UNIVERSITY OF NOVA GORICA
GRADUATE SCHOOL

STUDIES OF ASTROPHYSICAL VERY-HIGH ENERGY GAMMA-RAY EMISSION WITH THE PIERRE AUGER OBSERVATORY

DISSERTATION

Ahmed Mohamed Saleh Hassanin Khalil

Mentors: Assist. Prof. Dr. Sergey Vorobyev
Prof. Dr. Danilo Zavrtanik

Nova Gorica, 2017

UNIVERZA V NOVI GORICI
FAKULTETA ZA PODIPLOMSKI ŠTUDIJ

ŠTUDIJ ASTROFIZIKALNE EMISIJE GAMA ŽARKOV ZELO VISOKIH ENERGIJ Z OBSERVATORIJEM PIERRE AUGER

DISERTACIJA

Ahmed Mohamed Saleh Hassanin Khalil

Mentorja: doc. dr. Sergey Vorobyev
prof. dr. Danilo Zavrtanik

Nova Gorica, 2017

Abstract

In this study, the search for the very-high energy γ-ray emission using the data measured by the Auger low-energy scaler mode of surface detector (SD) array (Auger single particle technique (SPT) and/or Auger SD scalers) has been performed. The Auger scaler dataset from the years 2006-2015 has been analyzed to look for statistically significant excesses of the average scaler rate over the regular cosmic ray (CR) background. In addition to standard data quality selection, the corrections for the long-term evolution of the response of the water-Cherenkov detectors and the influence of atmospheric pressure were also considered. In the analysis, two different methods have been applied: the $\sigma - \delta$ method, which is sensitive to changes in scaler data on the timescale of seconds, and variability method, which is sensitive on timescale of minutes. The first method revealed in total 79 seconds of significant excesses above the CR background in the entire available dataset. These events do not coincide with any known gamma-ray bursts (GRBs) observed by other experiments. A majority of 77 seconds with excess in the average scaler rate were observed during the December 2015 Crab γ-ray flare. The second method unveiled 266 events with significant increase in the average scaler rate variability within 76 different dates in the period 2006-2015. Interestingly, about 2/3 of the detected excesses have occurred at sidereal times [3h, 9h] interval, when the Crab nebula was at least 20° above the horizon at the Pierre Auger Observatory, and the bulk of these excesses is in a good time correlation with the major Crab flares detected by the *Fermi*-LAT and AGILE γ-ray satellite. The assumption, that the average scaler rate excess variance originates from the detection of very-high energy γ-rays from the Crab nebula and pulsar is in agreement with the observed zenith angle distribution of the excess variance amplitude, peaking at $\theta \sim 57^{\circ}$ and manifesting a characteristic rapid decrease at larger zenith angles. The observed angular dependence reflects the typical effects of atmospheric absorption on the energy of secondary particles. The comparison of the Auger average scaler rate excess variability events to corresponding *Fermi*-LAT daily light curves of the Crab nebula shows a good correlation between both datasets, as 5 out of 7 strongest Crab γ-ray flares. The probability of observing those excess events by chance is significant at P-value <0.05 probability level. The capability and sensitivity of the Auger scaler mode to very-high energy γ-ray emission and the possible outbursts of the Crab nebula in the multi-TeV energy range was also assessed using the CORSIKA air shower and $\overline{\text{Off}}\underline{\text{line}}$ detector simulations. We can conclude that in the performed study the very-high energy γ-rays have been observed at the ground level, with energies exceeding 30 TeV. The capability to study γ-rays at these energies opens a new and interesting discipline to study variable astrophysical γ-ray emitters in sub-PeV energy range.

Keywords: Auger low-energy scaler mode, average scaler rate variability, GRBs, very-high energy γ-ray emission, the Crab nebula γ-ray flares, *Fermi*-LAT

Povzetek

V tem doktorskem delu smo opravili iskanje visokoenergijske emisije γ-žarkov z uporabo podatkov nizkoenergijskega "scaler" načina površinske detektorske mreže observatorija Pierre Auger. Analizirali smo nabor podatkov iz let 2006-2015 in iskali statistično pomembne presežke povprečne scaler stopnje nad rednim ozadjem kozmičnih žarkov (CR). Poleg standardne kvalitativne selekcije podatkov smo upoštevali popravke dolgoročnega razvoja odzivnosti Čerenkovih detektorjev in popravke povezane z vplivom atmosferskega tlaka. V analizi smo uporabili dve različni metodi: $\sigma - \delta$ metodo, ki je občutljiva na spremembe v podatkih na časovni skali sekund, ter variabilnostno metodo, ki je občutljiva na časovni skali minut. Prva metoda je razkrila 79 sekund pomembnih presežkov nad ozadjem CR v celotnem naboru podatkov. Ti podatki ne sovpadajo z znanimi izbruhi gama žarkov (GRBs), ki so jih opazili ostali eksperimenti. Večino dogodkov (77 sekund) s presežkom nad povprečno scaler stopnjo sovpada s povečano aktivnostjo Rakovice decembra 2015. Druga metoda je razkrila 266 dogodkov s pomembnim presežkom nad povprečno variabilnostjo scaler stopnje. Ti dogodki so se zgodili na 76 različnih dni v določenem časovnem okvirju (2006-2015). Presenetljivo, se je skoraj 2/3 presežkov zgodilo znotraj intervala siderskega časa [3h, 9h]. Ob tem času je Rakovica vsaj 20^{c}*irc* nad obzorjem observatorija Pierre Auger, velika večina teh presežkov pa je v dobri časovni korelaciji s povečanimi aktivnostmi Rakovice, ki sta jih zaznala satelit *Fermi*-LAT in satelit γ-žarkov AGILE. Predpostavka, da varianca presežka povprečne scaler stopnje izvira iz detekcije visokoenergijskih γ-žarkov iz Rakovice se sklada s porazdelitvijo variance presežka po zenitnih kotih. Vrh porazdelitve je pri $\theta \sim 57^{\circ}$, pri večjih zenitnih kotih pa ima porazdelitev značilen hitri padec. Kotna odvisnost kaže značilne učinke atmosferske absorpcije energije sekundarnih delcev. Primerjava dogodkov variabilnostne metode z ustrezno *Fermi*-LAT dnevno svetlobno krivuljo Rakovice kaže dobro medsebojno korelacijo (pet od sedmih najmočnejših povečanih aktivnosti Rakovice). Verjetnost naključne detekcije teh presežkov je pomembna pri verjetnostni stopnji P-vrednosti <0.05. Zmogljivost in občutljivost Auger scaler načina na visokoenergijsko emisijo γ-žarkov in morebitne izbruhe Rakovice v več-TeV energijskem območju smo ocenili preko simulacij s pomočjo programov CORSIKA in $\overline{\text{Off}}\underline{\text{line}}$. Po opravljeni raziskavi lahko zaključimo, da smo opazili visokoenergijske γ-žarke na površju z energijami nad 30 TeV. Sposobnost preučevanja γ-žarkov pri teh energijah odpira novo in zanimivo disciplino za raziskave variabilnih astrofizikalnih izvorov γ-žarkov v pod-PeV energijskem območju.

Ključne besede: Auger nizkoenergijski scaler način, variabilnost povprečne scaler stopnje, GRBs, visokoenergijska emisija γ-žarkov, γ-žarki iz povečane aktivnosti Rakovice, *Fermi*-LAT

Dedicated to my parents

Acknowledgements

I would like to express my sincere gratitude and appreciation to my supervisor Prof. Dr. Danilo Zavrtanik. I would like to thank him for his guidance, advices, and continuous support during my study. Also, I thank Assist. Prof. Dr. Sergey Vorobyev for his suggestions and everything. I would also like to thank my committee members for reading this thesis and their useful comments and suggestions.

The work with the Pierre Auger Collaboration has been a great experience for me and essentially enriched my knowledge. I would especially like to thank Roberto Mussa and Hernán Asorey, the Conveners of the CoGeo Task, for the very useful discussions and suggestions, which helped me a lot in my study. Indeed, I would like to express my deepest gratitude to Piera Luisa Ghia for her very helpful comments, valuable discussions, and nice explanation (grazie mille!). I would also like to thank many members from the Pierre Auger Collaboration, Xavier Bertou, Jimmy Masías Meza, Sergio Dasso, Julian Rautenberg, and others for their help via useful discussions. I would like also to acknowledge the use of the *Fermi*-LAT light curves of the Crab nebula and pulsar, which are publicly available on the official page of Monitored Source List Light Curves.

I would also like to express my appreciation to all the members of the Laboratory for Astroparticle Physics of the University of Nova Gorica, Andreja Gomboc, Samo Stanič, Andrej, Filipčič, Gabrijela Zaharijaš, Marko Zavrtanik, Lili Yang, Aurora Clerici, and others for their support. Also, I would like to acknowledge the previous members, Darko Veberič (hvala!), Maria Garzelli, Martin O'Loughlin, and Saeede Nafooshe.

My sincere thanks to my coworkers Gašper Kukec Mezek and Marta Trini for their wonderful support, encouragement, and help during this study. I wold like to thank so many people form the University of the Nova Gorica. Particular thanks to Tea Stibilj Nemec, Bojan Korecic, Marina Artico, Nadja Lovec, Maja Wagner, Erika Gojkovic, Sabina Zelinscek, Andreja Oblak and others for their help and support.

This thesis would not have been possible without the amazing support of my family. My sincere gratitude and appreciation to my family. Indeed, words cannot express how grateful I am to my parents for their unlimited support as well as all of the sacrifices that they have made for me.

I would also like to thank the Slovenian Research Agency for the financial support of my PhD research.

Contents

Introduction

The field of very-high energy (VHE; $\geq$30 GeV) γ-ray astrophysics has been connected to the research of cosmic rays (CRs) since their discovery by Victor Hess in 1912. It is widely believed that CRs, being mostly composed of protons and heavier nuclei, can be efficiently accelerated in astrophysical shocks originating in e.g. supernova explosions and propagating in the interstellar medium. During CR acceleration, neutral pions, which are produced in inelastic CR interactions with the ambient matter and radiation, subsequently decay into VHE γ-rays. Contrary to the charged CRs, photons are not deflected in cosmic magnetic fields, and thus provide information about the CR source directions in the sky, and the physical conditions at the CR production site.

At very-high energies, the fluxes of cosmic γ-rays decrease rapidly as a function of energy, which limits the number of photons that can be collected by the satellite-based detectors. However, indirect detection of the VHE γ-ray emission is possible from the ground, via measurements of particle cascades – "extensive air showers" (EAS) – induced by γ-rays in the interactions with the nuclei high in the atmosphere. Either the Cherenkov photons emitted in the air due to the passage of the charged relativistic shower particles, or the particles themselves (starting at higher TeV energies, energy threshold depending on the altitude of the experiment) are detected. Due to the large lateral spread of the shower particles and of the resulting Cherenkov light spot on the ground, large effective areas (above a few 10^5 m^2) can be reached. Whatever technique is used, it has to deal with a $\sim$3-4 orders of magnitude superior flux of showers induced by charged cosmic rays. The VHE γ-ray astronomy has emerged in 1989 as a result of the detection, at 9σ above the CR background, of the γ-ray signal from the **Crab nebula** at energies $>$100 GeV. This has been done using novel detector type at the Whipple Observatory, aimed to exploit the orientation and the shape of the images of rapid (a few ns) Cherenkov light flashes from air showers. The current generation of detectors employing this technique consists of arrays of the so-called imaging air Cherenkov telescopes (IACTs), which are much more sensitive than the pioneering instruments. More than 170 astrophysical sources (active galactic nuclei, supernova remnants, pulsars and other types of objects) have been detected at TeV energies, most of them during the last decade by the current IACT

arrays H.E.S.S., MAGIC and VERITAS. A new window for the exploration of the non-thermal Universe has thus been opened.

Another technique widely used in VHE γ-ray astronomy consists in measurement of shower particles using e.g. scintillators or water Cherenkov detectors distributed over large areas. This technique provides low energy threshold of few hundreds of GeV of γ-induced showers, due to deploying dense and huge surface detector arrays of very high altitudes with a very large duty-cycle ($\sim$100%). In contrast, the Cherenkov telescopes can be exploited only during clear nights near the new moon, so the corresponding duty cycle is no larger than $\sim$15%. In addition, EAS detector arrays simultaneously detect showers arriving from the large fraction of the sky, while IACTs have much smaller field of view (of a few degrees). The breakthrough in sensitivity of the EAS detection technique in the ground-based γ-ray astronomy has been made by the past Milagro and ARGO-YBJ γ-ray experiments. The currently running High Altitude Water Cherenkov (HAWC) experiment has higher sensitivity and lower energy threshold as compared to its predecessor Milagro. The new generation of VHE γ-ray experiments exploiting the EAS shower technique, such as LHAASO and HiSCORE, are being designed or constructed.

This study has been performed in the framework of the Pierre Auger Observatory, the world's largest hybrid cosmic ray experiment located in Argentina. By combining the sampling of shower particles reaching the ground, by water Cherenkov detectors (WCDs), with nightly measurements of the fluorescence light induced by the EAS in the atmosphere, Auger determines the arrival directions, energy, and provides constraints for the mass of the primary ultra-high energy (UHE; $\geq 10^{17}$ eV) cosmic rays. The Surface detector (SD) array of the Pierre Auger Observatory, which consists of $\sim$1600 WCDs spread over an area of $\sim$3.000 km^2, has the capability to study the variations in the flux of low energy CRs using the low energy modes. Flux rates of secondaries can be obtained either from particle count rates (scaler mode) or from charge distribution of the pulses (histogram mode), detected by individual WCDs. In scaler mode, SD is sensitive to particles that deposit energy between $\sim$15 MeV and $\sim$100 MeV in a WCD, while in histogram mode the deposited energy range can be extended up to 1 GeV.

The goal of the presented doctoral work is to explore the possibility to use the low energy Auger SD scaler mode for detection of the variable astrophysical phenomena in the VHE domain. The huge total collecting area of the Auger SD detector of more than 16.000 m^2 and the high total rate of $\sim 1.8 \times 10^8$ scaler counts per minute lead to a statistical accuracy well below 0.1%. This allows us to search for significant excesses of the average scaler rate variability of astrophysical origin at the second and minute timescales. Such variability could be detected during γ-ray flares of Galactic and nearby extragalactic objects.

Among the Galactic objects, possible source candidates include cosmic ray "PeVatrons", i.e. young supernova remnants that can accelerate cosmic-ray protons up to the energy of the knee and even higher. Accordingly, the spectra of γ-rays resulting from interactions of accelerated protons with the ambient gas could reach ∼100 TeV. At such high energies, air shower particles reaching the ground might produce measurable signal in the Auger scalers, provided that the flux of primary γ-rays is high enough.

The γ-ray sky at energies above a few tens of TeV is largely unexplored. And the Nature is rich with surprises. An example: the Crab nebula, which has been considered for a few decades as a "standard calibration candle" due to its high-flux and stable emission in the hard X-rays and also in the VHE γ-rays, has shown unexpected variability during several flaring episodes, observed in the years 2010-2015 at the energies $E > 100$ MeV by the AGILE and *Fermi*-LAT γ-ray detectors. Earlier, in the year 1989, when the VHE γ-ray signal from the Crab has been for the first time detected by the Whipple IACT, three EAS detector arrays – the EAS-TOP array in Gran Sasso, Italy, the Kolar Gold Fields (KGF) in India, and the Baksan Air Shower Array (BASA) in the USSR – have observed on the same date excesses of events from the direction of the Crab. The reported excess corresponded to sub-PeV energies, much higher than those observed in the recent Crab flares.

This shows utility of the proposed new application of the low energy scaler mode of the Pierre Auger Observatory for the studies of variable astrophysical γ-ray sources at multi-TeV energies, which can hopefully enrich our knowledge about the non-thermal Universe.

In Chapter 1, an overview of the fields of cosmic rays and of VHE γ-ray astrophysics is presented. Chapter 2 describes the techniques of detection of VHE γ-rays, and introduces the Pierre Auger Observatory including its low-energy modes. The performed analysis of the scaler data are presented in Chapter 3. The sensitivity of the Auger SD scaler rate to multi-TeV γ-ray flares from the direction of the Crab nebula is investigated in Chapter 4. The Crab nebula and its pulsar, as well as the recent Crab's high-energy γ-ray flares are described in Chapter 5. The correlations of the observed episodes of strong Auger scaler rate variability with the Crab flares are investigated in Chapter 6. Finally, conclusions and future prospects are presented.

Chapter 1

Cosmic Rays and the Accompanying Gamma-Ray Emission

Since their discovery by Victor Hess in 1912, cosmic rays have an intrinsic impact on several fields of physics, including elementary particle and nuclear physics, astrophysics and cosmology. A wealth of new particles have been discovered as a consequence of cosmic ray studies, e.g. positrons (in 1932), muons (in 1937), and pions (in 1947). Plausible cosmic ray sources are natural particle accelerators, capable to produce particles with energies higher than any of the man-made particle accelerators. However, after more than a century of intensive studies, fundamental issues of cosmic ray physics, particularly at the ultra-high energies, are still open. Some of these issues are: (a) where do cosmic rays of the highest energies come from?; (b) what kind of particles are they?; (c) which acceleration mechanisms are responsible for such extreme energies?; (d) what are the spatial distributions of their sources?; (e) how do cosmic rays interact with the cosmic background radiation?; (f) have we discovered all secondary particles produced in their interactions with Earth's atmosphere?. The answer to these questions will improve our understanding of cosmic rays and their interplay with the connected topics from physics and astrophysics. This Chapter elucidates the current state of cosmic ray physics, so that a brief summary of the cosmic ray history, energy spectrum, mass composition and arrival directions are presented, in addition to, the plausible cosmic ray acceleration mechanisms and the energy losses during the propagation in the Universe are described. Furthermore, an overview of the very-high energy γ-rays and their origin, propagation, production mechanisms, and sources are also demonstrated.

This chapter is intended to present the current state of cosmic ray physics and the connected field of very-high energy (VHE; $E \geq 30\,\mathrm{GeV}$) γ-ray astrophysics. We start with a brief summary of the cosmic ray history. Then, the cosmic ray measurement results are described, including energy spectrum, mass composition, and arrival directions. The acceleration mechanisms of the ultra-high

energy cosmic rays and the energy losses during their propagation in the Universe are explained. We conclude the chapter with an overview of the processes of VHE γ-ray emission, including their propagation in the interstellar and intergalactic medium and production mechanisms. Moreover, an overview of different types of cosmic VHE γ-ray sources and the relevant emission models is presented.

1.1 Historical overview

In 1912, Victor Hess used balloon flights to measure the intensity of the ionizing radiation as a function of altitude [1]. He discovered that the ionization increased as the balloon went beyond $\sim$2000 m, contrary to his expectations. He concluded that a highly penetrating radiation entered the terrestrial atmosphere from outer space. This radiation might reach the lower layer of the Earth's atmosphere and be a reason of the discharge of the electroscopes observed well before Hess. As no decrease in the radiation power was observed neither at night nor during a Solar eclipse, Hess concluded that the ionizing radiation was not of Solar origin. Thus, it had a cosmic origin. In 1936, Hess was awarded the Nobel prize for his discovery of the cosmic radiation. The term "cosmic rays" has been introduced by Robert Millikan by analogy to the γ-rays, which were the most penetrating radiation known at that time [2].

The early studies of cosmic rays had as well an essential impact on the evolution of the particle physics, being the main experimental method until the appearance of the particle accelerators in 1950s. In 1928-1929, Bothe and Kolhoerster have employed newly invented (1928) Geiger-Mueller counters in a coincidence scheme to show that cosmic rays at ground contained very-high energy charged particles able to penetrate thick material. In 1927-1929 Skobeltzyn for the first time observed the cascades of secondary charged cosmic ray particles using a cloud chamber placed in the magnetic field. During the same period, Clay discovered that the cosmic ray intensity depends on the observation latitude (the so-called "latitude" effect), which meant that cosmic rays are deflected by the geomagnetic field and therefore have to consist mostly of charged particles. In 1932 Carl Anderson discovered a positron as a start for a series of new particles detected in cosmic rays. In 1936-1938 Vernov, Johnson and others independently found out that the primary cosmic rays are positively charged particles, due to the asymmetry in arrival intensity of secondaries between east and west directions, the so-called "azimuthal" or "East-West" effect predicted by Rossi in 1930.

In 1938, Pierre Auger had performed his first experiment of two distant detectors at high altitude in Alps to detect the cosmic ray particles, and thereafter he repeated his experiment in Pyrenees with larger distances [3] between the two detectors. He had then noticed that they detected simultaneous signals at a rate exceeding the one expected from random time coincidences. He had

thus discovered the cosmic ray-induced "extensive air showers" (EAS), i.e. showers of secondary particles produced as a result of the collision of the primary high-energy particle with air nuclei. Such cascades were observed up to the 300 m distance between the detectors, which means that P. Auger detected secondaries from primary cosmic rays with energies up to 10^{15} eV, i.e. several orders of magnitude above the highest energies that we reach today using man-made accelerators, of about 10^{12} eV. On February 6, 1942, the first detection of Solar cosmic rays by ionization chamber revealed that the Solar cosmic rays are connected with a flare and radio disturbances. In 1946, Zatsepin and his collaborators pioneered the studies of hadronic interactions in the EAS using arrays of particle detectors in the Pamir mountains. Phyllis Frier in 1948 had discovered that the primary cosmic rays contain heavy nuclei [4] of various elements, such as helium and iron.

In 1949, Enrico Fermi had suggested that cosmic rays are accelerated by scattering off moving magnetic clouds of magnetic irregularities which are permeated through interstellar medium. To reach higher energy per interaction, numerous arrays of shower particles started to be built and exploited in the 1950s all over the world. In parallel, studies of primary cosmic rays using detectors on balloons, rockets, and later on satellites started to be performed. In 1972, SAS-2 satellite mapped the Galactic multi-MeV gamma-ray emission, which allowed to conclude that the bulk of this emission has to result from the high-energy cosmic ray interactions with the interstellar medium. The studies of cosmic rays have been extended to the interplanetary space, e.g. by the detectors on the Voyager 1 and 2 missions lunched in 1977. In a series of balloon experiments in 1977-1982, anti-protons in cosmic rays have been discovered by Bogomolov and his colleagues. In 1990, the first spacecraft, Ulysses probe, was lunched into a high heliospheric latitude orbit to study by more details the properties of cosmic rays and the 3D picture of Solar wind.

Conceived in 1990s, the Pierre Auger Observatory has been built in Argentina and completed in 2008 as a pivotal experiment to bring the decisive steps in the studies of the ultra high energy cosmic rays (UHECRs). The understanding of the origin of the ultra-high energy cosmic rays has an essential impact on fundamental topics in particle physics, cosmology, and astrophysics of the most violent non-thermal phenomena in the universe. As an example, the astrophysical aspects of cosmic rays have unleashed several theoretical approaches, such as the theory of novas and supernovas, magnetohydrodynamics (MHD) and other plasma theories in astrophysics. In this relation, we mention the following milestones:

- 1934: Walter Baade and Fritz Zwicky had proposed that supernova explosions are the sources of cosmic rays [5].
- 1949: Enrico Fermi had suggested that cosmic rays are accelerated by bouncing off magnetic clouds of magnetic field irregularities, a mechanism known now as the second-order Fermi acceleration [6].

- 1977: Ian Axford, Egil Leer, and George Skadron had proposed that cosmic rays are accelerated by first-order Fermi acceleration in supernova shocks in a hot interstellar medium [7].

Cosmic rays have been studied in experiments underground, on the ground, in the atmosphere, and in the outer space. Despite all intensive studies and experiments of the UHECRs, their origin is still unknown [8–13].

1.2 Cosmic rays

Cosmic rays are very energetic, mostly charged particles that continually reach the Earth's atmosphere from outer space. Cosmic rays are dominantly protons, but they also contain light and heavy nuclei, such as helium and iron nuclei, respectively. The cosmic rays arriving at the top of the atmosphere are called *primary* cosmic rays. After a primary cosmic ray interaction with an atmospheric nucleus, a particle cascade, a *shower*, develops in the air. The products of this first CR interaction are called *secondary* cosmic rays. Cosmic rays of low and medium energies are classified into three categories due to their origin [9]:

1. **Galactic Cosmic Rays (GCR)**
   Galactic Cosmic Rays originate far outside our Solar System, most likely in supernova remnants in our Milky Way and in the nearby galaxies. The GCRs are protons and to a lesser extent heavier nuclei, with energies ranging from $\sim$0.1 GeV (a boundary set by the Solar modulation) up to at least the "knee" energies of the cosmic ray energy spectrum (see § 1.2.1).

2. **Solar Cosmic Rays (SCR)**
   Solar cosmic rays cover wide energy range approximately from 1 MeV to 10 GeV [14], mostly originate in Solar flares.

3. **Anomalous Cosmic Rays (ACR)**
   Low energy cosmic rays likely originate in the interstellar space beyond the heliopause. The composition of ACR differs from GCR and SCR [15], e.g., more abundant in helium and oxygen than protons and carbon, and their energies per charge extends up to 100 MeV [16].

4. **Ultra High energy Cosmic Rays (UHECRs)**
   Those cosmic particles of ultra high energies up to 10^{18} eV and extragalactic origin. The UHECR flux above 10^{20} eV is estimated to be from 0.5 to 1 event per square kilometer per century per stradian [10, 13]. Various experiments, such as the Pierre Auger Observatory, Akeno Giant Air Shower Array (AGASA), and High Resolution Fly's Eye (HiRes),

have measured the UHECR spectrum [8, 11]. The Pierre Auger Observatory has measured the UHECR spectrum with high statistical accuracy from energy range $\sim 10^{18}$ eV to above $\sim 10^{20}$ eV [17].

The flux of primary cosmic rays decreases rapidly with increasing cosmic ray energy. The measured cosmic ray energy spectrum extends up to ultra-high energies of a few 100 EeV $\equiv 10^{20}$ eV [8, 11], where their flux is estimated to be about 0.5 to 1 event per square kilometer per century per steradian [10, 13]. The *ultra-high energy cosmic rays* (UHECRs) have an extragalactic origin.

1.2.1 Energy spectrum

The energy spectrum of the primary cosmic rays, expressed as a number of CR (particle flux) detected per unit area, energy, solid angle, and time, is shown in Fig. 1.1, which summarizes the measurements by the past and current CR experiments. In very large energy intervals, the spectrum follows a power law shape $\frac{dN}{dE} \propto E^{-\gamma}$ with spectral index $\gamma \sim 2.7$. Such shape indicates that cosmic rays are produced by non-thermal processes [8, 11]. A few distinct spectral features can be seen.

At a prominent spectral break around a few 10^{15} eV, conventionally referred to as the knee, the spectrum steepens from $\gamma \sim 2.7$ to $\gamma \sim 3.1$. Up to the knee energies, cosmic rays most likely have galactic origin. From energy 4×10^{17} eV to 7×10^{17} eV, above the knee, there is a dim feature in the CR spectrum called the *second knee* where the spectrum slightly steepens. A more prominent spectral break, commonly referred to as the ankle, occurs around 5×10^{18} eV, at which the spectrum hardens again with $\gamma \sim 2.7$.

The cosmic ray particles beyond the ankle have an extragalactic origin, since their Larmor radius in Galactic magnetic fields exceeds the size of the Milky Way, and no anisotropy in the CR arrival directions with respect to the Galaxy is observed (see § 1.2.6 about the CR arrival directions distribution).

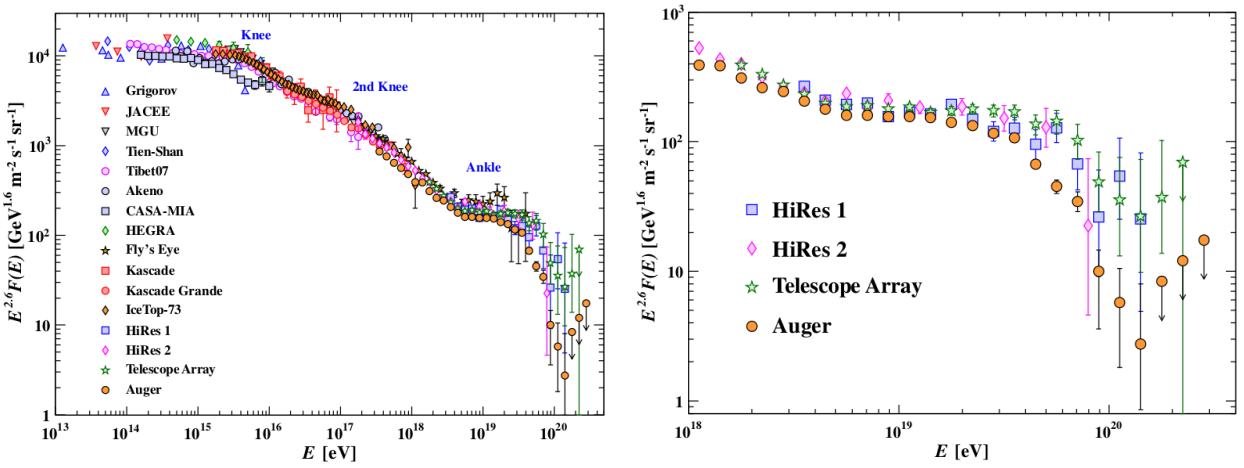

FIGURE 1.1: Left panel shows cosmic rays all-particle energy spectrum, measured by different experiments [18], and multiplied by $E^{2.6}$ to highlight the spectral features: the *knee* at a few 10^{15} eV, the weaker *second knee* at $\sim 10^{17}$ eV, the *ankle* at $\sim 5\times 10^{18}$ eV, and a CR flux suppression above $\sim 4\times 10^{19}$ eV. Right panel presents a zoom of the cosmic ray energy spectrum as measured at EeV energies [19–21], featuring the ankle and the flux suppression.

Finally, above $\sim 4\times 10^{19}$ eV the strong suppression of the CR flux is observed. We will describe now the reasons of this suppression.

1.2.2 UHECR energy losses and GZK cut-off

Soon after the discovery [22] of the cosmic microwave background (CMB) radiation by Penzias and Wilson in 1965, Greisen [23], and independently Zatsepin and Kuzmin [24] predicted a strong suppression of the primary CR flux above $\approx 5\times 10^{19}$ eV. Such spectral feature (baptised after the authors of the prediction as the GZK-cutoff or GZK-suppression) would manifest in the case of sources accelerating CR protons, and uniformly distributed throughout the Universe, as a result of a well-known pion photo-production processes:

$$\begin{aligned} \mathrm{p} + \gamma_{\mathrm{CMB}} &\rightarrow \mathrm{n} + \pi^{+}, \\ &\rightarrow \mathrm{p} + \pi^{0}. \end{aligned} \tag{1.1}$$

The properties of this process (see e.g. [25]) are measured with precision in the accelerator experiments in the interactions of photon beams with target protons. In each pion-production process, proton loses in average 20% of its energy. Charged and neutral pions in (1.1) decay, producing so-called GZK or cosmogenic neutrinos and photons. As a consequence of such drastic energy

losses, protons would rapidly lose energy until it falls below the reaction threshold, which corresponds to ∼50 EeV for a ultra-relativistic proton in collision with a CMB photon. The sources of the UHECR protons have therefore to be located nearby, within a ∼100 Mpc distance from Earth (the corresponding volume is commonly designated as GZK sphere). In 1970s, it has been shown [26] that the flux of heavier UHECR nuclei would be suppressed at similar or slightly smaller energies (depending of CR species), due to photo-dissociation on CMB photons. Both protons and nuclei also produce electron-positron pairs in the interactions with CMB photons. The reaction $p + \gamma_{CMB} \rightarrow p + e^+ + e^-$ has a smaller threshold energy $E_{th} \sim 5 \times 10^{17}$ eV than the photo-pion production. The process is dominant for sub-GZK protons, with maximal losses around 20 EeV, however, the corresponding loss distance (see Fig. 1.2) exceeds 1 Gpc at all energies.

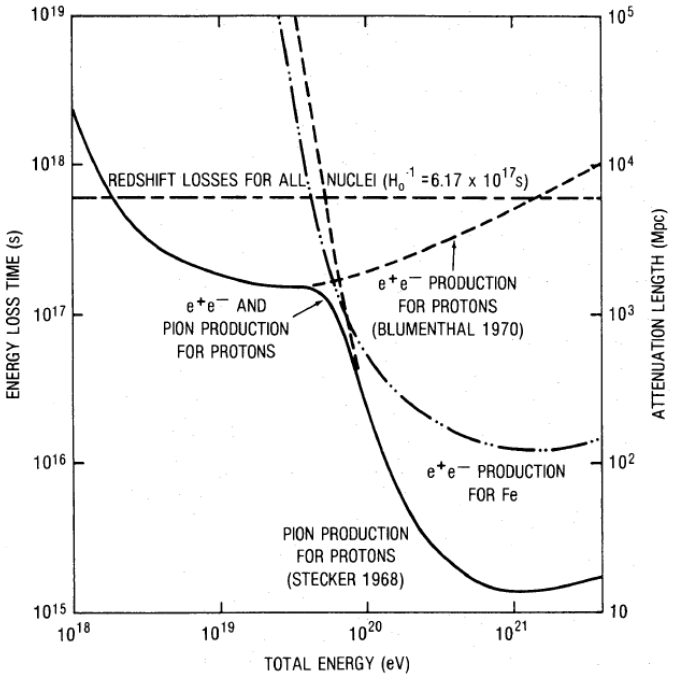

FIGURE 1.2: Time of energy loss and attenuation length for protons from pair production, redshift, and photo-pion production losses. The attenuation length resulting from pair production losses is also shown for Fe nuclei. Taken from Ref. [26].

The High resolution Fly's Eye (HiRes) has been the first experiment to establish the flux suppression at ∼60 EeV [19, 27, 28]. This result has been soon confirmed [29, 30] by Auger spectral measurements with higher statistical significance and superior data quality. The flux suppression has been recently confirmed by Telescope Array (TA) [20, 31]. However, recent combined measurement of the UHECR spectrum and composition by Pierre Auger experiment [32] suggests more complex interpretation of the observed CR flux suppression, in which both the energy loss processes and the maximal energy attainable in the UHECR sources seem to play a role.

1.2.3 Extensive air showers and their models

When a high-energy cosmic particle (e.g. primary γ-photon or nucleus) reaches the upper part of the Earth's atmosphere, it interacts with the air nuclei producing an extensive air-shower (EAS) of secondary particles, shown in Fig. 1.3.

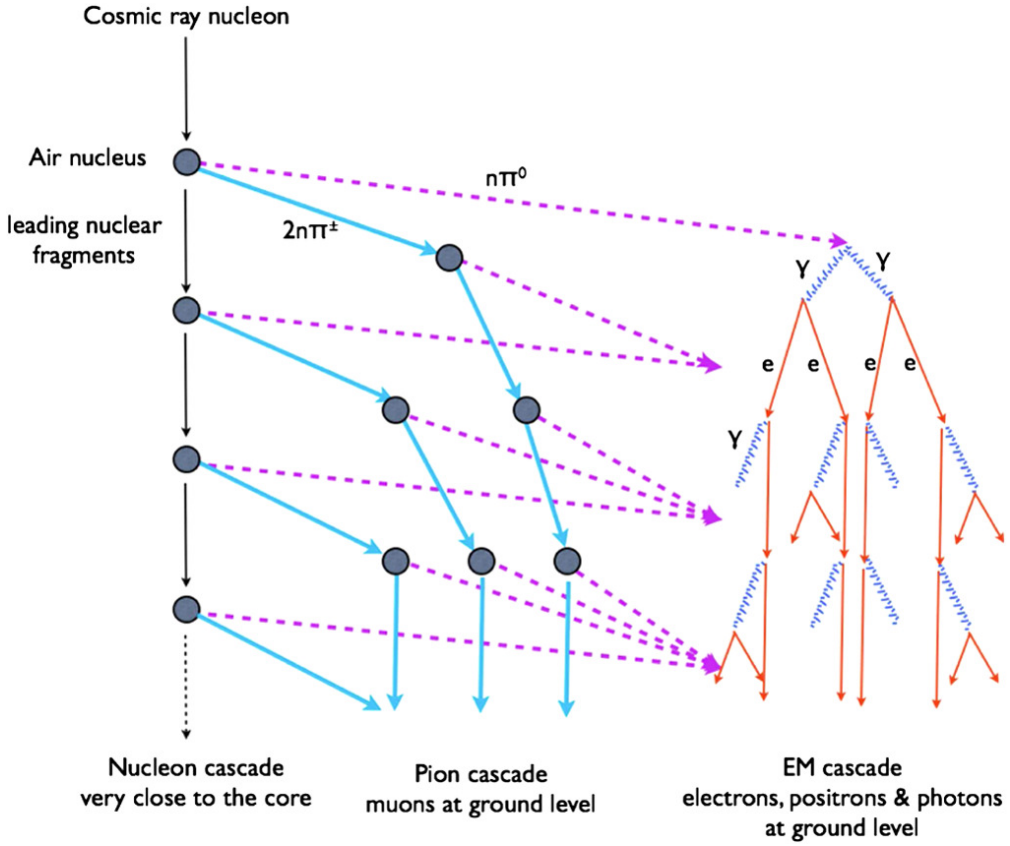

FIGURE 1.3: A scheme of an extensive air-shower (EAS) induced by a primary cosmic ray nucleon in the atmosphere, which shows the link between the EAS components. Taken from Ref. [33].

These secondaries go through further interactions with other nuclei in the atmosphere, so that a cascade of secondaries is generated along the trajectory of the primary particle, with lateral extent (lateral shower development) around it. The lateral shower development is due to: a) the traverse momenta of the newborn pions and kaons; b) the multiple Coulomb scattering the shower electrons. Three main EAS components can be distinguished: electromagnetic (γ, e^-, e^+), muonic (μ^+, μ^-), and hadronic (mainly $\pi^\pm$, π^0, n, p, $K^\pm$, K^0). The electromagnetic cascade is the dominant EAS component carrying the largest fraction of the total energy deposited in the atmosphere ($\sim$85%). The remaining $\sim$15% of the shower energy is shared between hadrons $\sim$4%, muons $\sim$10%, and neutrinos $\sim$1% representing altogether $\sim$1% of secondaries.

The electromagnetic (EM) shower component is mainly generated via $e^- e^+$ pair production by γ-rays, as well as via Bremsstrahlung (braking) radiation by electrons and positrons in interactions with atomic nuclei. As shown in Fig. 1.3, the EM component is fed by hadrons via decay of neutral and charged pions. In the following two sections, we summarize an extension by Matthews [34] of the Heitler model [35] of electromagnetic cascades in air-showers, which takes into account development of hadronic shower component.

Heitler model of the electromagnetic cascade According to the original Heitler model, illustrated in Fig. 1.4 (a), a photon interacts with the air nuclei at the top of Earth's atmosphere producing $e^- e^+$ pair of equal energy.

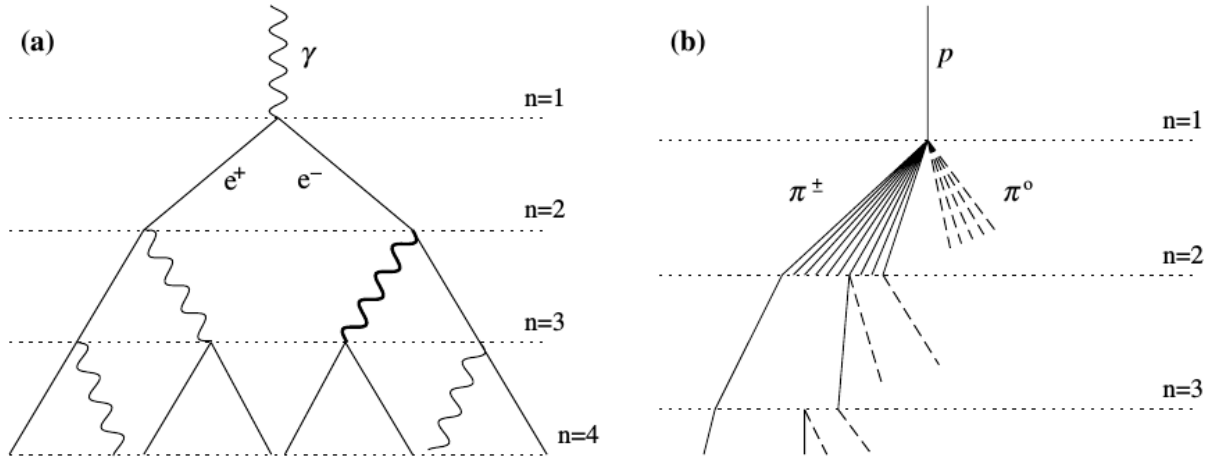

FIGURE 1.4: Schematic view of the Heitler model for electromagnetic (a) and hadronic (b) showers. Taken from Ref. [34].

Thereafter, an electron/positron travels single splitting depth of a distance $d = \lambda_r \ln 2$, and hence radiates single photon, where λ_r is the radiation length in the medium ($\lambda_r = 37$ g/cm^2 in the air) and d is the distance required for the electromagnetic particle to lose half of its energy via radiation. In each splitting depth, photons produce $e^- e^+$ pair of equal energy, while electrons and positrons lose half of their energies via Bremsstrahlung emission for a single resultant photon.

Let us assume that the shower has been initiated by a single photon with an energy E_0. Under the considered model, the electromagnetic cascade reaches its maximum size at a depth X_{max}, where $N = N_{max}$, and all particles have an energy ξ_c^e. Thus, the primary energy is related to N_{max} via

$$E_0 = \xi_c^e N_{max}. \tag{1.2}$$

The depth of shower maximum $X_{\max}$ is determined by specifying the number of splitting depths n required to reduce the particle energy to ξ_c^e. Since $N_{\max} = 2^n$, using Eq. 1.2 we obtain

$$n = \ln(E_0/\xi_c^e)/\ln 2. \tag{1.3}$$

Thus, $X_{\max}^{\gamma}$ of a pure electromagnetic cascade is given by

$$X_{\max}^{\gamma} = n\lambda_r \ln 2 = \lambda_r \ln(E_0/\xi_c^e). \tag{1.4}$$

After n splitting depths, the number of particles in cascade is $N_n = 2^n = e^{x/\lambda_r}$, each particle having energy E_0/N_n. When energies E of particles become too low to perform pair production or bremsstrahlung, the collisional energy losses start to dominate the radiative ones. This occurs when $E < \xi_c^e$, where ξ_c^e is the so-called critical energy [34] (ξ_c^e =85 MeV in air). The rate of increase of $X_{\max}$ as a function of primary energy E_0 shows the energy dependence of the position of the shower maximum, and for that reason it has been called elongation rate Λ^{γ}

$$\Lambda^{\gamma} \equiv \frac{dX_{\max}}{d\log E_0}. \tag{1.5}$$

Λ^{γ} can be used to investigate the energy evolution of the high energy cosmic ray composition and/or hadronic interactions. The elongation rate for the electromagnetic showers in the Heitler model is obtained by substituting $X_{\max}$ from Eq. 1.4 into Eq. 1.5, so $\Lambda^{\gamma} = \lambda_r \ln 10 = 2.3\lambda_r = 85$ g/cm^2. Heitler model allows to evaluate important parameters of electromagnetic cascades, such as $X_{\max}^{\gamma}$ and Λ^{γ}. These predictions are in a good agreement with detailed shower simulations, though the maximum number of particles $N_{\max}$ given by the Heitler model is overestimated by a factor of 2. The reason of this mismatch is that the energy losses of the shower particles are taken into account by the model only approximately. Additionally, the model overvalues the ratio of electrons/positrons to photons by a factor of 10, due to several reasons. In reality, more than a single photon can be emitted in the bremsstrahlung process [34]. Also, e^- e^+ pairs lose energy in the air more rapidly than assumed by the Heitler model.

However, the Heitler model correctly draws two important conclusions concerning the electromagnetic shower development: a) the maximum size of the shower $N_{\max}$ is proportional to the initial energy E_0 of the primary particle; b) the depth of shower maximum $X_{\max}$ achieved by the secondaries in the atmosphere increases logarithmically with E_0. These two characteristics have been investigated and confirmed by the simulations and real data acquisition.

Extension of the Heitler model to hadronic cascade Heitler model has been extended by Matthews [34] to describe the hadronic component of an extensive air-shower. In this extension, it is assumed that the hadronic showers are initiated by cosmic ray protons (primaries), and that the produced secondaries after each interaction are mainly pions, as shown in Fig. 1.4 (b). The characteristic length for hadronic cascade $\lambda_{\rm I}$, a hadronic interaction length, is approximated by Matthews as a constant. Its value for pions in air is $\sim$120 g/cm^2 within energy range 10 GeV-1 TeV. The Earth's atmosphere is conceived as layers of thickness $\lambda_{\rm I}\ln 2$. In each layer N_{ch} charged pions and $\frac{1}{2}N_{ch}$ neutral ones are produced. The neutral pions π^0 decay into electromagnetic cascade. The charged pions $\pi^{\pm}$ go through further interactions in consecutive atmospheric layers, hence hadronic cascade is generated. The interaction processes of $\pi^{\pm}$ proceed till a limit below the critical energy ξ_c^{π}, at which the decay length of $\pi^{\pm}$ ($\pi^{\pm}\rightarrow\mu^{\pm}+\nu_{\mu}$) becomes smaller than the distance to travel to the subsequent $\pi^{\pm}$ interaction, so no more $\pi^{\pm}$ are produced, and the hadronic cascade ends. The number of pions after n atmospheric splitting depths is $N_{\pi}=(N_{\rm ch})^n$, where $N_{\rm ch}$ is the pion multiplicity in each interaction. By assuming that the energy is equally divided between pion species, we obtain that after n layers pions carry the fraction $(2/3)^n$ of the primary energy E_0, while the remaining energy is converted into the electromagnetic cascade as a consequence of π^0 decays. Therefore, the energy of charged pions after n interactions is

$$E_{\pi}=\frac{E_0}{\left(\frac{3}{2}N_{\rm ch}\right)^n}. \tag{1.6}$$

We notice that after a certain number of interactions n, E_{π} is getting smaller than ξ_c^{π}. In a case of a shower initiated by a primary proton of 10^{15} eV, a pion energy reaches 20 GeV after 4 interactions. The critical energy ξ_c^{π} associated to such shower equals to 20 GeV, and it slowly decreases with increasing primary energy. For instance, $\xi_c^{\pi}=30$ GeV at $E_0=100$ TeV and $\xi_c^{\pi}=10$ GeV at $E_0=100$ PeV.

By assuming that at the critical energy ξ_c^{π} all pions decay into muons, and hence $N_{\mu}=N_{\pi}=(N_{\rm ch})^{n_c}$, we obtain $n_c=\ln(E_0/\xi_c^{\pi})/\ln(\frac{3}{2}N_{\rm ch})$ for the number of layer n corresponding to "critical" energy below which pion decays start to dominate over pion interactions. Thus, $n_c\ln N_{\rm ch}=\beta\ln(E_0/\xi_c^{\pi})$, where $\beta=\ln(N_{\rm ch})/\ln(\frac{3}{2}N_{\rm ch})$. Therefore, the number of muons in the shower is

$$N_{\mu}=\left(\frac{E_0}{\xi_c^{\pi}}\right)^{\beta}. \tag{1.7}$$

The primary particle energy is distributed between electromagnetic and hadronic components, $E_0=E_{\rm em}+E_{\rm h}$. Muons carry the energy of the hadronic part, which can be expressed as $E_{\rm h}=N_{\mu}\xi_c^{\pi}$. Hence, the fraction of the electromagnetic component reads

$$\frac{E_{\rm em}}{E_0} = 1 - \left(\frac{E_0}{\xi_c^{\pi}}\right)^{\beta-1}. \tag{1.8}$$

The depth of the shower maximum for proton-induced showers can be obtained using results for electromagnetic showers, Eq. 1.4. Taking into account that the first proton interaction occurs at an atmospheric depth $X_0 = \lambda_{\rm I} \ln 2$, and that subsequently each generated photon initiates an EM shower of energy $E/(3N_{\rm ch})$, $X^{\rm p}_{\rm max} = X_0 + \lambda_{\rm r} \ln\left[E_0/\left(3N_{ch}\xi_e^c\right)\right]$. Thus, the elongation rate in the case of hadronic showers is

$$\Lambda^{\rm p} = \Lambda^{\gamma} + \frac{d}{d\log E_0}(X_0 - \lambda_{\rm r}\ln(3N_{\rm ch})), \tag{1.9}$$

where Λ^{γ} is the elongation rate for the electromagnetic shower and $X_0 = \lambda_{\rm I}\ln 2$ is the first interaction depth for protons. As one can see, the elongation rate of proton showers is lower than the one of the photon-induced showers. Concerning showers induced by the nuclear primaries, the corresponding elongation rate can be evaluated using the superposition model.

The superposition model presents a plain view of nucleus-nucleus interaction between the atmospheric nuclei and a cosmic ray nucleus, in which the latter is represented by A nucleons, each having energy E_0/A and interacting separately. The resulting air shower is then a sum of showers from these nucleons induced at the same point, and its properties (the number of muons and the shower maximum) are related to the ones of a proton shower with the total primary energy E_0 in the following way:

$$N_{\mu}^{A} = N_{\mu}^{\rm p} A^{0.15} \tag{1.10}$$

$$X_{\rm max}^{A} = X_{\rm max}^{\rm p} - \lambda_r \ln A \tag{1.11}$$

At the same primary energy, the nuclear-initiated showers contain more muons than proton-initiated ones, as shown by Eq. 1.10. As an example, the number of muons generated in iron-induced showers is 1.8 times higher than in the proton-induced showers of same primary energy. The $X_{\rm max}$ of iron-induced showers is 150 g/cm^{-2} lower than the one of the proton showers at all energies (see Eq. 1.11), which leads to a constant shift between the elongation rates of protons and iron nuclei. Figure 1.5 summarizes the model predictions as well as the results from the detailed shower simulations.

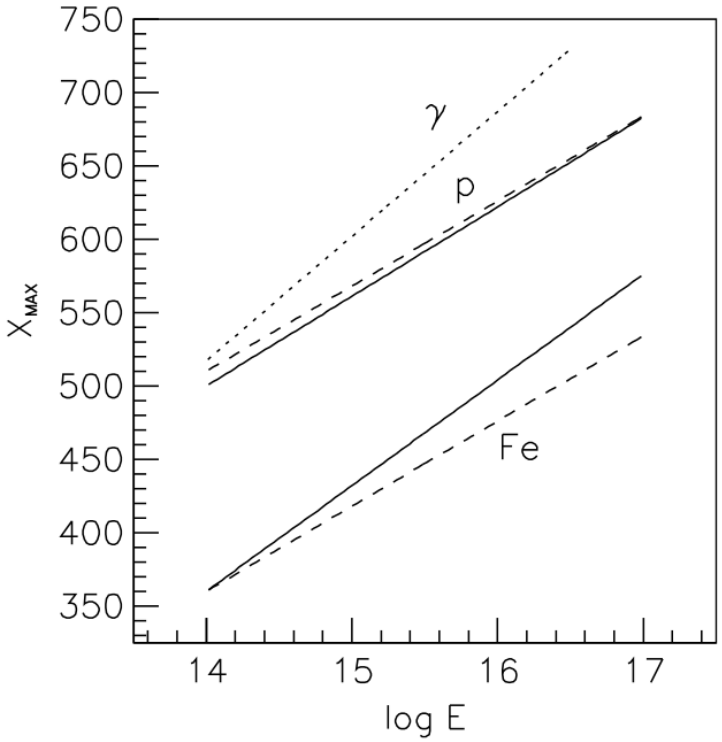

FIGURE 1.5: Depth of shower maximum $X_{\max}$ as a function of primary particle energy for photon, proton, and iron induced showers. Photon induced shower is shown by dotted line. Proton and iron induced shower are indicated by dashed line. The solid lines represent detailed simulations for p and Fe showers. Taken from Ref. [34].

The model, albeit simple, correctly predicts the elongation rate for protons ($\Lambda^{\mathrm{p}} = 58\,\mathrm{g/cm^2}$) and photons, though it underestimates the $X_{\max}$ values for nuclear primaries by about $100\,\mathrm{g/cm^2}$ at 100 PeV (the corresponding model predictions have been shifted upward by that amount on Fig. 1.5), due to neglecting of contributions of the π^0 production in the few first shower particle generations, as well of the effects of the leading particle production.

1.2.4 Composition of cosmic rays

The composition of cosmic rays with energies below $\sim 10^{15}$ eV is well determined via direct measurements taken from the space-based observations. The comparison between relative abundances of light and medium species for galactic cosmic rays and the corresponding abundances of elements in the Solar system shows significant differences between the abundances in two elemental sectors (see Fig. 1.6).

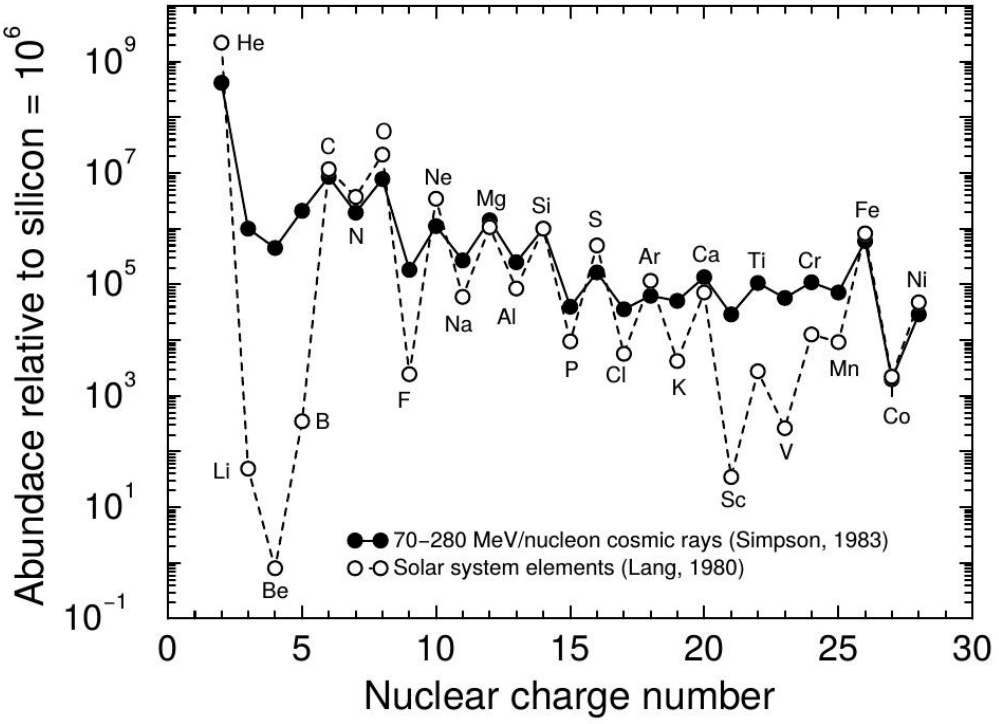

FIGURE 1.6: A comparison between relative abundances of light and medium nuclei in galactic cosmic rays (full circles) and the corresponding abundances of elements in the Solar system (open circles) normalized to Si $= 10^6$. Abundances of hydrogen (not shown in the figure) and helium in Solar system are higher than in the interstellar medium (ISM). Taken from Ref. [36].

Both abundances of Solar and Galactic species show the same trend, particularly, with tightly bound nuclei of even atomic number. However, two groups of elements - the group of (Li, Be, B) and the one of (Sc, Ti, V, Cr, Mn) present significantly higher abundances in cosmic rays than in the Solar system. All these features can be explained by a scenario in which primary cosmic rays are produced in the stellar nucleosynthesis, while the observed CR abundances result from spallation reactions during CR propagation in the interstellar medium [36]. There are two common approaches to estimate the chemical composition of the cosmic rays at PeV and higher energies, when the direct measurements are no longer possible. Either secondaries on the ground are sampled, or the emissions by the shower particles in the air (Cherenkov, fluorescence) are used. In all of these techniques, the primary composition is constrained using extensive MC simulations for different primary CR nuclei and applying comparison between the data and simulated events, performed on the statistical basis.

At the Pierre Auger Observatory, the shower development can be obtained via both the surface detector array (SD) and the fluorescence detector (FD). The large fluctuations in the shower development and the uncertainties in the hadronic interaction models make the primary particle identification not possible on event-by-event basis. The energy is reconstructed via measurements of

the longitudinal shower profile of the energy deposited in the atmosphere. More details about the measurements are available in chapter 2. The reconstructed depths of the shower maximum X_{max} and the corresponding elongation rate are used to discriminate between the primary CR species.

Figure 1.7 shows the average of measured values of the shower maximum $\langle X_{\mathrm{max}} \rangle$ for proton and iron nuclei, as well as $\langle X^{\mu}_{\mathrm{max}} \rangle$ for muons, along with the corresponding fluctuation RMS(X_{max}) and asymmetry of signal risetime Θ_{max} as a function of energy. All observables, both SD and FD related, suggest that the primary CR composition becomes heavier above the ankle energy of the UHECR spectrum. Concerning X_{max}, its systematic uncertainty $\leq$13 g/cm^2 (obtained combining the uncertainties in the atmospheric conditions, calibration, event selection, and event reconstruction) corresponds to $\lesssim$13% of the proton-iron separation predicted by the interaction models.

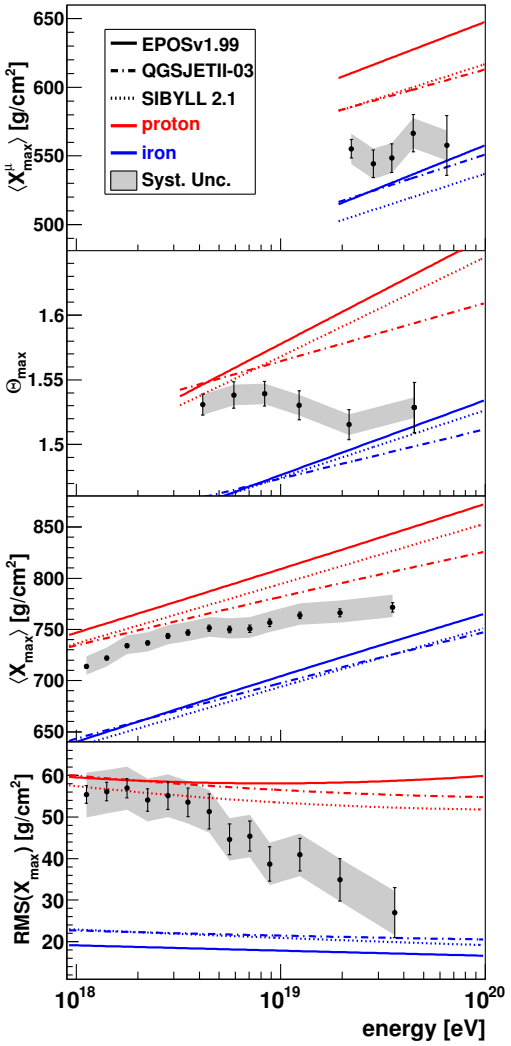

FIGURE 1.7: The composition-sensitive observables (RMS(X_{max}), $\langle X_{\mathrm{max}} \rangle$, Θ_{max}, $\langle X^{\mu}_{\mathrm{max}} \rangle$) as measured by the Pierre Auger Observatory and compared to the model predictions for proton and iron primaries, from three different interaction models (QGSJetII-03, SIBYLL 2.1, EPOS 1.99). The statistical and systematic uncertainties are indicated by error bars and shaded bands, respectively [37].

1.2.5 Origin of the highest energy cosmic rays

To interpret the UHECR measurement results, numerous production scenarios have been elaborated. The proposed models fall into two large categories [12, 13]. The "standard" UHECR production models assume the particle acceleration in non-thermal astrophysical environments and are thus called "bottom-up" scenarios. The other category of models supposes that at least a fraction of the highest energy cosmic rays may form as a result of decays of exotic objects such as super-heavy dark matter particles, topological defects etc. into standard model particles, i.e. in processes accompanied by energy decrease per particle, and for that reason such models are dubbed "top-down" scenarios.

Top-down scenarios In top-down scenarios, super-massive X-particles, originated from the high-energy processes in the early Universe and gravitationally bound in the galaxies and clusters of galaxies, undergo a chain of fragmentation processes, producing quarks and leptons. The quarks hadronize and form baryons and mesons. Decays of mesons, such as pions, produce leptons and photons. Thus, the observed extreme energy cosmic rays in top-down scenarios have to contain a considerable fraction (a few 10%) of photons. Two popular candidates for X particles are [13]:

- Topological defects such as cosmic strings, magnetic monopoles, domain walls, and extra dimensions.
- Cosmological relics of the early Universe, such as super-heavy dark matter particles.

The predicted energy spectra of the decay products (neutrinos, gamma-rays, as well as a small fraction of protons) of X particles in these scenarios follow the power law shape with spectral index of $\gamma = 1.5$, which is flatter compared to the bottom-up scenarios (see below), as well as to the measured slope of the UHECR spectrum.

Bottom-up scenarios The plausible UHECRs acceleration mechanisms involve interactions of individual cosmic ray particles with astrophysical shocks propagating in plasmas permeated by magnetic fields and induced currents [38]. The clouds of ionized gas in starburst or colliding galaxies hosting magnetohydrodynamic waves, giant lobes in radiogalaxies, supernova shock waves are the well-motivated candidates for acceleration sites. The dominating mechanism is thought to be associated with stochastic particle acceleration in magnetic clouds (second order Fermi acceleration) and strong shock waves (first order Fermi acceleration, which is known as *diffusive shock*

acceleration [6, 12, 39]). Another mechanism, the direct acceleration of charged particles by coherent electromagnetic fields, can take place near rotating compact objects, e.g. in the pulsar magnetospheres [12, 39].

Fermi acceleration mechanism In 1949, Enrico Fermi had suggested the original acceleration theory [6], in which the energy is transferred from a macroscopic plasma motion to a single charged particle via elastic interactions between the particle and the magnetic irregularities in plasma (magnetic clouds). After a sequence of collisions, the particle gains a fraction of energy of $\left\langle \frac{\Delta E}{E} \right\rangle \approx \frac{4}{3}\beta^2$, where $\beta = v/c$ and v is the velocity of magnetic irregularities with respect to the charged particle. This process is called the second order Fermi acceleration mechanism, as it is of a second order in β^2. The advantage of such mechanism is that it results in the power-law energy spectrum [6, 39]. The acceleration process is slow even for the supernova remnant (SNR) expanding shells, where $v \sim 10^4$ km/s, the average energy gain per particle collision is still small. Additionally, it is difficult to evade energy losses at the highest energies. Thus, the second-order Fermi acceleration mechanism is not efficient enough to explain the energy spectrum of the UHECRs.

The much faster and efficient, the first-order Fermi acceleration mechanism is known as "diffusive shock acceleration (DSA)". It implies an extension of the Fermi's original theory, in which the macroscopic motion is represented by astrophysical shocks. Shock waves are frequent in the Universe, e.g. in the SNR, which are believed to be the accelerator sites of the galactic cosmic rays.

All particles are repeatedly bounced back and forth within the shock wave frame and thus systematically gain energy [40]. Accordingly, particles gain a fraction of energy of $\left\langle \frac{\Delta E}{E} \right\rangle \approx \frac{4}{3}\beta$, where $\beta = v/c$ and v is the velocity of the shock wave, which is much larger than the typical velocity of the magnetic clouds. The mechanism leads as well to the power-law shape of the resulting energy spectrum [41]. Indeed, after k collisions between the particle and the shock, the initial energy E_0 will be accelerated to high energy $E = E_0(1+\xi)$. There are N cosmic charged particles that reach energy E as

$$N = N_0 P^k \tag{1.12}$$

$$E = E_0(1+\xi)^k, \tag{1.13}$$

where N_0 is the number of particles of initial energy E_0 and P is the probability that the particles escape the accelerator region. The above expression can be rewritten as

$$\frac{N}{N_0} = \left(\frac{E}{E_0}\right)^{\frac{\ln P}{\ln \beta}}. \tag{1.14}$$

The resulting differential flux of particles with energies between E and $E + dE$

$$N(E)dE = \text{constant} \times E^{-1+(\frac{\ln P}{\ln \beta})} dE, \tag{1.15}$$

which is thus following the power law with the spectral index $\gamma = -1 + (\frac{\ln P}{\ln \beta})$. From geometric considerations of the particle kinematics in collisions [41], $\ln P / \ln \beta = -1$. Therefore, the expected differential energy spectrum at the source follows the power law with $\gamma = -2$:

$$N(E)\, dE \propto E^{-2} dE. \tag{1.16}$$

Above certain energy, particles cannot be contained within the acceleration site and escape it. For example, the diffusive shock acceleration in supernova explosions is efficient only up to energies $\sim 10^5$ GeV per nucleon [13, 41].

Plausible acceleration sites and the Hillas diagram In 1984, A. M. Hillas evaluated [39] the capacity of various astrophysical sites to be cosmic ray accelerators. An essential role in containment of the charged particles within the acceleration region belongs to the magnetic fields. Therefore, by demanding that the Larmor radius of the particle, $r_L = E/(qB)$, does not exceed the size of the acceleration region, one can estimate the maximum particle energies that can be reached

$$E_{\max} < qBL, \tag{1.17}$$

where L is the size of the acceleration region and $q = Ze$ is the particle electric charge in units of the elementary charge e. The above inequality (1.17) is well known as the geometrical Hillas criterion for the potential cosmic ray accelerators. A number of astrophysical objects, satisfying to the Hillas criterion (1.18), have been suggested as possible UHECR accelerators. In the case where DSA is considered, the Hillas criterion involves in addition the shock velocity in the units of the speed of light in the vacuum, and the maximum attainable particle energy is

$$E_{\max} = \beta_s Z B L, \tag{1.18}$$

where $\beta_s = v_s/c$ is the shock velocity v_s ratio to the speed of light c. The UHECR source candidates can be found among various astrophysical sites distributed according to their linear size L and the magnetic field strength B in Fig. 1.8, known as the Hillas diagram.

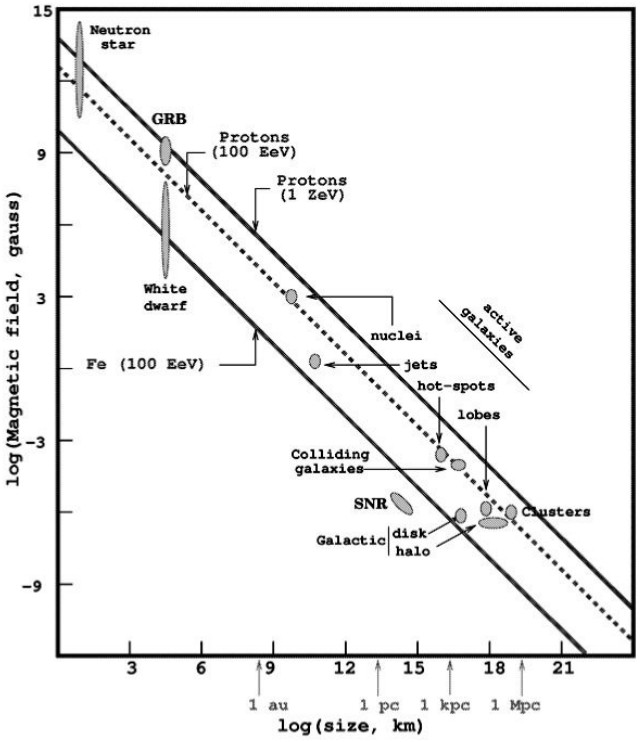

FIGURE 1.8: Hillas diagram shows linear size and magnetic field of possible astrophysical candidates for the UHECR acceleration. The sites above diagonal lines could in principle accelerate particles of the indicated species up to the indicated energies. Taken from Ref. [42].

Several object classes of the plausible UHECR accelerator sites are distinctly identified, including:

1. Neutron stars and their subcategories that exhibit the highest magnetic fields in the Universe:

   a. Pulsars are rapidly rotating neutron stars of order 10^4 m in diameter and a surface magnetic field about 10^{13} G. The Crab Pulsar and Vela Pulsar are famous examples of this class of objects, with rotational periods of 33 milliseconds and 89 milliseconds, respectively [43].

   b. Magnetars are young pulsars with surface magnetic field $\sim 10^{15}$ G.

   Pulsars are considered as powerful direct/one-shot acceleration candidates [39], though details of the particle acceleration mechanism are not well understood yet. The region between

the pole and the equator of length r can work as a circuit of an $emf \sim \frac{\omega B r^2}{c}$ (in cgs units) $\sim 10^{18}$ V for an aligned/parallel or oblique dipole. From this general consideration, the maximum energy [39, 44] that can be achieved in pulsars is

$$E_{\max} = \frac{\omega}{c} q B r^2. \tag{1.19}$$

Thus, a Crab-like pulsar ($\frac{\omega}{2\pi} \approx 30\,\mathrm{s}^{-1}$) could in principle accelerate electrons and protons up to 10 PeV, and the heavier nuclei up to Z times higher energies.

2. Active Galactic Nuclei (AGNs) are considered [45] the prime candidate sources for UHECR. They are thought to be powered by the matter accretion onto the central super-massive black hole in the range of 10^6 - $10^{9.5}$ $M_\odot$. This process may efficiently convert up to ~10% of the rest mass of the accreted matter into radiation.

   The electromagnetic emission from AGN spans across the entire spectrum up to multi-TeV γ-rays, with fluctuations on time-scales from several years down to a few minutes. Of special interest for the UHECR problem are the so-called "radio-loud" AGN having increased radio (5 GHz) to optical (B-band) flux ratio. These AGN, which make up about 15% of all AGN, produce collimated relativistic outflows (jets) of particles emerging from each face of the AGN accretion disk. The jetted AGN provide sufficient energetics/density for contributing significantly to the observed UHECR flux. A schematic diagram of the AGNs is presented in Fig. 1.9.

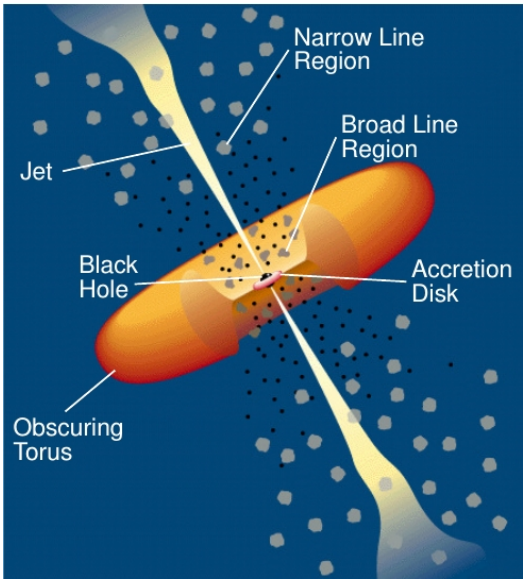

FIGURE 1.9: Schematic diagram of the AGNs [45]. The central black hole is surrounded by a luminous accretion disk, which ejects from each face collimated relativistic outflows (jets) of particles. The broad emission lines are generated in region of small clouds orbiting above the disk in the proximity of the central black hole, or they could be produced by the disk itself. A torus of dust obscures the broad-line region from the observer, with small angle of view with respect to the disk plane. Taken from Ref. [46].

3. Gamma Ray Bursts (GRBs) are the most luminous explosions in the Universe [47, 48] resulting either from the merger of binary neutron stars ("short" GRBs, $<$ few seconds) or the collapse of the massive stars ("long" GRBs). The intense γ-ray emission is followed by a longer lasting "afterglow" emitted at longer wavelengths, from X-ray to radio. Gamma-ray bursts are thought to be highly focused explosions, with most of the explosion energy collimated into two narrow ultra-relativistic jet. The particle acceleration is likely triggered by a system of the jet powerful internal (during GRB itself) and external (during afterglow) shocks involving the strong magnetic fields.

1.2.6 UHECR arrival direction distribution

The arrival direction distribution of the UHECRs, along with the spectrum and the mass composition, is crucial in order to understand their origin and nature. UHECR anisotropies at different angular scales provide valuable information on the plausible sources of cosmic rays and their propagation to the Earth [49, 50]. At **large angular scales**, anisotropies may help in pinpointing the transition from a Galactic to an extragalactic cosmic ray origin [51]. Indeed, a strong contribution of the Galactic component to the all-particle CR flux would result e.g. in a dipolar pattern with characteristic Galactic Center-related orientation and a larger amplitude than expected in the case of extragalactic cosmic rays. A dipolar anisotropy at the highest energies, where the CR are assumed to be extragalactic, could point to a collective diffusive propagation of the cosmic ray particles in extragalactic magnetic fields and/or to an anisotropy of the sky distribution of the UHECR sources. The Pierre Auger Collaboration investigated the large scale distribution of arrival directions of cosmic ray events with energies $E > 10^{18}$ eV detected by the surface detector array at zenith angles up to 80°. This is an update over previous analyses including inclined events with zenith angle $60° \leq \theta \leq 80°$, which allow $\sim$85% sky coverage and $\sim$30% more events.

The Rayleigh analysis [52] was applied to CR events with $E > 1$ EeV in order to search for harmonic modulation in the right ascension distribution of the event counting rates. Above 4 EeV, an additional harmonic analysis in azimuth, sensitive to the declination modulations, has been performed. The East-West technique [53] was employed at energies below 10^{18} eV, and harmonic analysis was applied to the difference in the rates between the eastern and western hemispheres. The obtained results are shown in Fig. 1.10.

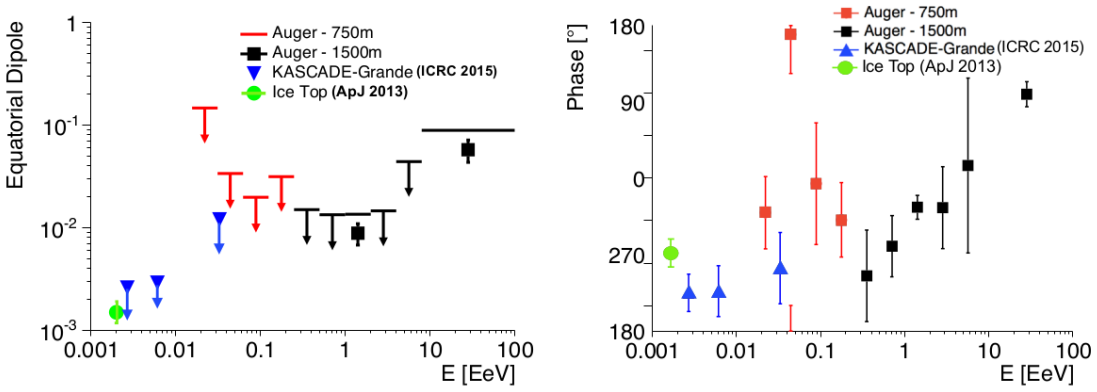

FIGURE 1.10: A summary of upper limits on the UHECR dipole equatorial component by the Pierre Auger Observatory [50], together with measurements at lower energies. Left panel shows the amplitudes in two energy bins with smallest P-values, 1.5×10^{-4} (between 1 and 2 EeV) and 6.4×10^{-5} (above 8 EeV). Right panel presents the phases of the first harmonic modulation in right ascension as a function of energy.

No significant deviation from isotropy has been found. The largest amplitude of the first harmonic in the right $r_1^\alpha = (4.4 \pm 1.0) \times 10^{-2}$, corresponding to the chance probability $P(\geq r_1^\alpha) = 6.4 \times 10^{-5}$, has been found for events above 8 EeV. Assuming a dipole in the large-scale distribution of the UHECR events, this leads to the total dipole amplitude $d = 0.073 \pm 0.015$ with a direction (α_d, δ_d) = $95^\circ \pm 13^\circ, -39^\circ \pm 13^\circ$. The similar results are obtained by the joint analysis of the all-sky CR distribution by the Pierre Auger Observatory and the Telescope Array experiments [54], when no assumption on the shape of the angular distribution is needed. This anisotropy could originate e.g. from an inhomogeneity in the distribution of the UHECR sources. It is interesting to note that the dipole phase above 8 EeV points roughly in the opposite direction with respect to the one below 1 EeV, which is in the approximate direction of the Galactic Center. Such behavior, together with the Auger composition studies, might be indicative of the transition between different UHECR components, e.g. generated by different classes of UHECR sources.

At the highest energies, magnetic deflections of the light nuclei are expected to decrease considerably (e.g. the expected deflection for 100 EeV proton in intergalactic magnetic field is of the order of $\sim 3^\circ$) and the analysis of anisotropies at **small and intermediate angular scales** can directly reveal the UHECR sources, e.g. via observation of the so-called magnetic multiplets [55]. A study of searches for anisotropies in the arrival directions of the highest energy CR events has been implemented by the Pierre Auger Collaboration. In this study 602 events of energy above 40 EeV, collected in 10 years of data, and corresponding to an exposure of 66452 $\mathrm{km^2\,sr\,yr}$ with a field of view ranging from -90° to +45° in declination. Several tests have been performed to search for anisotropies at different energy thresholds, up to 80 EeV, with different angular scales between 1° to 30°. Astrophysical structures, such as the Galactic Center and Galactic plane, Super-Galactic

Plane in the local Universe, and plausible UHECR acceleration site candidates have been used to investigate the correlations [49] with the highest energy Auger events. Moreover, the correlation with different populations of nearby extragalactic objects, such as Galaxies in the 2MRS catalog, AGNs detected by Swift-BAT (e.g., Seyfert I and II, blazars, and QSOs), radio Galaxies with jets and the Centaurus A Galaxy, have been tested. None of the implemented tests showed a statistically significant evidence of anisotropy. The strongest departures from isotropy was found for Auger events with energies $E > 58$ EeV on angular scale of 18° around Swift-BAT AGNs detected in hard X-rays (14 to 195 keV), within ∼130 Mpc and brighter than 10^{44} erg/s, whereas the penalized probability is ∼1.3% for such Swift AGNs catalog. A similar penalized probability of 1.4% has been obtained for events with $E > 58$ EeV and angular radius of 15°, contributing to the excess around the direction of a nearby (3-5 Mpc) powerful radiogalaxy Centaurus A (Cen A).

In a joint work, three analyses have been implemented [56, 57] to investigate correlations between the UHECRs detected by the Pierre Auger Observatory and the Telescope Array with diverse samples of neutrino candidates detected by the IceCube. The cross-correlation method implies the determination of the number of UHECR-ν pairs $n_p(\alpha)$ as a function of angular separation α, to be compared with the expectations with an isotropic distribution. None of analyses showed significant departure from isotropy. The smallest post-trial P-value of 5×10^{-4} has been obtained in the cross-correlation analysis between the UHECR events and IceCube high-energy cascades, for an angular separation of 22°. The sky distribution of events by the three experiments is shown in Fig. 1.11. The excess of pairs arises mostly in the sky region where Telescope Array has reported an excess of events, so-called "hot spot" [58], as well in the region close to the radio-galaxy Cen A and to the Super-Galactic Plane in the local Universe, where a smaller excess has been observed in Auger data. This interesting trend will be further jointly monitored by the three experiments.

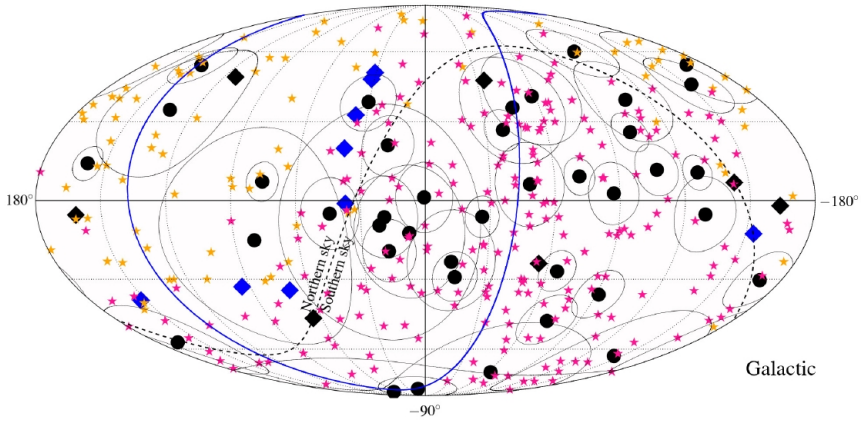

FIGURE 1.11: Galactic coordinates of the arrival directions [57] of the UHECRs detected by the Pierre Auger Observatory (magenta stars) and the Telescope Array (orange stars), and of the very-high energy neutrino candidates observed by the IceCube: cascades (black dots), tracks (black diamonds), tracks of the through-going muon sample (blue diamonds). The blue curve denotes the Super-Galactic Plane in the local Universe. Angular errors are indicated by the circles around the IceCube cascade events.

Anisotropies in the arrival directions of the UHECRs had been anticipated to unambiguously identify their sources. Despite the large exposure reached by two major contemporary detectors, the Pierre Auger Observatory and the Telescope Array, no significant anisotropy has been detected in the UHECR sky, which is unexpectedly isotropic, except for a few interesting anisotropy hints at both large and small angular scales. The better knowledge of mass composition of individual CR events and higher event statistics, especially at the UHECR flux suppression region, are vital to advance our understanding of the energy spectrum and the sky arrival distribution of the extreme energy cosmic rays. The required data improvements are therefore at heart of the upcoming upgrades of the Pierre Auger Observatory [59] and Telescope Array [31, 60] experiments.

1.3 Very-high energy γ-rays

The very-high energy γ-ray astrophysics is a recent and rapidly evolving discipline, which studies astrophysical sources of γ-ray photons, those of energy range [61] between ∼30 GeV and ∼30 TeV. Such γ-ray photons are produced directly from nuclear and high-energy processes, and convey physical information about their astronomical objects. The discovery of more than 100 very-high energy γ-ray sources is one of the most remarkable achievements in the astrophysics within the last decades.

In 1958, Morrison proposed the search for astrophysical γ-ray sources [62] at ∼100 MeV energy range. In 1960, Cocconi had predicted a very-high TeV γ-ray flux from the Crab and various astrophysical sources, which can be detected via measuring EAS with atmospheric Cherenkov detectors of high altitude [63]. Prior to such prediction, Galbraith and Jelley had detected the first Cherenkov radiation produced in the air by cosmic rays in 1953 [64]. The TeV astrophysics was firmly established as a consequence of the detection of steady γ-ray emission from the Crab Nebula at energies >100 GeV by the Whipple Collaboration [65] in 1989. Such early detection of γ-ray photons from the Crab Nebula had significant impact in developing the imaging atmospheric Cherenkov telescope (IACT), which provides intrinsic tool in discriminating between the γ-ray initiated showers and CR background. In 1990s, the nearby blazars Markarian 421 [66] and Markarian 501 [67] were the first extragalactic sources detected by the Whipple Collaboration, as well as the application of the stereo imaging technique by the HEGRA array [68]. A new generation of IACTs have been released with high sensitivity for VHE γ-ray emission, such as H.E.S.S., MAGIC and VERITAS.

Leptonic origin of the VHE γ-ray emission The TeV γ-ray radiation is primarily produced through interaction of low-energy photons (of stellar or synchrotron origin) with high-energy electrons and positrons via the so-called *inverse Compton* (IC) scattering [69], in which leptons loose

fraction of their energies. In magnetic fields, high-energy leptons can also produce synchrotron photons of energies reaching the low-energy γ-ray domain. These low energy synchrotron photons are up-scattered by the same population of leptons that originate them. Such process is know as *synchrotron self-Compton* (SSC) emission, which is thought to contribute significantly in TeV γ-ray emission from e.g supernova remnant and active galactic nuclei. These two processes are known as "leptonic interactions".

Hadronic origin of the VHE γ-ray emission High-energy protons and nuclei interact with matter, which exists in denser regions of interstellar medium through nuclear interactions. Mainly [69] neutral mesons π^0 are produced, which decay into γ-rays. Such processes of nucleons and mesons interactions are called "hadronic" interactions, in which the decay

$$\pi^0 \rightarrow \gamma + \gamma, \tag{1.20}$$

shows that the γ-ray energy spectrum peaks at $m_0 c^2/2 \approx 68\,\mathrm{MeV}$ (few orders of magnitude above the threshold energy for particle production). Then the spectral energy decreases smoothly showing a power law with spectral index approaching the one of the incident particle. The resultant γ rays can also proceed through hadronic interaction

$$\gamma + \mathrm{p} \rightarrow \pi^0 + \mathrm{p}. \tag{1.21}$$

Several γ-ray sources were detected at energies $E > 100\,\mathrm{MeV}$, and they emit non-thermal photons over the whole electromagnetic spectrum. The γ-ray differential flux $d^3N_\gamma/(dE\,dt\,dS)$ decreases very rapidly with energy [69]. The spectral energy distribution (SED) shows the quantity

$$E^2 \frac{d^3N_\gamma}{dE dt dS} = E \frac{d^3N_\gamma}{d\ln E dt dS}, \tag{1.22}$$

which indicates the power received from the γ-ray emitters by unit area S per unit energy E. The SED shows non-thermal emission from radio domain to the highest energies exhibiting power-law dependence on the energy. The Crab Nebula and the PKS 2155-304 are prominent sources for galactic and extra-galactic γ-ray emission, respectively.

Figure 1.12 shows the spectral energy distributions of two different sources; the Crab Nebula (galactic source) and the active galactic nucleus PKS 2155-304 (extra-galactic source). The SEDs of the two sources show a two-component structure, the first peak is due to synchrotron radiation

and the second one is a consequence of inverse Compton scattering. The specification of the SED of the PKS 2155-304, which is a variable source, demands simultaneous observations at different wavelengths.

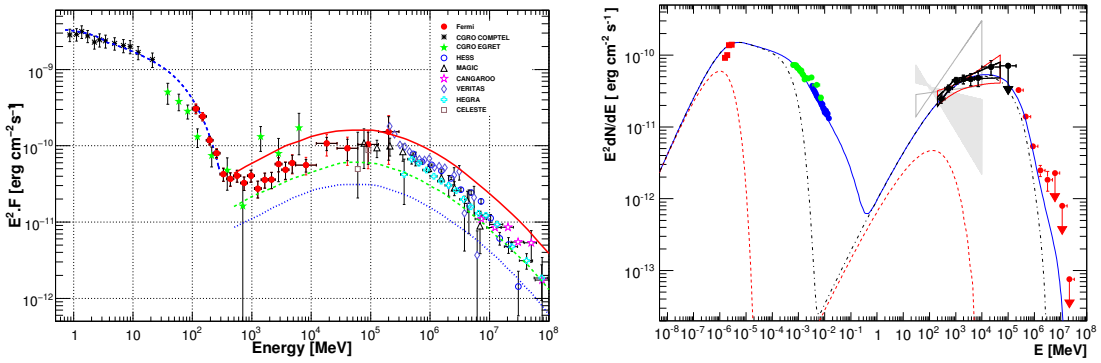

FIGURE 1.12: Broad spectral energy distributions ($E^2d^3N_\gamma/dEdtdS$) of two different non-thermal photon emitters from radio energy band to very-high energy γ-rays. *Left plot:* an example of the SED of a galactic source [70] (the Crab Nebula). *Right plot:* an example of the SED of an extra-galactic source[71] (the active galactic nucleus PKS 2155-304). The photon energy spectrum of the two sources can be approximated by power laws only in a limited energy range.

The variability dependence, which allows to constrain theoretical models of emission of γ-ray objects, might thus be found at different domains of the photon energy spectrum. It is obvious that the SEDs describe power-law at specific energy domains. The photon energy spectra is known to be "soft" (synchrotron bump) if the photon index $\gamma > 2$, and "hard" (IC bump) in case of $\gamma < 2$.

1.3.1 Production mechanisms of γ-ray emission

The γ-ray emission traces cosmic ray astrophysical accelerators and propagation of cosmic rays, e.g. diffuse γ-ray emission from the Milky Way. In the following, we will discuss the main mechanisms of the astrophysical γ-ray emission.

The main process of the VHE γ-rays production is the interactions of cosmic charged particles (nuclei or electrons) with the interstellar medium or radiation fields, however, there is a possible production by the top-down scenarios, which implies the decay of heavy particles (discussed in § 1.2.5). The γ-ray production rate gives indications for densities of cosmic ray (CR) particles and their plausible sources. They propagate away from the acceleration sites through diffusion in magnetic fields, convective follows, or bulk motions [72]. Cosmic γ-rays emitted from distant sources experience attenuation during their traveling in the intergalactic space. The interaction of γ-rays with the background photons, either starlight (infrared background radiation) or CMB, is considered the main process of the γ-ray absorption. At energies above ∼30 GeV, the interaction

of γ-rays with the starlight is dominant, while at higher energy range (TeV-PeV) the interaction of γ-rays with 2.7 K CMB photons is significant. Thus, the attenuation length of γ-rays reaches its minimal value of a few kpc, comparable to the distance to the center of the Milky Way (see Fig. 1.13).

The Universe is partly transparent to the UHE photons, however, Auger upper limits on the EeV photons has been obtained at this energy domain (see e.g., [73–76]).

The TeV γ-ray astrophysical emission is explained by non-thermal emission mechanisms, such as synchrotron radiation, curvature radiation, relativistic electron Bremsstrahlung, and inverse Compton scattering.

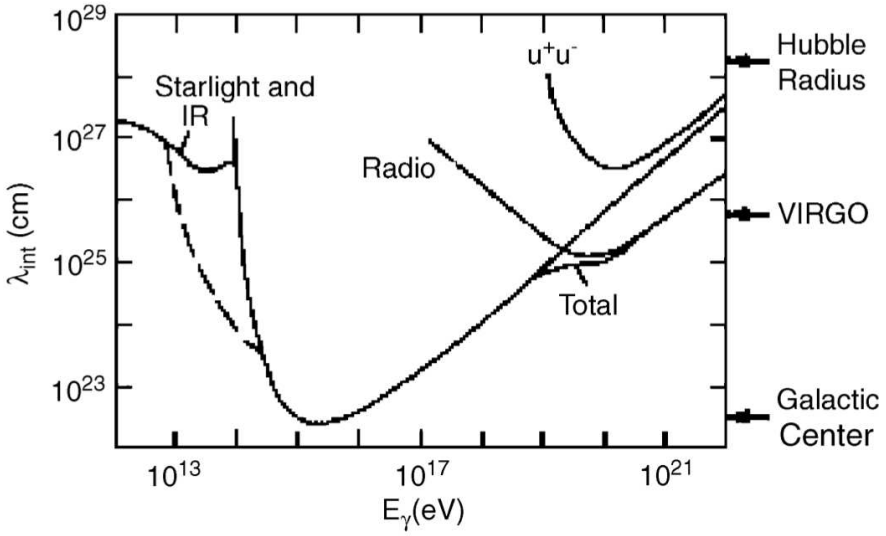

FIGURE 1.13: The attenuation length of the VHE γ-rays in the Universe, as a consequence of their interaction via pair-production with the low energy photons. The interaction of the VHE photons with the 2.7 K CMB photons results in the dominant absorption length at energy $\sim 10^{15}$ eV. Taken from Ref. [77].

Synchrotron radiation is observed in betatron experiments on the Earth [72], and considered as the main non-thermal process in TeV astrophysics. Two ingredients are required to have synchrotron radiation; magnetic field and relativistic charged particles (generally electrons). This kind of radiation is produced by the action of the relativistic Lorentz force (Eq. 1.23) which makes particles gyrate around magnetic field lines, with a Larmor radius r_L and pitch angle θ. The magnetic field doesn't exert work on particles, no change in particles energy can happen, except for energy losses due to the synchrotron radiation itself [78].

$$F_L = \frac{d}{dt}(\gamma m v) = \frac{e}{c}\mathbf{v} \times \mathbf{B}, \tag{1.23}$$

with parallel and perpendicular components:

$$F_{L\parallel} = ev_{\parallel}B = 0 \tag{1.24}$$

$$F_{L\perp} = \gamma m\frac{dv_{\perp}}{dt} = e\frac{v_{\perp}}{c}B. \tag{1.25}$$

Synchrotron radiation is playing a crucial role in indirect production of TeV photons via the synchrotron self-Compton process (SSC), as it is elucidated in § 1.3 and Fig. 1.14.

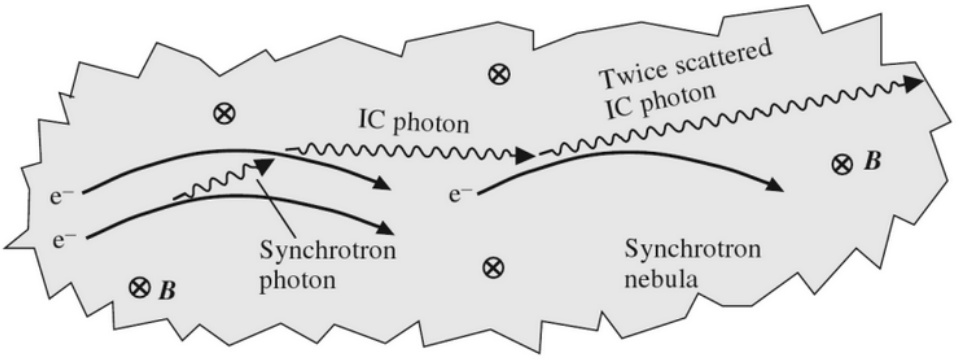

FIGURE 1.14: An example of synchrotron self-Compton (SSC) process in nebula. The magnetic field $\boldsymbol{B}$ is pointed into the page. Synchrotron photons are emitted as a consequence of high-energy electrons, which are produced in high-radiation energy density in the nebular media. Then, the photons experience inverse Compton (IC) scattering to high energies by the same population of electrons. With a significant probability of second IC scattering, the electron energy is rapidly diminished. Taken from Ref. [79].

Two examples of the SSC emission, of galactic and extragalactic origins. In each case the spectral energy distribution shows two maxima that belong to synchrotron radiation (low-frequency bump) and IC radiation (higher-frequency bump). The Crab Nebula again is an example of IC scattering, since the observed synchrotron radiation from the Crab indicates that the surprising galactic source contains very-high energy electrons gyrating in magnetic field of intensity reaching $\sim$10 nT. The second example are blazars. The typical SEDs of the blazars, e.g. the PKS 2155-304, are two-peaked like the Crab SED. Low-frequency peak is attributed to synchrotron radiation, while the peak at higher frequency denotes the IC scattering (see Fig. 1.12 and § 1.3).

Curvature radiation Astrophysical environments of strong magnetic field intensity $B = 10^{12}$ G are the host of this kind of radiation [79]. The motion of electrons in such media are damped by synchrotron radiation. Particles are constrained to closely follow magnetic field lines gyrating with a velocity normal to the field lines $\phi \approx \pi/2$. Such curved magnetic lines make the particles radiate photons. If the velocity of the particles is directed along the field lines, with $\phi \approx 0$, only

a small fraction of the electron's bulk motion will be orthogonal to the field lines. In this case, the energy of the radiated photons is small, and the very-high energy electrons can survive in the given magnetic field without dramatic energy losses. The curvature radiation relies on the electron energy, magnetic field strength, and the curvature of the magnetic field lines. The SED of photons radiated in this case resembles the one of synchrotron radiation. Both mechanisms are effective and vital in photon production processes in pulsars and supernova remnants (SNRs).

Relativistic electron Bremsstrahlung Bremsstrahlung means breaking radiation, since the electrons rapidly decelerates when they pass close by massive ions [80] and remain free (unbound to the collision center). Therefore, it is called free-free emission in astrophysical plasmas, and generally describes continuum radiation emitted as a result of Coulomb interactions or "collisions" between charged particles. In HE astrophysics, Bremsstrahlung is a crucial radiation mechanism, as it can likely interpret wide range frequencies of non-thermal emissions, e.g. the X-ray emission from the Sun and other X-ray sources, except for the X-ray emission from the Crab Nebula [81], which is basically synchrotron emission. Moreover, it is a vital mechanism in studying diffuse galactic emission, in particular, at energies $E < 200\,\mathrm{MeV}$. In VHE γ-ray astrophysics (SNRs and pulsars), Bremsstrahlung is not considered as a major process.

Inverse-Compton scattering Inverse-Compton (IC) scattering is the process in which low energy photons (synchrotron photons) gain energy through their collisions with relativistic electrons. Electrons give energy to photons rather than the opposite [79]. For a population of photons encounters free energetic electrons, which might not be relativistic. If the average energy of the electrons is much higher than the photons one, the photons will be scattered to very-high energies via IC scattering processes, and could significantly contribute to TeV γ-ray emission. If electrons are less energetic, photons on the other hand will be scattered to low energies. This modification of the photon spectra by single or multiple IC scattering is known as *Comptonization*.

The IC scattering is significant process in the nebular media, jets in the active galactic nuclei, and clusters of galaxies [79]. In jets, X-ray photons can be boosted up to VHE γ-ray energies. High-energy electrons in magnetized nebula radiate synchrotron photons, which may then interact with the same population of the energetic electrons which produced them, via IC process, and hence such synchrotron photons reach extremely-high energies. This is known as the synchrotron self-Compton (SSC) process (see e.g. shown in § 1.3 and Fig. 1.14).

The inverse-Compton scattering as well as synchrotron self-Compton models can explain the delay timescale of the high-energy emission of the γ-ray burst, e.g. GRB 080916C [82], which was discovered by the Fermi Large Area Telescope (*Fermi*-LAT). The SED of such event has extremely

broad energy range from 8 keV-300 GeV, and its prompt emission shows two components. The first component is due to synchrotron self-Compton radiation of accelerated electrons in the internal shock of the jet, at energy of order of MeV range. The later one represents the high-energy component, which arises from inverse-Compton scattering of X-ray photons resulted in the expanding of same electrons populated in the jet. The inverse-Compton mechanism could explain other short or long lasting *Fermi*-LAT GRBs.

Gamma-ray bursts and their emission mechanisms Gamma-ray bursts (GRBs) are the most energetic and luminous electromagnetic events in the Universe after the Big Bang. They are characterized by a sudden and bright emission of γ-rays within a short time interval lasting from few milliseconds to hundreds of seconds [47, 48]. After their discovery in 1967 [83] by the Vela satellites, however, such discovery was publicly announced in 1973. The Burst and Transient Source Explorer (BATSE) instrument was successfully studying the GRB emission at the energies ranging from 20 keV up to $>$1 MeV. Such study showed that the GRBs are isotropically distributed in the sky and strongly supported the hypothesis of the extragalactic (cosmological) origin of the GRBs suggested by Meegan [84]. Prior to these observations taken by the BATSE detector, the γ-ray bursts were believed to be young neutron stars in the galactic plane [85].

In 1997, the first detection of GRBs in X-ray domain was achieved by the Beppo-SAX satellite [86], which provided a suggestion on a possible relation between GRBs and massive star (supernova or even hypernova) explosions [87]. Such detection has proved that the GRBs have cosmological distances comparable to the ones of quasars. Other satellite instruments: HETE-2, INTEGRAL, Swift, and *Fermi*-LAT [88–91] have further contributed to GRBs studies. The ensemble of the current data supports the hypothesis that the GRBs occur as the result of astronomical explosions either during the merge of massive compact objects, such as neutron stars (for short GRBs), or in the collapse of massive stars (for long bursts), a process leading to a black hole formation. Thus, the observations of γ-ray bursts are crucial for our understanding of the GRB progenitors, as well as of the processes of high-energy particle acceleration and of the accompanying γ-ray emission. The bright γ-ray burst GRB 130427A, which was detected by the *Fermi*-LAT [92], showed the largest fluence, highest γ-energy photon (95 GeV), and longest duration (20 hr). This GRB event is one of the largest isotropically energy releases observed from γ-ray burst.

There are several theoretical models that can explain the cosmological origin of GRBs, e.g. the fireball shock [93], unsteady outflow [94], and blast-wave scenarios [95]. These mechanisms aim at estimating the range of parameters of expansion bulk Lorentz factor and density of external steady medium, and allow to investigate the γ-ray production and timescale appropriate for observable bursts.

The fireball [96] is an opaque spherical cloud of photons and gas. It is formed when a large amount of radiative energy is suddenly released into a compact region, whereas copious $e^{\pm}$ pairs are released. The fireball shock model can explain the GRBs of cosmological origin, as well as it shows a consistency with the photon energies and timescales of the observed γ-ray bursts. Originally, the mechanism conceives that the energy released due to a relativistic fireball expansion can be reconverted into radiation, after an interaction between fireball and external steady medium.

In 1992, Rees and Mészáros [93] suggested that a homogeneous baryon-dominated fireball of energy $E_{\rm f}$ expands adiabatically in the comoving frame. The internal thermal motions approaches relativistic limit, with high Lorentz factor $\Gamma_{\rm f}$, and goes to bulk kinetic energy expansion. The density of the internal material $n_{\rm b} \propto t_{\rm com}^3$, where $t_{\rm com}$ is the time measured w.r.t comoving frame of the expanding material. In the case that the fireball bumps up against a stable external medium of negligible thermal energy and a boundary $\rho_{\rm ext}$, a shock wave moves a head of the fireball into that steady external medium with a Lorentz factor $\sqrt{2}\Gamma_{\rm f}$. Hence, a reverse shock is constructed and propagates back into the fireball. The fireball starts to decelerate, with boundary $r_{\rm dec}$. Its energy reaches

$$E_{\rm f} \sim \frac{4}{3}\pi \rho_{\rm ext} \Gamma_{\rm f}^2 r_{\rm dec}^3. \tag{1.26}$$

This occurs when fireball ejects a mass (mainly baryonic matter) of $\Gamma_{\rm f}^{-2} E_{\rm f}/c^2$, corresponding to $\sim 10^{-9} M_{\odot}$ and a deceleration radius of $r_{\rm dec} \sim 10^{16}$ cm. If the deceleration becomes significant, a reversible process occurs, in which the fireball reconvert its bulk kinetic energy into thermal energy that can be radiated away, in cases of short cooling timescales. A part of the fireball shell, which moves towards a distant observer, has an apparent speed $\sim 2c\Gamma_{\rm f}^2$. The major of the observed radiation comes from parts of the fireball of Doppler factor $\geq \Gamma_{\rm f}$. The fireball would have a bolometric luminosity of peak of order of $L \sim E_{\rm f} c \Gamma_{\rm f}^2 / r_{\rm dec}$ at time $t \sim r_{\rm dec}/c\Gamma_{\rm f}^2$, then the luminosity decays rapidly. The fireball mechanisms succeeded to explain the total energy issue of the observed bursts of longer timescale, those events followed by slowly fading emission at longer wavelengths (afterglow radiation). The mechanism takes into account the dynamical timescale at deceleration radius, and it is the standard model of the γ-ray bursts.

The unsteady outflow model is operating in compact stellar-mass mergers, in which unsteady mass or energy flux is generated on a short timescales from 10^{-3} to 10 s. The energy is released as an outflow with high Lorentz factor Γ. With respect to comoving frame relative motions of outflowing material reach the relativistic limit, with fluctuating Γ by a factor of ∼2 around its mean value, and then internal shocks are produced. Shocks of $\Gamma \sim 10^2$ take place outside the photosphere of the compact stellar object. These shocks therefore accelerate the particles and essential fraction of the

total outflow energy is converted into non-thermal radiation. This mechanism can interpret GRBs occur at cosmological distances [94].

Some models can explain the detection of TeV photons [97] produced in a GRB: (a) inverse-Compton scattering of ambient photons from relativistic electrons in the burst field; (b) proton-synchrotron emission; (c) inelastic scattering of relativistic protons from pervasive photons. This inelastic scattering leads to high-energy π^0, which decay into HE photons.

VHE photons from GRBs The observations of GeV photons postulated that the relativistic outflows must have bulk Lorentz factors of $\Gamma \gtrsim 10^2$. These Lorentz factors lead to synchrotron spectra that can be extended to 100 MeV in the observer frame, while inverse Compton (IC) scattering of such synchrotron photons result in spectra of GeV and TeV counterparts. TeV photons from GRBs of high redshifts likely lose energies by $\gamma\gamma$ pair production, either in the source itself or in intergalactic medium.

In some cases nucleons dragged into the fireball can obtain energies of order of 100 GeV bulk kinetic energies in the observer frame. These particles can go through inelastic collisions, which result in pions, muons, neutrinos, electrons, and positrons. Neutrino and γ-ray spectra of 1-30 GeV is therefore expected from pion decay due to interactions within expanding plasmas and surrounding/external medium. These interactions rely on the neutron/proton ratio and fireball inhomogeneities [47], while those of surrounding medium depend on the external gas density and its distribution. Neutron star mergers (NS-NS mergers) are plausible sources for GRB, as they provide neutron-rich outflows, and hence neutrinos and photons from np collisions are expected at energies 5-10 GeV.

GRBs emerged from NS mergers offer essential possibility for interferometric gravitational wave detections, e.g., the Laser Interferometer Gravitational-Wave Observatory (LIGO), however, the first gravitational wave (GW) event GW150914 was arisen from the merger of a black hole binary [98]. In this connection, LIGO can provide important clues to the origin of short and long GRBs, either from NS-NS or neutron star-black holes (NS-BH) mergers, or from collapse of massive stars, which can help in investigating the relationship between long period GRBs and SNRs.

UHE photons from GRBs Electron inverse Compton in external and internal shocks is anticipated to release ultra-high energy photons [47] in the range of GeV and beyond. Prompt MeV radiation produced in internal shocks is amplified to ultimately obtain IC GeV photons from external shocks, which could explain the delayed GeV emission observed in some GRB events. The IC GeV photon counterpart is significantly crucial and predominated than possible proton or electron synchrotron components at GeV-TeV energy range.

The decay of π^0 from $p\gamma$ interactions, which occur between shock-accelerated protons and MeV photons produced in the shocks, presents other contributor to this energy range. In baryonic GRB outflows present possible contributor to GeV photon component, since *pn* inelastic collisions lead to pions production, including π^0, which decay to UHE photons that can cascade down to lower energies of GeV range. Therefore, the resultant GeV spectra at energy range 1-10 GeV of bursts of redshift $z \lesssim 0.1$ can be detectable with several detectors, such as *Fermi*-LAT and GLAST.

Interestingly, EGRET has observed GeV photons up to 20 GeV, and this helped to constrain the bulk Lorentz factor of the outflows, as energy and compactness optical depth of the photons depend on it. Thus, the lower limit of the bulk Lorentz factor of the outflow is constrained to the range of 300-600 for number of bursts detected by EGRET. Though, some GRBs are relevant to Lorentz factor of 850, at which TeV photons are liberated from the source.

Since the Earth's atmosphere is not transparent to γ-ray radiation, one can detect them using on-board detectors. *Fermi*-LAT [99] is an example of the current operating satellites and considered one of the most powerful space detectors. It is designed for deep sky survey at very large field of view of order of 2 steradian. *Fermi*-LAT is observing high-energy γ-rays in the energy range from ∼20 MeV to more than 300 GeV. Such domain of observations is complemented by smaller range detector of X-ray and γ-ray satellite, such as AGILE (Astro-rivelatore Gamma a Immagini LEggero) [100, 101]. Above 10 GeV γ-ray fluxes show low statistics, and the effective detection area of *Fermi*-LAT doesn't help in providing adequate statistics for comprehensive spectral studies in the VHE range. The indirect ground-based observations of VHE γ-ray emission complement the satellite-based observations in investigating the spectral and variability features of the γ-ray emitters.

1.3.2 Sources of VHE γ-rays

The disciplines of HE and VHE astronomy have revealed numerous sources of non-thermal emission, and they are classified, according to their origin, into two categories, galactic and extragalactic sources.

Extragalactic sources Extragalactic γ-ray emitters are mainly blazars, those active galactic nuclei (AGNs) whose jets are directed to the Earth. Radio galaxies, starburst, spiral galaxies, and γ-ray bursts are further considered as γ-ray extragalactic sources. The γ-ray emission emanated from these sources is constrained by absorption processes of γ-rays over their long path to the Earth by, e.g., interaction with extragalactic background light (EBL), which results in $e^{\pm}$ pairs. The impact of such absorption processes have been observed in TeV γ-ray regime from AGNs,

and hence their estimation allows to measure the density of background photons [69]. As it is mentioned in § 1.2.5, AGNs release relativistic jets powered by accretion onto a central nucleus, whereas a super-massive black holes are harbored. Their emission properties are yielded by the widely accepted AGN standard model, which relies on orientation of the AGN relative to the line of sight. The Seyfert Galaxies, Radio Galaxies, and Quasars are three broad types of AGNs. The basic components [78] of AGNs are:

a. **A black hole** of a mass from millions to billions of Solar masses. The black hole is likely spinning in the nucleus of the Galaxy.

b. **An accretion disk** is major source of the power. It is composed of matter orbiting around super-massive black hole attracted by its gravity to form the disk.

c. **An X-ray corona** is a hot layer surrounding the accretion disk.

d. **An obscuring torus** is located at several parsecs (1 parsec $\approx$ 3.26 light years) from the black hole, and it absorbs a fraction of the radiation produced by the disk to re-emit it in the infrared.

e. **A Broad Lines Region (BLR)** is a region of small moving clouds, orbiting above the disk, with speed $\sim$300 km s^{-1} at a distance approaching one parsec ($\sim 10^{17}$-10^{18} cm) from the halo. These clouds absorb $\sim$10% of the ionizing radiation of the disk, and re-emit it in a form of broaden observed lines via Doppler shifts.

f. **A Narrow Lines Region (NLR)** is a region at large distance $\sim$100 pc, where the moving clouds are less dense and slower than the ones of the BLR.

g. **Jets**, about 10% of the AGNs are able to eject material from their accretion disks at a relativistic speed into two opposite directions. The jet emission is highly beamed, and its aspect relies on the angle of view or the orientation. AGNs in which jets are pointing to the Earth are called *blazars*, while AGNs of jets pointing away the Earth are called *radio–galaxies*.

AGNs are generally divided into two essential categories of different accretion modes and physical emission processes [102]:

- **Thermal emission (disk dominated AGNs)**
  Collected matter is falling into a thin disk and emits thermal radiation. The distribution of the black-body emission is Comptonized by the effect of hot corona above the disk. Hence a power-law X-ray emission is produced. Such group of objects are known as QSOs (or

Seyfert galaxies), and they represent 90% of the AGNs. Their emission is basically shown in the optical or X-rays regimes, without releasing significant nuclear radio emission. The Comptonizing electron population is not highly enough to obtain relativistic beaming effect, which is able to boost the emission to further cosmological distances, and their resultant emission is distributed isotropically. Therefore, no QSOs have been uniquely discovered by the *Fermi*-LAT or imaging atmospheric Cherenkov telescopes.

- **Non-thermal emission (jet-dominated AGNs)**
  Population of VHE electrons, which has been accelerated in the relativistic jets, interacts with the ambient magnetic field of the jets and emits synchrotron photons distributed over broad energy range from the radio to X-ray. Such population of electrons can provide high energetic photons, through the interaction with surrounding photons or external radiation fields, e.g., ultraviolet (UV) radiation from the accretion disk or the infrared (IR) radiation from the surrounding torus, via synchrotron, SSC, or IC processes. Thus, the resultant spectral energy distribution of these class of objects presents a feature characterized by two distinct peaks.

  In the Coulomb field of a proton, photons emerged via proton synchrotron can be converted into a pion. The neutral pions then decay into γ photons that produce electromagnetic cascades. These objects show non-thermal emission components, with significant luminosity indicating the jet power. The radio-loud AGNs is an example of non-thermal dominated active galactic nuclei.

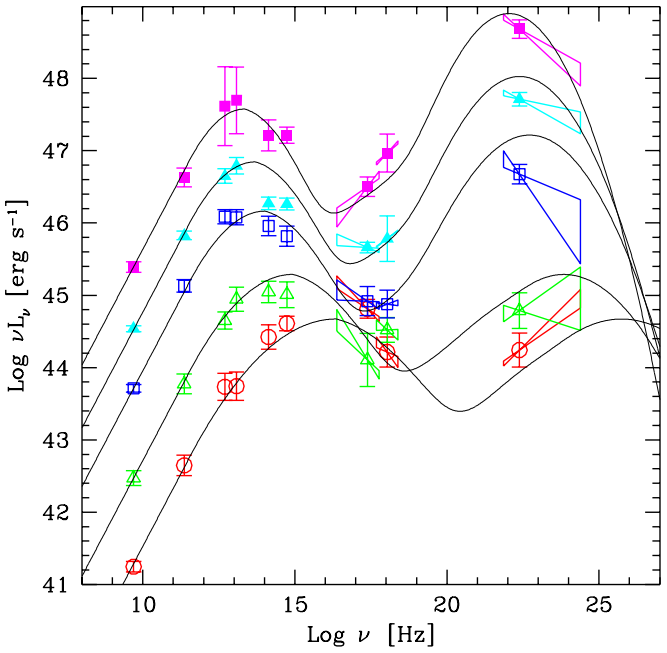

FIGURE 1.15: Spectral energy distributions of different blazars as a function of source luminosity from flat spectrum radio quasar (FSRQ) represented by top curve to high synchrotron peaked (HSP) indicated by bottom curve. Taken from Ref. [102].

Based on the properties of their spectra obtained in optical domain (see Fig.1.15), blazars are moreover subdivided into two main subcategories, namely, flat spectrum radio quasars (FSRQ) and BL Lacs [102], which are very compact radio sources. The FSRQs show broad optical emission lines with SEDs peak at energies lower than 1 eV, as the maximum particle energy obtained within the jet is limited by IC scenario to soft γ-ray band. Hence, no continuous TeV component has been detected from the FSRQ, however, they can flare in TeV energies. On the contrary, BL Lacs (Blazars of the BL Lac type) can emit profuse TeV emission with a broadband SED.

Extragalactic γ-ray emitters (mostly blazars) include about 40% of the detected VHE γ-ray sources, with the known redshifts ranging up to 0.944 [103]. Most of these objects exhibit burst-like variability, e.g., M 87 (z = 0.004), Mrk 421 (z = 0.030), Mrk 501 (z = 0.034), Mrk 180 (z = 0.045), PKS 0548-322 (z = 0.069), BL Lacertae (z = 0.069), PKS 2005-489 (z = 0.071), PKS 2155-304 (z = 0.116), 1ES 1011+469 (z = 0.212), and 3C 279 (z = 0.536). Some of these sources exhibit burst-like variability on short timescales [72] from a few minutes to a few tens of minutes, such as Mrk 421 and PKS 2155-304, however, γ-ray emission from AGN like M 87 and 3C 279 show variability over longer timescales up to days. There are other classes of extragalactic objects, which are expected to emit VHE γ-ray emission at a certain level close to the sensitivity of the contemporary γ-ray detectors. Such classes include starburst galaxies, GRBs, galaxy clusters, normal galaxies, and the UHECR plausible sources.

Galactic sources Our Galaxy harbors PeV accelerators (PeVatrons), which are able to accelerate charged particles to VHE of a few Peta-electronvolts, as well as TeV accelerators that can accelerate particles to tens of TeV energies. Supernova remnants (SNRs) are the main candidate for galactic CRs (below the knee) of energies up to PeV, since relativistic particles of very-high energy are generated via diffusive shock acceleration (DSA) that occurs in SNRs shock (see § 1.2.5). In SNRs environments, TeV γ-rays of hadronic origin arise from pp interactions, through the production and decay of π^0 [101, 104]. At few tens GeV energies, the spectral energy distributions is relatively steep with spectral index larger than 2, while it becomes harder at highest energies. These features have been observed by the IACT instruments of large field of view. The present generation of Cherenkov telescopes (H.E.S.S., MAGIC, and VERITAS) has discovered population of supernova remnants (SNRs) in the Galactic plane [105] at very-high energy γ-rays. Some of these VHE SNRs show a shell-type structure (SNR-shell, e.g., RX J1713.7-3946, RX J0852.0-4622, RCW 86, SN 1006, and HESS J1731-347), which can accelerate electrons or hadrons to ∼100 TeV for leptonic emission and few hundred TeV in case of hadronic acceleration. SNR-shells are not the only sources for GCRs produced via diffusive shock acceleration. An alternative scenario of particle acceleration is allowed via strong shocks, which result in colliding wind binaries (CWBs) [106] driven from massive stars in binary systems.

H.E.S.S. telescope array has observed very-high energy γ-ray emission resulted from particle acceleration processes in proximity of the young massive stellar cluster Westerlund 1 (Wd 1), which is a possible source of galactic VHE emission. In this connection, a study [104] of large photon statistics of 10 years collected by H.E.S.S. allowed to investigate the diffusion of VHE emission of the molecular gas region, which surrounds the galactic center. Such region expands out to radii $r \sim 250\,\mathrm{pc}$ and $r \sim 150\,\mathrm{pc}$ in the direction of positive and negative galactic longitudes, respectively.

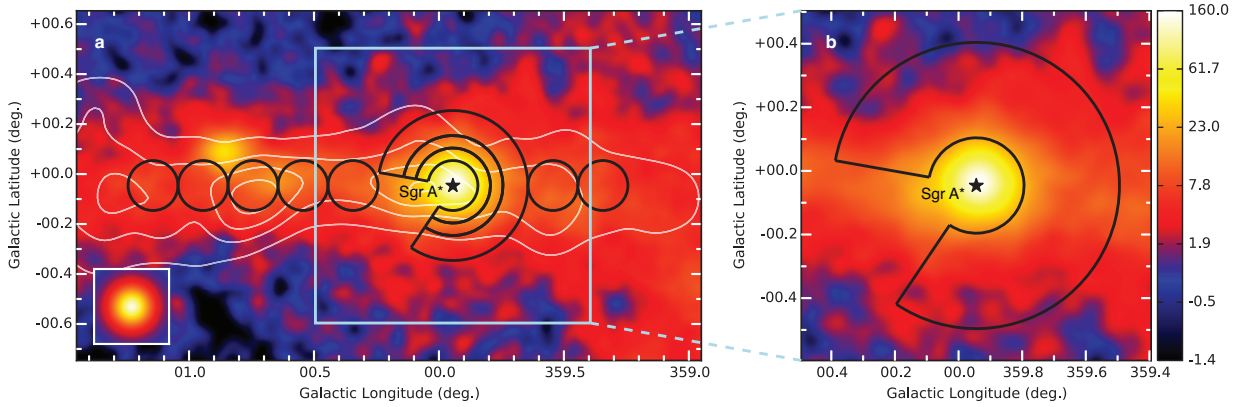

FIGURE 1.16: Image of VHE γ-ray of the galactic center region, from a torus centered at Sagittarius (Sgr) A*. *Left panel:* the black lines refer to the regions used to calculate CR energy density within the central molecular region. The density distribution of molecular gas is indicated by the white contour lines. The inset shows simulation of a point-like source. *Right panel:* a zoom view of the inner region of ∼70 pc used to build up the diffusion emission spectrum. Taken from Ref. [104].

H.E.S.S. survey of the inner galactic plane showed a strong correlation between the brightness distribution of VHE γ-rays and locations of massive gas-rich clumps in the galactic center. Therefore, VHE γ-ray emission of hadronic origin can be liberated, e.g., the energy spectrum of diffusive γ-ray emission from a torus centered at Sagittarius (Sgr) A* (see Fig 1.16) has been found to obey power-law, with a photon spectral index $\gamma \approx 2.3$ at energies up to tens of TeV.

The pulsar wind nebula G 359.95-0.04 is other potential source of VHE emission, which might have diffuse origin peaks toward the direction of the galactic center. The production of VHE γ-rays in galactic center from the IC scattering of electrons is possible as well.

The Crab nebula and its pulsar is a remarkable source for galactic VHE emission, either steady or pulsed γ-ray. Though, the large and deep observations of the Crab, many features are still a matter of intensive study. For instance, the rapid high energy flares from the Crab Pulsar Wind Nebula (PWN), with short timescale of 6 hr. Such kind of flares have been observed and reported recently by the *Fermi*-LAT and AGILE collaborations [107]. The VHE observations of PWNe have presented them as one of the most effective galactic sources for the VHE γ-ray production. The detection of these objects outside the Milky Way is also possible, e.g., PWNe of the Large Magellanic cloud (LMC) (see e.g. in [108]).

Chapter 2

Cosmic Ray Experiments

There have been great advances since initial experiment by Victor Hess aimed to achieve large statistics and precision of the extreme energy cosmic ray measurements. In 1963, John Linsley published an article about the first detection of a cosmic ray of energy exceeding 10^{20} eV [8, 12, 13, 109]. The highest energy (320 EeV) CR event was recorded on 15 October 1991 by the pioneer fluorescence experiment Fly's Eye. Important advances in the UHECR detection techniques came during the 1990s with the implementation of larger surface arrays or improved large exposure telescopes, sensitive for detection of the associated air shower emissions (fluorescence, Cherenkov etc.) in large air volumes. The largest air shower array at the epoch was the Akeno Giant Air Shower Array (AGASA) experiment in Japan. AGASA consisted of 111 scintillator detectors distributed over an area of 100 km^2, accompanied by a more compact array of 27 muon detectors (concrete shielded proportional counters). Also, the High Resolution Fly's Eye (HiRes) experiment, which consisted of two fluorescence detectors separated by 12.6 km, operated in 1997-2006 in the western Utah desert.

In order to significantly improve the statistics and the measurement accuracy of the rare UHECR events, the Pierre Auger Observatory, largest ever CR hybrid detector, has been conceived in the 1990s as the synergy of the previous efforts, and built in 2004-2008. Constructed near the town of Malargüe in Argentina, the Observatory is run and maintained by an international collaboration of scientists and engineers from 18 countries. The Auger experiment features a very large array of water Cherenkov detectors spanned over an area of 3.000 km^2 with 1.5 km spacing. This surface detector (SD) array is overlooked by fluorescence detectors [110] located at four sites.

In this work, we focus only on the detection of the VHE γ-ray emission using the low-energy scaler mode of surface detector (SD) array of the Pierre Auger observatory.

2.1 VHE γ-ray basic detection techniques

Cosmic γ-rays of low energy have been primarily observed by satellites, such as *Fermi*-LAT and AGILE γ-ray detectors. At energies above tens GeV, γ-rays are detected by ground-based instruments of extremely large collecting area [111, 112], through measuring the extensive air shower (EAS) via detecting the Cherenkov light in the air or the particle flux on the ground (see § 1.2.3). The lateral spread of secondaries of both hadron and γ-ray induced showers can cover large area of hundreds of meters (shower footprint). Detectors within that footprint can thereby observe the primary particles, giving an effective area, which could be many order of magnitude greater than the actual physical size of the ground-based detector. The ground-based detectors go into two approaches: (a) imaging atmospheric Cherenkov telescopes (IACTs); (b) extensive-air shower (EAS) detection technique.

Imaging atmospheric Cherenkov telescopes (IACTs) The imaging air Cherenkov telescopes have been evolved in the last decade, to detect very-high energy γ-ray emission. The IACTs measure extensive air showers (EAS) induced by VHE-γ photon by observing the Cherenkov radiation in the air (see Fig.2.1).

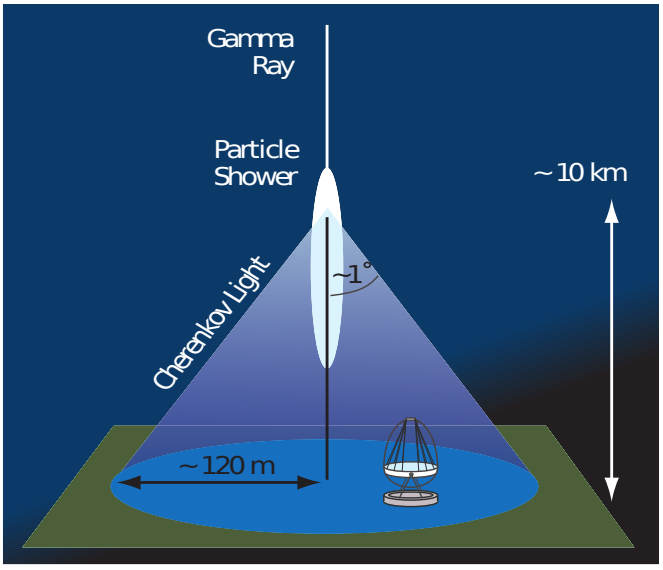

FIGURE 2.1: Schematic view of imaging atmospheric Cherenkov telescopes (IACT). Taken from Ref. [112].

A telescope of 10 m diameter mirror and multi-channel camera of pixel size of ∼1/4° with a field-of-view of ∼3° can effectively detect the EAS induced by primary γ-ray of energy ≥100 GeV [101]. The showers can be measured at ground level across distances of order of 100 m, which implies a huge detection area $A_{\rm eff} \geq 10^4\,{\rm m}^2$ of primary γ-rays. The total number of photons contained in

the observed Cherenkov light image is proportional to the energy of the primary photon deposited in the atmosphere. The arrival direction of the γ-ray photon is determined and correlated by the orientation of the image taken by the IACT technique, in addition to, the shape of such image provides information about the type of the primary particle which initiated the shower, e.g., photon, proton, or iron. A minimum detectable energy flux of the order of 3×10^{-13} erg/cm^{2}s can arise from a primary photon at energies around 1 TeV, which is much higher than energy deposited at GeV domain in space-based detectors. The space instruments can not achieve the performance obtained by the ground-based detectors of very large collection area at TeV energy sector, such as the High Energy Spectroscopic System (H.E.S.S.) [113], Very Energetic Radiation Imaging Telescope Array System (VERITAS) IACT arrays [114], and Major Atmospheric Gamma Imaging Cherenkov (MAGIC) telescopes [115]. The high flux sensitivity and relatively large (3-5 degrees diameter) field of view of the current IACTs allow to study point-like and extended sources with angular resolution $\sim 1^\circ$. However, the IACT arrays have low duty-cycle $\sim$10% (moonless clear nights) and limited potential in searching for astronomical extended structures, such as the galactic plane diffuse emission and huge radio lobes of the nearby radio galaxy Centaurus A. The IACT arrays have been very successful in discovering a variety of astrophysical sources emitting VHE γ-rays. Among detected TeV sources of Galactic and extragalactic origins are the Crab Nebula and blazars, a subclass of Active Galactic Nuclei (AGNs).

Above a few tens of GeV (at very-high energies, VHE), the current arrays of IACTs have not detected any γ-ray burst so far. The Cherenkov Telescope Array (CTA) [116, 117] launches the next generation of ground-based very-high energy γ-ray instruments, and will hopefully observe the VHE γ-ray emission from GRBs and help to clarify the emission mechanism in the GRBs. The CTA will serve broad astrophysics community through providing a deep insight into the non-thermal high-energy Universe.

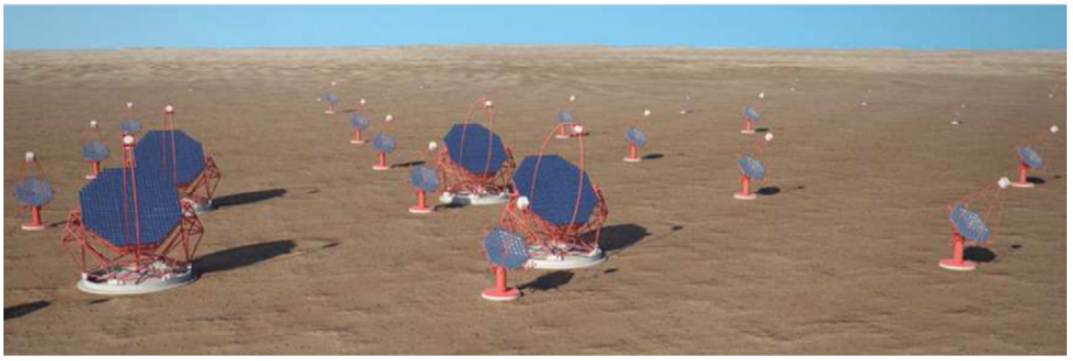

FIGURE 2.2: Schematic view of CTA array. The CTA experiment launches the next generation of ground-based very-high energy γ-ray Observatory. Taken from Ref. [117].

A Schematic view of the CTA array is shown in Fig. 2.2. The CTA Observatory will have two sites of ∼50-100 telescopes and aspires to achieve all-sky survey (more than 1000 astronomical sources) with high sensitivity by about an order of magnitude, and to cover four decades of energy from a few tens of GeV to above 100 TeV. Each shower cascade will be simultaneously imaged stereoscopically by the multiple CTA telescopes, which will be capable of reconstructing the properties of primary γ-ray from resultant images. The main CTA scopes are: (a) understanding the origin of cosmic rays and their origin; (b) elucidating the cosmic particle acceleration mechanisms (e.g., particle acceleration mechanisms around the black holes) and their nature; (c) investigating the nature of matter and the physics beyond the Standard Model by, e.g., exploring the dark matter and quantum gravity effects. All these promising goals can only be fulfilled through combination of different size telescopes, large ones for the lowest energies, medium ones for the core energy range, and small ones for highest energies. In order to improve the sensitivity at highest energies, CTA project requests a collection area of the order of 10 km^2. This assures that numerous telescopes are distributed over large area [117].

EAS detection technique The EAS detection technique (non-imaging technique) was originally designed for cosmic ray observations at PeV-EeV energy domain. It essentially relies on two [101] instrumental trends: (a) scintillators; (b) water Cherenkov detectors, both spanned over large areas. Such detection technique has been adapted to be used in γ-ray astronomy with continuous sky survey through lowering the energy threshold, via deploying dense and huge surface detector arrays at very high altitudes with high duty-cycle (∼100%). These intrinsic factors assure a low energy threshold of order of few hundreds of GeV of γ-initiated showers. Therefore, both scintillators and water Cherenkov detectors are widely used in ground-based γ-ray detectors, such as, Astrophysical Radiation with Ground-based Observatory at YangBaJing (ARGO-YBJ), Milagro γ-ray experiments, Large High Altitude Air Shower Observatory (LHAASO), and High Altitude Water Cherenkov experiment (HAWC) Observatory.

ARGO-YBJ Observatory is located in Tibet, China at an altitude of 4300 m a.s.l.. The Observatory is utilizing the "shower" and "scaler" modes in measuring the EAS by detecting particle fluxes on the ground level. The shower mode allows to deeply study the hadronic component of cosmic rays in 1 TeV-1 PeV energy range, while scaler mode presents unique opportunity in detecting the low energy transient phenomena at energy range from 1 to 100 GeV, e.g., GRBs and Solar flares [118, 119].

Milagro γ-ray detector is located in the Jemez Mountains near Los Alamos, New Mexico at the Fenton Hill Observatory site, and it is covering significant part of the sky (Northern Hemisphere).

The detector is sensitive to γ-ray emission at energies start from 1 to 100 TeV, with a peak sensitivity from 10 to 50 TeV based on the spectrum and declination of the astronomical source. These possibilities enabled the Milagro Collaboration to search for new classes of γ-ray sources [120], which lead to spectacular discoveries of VHE transient phenomena.

LHAASO detector for ground-based γ-ray astronomy was proposed in order to enrich the regime of VHE with crucial information about γ-ray emission and sources of both galactic and extragalactic origin [121] at Yangbajing, Tibet, China. LHAASO is proposed to be a large air shower particle detector array of 1 km^2 at 4300 m a.s.l. It will composed of many sub-arrays [122] for detecting the electromagnetic and muonic components of air shower produced above 100 GeV.

HAWC is one of the recent γ-ray experiments, and is situated close to Sierra Negra, Mexico, at high altitude of 4100 m a.s.l.. Its sensitivity is comparable to *Fermi*-LAT at 1 GeV, and hence the capability to observe GRBs [123, 124] up to 30 GeV. Therefore, HAWC will serve as a complementary detector to *Fermi*-LAT in continuous monitoring of more than 1 steradian fraction of the sky at TeV energy domain [101]. Its low energy threshold will allow to detect the brightest GRB events, such as GRB 090510 and GRB 090902b, which were observed by *Fermi*-LAT. The Observatory shall provide data about the high-energy spectra of GRBs, which will assist our understanding about pair production attenuation in the GRB jets and extragalactic background light absorption, as well as set the highest energy limit, at which GRBs accelerate particles.

The Hundred*i Square-km Cosmic ORigin Explorer (HiSCORE) [125] aims to detect cosmic rays at energies from 100 TeV to 1 EeV, as well as γ-rays from 10 TeV to several PeV. The main goal of HiSCORE is to investigate cosmic ray composition, spectral measurements at Galactic-extragalactic transition range, the origin of cosmic rays, and the detection of VHE γ-ray emission from galactic PeV sources (PeVatrons).

The current generation of IACT arrays (H.E.S.S., MAGIC, and VERITAS) with *Fermi*-LAT and AGILE satellites, along with the present or planned air shower experiments (e.g., ARGO-YBJ, Milagro, LHAASO, HAWC, and HiSCORE) have revealed new realm of γ-ray astronomy, with improving hadronic background suppression and better sensitivity of individual shower detectors. The combination of these observational facilities allow to explore the Universe above a few tens of GeV energy range, as the detection range has been extended from 30 MeV to >30 TeV [111]. This could help in discriminating between IC emission from relativistic electrons (dominant in the Crab and some blazars), and π^0 decay resulting from hadronic interactions.

A comparison between sensitivity for point sources survey of the new generation air shower detectors (LHAASO, HAWC, and HiSCORE) and next generation CTA is presented in Fig. 2.3.

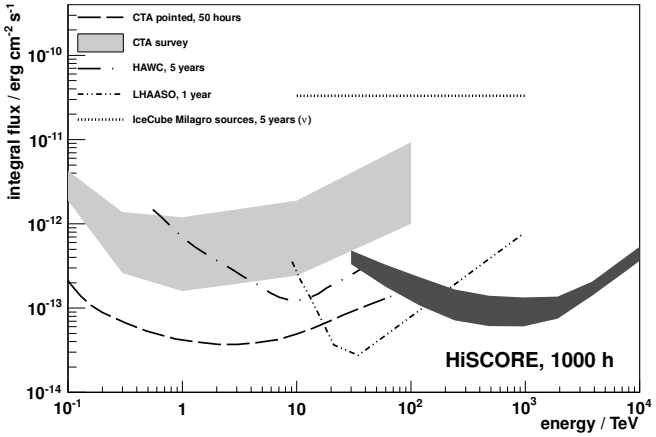

FIGURE 2.3: Sensitivity of the new generation air shower detectors and next generation CTA for point sources survey at multi-TeV energies [126]. HiSCORE sensitivity for point source survey, after 1000 h of exposure, is compared with sensitivities from CTA and other experiments. The CTA sensitivity [127] for 50 h pointed observation is provided for reference. Taken from Ref. [126].

Longitudinal development of electromagnetic showers As it is discussed in Chapter 1, photons are dominant in electromagnetic shower, and they produce $e^{\pm}$ pairs, which give photons via bremsstrahlung process. The detectability of the VHE γ-ray emission by ground-based detectors depends on the energy of primary γ-ray and zenith angle. The data shown in Fig. 2.4 provides convincing evidence that at high altitude above ∼3.000 m a.s.l. the γ-induced showers with primary energies above a few tens GeV are reaching the ground level.

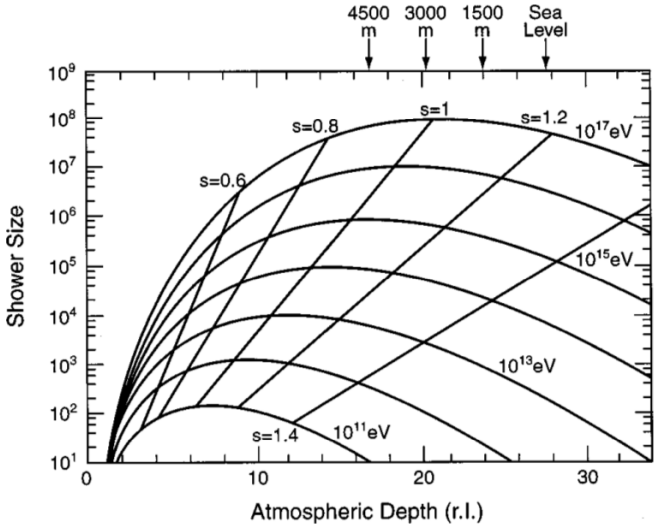

FIGURE 2.4: Longitudinal development of an extensive air shower. Taken from Ref. [128].

At lower altitudes the secondary particles in showers with primary energy of sub-TeV range reach the ground level, and hence sampled by the EAS detection techniques. The γ-induced showers from primaries of sub-PeV are likely detected at the sea level. The Pierre Auger Observatory is located

at average altitude of ∼1.420 m a.s.l., at which the γ-induced showers with primary energies below a few 100 GeV are absorbed before reaching the ground. On the contrary, the secondary particles of showers with primary energy in the TeV range can reach the Auger surface detector (SD). Consequently, Pierre Auger Observatory is able to detect the VHE γ-ray emission in TeV-PeV energy domain from the astrophysical sources, such as the Crab nebula and AGNs of the blazar type, through employing the *Auger low-energy scaler mode* - "the single particle technique (SPT)" or "SD scalers" [129].

2.2 Pierre Auger Observatory

The Pierre Auger Observatory is the world's largest detector of ultra-high energy (UHE; $>10^{18}$ eV) cosmic rays (CR), allowing to study these extreme energy particles with unprecedented statistics, and with combination of different detection techniques (hybrid detection) for better understanding of systematic uncertainties [130, 131]. The Observatory is located at Pampa Amarilla near Malargüe, in the province of Mendoza, Argentina at 35° S and 69° W. A map of the Observatory is shown in Fig. 2.5.

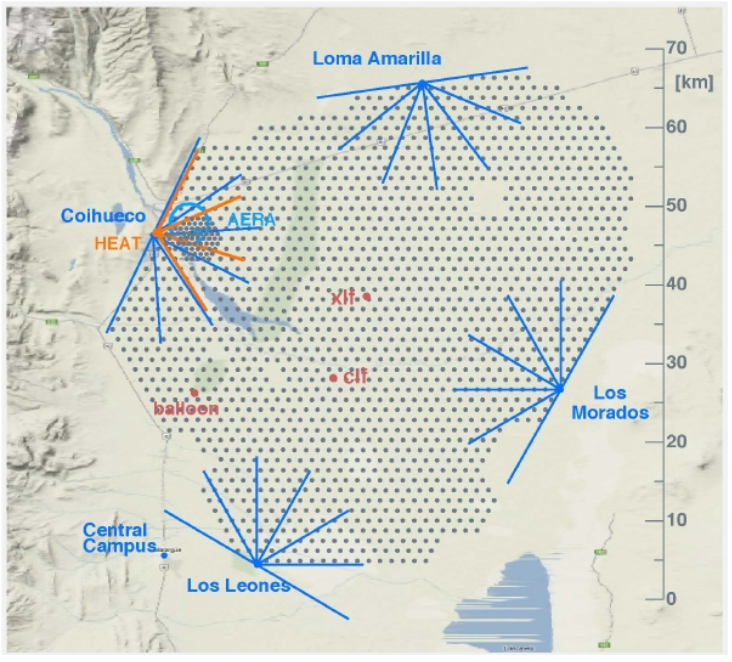

FIGURE 2.5: Schematic view of the Pierre Auger Observatory site [132]. The individual surface detectors of the SD array are shown by a regular grid of dots. The four sites of the fluorescence detector (FD) telescopes and the azimuthal field of view for each individual telescope are shown in blue. The Pierre Auger Observatory extensions at the proximity of the Coihueco FD site include the HEAT high elevation fluorescence telescopes for the hybrid detection of lower energy atmospheric showers developing over the densely placed surface detectors (the infill array) and the co-located AMIGA muon detector array. The AERA array of radio detectors, indicated by the blue circle, is located at the same area as well. The atmospheric monitoring stations are illustrated in red.

The Observatory is composed of two main components, which are the *surface detector* (SD) and the *fluorescence detector* (FD). The Observatory entered into operation at the end of the prototyping phase (Auger Engineering Array) in January 2004, with 154 individual surface detectors and one fluorescence telescope at that time, and has been in the construction phase till its completion in June 2008.

2.2.1 Location

The location of the Observatory has been chosen for the following reasons: (a) the mean altitude of ∼1.420 m a.s.l. and atmospheric depth of 879 g/cm^2 allow to detect e.g. the UHECR-induced air showers at the ground level; (b) relatively flat large area, 3.000 km^2, to allow detectors deployment and assure good wireless data transfer; (c) good climate conditions with dry atmosphere and minimal aerosol contents which satisfy the operating conditions of the fluorescence detectors; (d) proximity to the town of Malargüe helps to access the infrastructure demands.

The main building of the Pierre Auger Observatory is located at the town of Malargüe, where the offices of the permanent staff, laboratories for detectors maintenance, assembly hall, and the Central Data Acquisition System (CDAS) are localized. In this chapter, the main Auger detector components (the SD in § 2.2.2 and the FD in § 2.2.5) and the recent enhancements (in § 2.2.6) of the Observatory are described.

2.2.2 Surface Detector

The Surface Detector (SD) array [133] of the Pierre Auger Observatory consists of ∼1600 water Cherenkov detectors on a regular triangular grid with 1.5 km separation between the neighbor stations. The SD array spans an area of ∼3.000 km^2, and the SD detector is represented by a dot in Fig. 2.5. Each SD detector records Cherenkov light, which is produced as a consequence of the passage of the charged particles of cosmic ray air showers (mostly muons, electrons, and $e^{\pm}$ pairs) through the water contained in the detector, with a duty cycle of ∼100%.

The SD array is fully efficient in probing cosmic ray secondaries, produced by primary cosmic rays of energies above 3 EeV arriving at zenith angles below 60°. A low energy extension of the SD array has been implemented by deploying additional 60 WCD as denser array, namely *graded infill array* or *infill array* [134], shown as denser dots in Fig. 2.5. The *infill* detectors are a part of the AMIGA enhancement and will allow to detect cosmic rays down to 3×10^{17} eV [134, 135].

Design of individual water Cherenkov detectors Each station of the SD array is a cylindrical detector of diameter 3.6 m and 1.6 m high. The detector is filled with 12 tons of a highly purified water overlooked by three 9" photomultiplier tubes (PMTs) positioned uniformly at 1.2 m from the center of the detector in an equilateral triangle. The highly purified water assures high level of transparency by preventing the growth of the micro-organisms. The body of the detector is made of high density polyethylene resin of 12.7 mm thick, walls of two layers, which is opaque to external light. The external layer of the wall is in beige color, in order to minimize the heat and light absorption, while the internal one is in black. The detector liner, where the water is contained, is made of polyolefin-Tyvek film to diffusely reflect the UV Cherenkov light produced by the passage of the charged particles through the water, as the Tyvek® has high reflectivity to the ultraviolet light.

It has been planned that the Observatory will be running for more than 20 years, so each component of the water-Cherenkov detector has been designed for such long lifetime. So, the SD station is an autonomous unit, equipped with two Solar panels, which are able to recharge the 12 V batteries of the detector and to provide a 10 W power.

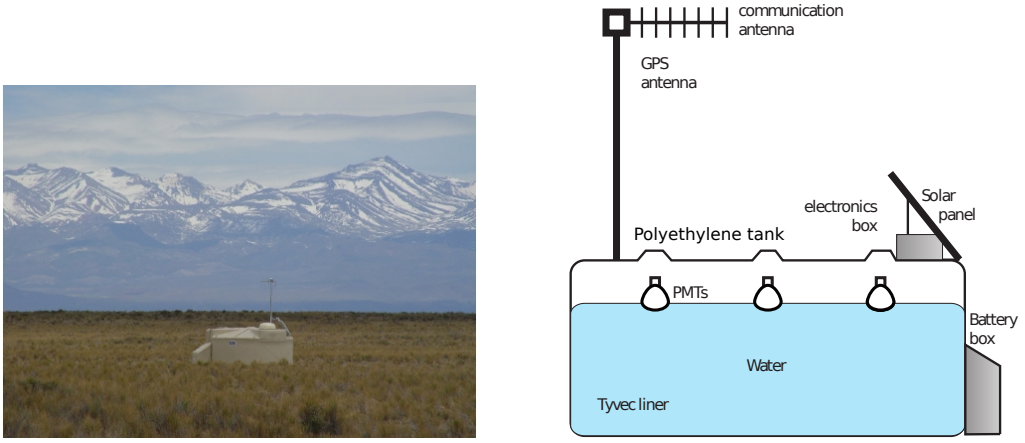

FIGURE 2.6: A photo and schematic view of the water-Cherenkov detector [131, 136] deployed in the Auger field. Various components are shown and described in the text.

The Cherenkov light is collected by the three PMTs, where the signal is extracted from the anode and the last dynode. The signal of dynode origin (high gain) is being amplified by a factor of 32 to extend the dynamic range, and the one of anode origin (low gain) is utilized when the dynode is getting saturated by the large amplitude signals. Each station thus provides 3 high gain and 3 low gain signals. These signals are read by the front-end electronics, which comprises six 10 bit 40 MHz Fast Analog to Digital Converters (FADCs).

The digitized signals are sent to the station trigger block. The detector trigger time, crucial for event reconstruction, is measured with a precision of $\sim$8 ns using the Global Positioning System

(GPS) units. The output signals, which pass a certain trigger level, are transmitted to the closest FD location by a radio antenna fixed on the detector surface (see Fig. 2.6), where they are transferred via communication towers to the CDAS building in Malargüe for further processing (higher trigger levels).

Calibration The SD detector is measuring the Cherenkov light produced by the passage of the shower particles through the water contained in the detector. The calibration of the SD station is carried out locally and automatically, since the total bandwidth from each SD station to the CDAS is limited to ∼1200 bits per second [137], which impedes remote calibration. Consequently, a common calibration unit for all detectors is implemented, which is the signal produced by a vertical and central through-going muon (VCT), called vertical equivalent muon (VEM). The purpose of the SD calibration processes is to determine the corresponding value for 1 VEM in electronic unit. This calibration unit is also employed in the SD simulations.

The signal collected in charge histogram by through-going atmospheric muons is providing an intrinsic tool in estimating the value of the vertical equivalent muon (VEM). The calibration of SD station is performed systematically every minute [138], whereas another histogram of low energy secondaries is yielded for ∼10.000 events.

In order to perform the SD calibration, some quantities are determined: (a) charge deposited in PMT by Cherenkov light from VCT muon (Q_{VEM} or VEM); (b) peak of the charge histogram ($Q^{\mathrm{peak}}_{\mathrm{VEM}}$) which is ∼1.09 VEM summed over the 3 PMTs to measure the total signal, while the individual PMTs measure the closest portion of the signal 1.03 ± 0.02 VEM for each PMT; (c) pulse height of Cherenkov light from VCT muon (I_{VEM}); (d) peak of the pulse height histogram ($I^{\mathrm{peak}}_{\mathrm{VEM}}$); The SD detector sensitivity to atmospheric muons results in the charge and pulse height histograms shown in Fig. 2.7. The shift with respect to the dashed histograms obtained with an external calibration unit, and is a consequence of the asymmetry in the muon track length distribution and also the effect of SD station light collection efficiency. In order to implement the SD detector calibration in VEM units, three steps are prerequisite:

1. adjust the high voltage for each PMT till obtaining $I^{\mathrm{peak}}_{\mathrm{VEM}}$ at 50 ch.
2. continually perform a local calibration to determine $I^{\mathrm{peak}}_{\mathrm{VEM}}$ in units of ADC channels to adjust the electronics trigger level.
3. determine the value of $Q^{\mathrm{peak}}_{\mathrm{VEM}}$ using charge histograms and apply the conversion from $Q^{\mathrm{peak}}_{\mathrm{VEM}}$ to 1 VEM to obtain a conversion from the integrated PMT signals to VEM units.

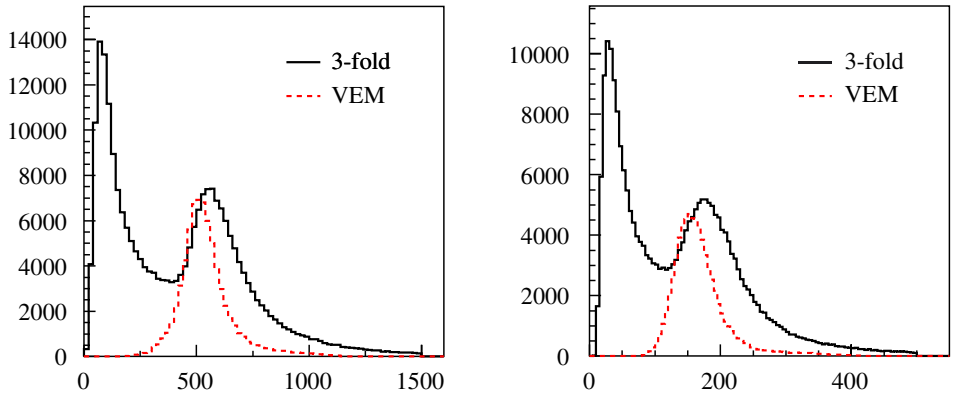

FIGURE 2.7: Charge (first panel) and pulse height (second panel) histograms for SD station. The signal is extracted from the 3 PMTs and summed over the three of them to measure the total signal. The solid distribution in both plots shows two peaks. The first peak is a consequence of the trigger effect of the low energy secondaries, while the second one is caused by the vertical through-going atmospheric muons. The dashed distribution in both plots represents vertical and central muons (VEMs) triggered by an external muon telescope [137].

The calibration parameters mentioned above ($Q^{\text{peak}}_{\text{VEM}}$ & $I^{\text{peak}}_{\text{VEM}}$) are specified every 60 s and transmitted with each triggering event to the central data acquisition system (CDAS). Subsequently, each event includes considerable amount of information about the SD detector in a minute time scale.

2.2.3 Trigger system

The bulk of the data acquisition is provided by the surface detector, due to its high duty cycle of ∼100%. The data are transmitted from each detector to the central data acquisition system (CDAS) via wireless communications. The SD trigger system [139] is set in a hierarchical form (see Fig. 2.8).

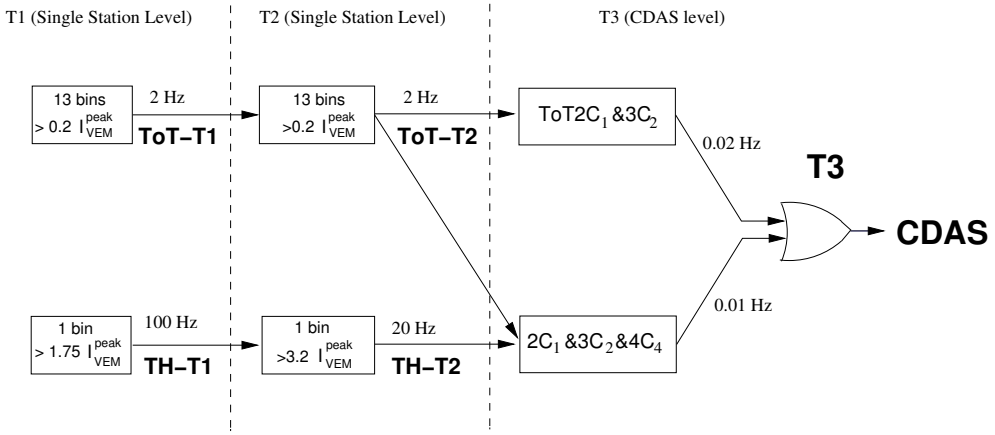

FIGURE 2.8: The trigger regime of Auger SD array [139].

Each trigger level diminishes the station background rate, and it becomes more strict to the real events amongst rich random muon-background. Two levels of triggers called T1 and T2 are performed *locally* to each individual detector. Higher level, array-wide triggers T3, T4, and T5 aim to select shower events. The T3 level (first offline level) decides whether the event is written to the CDAS database. T4 and T5 are pure offline triggers.

Local detector triggers T1 and T2 are two levels of triggers applied locally to each single detector. There are two trigger modes at both T1 and T2 level, which are optimized to detect the electromagnetic and muonic components of air showers. The threshold trigger TH-T1 assures coincidences above 1.75 VEM from the 3 PMTs in one bin, thus reducing the background rate due to atmospheric muons from $\sim$3 kHz to $\sim$100 Hz. TH-T1 is helpful in the detection of very fast (200 ns) inclined shower events containing mostly muons. The time over Threshold (ToT-T1) trigger selects coincidences above a threshold peak of $0.2\, I_{\mathrm{VEM}}^{\mathrm{peak}}$ in 2 out of 3 PMTs. ToT requires at least 13 FADC bins, i.e. 325 ns, in a sliding window of 120 bins (equivalent to 3μs). The ToT trigger is optimized for low amplitude time-extended signals typical for the electromagnetic shower component. The resulting ToT trigger rate at each station is about 1.6 Hz.

The second level T2 trigger is implemented in the local station software to reduce the rate of signals per station to $\sim$20 Hz. This reduction is crucial to resolve the limitation issue of the communication system bandwidth between the SD stations and the central campus. All ToT-T1 are systematically promoted to ToT-T2 triggers, while TH-T1 triggers pass further higher threshold of peak $3.2\, I_{\mathrm{VEM}}^{\mathrm{peak}}$ of a 3-fold coincidence in the 3 PMTs. The resulting T2 triggers are used to form the third level trigger, T3.

Since June 2013, two new triggers have been installed in the software of all local stations, in order to increase the sensitivity of the individual surface detectors to low energy air shower signals, thus extending the energy reach of the SD. The triggers are dubbed the Time over Threshold deconvolved (ToTd), and the Multiplicity of Positive Steps (MoPS). Both triggers are similar to ToT, however, in the first one additional deconvolution is performed to the traces signal before applying the ToT condition, in order to take into account the exponential decay of the signals. The second one counts the number of positive steps within the 3μs sliding window above the noise and below the moderate signal amplitude. The application of these more sophisticated triggers minimizes the influence of single muons, as well as improves the trigger efficiency for photon and neutrino showers.

Surface array triggers The third level trigger T3 is the first trigger for the whole SD array. The trigger is executed at the central data acquisition system (CDAS), based on the spatial and temporal

distribution of T2 triggers. Data from all T2 triggered stations are sent to CDAS, where the search of real events is implemented. The T3 trigger has two different modes named ToT2C1 & 3C2. The first mode, ToT2C1, requires 3-fold coincidences from at least three detectors that verify the ToT-T2 criteria, and also fulfill a minimum compactness requirements. Namely, one of the three detectors must be in the first crown of neighbor stations, i.e. the 6 closest surrounding stations, and the other stations have to be located within the second crown (see left panel of Fig. 2.9). The rate of events selected via this trigger mode, ∼1600 events per day, from UHE cosmic ray showers, 90% of them are physical events for real cosmic showers, mostly vertical showers.

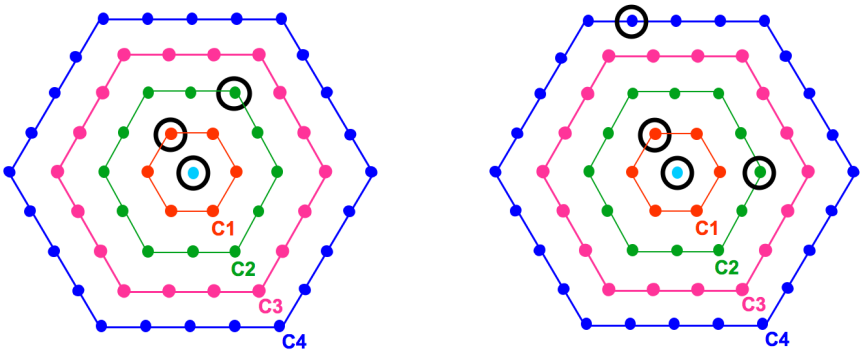

FIGURE 2.9: An example of the T3 trigger configurations. Left panel shows ToT2C1 & 3C2 modes. Right panel presents 2C1, 3C2, & 4C4 modes. C1, C2, C3, and C4 denote the first, second, third, and fourth sets of neighbors, respectively, at distance of 1.5, 3, 4.5, and 6 km from a given detector [139].

The second one, 3C2, requires 4-fold coincidences from four stations which pass the ToT-T2 conditions, as well as the minimal event compactness requirements have to be attainable. In this case the configuration is less compact than for the previous mode of ToT2C1. Namely, among the four fired detectors, one station may be as far away as the fourth hexagon, if a station is within the first hexagon and another station is no further than the second hexagon. The configurations of this mode are named 2C1&3C2&4C4 and are showing the right panel of Fig. 2.9. The 3C2 trigger mode is more effective for horizontal showers, which have larger footprint on the ground. The rate of events obtained by this mode is ∼1200 events per day, ∼10% of them are from UHE cosmic ray showers.

Physics trigger The T4 trigger is applied to T3 triggered data to select the real events with an estimated zenith angle of $\theta < 60^{\circ}$ from accidental coincidences. This physics trigger has two modes called 3ToT and 4C1. The 3ToT requires three adjacent detectors in a triangular pattern that have passed the ToT-T2 criteria. Additionally, the trigger times in the three detectors have to fit a plane shower front propagating with the speed of light. More than 98% of T3 triggering events are showers with a median energy $\sim 6 \times 10^{17}$ eV. The second mode of this trigger is 4C1, which

requires four nearby stations that have passed T2 trigger of any type. The possible topologies of the T4-4C1 trigger are shown in the right plot of Fig. 2.10.

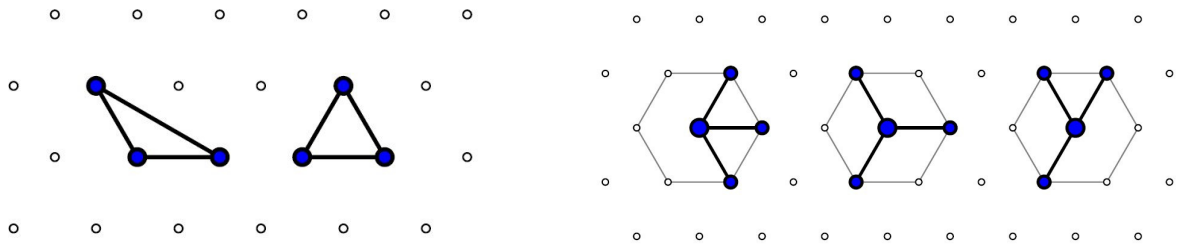

FIGURE 2.10: Examples of the T4 trigger configurations [140], for the T4-3ToT (left panel), and the T4-4C1 (right panel) modes.

The trigger times have to be compatible with a plane shower front of speed of light, i.e. time compatibility among the triggered stations is required, as the difference in trigger start time must be lower than the distance among the stations divided by the speed of light. At zenith angles below 60°, the 4C1 trigger mode identifies with efficiency of ∼100% air showers with a median energy $\sim 3 \times 10^{18}$ eV.

Quality trigger The T5 quality trigger is the highest level trigger and ensures that only those events that can be reconstructed with a known energy and sufficient angular accuracy to improve the quality of the measured Auger energy spectrum. One objective of the T5 event selection is to filter events of partially missing signals that have their shower core near the border or any gap of the SD array. In those cases parts of the shower are probably missing and the real core position could be located outside the array. This would also lead to wrong primary energy estimations. The adopted T5 trigger requires that the detector with highest signal (hottest detector) must have at least 5 working detectors among its 6 closest neighbors at the time of the event detection and that the reconstructed shower core must be inside an equilateral triangle of working stations (see Fig 2.11).

The quality trigger aims to select high quality events, which are triggered well within the array, not on its border. Thus, the trigger assures that the shower core is properly reconstructed. The T5 trigger requires that the detector of highest signal must be surrounded by a full hexagon of active stations at the time of the event, as it shown in left panel in Fig. 2.11.

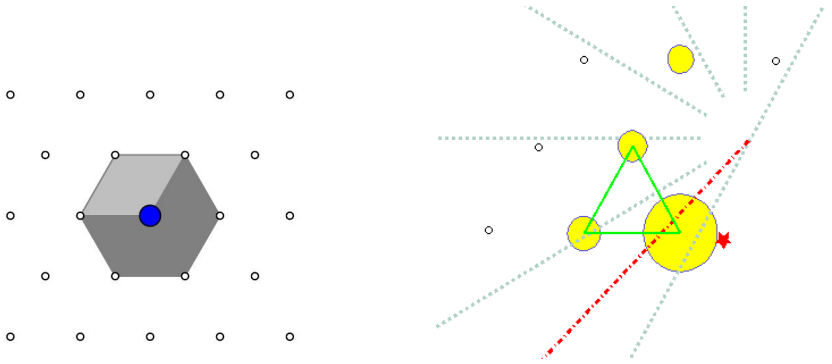

FIGURE 2.11: Left panel shows the T5 configuration [140] of a central station (blue), which received the largest signal and surrounded by 6 active stations. Right panel provides an example for non-T5 hybrid event shower, which falls on the edge of the SD array (right plot). The event is triggered by four SD detectors, indicated by filled circles, while open circles represent non-triggered ones. The size of the filled circles is proportional to the signal measured by the detector. Dashed dotted lines refer to the shower reconstructed by the FD telescope, and indicates that the shower core is located within the triangle of the detectors. In this case the event is reconstructed by 4 SD stations and one FD telescope [139].

The T5 trigger is efficient in eliminating edge array events as well as the events that have core close to a temporarily non-working detector (e.g. due to a malfunction or maintenance), however, its application could reduce the effective area by 10%.

2.2.4 Auger SD low energy modes

The low-energy modes of the Auger surface detector array has the capability to observe low-energy cosmic rays of primary energies ranging from 10 GeV to few TeV, via measuring variations in the flux of low-energy secondary particles reaching the ground level. It consists of two essential components of CR background recording: (a) the scaler mode; (b) histogram mode.

The scaler mode is particle background counter, and known as Auger single particle technique (SPT) or Auger scalers. It is installed on the entire SD array, since March 2005, and it got an updated version on September same year. Auger SD scalers record the number of signals detected above very low threshold of 3 FADC counts up to 20 FADC counts above the detector baseline, corresponding to deposited energy E_d in each individual detector between $\approx$15 MeV to $\approx$100 MeV [141–143]. The data are recorded every second, with a typical counting rate of $\sim$2 kHz and huge statistics of $\sim 1.8\times10^8$ counts/minute. The Auger scaler rate is mainly designed to search for gamma-ray bursts (GRBs) and study the modulation of Galactic cosmic rays (GCRs) due to the Solar activity (e.g., Forbush decreases and Solar cycle modulation). The Auger scalers is also very useful tool in studying and monitoring the long-term stability of the SD array.

The histogram mode is originating from the properties of the pulse signals produced by the particles interacting with the water contained in the detector. The histograms are constructed at each SD detector from the peak of each signal (peak histograms), and from the total charge deposited at the three PMTs of each detector (charge histograms). It is therefore possible to construct histograms of $E_d \sim 1$GeV, after the implementation of calibration process. The data of the histogram mode allow us to study the variations in the low-energy cosmic ray flux in different deposited energy channels (see e.g. [142–144])

This study is focused on the analysis of the data obtained using the Auger scaler mode, see details in Chapter 3.

2.2.5 Fluorescence Detector

The fluorescence detector (FD) is the second component of the Pierre Auger Observatory [145]. The FD is basically designed to measure the details of the longitudinal showers with high accuracy via measuring the faint fluorescence light. The secondaries of the extensive air shower (EAS) excite the atmospheric nitrogen molecules, so that fluorescence light in the range of 300-430 nm is emitted. This light is observed in dark moonless nights, i.e. the observational periods are restricted to the dark nights of a good weather conditions with a duty cycle of $\sim$15%.

The FD measures the rate of fluorescence emission, whereas the *longitudinal development profile* $\frac{dE}{dX}(X)$ of the EAS is specified as a function of atmospheric slant depth X. Subsequently, it can measure the energy of the primary cosmic particle by estimating the total energy dissipated electromagnetically, via the integral of the longitudinal development profile $\frac{dE}{dX}(X)$. This energy is considered as $\sim$90% of the total energy of the primary cosmic rays, and the remaining 10% represents the so-called *invisible energy*, which could be carried by neutrinos and high energy muons that haven't deposited their energy in the atmosphere, as they need long path to release their energies at the ground level.

Design The fluorescence detector (FD) consists of 24 Schmidt telescopes distributed in four observational sites, which are Los Leones, Cohiueco, Loma Amarilla, and Los Morados, located on the perimeter of the SD array. At each FD site six telescopes exist, each of them has a field of view of $30^\circ \times 30^\circ$ in azimuth and elevation. The telescopes are directed towards the SD array interior, so the six telescopes in each observational site cover 180° in azimuth angle. The telescopes arrangement inside an observational site is shown in Fig. 2.12.

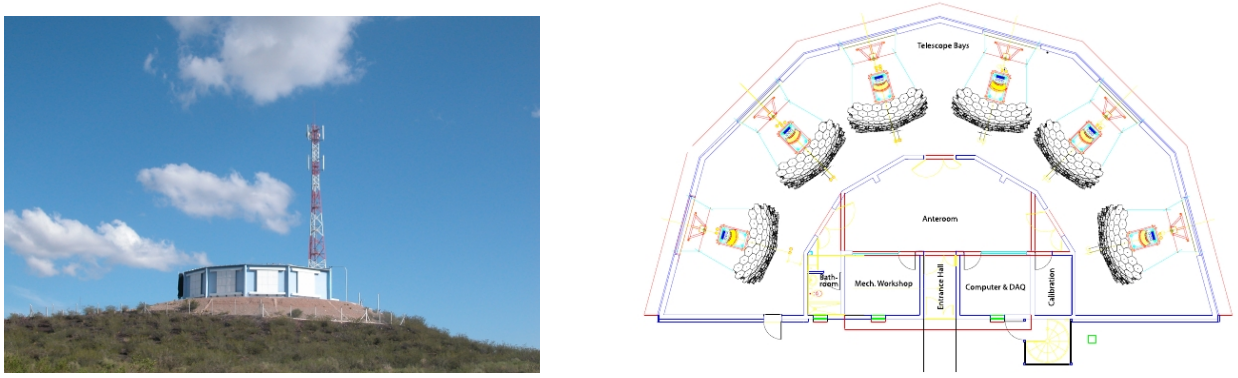

FIGURE 2.12: A photo and schematic view for one FD site (Los Leones) with six fluorescence telescopes [131, 145].

The telescopes are protected in a clean climate-controlled building. As an example, one fluorescence telescope is depicted in the left plot of Fig. 2.13.

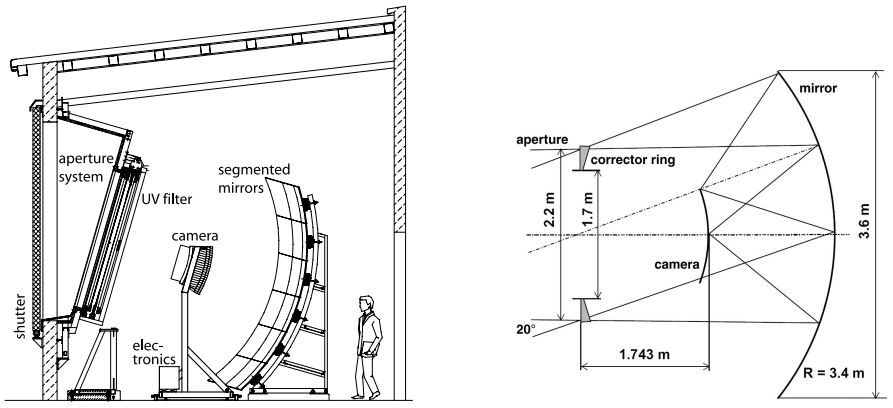

FIGURE 2.13: Left panel presents schematic view of one fluorescence telescope [145]. Right panels shows the geometrical design of the telescope optical system and its basic components.

The optical system in the fluorescence telescope is composed of a filter at the entrance of a large window that contains a heavy shutter to protect the entire system, a circular aperture, a corrector ring, a mirror and a camera with PMTs. Its geometrical design is shown in the right plot of Fig. 2.13. The florescence light is coming to enter through the large windows of a filter that allows the passage of the UV light only. The air-fluorescence light from nitrogen enters through a large window of UV-passing filter and a Schmidt optics corrector ring. Each telescope has a mirror of $10\,\mathrm{m}^2$ that overlooks a camera of 440 pixels and photomultiplier light sensors. These pixels digitize the light pulses every 100 ns, and then trigger levels are applied hierarchy to detect and measure the cosmic showers.

2.2.6 Recent Enhancements

The Pierre Auger Observatory has been enhanced with three new detectors, which are Auger muons and infill for the ground array (AMIGA) [146], the high-elevation Auger telescopes (HEAT) [131, 147], and the Auger engineering radio array (AERA) [148, 149]. These new detectors are aiming at expanding the detection threshold of the cosmic rays down to 10^{17} eV by providing a better measurements of muonic component.

Chapter 3

Analysis of the Auger SD Scaler Rate

The scalers and/or the single particle technique is a background measuring mode, and it has been used for GRB search by many cosmic ray experiments, such as INCA in Bolivia [150], EAS-TOP in Italy [151], ARGO-YBJ in Tibet [152, 153], and Andyrchy EAS array in Russia [154, 155], albeit no GRB candidate has been detected so far. The Auger scalers have been set on each individual SD detector since March 2005, and got an updated version in September 2005. The aim of the Auger SD scalers is substantially to investigate candidates for the γ-ray bursts and to pursue the monitoring studies [156–158]. Auger SD scalers are recording the rate of low-energy cosmic ray particles that deposit energy in a range of 15 MeV$\lesssim E_d \lesssim$100 MeV in the water-Cherenkov detectors of the SD array [129, 159–161], which corresponds to a threshold of 3 FADC counts up to 20 FADC counts above the detector baseline. The average rate per detector is $\sim$2 kHz, with large statistics of $\sim 1.8\times10^8$ count/minute, which allows to study modulations of Galactic cosmic rays (GCRs), transient phenomena related to the Solar activity at the weekly (Forbush decreases), and the Solar Cycle at long timescales [141, 158].

The first long-term analysis of GCR flux has been obtained by the Auger Collaboration [142] using the data measured by the Auger SD low-energy modes (scalers and histogram), which showed their sensitivity to the Solar Cycle variation. Therefore, the Solar modulation of GCR flux has been monitored over 8-year period. Furthermore, a good correlation is found between the Auger low-energy modes and data from Neutron Monitors of different rigidity cut-offs, as well as a global maximum in GCR flux is observed in 2009 by both Auger low-energy modes and Neutron Monitors, as a consequence of the Solar minimum that took place in that year.

At a short-timescale (second) the Auger SD scalers have been proposed to search for γ-ray burst (GRB) emission [156, 157, 162], which can be detected as a significant excess of the number of

detected particles above the regular cosmic rays (CR) background level. The signal above the CR background can be probed using, e.g., the $\sigma - \delta$ method [163].

In § 3.1, the data measured by the Auger SD scaler from ten-year period (2006-2015) have been analyzed. The standard data quality cuts, i.e, no detectors with abnormal rate or Area over Peak (AoP) values, no selection for acquisition periods of low number of active detector or lightning/strong wind, have been performed. Additionally, the corrections for the long-term evolution of the SD detector response (aging factor/AoP parameter) and the influence of atmospheric pressure are applied to the dataset. In § 3.2 and § 3.3, the search for statistically significant excesses of the average scaler rate over the CR background, which can be relevant to the very-high energy γ-ray emission, is performed using the $\sigma - \delta$ method of a short (one second) timescale and variability method of intermediate (minutes) timescale.

3.1 Data cleaning and corrections

In order to search for candidates for either γ-ray bursts or astronomical γ-ray flares using the Auger SD scalers [141, 156], the following data cleaning steps and corrections are done by:

1. discarding the data taken during thunderstorms[1] or at the wind speed exceeding 70 km/h, to evade artificial excess in count rate in the surface detectors[2],

2. removing the periods of low number of active stations, when the loss is larger than 5% compared to a median value, which is verified over a few consecutive days,

   The percentage of the loss in the data, is shown in Fig. 3.1 and Tab. 3.1, including the periods excluded from the whole dataset (2006-2015) for the following reasons:

   - lightning periods,
   - strong wind ($>$70 km/h),
   - change in the number of working detectors, exceeding 5% with respect to the median value,
   - major SD acquisition instabilities, the so-called "T3 bad periods" [164–166].

[1] To search for lightning periods in the Auger SD data acquisition, we have used the function *IsLightningEvent()* from CDAS/Ec package [164, 167]. Whenever the lightning event was found, all data within $\pm$1 hour around its time have been excluded. The resulting list of lightning periods represents the union of such 2-hour intervals.

[2] A very strong wind ($>$70 km/h) generates static charging of the plastic detectors. Consequently, an artificial excess in the count rate in the detectors is recorded [168].

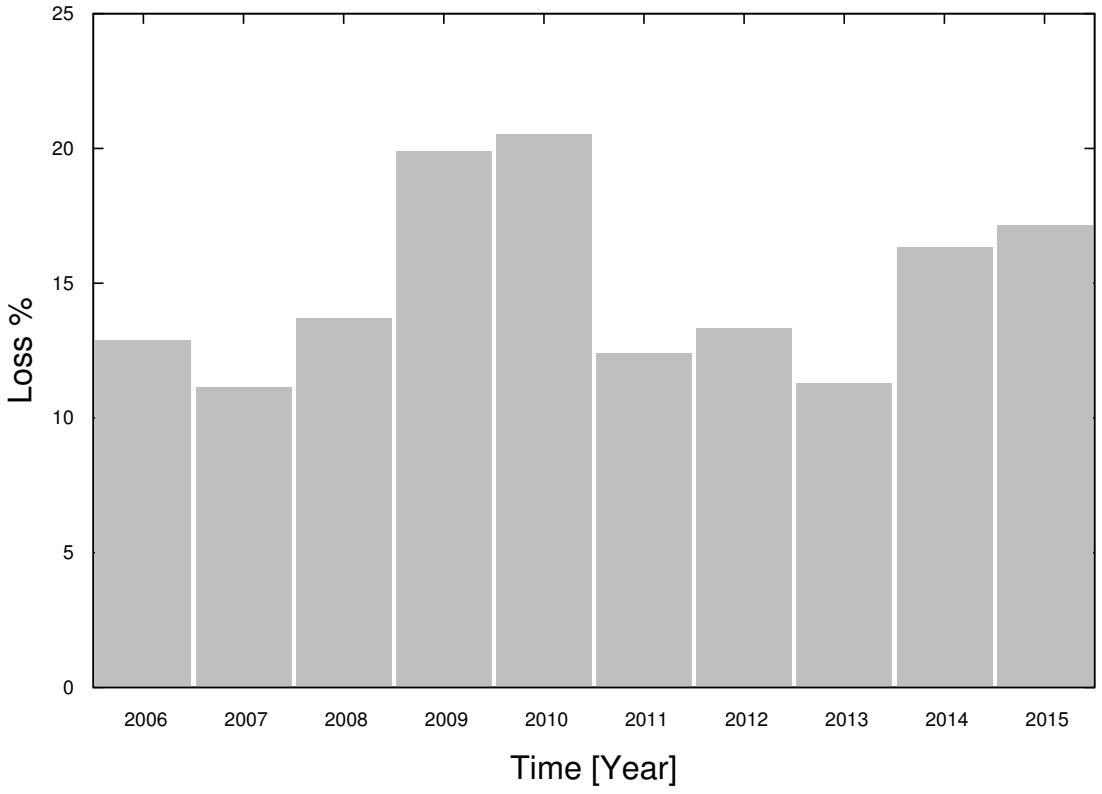

FIGURE 3.1: Scaler data fraction excluded per year in the period 2006-2015.

Date [yyyy]	Lightning [%]	Strong wind [%]	Change in the number of active detectors [%]	SD instabilities-T3 [%]	Total loss [%]
2006	1.52	0.48	10.80	0.19	12.88
2007	3.11	0.18	7.66	0.57	11.13
2008	3.82	0.46	9.49	0.34	13.69
2009	2.08	0.25	19.39	0.16	19.88
2010	2.57	0.14	19.00	0.18	20.51
2011	3.10	0.09	9.68	0.62	12.38
2012	3.46	0.05	18.70	1.78	13.34
2013	3.73	0.02	7.82	1.05	11.28
2014	3.12	0.09	11.94	1.61	16.32
2015	4.54	0.00	10.71	3.15	17.13

TABLE 3.1: Percentage of the loss in Auger scaler data (2006-2015) due to the different quality cuts.

3. excluding from the analysis detectors with an abnormal rate distribution, which could manifest e.g. noisy or unstable baselines, unstable PMTs etc,

4. skipping stations which record counts less than 500 Hz,

5. skipping 2.5% of highest and 2.5% of lowest counts for each second,

6. correcting for the Area over Peak (AoP) parameter of detector aging [141, 142, 169],

7. correcting for the atmospheric pressure and

8. calculating the average scaler rate for each second.

3.1.1 Correction for the Area over Peak

The Area over Peak (AoP) ration [141, 142, 169] of the muon signals is an indicator of the detector pulse response to individual muons. It is defined as the ratio of the deposited charge (VEM_{q}) to the peak (VEM_{p}) of the pulses resulted from the passage of single vertical muon trough the water volume contained in the water Cherenkov detector

$$AoP = \frac{VEM_{\mathrm{q}}}{VEM_{\mathrm{p}}}. \tag{3.1}$$

The importance of the AoP ratio comes from the fact that the output PMT signal from a single vertical muon in Auger water Cherenkov detectors shows a prompt increase followed by an exponential decay, which is basically contingent on single/multiple reflections of the Cherenkov light by the inner liner wall of the individual detector. As the decay part of the signal relies strongly on the reflection coefficient of the detector liner and the transparency of the water, the AoP ration of the signal is an intrinsic tool for monitoring the detectors response, including scaler rate, and is also used for specifying the detectors that show abnormal distribution of the count rate. The correlation between the scaler rate and Area over Peak shown in Fig. 3.2.

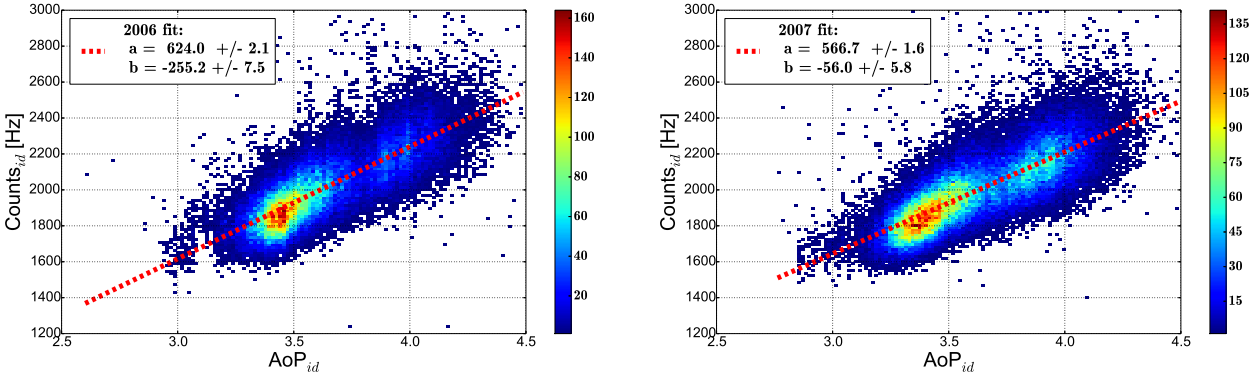

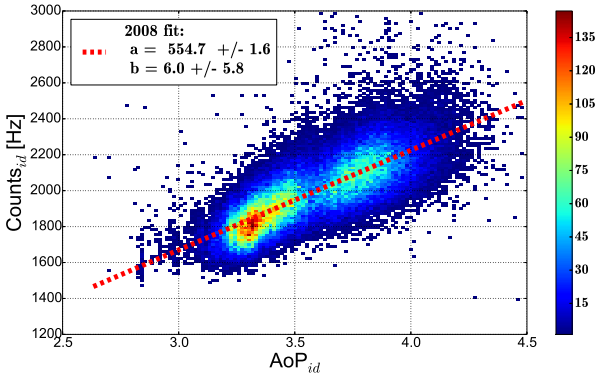
2008 fit:
a = 554.7 +/- 1.6
b = 6.0 +/- 5.8
Counts$_{id}$ [Hz]
AoP$_{id}$

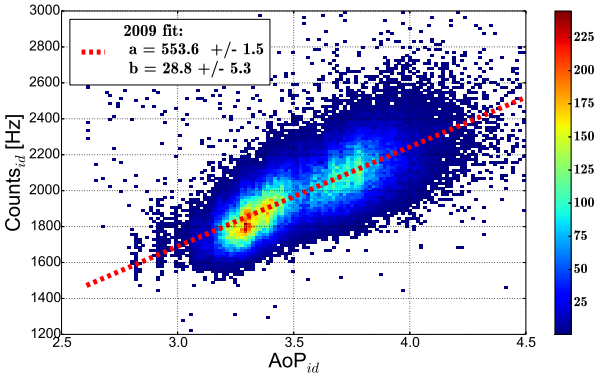
2009 fit:
a = 553.6 +/- 1.5
b = 28.8 +/- 5.3
Counts$_{id}$ [Hz]
AoP$_{id}$

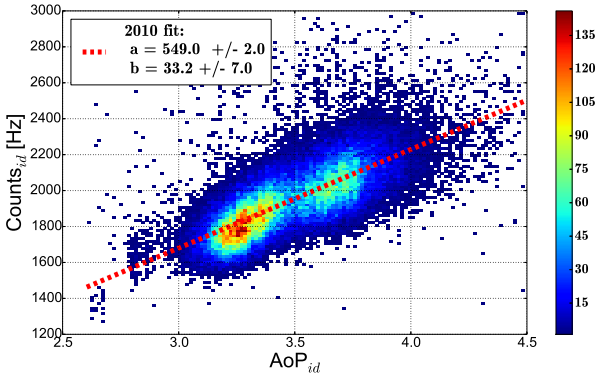
2010 fit:
a = 549.0 +/- 2.0
b = 33.2 +/- 7.0
Counts$_{id}$ [Hz]
AoP$_{id}$

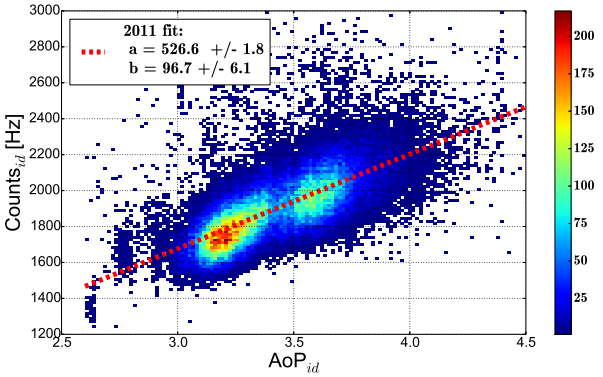
2011 fit:
a = 526.6 +/- 1.8
b = 96.7 +/- 6.1
Counts$_{id}$ [Hz]
AoP$_{id}$

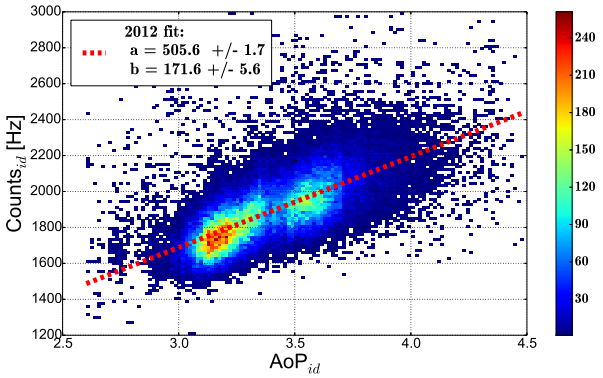
2012 fit:
a = 505.6 +/- 1.7
b = 171.6 +/- 5.6
Counts$_{id}$ [Hz]
AoP$_{id}$

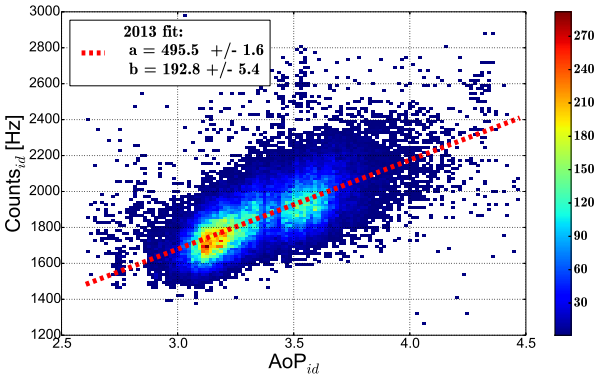
2013 fit:
a = 495.5 +/- 1.6
b = 192.8 +/- 5.4
Counts$_{id}$ [Hz]
AoP$_{id}$

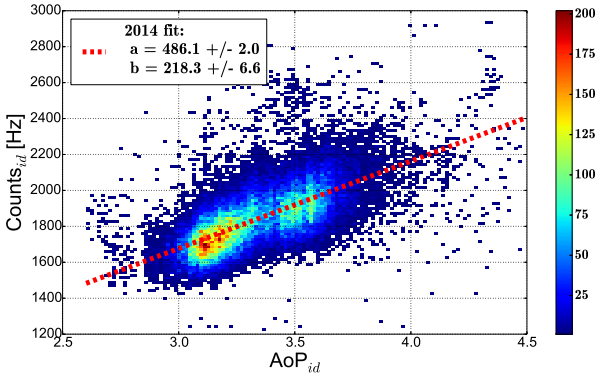
2014 fit:
a = 486.1 +/- 2.0
b = 218.3 +/- 6.6
Counts$_{id}$ [Hz]
AoP$_{id}$

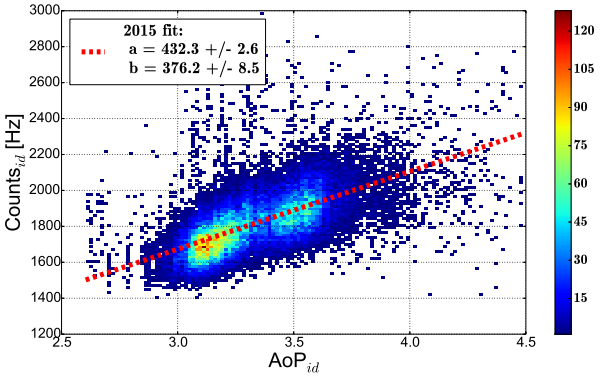
2015 fit:
a = 432.3 +/- 2.6
b = 376.2 +/- 8.5
Counts$_{id}$ [Hz]
AoP$_{id}$

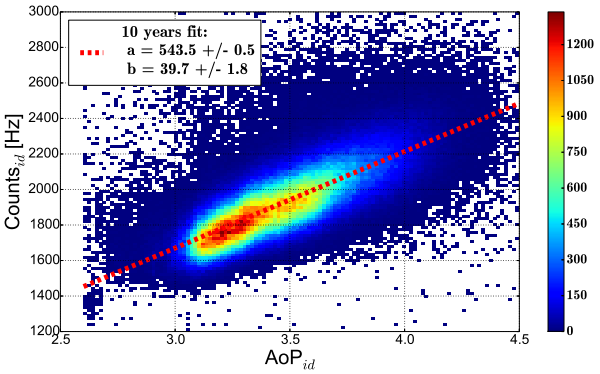

FIGURE 3.2: Two dimensional histograms show correlation between the AoP values and SD scaler rate for the years 2006 to 2015. The data are plotted every five days, with a separate figure for each year, besides the linear fit results represented by the dashed lines. The last panel shows a joint fit of the data from the ten years, resulting in a linear coefficient $a = 543.5 \pm 0.5$.

The linear correction of the rate of individual detectors is performed using Eq. 3.2

$$S_{id}(t)^{corr/AoP_{id}} = S_{id}(t) - a(AoP_{id}(t) - \langle AoP_{id}(t)\rangle), \tag{3.2}$$

where $S_{id}(t)$ and $AoP_{id}(t)$ are the scaler rate of detector *id* and the Area over Peak value (averaged over the 3 PMTs) at a given time t, respectively.

With respect to Fig. 3.2, a strong correlation is found between the scaler rate and the AoP values. Detectors of large AoP values shows large scaler rate. This can be interpreted as detectors of large AoPs exhibit higher response to individual particles than the ones of smaller AoP values. The bulk of AoPs ranges from ∼3 to ∼4, which is mainly the range dedicated to regular detectors. The values of the yearly linear coefficients and scaler rates S_{id} with AoP_{id} show gradually decrease over time, shown in Fig. 3.3.

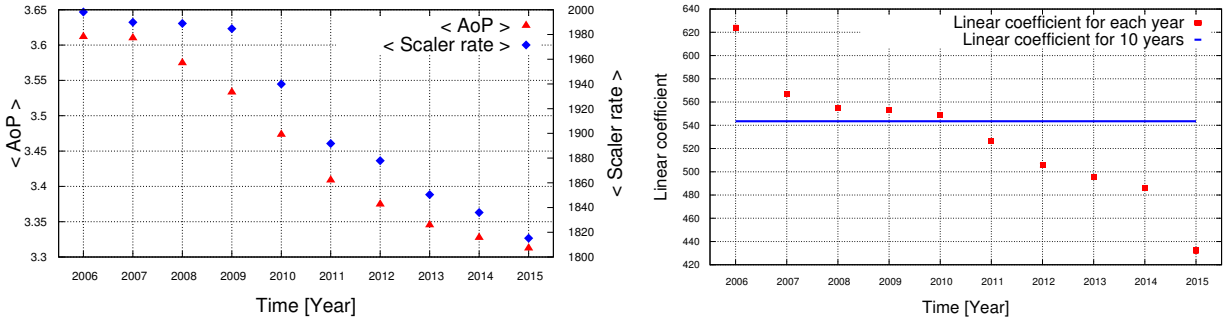

FIGURE 3.3: A common decline behavior of the response of the Auger detectors. Left panel presents the diminution of the average AoP and scaler rate values over ten years. Right panel shows the decline of the linear coefficient obtained per each indicated year in Fig. 3.2, as well as the horizontal line represents the slope value for the ten years (2006-2015).

3.1.2 Correction for atmospheric pressure

The Pierre Auger Observatory has various weather stations, which enable us to measure atmospheric parameters, such as atmospheric pressure, temperature, and air density. These atmospheric variables affect the development of extensive air showers produced by cosmic ray of high energies at the top of the atmosphere. Therefore, the weather measurements, which are recorded every 5-minute intervals, are essentially used for many studies, e.g., the search for large scale anisotropies and space weather [170]. The atmospheric pressure tends to attenuate energy of air shower particles before they reach the ground level. Hence, the measured flux of secondaries at ground level is significantly modulated by atmospheric pressure. This implies the well-known anti-correlation [141, 142, 144] between the average scaler rate and atmospheric pressure (see an example in Fig. 3.4).

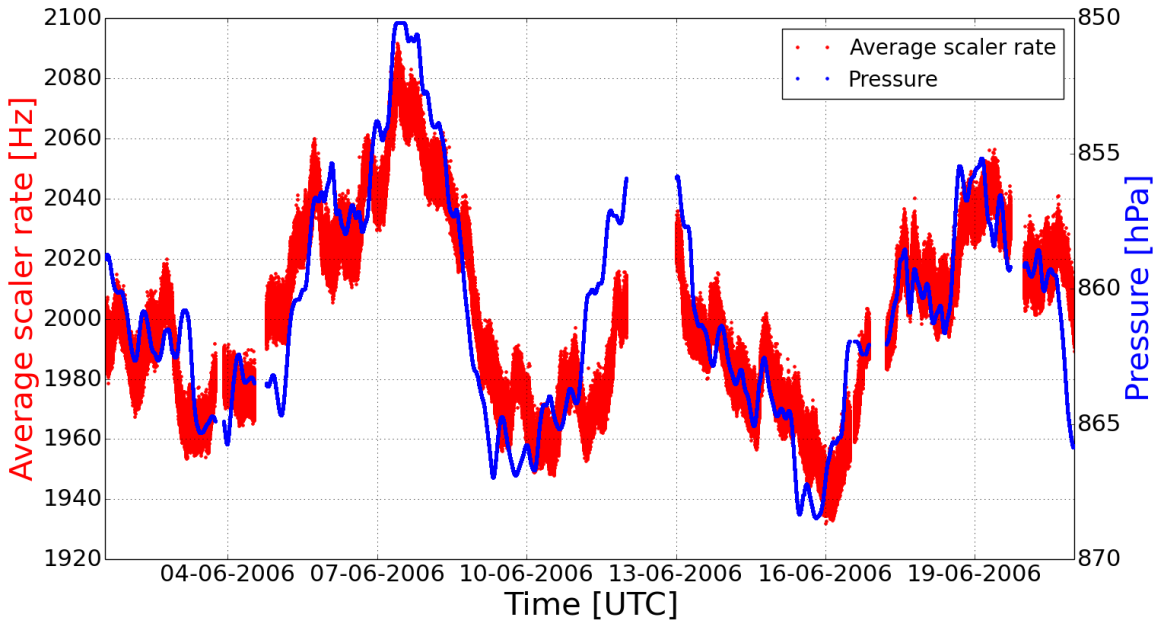

FIGURE 3.4: An example of anti-correlation between the average scaler rate (left axis) and the atmospheric pressure (right axis) of a 3-week period. The pressure measurements are obtained from the weather station of the Central Laser Facility of the Pierre Auger Observatory.

The anti-correlation between average scaler rate versus atmospheric pressure is obtained from 8-year period (2006-2013) in Fig. 3.5, along with the linear fit results.

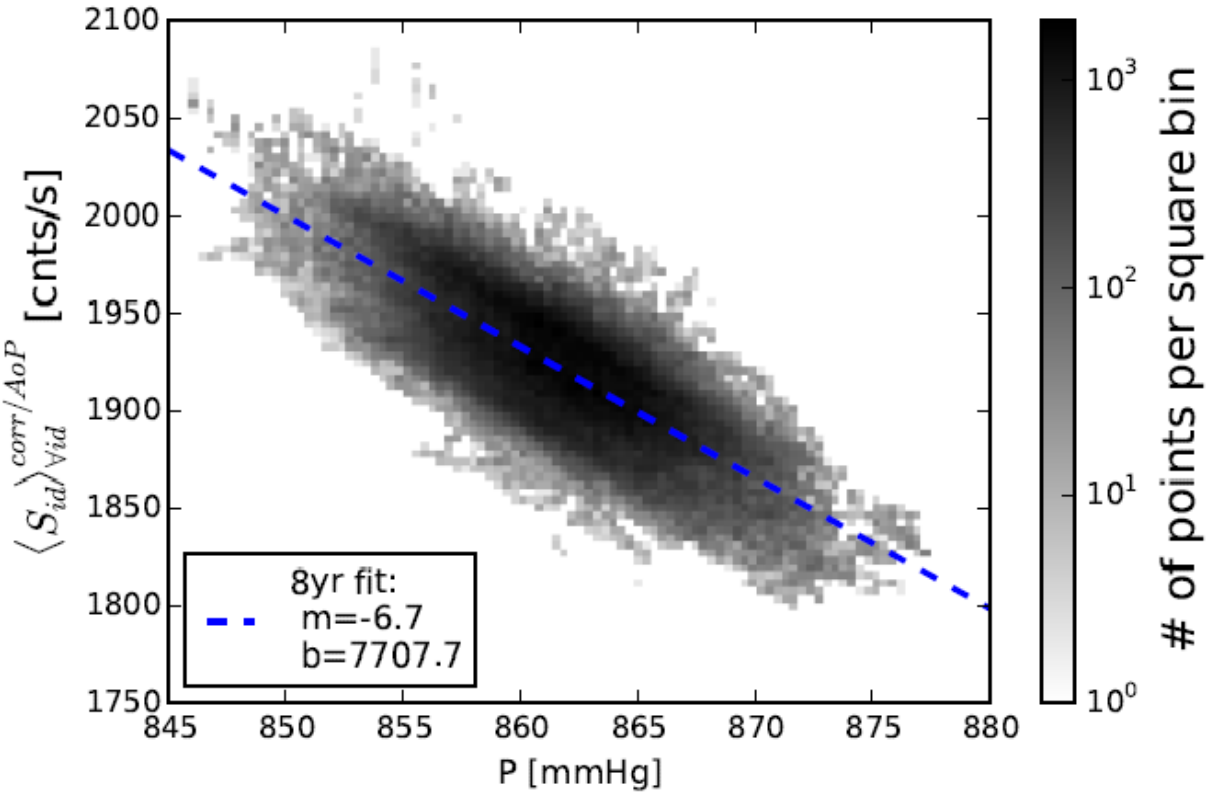

FIGURE 3.5: Two dimensional histogram of anti-correlation between the corrected scalers $S_{id}^{corr/AoP}$ and atmospheric pressure p, along with the linear fit results over 8-year period from 2006 to 2013. The gray scale indicates the number of data points per square bin over the eight years. This result is obtained by the Auger Collaborators and taken from Ref. [141].

The atmospheric pressure affects the development of air showers in the atmosphere, and hence the flux of detected particles. In order to obtain a physical signal, the average scaler rate has to be corrected for the effect of atmospheric pressure using Eq. 3.3

$$\langle S^{corr/AoP}(t)\rangle^{corr(p)} = \langle S^{corr/AoP}(t)\rangle - a(p(t) - \langle p(t)\rangle), \tag{3.3}$$

where $\langle S^{corr/AoP}(t)\rangle$ is the corrected scaler rate for the AoP, a is the linear coefficient -6.7, and $p(t)$ is the atmospheric pressure value at a given time t.

3.1.3 Long-term average scaler rate (2006-2015)

The long-term average scaler rate for both raw and cleaned scaler data is obtained after performing the prior data cleaning steps and corrections (see Fig. 3.6).

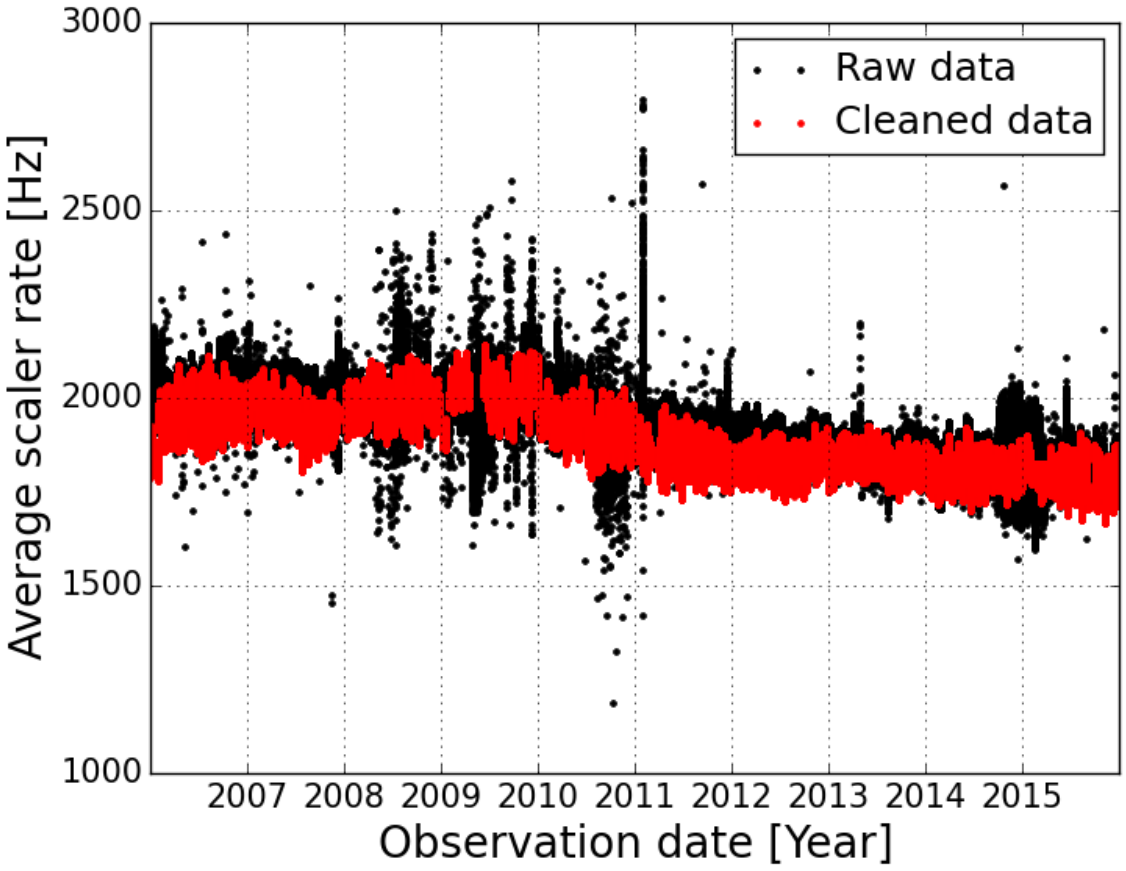

FIGURE 3.6: Long-term average scaler rate for the years 2006-2015. Black dots show raw scaler data. Red dots represent cleaned and corrected scaler data for the AoP and atmospheric pressure effects.

The long-term average scaler rate shows a good correlation with the rate evolution of low-energy cosmic rays detected by the Neutron Monitors [142]. A global maximum in the average scaler rate is obviously observed in the year 2009, due to an increase in the GCR flux during the Solar minimum that took place in that year.

The Neutron Monitors are ground-based detectors designed to measure the flux of low-energy cosmic rays and their variations with different timescales (e.g., Solar Cycles, Forbush decreases, and ground level enhancements) at ground level. The comparison between the Auger scaler rate and the data from Neutron Monitors of different rigidity cut-offs showed a good correlation (see Fig. 3.7), in which the Solar modulation of GCR flux has been monitored [142] over 8-year period by Auger SD scalers for the first time (see Fig. 3.7).

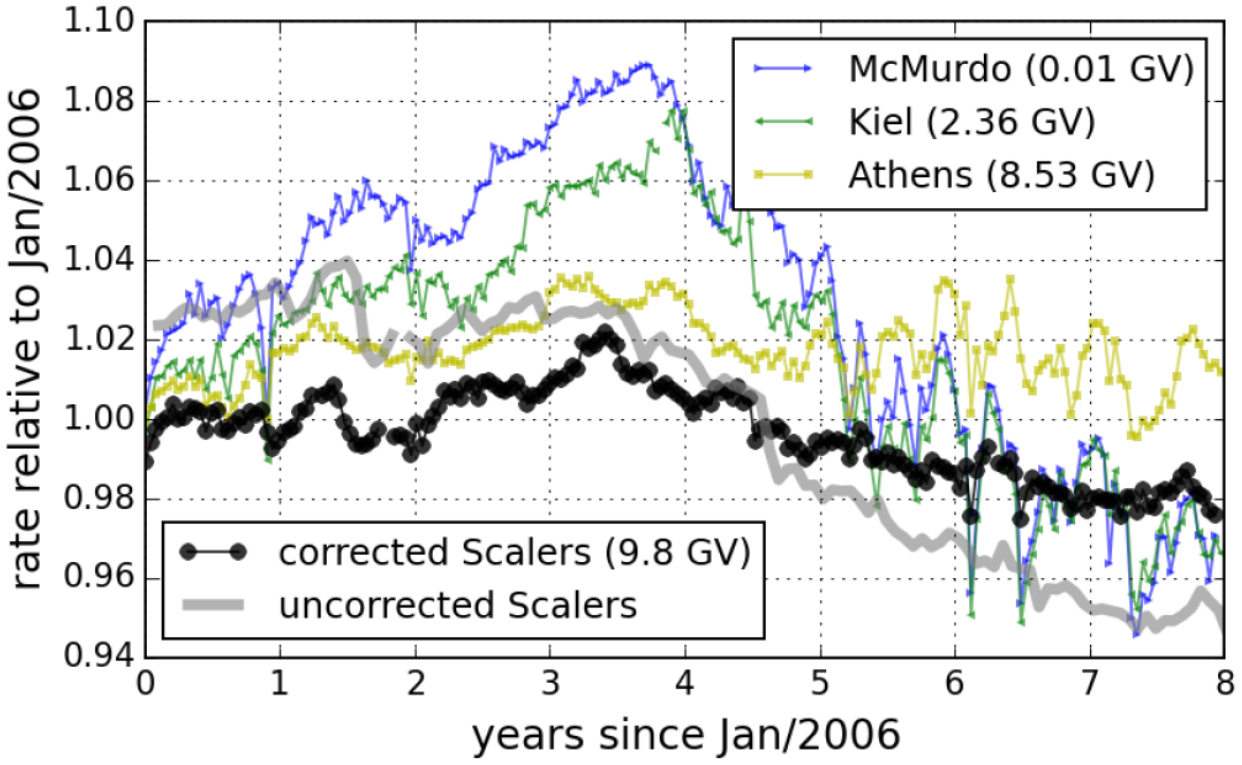

FIGURE 3.7: A comparison of the Auger SD scalers with data from Neutron Monitor stations of different rigidity cut-offs over 8-year period (2006-2013). Black dots represent Auger scaler dataset, which is corrected for pressure and AoP. Gray line indicates Auger scalers without AoP correction. A good correlation is found between Auger scalers and the Neutron Monitor measurements for different rigidity cut-offs. A global maximum in GCR flux is observed by Auger SD scalers and Neutron monitors. This result is obtained by Auger Collaborators and taken from Ref. [142].

In this work the search for the very-high energy γ-ray emission at a second and minute timescales is implemented using the data measured by the Auger low-energy scaler mode (see § 3.2 and § 3.3).

3.2 $\sigma - \delta$ method

A cascade of secondary particles is produced, when high energy photons from a GRB event bombard the Earth's atmosphere. The GRBs can be probed as an increase of the count rate in all detectors [171]. Several methods have been used to estimate the excess above the CR background, such as $\sigma - \delta$ method [156, 163] and the normalized fluctuation function [172]. These methods give a normally distributed observable pertained to global variation of the count rate in individual detectors.

In order to search for the GRB candidates, which can be observed as significant excesses above the regular CR background, with the Auger SD scalers, the $\sigma - \delta$ method has been implemented.

The $\sigma - \delta$ is a non-linear method of background subtraction [163]. The method is optimized for a second-timescale and implies a comparison between the current rate r and the expected one R, with fluctuation $\sigma = 10$ and elementary increment/decrease $\delta = 0.1$ Hz. Thus, an expected rate for each second is specified, in the sense that the expected rate R converges to the current one by $\delta = 0.1$ Hz. Both σ and δ are arbitrary values. The fluctuation Δ of the current rate for a specific second is given by

$$\Delta = \frac{r - R}{\sqrt{r/N}}, \tag{3.4}$$

where N is the number of active detectors of that second. The implementation of the $\sigma - \delta$ method over cleaned Auger scaler data reveals 79 seconds of excesses ($\geq 5\sigma$) from the mean of distribution of the average scaler rate fluctuation, shown in Fig. 3.8 and Tab. A.1.

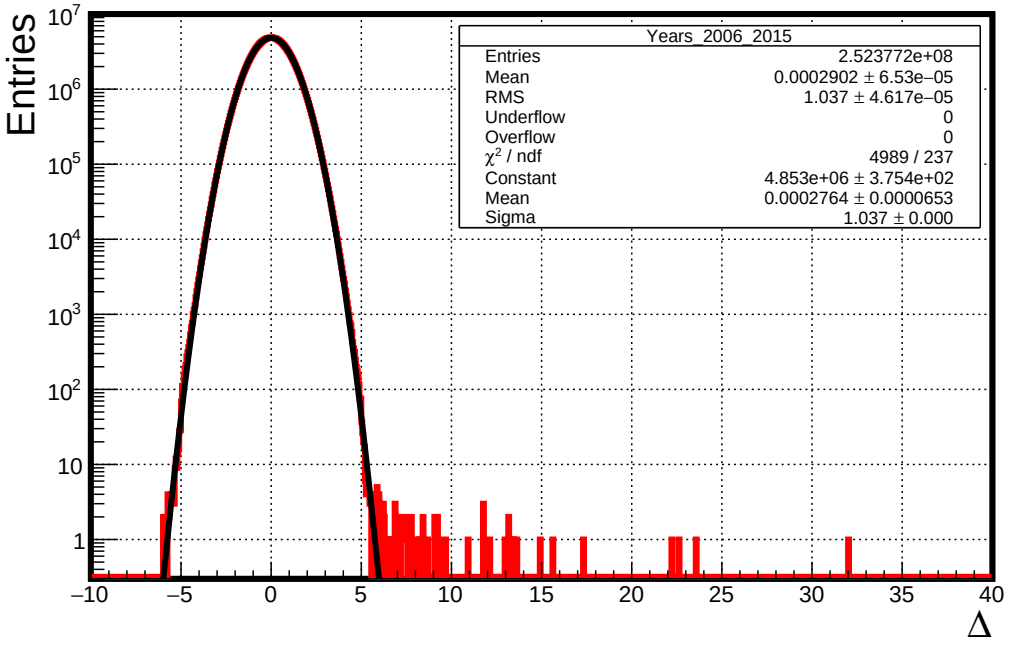

FIGURE 3.8: Average scaler rate fluctuation for the years 2006-2015 obtained using $\sigma - \delta$ method. Several seconds of excesses in the average scaler rate are revealed above the CR background.

The background subtraction/fluctuation is calculated using Eq. 3.4, and represented by the underlaying Gaussian distribution in Fig. 3.8. The parameter Δ can be used directly to search for statistically significant excess, which can be a consequence of GRB event. Such significant excesses are shown on the positive side of the histogram in Fig. 3.8, and explained as an increase of the flux of secondary particles at the ground level.

The seconds of excesses are distributed over two dates, which are October 28, 2008 and December 31, 2015. Such dates of excesses in the average scaler rate show high quality data of SD

array stability and good weather conditions (no period of strong wind is recorded by Auger space weather stations), however, two lightning events are triggered at GPS seconds 1135540667 and 1135541601, as well as one lighting event at GPS second 1135630788 by the CDAS lightning sensor on December 30 and 31, 2015, respectively. These seconds of lighting events are far from the time of the observed excesses, albeit the observed excesses within the time interval [0h, 1h] UTC could be relevant to the lightning events of the night before (December 30, 2015). The average scaler rate measurements of those two dates are shown in Fig. 3.9.

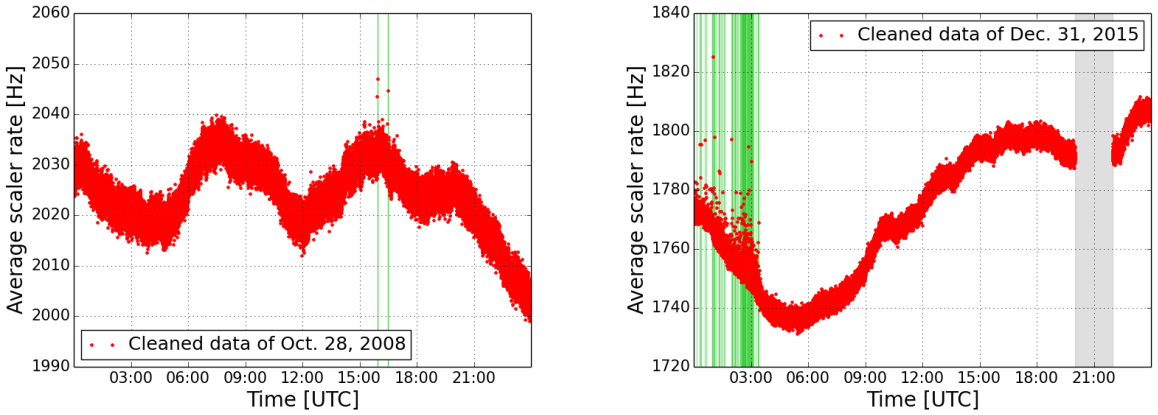

FIGURE 3.9: Average scaler rate of October 28, 2008 (left plot) and December 31, 2015 (right plot). The green vertical lines indicate the seconds of excesses observed by the $\sigma - \delta$ method in both plots. The gray band in the right plot shows lightning period cut on December 31, 2015.

3.2.1 Scaler rate distributions of the probed seconds of excesses

During GPS second 909244576, 277 detectors showed an increase in the count rate at a level $>1\sigma$, corresponding to $\sim$115 Hz from the main value of the count rate distribution of the second of excess, where $\sigma = \left(\sigma_{s_{before}} + \sigma_{s_{after}}\right)/2$ specified with respect to the previous (of $\sigma_{s_{before}}$) and next second (of $\sigma_{s_{after}}$) to the second of excess. At GPS second 909246605, there are 285 detectors of excess in the count rate at a level $>1\sigma$, corresponding to $\sim$120 Hz from the main value of the count rate distribution of the second of excess.

The distribution of the corrected SD count rate for AoP and atmospheric pressure influence, within the time of excesses, is shown in Fig. 3.10.

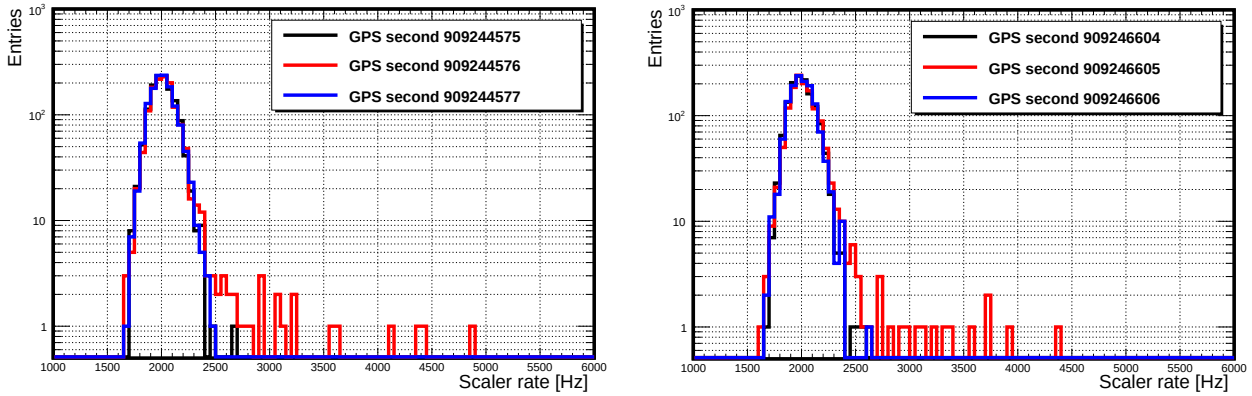

FIGURE 3.10: Scaler rate distributions of the two seconds of excesses observed in October 2008 using the $\sigma - \delta$ method. Left panel shows scaler rate distribution from the entire SD array (corrected for the AoP and atmospheric pressure) for GPS second 909244576 of excess (marked in red), at 6.3σ level in the average scaler rate. Right panel presents scaler rate distribution from the whole SD array (corrected for the AoP and atmospheric pressure) for GPS second 909246605 of excess (marked in red), at 8.3σ level in the average scaler rate. In both plots the rate distribution of the previous and next second to the one of excess is marked in black and blue, respectively.

The detectors of excesses in the count rate, in both seconds of October 28, 2008, are distributed over the whole SD array (see Fig. 3.11), with a contribution from the infill array.

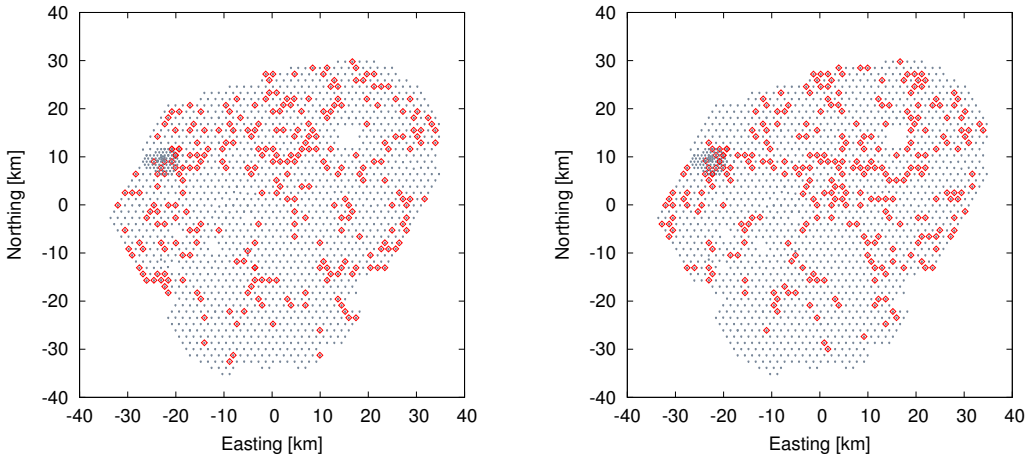

FIGURE 3.11: Maps of detectors of excesses observed in October 2008. *Left panel:* map of detectors of excesses observed at GPS second 909244576. *Right panel:* map of detectors of excesses observed at GPS second 909246605. The detectors of excesses of both seconds are distributed over the whole SD array, with a contribution from the infill array (dense points on the plots).

Both excesses are not coincident with any GRB trigger time. The GRB 081028A [173] is the only event detected on that date by *Swift* satellite at 00:25:00 UTC, with late-time afterglow re-brightening and redshift $z = 3.038$. With respect to the Auger site, this GRB was at elevation of 2.7° and -4.2° at the GPS second 909244576 (of the first excess) and GPS second 909246605 (of the second excess), respectively. Therefore, no possibility for these two seconds of increase in the count rate to be attributed to such GRB event. Interestingly, no significant excess has been

observed in the average scaler rate beyond October 2008, except for those 77 seconds of increase in the count rate probed in December 31, 2005, see an example in Fig. 3.12. The rest of the 77 seconds distributions are listed in A.2

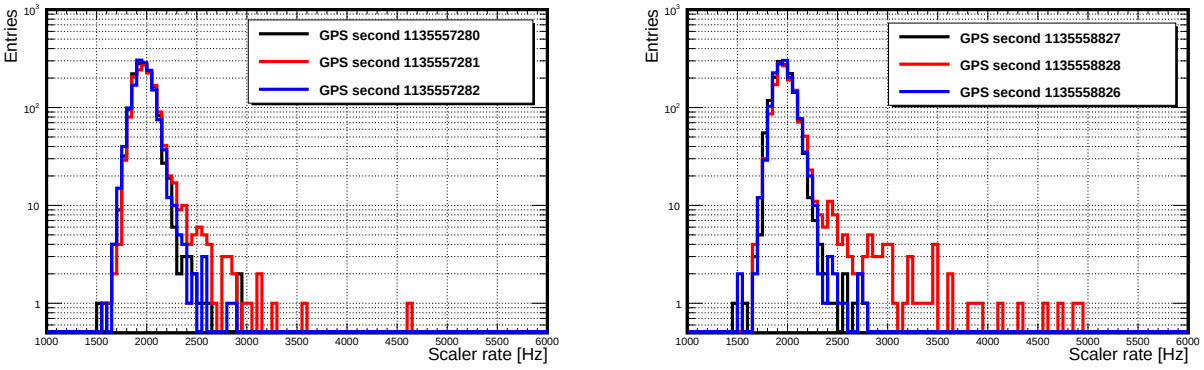

FIGURE 3.12: An example of scaler rate distributions of two seconds out of 77 seconds of excesses observed in December 2015. Left panel shows scaler rate distribution (corrected for the AoP and atmospheric pressure) for the GPS second 1135557282 of excess (marked in red), at 13.4σ level in the average scaler rate. Right panel presents scaler rate distribution (corrected for the AoP and atmospheric pressure) for the GPS second 1135558828 of excess (marked in red), at 32σ level in the average scaler rate. In both plots the rate distribution of the previous and next second to the one of excess is marked in black and blue, respectively.

An increase in the count rate is observed at the GPS 1135557281, with 370 detectors of excesses above $>1\sigma$ level, corresponding to $\sim$86 Hz from the mean value of the count rate distribution of this second of excess. Another example is the GPS 1135558828, at witch 385 detectors recorded excesses in the count rate $>1\sigma$ level. Namely, $\sim$87 Hz from the mean value of the count rate distribution of the second of excesses. The detectors of excesses are mapped in Fig. 3.13.

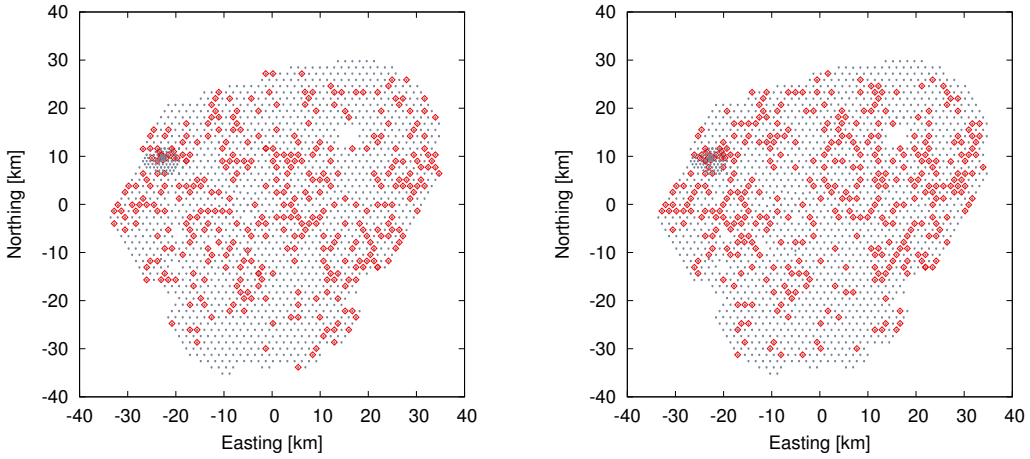

FIGURE 3.13: Maps of detectors of excesses observed in December 2015. *Left panel:* map of detectors of excesses observed at GPS second 1135557281. *Right panel:* map of detectors of excesses observed at GPS second 1135558828. The detectors of excesses of both seconds are distributed over the whole SD array, with a contribution from the infill array (dense points on the plots).

No GRB was detected by any experiment on that date of December 2015. The Crab nebula was the only source flaring at that time of the observed excess [174], and its γ-ray emission was observed by *Fermi*-LAT at HE level (E >100 MeV), see details in § 5.4 and § 6.1.7. The Crab nebula was above horizon with elevation >20° at the Pierre Auger Observatory site for more than 5 hr, during the time of the observed excesses, on December 31, 2015 (see Fig. 3.14).

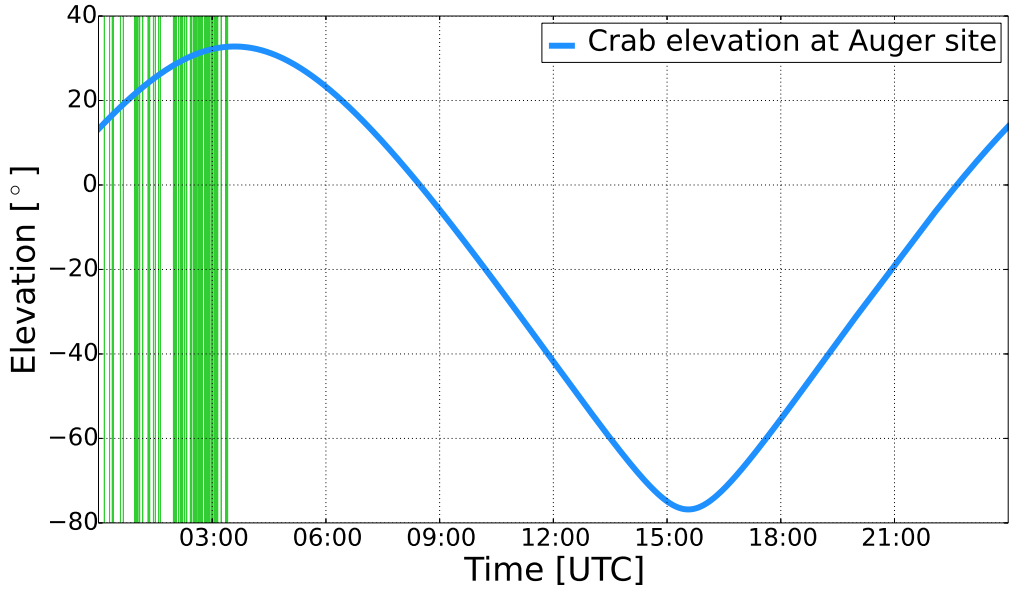

FIGURE 3.14: The Crab nebula elevation is shown as a function of time at the Pierre Auger Observatory site, on December 31, 2015. The green vertical lines mark the 77 seconds of excesses, which are detected by using the $\sigma - \delta$ method. The majority of the 77 seconds of excesses took place when the Crab was at high elevation >30° with respect to Auger site.

The large number of SD scalers (>1660) and the low deposited energy in each detector (15 MeV$\lesssim E_d \lesssim$100 MeV) propose the hypothesis that the probed excesses in the Auger SD scalers, on a second-timescale, could have astrophysical origin. In particular, the 77 seconds of excesses, which are occurred when the Crab nebula was flaring at the Malrgüe sky, on December 31, 2015. This suggests us to expand the search for very-high energy γ-ray emission, using the data measured by Auger low-energy scaler mode, to minute-timescale.

3.3 Variability method

In order to search for the excesses above the CR background on a minute-timescale, a test for variability [175, 176] has been applied to the cleaned and corrected Auger scalers dataset, which showed its sensitivity to variations of low-energy cosmic ray fluxes at different timescales. The average scaler rate over the whole SD array shows diverse features (see Fig. 3.6 and Fig. 3.9).

Each detector has different altitude, so that the detectors baselines are fluctuating. Accordingly, it is very important to specify the baseline of the average scaler rate, above which the search for the excess is implemented. To quantify the baseline, we have calculated the variability (*normalized excess variance* σ^2) of the average scaler rate over the entire SD array for each consecutive 5-minute intervals, using

$$\sigma^2 = \frac{1}{N\mu^2}\sum_{k=1}^{N}[(\chi_k-\mu)^2-\sigma_k^2]. \tag{3.5}$$

In Eq. (3.5), χ_k and σ_k are the average scaler rate and the corresponding error for the second k, respectively, where $(k=1,2,\ldots,N)$, $N=300$ is the number of the average rate measurements, and μ is the unweighted average of the χ_k values. The error given by σ_k parameter ranges from 1 to 2 Hz.

The choice of the interval length of 5 minutes allows us, on one hand, to have a large sample of average rate measurements, and on the other hand, to possibly probe the variability time structure, since this time interval is smaller than typical durations of the observed TeV γ-ray sources (see e.g. [177, 178]).

The error of the excess variance[3] reads

$$\sigma_{err}/(\mu^2\sqrt{N}), \text{ where } \sigma_{err}^2 = \frac{1}{N-1}\sum_{k=1}^{N}([(\chi_k-\mu)^2-\sigma_k^2]-\sigma^2\mu^2)^2. \tag{3.6}$$

The variability test Eq. (3.5) has been used in the X-ray astronomy, e.g., in the analysis of the data sample, which is taken by ASCA satellite [179], of 18 Seyfert 1 galaxies to investigate their X-ray properties. The light curves of the 18 Seyfert 1 galaxies showed diversity of variability feature, as each source exhibited different amplitudes of count rate variability. Therefore, the variability test has been used to quantify the "normalized excess variance" for each light curve on the minute and hour timescales. None of the 18 Seyfert 1 galaxies showed significant excess in the hard X-ray flux (see Ref. [175]).

The variability method has also been performed [180] to calculate the "excess variance" for the data measured by SMARTS [181] and *Fermi*-LAT [182], in order to monitor 12 γ-ray bright blazars in the optical and infrared wavelengths.

In the Pierre Auger Observatory, the variability test is implemented for the whole cleaned and corrected Auger scalers data for the AoP and atmospheric pressure effect, from 2006-2015. As an

[3]There is a mistype in the expression for the error in [175], which has been corrected in [176].

example of the variability test application, the distribution of σ^2 values for the days of July 9, 2006 and April 27, 2013 are shown as a function of time in Fig. 3.15.

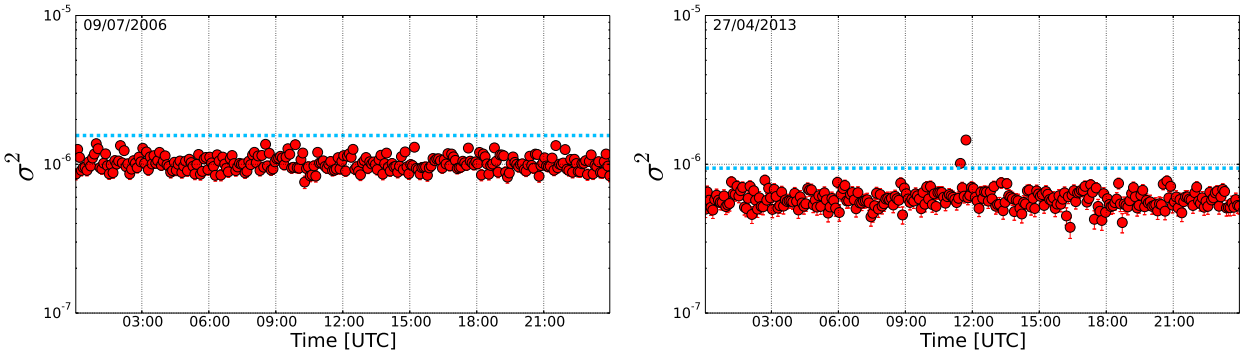

FIGURE 3.15: Two examples of application of the variability test to the average scaler rate as a function of time. Left panel shows the distribution of σ^2 values for the date of July 9, 2006. No significant excess variance has been observed on that date. Right panel presents the distribution of σ^2 values for the date of April 27, 2013. Two bins of 5-minute intervals of the average scaler rate show significant excesses $>5\sigma$ level, around 12 h UTC. The horizontal dashed line shows the 5σ significance level. The SD array was stable on both dates, and the weather conditions were good. As it is expected from the long-term evolution of the SD detector response (detector aging factor), the baseline of the variability distribution (σ^2) decreases over the years.

The histograms of the σ^2 values of the same two dates are shown in Fig. 3.16.

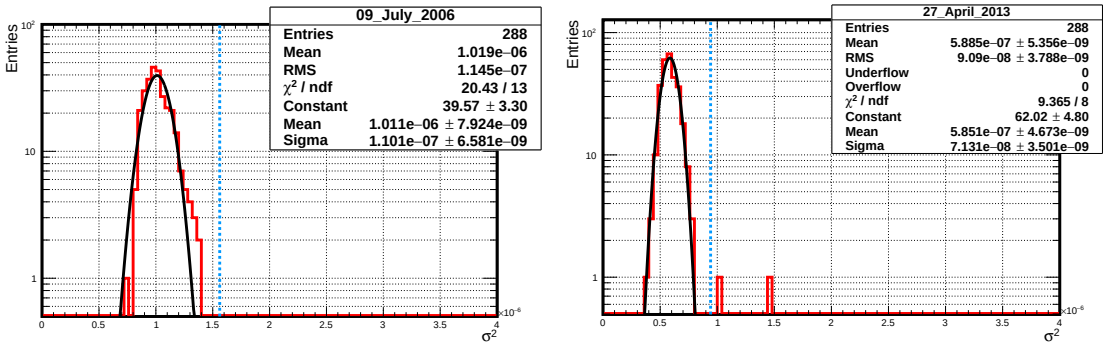

FIGURE 3.16: Two examples of histograms of average scaler rate variability. The histogram of the σ^2 values of the date of July 9, 2006 is shown in the left plot, with no significant excess in the average scaler rate variability. The histogram of the σ^2 values of the date of April 27, 2013 is presented in the right plot, with significant excesses $>5\sigma$ level. The vertical dashed line shows the 5σ significance level. As a consequence of the detector aging factor, the value of the baseline of σ^2 distribution of the date of April 27, 2013 is smaller than the one of July 9, 2006.

Figures 3.15 and 3.16 show two examples of the application of the test of variability to a couple of dates of average scaler rate measurements. No significant excess variance has been observed on the date of July 9, 2006. In contrast, the date of April 27, 2013, which shows two bins of significant excesses variability. The bin length is successive 5-minute intervals of average scaler rate of $\sim$2 kHz per detector, i.e., 300 seconds of average scaler rate measurements over the whole

SD array. The detected excesses are well above a significance level of 5σ (i.e., $> \mu + 5\varsigma$; where μ and ς are the mean and standard deviation (σ) values of the Gaussian fit, respectively) of the variability baseline distribution of that date. This means that the integral of the increase in average scaler rate of each bin of excess is above $\sim$2869 counts per the 5-minute intervals. So, we have an increase above $\sim$10 Hz for each average scaler rate value within the 5-minute intervals of the two bins of excesses, which are probed on April 27, 2013.

The variability method is performed for the whole cleaned and corrected Auger scaler measurements from the ten-year period (2006-2015) on a day-by-day basis. Consequently, 266 5-minute intervals of significant excesses of the average scaler rate variability are detected on 76 different dates. The distribution of the entire excesses as a function of time is presented in Fig. 3.17.

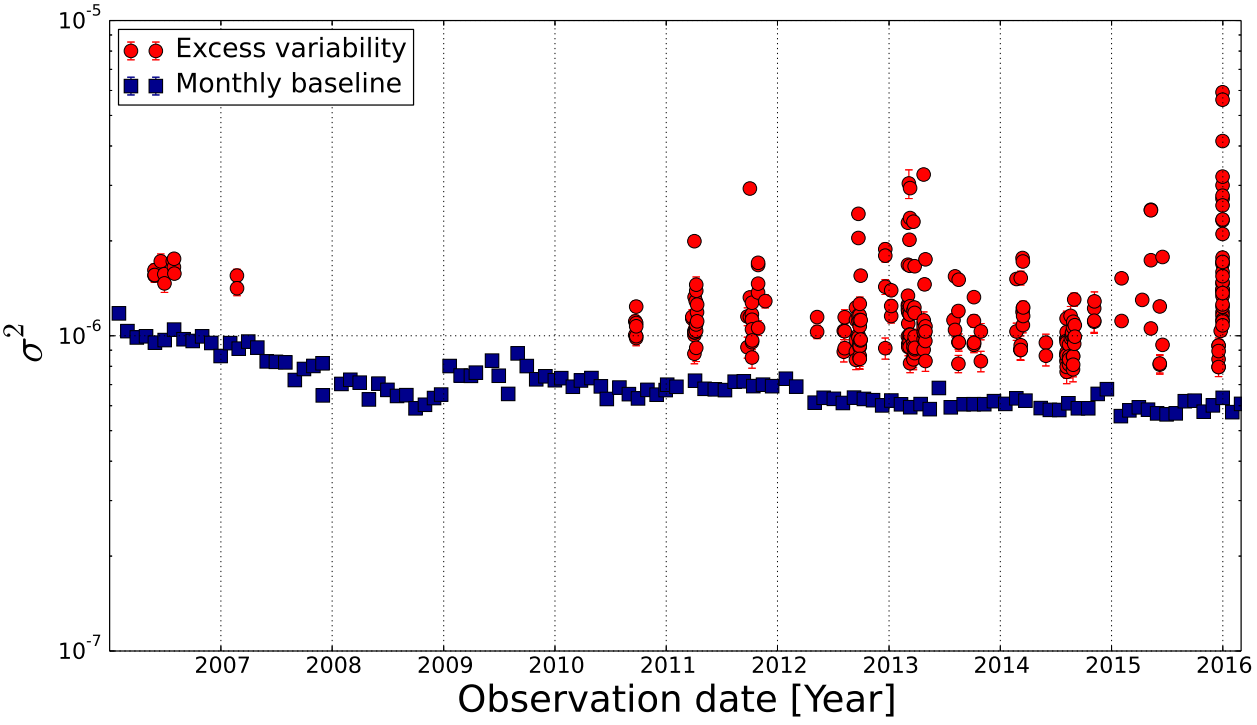

FIGURE 3.17: The detected excesses of the average scaler rate variability (266 5-minute intervals) in the ten-year period (2006-2015) are $\geq 5\sigma$ level, and spread over 76 different dates. The monthly baseline of the average scaler rate variability, which is plotted from January 2006 to February 2016, shows slow decrease throughout the years.

The SD array showed high stability during the 76 dates (out of ten-year period) of the observed excesses under good weather conditions. The values of all bins of significant excesses are listed in Tab. A.3. In the following, we present the histograms of the average scaler rate variability and its baseline for each year separately from 2006 to 2015.

3.3.1 Distributions of the average scaler rate variability (2006-2015)

By means of the variability method described in 3.3, and applied to the cleaned and corrected Auger scalers, the distributions of the average scaler rate variability from 2006 to 2015 are shown for each year in Fig. 3.18.

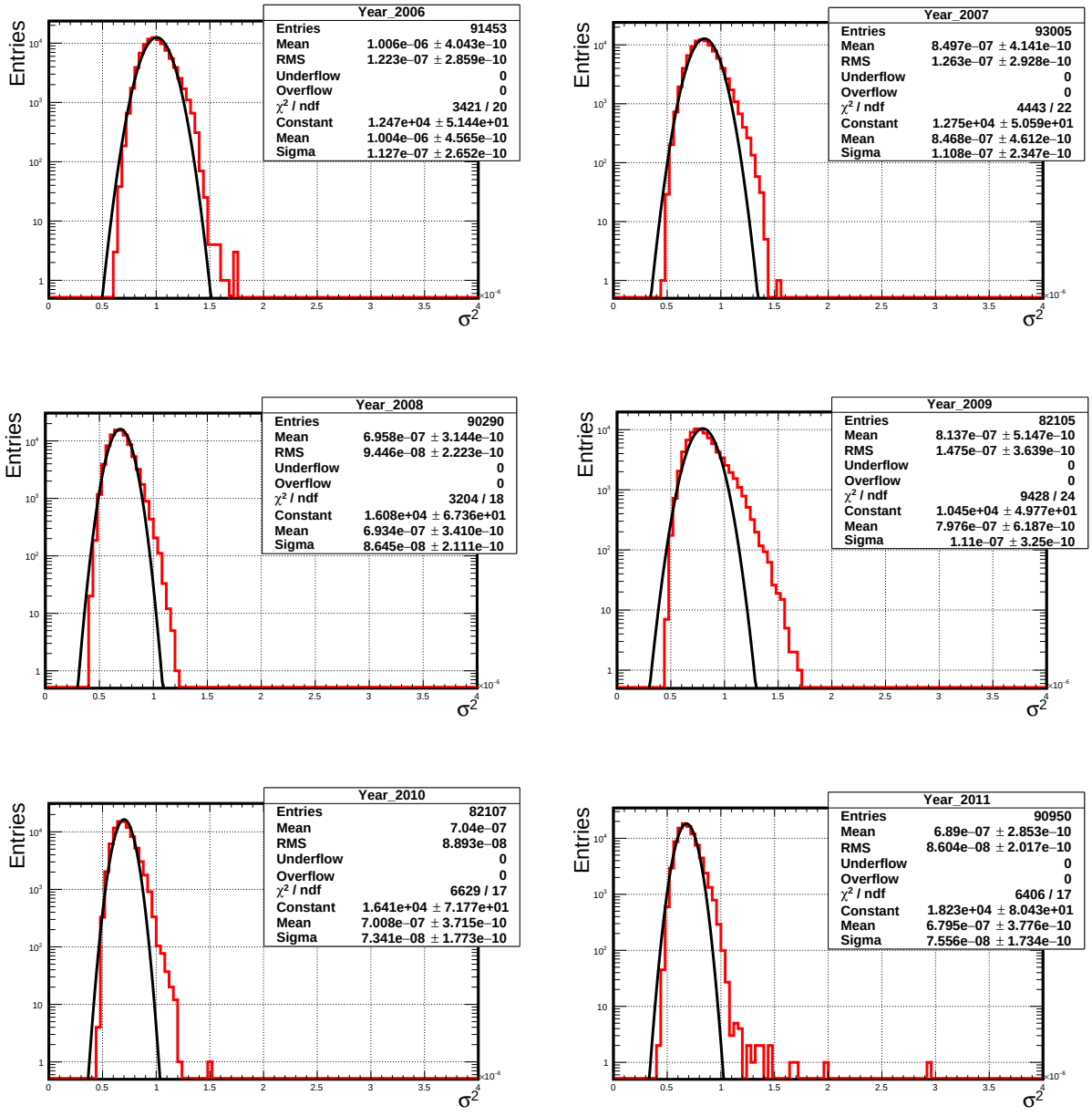

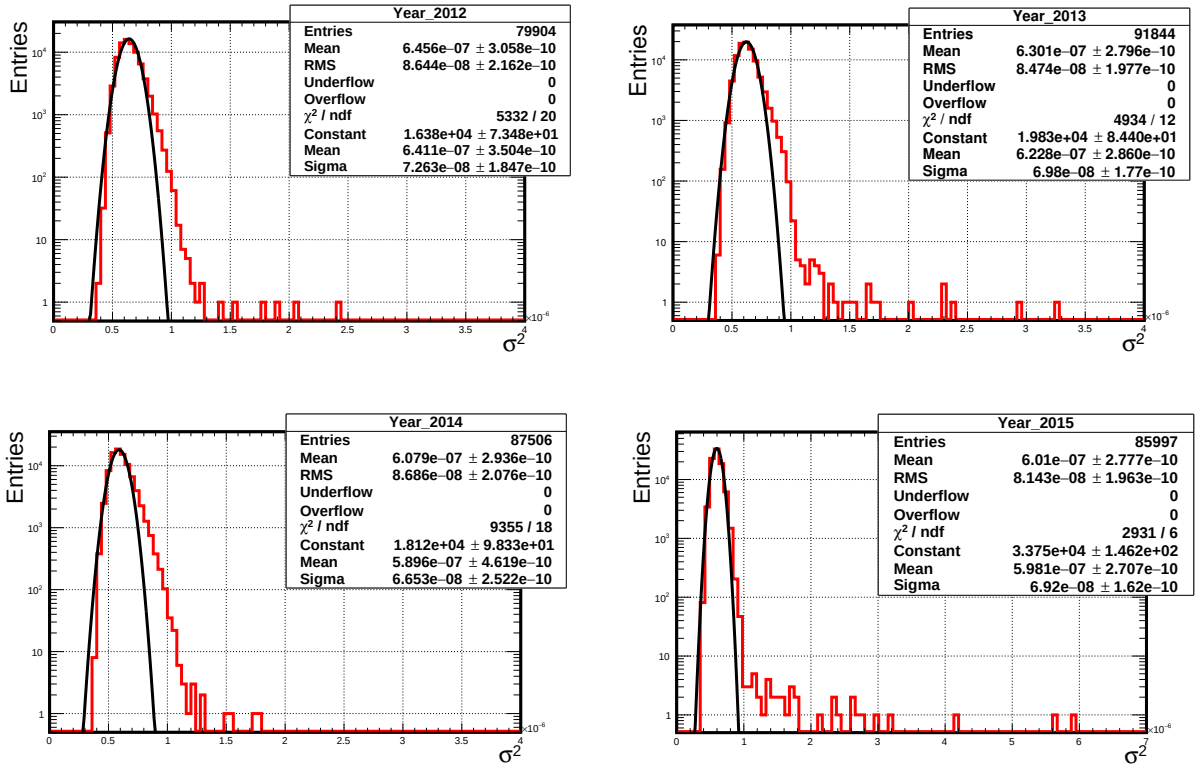

FIGURE 3.18: Average scaler variability histograms for the years 2006-2015. The excess variance values σ^2 for each 5-minute intervals are satisfying the data quality requirements. Lot of small excess variance amplitudes are observed over the whole dataset. The significant excesses are $\geq 5\sigma$ the daily baseline of the average scaler rate variability.

Figure 3.18 shows the yearly distributions of the excess variance values σ^2 of each five-minute interval satisfying the quality cuts. The significant variability observed in average scaler rate from the years 2006-2015 (see Tab. A.2) appears as a clearly distinct feature on the σ^2 distributions. The σ^2 method showed its sensitivity to variability changes of average scaler rate. These changes can have, on one hand, astrophysical and Solar orgins, and on the other hand, artificial origin, such as drastic change in the number of the active detectors over the entire SD array and detector response. We can see on the positive side of the yearly σ^2 distributions (2006-2015), a plenty of small excess variance, and then the significant excess variability $\geq 5\sigma$ significance level on a day-by-day basis. All these excesses distort the Gaussian shape of the σ^2 distributions. On the year 2009, a Solar minimum has been observed [142]. This means that an increase in low-energy CR flux, which results in a global excess in average CR background rate (shown in Figs. 3.6 and 3.7 during the year 2009). Also in the year 2010, the excess variance σ^2 shows global excess on the positive side of the histogram, corresponding to an increase in average scaler rate over the interval from January-July 2010. Such increase in average scaler rate could be explained as an impact of the deep Solar minimum of 2009. Moreover, the change in th number of active detectors in these two years (2009 and 2010) was the highest over the 10-year period (see Fig. 3.1 and Tab. 3.1). The corresponding baseline variability of the years 2006-2015 is presented in Fig. 3.19.

Baseline distributions of the average scaler rate variability (2006-2015) We show in Fig. 3.19 the distributions of the baseline of average scaler rate variability, and its evolution in 2006-2015. The baseline is calculated on a day-by-day basis by specifying the median value of the excess variance distribution σ^2 per day.

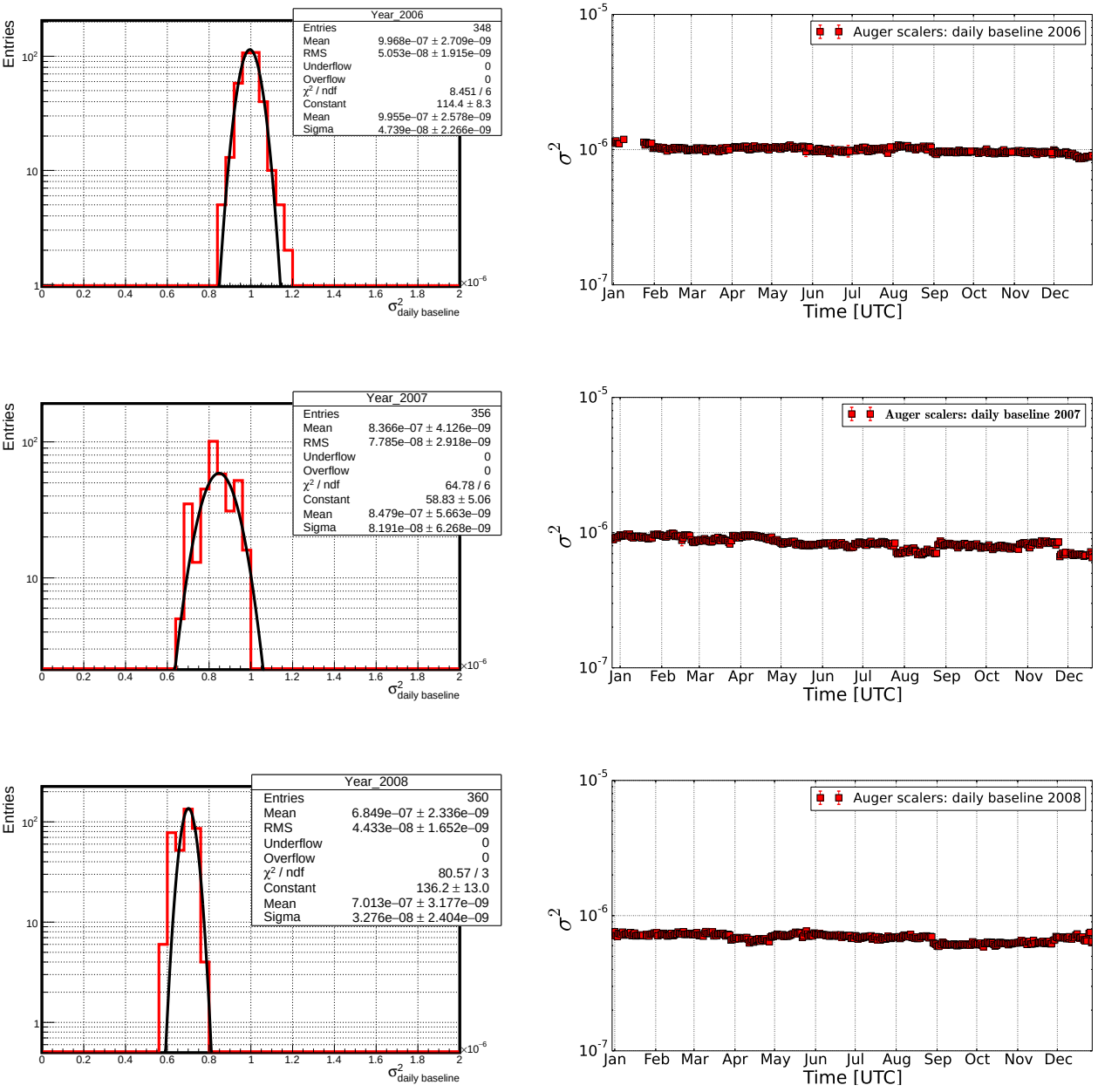

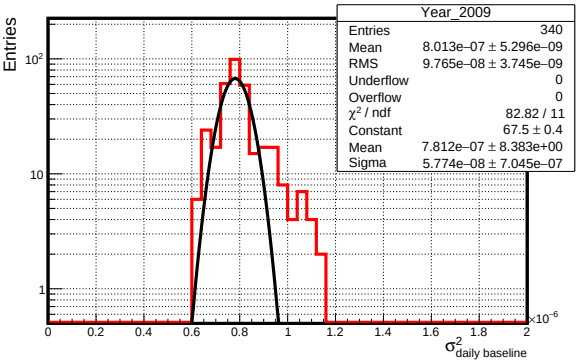
Year_2009
Entries 340
Mean 8.013e–07 ± 5.296e–09
RMS 9.765e–08 ± 3.745e–09
Underflow 0
Overflow 0
χ² / ndf 82.82 / 11
Constant 67.5 ± 0.4
Mean 7.812e–07 ± 8.383e+00
Sigma 5.774e–08 ± 7.045e–07
Entries
σ² daily baseline

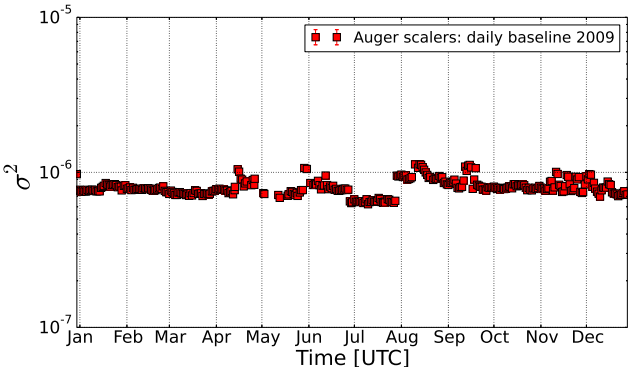
Auger scalers: daily baseline 2009
σ²
Jan Feb Mar Apr May Jun Jul Aug Sep Oct Nov Dec
Time [UTC]

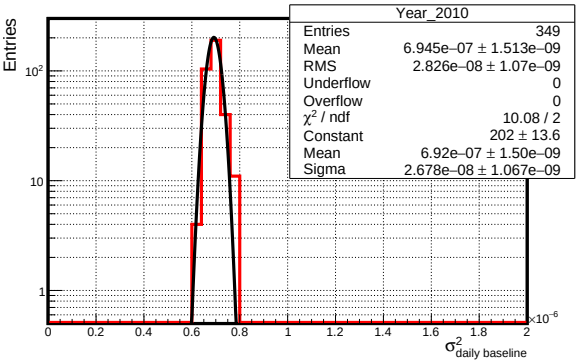
Year_2010
Entries 349
Mean 6.945e–07 ± 1.513e–09
RMS 2.826e–08 ± 1.07e–09
Underflow 0
Overflow 0
χ² / ndf 10.08 / 2
Constant 202 ± 13.6
Mean 6.92e–07 ± 1.50e–09
Sigma 2.678e–08 ± 1.067e–09
Entries
σ² daily baseline

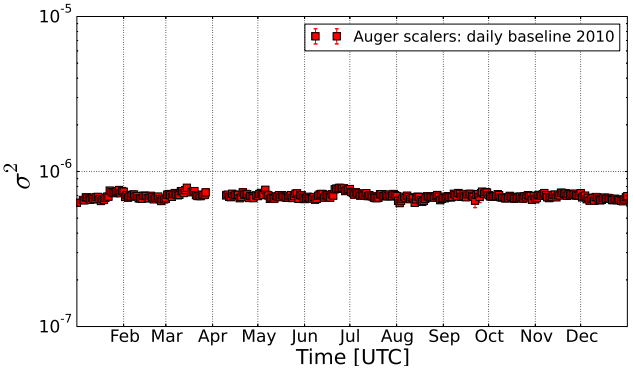
Auger scalers: daily baseline 2010
σ²
Feb Mar Apr May Jun Jul Aug Sep Oct Nov Dec
Time [UTC]

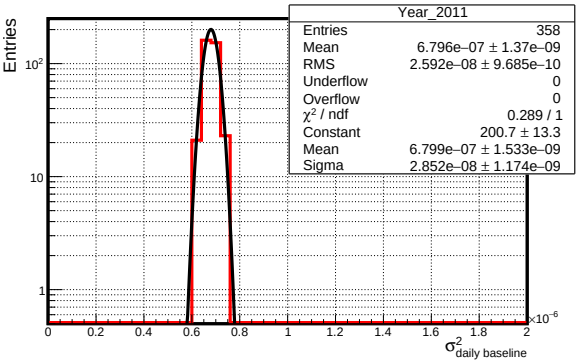
Year_2011
Entries 358
Mean 6.796e–07 ± 1.37e–09
RMS 2.592e–08 ± 9.685e–10
Underflow 0
Overflow 0
χ² / ndf 0.289 / 1
Constant 200.7 ± 13.3
Mean 6.799e–07 ± 1.533e–09
Sigma 2.852e–08 ± 1.174e–09
Entries
σ² daily baseline

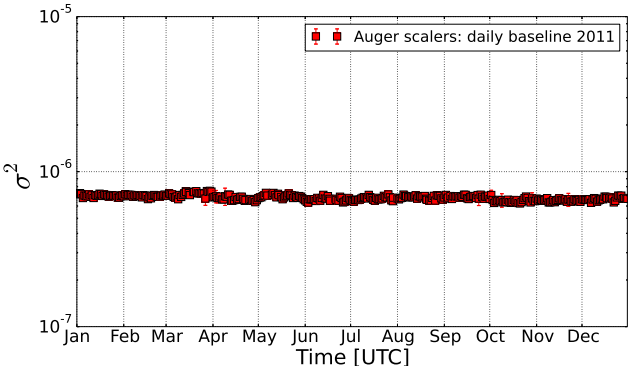
Auger scalers: daily baseline 2011
σ²
Jan Feb Mar Apr May Jun Jul Aug Sep Oct Nov Dec
Time [UTC]

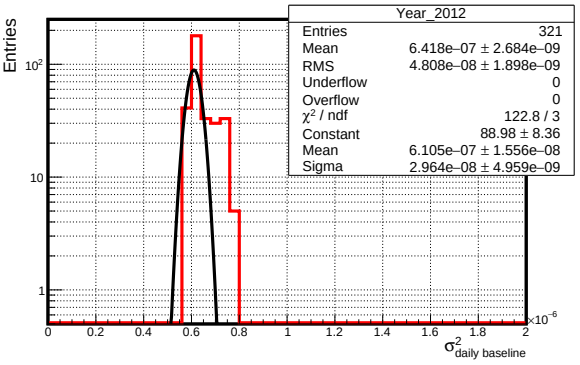
Year_2012
Entries 321
Mean 6.418e–07 ± 2.684e–09
RMS 4.808e–08 ± 1.898e–09
Underflow 0
Overflow 0
χ² / ndf 122.8 / 3
Constant 88.98 ± 8.36
Mean 6.105e–07 ± 1.556e–08
Sigma 2.964e–08 ± 4.959e–09
Entries
σ² daily baseline

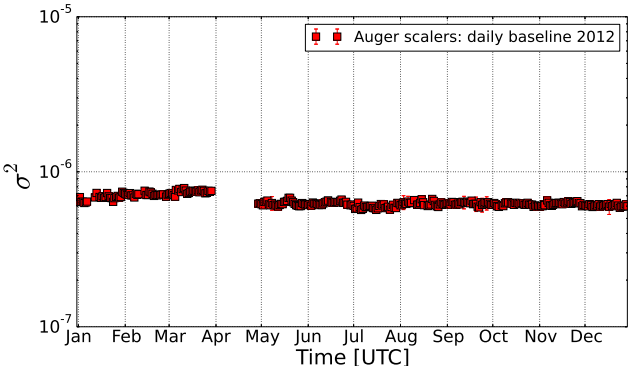
Auger scalers: daily baseline 2012
σ²
Jan Feb Mar Apr May Jun Jul Aug Sep Oct Nov Dec
Time [UTC]

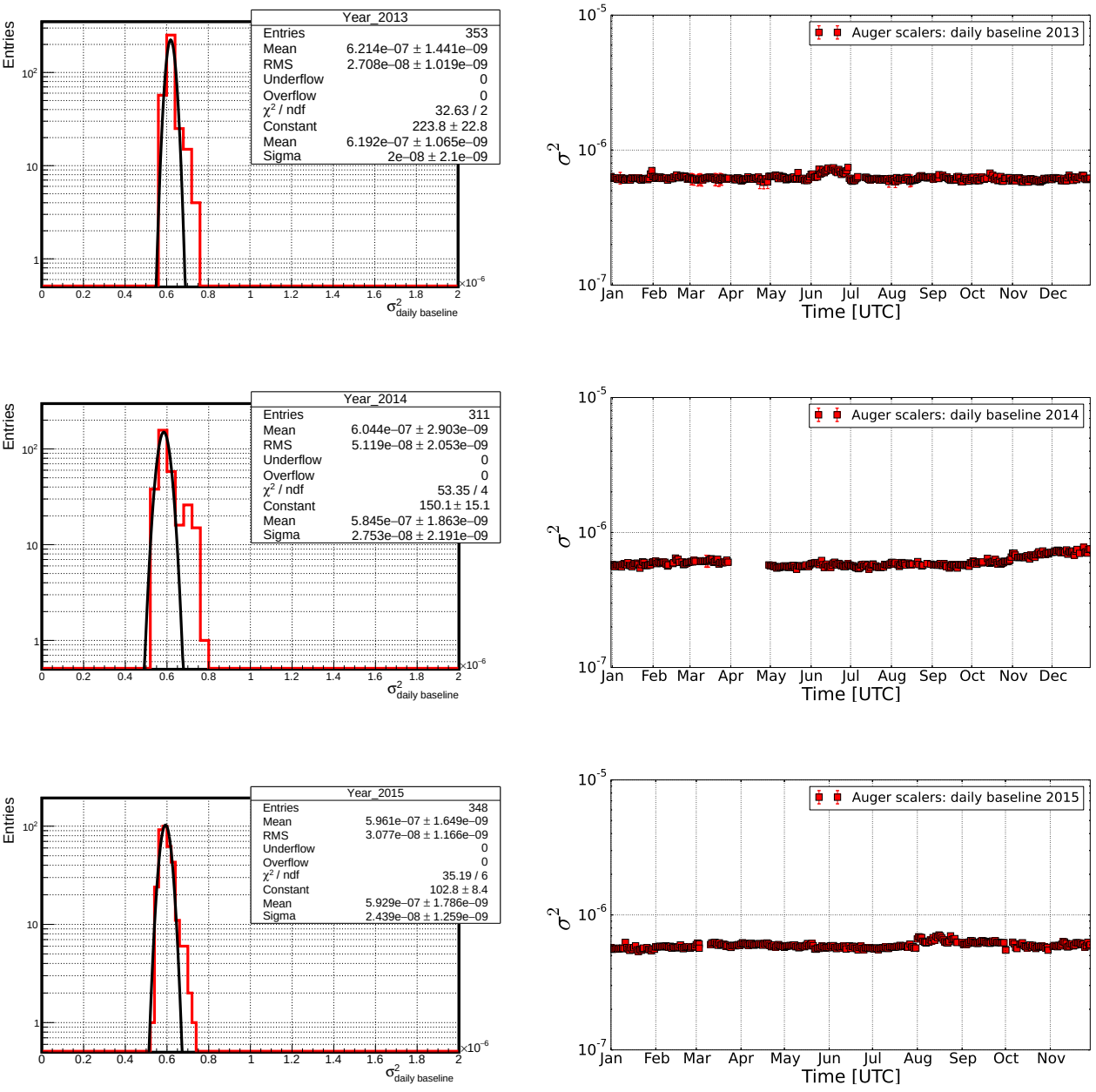

FIGURE 3.19: Distributions of the baseline of average scaler rate variability, and its evolution in the years 2006-2015.

We notice that the baseline of the average scaler rate variability σ^2 declines over the years. Such decline behavior is shown prior by the long-term evolution of the AoP parameter and the average scaler rate for the ten-year period (see Figs. 3.3 and 3.6). The evolution of the yearly average scaler rate variability and its baseline over the ten years (2006-2015) are presented in Fig. 3.20, along with the average value of the scaler rate per each year.

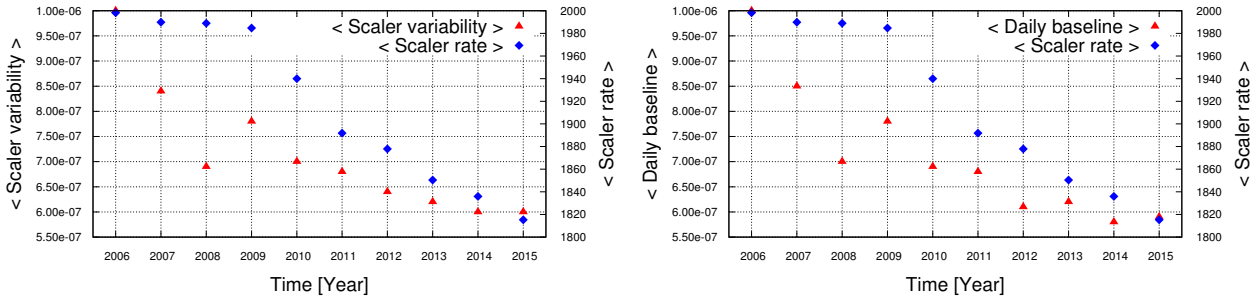

FIGURE 3.20: Distributions of average scaler rate variability and its baseline with average values of count rate from 2006 to 2015. As it has been expected from the SD detector response, due to the aging factor, as well as the change in flux of the low-energy cosmic rays, a common decline behavior is shown in the data taken from 2006 to 2015. Additionally, a global maximum in the variability of average scaler rate is recorded in 2009, corresponding to the Solar minimum occurred in that year.

The average of scaler rate variability and its baseline adhere decline behavior and show a global maximum in the year 2009, which has the widest excess variance distribution over the ten year period. In 2009, we observe large number of small excess amplitudes, which can be a consequence of increase of GCR fluxes during the Solar minimum occurred in the same year. The whole trend shown in Fig. 3.20 is consistent with the long-term evolution of the low-energy cosmic ray fluxes and the SD aging factor, as it has been studied previously by our Collaborators in Refs. [141, 142, 144].

To summarize, Figs. 3.18, 3.19, and 3.20, allow to conclude that the variability method/excess variance σ^2 is sensitive to short and long-term variability changes in average scaler rate. On a short-term variability, there have been 266 5-minute intervals of significant excesses observed in average scaler rate, over 76 dates from the years 2006 to 2015. Furthermore, a plenty of small excess variance amplitudes are observed and clearly visible on the positive side of the yearly σ^2 distributions in Fig. 3.18 from 2006 to 2015. On a long-term variability, the variability method can be employed to monitor the long-term evolution of low-energy CR fluxes (CR background), in addition to, the detector response over the years.

As a first guess to investigate the origin of the significant excess variance obtained using the variability method, the sidereal times and zenith angles distributions of the observed excesses are shown in § 3.3.2.

3.3.2 Sidereal time and zenith angle distributions of the observed excesses

Except for a few excesses in 2006 and 2007, the bulk of the significant excess variability has been observed in the years 2010-2015. The distribution of the sidereal times of the excesses, i.e., the right

ascensions of the meridian transiting to the North with respect to the Pierre Auger Observatory site is shown in Fig. 3.21.

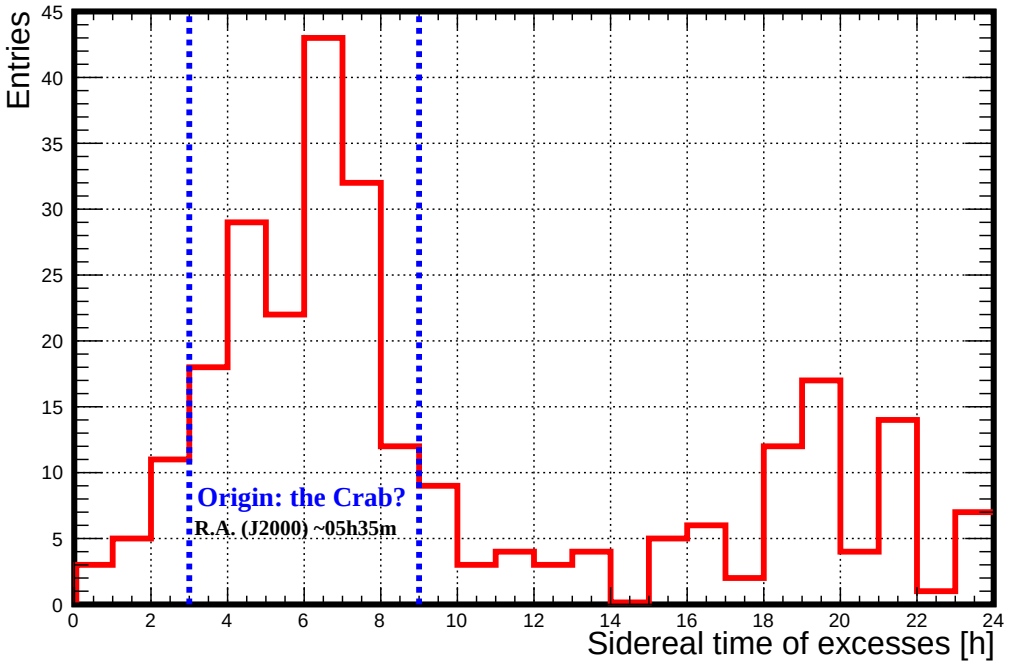

FIGURE 3.21: The sidereal times distribution of the detected excesses. The majority of the excess variance entries are occurred at the sidereal time intervals from 3h to 9h (region restricted between the blue dashed lines), which might be relevant to the location of the Crab nebula and pulsar, which was above the horizon with respect to Auger site.

The distribution of the sidereal times of the excesses shows a bulk of entries at the [3h, 9h] interval. This range corresponds to the Galactic "anti-center". Thus, there is already considerably restricting list of plausible Galactic objects, which are suitable to explain the excesses of sidereal times from 3h to 9h. The Crab nebula is among the brightest source candidates. The Crab has an appropriate location (the Crab's right ascension R.A. (J2000) is ∼05h 35m), which could present the Crab as a plausible candidate for the majority of the significant excesses observed at sidereal time intervals from 3h to 9h.

Assuming that the Crab nebula and pulsar is the source candidate for the observed excesses. The zenith angle of the Crab nebula with respect to the Pierre Auger Observatory site, at the moments of the detected excesses is shown in Fig. 3.22

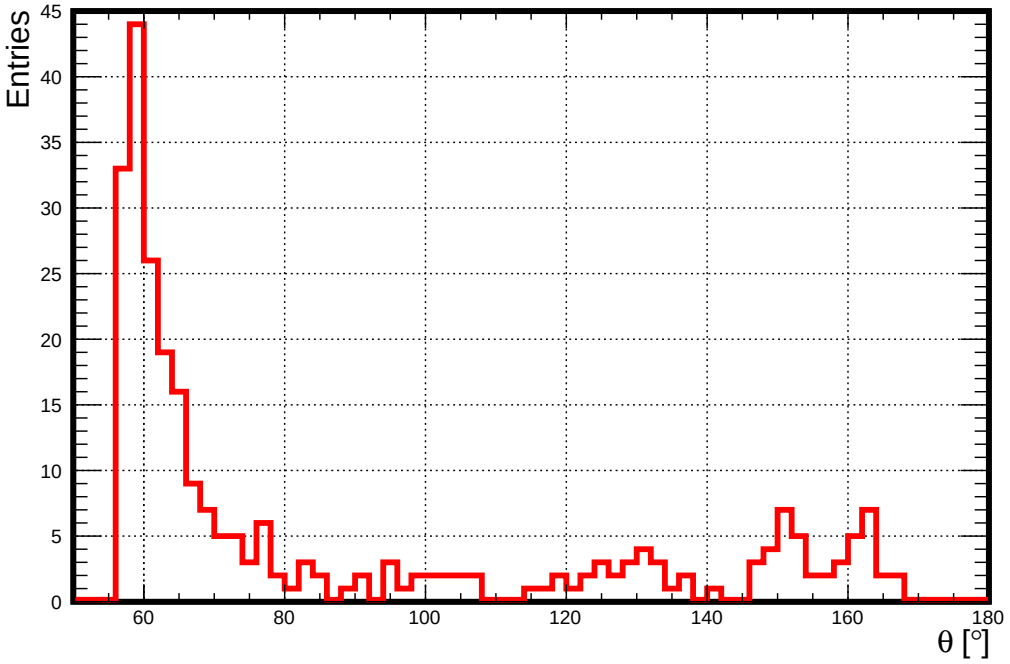

FIGURE 3.22: The zenith angle distribution of the Crab nebula with respect to the Pierre Auger Observatory site, at the time of the observed excesses. The zenith angles of the majority of the excesses range from ∼57° to ∼70°, and took place when the Crab nebula was above the horizon, at elevation >20° with respect to the Pierre Auger Observatory site.

Both distributions of the sidereal times and zenith angles could provide a first guess for astrophysical candidates for the strong observed variability. About 2/3 of the observed variability occurred when the Crab nebula was at Malrgüe sky, with an elevation >20°. The distribution of the zenith angles peaks at ∼57°, which is corresponding to the Crab transit at the Pierre Auger Observatory sky, and shows a rapid decrease of the number of bins of excess amplitude with large zenith angles. The values of the zenith angles of the Crab nebula, with respect to Auger site, are plotting versus the excess variance amplitudes in Fig. 3.23.

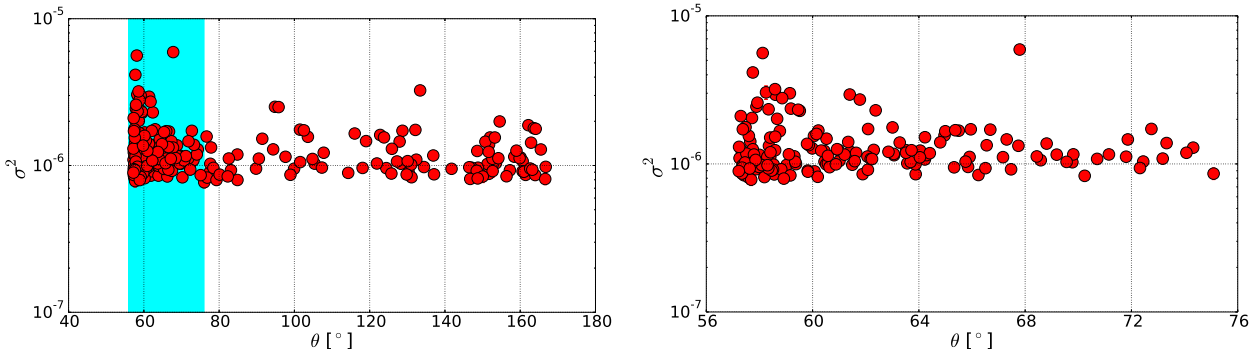

FIGURE 3.23: *Left panel:* the Crab nebula zenith angle, with respect to Auger site, versus the amplitude of the observed significant excesses (2006- 2015). A vertical cyan band highlights the excesses corresponding to the Crab zenith angle < 76°. *Right panel:* a zoom of this range.

Figure 3.23 can reveal an interesting dependence of the excess variance amplitudes on the Crab's zenith angle, as the values of excess variance amplitude σ^2 decrease with increasing zenith angle. This dependence might be interpreted as the influence of the atmospheric absorption, which increases the energy threshold of the detection of the very-high energy γ-ray emission at large zenith angles.

The results obtained by applying the $\sigma - \delta$ (§ 3.2) and variability (§ 3.3) methods to the clean and corrected Auger scaler data appear to suggest the first hints of astrophysical origin for the observed significant excesses in the Auger SD scalers, at both second and minute timescales.

Before going to further search for the very-high energy γ-ray emission from the Crab nebula and pulsar or other astrophysical TeV γ-ray emitters, a feasibility cross-check is a necessary step for sensitivity of the Auger SD scalers to the very-high energy γ-ray emission (see Chapter 4 for details).

Chapter 4

Sensitivity of the Auger SD Scaler Rate to Multi-TeV Gamma-Ray Flares

The low-energy scaler mode of Auger surface detector (SD) array has a large collecting area of $\sim 1660 \times 10\,\mathrm{m}^2$ and low deposited energy in each detector ($15\,\mathrm{MeV} \lesssim E_d \lesssim 100\,\mathrm{MeV}$), which enable us to observe low-energy CRs of primary energies up to few TeV, by measuring the flux variations of low-energy secondary particles at ground level. Therefore, by using the Auger SD scalers, we are able to investigate variability studies of astrophysical and Solar origins at different timescales: (a) second-variations - the search for GRBs; (b) minute-variations - the detection of astrophysical VHE γ-ray emission; (c) day to week-variations - the observations of daily modulation and Forbush decreases; (d) year-variations - the monitoring of Solar Cycle. This study develops, in the framework of the Pierre Auger Observatory, the search for the non-thermal emission of cosmic γ-rays at multi-TeV domain. The Pierre Auger Observatory is located at Argentina at 35° S and 69° W, with mean altitude of $\sim$1.420 m a.s.l., at which the γ-induced showers of primary energies below a few 100 GeV are absorbed before reaching ground level.

This Chapter is meant to investigate sensitivity of the Auger low-energy scaler mode to multi-TeV γ-ray flares from the direction of the Crab nebula, with respect to the Pierre Auger Observatory. A MC simulation of both extensive air shower development in the atmosphere and detector response is performed for a photon of fixed energy and zenith angle. In § 4.1, the CORSIKA air shower simulation is performed at fixed energy ranges (E_γ: 10, 30, 100, 300, and 1000 TeV), with six Crab zenith angle (θ_{CRAB}: 57.2°, 59.9°, 61.9°, 63.8°, 66°, and 69.9°) at the Pierre Auger Observatory sky. We present in § 4.2 the results obtained using the $\overline{\mathrm{Off}}\underline{\mathrm{line}}$ detector simulation. In § 4.3, we carry out a cross-check of scaler simulated γ-ray signal, from the direction of the Crab, with CR background.

4.1 CORSIKA air shower simulation

Air shower simulations serve as an essential tool in designing air shower experiments, as well as the CR data analysis. We perform air shower simulation for photon-induced showers using CORSIKA [183] version 7.4005. The QGSJET-II-04 [184] and FLUKA 2011.2c-1 hadronic interaction models are used with no thinning at different energy ranges (E_γ: 10, 30, 100, 300, and 1000 TeV), for six Crab zenith angle ($\theta_{\rm CRAB}$: 57.2°, 59.9°, 61.9°, 63.8°, 66°, and 69.9°) with respect to the Pierre Auger Observatory. The SLANT option is applied to the arrival direction of the Crab. We simulated 2×10^3 showers per energy range per Crab zenith angle, i.e. 12×10^3 showers over the Crab trajectory per energy range.

4.1.1 Longitudinal shower profiles

From shower development in the atmosphere, we can specify the total number of secondaries (γ, e^-, e^+, μ^-, μ^+) as a function of atmospheric depth. The secondary particles, which induce a signal in the detector, of a photon-induced shower at multi-TeV energies for different Crab zenith angle reach the ground level at the Pierre Auger Observatory site and travel further it (see an example in Fig. 4.1).

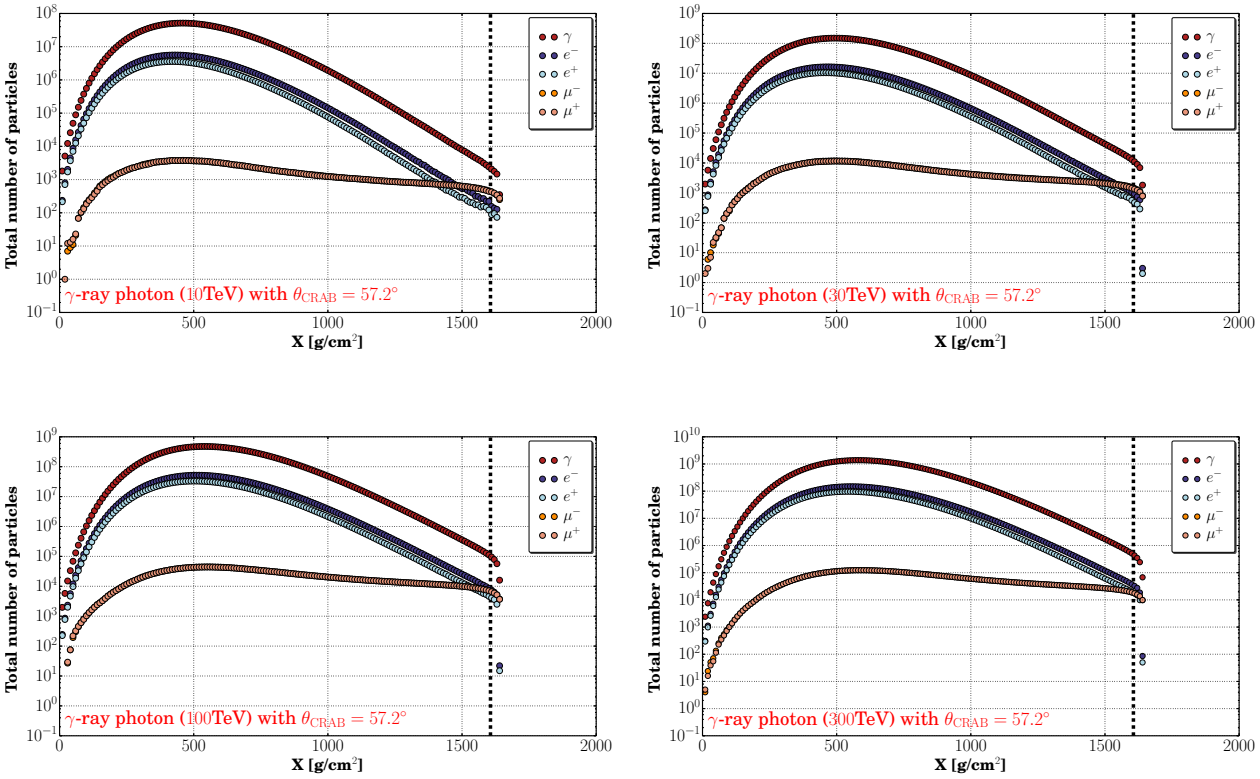

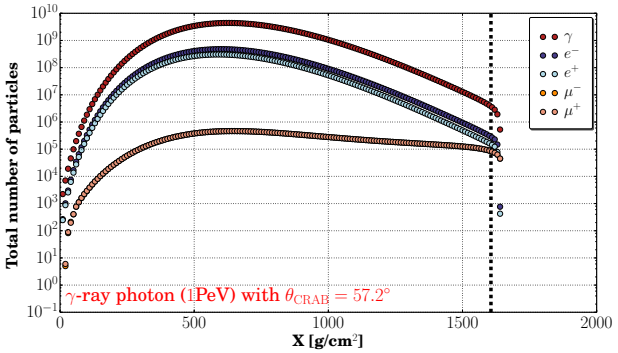

FIGURE 4.1: An example of longitudinal shower profiles of secondaries of photon-induced showers from the direction of the Crab nebula ($\theta_{CRAB} = 57.2°$) with respect to Auger site. The secondaries from inclined photon-induced showers reach the ground level at the Pierre Auger Observatory. The black vertical dashed lines indicate atmospheric depth values at the ground.

The rest of longitudinal shower profiles at multi-TeV energies and Crab zenith angles (from 59.9° to 69.9°) is shown in B.1.

4.1.2 Lateral distribution of secondaries

The lateral distributions of secondaries (γ, e^-, e^+, μ^-, μ^+) at the ground from photon-induced showers of fixed energies 10, 30, 100, 300, and 1000 TeV, with Crab zenith angle $\theta = 57.2°$, is presented in Fig. 4.2. The traverse (x-direction) and the longitudinal (y-direction) components of the simulated showers are presented in the left and right column histograms, respectively.

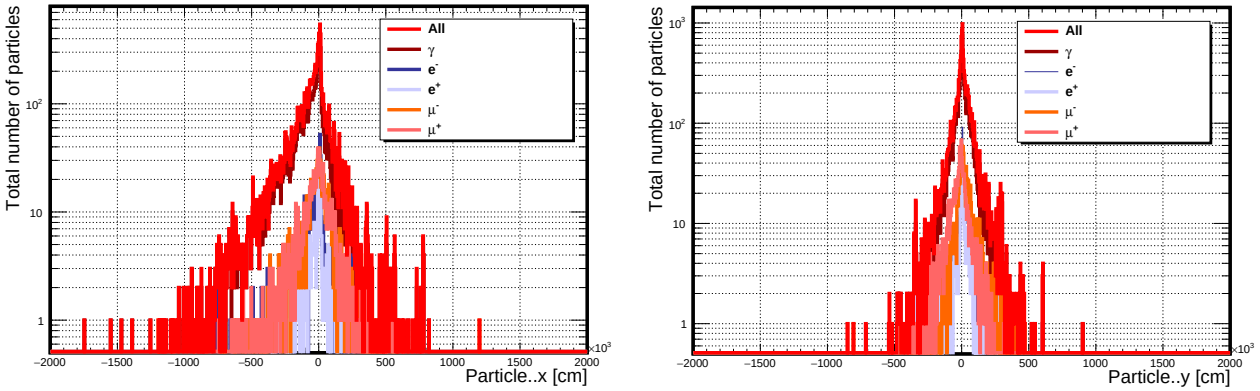

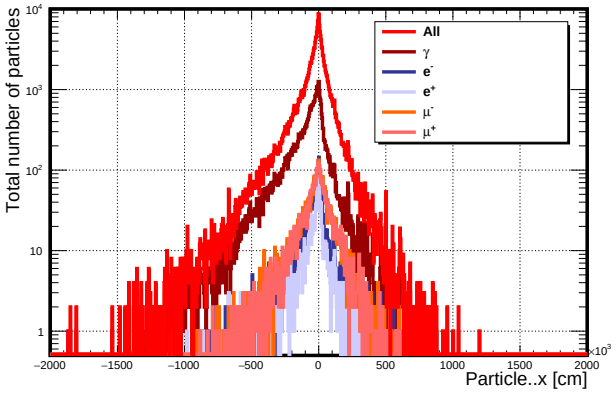
Total number of particles
Particle..x [cm]
All
γ
e⁻
e⁺
μ⁻
μ⁺

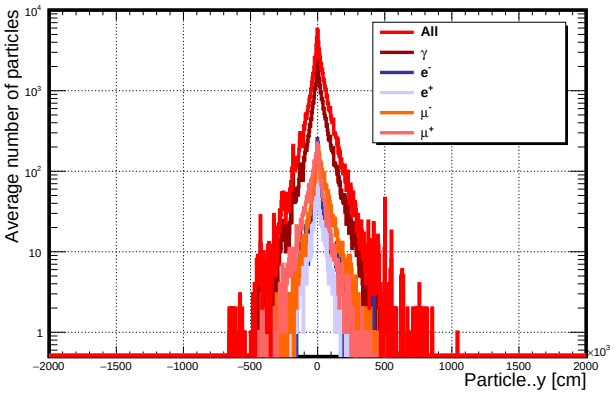
Average number of particles
Particle..y [cm]
All
γ
e⁻
e⁺
μ⁻
μ⁺

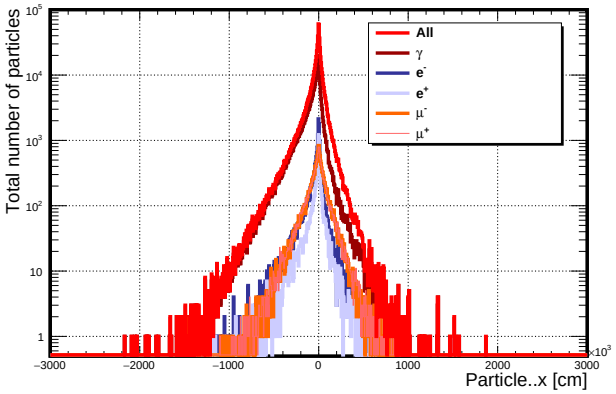
Total number of particles
Particle..x [cm]
All
γ
e⁻
e⁺
μ⁻
μ⁺

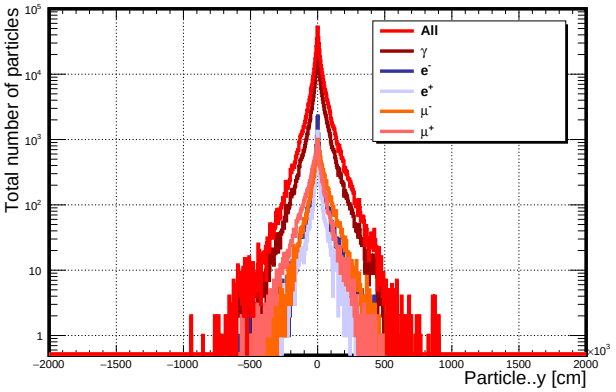
Total number of particles
Particle..y [cm]
All
γ
e⁻
e⁺
μ⁻
μ⁺

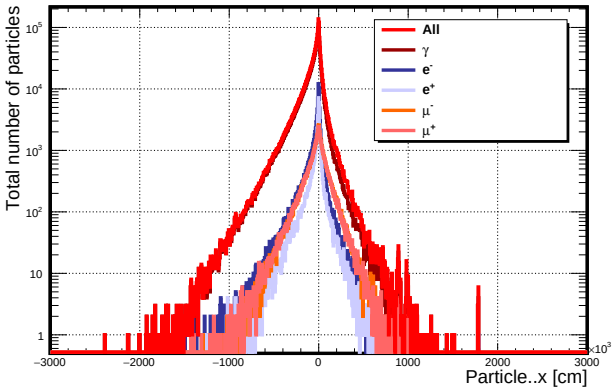
Total number of particles
Particle..x [cm]
All
γ
e⁻
e⁺
μ⁻
μ⁺

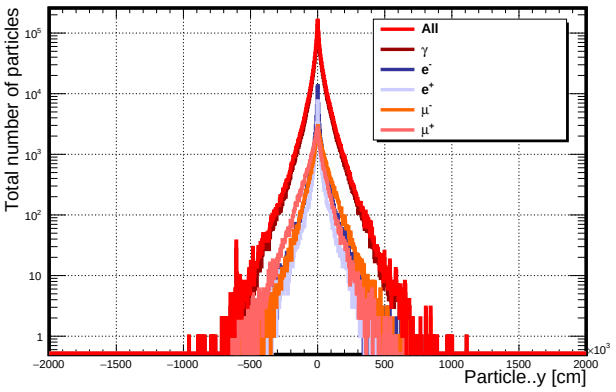
Total number of particles
Particle..y [cm]
All
γ
e⁻
e⁺
μ⁻
μ⁺

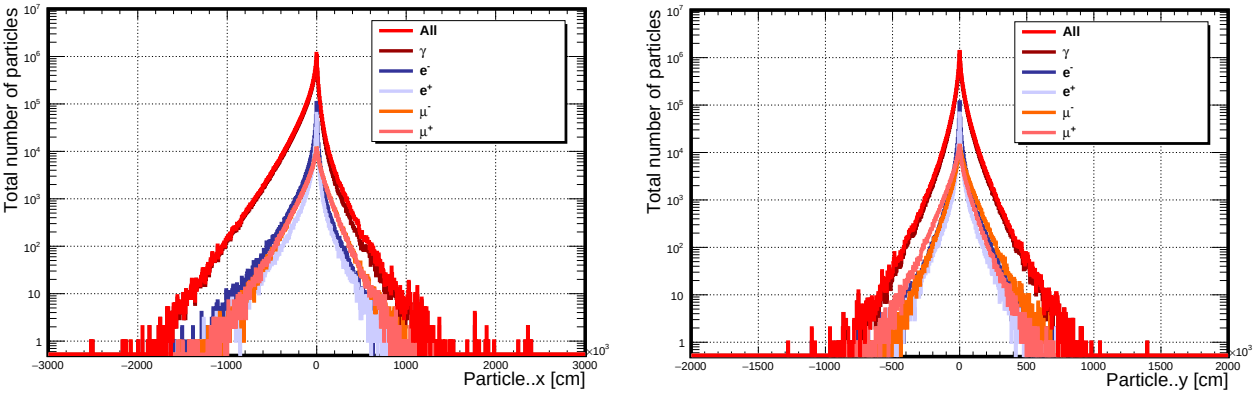

FIGURE 4.2: An example of lateral distribution of secondaries resulted from γ-ray showers at multi-TeV energies, with zenith angle 57.2°.

The lateral distributions of secondaries resulted from photon-induced showers at multi-TeV energies have widths of hundreds of meters, quite comparable to the Auger SD grid size. This can suggest that the Auger SD scalers can detect γ-ray shower with high detector multiplicities. The rest of lateral distributions of secondaries at multi-TeV energies and Crab zenith angles (from 59.9° to 69.9°) is shown in B.1. In the following we present the results obtained from the $\overline{\text{Off}}\underline{\text{line}}$ detector simulation.

4.2 $\overline{\text{Off}}\underline{\text{line}}$ detector simulation

The Auger $\overline{\text{Off}}\underline{\text{line}}$ analysis framework is a detector simulation [185] used in calibration studies and investigating the detector response to the signal produced from the UHECRs in both surface and fluorescence detectors of the Pierre Auger Observatory. Prior to applying the Auger $\overline{\text{Off}}\underline{\text{line}}$ detector simulation to photon-induced showers, the local trigger parameters `(T1&T2)` in the `TankTriggerSimulator` module, of the Auger SD array, are set to verify the trigger conditions of the low-energy scaler mode. Namely, the counts of events from 4 FADC up to 20 FADC above the detector baseline are selected (see examples of FADC traces of simulated signals in B.2). Large statistics of photon-induced showers (2×10^3 per energy range per zenith angle) at multi-TeV energies, with several zenith angle over the Crab trajectory at Malargüe sky, are detector simulated for 200 times. This means that 4×10^5 simulated events per energy range E per zenith angle θ. As an example, maps of the detectors of γ-ray signals passing the scalers trigger at energies 10, 30, 100, 300, and 1000 TeV, with zenith angle $\theta = 57.2°$ are shown in Fig. 4.3.

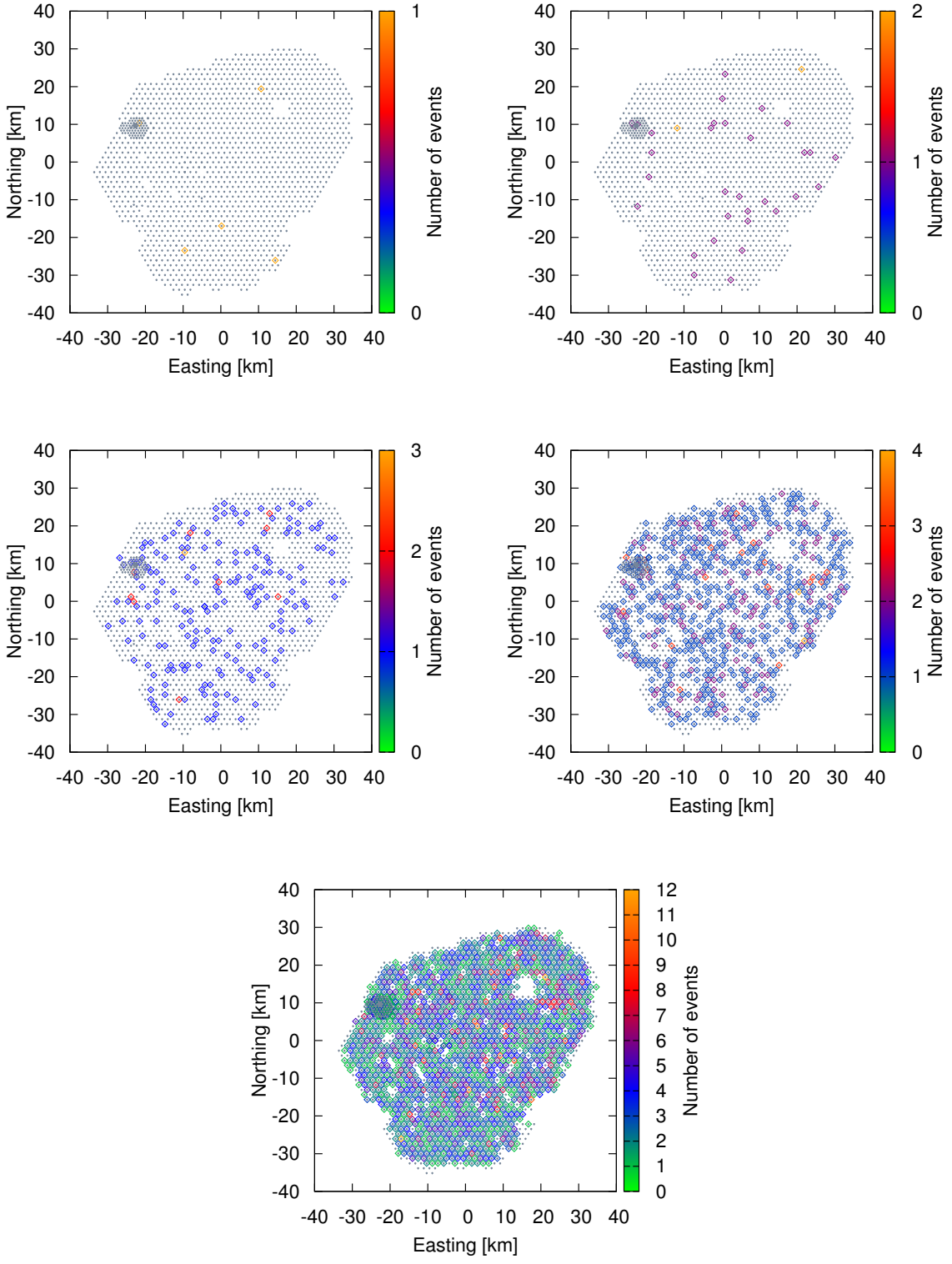

FIGURE 4.3: An example of maps of detectors of γ-ray signal at multi-TeV energies and zenith angle 57.2° at Auger sky. Large number of simulated events (4×10^5) at primary photon energies (10, 30, 100, 300, and 1000 TeV), with zenith angle $\theta = 57.2°$, are simulated. Detector multiplicities are clearly visible at high energies >30 TeV.

The rest of the maps of different Crab zenith angles at Auger sky is shown in B.2. The total and mean number of particles, which survive scaler trigger, per primary photon energy E per Crab zenith angle θ is shown in Fig 4.4.

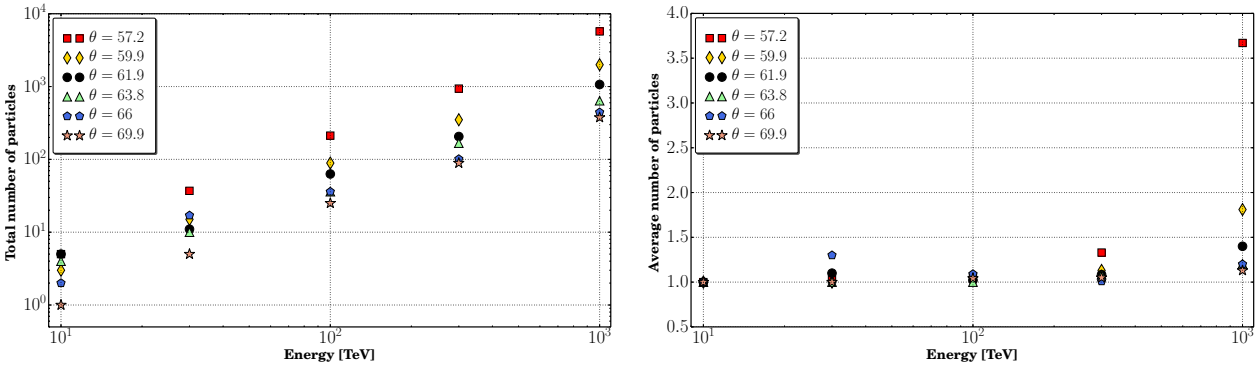

FIGURE 4.4: The total and mean number of particles detected in the detectors, from simulations of photon-induced showers at multi-TeV energies, as a function of primary photon energy for different Crab zenith angle. Left panel shows the total number of particles passing scaler trigger per energy range per zenith angle. Right panel represents the mean number of particles of scaler trigger, with high detector multiplicities at high energies and low Crab zenith angle.

In Fig. 4.4, the dependence of the number of particles on the primary photon energy and zenith angle is shown. Large number of particles are detected by the Auger SD scalers at multi-TeV energies, with Crab zenith angles ranging from ∼57° and ∼70° at Auger sky. The SD scalers see more particles from γ-ray showers at low Crab zenith angle than the high ones. At large zenith angle the influence of the atmospheric absorption, which increases the energy threshold of detection of very-high energy γ-ray emission, is obvious. The particles counting is based on single PMTs. Namely, if one or the three PMTs per individual detectors verify the scaler trigger, only one particle is counted. The number of triggered detectors and corresponding collecting area are presented in Fig. 4.5.

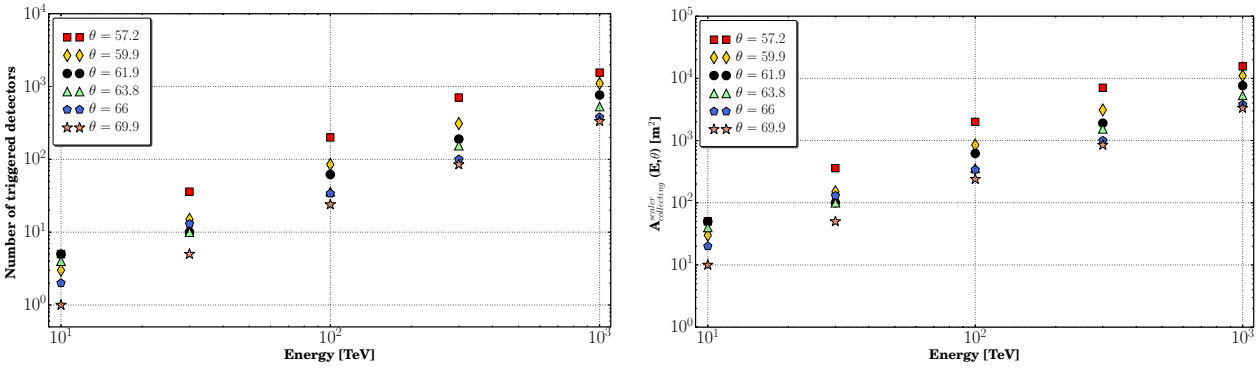

FIGURE 4.5: The number of triggered detectors (left plot) and corresponding collecting area (right plot) of particles passing scaler trigger, from photon-induced showers at multi-TeV energies, per primary photon energy per Crab zenith angle. The number of triggered detectors and corresponding collecting area increase with primary photon energy and low Crab zenith angle.

Since Auger SD scalers is installed on the entire SD array (more than 1660 detectors of area of $10\,m^2$ each), large collecting area is achieved at multi-TeV energies, for different zenith angles over the whole Crab trajectory at Malrgüe sky. The efficiency of particle detection by Auger SD scalers is an essential parameter for sensitivity calculus, and gives the number of detected particles N_{obs} from N_{thrown} thrown secondaries over the SD array. The scaler efficiency is specified using

$$\eta^{scaler} = \frac{N_{obs}(E,\theta)}{N_{thrown}(E,\theta)}, \tag{4.1}$$

where N_{obs} is the number of triggering particles, which survive scaler trigger, in at least one PMT (from 4 FADC bin up to 20 FADC bin above the detector baseline), and N_{thrown} is the number of detector simulated showers (4×10^5 simulated events) by using the Offline. Figure 4.6 presents particle detection efficiency with scaler mode as a function of primary photon energy, with different Crab zenith angles.

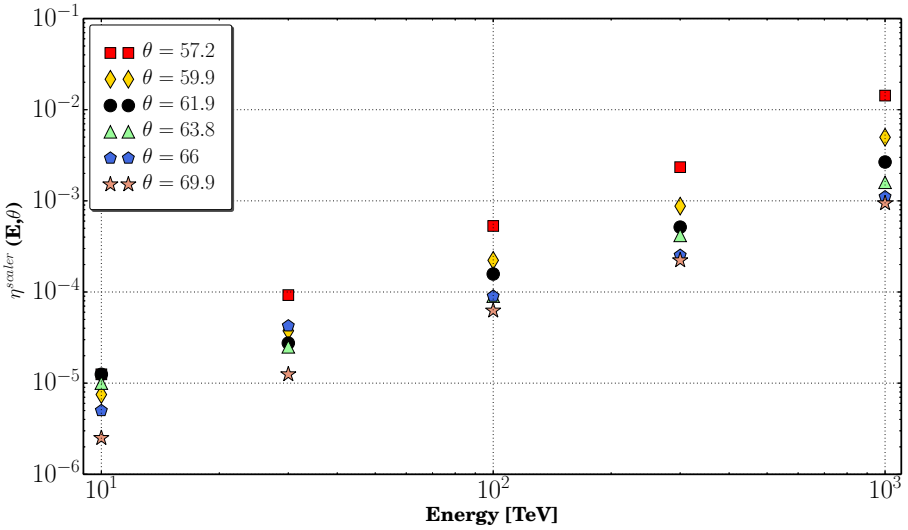

FIGURE 4.6: Auger SD scaler trigger efficiency at multi-TeV energies as a function of primary photon energy, with different Crab zenith angles.

Auger SD scalers show reasonable efficiency at multi-TeV energies. The quantities of N_{obs} and N_{thrown} are obtained from detector simulation. The effective area is the actual size of the detector, which is sensitive to detect extensive air showers. It is also an intrinsic quantity for any sensitivity calculations, and depends on several parameters such as the primary particle energy and its arrival direction. In case of inclined γ-ray showers from the Crab nebula, the effective detection area of Auger SD scalers at multi-TeV domain and different Crab zenith angles can be obtained using

$$A^{scaler}_{effective} = A_{thrown} N_{PMT} \eta^{scaler} \cos\theta, \tag{4.2}$$

where A_{thrown} (as an approximation) is the active area of the SD array ($1660\times10\,\mathrm{m}^2$), over which the simulated showers are thrown, and N_{PMT} is the average number of triggered PMTs due to γ-ray photon at energy E and zenith angle θ. The quantities of N_{PMT} and η^{scaler} are obtained from detector simulation. The effective detection area of Auger SD scalers as a function of primary photon energy for different Crab zenith angles is shown in Fig. 4.7.

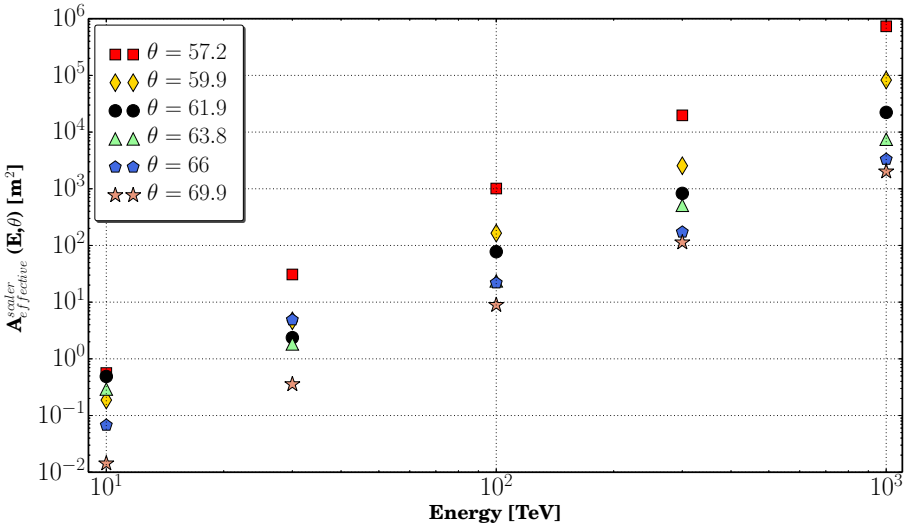

FIGURE 4.7: Effective detection area of Auger SD scalers at multi-TeV energies as a function of primary photon energy, with different Crab zenith angles.

The effective detection area of Auger scalers for VHE γ-ray emission from the direction of the Crab nebula with respect to Auger site is high, and reaches many order of magnitude ($\sim10^5\,\mathrm{m}^2$) greater than the actual geometrical size of the detector, at sub-PeV energy domain.

4.3 Expected sensitivity of Auger SD scalers to VHE γ-ray emission

The very-high energy γ-ray emission can be detected by the "single particle technique" (scalers) at ground level, as a significant excess in the average scaler rate from the entire SD array [171]. This means that the counting rate summed over the whole detectors has to be significantly higher than the CR background fluctuations. The condition for a given flux to be detected at the ground level is therefore given by

$$\Phi_\gamma = \int_{E_{min}}^{E_{max}} n_{obs}(E,\theta)\frac{dN}{dE}dE \geq \frac{\mathcal{S}}{A\cos\theta}\sqrt{\frac{B}{N_{det}T_{exp}}}, \tag{4.3}$$

where $n_{obs}(E,\theta)$ is the average number of particles that survive scaler trigger (obtained from detector simulation and presented in the right panel of Fig. 4.4), from photon-induced showers at energy E and zenith angle θ, dN/dE is the photon differential spectrum, as N is the number of photons at energy E, $\mathcal{S}$ is statistical significance (we set $\mathcal{S}=5$), A is the area of the detector ($10\,\mathrm{m}^2$), B is the background counting rate ($2\,\mathrm{kHz}$), N_{det} is number of detectors (1660), T_{exp} is the exposure time of the γ-ray source ($5\,\mathrm{minutes}$), and E_{min} and E_{max} are 10 TeV and 1PeV, respectively. Right hand side of Eq. 4.3 represents the detection threshold $\left(\mathrm{s}^{-1}.\mathrm{m}^{-2}\right)$, which changes as $(T_{exp}N)^{-1/2}$. Accordingly, the detection of γ-ray photons from weak flux sources, at the ground level, requires big number of detectors and long source exposure time. The Pierre Auger Observatory provides huge number of surface detectors (>1660) spanned over $3.000\,\mathrm{km}^2$ and large effective detection area, at multi-TeV energies, of the order of $\sim 10^5\,\mathrm{m}^2$ with scaler mode. These privileges can enable us to detect possible multi-TeV γ-ray flares from the Crab nebula, which has transit time of $\sim 6\,\mathrm{hr}$ at Auger.

Let us postulate γ-ray spectrum of a simple power law shape, with no energy cut-off, such as $dN/dE = -\mathcal{K}E^{-\gamma}$, where $\mathcal{K}$ and γ are the normalization factor and spectral index, respectively. The number of observed photons, from a Crab-like point-source, at ground level is

$$N_\gamma = \eta^{scaler} T_{exp} \int_{E_{min}}^{E_{max}} \mathcal{K}E^{-\gamma} A^{scaler}_{effective}(E,\theta)dE. \tag{4.4}$$

The normalization factor $\mathcal{K}$ is estimated using Eq. 4.3 per each energy range E, averaged over the Crab trajectory (6 zenith angles, from 57.2° to 69.9°) at the Pierre Auger Observatory sky, with different spectral indices and exposure time T_{exp} of 5 minutes per each zenith angle. In Eq. 4.4, the number of observed particles N_γ at the ground is calculated for each energy bin, whereas E_{max} reads 10, 30, 100, 300, and 1000 TeV. Figure 4.8 shows the number of particles, which are detected in the detector, as a function of primary photon energy over the Crab trajectory, with different spectral index values.

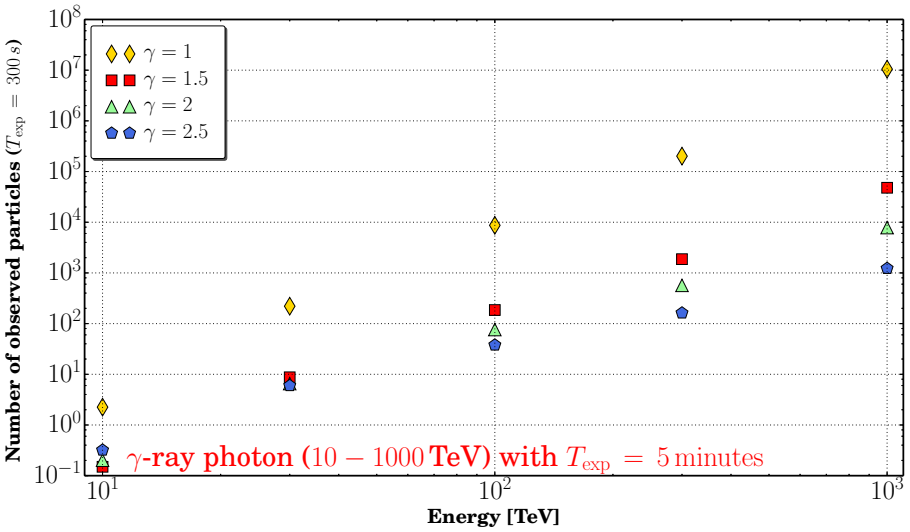

FIGURE 4.8: Number of observed particles in the detector as a function of primary photon energy, with different spectral indices, over the Crab trajectory (from 57.2° to 69.9°) at Malrgüe sky. The exposure time is 5 minutes per each zenith angle.

The number of observed particles at the ground level significantly increases with the primary photon energy, and is spectral index dependence. At VHE γ-ray emission, above 10 TeV, more particles can be observed with very hard spectral index ($\gamma = 1, 1.5$) than the hard ones ($\gamma = 2, 2.5$). The corresponding fluence of N_γ observed particles at the ground is

$$\mathcal{F} = \frac{N_\gamma \int_{E_{min}}^{E_{max}} E^{-\gamma+1} dE}{\int_{E_{min}}^{E_{max}} E^{-\gamma} A_{effective}^{scaler}(E,\theta) dE}. \tag{4.5}$$

The observed fluence is shown in Fig. 4.9, and calculated for each energy bin, with exposure time of 5 minutes per each zenith angle over the Crab trajectory. Particle fluence depends on primary photon energy and spectral index value. We observe higher fluences with very hard spectral indices than the hard ones. This dependence is clearly visible in Fig. 4.9 at energies >10 TeV.

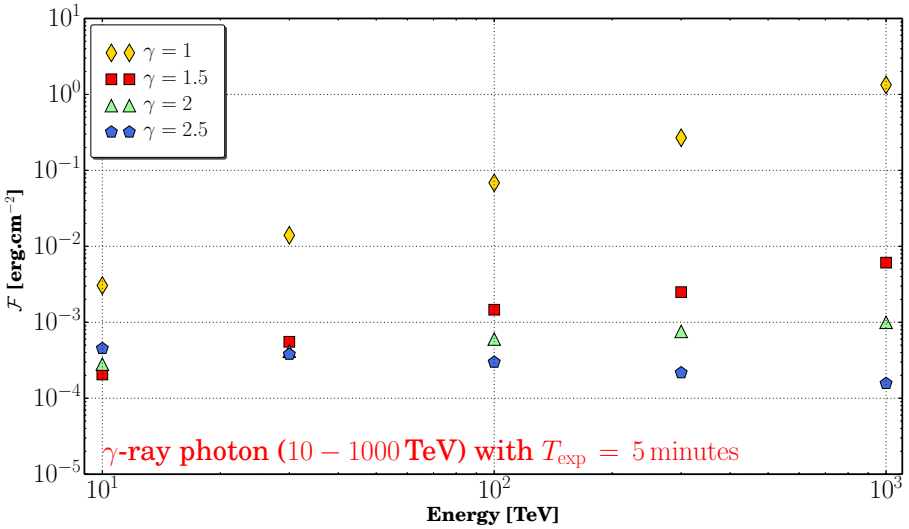

FIGURE 4.9: Observed fluence as a function of primary photon energy, with exposure time of 5 minutes and different spectral indices.

With respect to Fig. 4.8 and 4.9, Auger SD scalers are sensitive to multi-TeV γ-rays. We observe at 10 TeV higher particles and fluences with hard spectral indices ($\gamma = 2, 2.5$) than very hard one ($\gamma = 1.5$). In contrast, at energies >30 TeV up to 1 PeV, the particle fluences are higher with very hard spectral index than the hard ones.

In the following we calculate the *event rate* at each energy range for different Crab zenith angles with respect to the Pierre Auger Observatory site. The event rate is then added to real background data, and hence the search for significant excesses on a minute timescale is performed using the variability method, which is presented in § 3.3.

4.3.1 Event rate with CR background data

The background is a consequence of the convolution of all secondary particles from cosmic ray air showers (mostly hadronic) produced at the top of the atmosphere. The background rate is roughly constant flux, and depends on the altitude and the geomagnetic latitude of the observatory. The typical average scaler rate of the Pierre Auger Observatory is ∼2 kHz for all detectors. The event rate and/or number of observed particles per second by the entire SD scalers, from a given spectrum is given by Eq. 4.6, and shown in Fig. 4.10.

$$\mathcal{E}_\gamma = \eta^{scaler} \int_{E_{min}}^{E_{max}} \mathcal{K} E^{-\gamma} A_{effective}^{scaler}(E, \theta) dE. \tag{4.6}$$

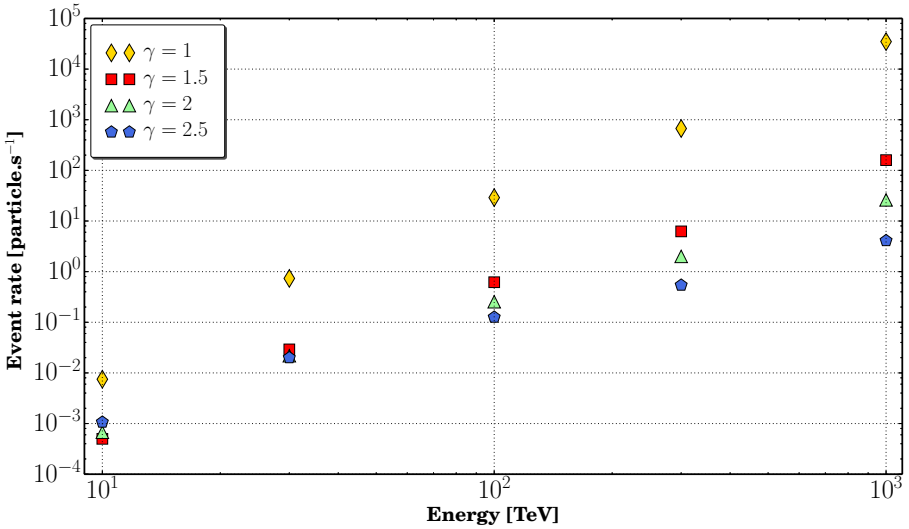

FIGURE 4.10: Event rate of SD scalers at multi-TeV energies with very hard and hard spectral indices.

In order to cross-check the excess that we expect from γ-ray flares, we add the estimated event rate to real CR background measurements, which are observed by the low-energy scaler mode. We have selected a date of high quality data and good weather conditions. Namely, the SD array was stable and no missing data acquisition. Additionally, no bad periods, no strong wind, and no thunderstorms, which strongly affect the detector response, are recorded. No significant excesses $\geq 5\sigma$ are observed over the selected background data by using the variability method on a minute timescale. The corresponding variability of the selected background date is shown in Fig 4.11.

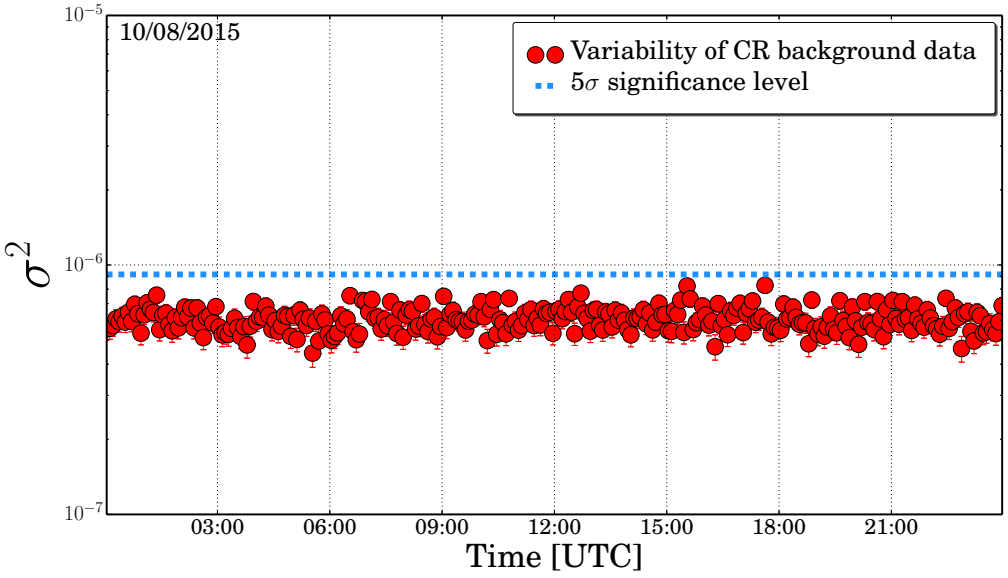

FIGURE 4.11: Average scaler rate variability of August 10, 2015. The horizontal dashed line shows the 5σ significance level. The excess variance σ^2 is calculated every successive 5-minutes interval (288 bins per date). No significant excesses $\geq 5\sigma$ are observed over the average background rate of this date.

The histogram of the excess variance σ^2 of the background date is shown in Fig. 4.12.

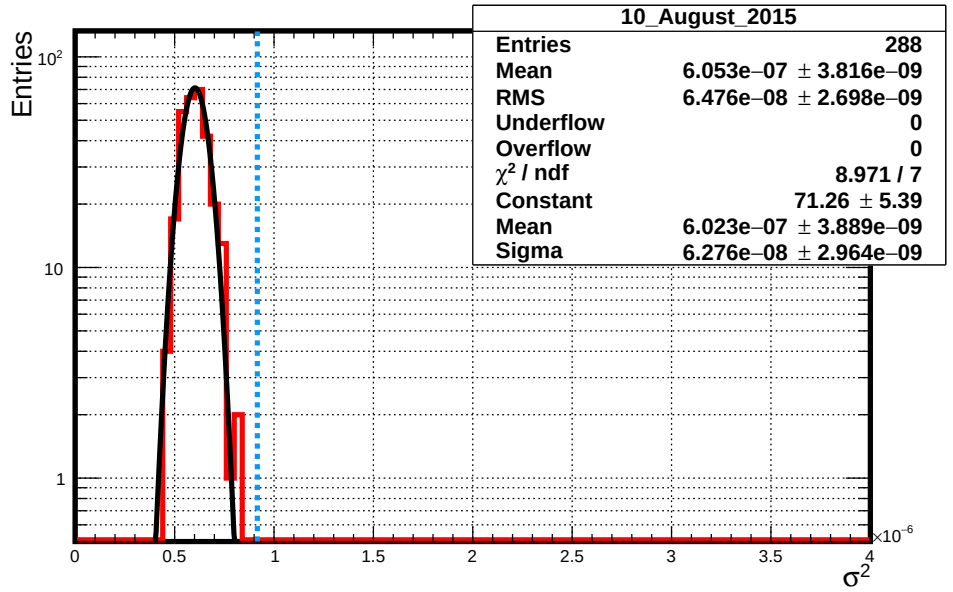

FIGURE 4.12: Histogram of average scaler rate variability of August 10, 2015. No significant excesses $\geq 5\sigma$ level are observed. The vertical dashed line shows the 5σ significance level.

The simulated γ-ray signal (number of particles per second from the entire SD array) from the direction of the Crab nebula at sub-PeV energies is added to consecutive 300 seconds of average scaler rate (CR background measurements). Then, the search for statistically significant excesses of the simulated signal at multi-TeV γ-ray is performed on a minute timescale by using the variability method (see Figs. 4.13, 4.14, 4.15, and 4.16).

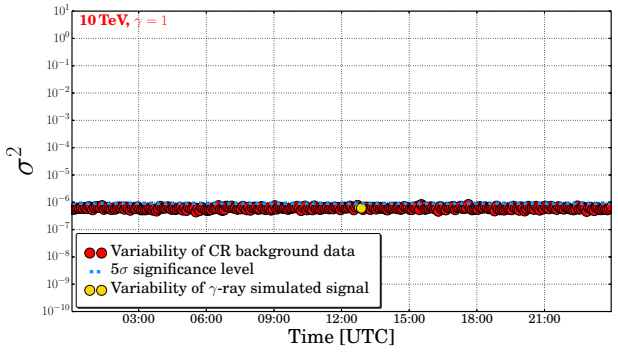

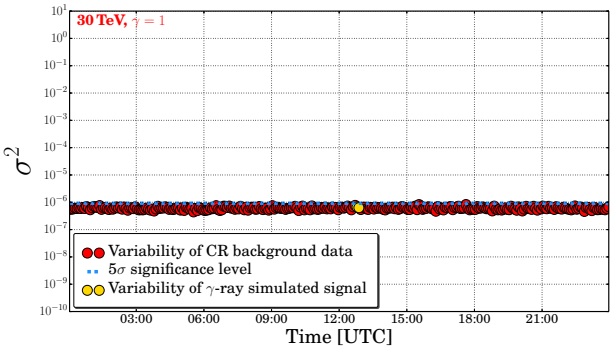

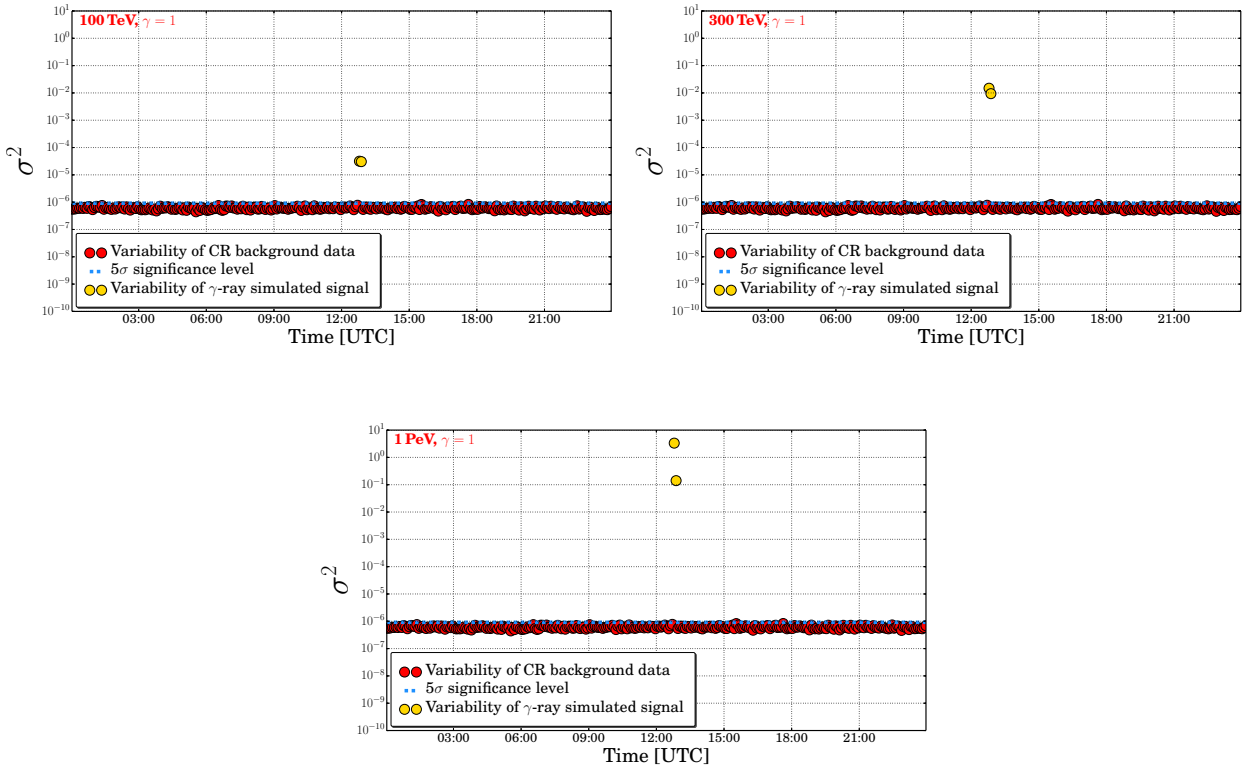

FIGURE 4.13: Daily variability plots of average scaler rate (background data) with the Crab simulated signal at multi-TeV energies and spectral index $\gamma = 1$. The event rate is added to 300 seconds of the average background rate. The measurements are corrected for the AoP and atmospheric pressure influence. We observe significant excesses $>5\sigma$ at 100, 300, and 1000 TeV with very hard spectral index $\gamma = 1$.

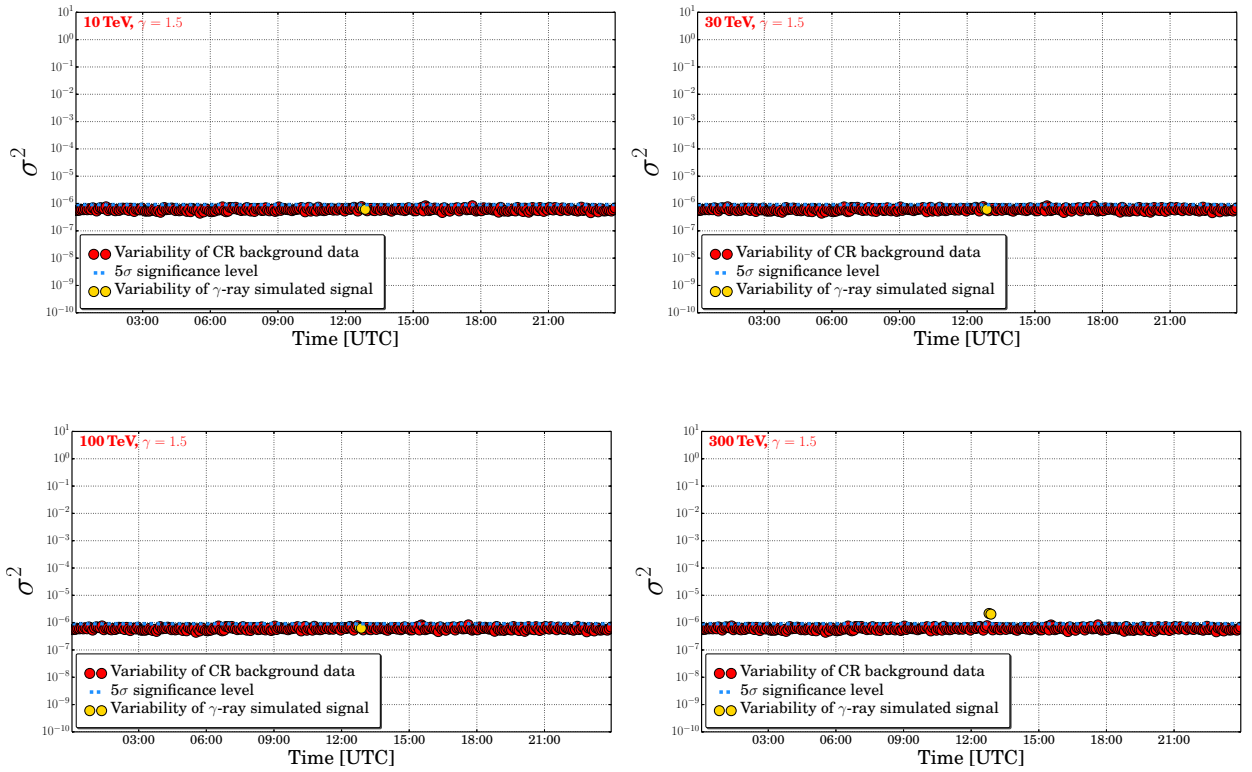

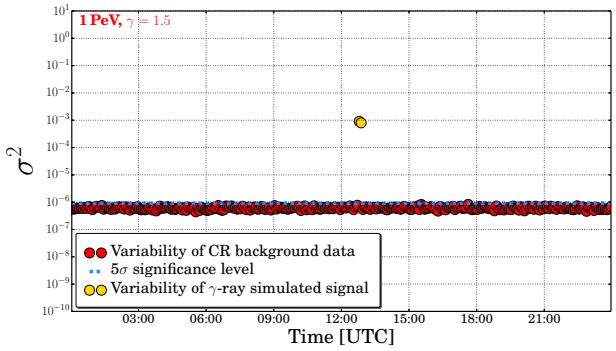

FIGURE 4.14: Daily variability plots of average scaler rate (background data) with the Crab simulated signal at multi-TeV energies and spectral index $\gamma = 1.5$. The event rate is added to 300 seconds of the average background rate. The measurements are corrected for the AoP and atmospheric pressure influence.

We observe significant excesses $>5\sigma$ at energies above 100 TeV with very hard spectral index $\gamma = 1.5$.

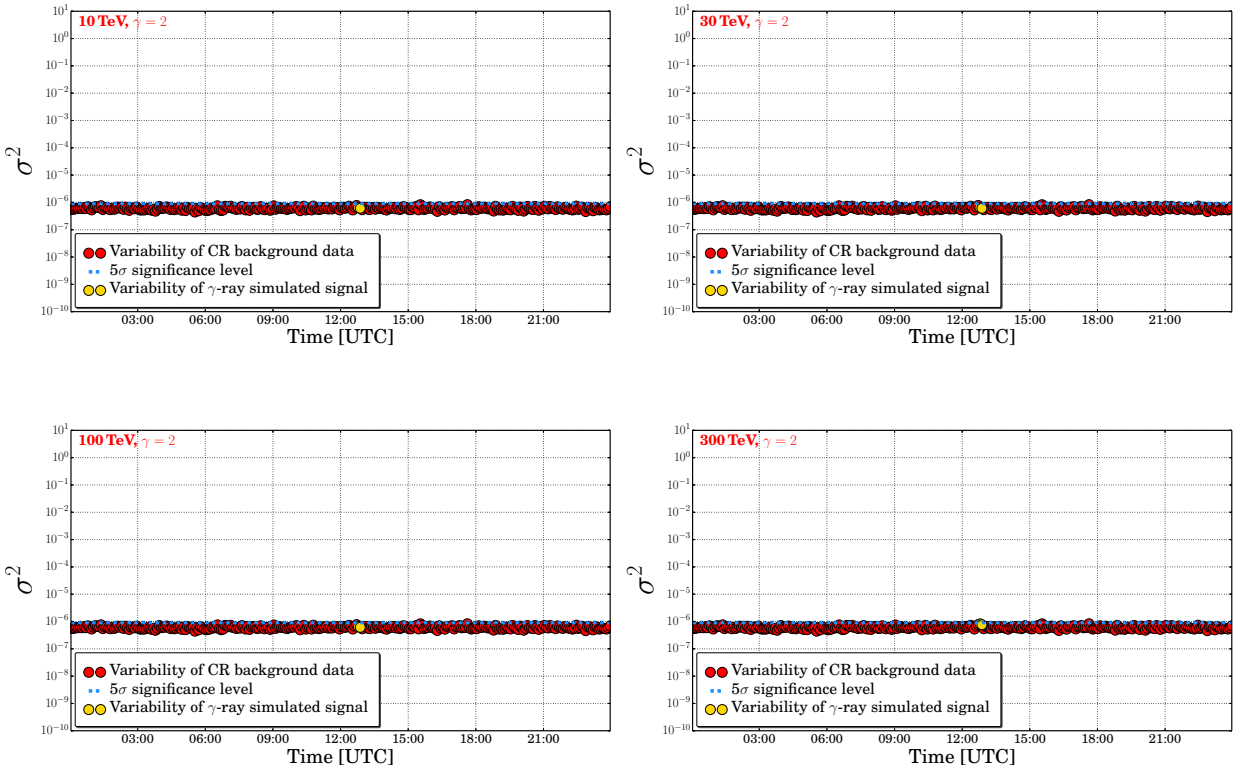

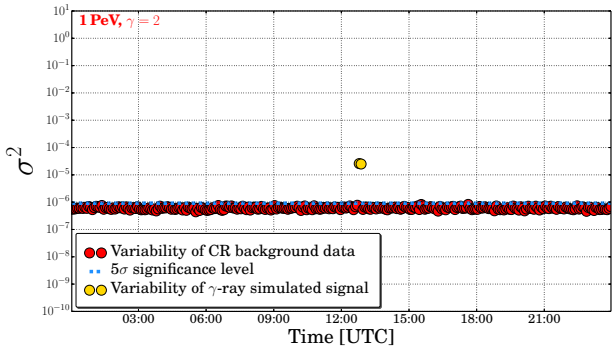

FIGURE 4.15: Daily variability plots of average scaler rate (background data) with the Crab simulated signal at multi-TeV energies and spectral index $\gamma = 2$. The event rate is added to 300 seconds of the average background rate. The measurements are corrected for the AoP and atmospheric pressure influence. We observe significant excesses $>5\sigma$ at 1 PeV with hard spectral index $\gamma = 2$.

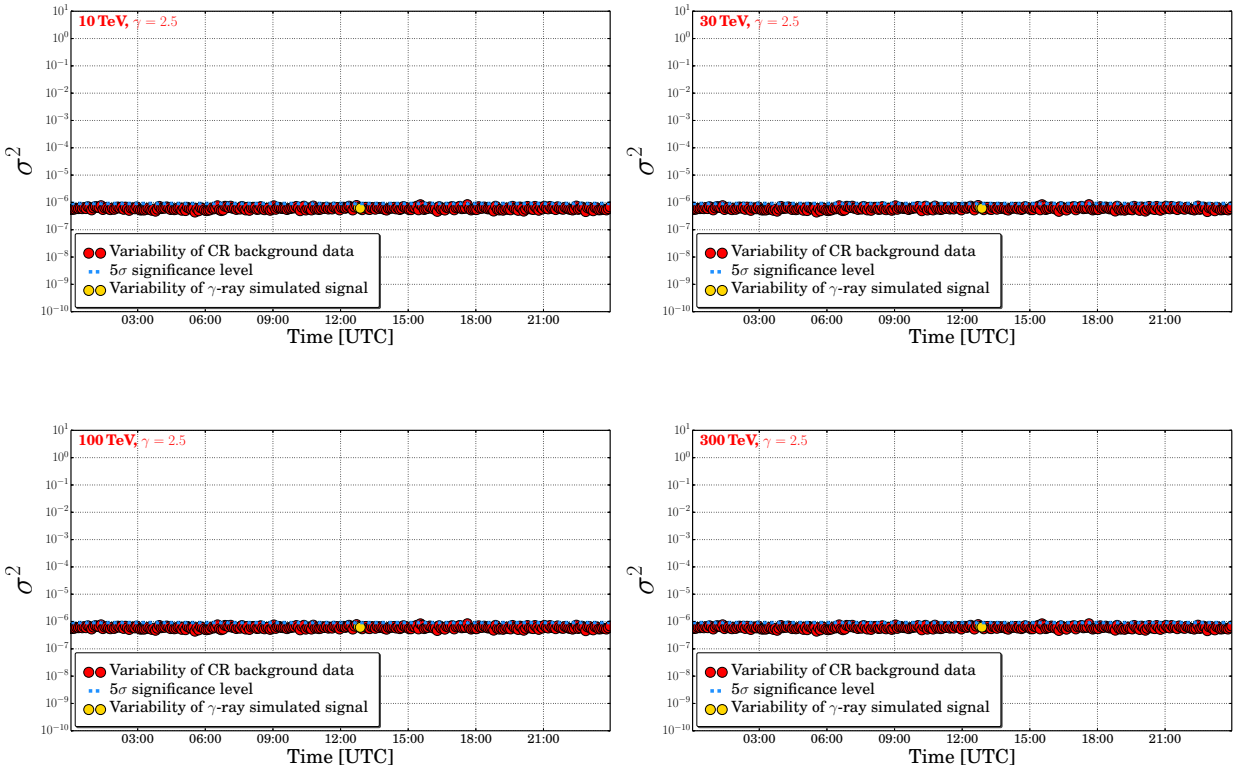

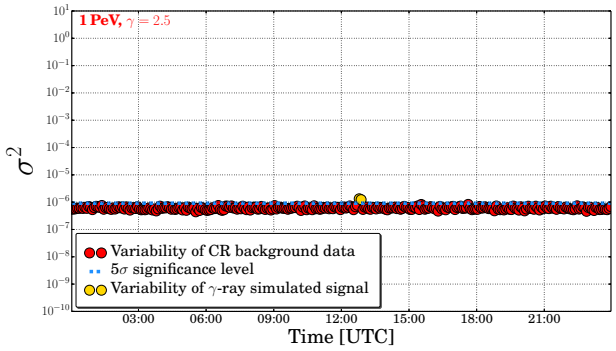

FIGURE 4.16: Daily variability plots of average scaler rate (background data) with the Crab simulated signal at multi-TeV energies and spectral index $\gamma = 2.5$. The event rate is added to 300 seconds of the average background rate. The measurements are corrected for the AoP and atmospheric pressure influence. We observe significant excesses $>5\sigma$ at 1 PeV with hard spectral index $\gamma = 2.5$.

Significant excesses (above 5σ significance level) of the simulated γ-ray signal from the Crab nebula are clearly visible on the average background rate variability, at 100, 300, 1000 TeV γ-ray, with very hard and hard spectral indices. The obtained simulation results can confirm expectations of the sensitivity of the Auger low-energy scaler mode to γ-ray flares from the direction of the Crab nebula, with respect to the Pierre Auger Observatory site, as well as from hard and very hard spectrum sources.

The detection of γ-ray emitters, such as the Crab nebula, by the ground-based instruments leads to better understanding to their structure, besides, acceleration processes, interactions, and propagation of the non-thermal particles of Galactic and extragalactic origins. The Crab nebula has served for long time as a standard calibration candle in several astronomical disciplines, such as X-ray and γ-ray astronomy, due to its stability and strong emission of high flux. Such surprising source imposes challenges to the theory of astroparticle acceleration and the models of γ-ray emission, as the Crab finally switched to be a variable source, with emitting VHE γ-ray flares. In 1989, there have been results that the Crab emission reached VHE domain at energies >100 TeV. Such early detection of the Crab nebula γ-ray outburst had been carried out by several experiments of EAS technique, such as the Kolar Gold Fields (KGF), the Baksan Air Shower Array (BASA) [186], and finally by the EAS-TOP array [187]. Recently, the AGILE and *Fermi*-LAT γ-ray detectors have frequently detected an enhanced γ-ray emission at energies $E > 100$ MeV from the direction of the Crab nebula. In the following we present a review of the Crab nebula and pulsar, with a focus on the observed γ-ray flares (see details in Chapter 5).

Chapter 5

The Crab Nebula and its Pulsar

The Crab (the Crab nebula and its pulsar) is the remnant of the historical supernova explosion observed by the Chinese astronomers on July 4, 1054 AD. A "guest star" was visible for three weeks during the daytime, and for 22 months at night [107, 188]. The Crab nebula was primarily identified in 1731 by an English astronomer John Bevis. In 1758, the nebula was independently rediscovered by Charles Messier, who was interested in observing comets. Messier founded a small nebulous/cloudy source in the constellation of Taurus, while following a bright comet of 1758. He then included such nebulous object as a first entry in his famous catalog of comet-like objects [189], which ultimately became the most famous catalog of galaxies, star clusters and nebulae in the field of astronomy. The Crab nebula was named by William Parsons, 3rd Earl of Rosse, who used a 36-inch telescope to observe the source in 1840, and hence he produced a drawing (first depiction of the nebula) that looked like a Crab [190].

The development of the astronomical photographic methods in the last ninetieth allowed to study the Crab nebula. First photograph was obtained by Isaac Robert in 1892, who noticed that the Crab nebula doesn't resemble any known object at that time. Robert's conclusion had been confirmed later, when Keeler, Curtis, Ritchey, and other astronomers made more photographs of the Crab nebula, which revealed its filamentary structure [191]. The Crab nebula was one of the first sources studied, during early spectroscopic observations of the sky that had been started by Vesto Slipher in 1913 at the Lowell Observatory. Slipher had inferred from his spectroscopic measurements that the Crab nebula was expanding at velocity of $\sim$1.000 km s^{-1} [192]. Through tracing the expansion back, the naked-eye visibility of the nebula from the Earth was quite possible about 900 years ago since that time, which backs to the Chinese historical record of the "guest star" in 1054 AD, from the same sky location. Such result is considered as a first connection of the Crab nebula to the bright supernova (SN) of 1054 AD, i.e., the Crab is the first identified supernova remnant (SNR).

In 1921, Lampland observed fluctuations in brightness of the Crab nebula, besides, possible changes in its position and structure [193]. John Charles Duncan, in the same year, studied the Crab nebula changes. He measured the resulting displacements of 12 symmetrical nebulous point with respect to comparison stars, over time interval of $\sim$11 years. Duncan in his study (see [194]) illustrated that the Crab nebula is expanding. Knut Lundmark had presented in Ref. [195] evidences of the proximity of the Crab nebula to the SN of 1054 AD.

Walter Baade in 1942 had presented observations of detailed structure [196] of the Crab nebula, and proposed that an exciting star near the center of the nebula could be its origin. In 1973, Virginia Trimble had presented several methods [197] to compute the distance to the Crab nebula. The Trimble's analysis allowed to estimate the distance to the nebula $\sim$1.9 kpc, which is consistent with the currently used value of 2 kpc.

The electromagnetic emission of the Crab nebula has been detected over 20 decades in energies, from radio waves to γ-rays of at least a few 10 TeV. The Crab holds a unique place in astrophysics by constantly providing new observational results and by stimulating new theories to explain the observations. It became the first radio source (1949) and the first X-ray source (1963) identified with a Galactic object other than the Sun; the first source for which linear polarization, characteristic of a synchrotron emission, has been observed (1954); the first remnant of a historical supernova for which a pulsar has been detected (1968) and optically observed (1969). With the development of very high-energy (VHE; $E \gtrsim 100$ GeV) γ-ray astronomy, the Crab nebula became the first object firmly detected (1989) at TeV energies using the imaging atmospheric Cherenkov technique. The same technique has been used to detect (2008) the VHE γ-ray emission of the Crab pulsar, challenging the models of the VHE γ-ray emission in pulsar magnetospheres. The Crab remains an authentic laboratory for studying the non-thermal processes in the Universe, as shows the recent detection of high-energy (HE; $E \gtrsim 100$ MeV) γ-ray flares from the nebula by AGILE and *Fermi*-LAT satellite detectors [107]. The AGILE data can be found at the ASI Data Center [198]. The *Fermi*-LAT team has monitored numerous light curves of bight and transient sources. The dataset of the monitored sources is available at the Fermi Science Support Center [199].

5.1 The Crab supernova remnant

The Crab nebula is the prototype of compact synchrotron nebula (pulsar-powered nebula), which is conventionally known as a pulsar wind nebula (PWN). The pulsar wind nebulae (PWNe) are commonly known as bubbles of relativistic particles and magnetic field produced as a consequence of the interaction of the ultra-relativistic wind, emerged from a rapidly rotating neutron star, with the supernova remnant (SNR) or the ambient medium. Hence, the nebula is continuously powered

by the ultra-relativistic magnetized wind from the young rapidly rotating pulsar located at Its center. The nebula is confined within a no-relativistic medium, the wind therefore terminates at ensemble of shock waves, which fills the nebular medium (see Fig. 5.1). This energy from the pulsar produces large bubble of relativistic fluid that emits **synchrotron radiation** [200, 201] from the radio to γ-ray energy domain.

FIGURE 5.1: A composite Hubble Space Telescope image of the Crab nebula made using red, green, and blue filters. The thermal filaments, composed of ejecta of the exploded star, dominate the outer part of the remnant, and reveal a sophisticated structure of the magnetic field within the nebula, at which the relativistic particles propagate in the outer nebula region. The central part of the Crab shows the axial symmetry of the bluish synchrotron emission of the relativistic electrons, which results from the rotation of the young and energetic pulsar that powers the nebula. Taken from Ref. [188].

A Crab-like SNR has a filled central part, which is brighter than the periphery, contrary to the shell-type SNR. We will now describe successively the Crab pulsar, the synchrotron nebula, and the expanding ejecta.

5.1.1 The Crab pulsar

The Crab pulsar is a relatively young and energetic neutron star located in the center of the Crab nebula. It has a spin period of $P = 33.6\,\text{ms}$, which is slowed-down by $\dot{P} = 4.21 \times 10^{-13}$. Under the

assumption of a uniform density sphere of a radius 10 km and a mass of 1.4 $M_\odot$, the Crab pulsar has moment of inertia $I \approx 1.1 \times 10^{45}$ g cm^2, and its spin-down luminosity is $L_{\rm spin} = 4\pi^2 I \frac{\dot{P}}{P^3}$, which equals to 130.000 $L_\odot$. A small fraction of pulsar's spin-down energy loss $\sim$1% is emitted in pulsed electromagnetic radiation, while the rest goes to a combination of magnetic dipole radiation and ultra-relativistic wind, and is then converted into synchrotron emission of the Crab nebula [188]. The Crab pulsar is powering the nebula, and has been intensively studied in all frequencies from radio waves to gamma rays, showing atypical emission properties with respect to other known pulsars at both ends of the electromagnetic spectrum.

At **radio waves**, the Crab pulsar belongs to a dozen of pulsars, among $\sim$1800 currently detected, from which the so-called "giant" radio pulses [202, 203] have been observed. The name of "giant" pulses is attributed to occasional individual radio pulses, which intensity surpasses the one of the "normal" pulses by a large factor ($>$1000). The fine structure of the Crab giant pulses, as short as 2 ns, corresponds to a size of emitting region of only $\sim$60 cm, thus to the smallest objects ever detected outside of the Solar System. The equivalent brightness temperature of the Crab giant radio pulses exceeds 5×10^{37} K, which ranges them among the brightest radio transients in the Universe. Historically, the Crab pulsar has been discovered [204] due to its giant radio pulses; the period of "normal" pulses has been measured [205] a few weeks later after the discovery, with the help of the radiotelescope in Arecibo.

At **VHE γ-rays**, an unexpectedly slow spectral decay has been measured by MAGIC [206–208] and VERITAS [209] experiments. There is no spectral cutoff in the pulsed γ-ray emission up to the energy of 400 GeV, contrary to all other ($\sim$120) pulsars in the second *Fermi*-LAT pulsar catalog [210], in which γ-ray show spectra cutoff around 1 GeV.

5.1.2 The synchrotron nebula

The Crab synchrotron nebula results from the interaction of the ultra-relativistic and highly magnetized plasma of $e^\pm$ pairs injected by the pulsar, with the thermal ejecta from the supernova explosion. Upstream of the pulsar wind termination shock (seen as the bright innermost ring surrounding the pulsar on Fig. 5.2), the wind is dominated by the kinetic energy of the flow and is not luminous. At the shock, the wind particles are accelerated up to 10^4 TeV and randomized in their angle with respect to the ambient magnetic field. The radiation produced by these particles downstream of the termination shock is then seen as the synchrotron nebula. The synchrotron nebula fills a volume which can be approximated by an ellipsoid with a major axis of 4.4 pc and a minor axis of 2.9 pc and is tilted to the plane of the sky by 30° [107]. The Chandra X-ray image shows an axisymmetric

structure around the pulsar's rotation axis, with a torus and a jet. The torus-jet structure doesn't show strong spectral variations from infrared to X-ray energies.

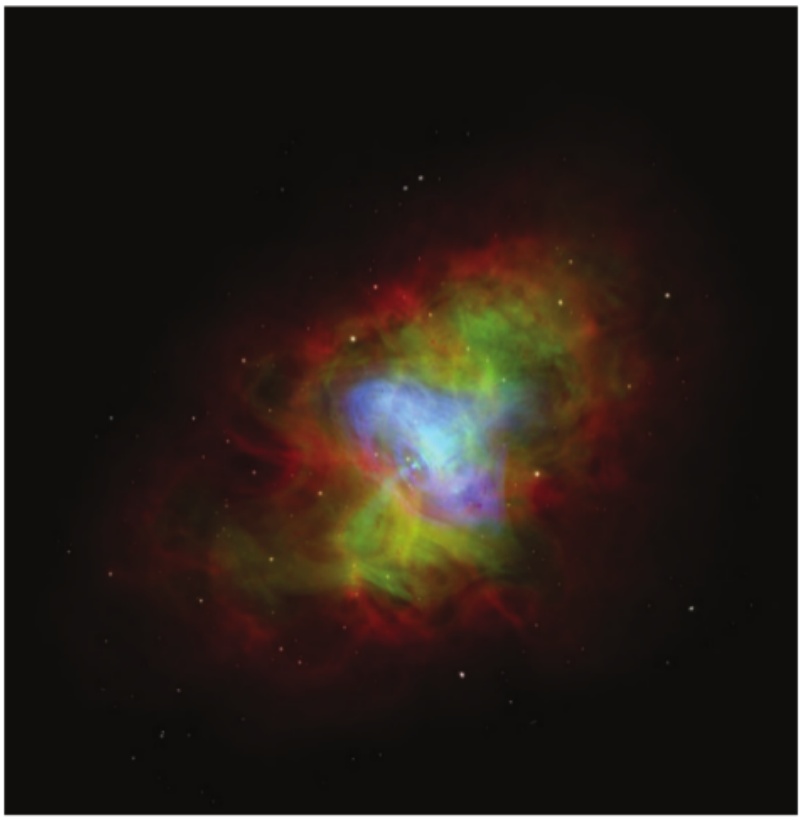

FIGURE 5.2: A composite multi-wavelength image of the Crab synchrotron nebula shows Chandra X-ray in blue, HST visible light in green, and VLA radio in red. The pulsar is located at the center of the nebula and marked in bright blue. The nebula is symmetrical around the axes, shown by the X-ray torus and jets. Near to the center of the nebula, where the electrons are injected, the emission from high-energy electrons is brightly shown. The emission gets softer as the observer moves outward far from the center, where adiabatic and radiative losses occur. At the edge of the nebula, the low-energy radio emission by electrons is predominant. Taken from Ref [107].

The emission from the nebula is linearly polarized from radio to hard X-rays, confirming its synchrotron origin, and the distribution of the polarization angle reveals the complex structure of the magnetic field within the nebula. The size of the nebula increases at lower frequencies (see Fig. 5.2), which reflects the processes of radiative cooling of electrons, as they are moving away from the nebula center by convection and diffusion. The average spectral energy distribution (SED) of the Crab nebula and pulsar is shown in Fig. 5.3.

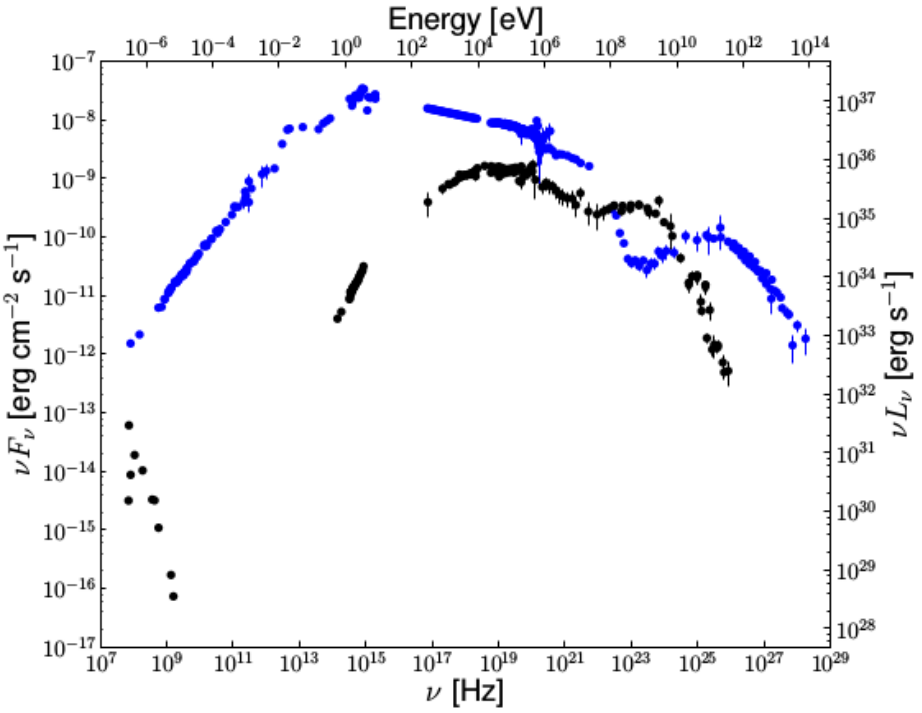

FIGURE 5.3: The spectral energy distribution of the average emission of the Crab nebula (blue) and the Crab pulsar (black). The low frequencies of radio band $\lesssim$1 GHz appeared on the plot are caused by non-contemporaneous records, which could be affected by time varying interstellar scintillation. The luminosity given on the right axis is calculated at a distance of $\sim$2 kpc. Taken from Ref. [107].

The spectrum of the synchrotron nebula follows a power law shape at large energy ranges up to MeV γ-rays, which gets progressively steeper at higher energies. The first change of the spectral index occurs in the near infra-red, where also a bump due to the thermal emission of the dust within the nebula is observed. The lifetime of the electrons with respect to the synchrotron energy losses τ_{syn} gets smaller than the nebula age at frequencies $>10^{13}$ Hz. This implies that the pulsar continuously ejects electrons into the nebula, in order to maintain stability of the emission. The stability of the Crab nebula emission besides its high flux at 30 keV (X-rays) allowed to use it as a standard calibration candle in the X-ray astronomy. This led the astronomers to express the flux from other X-ray astronomical sources in "Crab" flux unit, e.g. Crab, milliCrab, etc. The Crab flux unit has been utilized by the community of γ-ray astronomy as well, since the development of the ground-based γ-ray astronomy provided the possibility to study the very-high energy (VHE; $E \geq$ 30 GeV) via employing indirect detection techniques (see § 2.1).

Besides the main **synchrotron** component extending up to $\sim$1 MeV, we note on Fig. 5.3 a spectral hardening above this energy, followed by a rapid cut-off towards $\sim$150 MeV. This variable part of the SED, discovered by COMPTEL and EGRET telescopes onboard the Compton Gamma-Ray Observatory in the years 1990, is interpreted as a synchrotron emission of the population of electrons, which is attributed to variable and compact structures of the typical size of $\sim 0.2''$

observed by ROSAT, Chandra, VLA and Hubble Space Telescope. These structures - called wisps, knots etc. [188] - represent local electron over-densities in the proximity of the terminal shock of the pulsar wind, and also along the jet. In total, the synchrotron emission from the Crab nebula has integrated luminosity of $\sim 1.3 \times 10^{38}\,\mathrm{erg\,s^{-1}}$, i.e. $\sim$26% of the energy injected into the nebula by the pulsar, which shows the high conversion efficiency.

The presence in the Crab nebula of relativistic electrons and dense photon fields results in efficient **inverse Compton** scattering of low energy photons to the VHE range. The corresponding SED component, peaking around 100 GeV (see Fig. 5.3), has been predicted by Gould [211] as early as in 1965. However, almost a quarter of century of development of the measurement techniques was necessary to detect this VHE γ-ray emission above the cosmic-ray background using the atmospheric Cherenkov imaging.

5.1.3 Expanding ejecta of the exploded star

The thermal filaments of the Crab nebula are composed of the material of the atmosphere of the progenitor star, and consist mostly of the ionized helium and hydrogen, along with smaller admixture of heavier elements. The observations of the filaments show that their expansion velocities range from $\sim$700 km/s to $\sim$1800 km/s with a characteristic velocity $\sim$1500 km/s at the visible edge of the nebula. Tracing back the expansion of the Crab, one obtains the estimate of the age of the remnant several decades smaller than the true one, which implies that ejecta are moving $\sim$100-300 km s$-$1 faster than the free expansion velocity. This accelerated expansion is due to the pressure on the ejecta exerted by the confined synchrotron nebula.

Spectroscopic studies of the Crab filaments allow to estimate their mass to be of order 2-5 $\mathrm{M_\odot}$. Together with the pulsar (1.4 $\mathrm{M_\odot}$), this is less than the mass (at least 8 $\mathrm{M_\odot}$) required for a progenitor of a Type II (core collapse) supernova. The kinetic energy of the Crab filaments, of $\sim 3 \times 10^{49}$ erg, is also a factor of 30 less than the typical values of $\sim 10^{51}$ erg observed in the ejecta of the Type II supernovae. The missing mass and kinetic energy are attributed to an additional remnant component, with a radius a few times larger than the observed Crab, freely expanding into a tenuous cavity of interstellar medium (with a size of $\sim$130 pc) surrounding the Crab, which makes its detection extremely difficult. The recent measurements, by the Hubble Space Telescope, of the blue shift of the C IV absorption line in the spectrum of the Crab pulsar allowed to set conservative lower limits on the mass ($M > 0.3\,\mathrm{M_\odot}$) and the kinetic energy (KE $> 1.5 \times 10^{49}$ erg) of this additional component of the ejecta of the Crab SNR [188].

5.2 Steady high-energy γ-ray emission of the nebula

The cosmic γ-rays can be detected at higher energies $>10^{11}$ eV [212] by observing the atmospheric Cherenkov light produced in the accompanied extensive air showers (EAS). By the use of the ground-based atmospheric Cherenkov technique, early observations of the Crab γ-rays EAS have been implemented over six dark nights of good measuring conditions in November 1971 by the Smithsonian Astrophysical Observatory. In that study 68 drift scans on the Crab were obtained. Each drift scan centered on ∼1-minute transit time of the Crab for ∼20-minute duration, followed by 31 additional scans taken over three dark nights in December. These measurements for the Crab EAS ended with a detection of 4.5σ excess at the optical interpulse phase. The detection of TeV γ-ray emission from the Crab nebula not only asserts the Compton synchrotron model, but is also considered as a direct tool for magnetic field measurements. The observations of γ-ray flux ($4.4\pm1.4\times 10^{-11}$ photon cm^{-2} s^{-1}) from the Crab nebula at energy ≥ 0.25 TeV have been reported by the Smithsonian Astrophysical Collaboration in 1972 [213]. The detection has been achieved at a level of 3.1σ in a period averaged over three-year measurements. The study concluded that the γ-ray flux from the Crab could vary over time, with a significant flux of $1.21\pm0.24\times 10^{-10}$ photon cm^{-2} s^{-1} in a period of 60-120 days after a major spin-up of the Crab pulsar NP 0532. The significant excess detected in the Crab γ-ray flux was at 5σ level with energy of $\sim 10^{12}$ eV.

The electro-optical equipment is the only difference between both previous reports of the year 1972. A new photomultiplier (RCA C31000N) of higher quantum efficiency in ultraviolet band had been used in the first study reported by Grindlay in Ref. [212]. These studies had essentially relied on ON/OFF ratio of the counting rate. No imaging of atmospheric Cherenkov light had been used.

In the period between November 11, 1988 and March 8, 1989, under proper weather and sky conditions, the Crab nebula was detected at energies >100 GeV by the Whipple 10 m telescope via improving the technique of the atmospheric Cherenkov [65, 214, 215]. The Whipple 10 m γ-ray telescope used a 37 pixel camera, and the Crab detection was declared as a **steady** (unpulsed) signal at 9σ level, which corresponds to a flux of 1.8×10^{-11} photon cm^{-2} s^{-1} and energy >0.7 TeV. The γ-ray spectrum from the Crab nebula has been measured in 500 GeV-8 TeV energy range by the Whipple Collaboration. The spectrum was obtained for this energy range (GeV-TeV) by the power-law fit of a form $\Phi_\gamma = (3.25\pm0.14\pm0.6)\times10^{-7}\times E^{-2.44\pm0.06\pm0.04-0.151\log_{10}(E)}$ photon m^{-2} s^{-1} TeV^{-1}, where E is energy in TeV with integral flux >1 TeV is given by $(2.1\pm 0.2\pm0.3)\times10^{-7}$ photon m^{-2} s^{-1}. Such detection was confirmed independently [214, 216] using two optical reflectors of 11-meter diameter at Sandia Laboratory in Albuquerque. Therefore, the Whipple telescope firmly detected the Crab nebula as a steady γ-ray emitter at TeV energies using imaging atmospheric Cherenkov technique.

A bit later, new set of observations had been performed using an improved camera on the Whipple 10 m telescope [214]. Such improvement resulted in another detection for a steady (unpulsed) Crab nebula signal at 20σ level reported in 1991. The Crab nebula energy spectrum was obtained at energy range (0.4-4) TeV, with a flux of a form $N(E) \times dE = 2.5 \times 10^{-10}(E/0.4\,\mathrm{TeV})^{-2.4\pm0.3}$ photon $\mathrm{cm}^{-2}\,\mathrm{s}^{-1}$ TeV^{-1}. This 20σ of the Crab nebula detection by the Whipple Collaboration is widely accepted by the community of γ-ray astronomy [217], as the detection of the Crab nebula at such highest energies was confirmed by the observations carried out by the ASGAT TeV γ-ray telescope in southern France [218], as well as the THEMISTOCLE Collaboration [219]. ASGAT used different instrumental design to observe the Crab nebula for 50 hr in the period between 1991 and 1992. Such design was basically based on measurements of the Cherenkov light front via employing an array of independent detectors. THEMISTOCLE array, which composed of 18 Cherenkov detectors, declared the detection of Crab nebula in 1993 at 5.8σ level at (3-15) TeV energy range.

During other set of observations that took place between November 1994 and March 1997, the Whipple 10 m γ-ray telescope was searching for a pulsed TeV emission from the Crab pulsar. The total period of the observations was 73.4 hr and the telescope was operating at its lowest energy threshold with spectral analysis techniques. No γ-ray signal of 33 ms pulsations has been found within the energy band 250 GeV to 4 TeV [220]. The Whipple telescope was taking regular measurements for the Crab nebula till its decommissioning in 2011. Therefore, a search for short-term flares in the extended VHE of the Crab nebula was carried out by the Whipple telescope over the 10-year period of a Crab dataset. No evidence for a significant Crab flaring activity has been found by the Whipple telescope [221].

The development of the Imaging Atmospheric Cherenkov Telescopes (IACTs) technique was necessary during the last decades to detect such VHE γ-ray emission above the cosmic ray background. Thus, the Crab nebula γ-ray emission from the inverse Compton component has been detected by several ground-based experiments via hiring arrays of the IACTs technique, such as the High Energy Gamma Ray Astronomy (HEGRA) [222], H.E.S.S. [223], MAGIC telescopes [224], and VERITAS [225, 226].

The HEGRA experiment has observed the Crab nebula and its pulsar for ∼400 hr from the period between 1997 to 2002 [222]. The differential energy spectrum of the accumulate dataset from the Crab has been fitted by a power-law in the form $\Phi(E)/dE = \Phi_0 \times (E/\mathrm{TeV})^s$, where $\Phi = (2.83 \pm 0.04_{\mathrm{stat}} \pm 0.6_{\mathrm{sys}}) \times 10^{-11}$ photon $\mathrm{cm}^{-2}\,\mathrm{s}^{-1}\,\mathrm{TeV}^{-1}$ and $\gamma = -2.62 \pm 0.02_{\mathrm{stat}} \pm 0.05_{\mathrm{sys}}$. The Crab spectrum obtained by HEGRA extends up to energy $E = 80$ TeV, which is well consistent with calculus of the inverse Compton scattering of numerous photons in the nebula. The emission region is constrained to a size less than $2'$ at energies between 1 and 10 TeV. At energies >30 TeV,

the size is constrained to less than $3'$. No evidence for a pulsed emission has been found by the HEGRA experiment.

The Crab nebula was observed for 22.9 hr in the period between October 2003 to January 2005 by the H.E.S.S. stereoscopic Cherenkov telescope array [223]. The measurements of the Crab flux are taken at different sectors of zenith angles ranges from 45° to 65°. A distinct signal with over 7500 excess events has been detected by the H.E.S.S. telescope. The SED has been found to obey a power-law with observed integral flux $(2.26 \pm 0.08_{\rm stat}) \times 10^{-11}$ photon cm^{-2} s^{-1} and an exponential cutoff. The photon spectral index $\gamma = 2.39 \pm 0.03_{\rm stat}$ and the cutoff energy $E_{\rm cutoff} = 14.3 \pm 2.1_{\rm stat}$ TeV at energies between 440 GeV to 40 TeV.

The MAGIC telescope has collected a data of 69 hr of the Crab nebula in the period between October 2009 and April 2011. The SED of the Crab nebula was obtained by the MAGIC stereoscopic software with unprecedented precision from 50 GeV to 3 TeV. The daily light curve of the Crab nebula at energies >300 GeV has been presented by the MAGIC Collaboration in Ref. [224] from October 15, 2009 to April 6, 2011. The average flux of the Crab nebula at HE γ-ray emission is $\Phi_{>300\,\rm GeV} = (1.20 \pm 0.08_{\rm stat} \pm 0.17_{\rm sys}) \times 10^{-10}$ photon cm^{-2} s^{-1}.

5.3 High-energy γ-ray emission of the pulsar

Intensive studies for the Crab have been performed by the space-based observations. The overall Crab nebula flux showed a decline of ∼7% (70 milliCrab) at 15-50 keV energy range in the period 2008-2010. This decrease in the Crab flux was observed by the *Fermi* Gamma-ray Burst Monitor (GBM) and confirmed by three additional detectors; the Swift Burst Alert Telescope (Swift-BAT), the Rossi X-ray Timing Explorer Proportional Counter Array (RXTE-PCA), and the International Gamma-Ray Astrophysics Laboratory Imager on Board (INTEGRAL-IBIS). According to these measurements from four independent spacecrafts, the nebula X-ray and γ-ray emissions varies at a level of ∼3.5% yr^{-1} [227, 228].

Roughly a 30 year-long effort has been exerted by the ground-based γ-ray observations, in order to detect the Crab pulsar at VHE γ-rays. The pulsed emissions from the pulsars are described by two common models; the polar cap and outer gap models. The detection of a pulsed γ-ray emission from the Crab pulsar was claimed for the first time by the KGF and Baksan experiments, during the February 1989 Crab flare (discussed in § 5.4). The two detectors pointed to possible periodicity of the detected emission at likely sub-PeV γ-rays, as it was consistent with the period of the Crab pulsar. Later, the search for the Crab pulsar signature was implemented by several previous

experiments, such as the Whipple Observatory, ASGAT TeV γ-ray telescope, and THEMISTOCLE Collaboration, and no evidence for the Crab pulsar periodicity had been found. However, the EGRET detector aboard the Compton Gamma Ray Observatory detected pulsed γ-ray emission from the Crab pulsar [229, 230] at GeV energies.

In 2004, the MAGIC Collaboration searched for pulsed γ-ray from the Crab pulsar. No evidence has been found for pulsed emission at the expected frequency in the data taken at that period [230]. In 2009, the MAGIC Cherenkov telescope reported on the detection of pulsed γ-rays from the Crab pulsar [231] at VHE range above 25 GeV. The energy spectrum of the Crab pulsar has been specified and is shown in Fig. 5.4. The trigger threshold of the MAGIC telescope has been reduced to 25 GeV from 50 GeV, which made such detection possible. The pulsed signal has been detected at 6.4σ level.

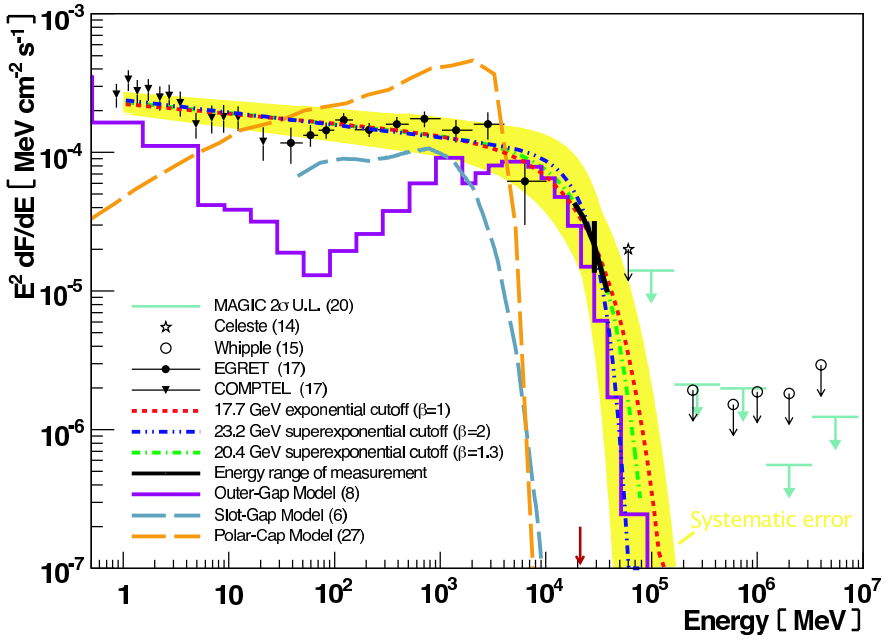

FIGURE 5.4: The SED of the Crab pulsar measured by MAGIC and various experiments. The solid circles and triangles show the pulsar flux measured by EGRET, while MAGIC is indicated by the horizontal lines with arrows on the right. The open circles and star with arrows represent the upper limits of several previous detectors, e.g. Whipple & CELESTE. Taken from Ref. [231].

In case of assuming an exponential cutoff $(\Phi \times \exp(-E/E_0))$, the detected signal is compatible with cutoff energy $E_{\text{cutoff}} = 17.7 \pm 2.8_{\text{stat}} \pm 5.0_{\text{sys}}$ GeV. On the other hand, if the super-exponential cutoff is supposed $(\Phi \times \exp(-E/E_0)^2)$, the measured signal shows a consistency with cutoff energy $E_{\text{cutoff}} = 23.2 \pm 2.9_{\text{stat}} \pm 6.6_{\text{sys}}$ GeV. A study of the very high-energy spectral tail of the Crab pulsar has been extended up to 400 GeV by the MAGIC Collaboration and reported in January 2016 [232].

The analyses of good quality Crab measurements of ∼320 h from February 2007 to April 2014 resulted in a detection of a pulsed γ-ray emission from the Crab pulsar at energies up to 1.5 TeV. The energy spectrum shows two peaks that obey two different power-law functions from 70 GeV to 1.5 TeV. Such feature is in agreement with the spectra measured by the *Fermi*-LAT above 10 GeV, as illustrated in Fig. 5.5.

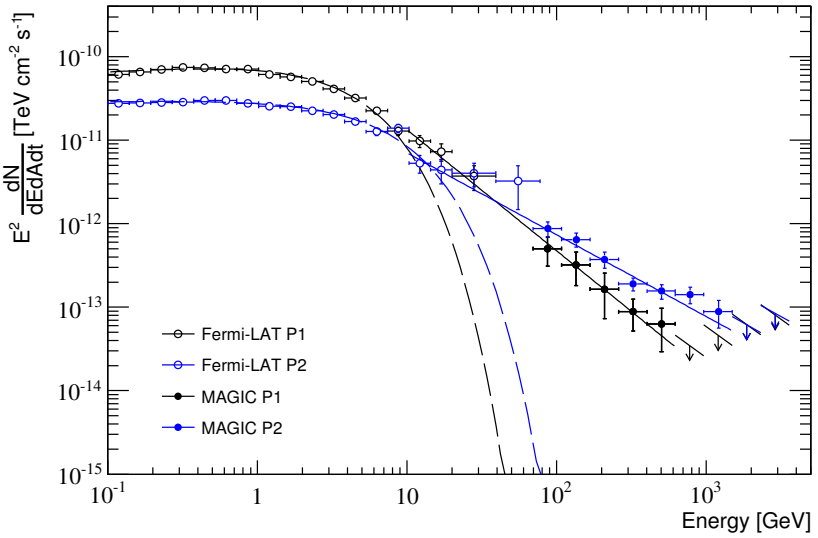

FIGURE 5.5: The SED of the Crab pulsar measured by *Fermi*-LAT and MAGIC at HE and VHE. The open circles indicate the Crab pulsar peak 1 (black) and peak 2 (blue) measured by *Fermi*-LAT. The solid circles show the Crab pulsar peak 1 (black) and peak 2 (blue) detected by MAGIC. The dashed lines refer to power-law fit functions of the *Fermi*-LAT data with an exponential cutoff. The solid lines represent power-law functions that fit both measurements (joint *Fermi*-LAT/MAGIC) at energies $E > 10$ GeV. The slope of the arrows denotes the upper limits to the differential flux at 95% CL, which calculated under the assumption that the power-law spectrum is verified. Taken from Ref. [232].

A pulsed γ-rays emission from the Crab pulsar has also been detected at energies >100 GeV [209] by the VERITAS array of atmospheric Cherenkov telescopes. The SED of the pulsed γ-ray emission is described by a broken power-law with an exponential cutoff between 100 MeV and 400 GeV (see Fig. 5.6).

The SED of the Crab pulsar is described by an exponential cutoff $\Phi(E) = A(E/E_0)^s \exp(-E/E_{\text{cutoff}})$ at energy $E > 1$ GeV, which yields a good fit parametrization for the *Fermi*-LAT and MAGIC Crab pulsar spectrum. The VERITAS flux measurements are compatible with spectral shape of a broken power-law. A fit of a broken power-law in the form of $A(E/E_0)^s[1+(E/E_0)^{s-\beta}]$ for the VERITAS and *Fermi*-LAT data leads to χ^2 value of 13.5 for 15 degree of freedom, where the fit parameters $A = (1.45 \pm 0.15_{\text{stat}}) \times 10^{-5}\,\text{TeV}^{-1}\,\text{cm}^{-2}\,\text{s}^{-1}$, $E_0 = 4.0 \pm 0.5_{\text{stat}}$ GeV, $\gamma = -1.96 \pm 0.02_{\text{stat}}$ and $\beta = -3.52 \pm 0.04_{\text{stat}}$.

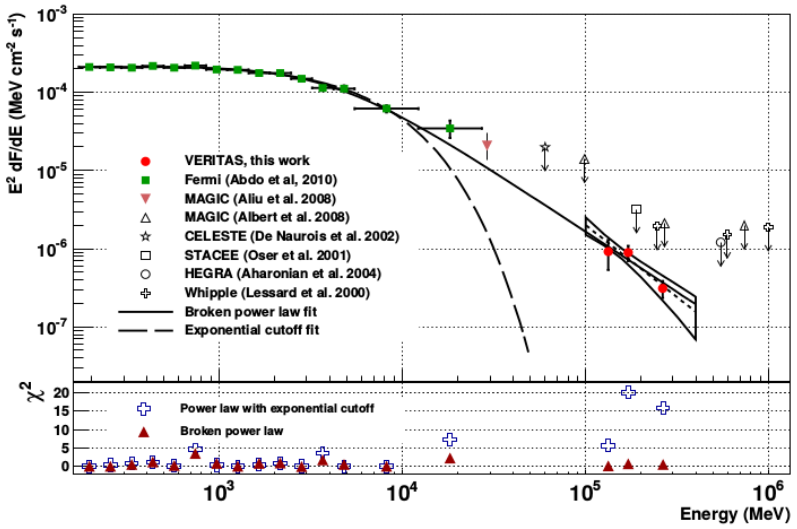

FIGURE 5.6: The spectral energy distribution (SED) of the pulsed γ-ray emission from the Crab pulsar. Red spots indicate VERITAS flux measurements using spectral reconstruction method. The bow tie gives the flux measurements done by VERITAS using a different method of forward-folding method. The dotted line enclosed in the bow tie represents the best power-law spectrum fit with statistical uncertainties for VERITAS data. The *Fermi*-LAT data are given by green squares and reddish triangle present MAGIC flux measurement. The open signs (triangle, star, square, circle, and cross) refer to the upper limits of MAGIC telescope, CErenkov Low-Energy Sampling and Timing Experiment (CELESTE), Solar Tower Atmospheric Cherenkov Effect Experiment (STACEE), High-Energy-Gamma-Ray Astronomy (HEGRA), and Whipple. The solid line denotes a broken power-law fit for the data taken by VERITAS and *Fermi*-LAT. The dashed line gives the fit results of a power-law spectrum multiplied by an exponential cutoff. The χ^2 values are plotted below the SED to visualize the deviations of the best fit parameters of the flux measured by *Fermi*-LAT and VERITAS. Taken from Ref [209].

The detection of γ-ray emission at energies $E > 100\,\mathrm{GeV}$ imposes strong primary conditions on the γ-ray radiation mechanisms, since two different plausible radiation scenarios could be dominant; the curvature radiation and the inverse Compton scattering. By assuming a balance between acceleration gains and radiative loss processes by curvature radiation, the break in the γ-ray spectrum is expected to be at $E_{\mathrm{break}} = 150\,\mathrm{GeV}\,\eta^{3/4}\,\xi^{1/2}$, where η is the acceleration efficiency ($\eta < 1$) and ξ is the radius of curvature (light-cylinder radius unit).

5.4 Enhanced high-energy gamma-ray emission of the Crab

The Crab nebula is used to calibrate X-ray and γ-ray telescopes and to cross-check their functionality over time. Nevertheless, variabilities in the Crab flux at high-energy (HE; $E > 100\,\mathrm{MeV}$) γ-rays have been recently revealed by the Fermi Large Area Telescope (*Fermi*-LAT) and AGILE satellites during the so-called *Crab γ-ray flares* [228, 233, 234], e.g. October 2007, February 2009, and September 2010 Crab flares. The Crab γ-ray flares are detected in energy range between the synchrotron and inverse Compton components of the spectral energy distribution. The synchrotron

component shows average flux of $\Phi_\gamma = (6.1 \pm 0.2) \times 10^{-7}$ photon cm^{-2} s^{-1} and the inverse Compton component is $\Phi_\gamma = (20.4 \pm 0.1) \times 10^{-7}$ photon cm^{-2} s^{-1} [107]. The synchrotron component of the nebula exhibits a variable feature over wide timescales, and it explains the X-ray and γ-rays spectra up to ∼100 MeV energies. However, the inverse Compton component of the nebula and pulsar emissions are found to be constant in time with measurement accuracies, and it models the emissions at **very-high energies** between GeV and TeV.

During the quiescent state, the flux remains below the *Fermi*-LAT detection threshold on a long timescale of several months, with a flux upper limits well below the average flux level. The Crab flux can rapidly rise during flares for a time interval of order of hours-days. The spectral energy distribution (SED) around the peak flux of the flares is shown in Fig. 5.7.

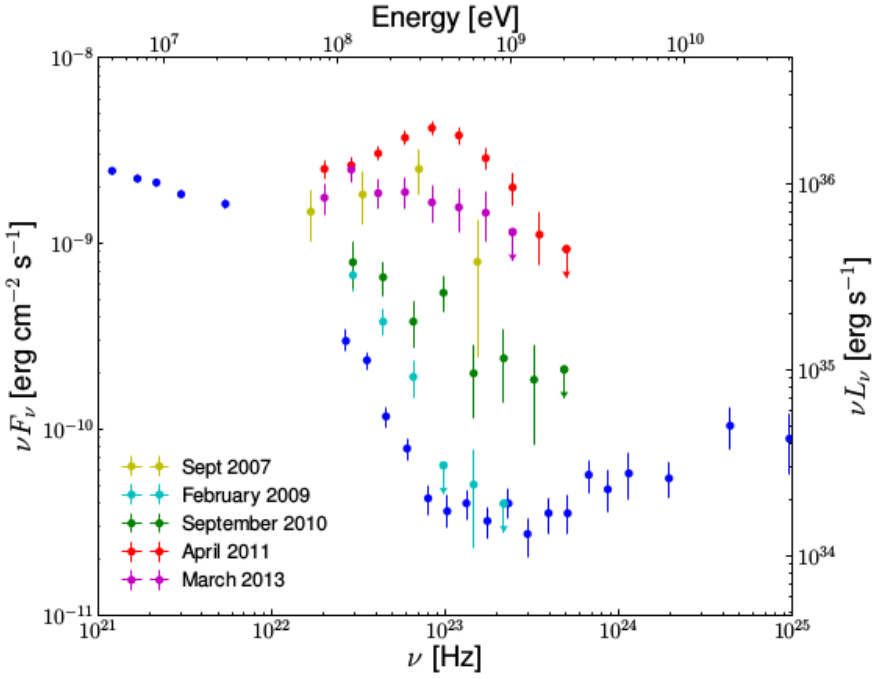

FIGURE 5.7: The spectral energy distribution (SED) at the maximum flux level for **five of six Crab nebula flares:** September 2007, February 2009, September 2010, April 2011, and March 2013, in a comparison with the average SED (blue). The synchrotron component of the Crab nebula possessed a peak flux $>3.5\times10^{-6}$ photon cm^{-2} s^{-1} for all flares detected as of September 2013. The July 2012 flare showed low intensity γ-ray emission, and its spectrum hasn't been published. The luminosity (right axis) was calculated for a Crab distance of ∼2 Kpc. Taken from Ref. [107].

According to Fig. 5.7, the Crab flares show distinct spectral behavior, e.g. the peak flux measured during the February 2009 flare increased by small increment, and no spectral changes were observed with respect to the average flux of the nebula. On the contrary, in the spectrum of the April 2011 flare, a new spectrum component with highest flux was observed.

The detection of VHE photons >1 GeV emphasizes that the electrons are accelerated to VHE of PeV range in the nebula. The γ-ray flares from the Crab nebula show high luminosities and high energy photons. Additionally, they help to constrain particle acceleration in PWNe or other plausible high-energy astrophysical sources, radiative processes in nebular media, and theoretical models applied to astrophysical plasmas environments. Several theoretical models have been proposed to explain the flare emission of photons with energies up to ∼1 GeV, such as the relativistic Doppler boost of the emission (e.g [235–237]), and the acceleration by the electric field in the reconnection layer in the pulsar magnetosphere [238, 239].

In the following, a focus on episodes of intense γ-ray flares from the Crab nebula is presented from early time of 1989 to present.

February 1989 Crab flare On February 23, 1989, an excess in the count rate was recorded from the Crab nebula at very-high energy band (VHE; $E > 100$ TeV) over a period less than 12 hr. The excess was primarily seen at the same UTC timescale by the Kolar Gold Fields (KGF) in southern India and the Tien-Shan air shower arrays, later by the Baksan Air Shower Array (BASA) [186] in valley of the northern Caucasus mountains in the USSR, and finally by the EAS-TOP array [187] in Gran Sasso, Italy. According to Baksan detector, 55 excess events above the CR-background were detected.

The time distribution of such events within the Crab cell is shown in the left panel of Fig. 5.8, along with the anticipated background distribution, which is normalized to the mean value of 34.1 events. The daily ON/OFF ration was attributed to 1.6, with statistical significance of 3.6σ level. The arrival directions of the showers are recorded in a millisecond timescale, from an area of $22^\circ \times 22^\circ$ in the right ascension and declination about the Crab direction. So, the phase analysis of the 55 events within the Crab cell was implemented, and the biggest number (6 out of 10) of excess events above the background were concentrated in the favored phase bin, as it is shown in the right panel of Fig. 5.8.

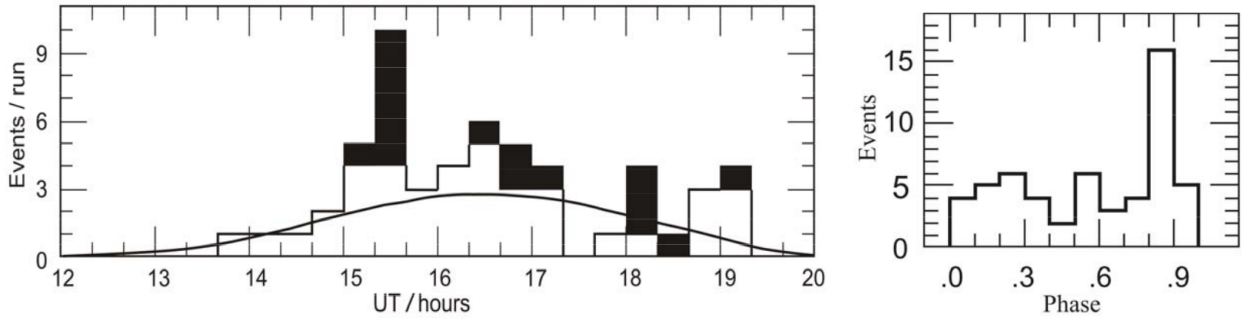

FIGURE 5.8: Left plot: time distribution of the number of excess events of the Crab cell above the CR-background detected by Baksan experiment during the February 1989 Crab flare [186, 240], a circle of a radius 2.5° around the source direction was chosen. The data were recorded every 20 min, and 8 background cells of the same radii were specified around the source cell. All background cells had equal solid angles with daily ON/OFF ratio, which is determined here as $8S/\sum_{n=1}^{8} B_n$, where S is the number of events in the source cells and B is the background cells. The expected CR-background is indicated by the smooth curve. The bins marked in black represent the excess events taken from the 9^{th} phase distribution bin, shown in the right panel. Right plot: the relative phase distributions of 55 events of the left panel, after barycentering the arrival times and using the pulsar period values and its derivative based on the Jodrell Bank Crab ephemeris.

It is obvious that the highest peak in the relative phase distribution, right plot of Fig. 5.8, is given by the 9^{th} phase bin. The excess events from such bin are marked in black in the left plot of the same figure. Thus, the main part of the excess events is located in a single phase bin, these events show a kind of **periodic** structure of 40 minute to 1 hr timescale, and distributed in three populations. The total duration of of the observation of this flare is several hours less than half a day.

The KGF and Tien-Shan air shower detectors had observed the flare in the same time interval from 13 to 16 UTC. Baksan and EAS-TOP experiments had confirmed the detection of the γ-ray outburst in the period 15-18 UTC and 17-20 UTC, respectively. The KGF group estimated the gamma ray flux at energy $E > 100$ TeV as $\Phi_\gamma = (8 \pm 2) \times 10^{-12}$ photon cm^{-2} s^{-1}, with a significant excess of 4.1σ level, the flux measured by EAS-TOP was $E > 100$ TeV as $\Phi_\gamma = 2 \times 10^{-12}$ photon cm^{-2} s^{-1} at energy threshold of 200 TeV, with a significant excess $>1.4\sigma$.

Figure 5.9 shows the Crab zenith angle and the count rate during the flare as seen by three independent experiments: the KGF, Baksan, and EAS-TOP. No reports about the February 1989 Crab γ-ray flare had been provided by the more eastern air shower arrays, such as the Japanese Akeno SPICA and Ohya Mine. The same thing with the more western experiments, e.g. HEGRA, which gave no evidence about the flare.

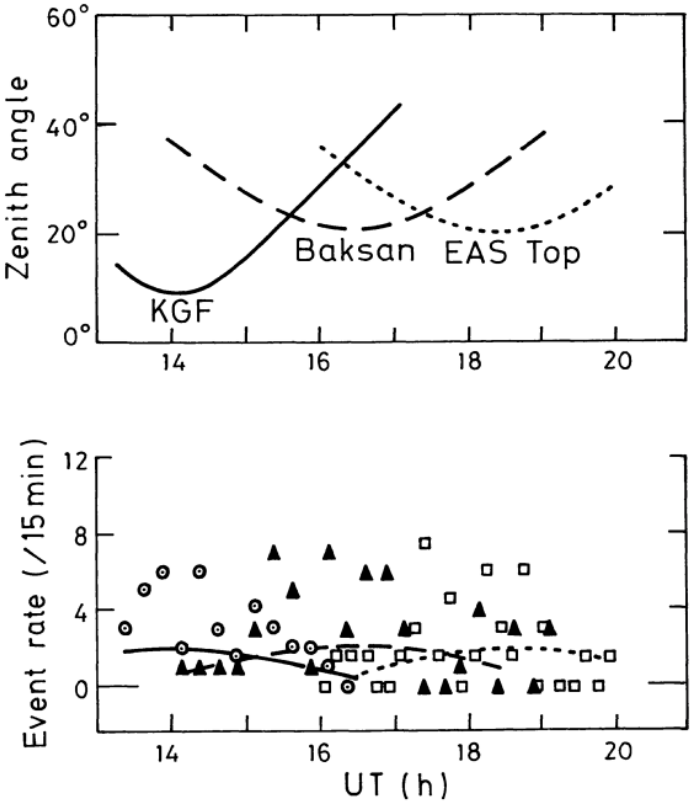

FIGURE 5.9: Top plot: the Crab zenith angle as a function of time with the Kolar Gold Fields, Baksan, EAS-TOP arrays. Bottom plot: event rate from the Crab direction as seen by the three independent detectors: Kolar Gold Fields (KGF), Baksan, and EAS-TOP shown by open circles, filled triangles, and open squares, respectively. The background is indicated by solid, dotted, and dashed lines. Taken from Ref. [217].

Recently, the γ-ray outbursts from the Crab nebula have been frequently detected by the AGILE and *Fermi*-LAT satellite detectors.

October 2007 Crab flare The AGILE satellite observed the Crab nebula in a pointing mode in the period between mid-2007 to mid-2009. The AGILE observations included the spinning mode, which has been started in November 2009. AGILE detected a remarkable γ-ray flare from the Crab nebula [233] in October 2007, before *Fermi*-LAT started the observations. The flare lasted for ∼2 weeks, shown in Fig. 5.10. The peak flux is recorded on October 7, 2007, with an integral flux $\Phi_\gamma = (8.9 \pm 1.1) \times 10^{-6}\,\text{photon}\,\text{cm}^{-2}\,\text{s}^{-1}$ and spectral index $\gamma = 2.05 \pm 0.13$ for a 6.2σ detection level above the Crab's steady state flux, where the average flux value (nebula+pulsar) was $\Phi_\gamma = (2.2 \pm 0.01) \times 10^{-6}\,\text{photon}\,\text{cm}^{-2}\,\text{s}^{-1}$ in energy range 100 MeV to 5 GeV and the spectral index $\gamma = 2.13 \pm 0.07$.

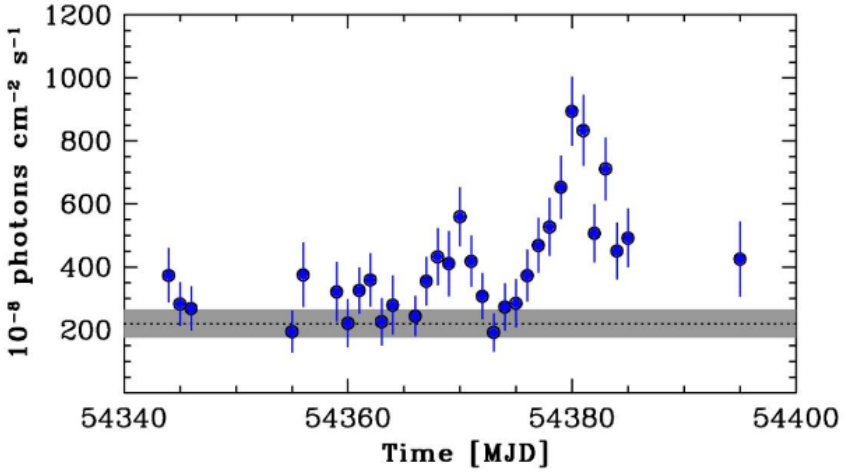

FIGURE 5.10: Daily light curve of the total flux of the Crab nebula detected by AGILE at energy range 100 MeV to 5 GeV during the γ-ray flaring periods in 2007. The flare lasted for ∼2 weeks and the flux showed maximum value on October 7, 2007. Taken from Ref. [233].

During and after the flare, there was no evidence seen by AGILE for pulsar γ-ray signal variation. Therefore, the flare is likely a consequence of non-pulsed relativistic shock emission generated in the nebula.

February 2009 Crab flare In February 2009, *Fermi*-LAT has detected an enhanced γ-ray emission from the Crab nebula. The flare hasn't been observed by AGILE, as the detector was scanning other sector of the sky. The period of this flare was ∼16 days, illustrated in Fig. 5.11.

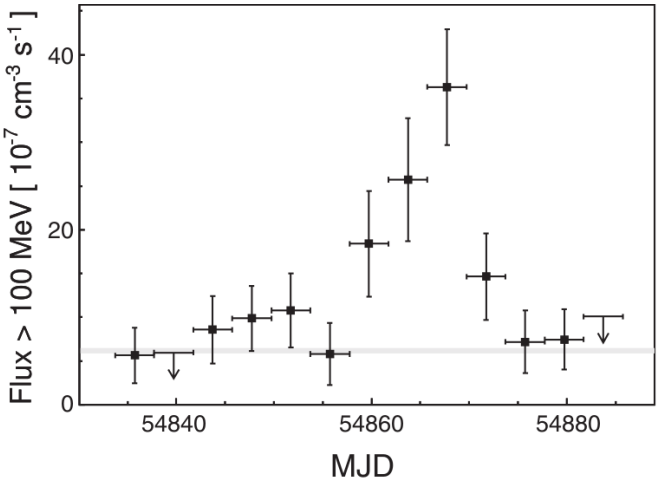

FIGURE 5.11: Daily light curve of the Crab nebula detected by *Fermi*-LAT during the γ-ray flaring periods in February 2009. The flare lasted for ∼16 days, and the flux has been significantly increased by a factor 3.8 ± 0.5 the average flux value represented by the gray band. Taken from Ref. [228].

The γ-rays were emitted via synchrotron radiation, as the nebular electrons were accelerated to (VHE; $E = 10^{15}$ eV) in a region smaller than 14×10^{-3} pc [228]. The flux has been significantly increased by a factor 3.8 ± 0.5 the average flux value, which is $>8\sigma$ level and the integral flux was $\Phi_\gamma = (23.2 \pm 2.9) \times 10^{-7}$ photon cm^{-2} s^{-1} at energies $E > 100$ MeV between the period January 26, 2009 to February 11, 2009. The flare has showed a soft spectrum of spectral index $\gamma = 4.3 \pm 0.3$.

September 2010 Crab flare On September, 2010, an increased γ-ray emission from the Crab has been detected at energies $E > 100$ MeV by AGILE [233]. The γ-ray emission reached its maximal flux during the nights between 19 and 21 September, with average flux of $\Phi_\gamma = (7.2 \pm 1.4) \times 10^{-6}$ photon cm^{-2} s^{-1}, corresponding to an excess of 4.8σ above the average flux $(2.20 \pm 0.15) \times 10^{-6}$ photon cm^{-2} s^{-1} [241] and spectral index $\gamma = 2.03 \pm 0.18$. The flare detection has been subsequently confirmed by *Fermi*-LAT [228], with a duration of ∼4 days. The integral flux at energies $E > 100$ MeV was $\Phi_\gamma = (33.8 \pm 4.6) \times 10^{-7}$ photon cm^{-2} s^{-1}, increased by a factor 5.5 ± 0.8 the average flux, and showed a significant excess $>10\sigma$ level in the time interval between September 19 and September 22 (see Fig. 5.12).

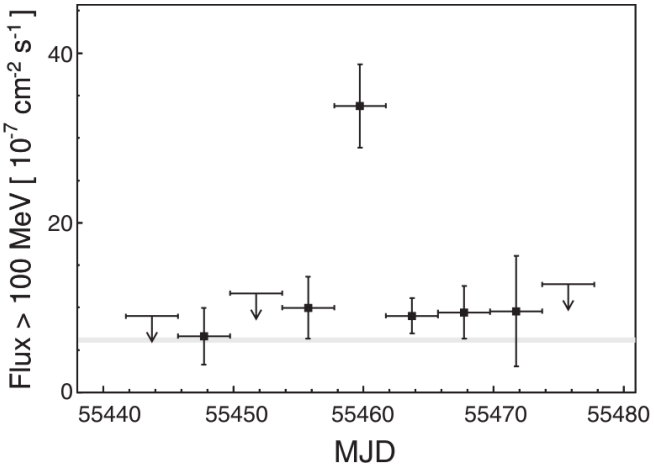

FIGURE 5.12: Daily light curve of the Crab nebula detected by AGILE and *Fermi*-LAT during the γ-ray flaring periods in September 2010. The flare duration was ∼4 days, and the flux has been significantly increased by a factor 5.5 ± 0.8 the average flux value indicated by the gray band. Taken from Ref. [228].

The energy spectrum of this flare was significantly harder than previous one, with a spectral index $\gamma = 2.7 \pm 0.2$ at energy above 1 GeV and 3σ level. The average γ-ray power released during this flare and the previous one of February 2009 was $\sim 4 \times 10^{36}$ erg s^{-1} in a case of isotropic emission. The emission from the pulsar hasn't shown significant variations during the month and the 4-day time interval of the flare. Additionally, no significant change in the synchrotron component was detected neither in X-ray nor at low frequencies above the average flux level during the flare period.

The INTEGRAL [242] made observations of the Crab during the period of the flare from September 12 at 10:32 to September 19 at 12:48 via using the ISGRI detector. No significant excess in the Crab flux has been found in the energy ranges 20-40, 40-100, and 100-400 keV (hard X-ray) energy bands.

The Swift-BAT X-ray didn't detect variations [243] in the Crab flux larger than 5.5% at energies 15-50 keV, with 1σ with respect to the mean flux during the period of the flare. A ToO Chandra/ACIS-S3 observations were also implemented for 5 ks. All of the nebula was observed with the Chandra resolution, except for the $2''$ region surrounding the pulsar, so that, the pulsar was missing from the resultant image. Nothing especially unusual was observed [244] in the image, except for: a) A $3''$ extension of the enhancement (or bright knot) of the jet at $\sim 6''$ south-east of the pulsar which propagated outwards and faded in brightness. This knot wasn't aligned with the jet. A similar extension was seen in Chandra ObsId 2001 (2001-Jan-31). b) the large scale structure (of order of an arc-minute or more) of the X-ray jet to the south-east has changed significantly from what it was observed several years ago, and this significant change could be unrelated to the γ-ray flare. The jet clearly exhibits the same "firehose-instability-like" structure as seen in Vela SNR.

The flare was detected by the ARGO-YBJ air shower detector [245] from 17 to 22 September 2010, with statistical significance of 4σ level. This was corresponding to a flux $\sim$3-4 times higher than the average value at a median energy of $\sim$1 TeV. The ARGO-YBJ experiment proposed that the enhanced emission at TeV energies from the Crab nebula extended up to September 27, 2010, more than what other experiments detected at low energies.

The September flare was observed also by the MAGIC telescope at a VHE range via stereoscopic mode [246].

The MAGIC observations of the Crab lasted 58 minutes on September, 20, 2010, and no significant variability was detected in the flux or the spectral shape at energy $E = 1$ TeV. The Crab was observed in the period of the flare by the VERITAS telescope at energy range from 200 GeV to 3 TeV [221, 247]. The observations occurred on four nights of September 17, 18, 19, and 20, 2010, with a total time interval of 120 minutes. A strong γ-ray signal was detected by VERITAS at 40σ above CR-background, however, the measured flux during the period of the flare is in agreement with the previous year observations of the Crab nebula. Hence, no change in the measured flux or spectral shape at VHE has been observed by VERITAS experiment, which is in a full accord with the results obtained by MAGIC telescope.

April 2011 Crab flare An intense and fast γ-ray flare from the Crab nebula above 100 MeV was detected by *Fermi*-LAT [248, 249] and AGILE-GRID [250, 251] in April 2011. The flare

lasted ∼9 days, and the observed flux was ∼10 times higher than the one of the steady state [252]. A spectacular time variability was detected during the flare, with a highest peak flux of $\Phi_\gamma = (22 \pm 0.85) \times 10^{-6}$ photon cm^{-2} s^{-1} [253]. The exceptionally high flux allowed to measure the SED and its evolution over time. A new spectral component was investigated from the synchrotron emission of electrons accelerated up to (VHE; $E = 10^{15}$ eV) in the nebula, after subtracting the steady emission form the pulsar and the IC component of the nebula, at which the flux reached a maximum value in the period between April 15, 2011 to April 16, 2011. The integral flux measured by both detectors is shown in Fig. 5.13.

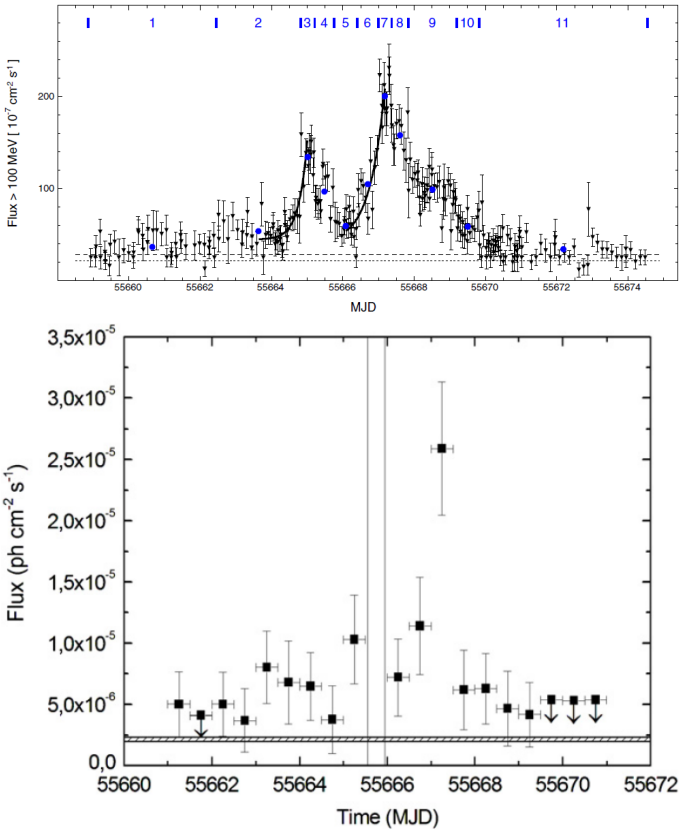

FIGURE 5.13: Daily light curve of the Crab nebula [249, 251] detected by *Fermi*-LAT (top) and AGILE-GRID (bottom) during the γ-ray flaring periods in April 2011. The flare time interval was ∼9 days. Top: The dotted line represents the average flux from IC (nebula and pulsar) for 33 month. The dashed line indicates the flux of average synchrotron nebula. The solid black line shows the best fit obtained from $\Phi_{\gamma,p}(E) = \Phi_{P,0}\,(E/1\,\mathrm{GeV})^{-\gamma_P} \exp(-E/E_{P,c})^k$, where $\gamma_p = 1.59 \pm 0.01$, the curvature index $k = 0.43 \pm 0.01$, and the energy break $E_{P,c} = (504 \pm 63)$MeV. The function is normalized by setting an initial flux value of $\Phi_{\gamma,P,0} = (8.1 \pm 0.50) \times 10^{-10}$ photon cm^{-2} s^{-1}. The vertical blue lines refer to the intervals of constant fluxes within statistical uncertainties. The numbers at the top of the plot gives time windows used in the analyses. The integral flux at energy $E > 100$ MeV was $\Phi_{\gamma,P} = (20.4 \pm 0.10) \times 10^{-7}$ photon cm^{-2} s^{-1}. Bottom: The gray horizontal band shows the average flux of the pulsar and nebula. The gray vertical band denotes the loss time interval in the data. The integral flux was given at energy above 100 MeV by AGILE-GRID in period between April 10 to April 19, 2011 is $\Phi_{\gamma,P} = (26 \pm 5) \times 10^{-6}$ photon cm^{-2} s^{-1}.

No enhanced change in the synchrotron nebula emission was found at lower and higher energies,

from radio to X-rays frequencies. Also, no pulsations in the γ-ray flare emission were detected, in addition to, the pulsar showed no evidence for significant variabilities in its flux or spin-down period. The Chandra was observing the Crab for 5 ks with the ACIS instrument using a custom window on a 0.2s frame time. The structure of the whole nebula, except for the 2″ region surrounding the pulsar, was observed with Chandra resolution. The observations occurred at the period between April 12, 12:24 UT and April 13, 23:33 UT revealed [254] a new knot, coinciding with the initial position[1] of the faded knot reported during the September 2010 flare (see § 5.4).

The Crab was also observed for 1.8 ks by the ToO Swift/XRT [255] in windowed timing (WT) mode started at April, 12 at 18:39:29 UTC. A preliminary spectral analysis showed no significant increase in the Crab's flux, as the spectral parameters and flux values are well consistent with previous Swift/XRT Crab measurements.

The MAGIC telescope observed the Crab nebula during the flare period for 140 minutes, from April 11, 2011 to April 14, 2011. The observations were implemented under strong moonlight conditions. Based on the preliminary analysis of the data sample taken in that period, no significant increase was found in the flux [256].

ARGO-YBJ detector observed the Crab for 34.4 hr from April 11, 2011 to April 17, 2011, and an excess of events was reported with $\sim 3.4\sigma$ [252], while $\sim 0.62\sigma$ was expected for the steady Crab flux.

July 2012 Crab flare *Fermi*-LAT observed low-intensity Crab nebula flare as a significant excess in the γ-ray emission [253, 257]. According to the preliminary analysis done by the *Fermi*-LAT Collaboration, the γ-ray flux reached a maximum value of $\Phi_\gamma = (2.75 \pm 0.10) \times 10^{-6}\,\mathrm{photon\,cm^{-2}\,s^{-1}}$ on July 3, 2012 (see Fig. 5.14) at high-energy (HE; $E > 100\,\mathrm{MeV}$).

This flux value is a factor of 2 greater than the average flux (pulsar and nebula) at a steady state $\Phi_\gamma = (2.75 \pm 0.02) \times 10^{-6}\,\mathrm{photon\,cm^{-2}\,s^{-1}}$ reported in the second *Fermi*-LAT [258] catalog (2FGL). The flare showed a short time flux variation form 3 to 6 hr time interval, with average fluxes $\Phi_\gamma = (5.10 \pm 1.30) \times 10^{-6}\,\mathrm{photon\,cm^{-2}\,s^{-1}}$ measured on the third night of July.

[1] The error on the positions is 0.5″

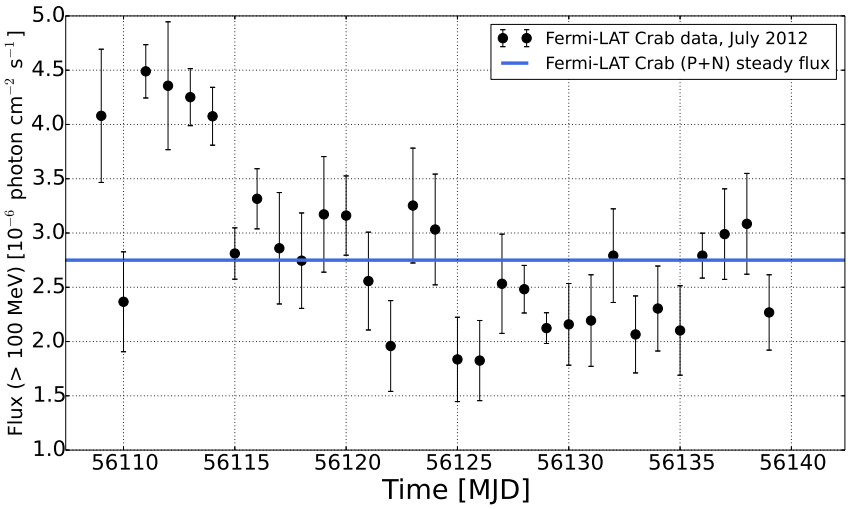

FIGURE 5.14: Daily light curve of the Crab nebula obtained by *Fermi*-LAT during the July 2012 Crab γ-ray flare. The data are plotted from the official page [259] of *Fermi*-LAT Crab's daily light curve.

The *Fermi*-LAT detection to the July Crab flare was followed by observations implemented in the same day by the ARGO-YBJ air shower detector [260]. The initial analysis of the data showed events with statistical significance excess of $\sim 4\sigma$ from the Crab nebula, corresponding to a flux value of $\sim$8 times higher than the average Crab emission at a median energy of $\sim$1 TeV. However, no significant excess was detected in the days between July 4^{th} to July 6^{th}.

ARGO-YBJ experiment monitors the northern sky constantly at energies higher than 0.3 TeV, with a field of view of $\sim$2 sr and a duty cycle of $\sim$85%. A long-term observations to the Crab nebula [252, 261] over a five-year timescale were carried out by ARGO-YBJ in the period from August 2008 to February 2013, shown in Fig. 5.15.

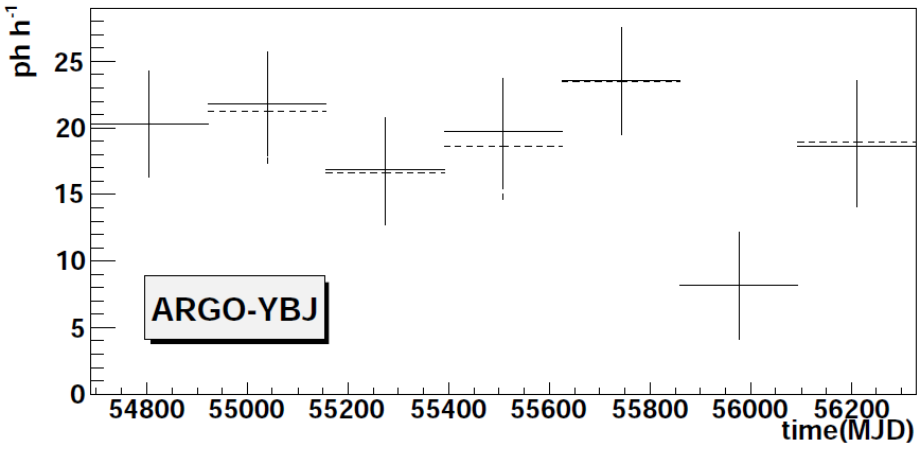

FIGURE 5.15: The Crab nebula flux measured by ARGO-YBJ air shower detector over a five-year timescale. The dashed line indicates the flux measurements of non-flaring days. Taken from Ref. [261].

The observations taken by the ARGO-YBJ experiment from the five years of operation has been reanalyzed, in order to study the variability in the Crab nebula emission at energy range 0.5-20 TeV. The study concludes that a higher sensitivity is required for a firm detection of the VHE γ-ray flux variability. Furthermore, the ARGO-YBJ long-term Crab light curve is compatible with a uniform flux with a probability of 0.11. However, the Crab flux measured by the ARGO-YBJ detector is higher than the Crab's average flux by a factor of 2.4 ± 0.8, and it showed a correlation with the corresponding *Fermi*-LAT light curve, shown in Fig. 5.16.

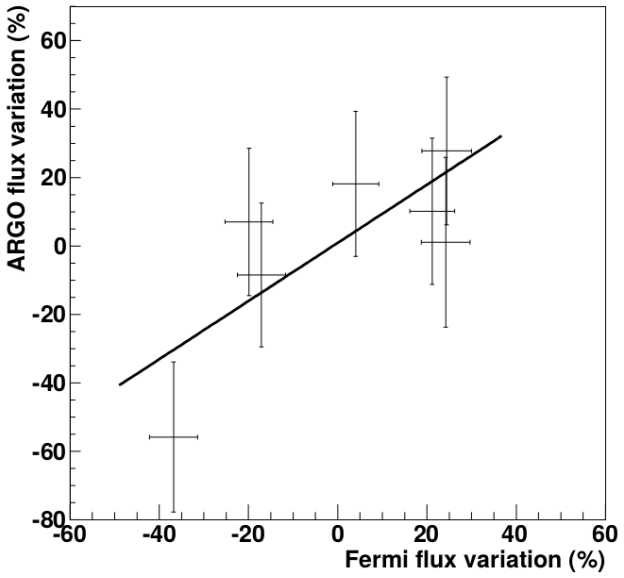

FIGURE 5.16: Variation percent of the Crab nebula flux measured by *Fermi*-LAT and ARGO-YBJ. Taken from Ref. [261].

March 2013 Crab flare In March 2013, an enhanced γ-ray emission from the Crab nebula was detected by *Fermi*-LAT [234, 262] and AGILE-GRID [263, 264]. The flare lasted for ∼2 weeks, shown in Fig. 5.17. The observed flux showed a variability of ∼5 hr at energy $E > 100$ MeV from the pulsar and nebula.

The maximum flux observed had a value of $\Phi_\gamma = (12.5 \pm 0.8) \times 10^{-6}$ photon cm^{-2} s^{-1} on March 6, 2013, which corresponds to an increase of a factor 6 the quiescent average flux. The observations carried out by AGILE-GRID showed a significant flux $\Phi_\gamma = (7.4 \pm 2.2) \times 10^{-6}$ photon cm^{-2} s^{-1} at 6σ level, which is consistent with the *Fermi*-LAT measurements.

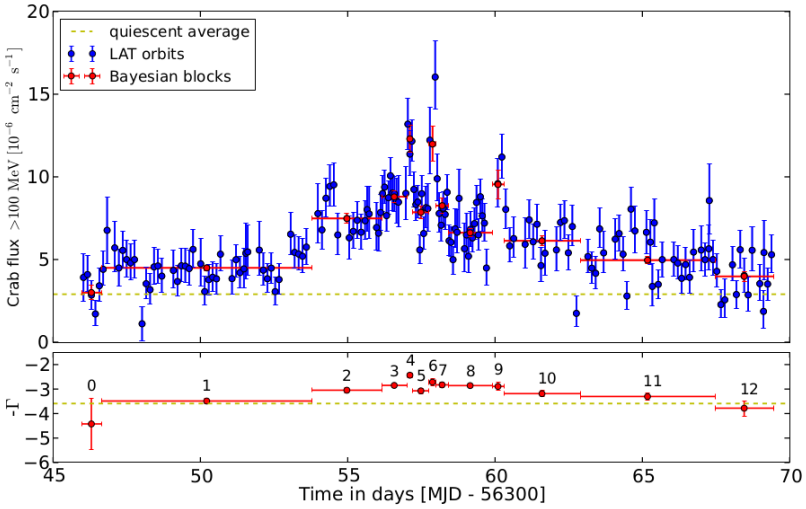

FIGURE 5.17: Daily light curve of the Crab nebula obtained by *Fermi*-LAT during the March 2013 Crab γ-ray flare. Top: The orbit-binned light curve is shown in blue, while red spots indicate fluxes obtained from the Bayesian blocks analysis, which implies the sum of the fitted synchrotron flux of the steady pulsar and the nebula fluxes from IC component. Bottom: Time evolution of the spectral index of the fitted power-law model ($\frac{dN}{dE} \propto E^{-\gamma}$) from the Bayesian blocks is illustrated. The yellow-dotted line represents average spectral index of the synchrotron component overall flare time interval. Taken from Ref. [234].

The INTEGRAL was observing the Crab nebula since March 2, 2013 at 06:56 UTC (Rev 1268-1269). The IBIS/ISGRI average rates during Rev 1268, with 4 energy bands in the 20 keV-200 keV energy range, showed a consistency between the pre-flare (Rev 1268) and the flare periods (Rev 1269) [265]. The IBIS/SPI data spectral analysis in the period between March 2, 08:43 UTC and March 5, 14:13 UTC was carried out using a broken power-law model, which allowed to establish the Crab X-ray spectrum. The resultant X-ray spectrum was stable during the whole period, i.e. before and during the γ-ray flare.

The observation of the Crab was extended to optical band during the γ-ray flare by the Asiago Quantum Eye (Aqueye) detector, which is mounted at the 182 cm Copernico telescope at Asiago Cima-Ekar. The pulsar [266] was observed by Aqueye for three nights started from March 2 22:18:38 UTC and stopped at March 4, 19:31:46 UTC. A preliminary analysis revealed a light curve with a time resolution of 336.6 microseconds. A fractional RMS of the light curve binned at 3 millisecond and including sky and nebular background is 12%-13%. No significant variations in the pulse shape have been detected during the three nights of the observations.

H.E.S.S array of Cherenkov telescopes observed the Crab for 5 successive days (March 6 to March 10, 2013) during the flare period, in order to search for the variability in the emission of the Crab nebula at very-high energies (VHE; $E > 100$ GeV). The observations taken by H.E.S.S. experiment showed no significant variabilities in the Crab flux [267] in energy range 1 TeV to 5 TeV. The variation in the integral flux measured at energy $E > 1$ TeV was limited to ∼63% and the one

measured at energy $E > 5$ TeV was limited to ∼78% at a 95% confidence level. This is in agreement with the non-variable long-term average Crab nebula flux measured by VERITAS telescope [268] during the March 2013 Crab nebula flare.

October 2013 Crab flare A significant increase in γ-ray emission from the Crab nebula was observed by *Fermi*-LAT [269] and AGILE [270] in the mid-October 2013. Based on the preliminary analysis of the *Fermi*-LAT, the daily average γ-ray emission measured on October 17, 2013 at high-energy level (HE; $E > 100$ MeV) from the Crab nebula showed a flux value of $\Phi_\gamma = (9.7 \pm 0.7) \times 10^{-6}$ photon cm^{-2} s^{-1}, presented in Fig. 5.18.

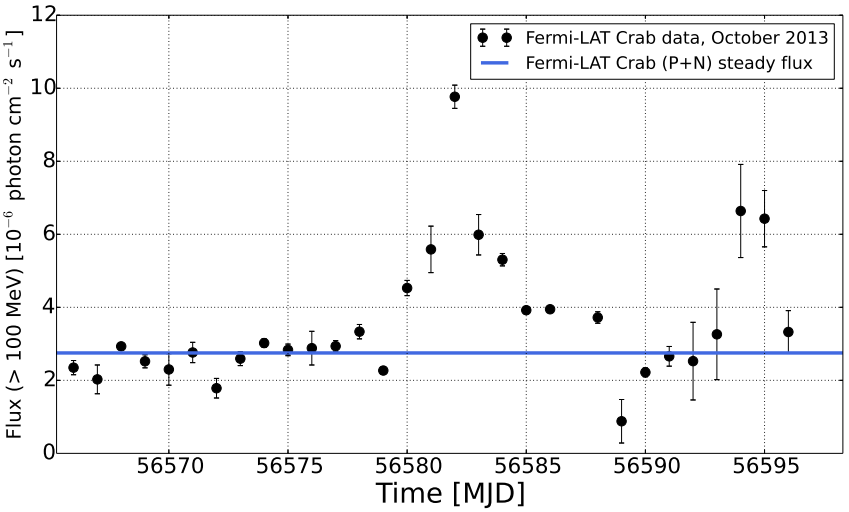

FIGURE 5.18: Daily light curve of the Crab nebula obtained by *Fermi*-LAT during the October 2013 Crab γ-ray flare. The data are plotted from the official page [259] of *Fermi*-LAT Crab's daily light curve.

This value is ∼3.5 greater than the average γ-ray flux (pulsar and nebula) $\Phi_\gamma = (2.75 \pm 0.02) \times 10^{-6}$ photon cm^{-2} s^{-1} [258]. The average flux value measured on the October 17 is comparable to the peak flux value recorded during the March 2013 flare, see e.g. [234, 262–264, 271, 272].

AGILE confirmed the *Fermi*-LAT observations via detecting an enhanced γ-ray emission from the Crab nebula on October 18, 2013. The measured flux was $\Phi_\gamma = (6.8 \pm 2.2) \times 10^{-6}$ photons cm^{-2} s^{-1}, with a significance ∼5σ level. According to AGILE measurements, the Crab flux returned to its standard level $\Phi_\gamma = (2.9 \pm 1.3) \times 10^{-6}$ photons cm^{-2} s^{-1} on October 20, 2013.

March 2014 Crab flare The *Fermi*-LAT has observed an enhanced γ-ray flux from the Crab nebula since March 6, 2014 [273], demonstrated in Fig. 5.19. The preliminary analysis performed by the *Fermi*-LAT Collaboration showed that the daily average γ-ray emission was consistent with a flux value of $\Phi_\gamma = (5.7 \pm 0.5) \times 10^{-6}$ photon cm^{-2} s^{-1} on March 10 at high-energy range (HE;

$E > 100\,\mathrm{MeV}$), which corresponds to a factor of 2 greater than the quiescent average flux (pulsar and nebula) $\Phi_\gamma = (2.75 \pm 0.02) \times 10^{-6}\,\mathrm{photon\,cm^{-2}\,s^{-1}}$ [258].

During the flare, the pulsar was detected in the optical band, separately from the brighter nearby stellar objects of 5″ to the nebula, by the 30 cm telescope of the Foligno Observatory of a Canon 350D, with a scale of 0.89 arcsec/pixel.

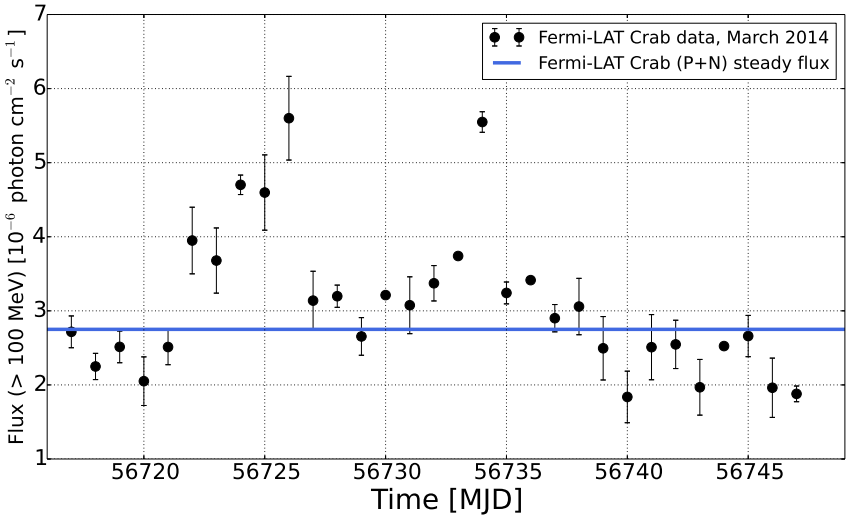

FIGURE 5.19: Daily light curve of the Crab nebula obtained by *Fermi*-LAT during the March 2014 Crab γ-ray flare. The data are plotted from the official page [259] of *Fermi*-LAT Crab's daily light curve.

Consequently, two series of unfiltered images of 15 minutes exposure were obtained. In the range V = 11 to 16.5, there were a large number of comparison stars (130 stars taken from the UCAC4 catalog) around the nebula. Hence, the pulsar magnitude was attributed to a value of $V = 16.3 \pm 0.2$. The background level was tricky to be released by reason of the presence of the emission emerged from the nebula. Therefore, several choices of the coronal area inner radius were used, in order to estimate the background level with typical uncertainties.

The measurements carried out by the Foligno Observatory concluded that the pulsar was essentially at its typical optical flux level, and no evidence [274] for an increase of a factor 2 has been found, which is not in agreement with the result reported at γ-ray frequencies.

August 2014 Crab flare In August 2014, *Fermi*-LAT detected a significant γ-ray emission from the Crab nebula [275] at high-energy range (HE; $E > 100\,\mathrm{MeV}$). The increase in the γ-ray flux started on August 15, with a gradual flux rise on the preceding days, shown in Fig. 5.20. A flux value of $\Phi_\gamma = (7.5 \pm 0.6) \times 10^{-6}\,\mathrm{photon\,cm^{-2}\,s^{-1}}$ was measured on August 18, which is ∼2.7 greater than the average γ-ray flux of quiescent level (pulsar and nebula) $\Phi_\gamma = (2.75 \pm 0.02) \times 10^{-6}\,\mathrm{photon\,cm^{-2}\,s^{-1}}$ [258]. The flare hasn't been reported by the IACT observations.

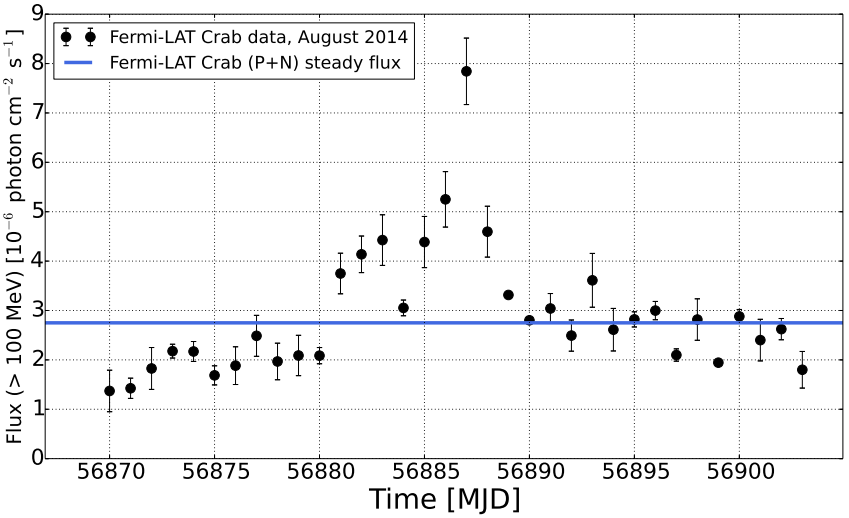

FIGURE 5.20: Daily light curve of the Crab nebula obtained by *Fermi*-LAT during the August 2014 Crab γ-ray flare. The data are plotted from the official page [259] of *Fermi*-LAT Crab's daily light curve.

December 2015 Crab flare In the last week of December 2015, an enhanced γ-ray emission was observed from the Crab nebula [174] by *Fermi*-LAT at high-energy level (HE; $E > 100\,\mathrm{MeV}$). The flux peaked at a value $\Phi_\gamma = (4.7 \pm 0.5) \times 10^{-6}\,\mathrm{photon\,cm^{-2}\,s^{-1}}$ on January 7 (see Fig. 5.21), which is a factor of ∼1.7 greater than the average γ-ray flux of the Crab's steady state [258] $\Phi_\gamma = (2.75 \pm 0.02) \times 10^{-6}\,\mathrm{photon\,cm^{-2}\,s^{-1}}$.

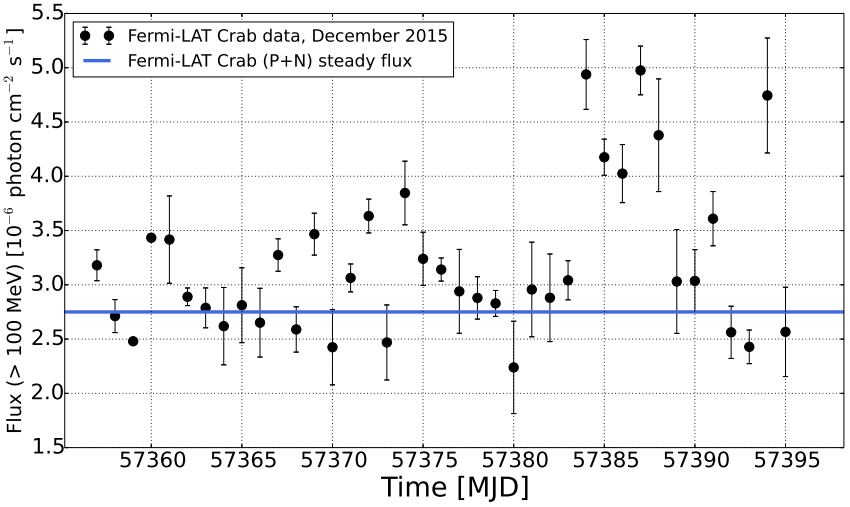

FIGURE 5.21: Daily light curve of the Crab nebula obtained by *Fermi*-LAT during the December 2015 Crab γ-ray flare. The data are plotted from the official page [259] of *Fermi*-LAT Crab's daily light curve.

The December flare is the last Crab flare reported to date (May 17, 2016), and it has provided the highest flux observed for the Crab at γ-ray frequencies since August 2014.

Chapter 6

Search for Astrophysical Gamma-Ray Flares

The search for statically significant excesses on a minute time scale has revealed **266** 5-minute intervals of significant excesses in average scaler rate variability. These 266 excess bins are distributed over 76 dates from the year 2006 to 2015. As we have discussed earlier in Chapter 3, the Crab γ-ray flares, which are summarized in Tab. 6.1, might be the origin of ∼2/3 of the observed excesses on a minute timescale.

Date	Experiments	Energy	Duration	Φ_γ [photon cm^{-2} s^{-1}]
October 2007	AGILE	100 MeV to 5 GeV	∼2 weeks	$2.2 \pm 0.01 \times 10^{-6}$
February 2009	*Fermi*-LAT	$E > 100$ MeV	∼2 weeks	$23.2 \pm 2.9 \times 10^{-7}$
September 2010	AGILE & *Fermi*-LAT	$E > 100$ MeV	∼4 days	$7.2 \pm 1.4 \times 10^{-6}$ $33.8 \pm 4.6 \times 10^{-7}$
April 2011	AGILE & *Fermi*-LAT	$E > 100$ MeV	∼9 days	$26 \pm 5 \times 10^{-6}$ $20.4 \pm 0.10 \times 10^{-7}$
July 2012	*Fermi*-LAT ARGO-YBJ	$E > 100$ MeV	∼1 week	$2.75 \pm 0.10 \times 10^{-6}$
March 2013	*Fermi*-LAT & AGILE	$E > 100$ MeV	∼2 weeks	$12.5 \pm 0.8 \times 10^{-6}$ $7.4 \pm 2.2 \times 10^{-6}$
October 2013	*Fermi*-LAT & AGILE	$E > 100$ MeV	∼1 week	$9.7 \pm 0.7 \times 10^{-6}$ $6.8 \pm 2.2 \times 10^{-6}$
March 2014	*Fermi*-LAT	$E > 100$ MeV	∼2 weeks	$5.7 \pm 0.5 \times 10^{-6}$
August 2014	*Fermi*-LAT	$E > 100$ MeV	∼2 weeks	$7.5 \pm 0.6 \times 10^{-6}$
December 2015	*Fermi*-LAT	$E > 100$ MeV	∼1 week	$4.7 \pm 0.5 \times 10^{-6}$

TABLE 6.1: A summary of observed Crab γ-ray flares from 2007 to 2015. The Crab nebula and its pulsar, in addition to, all observed Crab γ-ray flares from early time to December 2015 are discussed in Chapter 5.

Based on MC simulations in Chapter 4, the Auger low-energy scaler mode is sensitive to possible γ-ray flares from the Crab nebula, and thus it is capable of detecting VHE γ-ray at energies near to

100 TeV up to 1 PeV from hard and very hard spectrum sources. In this Chapter, we investigate the origin of the significant excesses observed in average scaler rate variability. In particular, the significant *Crab-compatible* variability. Therefore, we perform detailed comparison between Auger SD scaler excess variance and the corresponding significance of Crab γ-ray flux measured by the *Fermi*-LAT, which has started its mission since August 2008.

A good correlation is found between both datasets. The probability of observing those excesses by chance is quite small, corresponding to a P-value <0.0001, which is significant at $P < 0.05$ probability level. This means that a strong association is investigated between the observed Crab-compatible excesses and the γ-ray flares from the Crab nebula.

In § 6.1, we present the yearly Auger SD scaler rate variability and a comparison with the *Fermi*-LAT daily Crab light curves, starting from 2008 to 2015. From § 6.1.1 to § 6.1.7, we discuss with details all observed significant excess variability in average scaler rate, during Crab γ-ray flares observed by the *Fermi*-LAT and AGILE. A study of correlation between the significance of the excesses observed by Auger SD scalers and the γ-ray flare flux measured by *Fermi*-LAT is investigated in § 6.2.

6.1 Auger SD scaler rate variability and *Fermi*-LAT daily Crab light curves

We present all significant excess variance observed in the average scare rate from the years 2006 to 2015 and the daily Crab's light curves measured by the *Fermi*-LAT from 2008 to 2015. The daily and weekly *Fermi*-LAT Crab light curves are publicly available on the Monitored Sources List web page [199] from August 2008 up to present. The regularly updated plots are available in [259], and they show a sum of the pulsar and the nebula fluxes on daily and weekly timescales. It is worthwhile to mention here that the average photon flux above 100 MeV is $2.74 \pm 0.02 \times 10^{-6}$ cm^{-2} s^{-1} according to the second *Fermi*-LAT catalog of sources [258]. A comparable value of 2.72 $\pm$ 0.02$\times 10^{-6}$ photons cm^{-2} s^{-1} is yielded by the third *Fermi*-LAT source catalog [276], which has a four years of data. This flux value is considered to be the sum of contributions of the pulsar 2.34 $\pm$ 0.02$\times 10^{-6}$ cm^{-2} s^{-1}, nebula synchrotron 0.25 $\pm$ 0.01$\times 10^{-6}$ cm^{-2} s^{-1}, and nebula inverse Compton (IC) 0.13 $\pm$ 0.01$\times 10^{-6}$ cm^{-2} s^{-1}. We have noticed that the average Crab flux value beyond the year 2014 shows a small decrease compared to the other years. Such decline is clearly visible on the light curve plot [259]. Therefore, we have gotten the value of 2.37 $\pm$ 0.03$\times 10^{-6}$ photons cm^{-2} s^{-1} for the Crab flux (pulsar + nebula) in 2014, after excluding two months of flux data of Crab's flares (March and August). Since the Crab synchrotron nebula emission >100 MeV

varies on long timescales, see e.g. [249], the reason for such decline is not clear. The yearly average scaler rate variability is shown as a function of time from 2006 to 2015. The *Fermi*-LAT has started to take measurements since August 2008, we compare between both Auger average scaler rate variability and the *Fermi*-LAT daily light curves of the Crab nebula and pulsar from 2008 to 2015 (see Figs. from 6.3 to 6.10). Moreover, the average scaler rate variability of the years 2006 and 2007 are also shown in Figs. 6.1 and 6.2, respectively. The variability "baseline" of the daily excess variance, given by Eq. 3.5, is determined by taking a daily median value for the whole Auger scaler dataset.

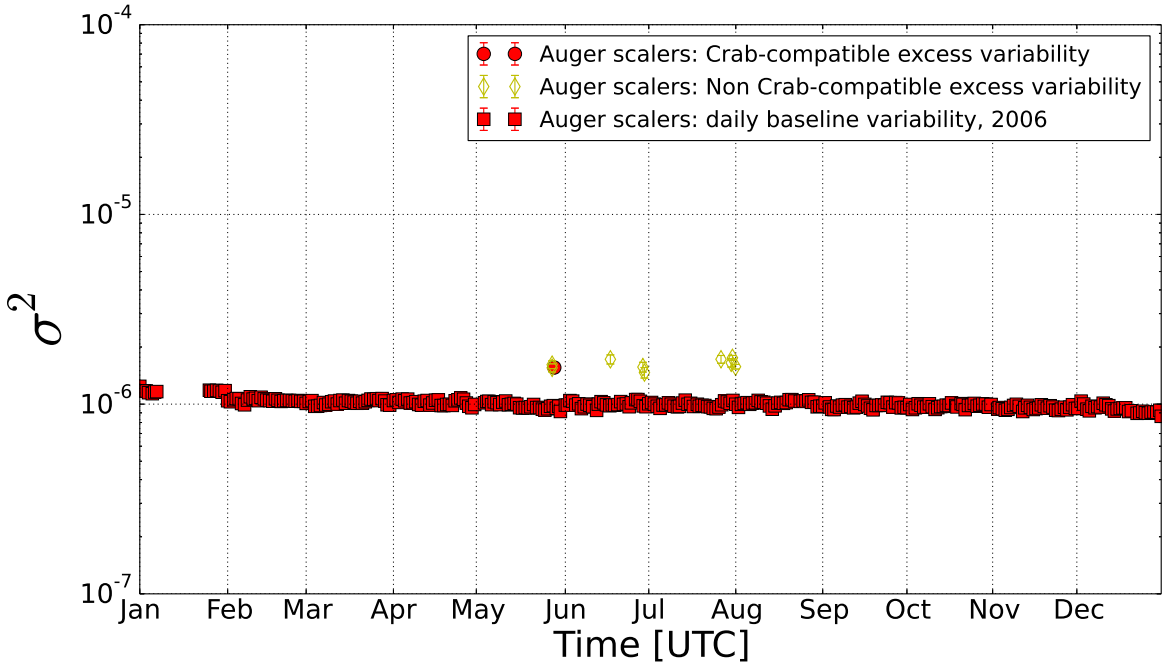

FIGURE 6.1: Auger average scaler rate variability in **2006**. The red circle denotes the five-minute Crab-compatible excess variability above the daily baseline shown by red squares. The yellow diamonds present the five-minute non Crab-compatible excess variability.

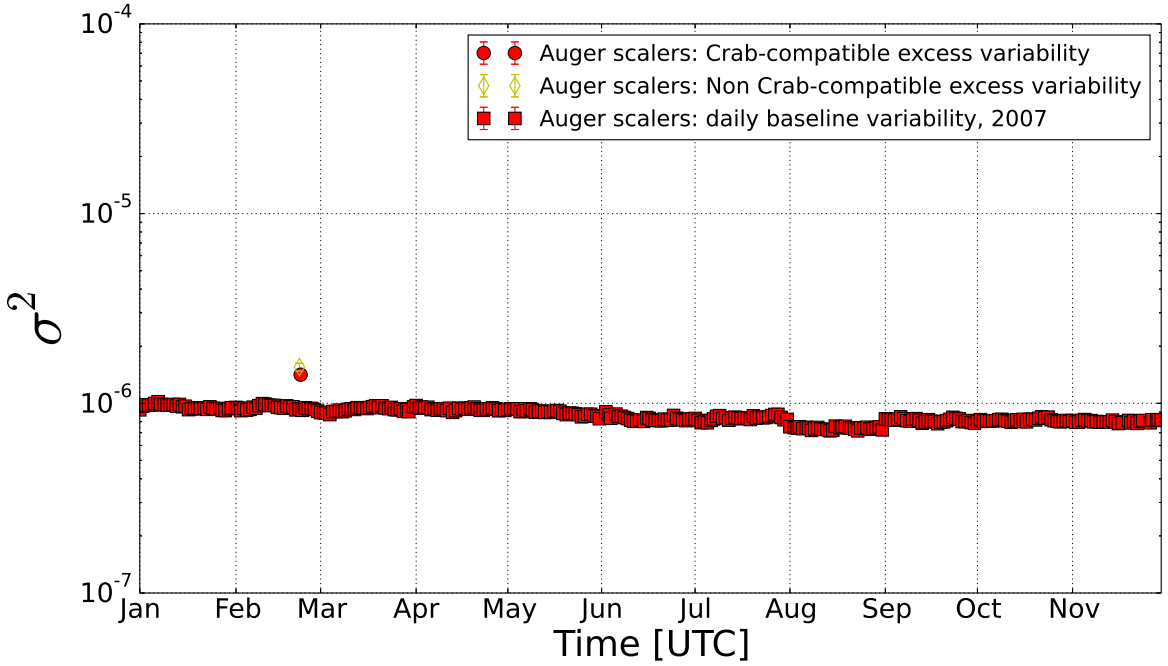

FIGURE 6.2: Auger average scaler rate variability in **2007**. The red circle denotes the five-minute Crab-compatible excess variability above the daily baseline shown by red squares. The yellow diamond presents the five-minute non Crab-compatible excess variability.

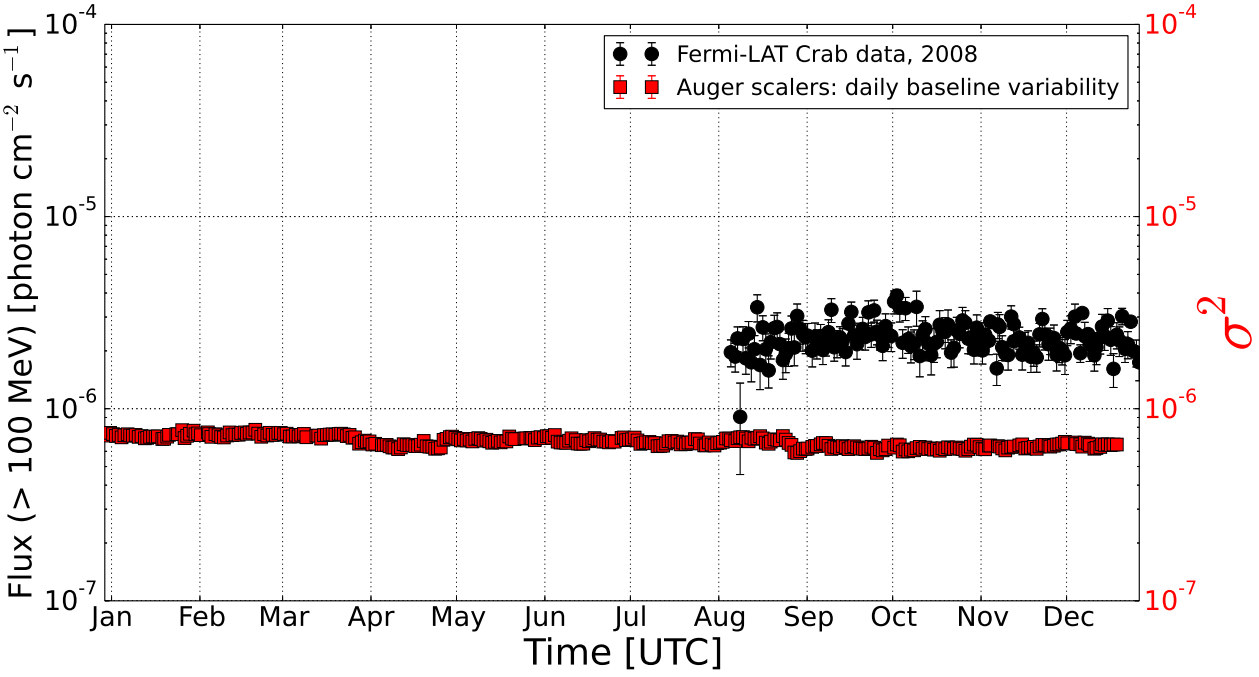

FIGURE 6.3: *Fermi*-LAT daily Crab light curve (black circles) versus Auger average scaler rate variability (red symbols) in **2008**. The daily baseline is shown by red squares. No Crab flares have been observed in this year by the *Fermi*-LAT or any other detector. Also, Auger SD scalers have not seen any significant variability in the average scaler rate during 2008.

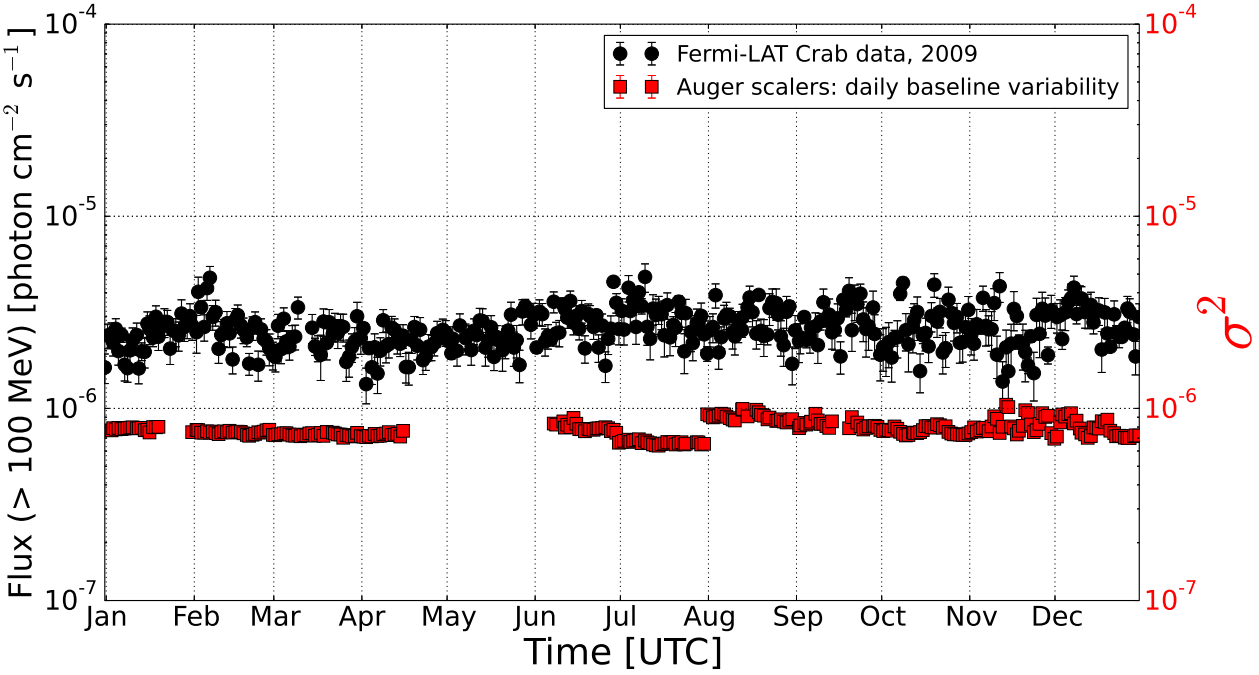

FIGURE 6.4: *Fermi*-LAT daily Crab light curve (black circles) versus Auger average scaler rate variability (red symbols) in **2009**. The red circles denote the five-minute Crab-compatible variability excesses above the daily baseline shown by red squares.

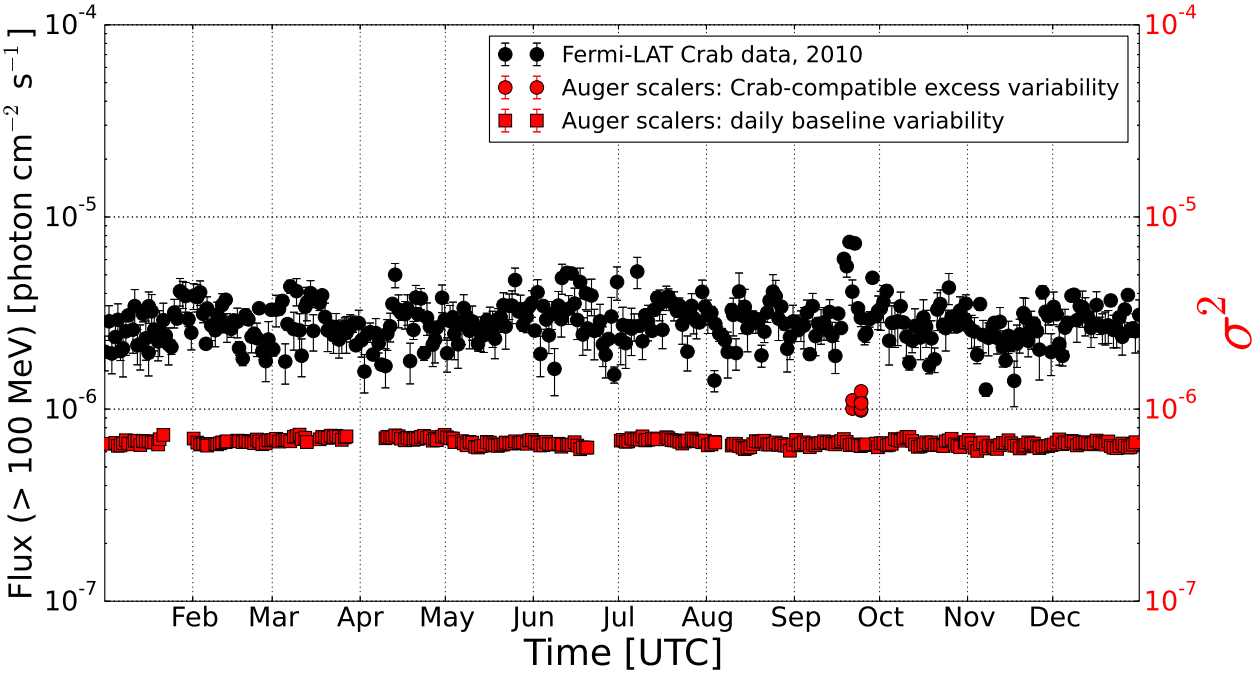

FIGURE 6.5: *Fermi*-LAT daily Crab light curve (black circles) versus Auger average scaler rate variability (red symbols) in **2010**. The red circles denote the five-minute Crab-compatible variability excesses above the daily baseline shown by red squares.

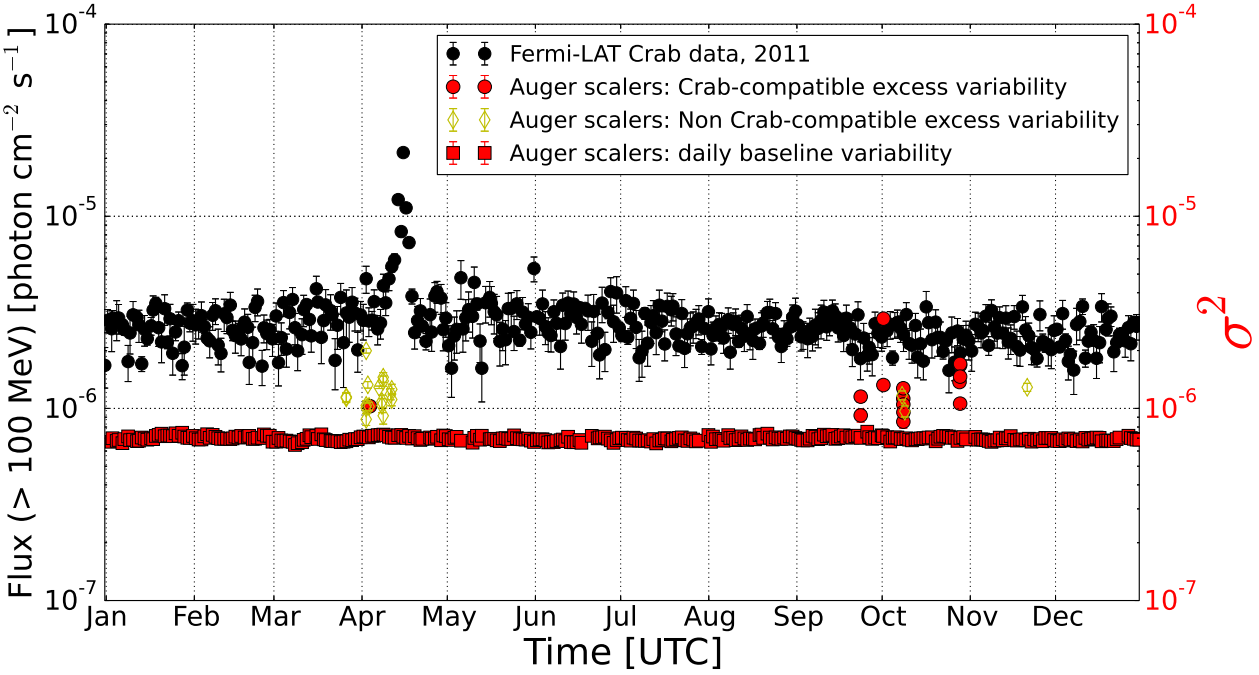

FIGURE 6.6: *Fermi*-LAT daily Crab light curve (black circles) versus Auger average scaler rate variability (red symbols) in **2011**. The red circles denote the five-minute Crab-compatible variability excesses above the daily baseline shown by red squares. The yellow diamonds present the five-minute non Crab-compatible excess variability.

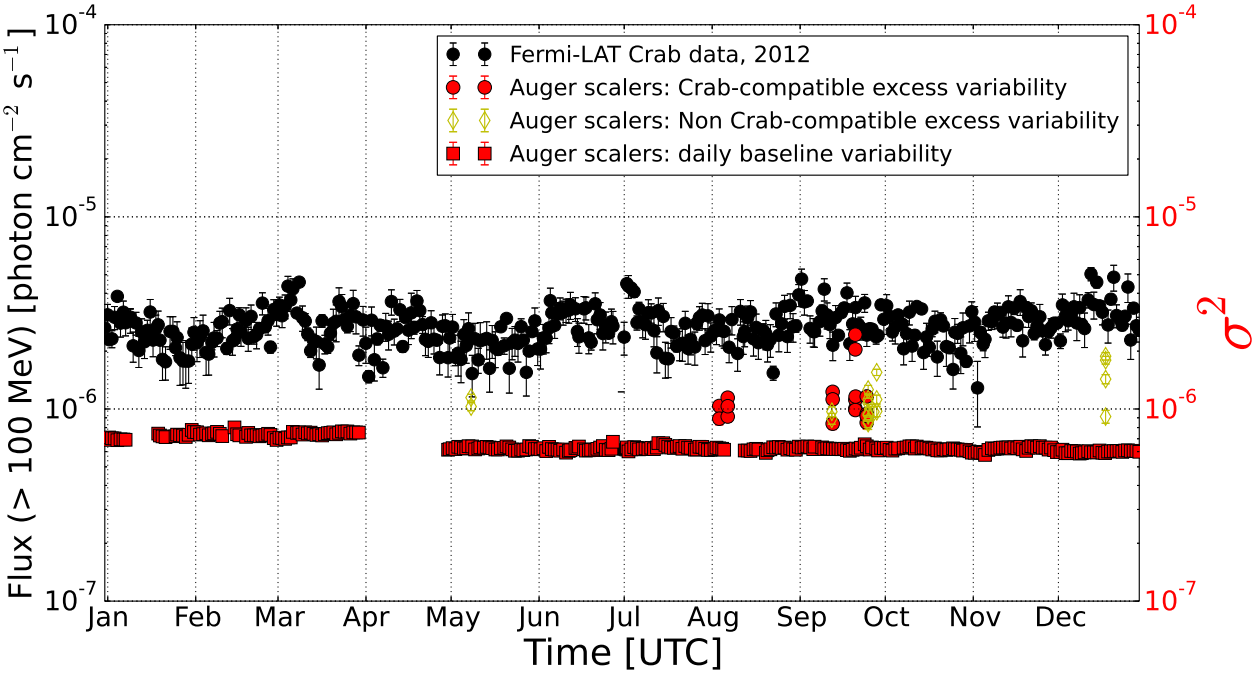

FIGURE 6.7: *Fermi*-LAT daily Crab light curve (black circles) versus Auger average scaler rate variability (red symbols) in **2012**. The red circles denote the five-minute Crab-compatible variability excesses above the daily baseline shown by red squares. The yellow diamonds present the five-minute non Crab-compatible excess variability.

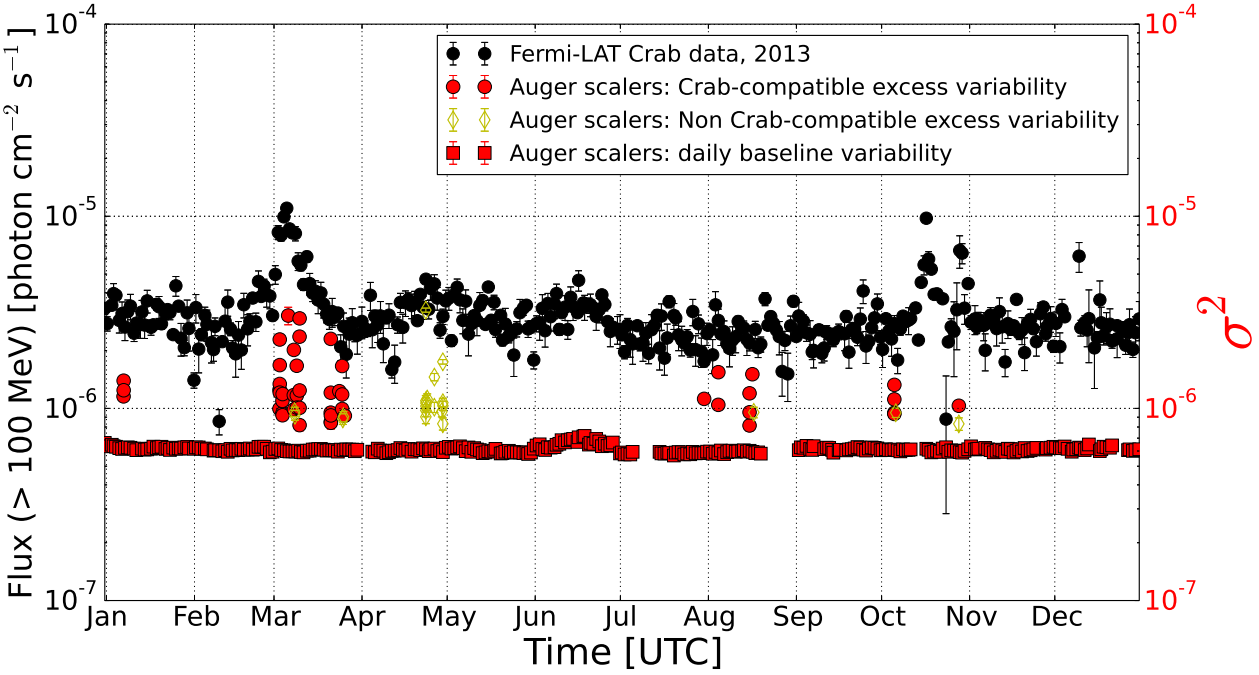

FIGURE 6.8: *Fermi*-LAT daily Crab light curve (black circles) versus Auger average scaler rate variability (red symbols) in **2013**. The red circles denote the five-minute Crab-compatible variability excesses above the daily baseline shown by red squares. The yellow diamonds present the five-minute non Crab-compatible excess variability.

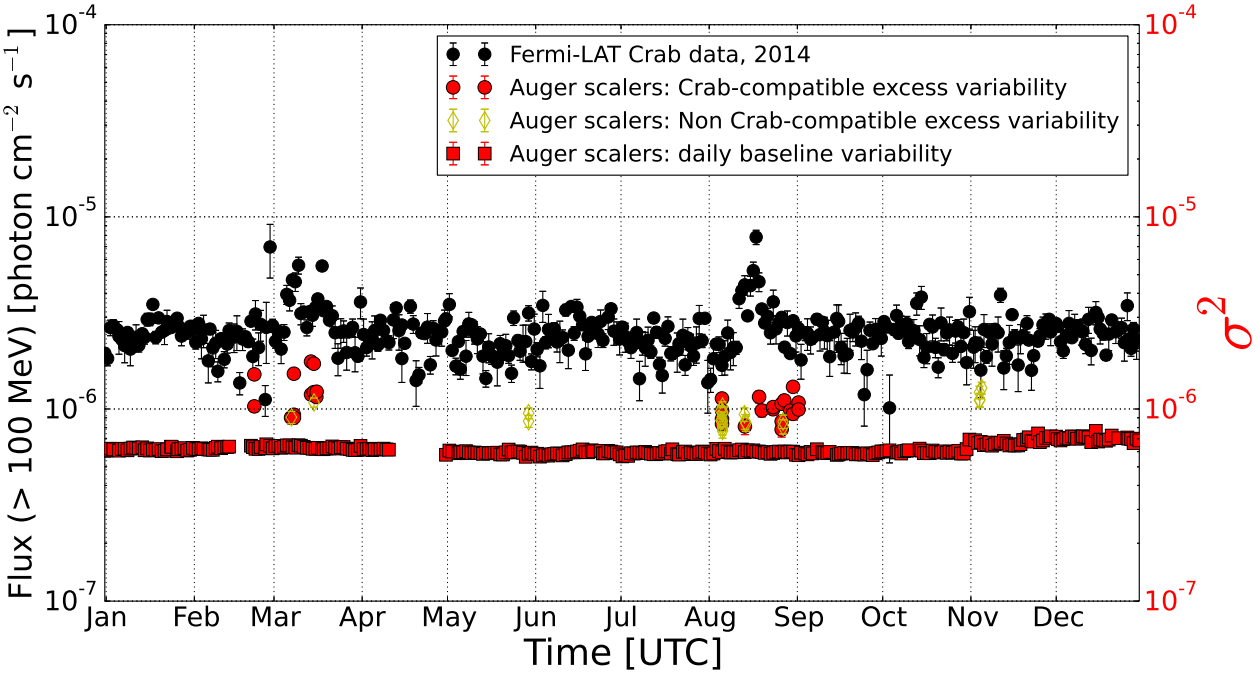

FIGURE 6.9: *Fermi*-LAT daily Crab light curve (black circles) versus Auger average scaler rate variability (red symbols) in **2014**. The red circles denote the five-minute Crab-compatible variability excesses above the daily baseline shown by red squares. The yellow diamonds present the five-minute non Crab-compatible excess variability.

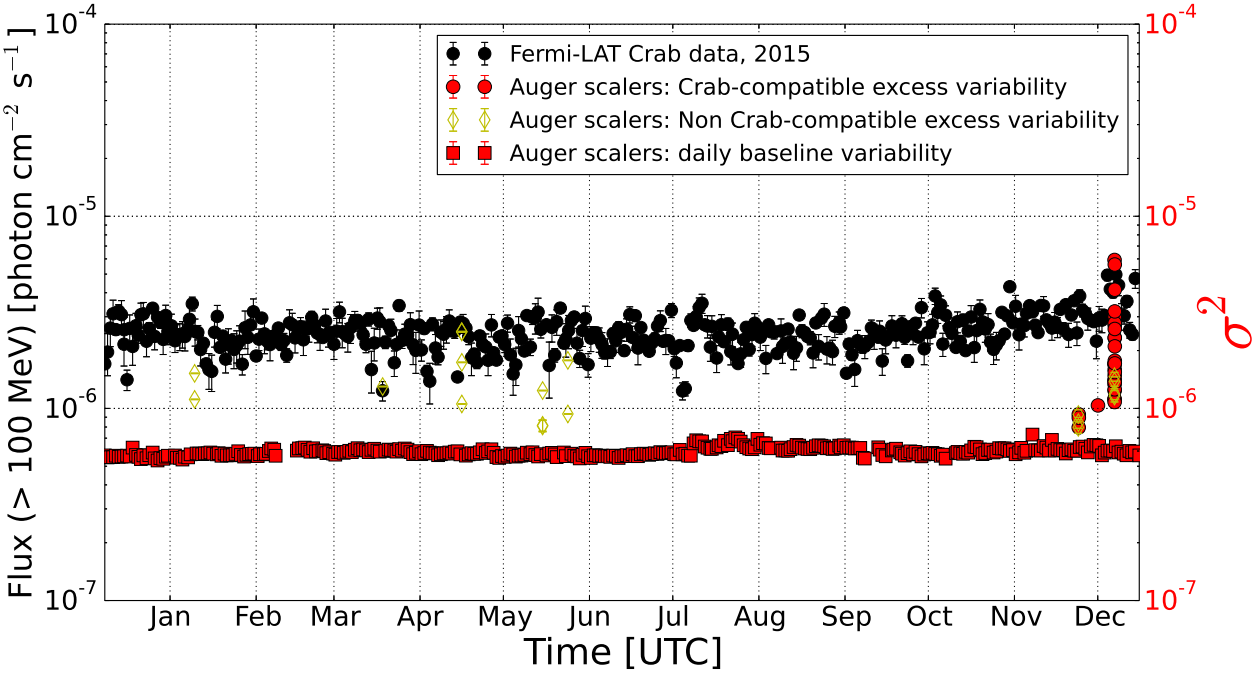

FIGURE 6.10: *Fermi*-LAT daily Crab light curve (black circles) versus Auger average scaler rate variability (red symbols) in **2015**. The red circles denote the five-minute Crab-compatible variability excesses above the daily baseline shown by red squares. The yellow diamonds present the five-minute non Crab-compatible excess variability.

The yearly variability plots are presented from 2006 to 2015 in Figs. 6.1 to 6.10. As we can see, there have been several episodes of significant Auger average scaler rate variability in a good correlation with the *Fermi*-LAT Crab γ-ray flux. In particular, **September 2010**, **March 2013**, **March 2014**, **August 2014**, and **December 2015** Crab γ-ray flares. A weak correlation has been found during **October 2013** Crab flare for one night (see § 6.1.4 for details). No excesses have been found during April 2011 Crab γ-ray flare, which is one of the strongest and shortest Crab flares. We have found ∼50 5-minute intervals of strong Crab-compatible excess variability (corresponding to ∼20% of the catalog excesses A.2) spread over 8 years. Such excesses occurred when the Crab was above 20° with respect to the horizon, but outside of the GeV γ-ray flaring episodes. In contrast, the years 2008 and 2009 showed no γ-ray activities from the Crab nebula and its pulsar. The lack of Crab γ-ray flares in those years (2008-2009) is in agreement with Auger average scaler rate variability, which showed no significant excesses over that time interval.

About 1/3 of the excesses detected in the average scaler rate could be relevant to some Galactic PeV sources (PeVatrons) at the galactic center, see § 1.3.2 for details. These excesses observed at sidereal times corresponding to the right ascensions of the center of the Milky Way.

6.1.1 Average scaler rate variability during September 2010 Crab γ-ray flare

As we have discussed earlier in § 5.4, an increased Crab γ-ray flux has been detected on 19 and 20 September by AGILE and confirmed by *Fermi*-LAT (see [228, 233]). No significant flux change has been found in X-rays, neither at lower frequencies, however, Chandra [244] and Hubble Space Telescope [277] have detected and followed up an enhanced emission from the fine arc-minute-size structures in the proximity of the pulsar.

During September 2010 Crab's γ-ray flare, only two dates, September 21 and 24, of significant excesses in the average scaler rate variability are observed. The excesses (7 bins) were occurred when the Crab nebula was flaring at $>20^{\circ}$ elevation with respect to Auger site. A comparison between the *Fermi*-LAT Crab daily light curve and the Auger scalers variability during September 2010 Crab nebula flare is presented in Fig. 6.11.

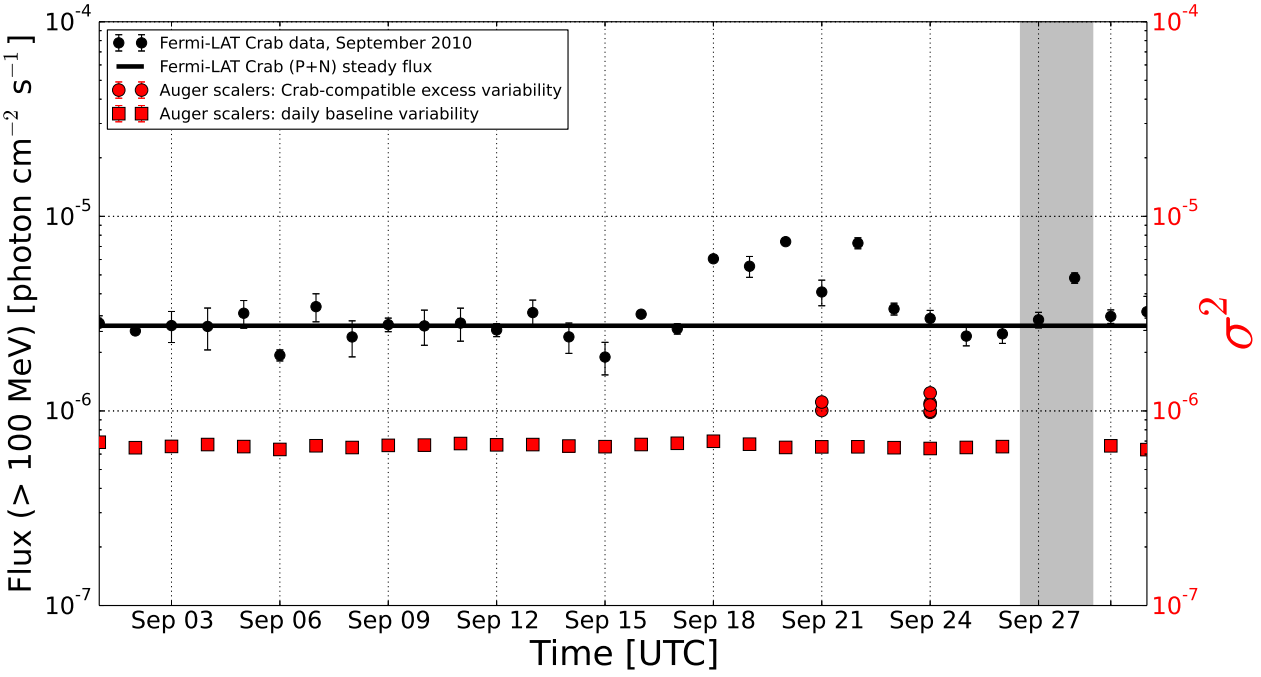

FIGURE 6.11: The daily significant variability in Auger average scaler rate *(right axis, red circles)* versus *Fermi*-LAT daily flux of the Crab nebula and pulsar *(left axis, black circles)* in **September 2010**. The red circles represent the observed excess variance per day, corresponding to the Crab zenith angle $< 70^{\circ}$, see tables 6.2 and A.2. The black solid line indicates the average Crab γ-ray flux ($E > 100$ MeV) according to the 3rd *Fermi*-LAT source catalog [276]. The red squares show the daily baseline of the average scaler rate variability. The gray band shows excluded dates of low quality scalers data (lightning & detector instability.)

During the γ-ray flare, the operation of the SD array was stable under good weather conditions. The variability plots of the dates of excesses are shown in Fig. 6.12.

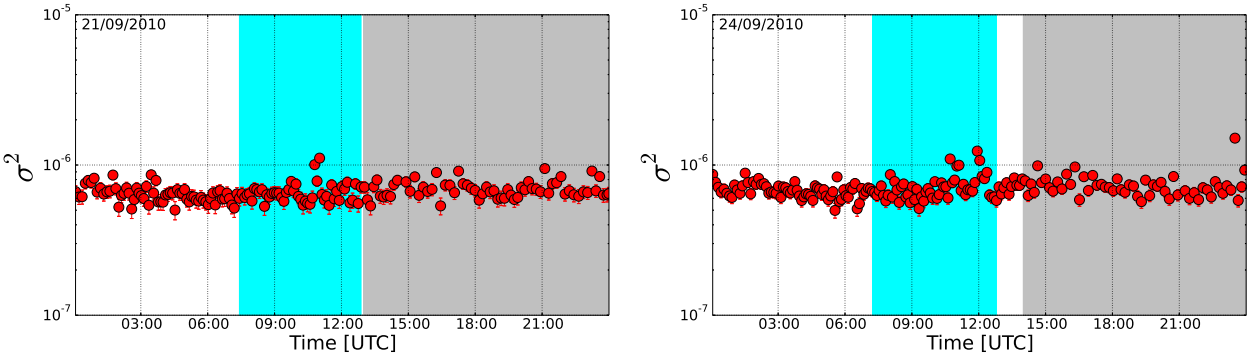

FIGURE 6.12: Daily variability plots of the dates of excesses in average scaler rate variability in September 2010, during the Crab γ-ray flare. The cyan vertical bands refer to the time interval corresponding to the Crab elevation >20° at the Pierre Auger Observatory site. The gray bands indicate interval of a loss in the number of active detectors.

Table. 6.2 shows the days of increased average scaler rate variability in September 2010 and the sum over Crab-compatible significant excesses, with $\theta_{CRAB} < 70°$. Furthermore, the number of 5-minute intervals of strong variability per each date is presented.

Date [yyyy-mm-dd]	Date [MJD]	Amplitude sum σ^2, $[10^{-6}]$	# of bins of excess
2010-09-21	55460	2.12 ± 0.07	2
2010-09-24	55463	5.39 ± 0.12	5

TABLE 6.2: Dates of increased variability in the average scaler rate in September 2010, during the Crab γ-ray flare. The observed excesses are Crab-compatible, with zenith angle $\theta_{CRAB} < 70°$.

According to Figs. 6.11 and 6.12, in addition to, Tab. 6.2, two dates of significant average scaler variability are consistent with the high-energy γ-ray flux detected by the *Fermi*-LAT.

6.1.2 Average scaler rate variability during April 2011 Crab γ-ray flare

The *Fermi*-LAT [249] and AGILE [251] have observed intense and fast Crab high-energy γ-ray flare in April 2011. As September 2010 Crab flare no enhanced variability in the synchrotron nebula emission has been found at lower energies, in addition to, the broadband pulsar flux and/or the spin-down pulsar period (pulsar glitches) haven't shown change. The Crab γ-ray flare of April 2011 hasn't been observed by the Cherenkov telescopes (see details in § 5.4), because of the small angular distance between the Sun and the Crab.

Auger fluorescence telescopes, covering zenith angles above 60° (except for the HEAT [131, 147] telescopes, which cover an elevation range from 30° to 58° above the horizon), appropriate for the Crab observation conditions in Malargüe, could in principle detect an excess of Cherenkov light

flashes in VHE γ-ray induced showers from the Crab direction. Unfortunately, the flare of April 2011 occurred close to the full Moon on April, 18, so that fluorescence data acquisitions were very sparse during the flare period.

During the flare episode observed by the *Fermi*-LAT, Auger SD scalers didn't show any strong variability for the time intervals, at which the Crab was high (>20°) above the horizon, see Fig. 6.13 and Tab. A.2.

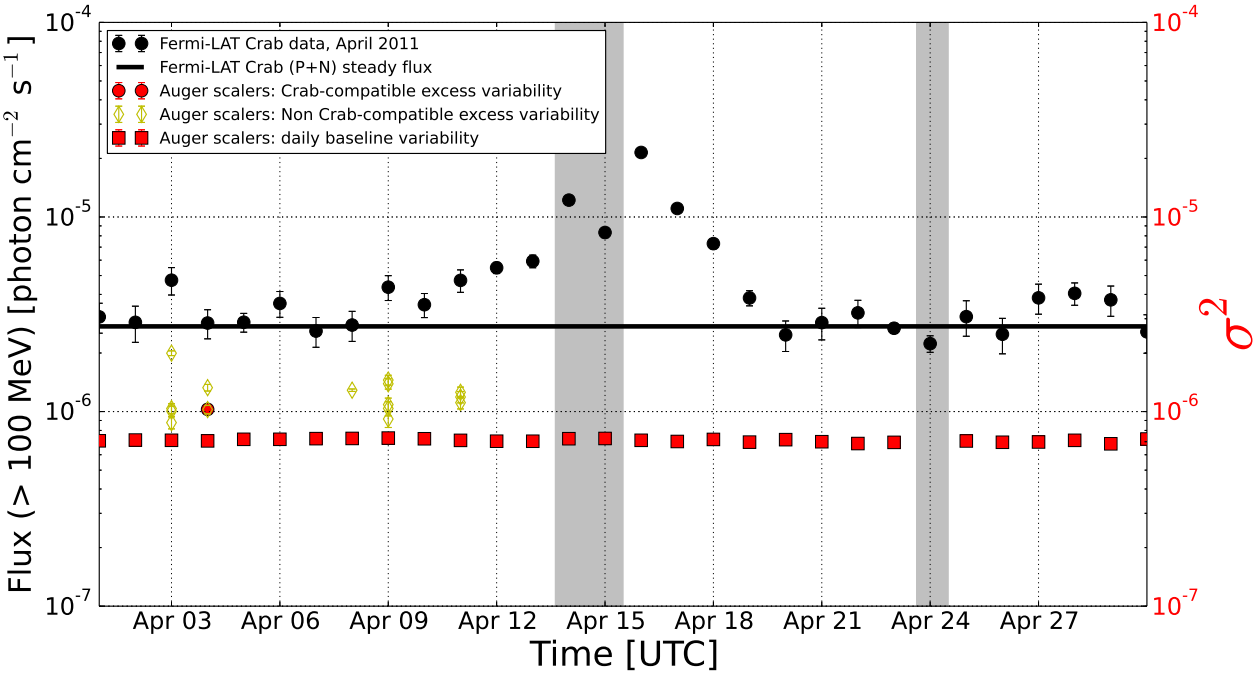

FIGURE 6.13: The daily significant variability in Auger average scaler rate *(right axis, red circles)* versus *Fermi*-LAT daily flux of the Crab nebula and pulsar *(left axis, black circles)* in **April 2011**. The red circles represent the observed excess variance per day, corresponding to the Crab zenith angle $< 70°$, see Tab. A.2. The black solid line indicates the average Crab γ-ray flux ($E > 100$ MeV) according to the 3^{rd} *Fermi*-LAT source catalog [276]. The red squares show the daily baseline of the average scaler rate variability. The yellow diamonds refer to non Crab-compatible excess variability observed over 5 dates. The gray bands indicate dates of SD instabilities. The date of April 24 has been excluded by reason of drastic change in the number of active detectors.

Figure 6.13 presents all significant excess variance in the average scaler rate variability during April 2011 Crab γ-ray flare observed by the *Fermi*-LAT. In that month, the operation of the SD array was stable, except for three dates (April 14, 15, and 24, which are marked in gray bands in Fig. 6.13). The loss in scaler acquisition on April 14 and 15 is 19.8% and 47.7% of the total daily measurements, respectively. The interval of SD instability started on April 13 around 21h UTC. The date of April 24 is excluded from the analysis by reason of drastic change in the number of active detectors.

We notice that Auger SD scalers recorded one date (April 4) of one bin of Crab-compatible excess variability, around 18h UTC, before the official episodes of the γ-ray flare announced by the *Fermi*-LAT. The daily variability plot of that date is shown in Fig. 6.14.

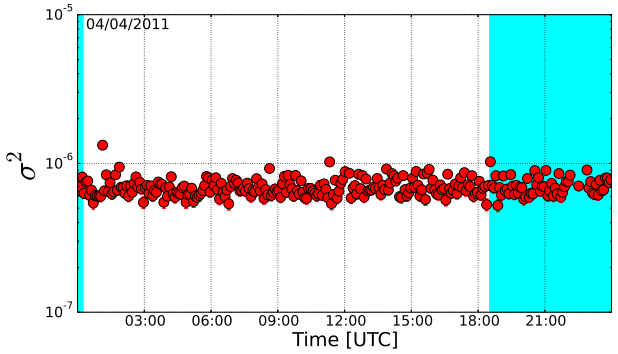

FIGURE 6.14: Daily variability plot of one date of excess in average scaler rate variability in April 4, 2011. On that date, one bin of Crab-compatible excess variability was observed, at 18h:33m:05s UTC, 5 days before the official episode of the Crab γ-ray flare detected by the *Fermi*-LAT. The cyan vertical bands refer to time interval corresponding to the Crab elevation $>20^\circ$ at the Pierre Auger Observatory site.

Also, on April 4, 2011, there are two episodes of non Crab-compatible excesses variability around 1h and 11h UTC (shown in Figs. 6.13 and 6.14, in addition to, Tab. A.2).

6.1.3 Average scaler rate variability during March 2013 Crab γ-ray flare

In the first week of March 2013, a strong γ-ray flare of the Crab nebula has been detected by the *Fermi*-LAT [234, 262] and AGILE-GRID [263, 264]. The flare lasted for more than two weeks.

The Crab nebula was observed by the VERITAS and H.E.S.S. experiments, during March 2013 γ-ray flare (see details in § 5.4). The VERITAS Observatory has collected 10.3 hours of data on the Crab in ten nights from March 2 to March 15, 2013. The average flux observed during the Crab's flaring state was consistent with the non-variable long-term average Crab nebula flux [268]. The H.E.S.S. Observatory has collected 4.4 hours of data on the Crab nebula in five consecutive nights on March 6 to March 10, 2013. The observational data taken during the flare concluded that no significant changes in the flux [267].

Auger SD scalers observed several dates of significant excess variance during March 2013 Crab γ-ray flare. The SD array was stable and the weather conditions were good during the month of the γ-ray flare. A comparison between Auger average scaler rate variability and *Fermi*-LAT daily Crab flux is shown in Fig. 6.15.

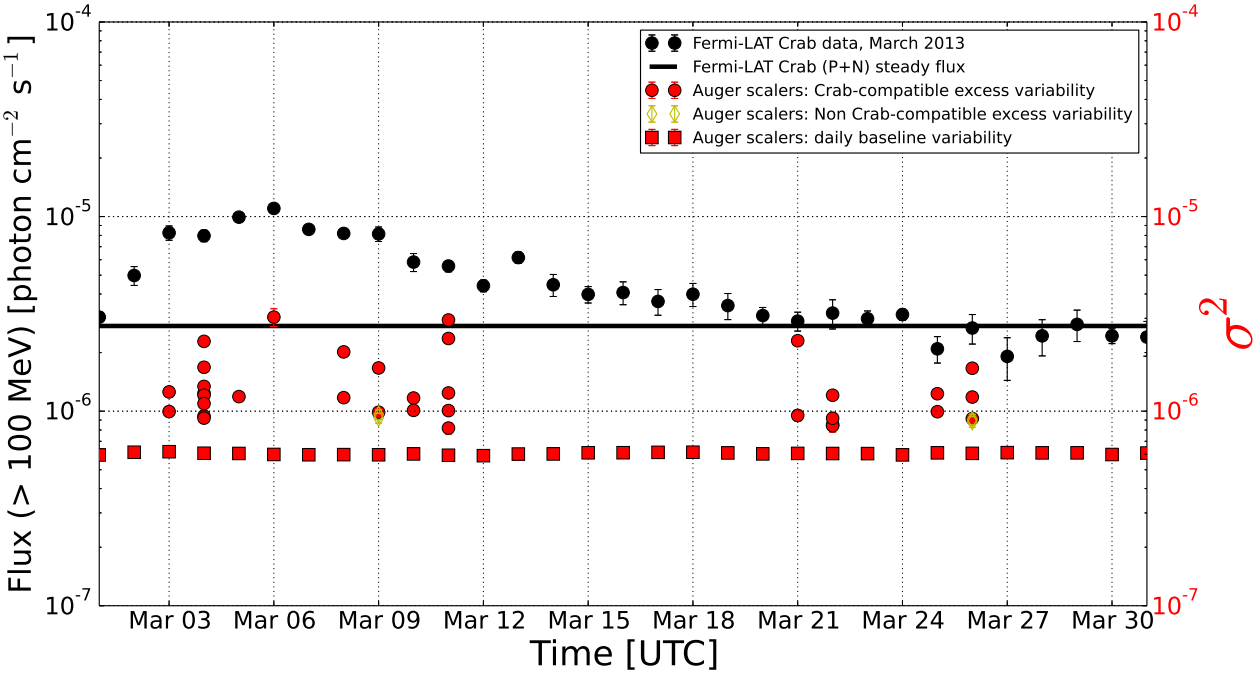

FIGURE 6.15: Daily significant variability in Auger average scaler rate *(right axis, red circles)* versus *Fermi*-LAT daily flux of the Crab nebula and pulsar *(left axis, black circles)* in **March 2013**. The red circles represent the observed excess variance per day, corresponding to the Crab zenith angle $< 70°$, see tables 6.3 and A.2. The black solid line indicates the average Crab γ-ray flux ($E > 100\,\text{MeV}$) according to the 3^{rd} *Fermi*-LAT source catalog [276]. The red squares show the daily baseline of the average scaler rate variability. The yellow diamonds refer to non Crab-compatible excess variability observed over 2 dates.

Figure 6.15 provides 12 episodes of significant variability in Auger average scaler rate during the γ-ray flare. Interestingly, a few dates of excesses have been detected at the end of the month, while the Crab flux has retrieved the quiescent level according to *Fermi*-LAT measurements. The total number of Crab-compatible excesses is 34 5-minute intervals. A small fraction (4 5-minute intervals) out of them is non Crab-compatible distributed over two dates. The variability plots of those dates of significant excess variance are presented in Fig. 6.16.

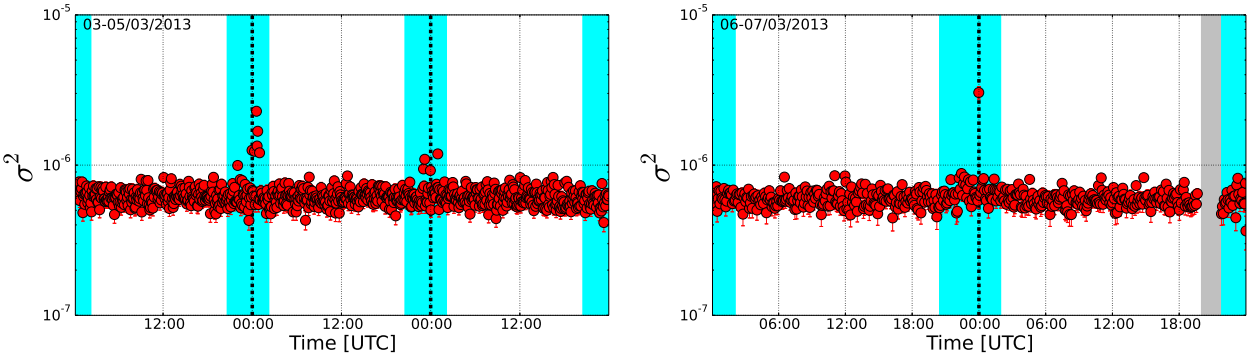

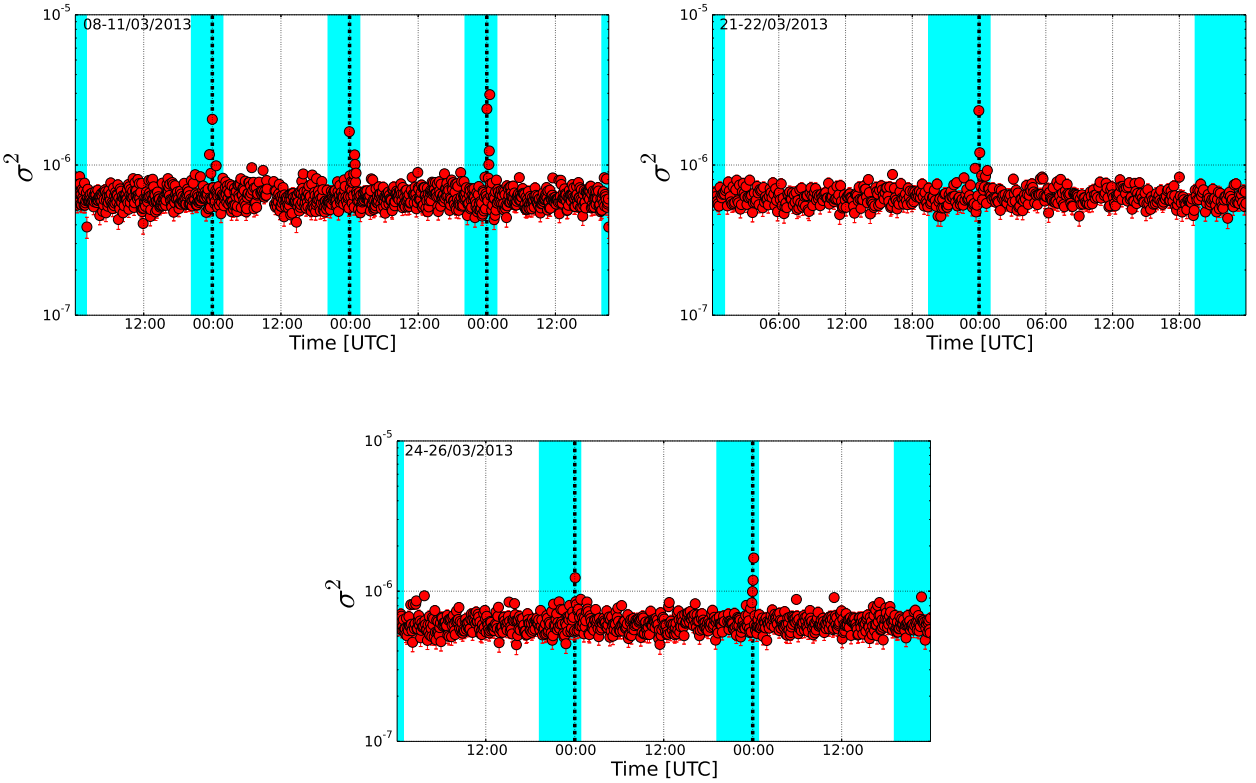

FIGURE 6.16: Daily variability plots of the dates of excesses in average scaler rate variability in March 2013, during the Crab γ-ray flare. The cyan vertical bands refer to the time interval corresponding to the Crab elevation >20° at the Pierre Auger Observatory site. The bands marked in gray indicate the periods of lightning excluded from the analysis.

The significant excesses coincide with the Crab transit periods, with zenith angle $\theta_{CRAB} < 70°$. Additionally, the bulk of excesses correlates with the episodes of the highest γ-ray flux measured by the *Fermi*-LAT. Table 6.3 shows the sum over Auger excess variance amplitudes and the number of 5-minute intervals of strong variability per each date.

Date [yyyy-mm-dd]	Date [MJD]	Amplitude sum σ^2, $[10^{-6}]$	# of bins of excess
2013-03-03	56354	2.25 ± 0.07	2
2013-03-04	56355	10.70 ± 0.16	8
2013-03-05	56356	1.18 ± 0.05	1
2013-03-06	56357	3.04 ± 0.32	1
2013-03-08	56359	3.19 ± 0.06	2
2013-03-09	56360	2.65 ± 0.06	2
2013-03-10	56361	2.18 ± 0.07	2
2013-03-11	56362	8.37 ± 0.09	5
2013-03-21	56372	3.25 ± 0.07	2
2013-03-22	56373	3.82 ± 0.12	4
2013-03-25	56376	2.22 ± 0.07	2
2013-03-26	56377	3.76 ± 0.09	3

TABLE 6.3: Dates of increased variability in the average scaler rate in March 2013, during the Crab γ-ray flare. The observed excesses are Crab-compatible, with zenith angle $\theta_{CRAB} < 70°$.

According to Figs. 6.15 and 6.16, in addition to, Tab. 6.3, 34 5-minute intervals of significant average scaler variability are observed during high-energy γ-ray flux detected by *Fermi*-LAT.

6.1.4 Average scaler rate variability during October 2013 Crab γ-ray flare

A short γ-ray Crab nebula flare ($E > 100$ MeV) has been reported by *Fermi*-LAT [269] on October 17, 2013. The γ-ray flare has been confirmed by AGILE on October 18, 2013, as a significant increase in the Crab's standard flux levels $\sim 5\sigma$ [270].

In the month of the γ-ray flare, we have found two dates of strong Crab-compatible variability in average scaler rate, see Fig. 6.17. The weather conditions were good and the SD array was stable, except for 4 dates of significant γ-ray flux observed by the *Fermi*-LAT. Those dates of SD instabilities and lightning events are excluded from the analysis, and marked in gray bands in Fig. 6.17.

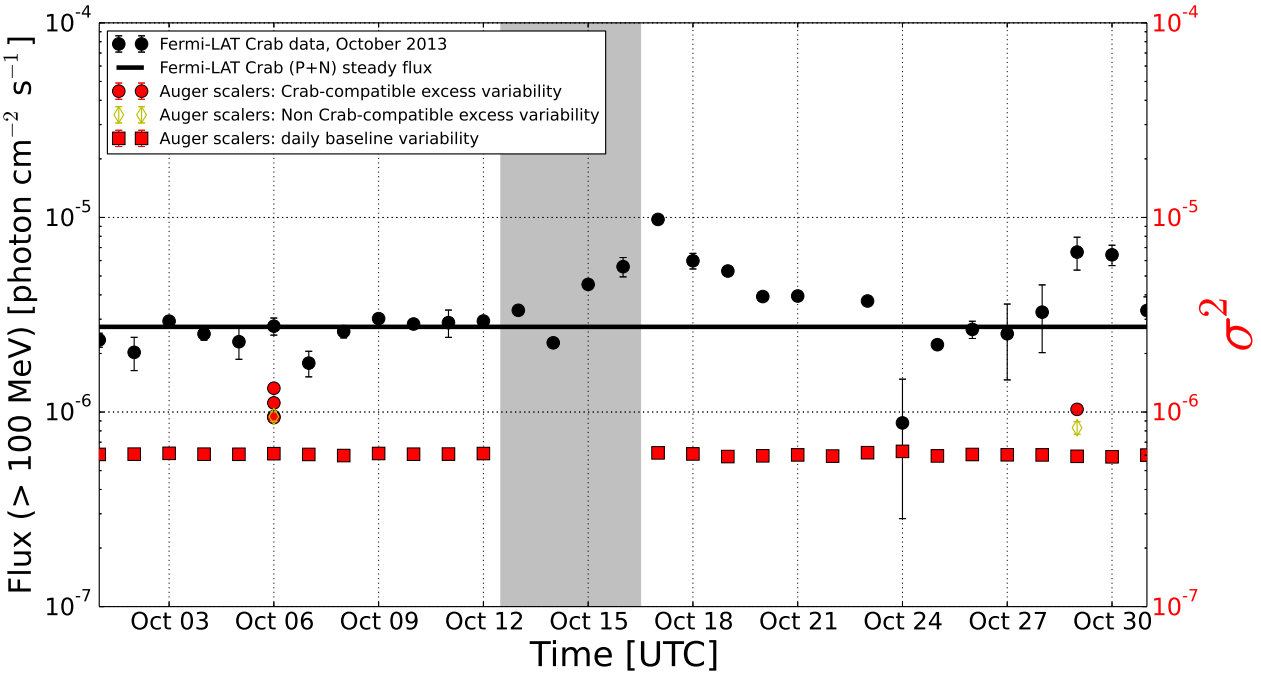

FIGURE 6.17: Daily significant variability in Auger average scaler rate *(right axis, red circles)* versus *Fermi*-LAT daily flux of the Crab Nebula *(left axis, black circles)* in **October 2013**. The red circles represent the observed excess variance per day, corresponding to the Crab zenith angle $< 70°$, see tables 6.4 and A.2. The black solid line indicates the average Crab γ-ray flux ($E > 100$ MeV) according to the 3^{rd} *Fermi*-LAT source catalog [276]. The red squares show the daily baseline of the average scaler rate variability. The gray bands show excluded dates of low quality data (SD array instabilities and lightning). The yellow diamonds refer to non Crab-compatible excess variability observed over 2 dates.

Both dates of excesses are outside of the major flare period declared by the *Fermi*-LAT Collaboration, albeit a significant flux of the factor of ~ 2.3 the steady Crab's flux has been detected by

Fermi-LAT in October 29, 2013, which is compatible with the strong variability observed by Auger SD scalers. The variability plots of those dates are shown in Fig. 6.18.

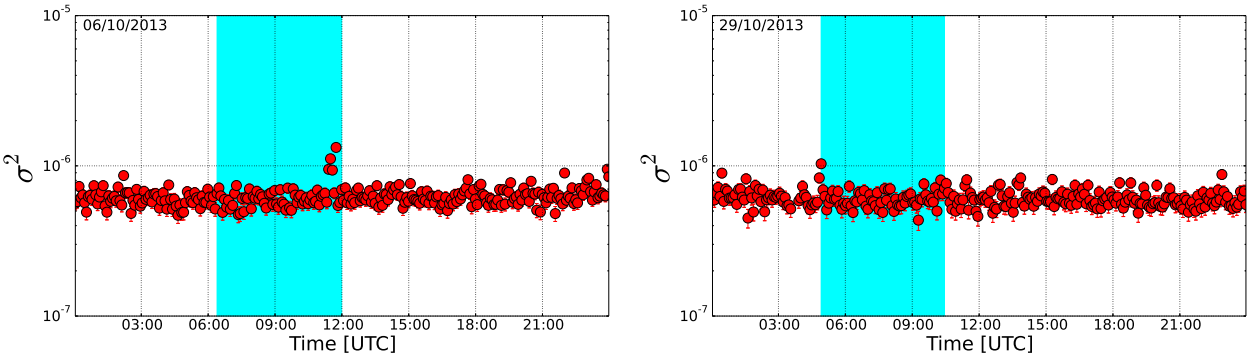

FIGURE 6.18: Daily variability plots of the dates of excesses in average scaler rate variability in October 2013, during the Crab γ-ray flare. The cyan vertical bands refer to the time interval corresponding to the Crab elevation $>20^\circ$ at the Pierre Auger Observatory site.

Table 6.4 shows the sum over Auger excess variance amplitudes and the number of 5-minute intervals of strong variability per each date.

Date [yyyy-mm-dd]	Date [MJD]	Amplitude sum σ^2, $[10^{-6}]$	# of bins of excess
2013-10-06	56571	4.32 ± 0.10	4
2013-10-29	56594	1.03 ± 0.06	1

TABLE 6.4: Dates of increased variability in the average scaler rate in October 2013, during the Crab γ-ray flare. The observed excesses are Crab-compatible, with zenith angle $\theta_{\mathrm{CRAB}} < 70^\circ$.

6.1.5 Average scaler rate variability during March 2014 Crab γ-ray flare

In March 2014, *Fermi*-LAT has observed γ-ray flare from the Crab nebula [273], as an increase in the daily-averaged γ-ray emission ($E > 100\,\mathrm{MeV}$).

During the month of this γ-ray flare, the Auger SD array was stable and the weather conditions were good. Auger SD scalers detected two Crab-compatible episodes of significant variability in average scaler rate. These two episodes are in a strong correlation with the Crab γ-ray flux measured by the *Fermi*-LAT (see Fig. 6.19).

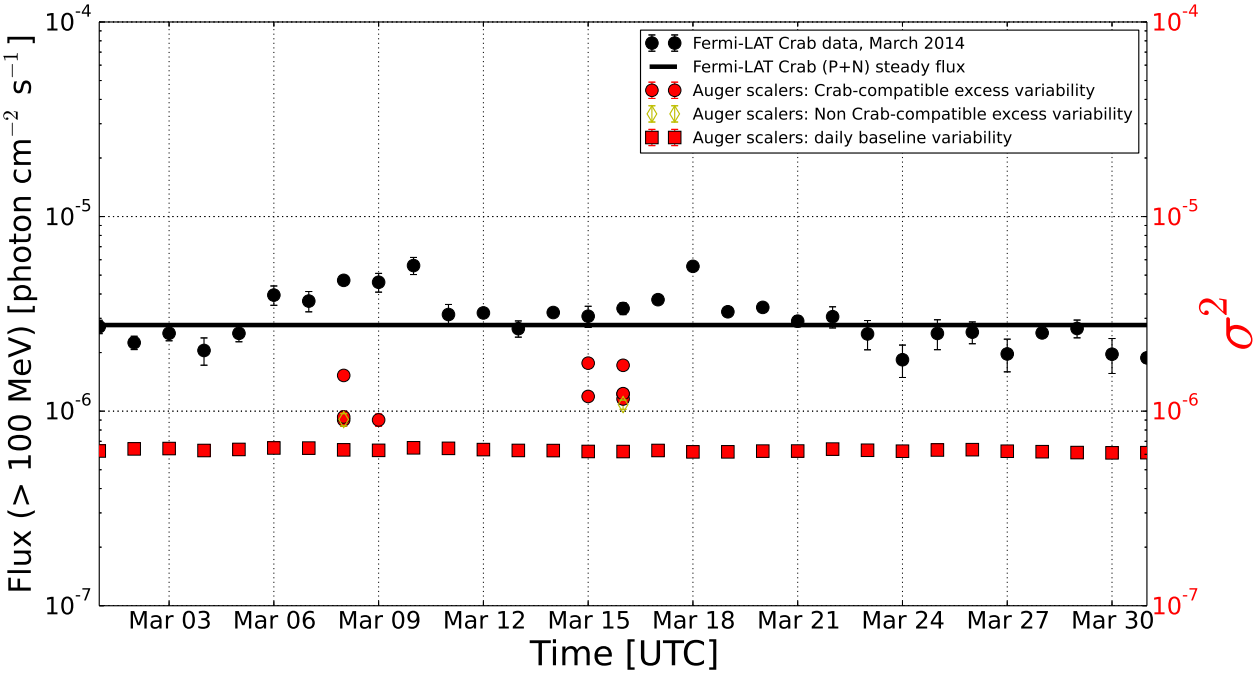

FIGURE 6.19: Daily significant variability in Auger average scaler rate *(right axis, red circles)* versus *Fermi*-LAT daily flux of the Crab nebula *(left axis, black circles)* in **March 2014**. The red circles represent the observed excess variance per day, corresponding to the Crab zenith angle $< 70^\circ$ (see tables 6.5 and A.2). The black solid line indicates the average Crab γ-ray flux ($E > 100$ MeV) according to the 3rd *Fermi*-LAT source catalog [276]. The red squares show the daily baseline of the average scaler rate variability. The yellow diamonds refer to non Crab-compatible excess variability observed over 2 dates.

The variability plots of the dates of significant excesses are shown in Fig. 6.20.

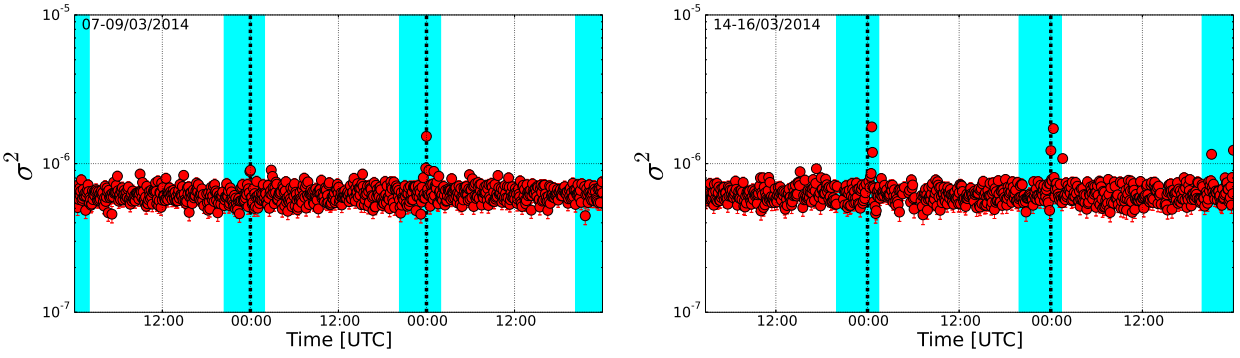

FIGURE 6.20: Daily variability plots of the dates of excesses in average scaler rate variability in March 2014, during the Crab γ-ray flare. The cyan vertical bands refer to the time interval corresponding to the Crab elevation $>20^\circ$ at the Pierre Auger Observatory site.

Table 6.4 shows the sum over Auger excess variance amplitudes and the number of 5-minute intervals of strong variability per each date.

Date [yyyy-mm-dd]	Date [MJD]	Amplitude sum σ^2, $[10^{-6}]$	# of bins of excess
2014-03-08	56724	3.35 ± 0.13	3
2014-03-09	56725	0.90 ± 0.07	1
2014-03-15	56731	2.95 ± 0.08	2
2014-03-16	56732	5.18 ± 0.11	4

TABLE 6.5: Days of increased variability in the average scaler rate in March 2014, during the Crab γ-ray flare. The observed excesses are Crab-compatible, with zenith angle $\theta_{CRAB} < 70^{\circ}$.

According to the daily variability plots in March 2013 (Fig. 6.16) and March 2014 (Fig. 6.20), a kind of similarity in the distribution of significant Crab-compatible variability has been found. Most of the excesses, which are observed during both March 2013 and March 2014 flares, have a tendency to occur around the midnight, at a certain time corresponding to Crab's high elevation $>20^{\circ}$ at Malargüe sky. The origin of such excess regularity is not known with certain, however, the results obtained from the individual detector analysis (see Appendix C) infer that many detectors have contributed to the strong scaler rate variability in both March 2013 and March 2014. This could investigate the hypothesis of the *periodicity* of a pulsed multi-TeV γ-ray Crab emission, as concluded by the analysis of the outburst of 23 February 1989 [65, 186, 187], discussed in § 5.4. In order to prove such hypothesis, further analysis of T2 trigger data should be provided, as well as an extension of the detector calibration (adding a nanosecond time stamp and maybe also additional thresholds) seems to be necessary for a future study.

6.1.6 Average scaler rate variability during August 2014 Crab γ-ray flare

In August 2014, another Crab γ-ray flare has been reported by the *Fermi*-LAT [275]. Since, the daily-averaged γ-ray emission ($E > 100$ MeV) from the Crab nebula was a factor of ∼2.7 greater than the average Crab γ-ray flux, which start to increase on August 15, 2014. Thus, a gradual flux rise has been observed on the following days (see Fig. 6.21 and details in § 5.4).

During the August γ-ray flare, Auger average scaler rate has shown 10 dates of a strong variability, illustrated in Fig. 6.22. We have noticed that the variability of August 6, 2014 provides a plenty of excesses over the whole date for both Crab-compatible and non Crab-compatible (see A.2), however, in all other dates most of the excess variability in scaler average rate are Crab-compatible ($\theta_{CRAB} < 70^{\circ}$). The SD array was stable and the weather conditions were good during the month of the γ-ray flare.

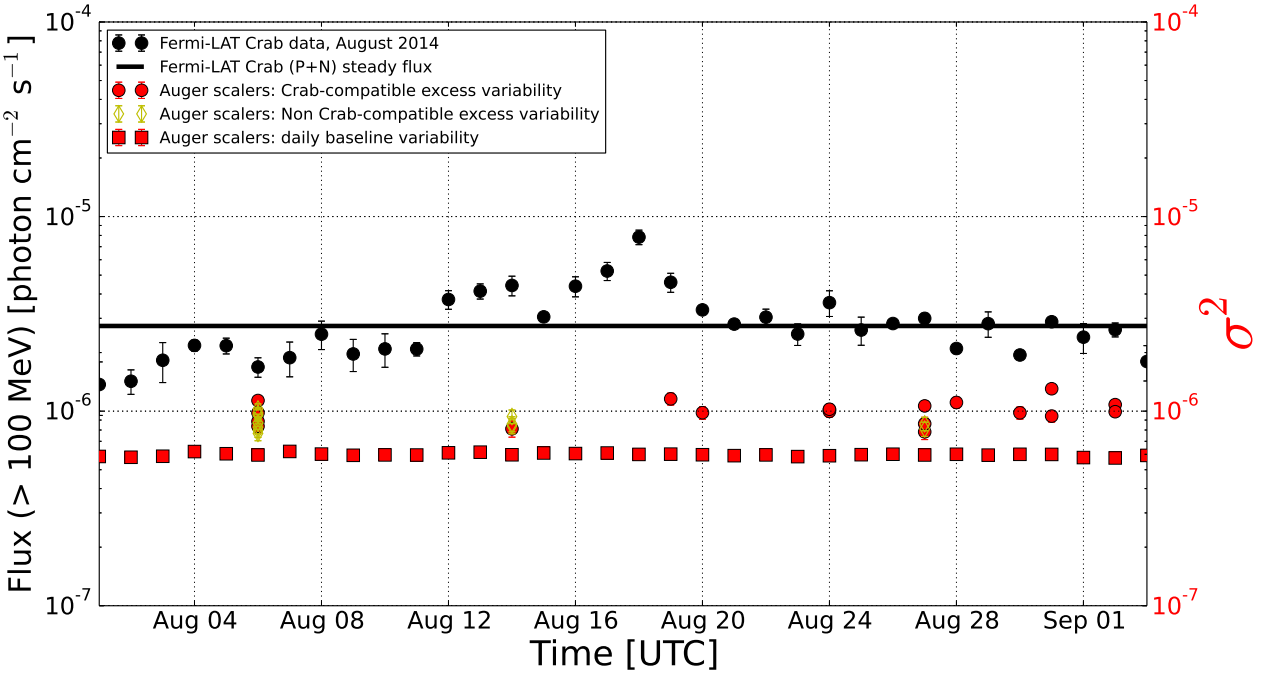

FIGURE 6.21: Daily significant variability in average scaler rate *(right axis, red circles)* versus *Fermi*-LAT daily flux of the Crab nebula *(left axis, black circles)* in **August 2014**. The red circles represent the observed excess variance per day, corresponding to the Crab zenith angle $< 70°$, see tables 6.6 and A.2. The black solid line indicates the average Crab γ-ray flux ($E > 100\,\mathrm{MeV}$) according to the 3^{rd} *Fermi*-LAT source catalog [276]. The red squares show the daily baseline of the average scaler rate variability. The yellow diamonds refer to non Crab-compatible excess variability observed over 3 dates.

The majority of the excesses are correlated with the significant γ-ray flux observed by the *Fermi*-LAT. The variability plots of such dates of significant excesses are presented in Fig. 6.22.

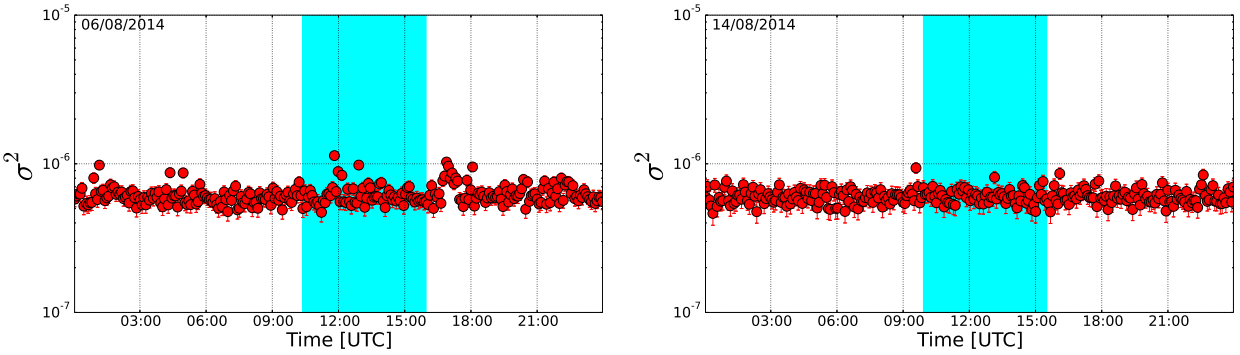

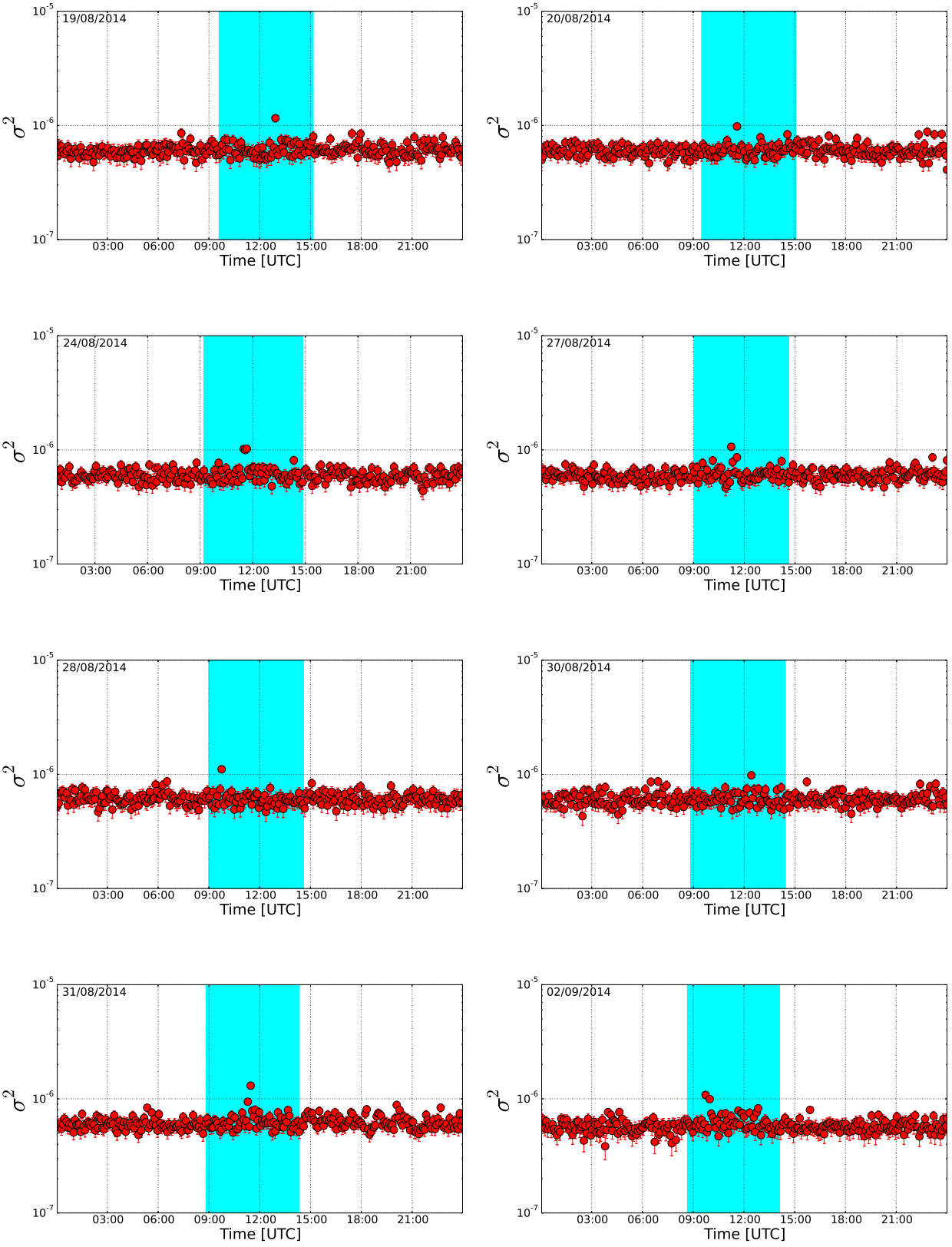

FIGURE 6.22: Daily variability plots of the dates of excesses in average scaler rate variability in August 2014, during the Crab γ-ray flare. The cyan vertical bands refer to the time interval corresponding to the Crab elevation >20° at the Pierre Auger Observatory site.

Table 6.6 shows the sum over the excess variance amplitudes and the number of 5-minute intervals of strong variability per each date.

Date [yyyy-mm-dd]	Date [MJD]	Amplitude sum σ^2, $[10^{-6}]$	# of bins of excess
2014-08-06	56875	3.84 ± 0.13	4
2014-08-14	56883	0.81 ± 0.08	1
2014-08-19	56888	1.15 ± 0.08	1
2014-08-20	56889	0.98 ± 0.07	1
2014-08-24	56893	3.04 ± 0.11	3
2014-08-27	56896	2.71 ± 0.12	3
2014-08-28	56897	1.10 ± 0.07	1
2014-08-30	56899	0.98 ± 0.07	1
2014-08-31	56900	2.25 ± 0.09	2
2014-09-02	56902	2.07 ± 0.05	2

TABLE 6.6: Days of increased variability in the average scaler rate in August 2014, during the Crab flare. The observed excesses are Crab-compatible, with zenith angle $\theta_{CRAB} < 70^{\circ}$.

According to Figs. 6.21 and 6.22, in addition to Tab. 6.6, Auger average scaler rate variability shows significant excesses during the Crab γ-ray flare. Interestingly, few dates of significant excesses are observed after the γ-ray flare. This behavior was also observed in March 2013 (see Fig. 6.15).

6.1.7 Average scaler rate variability during December 2015 Crab γ-ray flare

In December 2015, the *Fermi*-LAT has detected an enhanced γ-ray ($E > 100$ MeV) emission [174] from the Crab nebula (see details in § 5.4).

Auger average scaler rate has shown significant variability during three dates in December 2015. On each of these dates, there are strong variability time intervals compatible with the Crab elevation ($>20^{\circ}$) at Malargüe. No such significant variability has been found during January 1-8, 2016, as this period had unstable weather conditions, and hence bad period cuts, e.g., lightning and SD instability periods (see Appendix A.4 and A.5). A comparison of Auger SD average scaler rate variability and the daily Crab flux measured by the *Fermi*-LAT is presented in Fig. 6.23

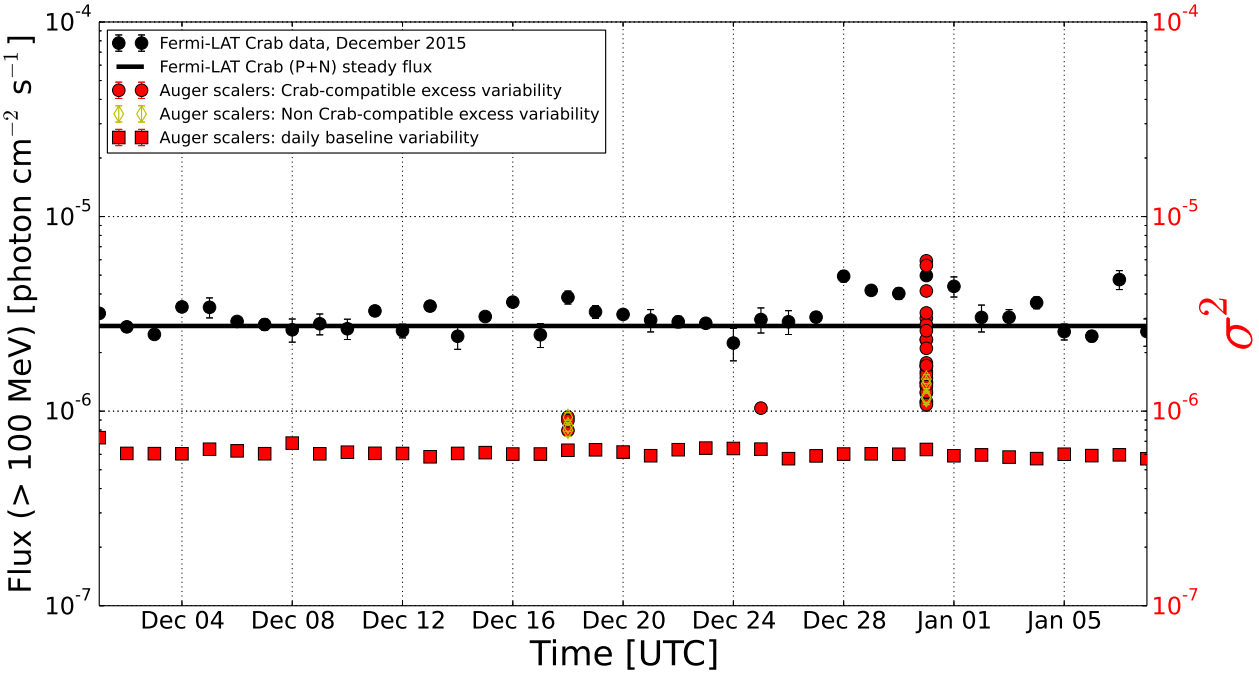

FIGURE 6.23: Daily significant variability in Auger average scaler rate *(right axis, red circles)* versus *Fermi*-LAT daily flux of the Crab nebula *(left axis, black circles)* in **December 2015 and January 1-8, 2016**. The red circles represent the observed excess variance per day, corresponding to the Crab zenith angle $< 70°$, see tables 6.7 and A.2. The black solid line indicates the average Crab γ-ray flux ($E > 100$ MeV) according to the 3rd *Fermi*-LAT source catalog [276]. The red squares show the daily baseline of the average scaler rate variability. The yellow diamonds refer to non Crab-compatible excess variability observed over 2 dates.

The variability plots of these strong Crab-compatible episodes are shown in Fig. 6.24. An especially strong variability has been observed on December 31, corresponding to the highest daily Crab's γ-ray flux detected by the *Fermi*-LAT [174] in 2015.

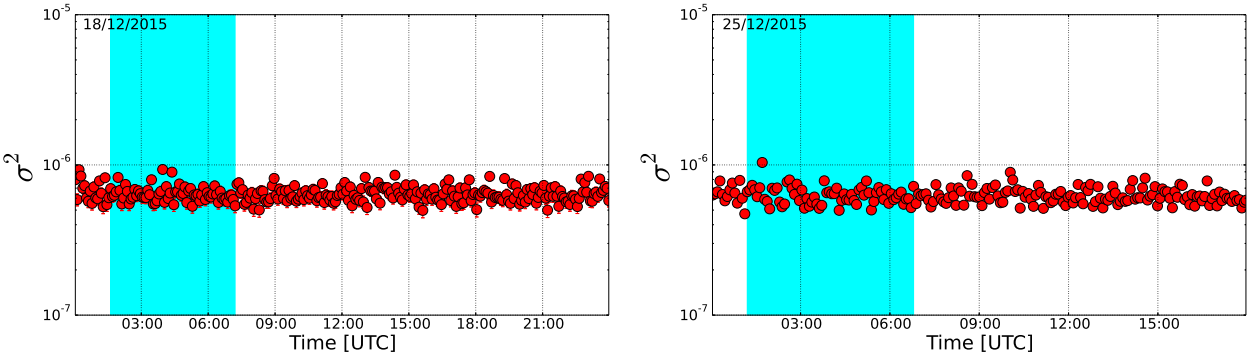

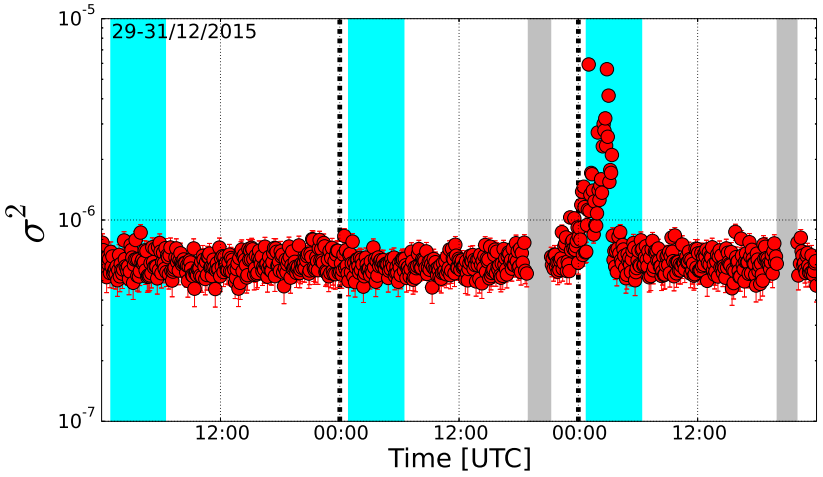

FIGURE 6.24: Daily variability plots of the dates of excesses in average scaler rate variability in December 2015, during the Crab γ-ray flare. The cyan vertical bands refer to the time interval corresponding to the Crab elevation >20° at the Pierre Auger Observatory site. The bands marked in gray indicate intervals of lightning events excluded from the analysis.

Table 6.7 shows the sum over the excess variance amplitudes and the number of 5-minute intervals of strong variability per each date.

Date [yyyy-mm-dd]	Date [MJD]	Amplitude sum σ^2, $[10^{-6}]$	# of bins of excess
2015-12-18	57374	2.62 ± 0.01	3
2015-12-25	57381	1.04 ± 0.003	1
2015-12-31	57387	59.55 ± 0.38	27

TABLE 6.7: Days of increased variability in the average scaler rate in December 2015 and January 1-8, 2016, during the Crab flare. The observed excesses are Crab-compatible, with zenith angle $\theta_{CRAB} < 70°$.

The three dates of significant average scaler rate variability are summarized in Tab. 6.7, and shown in Figs. 6.23 and 6.24. In Tab. 6.7, the excess variance of all five-minute intervals are added up in order to obtain the daily value. The exceptionally long and strong variability episode on **December 31** led to the highest daily Crab-compatible σ^2 value of $(59.55 \pm 0.38) \times 10^{-6}$ over the whole dataset from 2006 to 2015.

For the first time, the Crab flare occurred during the austral summer (November-February). This requires sub-array analyses with detailed weather cross-check, particularly, there are lightning events triggered on December 30, the day before the maximum strong variability, which is observed on December 31, 2015.

The Auger datafile (prod. v2r0) ad_2015_12_30_12h00.root for the date of the strong scaler rate variability contains 67 events, triggered by the lightning detection system (LDS) [278] in the period from the noon UTC of December 30 to the noon UTC of December 31, 2015. Only four of these events have abnormal "oscillating" FADC traces typical for the lightning-induced events (detector

id: 109, 255, 269, and 357), e.g., one identified event by the function *IsLightningEvent()* from the CDAS/Ec package [164] is shown in Fig. 6.25.

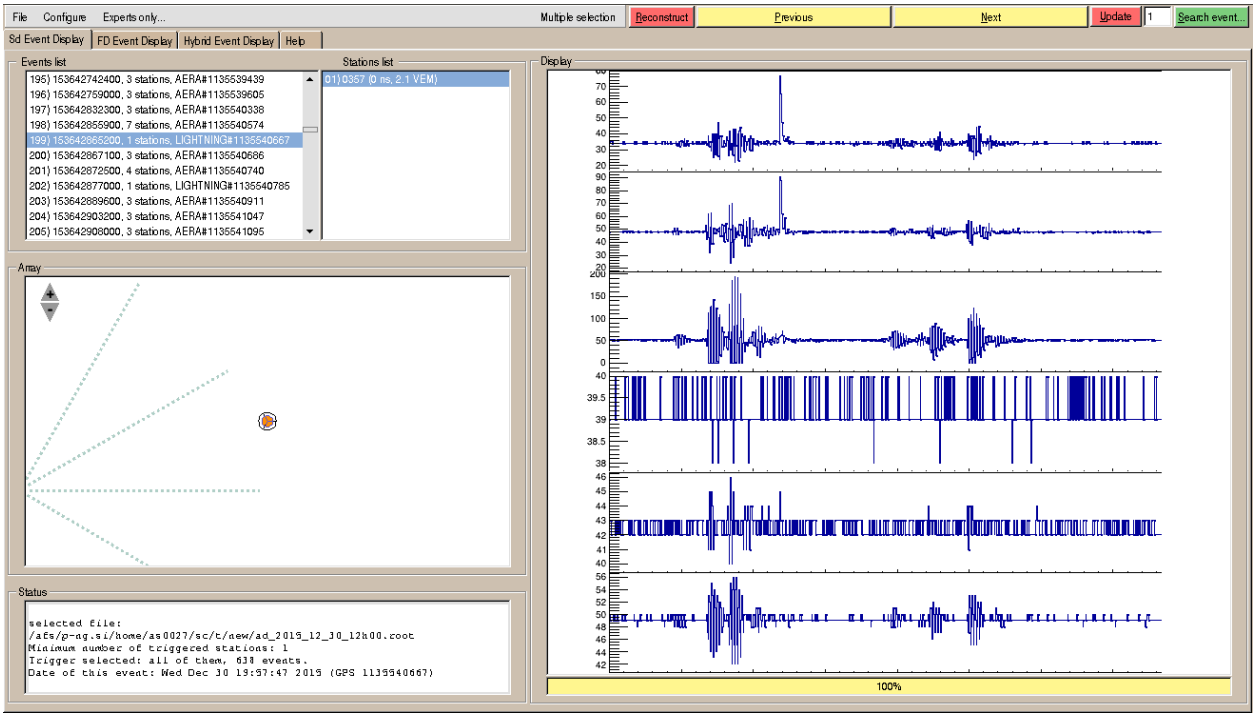

FIGURE 6.25: CDAS Event Display [164] view of the lightning event at GPS second 1135540667 (i.e. at 19 h57 m47 s UTC, Dec 30), in the period from the noon of December 30 till the noon of December 31, 2015. This lightning event has been identified using function *IsLightningEvent()* from CDAS/Ec package, and the whole array scaler data ±one hour around its time have been excluded. The corresponding lightning period is marked by a gray band on Fig. 6.24 and listed in Tab. A.23.

The remaining 63 events have normal FADC traces (see an example in Fig. 6.26).

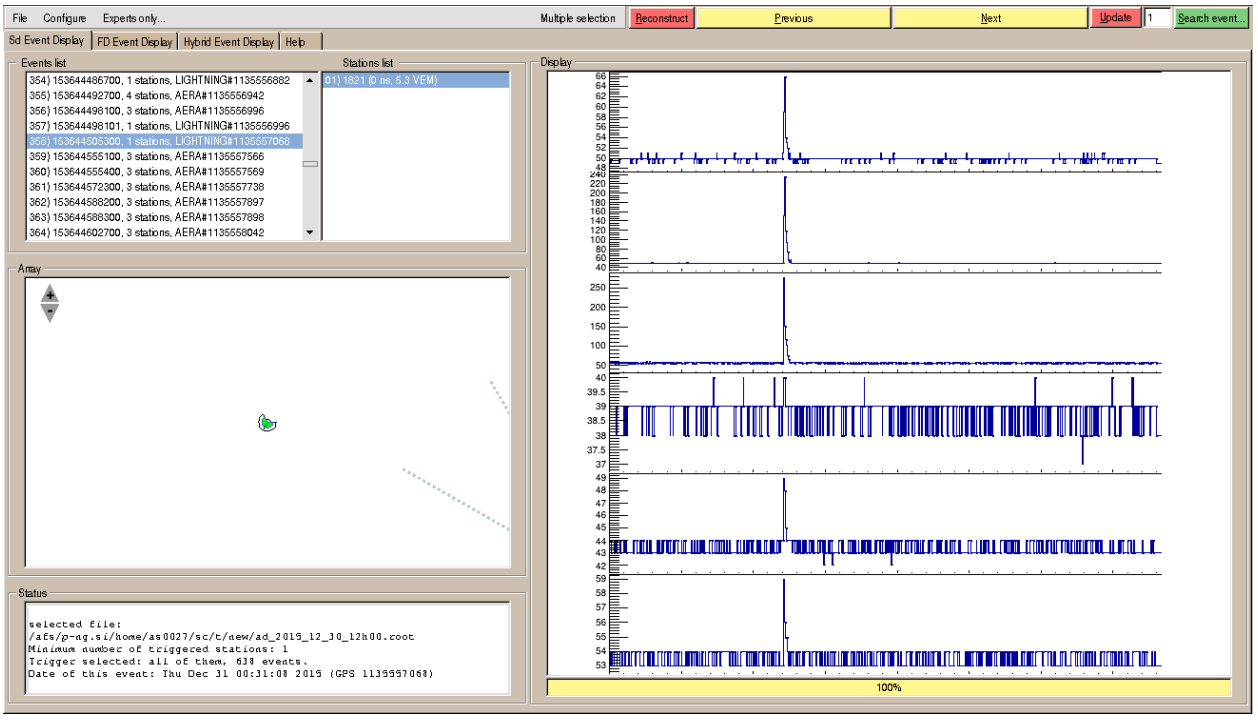

FIGURE 6.26: CDAS Event Display [164] view of the last Auger lightning trigger in the period from the noon of December 30 till the noon of December 31, 2015. An anomaly in operation of the first photomultiplier or the associated electronics is seen both on the high and the low gain waveforms. However, the waveforms of two other PMTs show a normal behavior, and the event has not been retained by the CDAS/Ec package as a lightning event.

The time distribution of the 67 lightning detector triggers is shown in Fig. 6.27 (blue histogram), as well as the number of five-minute interval bin of a significant average scaler rate variability detected on December 31, 2015.

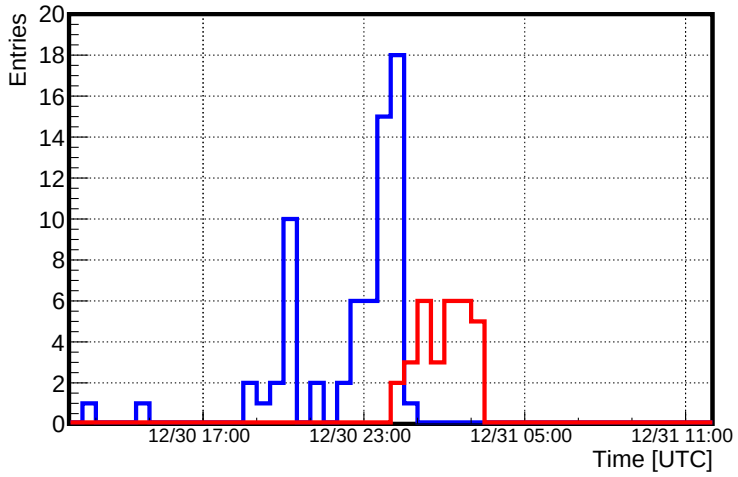

FIGURE 6.27: The distribution of Auger lightning detector triggers (in blue) and Auger scaler rate variability excesses (in red), in the period from the noon of December 30 till the noon of December 31, 2015.

The overlap of the two distributions is very small ∼1 hr length. The five-minute excess variance intersects with the lightning triggers between 0h and 1h UTC, Dec 31, corresponding to sidereal time range of [2h, 3h] and Crab zenith angle of the range of [68°, 74°]. We have extracted the events detected by the StormTracker lightning detectors [278] from the Auger Monitoring Database [279, 280], during the period of the Crab γ-ray flare. These events are mapped in the left plot of Fig. 6.28, and the 67 events triggered by the LDS in the right plot of the same figure.

Interestingly, there is no lightning trigger in the CDAS file after 0h 31m 08s UTC on December, 31, while multiple events have been recorded by the lightning detectors.

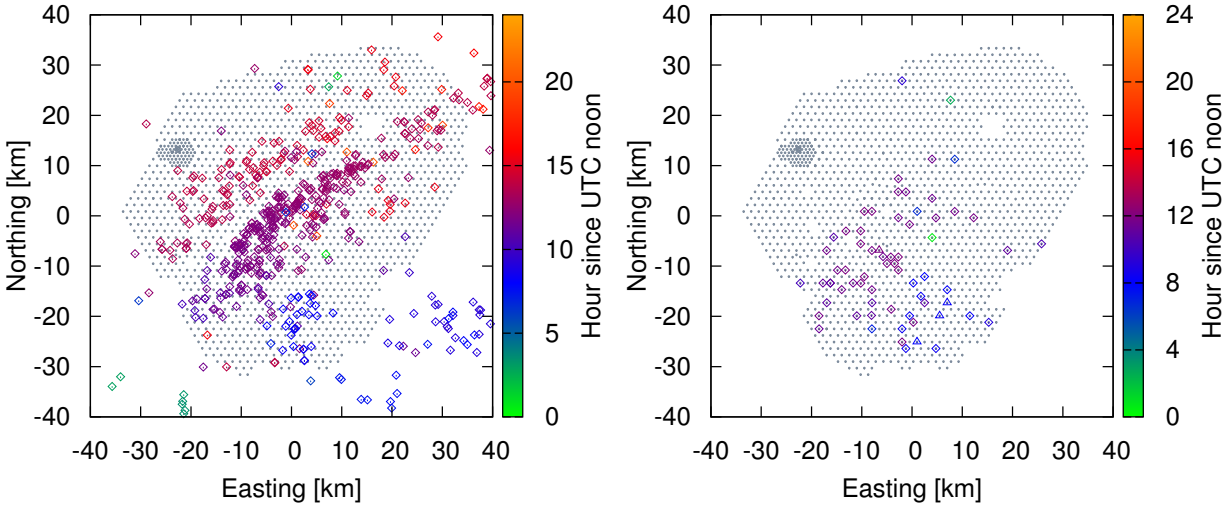

FIGURE 6.28: Maps and time of the events recorded by the StormTracker lightning detectors in December 30 and 31, 2015. *Left panel*: Map of the position and the time of the events recorded by the StormTracker lightning detectors [278]. *Right panel*: The 67 CDAS events triggered by the lightning detectors. Detectors with lightning-induced FADC traces (4 events out of 67) are marked by triangles on the right map.

The Auger data file corresponding to the next 24 hours, ad_2015_12_31_12h00.root, contains 27 triggers from the lightning detectors. Out of these 27 events, 24 occurred during a two-hour period between 19h 57m 10s UTC and 21h 59m 53s UTC on December 31, including the only event with lightning-induced traces, at GPS second 1135630788 (i.e. at 20 h59 m48 s UTC). Therefore, there was no interruption in operation of the lightning detectors and the corresponding triggers in CDAS during the date of December 31, 2015.

To summarize, the peak of the strong rate variability is in the time bin between 2 am and 3 am UTC, while the latest of the 67 events (only four detectors with anomaly in FADC traces, see e.g. 6.25, and remaining 63 events have normal traces, see Fig. 6.26) is at 0h 31m 08s UTC, Dec 31. The distribution of the lightning detector-triggered events agrees with the weather data recorded by the Malargüe airport weather station [281, 282] (weather worsening starting from 18h UTC (15h ART), Dec 30, strong thunderstorms at 0h UTC, Dec 31, almost clear sky at 3h UTC (0h ART) etc.).

Both data sets suggest that the thunderstorms cannot be the reason of the strong Auger scaler rate variability observed on the last date of the year 2015. The analysis of the average scaler rate variability using the Auger SD sub-arrays free from thunderstorms confirms this conclusion.

In contrast to all episodes of strong Auger average scaler rate variability, which are consistent with the HE γ-ray Crab flares, the strong variability in December 31, 2015 occurred during a period of thunderstorms typical for the austral summer (November to February).

Based on the data (time and location) provided by the lightning detectors [278], we are able to localize and exclude lightning contributions to the scaler rate measurements of December 30 and 31, 2015. Fig. 6.29 shows the subset of the lightning events from the distribution shown on the left map of Fig. 6.28, for the period of the strong average scaler rate variability from the midnight UTC to 4 UTC of December 31, 2015.

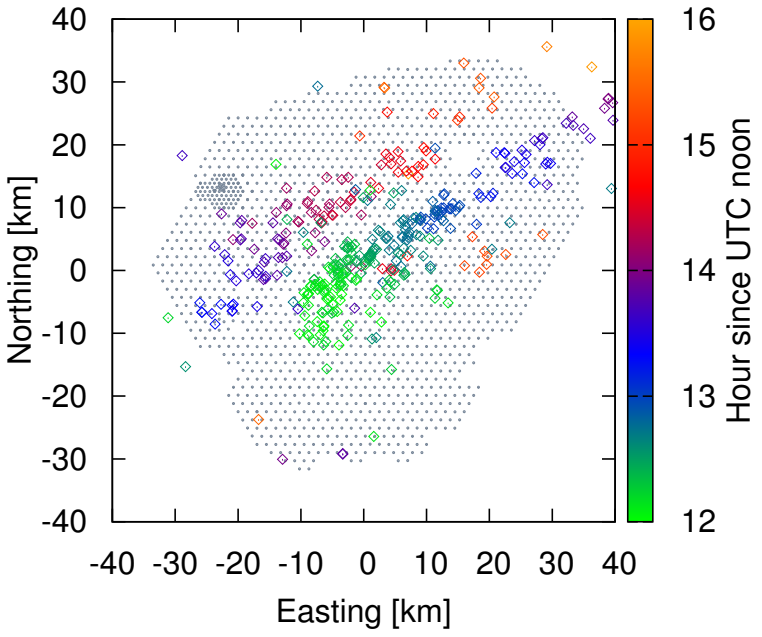

FIGURE 6.29: Position and time of events recorded by the StormTracker lightning detectors [278] for period of the strong average scaler rate variability from the midnight UTC to 4 UTC of December 31, 2015.

Therefore, we have applied the analyses to seven "thunderstorm-free" sub-arrays of the regular SD array. The location of these sub-arrays and the corresponding average scaler rate variability as a function of time are shown in Fig. 6.30.

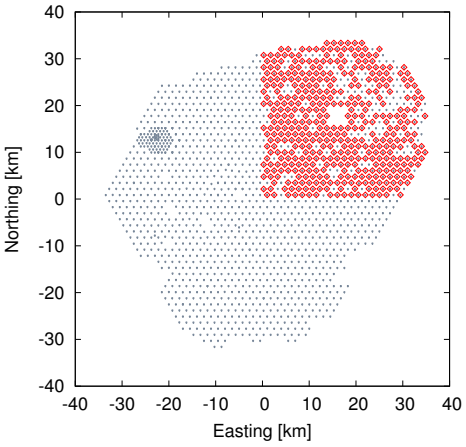
Northing [km]
Easting [km]
40
30
20
10
0
-10
-20
-30
-40

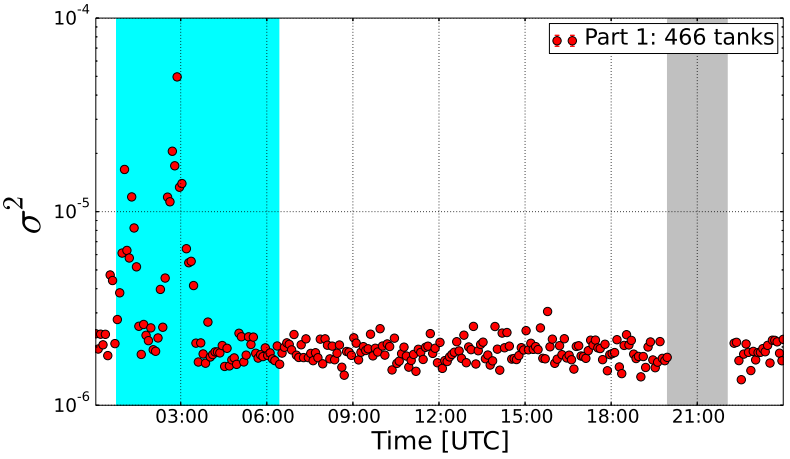
Part 1: 466 tanks
σ^2
10^{-4}
10^{-5}
10^{-6}
03:00
06:00
09:00
12:00
15:00
18:00
21:00
Time [UTC]

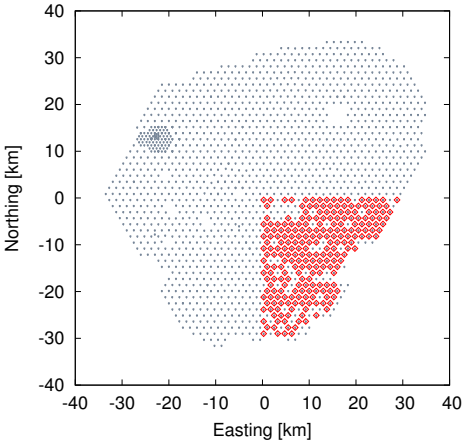
Northing [km]
Easting [km]
40
30
20
10
0
-10
-20
-30
-40

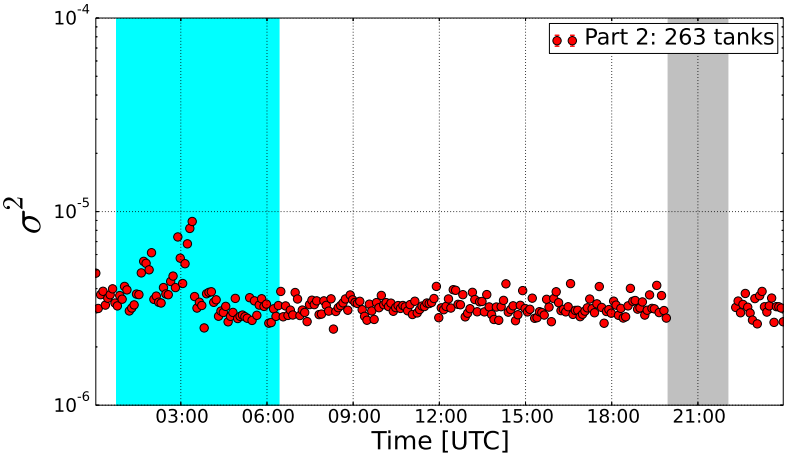
Part 2: 263 tanks
σ^2
10^{-4}
10^{-5}
10^{-6}
03:00
06:00
09:00
12:00
15:00
18:00
21:00
Time [UTC]

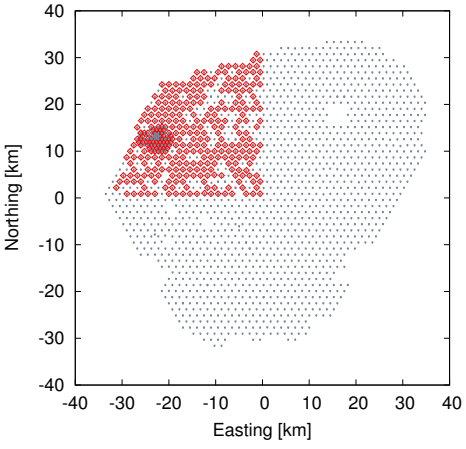
Northing [km]
Easting [km]
40
30
20
10
0
-10
-20
-30
-40

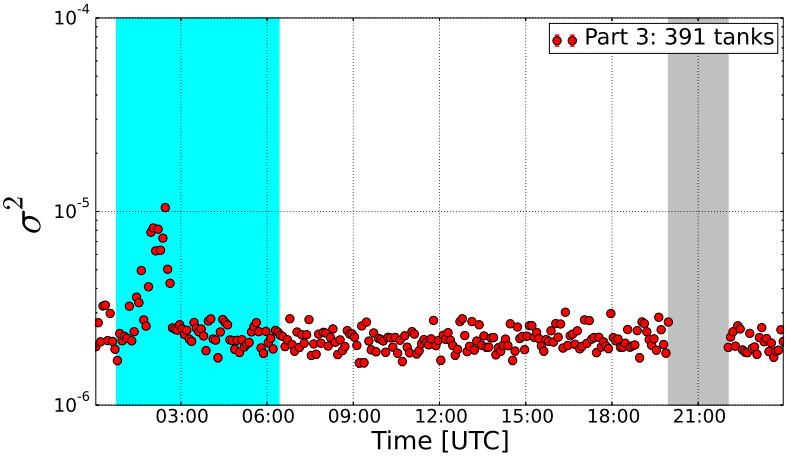
Part 3: 391 tanks
σ^2
10^{-4}
10^{-5}
10^{-6}
03:00
06:00
09:00
12:00
15:00
18:00
21:00
Time [UTC]

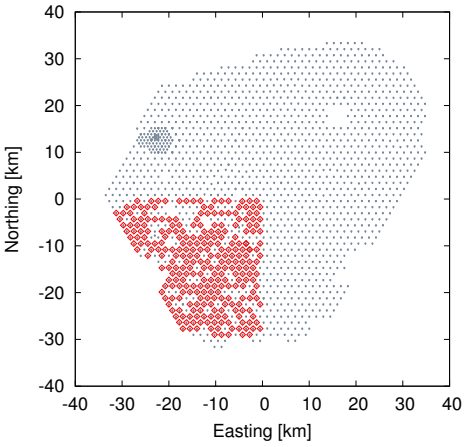
Northing [km]
Easting [km]
40
30
20
10
0
-10
-20
-30
-40

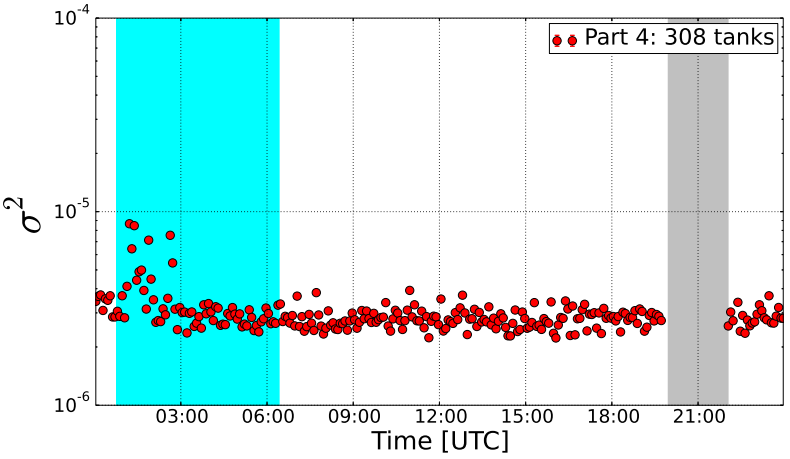
Part 4: 308 tanks
σ^2
10^{-4}
10^{-5}
10^{-6}
03:00
06:00
09:00
12:00
15:00
18:00
21:00
Time [UTC]

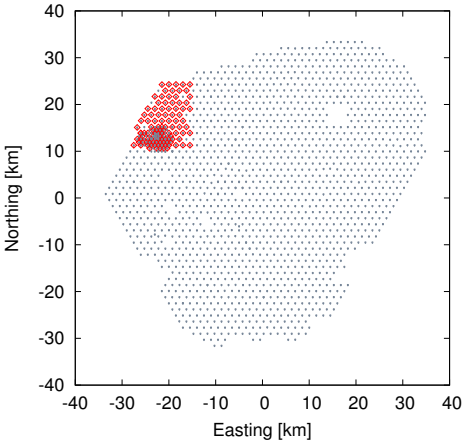
Northing [km]
Easting [km]
40
30
20
10
0
-10
-20
-30
-40

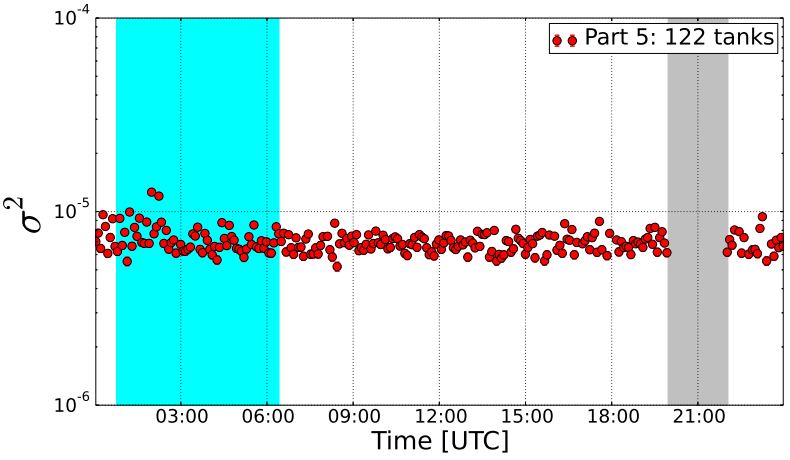
Part 5: 122 tanks
σ^2
10^{-4}
10^{-5}
10^{-6}
03:00
06:00
09:00
12:00
15:00
18:00
21:00
Time [UTC]

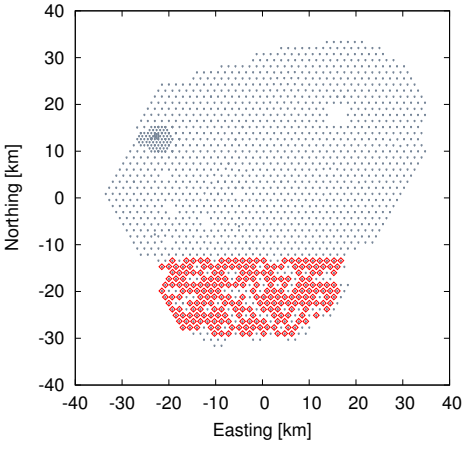
Northing [km]
Easting [km]
40
30
20
10
0
-10
-20
-30
-40

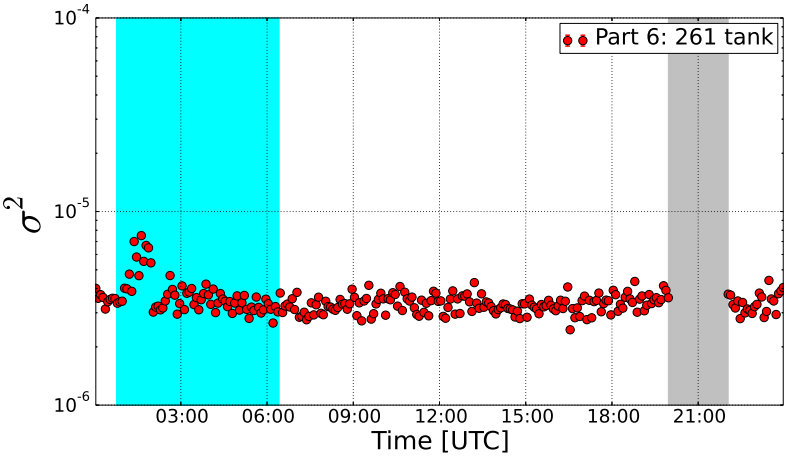
Part 6: 261 tank
σ^2
10^{-4}
10^{-5}
10^{-6}
03:00
06:00
09:00
12:00
15:00
18:00
21:00
Time [UTC]

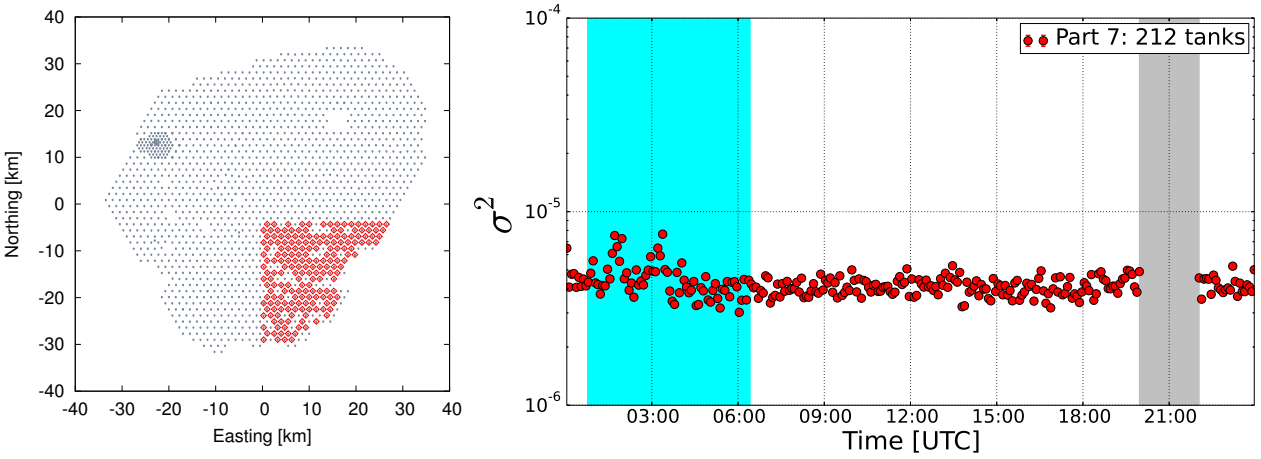

FIGURE 6.30: Using information from the lightning detectors, seven sub-arrays free from thunderstorms at the time interval of the strong average scaler rate variability on December 31, 2015 have been selected. *left column*: maps of diamond symbols indicate the locations of the Auger surface detectors of high quality data. *right column*: Average scaler rate variability as a function of time for each sub-array. The vertical cyan bands refer to strong excess variance in the average scaler rate in all sub-arrays, when the Crab nebula was flaring with elevation $> 20^{\circ}$ at the Pierre Auger site. The lighting contribution is visible in most of variability plots as small excess variance, within the UTC time interval $[0h, 1h]$. Such contribution is from the thunderstorm that occurred in the center of the array at beginning of that night (indicated by green color in Fig. 6.29). The gray bands denote period excluded from the analysis due to lightning-induced signals in the detectors, listed in Tab. A.23.

Figure 6.30 shows the average scaler rate variability detected in different parts of the array. Part 1 part 3, and Part 7 of the array revealed two maxima in the variability amplitude, separated in time by $\sim$1.5 hr interval. The variability pattern was found to depend on the sub-array location, as the two-peak structure, particularly, in the sub-arrays in the eastern part of the SD array. The time pattern of the average scaler rate variability observed on that date of December 31, 2015 resembles the results obtained by several other experiments during the outburst of very-high energy events from the Crab direction on February 23, 1989, which also consisted of several sequential maxima (discussed in § 5.4).

6.2 Correlation with the *Fermi*-LAT Crab γ-ray flux

We investigate the correlation between the significance of the observed excesses by Auger low-energy scaler mode and the Crab γ-ray flux measured by the *Fermi*-LAT, during 5 out of 7 strongest Crab γ-ray flares. The significance correlation is shown in Fig. 6.31.

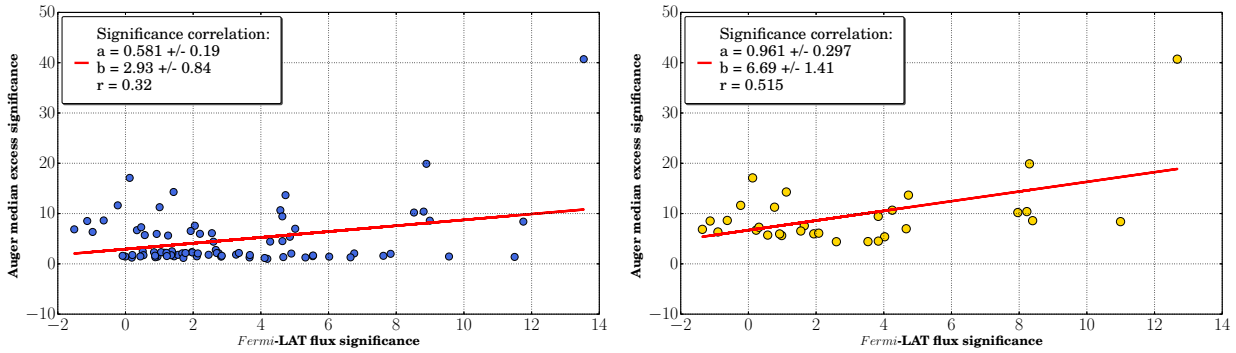

FIGURE 6.31: *Left panel*: Significance correlation between *Fermi*-LAT γ-ray flux of the Crab nebula and pulsar during the total interval of the γ-ray flares, with a linear coefficient $a = 0.581$ and Pearson correlation coefficient $r = 0.32$. *Right panel*: Significance correlation between Auger excess variance observed in average scaler rate and the corresponding *Fermi*-LAT γ-ray flux of the Crab nebula and pulsar, during the episodes of γ-ray flares, with a linear coefficient $a = 0.961$ and Pearson correlation coefficient $r = 0.515$. A correlation is found between both datasets taken during 5 major Crab γ-ray flares.

The significant excesses of both dataset are resulted from normal distributions, which are shown in Appendix D. The *Fermi*-LAT flaring flux significance is specified based on the yearly distribution of the Crab nebula and pulsar flux (see Fig. D.6). The significance correlation is studied for the data taken during 5 Crab γ-ray flares, which occurred in September 2010, March 2013, March 2014, August 2014, and December 2015. A significance of a median value of the 5-minute intervals observed in Auger average scaler rate is calculated per a date, and the corresponding significance in *Fermi*-LAT data is specified as well.

On a minute timescale, we have observed **266** 5-minute intervals of significant excesses in average scaler rate variability from the years 2006 to 2015. The transit time of the Crab nebula and pulsar at Auger sky is ∼6 hr, i.e., 1/4 of a day. A statistical test is prerequisite, in order to calculate the probability (*P*-value) that an excess is detected by chance during those 6 hours. The observed significant excesses in average scaler rate variability from the years 2006 to 2015 are presented in Tab. 6.8.

Crab γ-ray flare	Significance during flare episodes	Significance outside flare episodes	Total
Compatible	90	64	154
Non Compatible	37	75	112
Total	127	139	266

TABLE 6.8: Observed significant excesses in average scaler rate variability from 2006 to 2015. The total number of the observed excesses is 266 5-minute intervals detected over 76 dates from 2006 to 2015.

In Tab. 6.8, the total number of observed excess variance is divided into two main categories with $n = 2$ classes: category (a) significance during the γ-ray flare episodes; category (b) significance outside the γ-ray flare episodes; class (a) compatible excess variance with the flare; class (b) non

compatible excess variance with the flare. These categories and classes are based on the official episodes of the Crab γ-ray flares observed by the *Fermi*-LAT. Under the assumption that no association between the observed excesses and the Crab γ-ray flare, the expected numbers of significant excess variance is shown in Tab. 6.9.

Crab γ-ray flare	Significance during flare episodes	Significance outside flare episodes	Total
Compatible	73.5	80.5	154
Non Compatible	53.5	58.5	112
Total	127	139	266

TABLE 6.9: Expected numbers of significant excesses in average scaler rate variability.

We notice that the difference between the observed significance and expected is relatively big. The chi-square statistical test is given by

$$\chi^2_{df} = \sum_i \frac{(O_i - E_i)^2}{E_i}, \tag{6.1}$$

where the subscript df is the degree of freedom. O_i and E_i are the observed and expected values (see Tabs. 6.8 and 6.9) of the significance average scaler rate variability, respectively. The χ^2_1 value is 16.8 with degree of freedom $df = 1$. The corresponding P-value is $<$0.0001. This result is significant at $P < 0.05$ probability level. Therefore, we reject the null hypothesis. Namely, there is a strong association between the significant excess variance observed in Auger average scaler rate and the Crab γ-ray flares, as the probability to find such excesses by chance is very small (P_{chance} $<$0.0001).

The performed analysis on a minute timescale led to **266** 5-minute interval of significant excess variance in the average scaler rate (see excess catalog in A.2). About 2/3 of the observed excesses are Crab-compatible, i.e., occurred when the Crab was above horizon ($>20^\circ$ elevation) at the Pierre Auger observatory site. The comparison of the Auger average scaler rate excess variability to corresponding significance of *Fermi*-LAT daily light curves of the Crab nebula and pulsar shows a good correlation during 5 out of 7 strongest Crab γ-ray flares. Namely, during the HE γ-ray flares observed by the *Fermi*-LAT in September 2010, March 2013, March 2014, August 2014, and December 2015. A weak correlation is found between both datasets during October 2013 flare. Only one episode of strong excess variability coincides with significant Crab γ-ray flux measured by the *Fermi*-LAT outside the official duration of the flare. No exceptional flares have been observed from the Crab nebula and pulsar in the years 2008-2009, as well as the first half of 2015 and 2016. This is in agreement with Auger SD scalers variability, which hasn't revealed significant excesses relevant to the Crab in these time intervals. No significant excesses are found during October 2007,

February 2009, April 2011, and July 2012 Crab γ-ray flares. This backs to several factors, such as primary photon energy, spectrum, detector sensitivity, SD array stabilities, and weather conditions.

Interestingly, we see strong Crab-compatible excess variability on few dates before and after the official episodes of the Crab γ-ray flares, as seen by the *Fermi*-LAT. Such behavior is observed during April 2011, July 2012, March 2013, October 2013, August, 2014, and December 2015. This could be interpreted as a possible link between the plausible radiation scenarios of **HE** (synchrotron) and **VHE** (curvature and IC scattering) emissions in the Crab nebula and pulsar. Table 6.10 summarizes all excess variance observed in the average scaler rate from 2006 to 2015.

Crab-compatible and correlated with the flare	Crab-compatible but not correlated with the flare	Non-Crab compatible	Total	*P*-value
90	64	112	266	<0.0001

TABLE 6.10: All observed excesses and the *P*-value. The total number of the observed excesses is 266 5-minute intervals detected over 76 dates from 2006 to 2015. The probability of observing such excesses by chance is quite small <0.0001.

Auger SD low-energy scaler mode is capable of detecting the very-high energy γ-ray photons from the Crab nebula and pulsar and other TeV γ-ray emitters. The scaler mode seems to be a strong competitor in the VHE γ-ray astronomy and astrophysical variability studies.

Conclusions and Prospects

This thesis contributes to a search for the astrophysical very-high energy (VHE; $\geq$30 GeV) γ-ray emission using the Pierre Auger Observatory low-energy scaler mode. This mode, also known as the single particle technique, consists in counting the cosmic-ray (CR) particles depositing energy in excess of $\sim$15 MeV, and below $\sim$100 MeV in each individual water Cherenkov detector (WCD), which results in high total rate of $\sim$3 MHz per Auger Surface Detector (SD) array. This technique has been successfully exploited by the Auger Collaboration for the space weather and space climate studies, via measurements of the solar modulations of the Galactic cosmic ray flux at the weekly (Forbush decreases) and yearly (solar cycle) timescales. In the present work, the Auger scaler dataset from ten years (2006-2015) has been analyzed to search for variability of astrophysical origin at the short (one second) and intermediate (minutes) timescales, via probing statistically significant excesses of the average scaler rate above the regular CR background. The second-timescale variability is expected e.g. during the prompt emission phase of bright γ-ray bursts (GRB), while the minute-timescale is suitable for studies of the variability of astrophysical sources emitting γ-rays in the multi-TeV energy range, both in Galaxy (e.g. Galactic transient sources) and beyond (e.g. active galactic nuclei (AGN) during a flaring state).

A clean data sample has been selected after applying the standard data quality cuts. Namely, the detectors with abnormal rates or signal shape (monitored via the signal Area over Peak (AoP) values) have been excluded, as well as the acquisition periods with lightning/strong wind or considerably smaller number of working detectors due to e.g. connectivity problems. Furthermore, the corrections for the long-term evolution of the SD array response (examined via the AoP values of individual detectors) and for the influence of atmospheric pressure have been applied to the dataset.

On the **minute-timescale**, our analysis has revealed numerous episodes of strong Auger scaler rate variability. The majority ($\sim$2/3) of the observed variability excesses occurred at the sidereal times around the transit time of the Crab nebula at the Pierre Auger Observatory sky. Remarkably, during seven major Crab nebula γ-ray flares detected by *Fermi*-LAT and AGILE satellite detectors in the years 2010-2015 at high energies (HE; $\geq$100 MeV), there have been found five such *Crab-compatible* episodes of strong scaler rate variability in a good time correlation with the enhanced

HE γ-ray emission of the Crab as seen by the satellite detectors. In addition, if the Crab nebula origin is assumed, both the zenith angle distribution, and the dependence "excess amplitude-zenith angle" for the correlated excesses have a shape typical for atmospheric absorption effects on air showers.

The obtained results are consistent with an assumption that an additional sub-PeV γ-ray flux component originates from the Crab during periods of enhanced high-energy γ-ray emission. The presented results of shower and detector simulations allow to conclude that the energy of the sub-PeV photons, which contributed to the observed excesses of secondary particles counted by the Auger scalers, exceeds 30 TeV. Interestingly, the remaining ($\sim$1/3) scaler rate variability excesses correspond to the sidereal times of the inner Galaxy and may unveil some of the so-called Galactic PeVatrons, presumably young supernova remnants, possibly in association with molecular clouds or other dense environments.

On the **second-timescale**, no significant excess in the average scaler rate correlating with GRB prompt emission has been found. The majority (77 out of 79) of the detected excesses correspond to the exceptionally strong scaler outburst of December 31, 2015, which in turn correlates with the highest daily Crab γ-ray flux observed by *Fermi*-LAT in 2015.

It is interesting to note that during the previous Crab flares, the Auger scaler rate has shown only the minute-timescale variability. This may be related to the particularly strong and long lasting character of the scaler rate variability detected on the last date of the year 2015, which has been observed at the second-timescale as well.

To summarize, in the presented doctoral work the supposed utility of the "single particle technique" for the studies of transient astrophysical phenomena has been for the first time confirmed experimentally, via observations of the strong Auger scaler rate variability, correlated with the high-energy γ-ray flares of the Crab nebula, which have been detected in the years 2010-2015 by *Fermi*-LAT and AGILE satellite instruments.

Future prospects

We propose the following methods in order to confirm the Crab origin of the observed excesses in the Auger scaler rate variability:

- A densely placed infill array should allow a detection of VHE γ-rays from the Crab by a few neighbor tanks, and make it possible a proper reconstruction of the arrival direction. Due to

the denser tank deployment, the infill array will also be fully efficient starting from lower energies, at which the VHE γ-ray flux is higher.

- A study of the charge spectrum using calibration histograms could bring constraints on the composition of the primary particles detected when the scalers observe an excess, since the photon showers are expected to contain less muons.
- The most exciting Crab signature will be a detection of the Crab pulsar period in the times of T2 triggers of individual stations of the Auger Surface Detector during a future flare. The T2 time stamps have been saved since January 2016 in order to allow such periodicity studies. The analysis of the periodicity of the T2 arrival times has been implemented.

In the light of the studies presented in this doctoral work, the decision to host the CTA Southern Observatory in Chile, at the proximity of the ESO site in Paranal, opens interesting possibilities for the Pierre Auger Observatory, since CTA South will be exposed to nearly the same sky as the Auger site. A synergy between CTA large-size and mid-size telescopes and air shower arrays such as the HAWC experiment is expected in particular for studies of transient phenomena, such as GRBs and AGN flares, at energies up to a few TeV. EAS detector arrays will measure the brightest flares from hard spectrum sources and provide triggers for CTA telescopes, which will probe the VHE γ-ray spectra and light curves with higher sensitivity.

The large area of the Pierre Auger Surface Detector array, surpassing the one of all planned air shower arrays (LHASSO, HiSCORE, HAWC South), is an advantage and a necessary condition to perform a similar monitoring at higher sub-PeV energies, making also profit from the future small-size CTA telescopes in the Southern hemisphere with their improved sensitivity around 10 TeV. Such synergy between Auger and CTA Southern IACT array will certainly open a new window to the non-thermal phenomena at the PeV energy domain, which justifies additional studies of the ways to improve the Auger sensitivity to the VHE γ-ray showers.

Appendix A

Scaler rate analysis on the full SD array

A.1 Catalog of the excesses detected in the years 2006-2015 on a second time scale

GPS [s]	Date [yy/mm/dd]	UTC [hh/mm/ss]	σ	# of active detectors
909244576	2008-10-28	15:56:16	6.3	1274
909246605	2008-10-28	16:30:05	8.3	1272
1135555744	2015-12-31	00:09:04	6.2	1406
1135556254	2015-12-31	00:17:34	11.8	1406
1135556501	2015-12-31	00:21:41	7.4	1406
1135556617	2015-12-31	00:23:37	12.9	1406
1135557281	2015-12-31	00:34:41	13.4	1406
1135557547	2015-12-31	00:39:07	6.9	1406
1135558650	2015-12-31	00:57:30	7.3	1406
1135558709	2015-12-31	00:58:29	6.6	1406
1135558828	2015-12-31	01:00:28	32.0	1402
1135558941	2015-12-31	01:02:21	7.7	1404
1135559051	2015-12-31	01:04:11	17.3	1406
1135559118	2015-12-31	01:05:18	7.9	1406
1135559414	2015-12-31	01:10:14	7.6	1405
1135559904	2015-12-31	01:18:24	13.2	1406
1135559929	2015-12-31	01:18:49	6.2	1406
1135560071	2015-12-31	01:21:11	12.1	1406
1135560413	2015-12-31	01:26:53	6.0	1406
1135560584	2015-12-31	01:29:44	9.2	1406
1135560934	2015-12-31	01:35:34	6.2	1402
1135561069	2015-12-31	01:37:49	6.3	1404
1135562313	2015-12-31	01:58:33	22.2	1405
1135562452	2015-12-31	02:00:52	6.9	1406
1135562468	2015-12-31	02:01:08	9.1	1406
1135562561	2015-12-31	02:02:41	7.2	1406
1135562844	2015-12-31	02:07:24	6.0	1406
1135562999	2015-12-31	02:09:59	6.9	1406

Continued on next page

TABLE A.1: Significant excesses detected in average scaler rate (2006-2015) by using $\sigma - \delta$ method.

GPS [s]	Date [yy/mm/dd]	UTC [hh/mm/ss]	σ	# of active detectors
1135563058	2015-12-31	02:10:58	7.7	1406
1135563208	2015-12-31	02:13:28	13.2	1405
1135563406	2015-12-31	02:16:46	6.1	1406
1135563593	2015-12-31	02:19:53	7.8	1407
1135563918	2015-12-31	02:25:18	9.6	1406
1135564040	2015-12-31	02:27:20	13.6	1406
1135564186	2015-12-31	02:29:46	11.8	1406
1135564262	2015-12-31	02:31:02	9.1	1406
1135564299	2015-12-31	02:31:39	7.5	1406
1135564351	2015-12-31	02:32:31	7.3	1406
1135564403	2015-12-31	02:33:23	8.6	1406
1135564442	2015-12-31	02:34:02	6.9	1407
1135564488	2015-12-31	02:34:48	8.3	1406
1135564497	2015-12-31	02:34:57	11.8	1406
1135564544	2015-12-31	02:35:44	9.6	1406
1135564550	2015-12-31	02:35:50	7.5	1406
1135564661	2015-12-31	02:37:41	13.4	1406
1135564671	2015-12-31	02:37:51	8.4	1405
1135564786	2015-12-31	02:39:46	7.0	1406
1135564792	2015-12-31	02:39:52	6.0	1406
1135564818	2015-12-31	02:40:18	9.2	1406
1135564840	2015-12-31	02:40:40	6.9	1406
1135564931	2015-12-31	02:42:11	10.9	1407
1135564935	2015-12-31	02:42:15	7.4	1406
1135565012	2015-12-31	02:43:32	6.3	1406
1135565019	2015-12-31	02:43:39	8.2	1406
1135565050	2015-12-31	02:44:10	6.8	1406
1135565254	2015-12-31	02:47:34	6.1	1406
1135565325	2015-12-31	02:48:45	7.7	1406
1135565339	2015-12-31	02:48:59	8.7	1406
1135565404	2015-12-31	02:50:04	14.9	1406
1135565483	2015-12-31	02:51:23	7.1	1406
1135565529	2015-12-31	02:52:09	23.6	1406
1135565599	2015-12-31	02:53:19	6.9	1406
1135565622	2015-12-31	02:53:42	15.6	1406
1135565761	2015-12-31	02:56:01	7.8	1406
1135565771	2015-12-31	02:56:11	6.7	1406
1135565893	2015-12-31	02:58:13	9.1	1406
1135565961	2015-12-31	02:59:21	7.4	1406
1135566022	2015-12-31	03:00:22	22.6	1403
1135566068	2015-12-31	03:01:08	7.7	1404
1135566074	2015-12-31	03:01:14	6.7	1405
1135566254	2015-12-31	03:04:14	7.0	1406
1135566278	2015-12-31	03:04:38	6.4	1406
1135566288	2015-12-31	03:04:48	6.1	1406
1135566394	2015-12-31	03:06:34	6.3	1405
1135566534	2015-12-31	03:08:54	6.5	1404
1135566837	2015-12-31	03:13:57	8.4	1406
1135567275	2015-12-31	03:21:15	9.7	1406
1135567378	2015-12-31	03:22:58	7.3	1406
1135567469	2015-12-31	03:24:29	13.2	1406

TABLE A.1: Significant excesses detected in average scaler rate (2006-2015) by using $\sigma - \delta$ method.

A.2 Distributions of 75 seconds of excesses observed by the $\sigma - \delta$ method on December 31, 2015

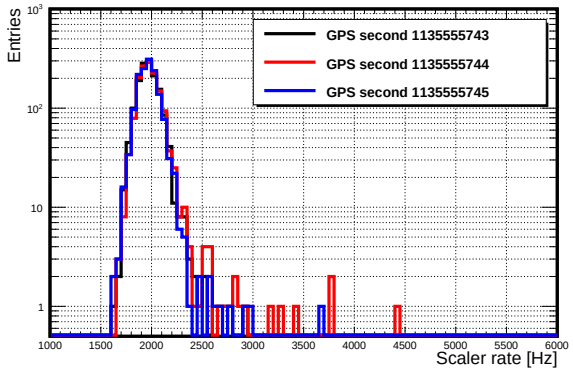

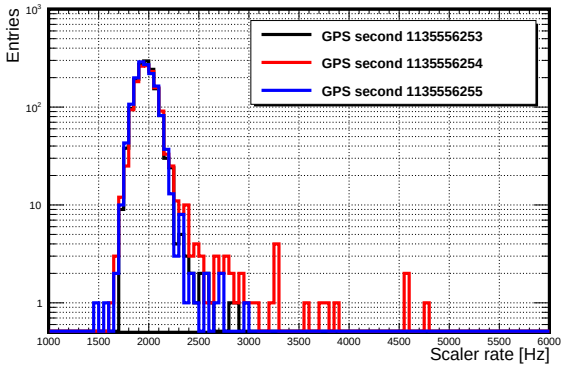

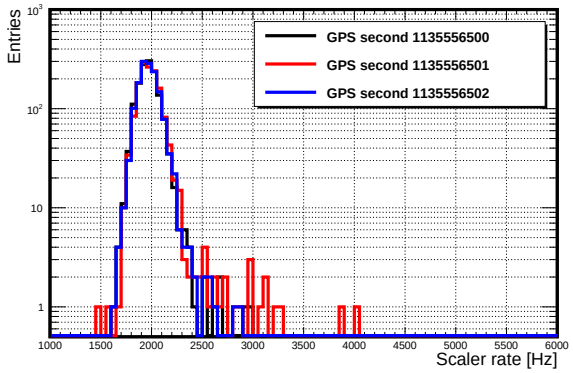

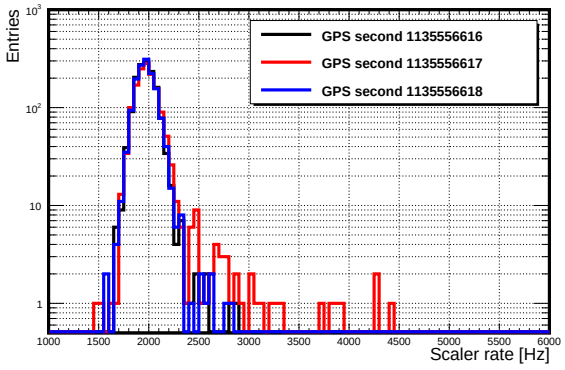

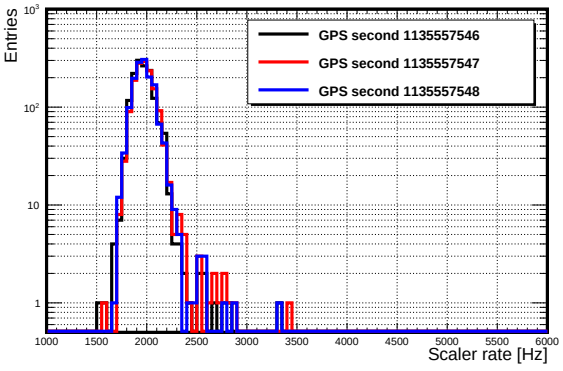

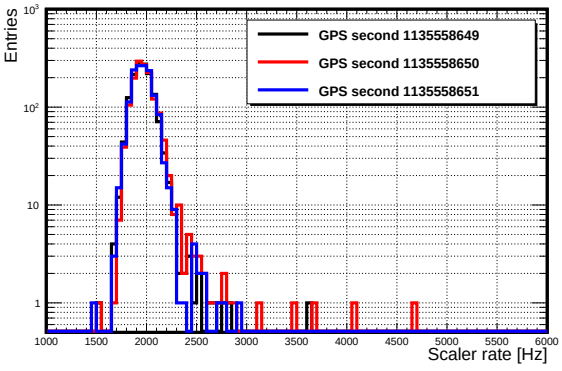

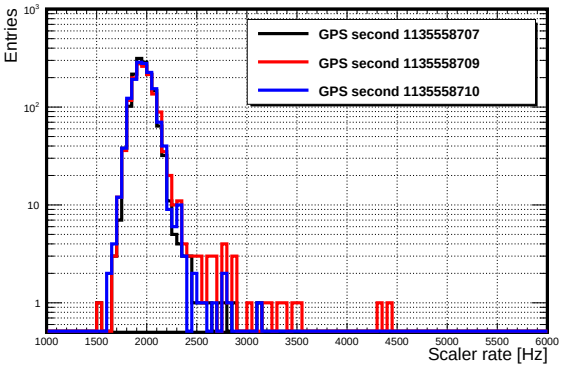
Entries
Scaler rate [Hz]
GPS second 1135558707
GPS second 1135558709
GPS second 1135558710

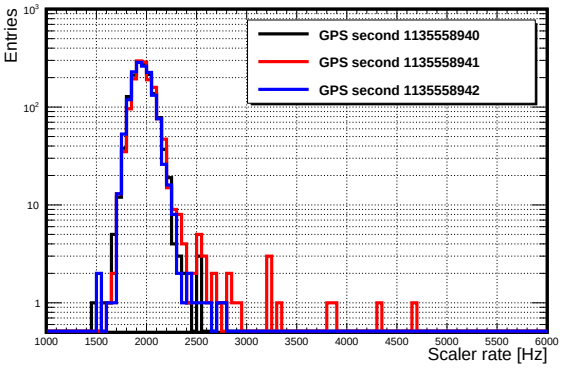
Entries
Scaler rate [Hz]
GPS second 1135558940
GPS second 1135558941
GPS second 1135558942

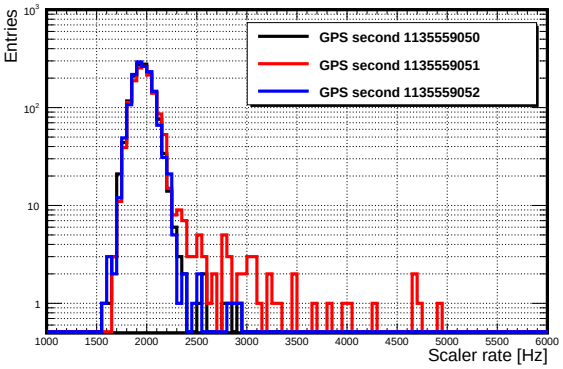
Entries
Scaler rate [Hz]
GPS second 1135559050
GPS second 1135559051
GPS second 1135559052

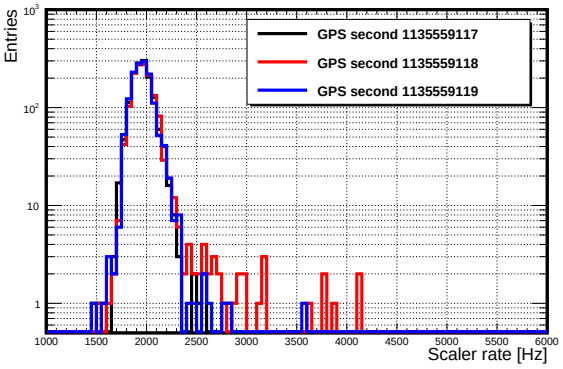
Entries
Scaler rate [Hz]
GPS second 1135559117
GPS second 1135559118
GPS second 1135559119

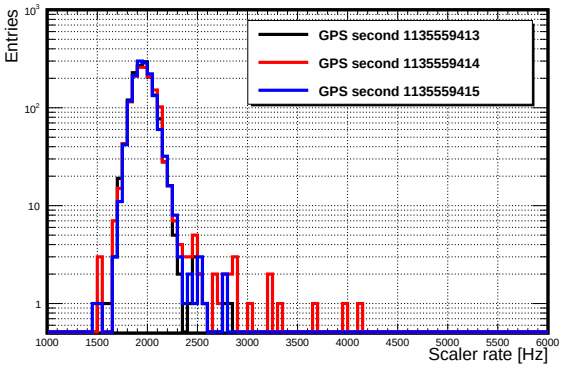
Entries
Scaler rate [Hz]
GPS second 1135559413
GPS second 1135559414
GPS second 1135559415

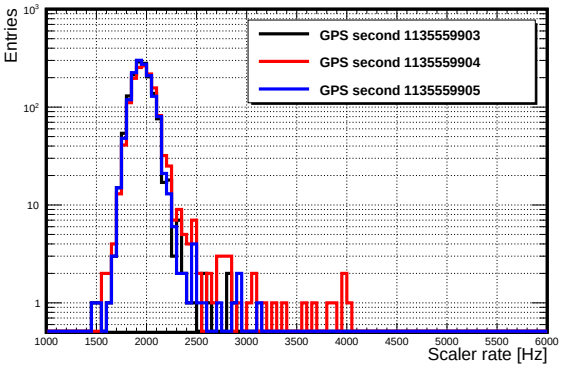
Entries
Scaler rate [Hz]
GPS second 1135559903
GPS second 1135559904
GPS second 1135559905

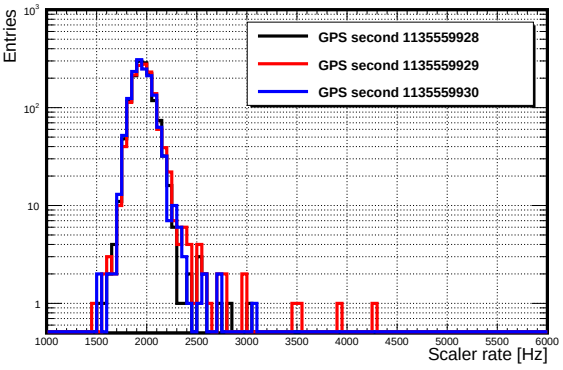
Entries
Scaler rate [Hz]
GPS second 1135559928
GPS second 1135559929
GPS second 1135559930

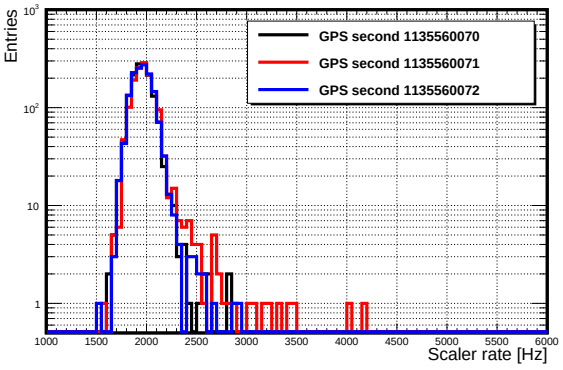
Entries
Scaler rate [Hz]
GPS second 1135560070
GPS second 1135560071
GPS second 1135560072

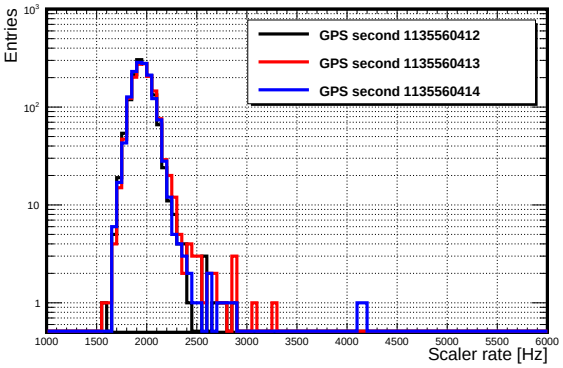
Entries
Scaler rate [Hz]
GPS second 1135560412
GPS second 1135560413
GPS second 1135560414

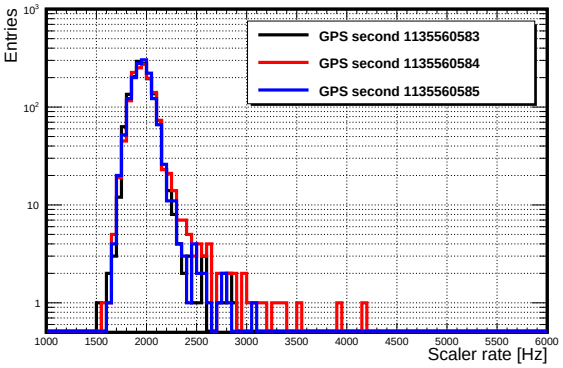
Entries
Scaler rate [Hz]
GPS second 1135560583
GPS second 1135560584
GPS second 1135560585

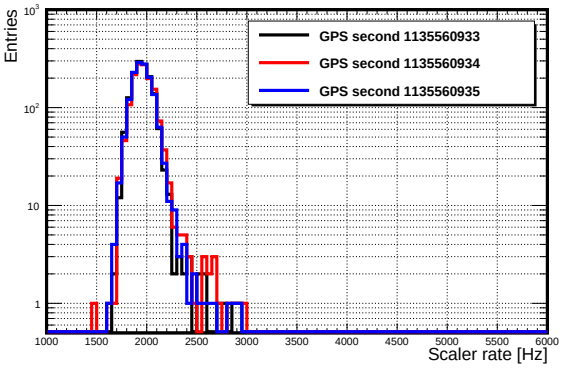
Entries
Scaler rate [Hz]
GPS second 1135560933
GPS second 1135560934
GPS second 1135560935

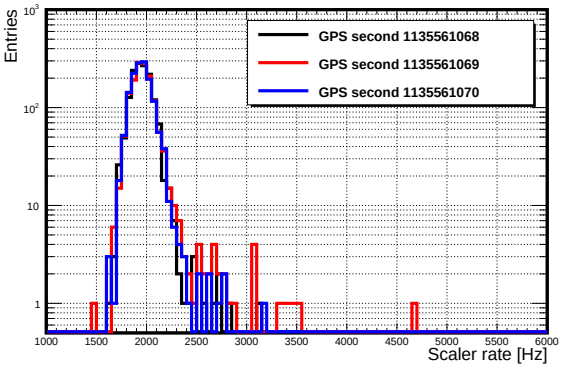
Entries
Scaler rate [Hz]
GPS second 1135561068
GPS second 1135561069
GPS second 1135561070

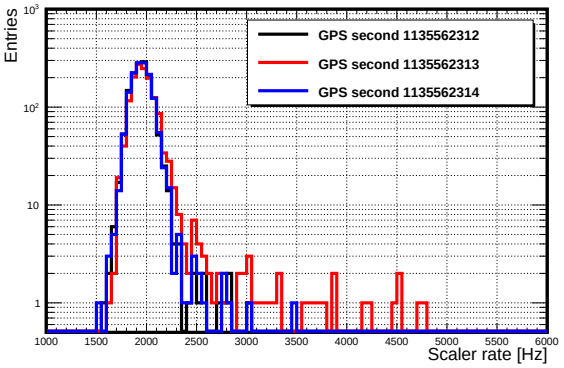
Entries
Scaler rate [Hz]
GPS second 1135562312
GPS second 1135562313
GPS second 1135562314

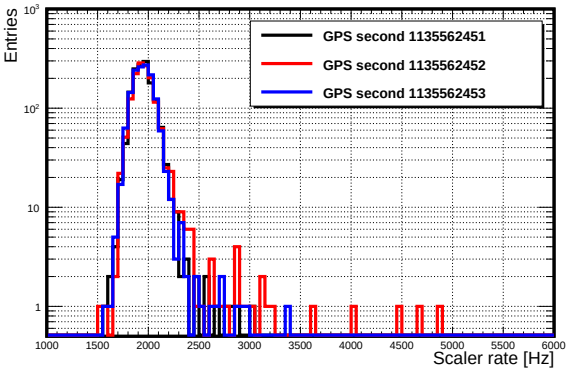
Entries
Scaler rate [Hz]
GPS second 1135562451
GPS second 1135562452
GPS second 1135562453

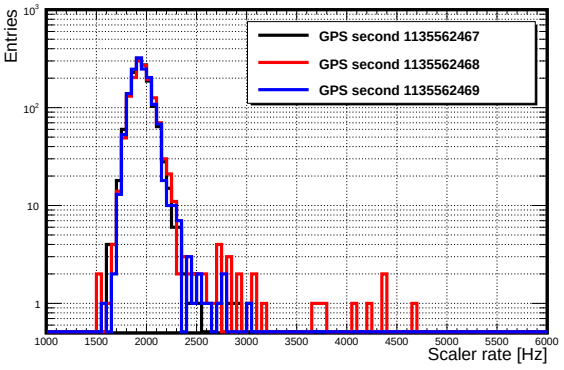
Entries
Scaler rate [Hz]
GPS second 1135562467
GPS second 1135562468
GPS second 1135562469

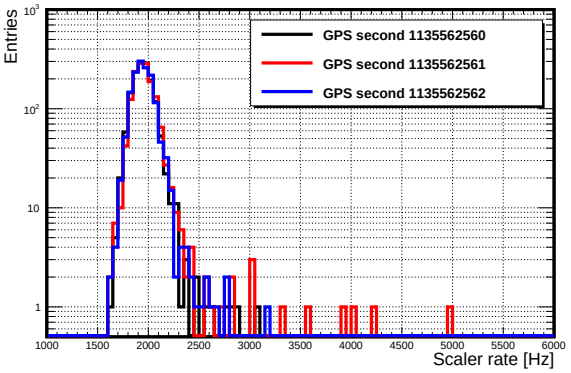
Entries
Scaler rate [Hz]
GPS second 1135562560
GPS second 1135562561
GPS second 1135562562

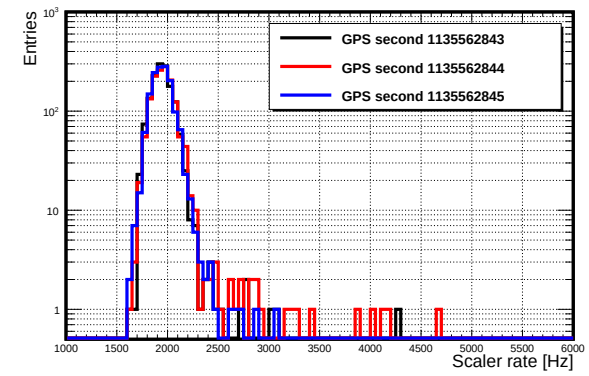
Entries
Scaler rate [Hz]
GPS second 1135562843
GPS second 1135562844
GPS second 1135562845

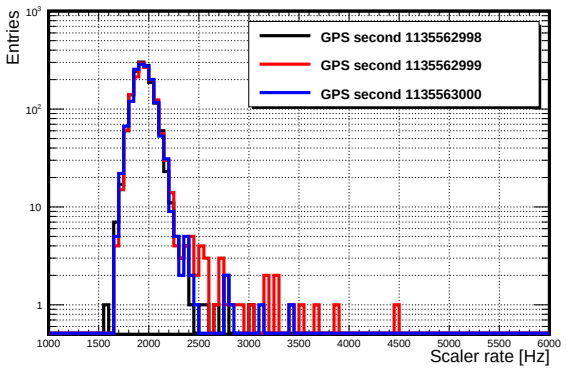
Entries
Scaler rate [Hz]
GPS second 1135562998
GPS second 1135562999
GPS second 1135563000

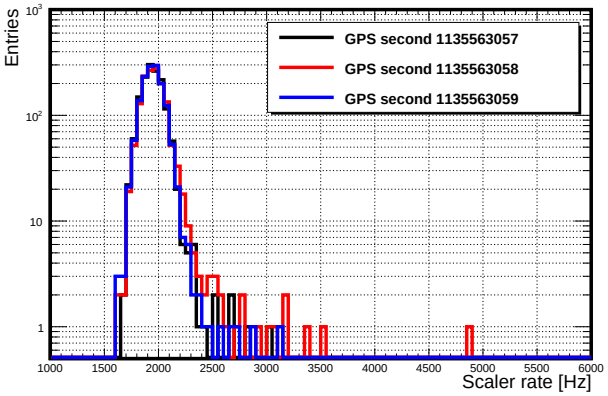
Entries
Scaler rate [Hz]
GPS second 1135563057
GPS second 1135563058
GPS second 1135563059

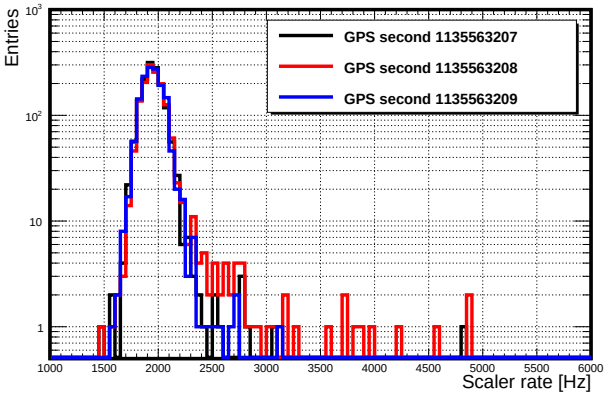
Entries
Scaler rate [Hz]
GPS second 1135563207
GPS second 1135563208
GPS second 1135563209

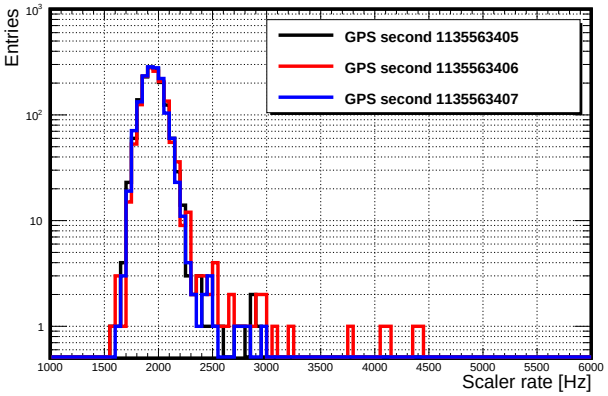
Entries
Scaler rate [Hz]
GPS second 1135563405
GPS second 1135563406
GPS second 1135563407

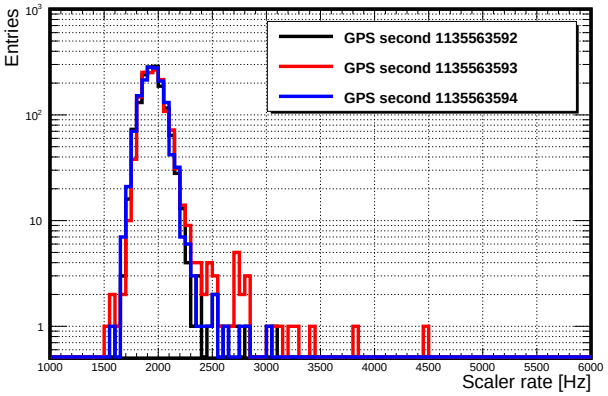
Entries
Scaler rate [Hz]
GPS second 1135563592
GPS second 1135563593
GPS second 1135563594

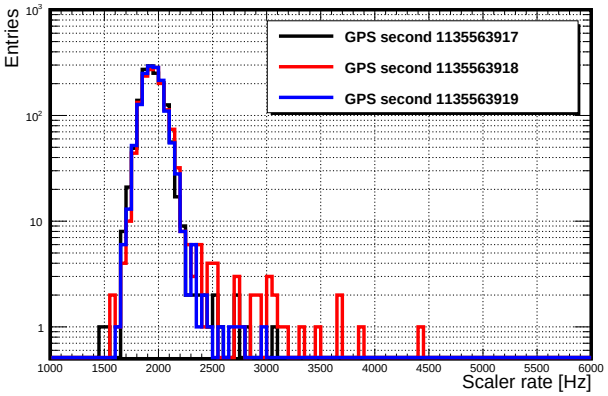
Entries
Scaler rate [Hz]
GPS second 1135563917
GPS second 1135563918
GPS second 1135563919

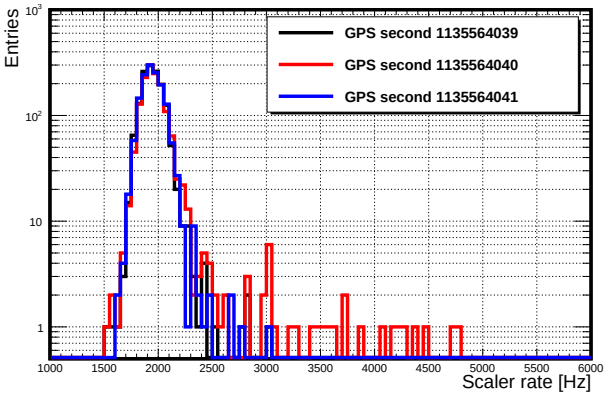
Entries
Scaler rate [Hz]
GPS second 1135564039
GPS second 1135564040
GPS second 1135564041

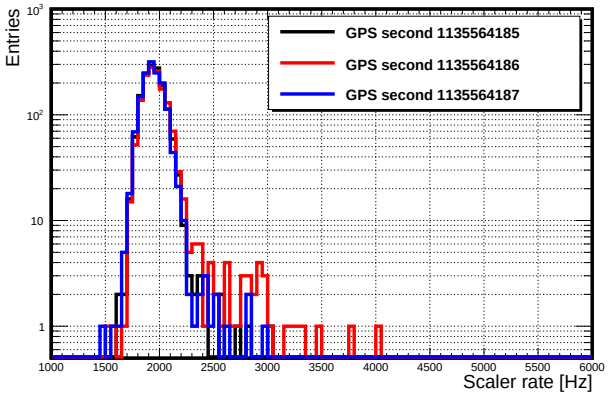
Entries
Scaler rate [Hz]
GPS second 1135564185
GPS second 1135564186
GPS second 1135564187

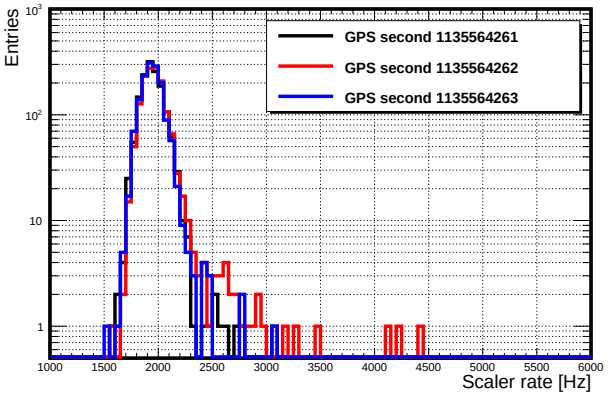
Entries
Scaler rate [Hz]
GPS second 1135564261
GPS second 1135564262
GPS second 1135564263

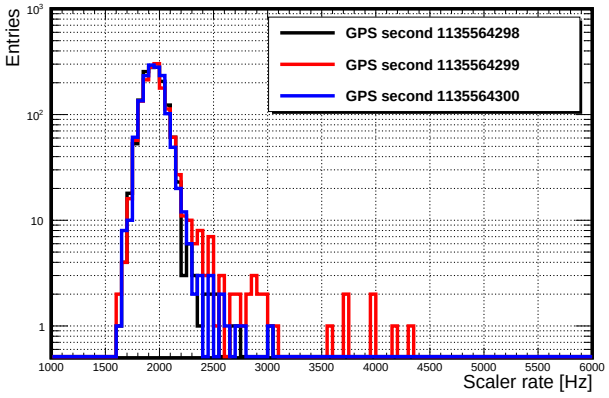
Entries
Scaler rate [Hz]
GPS second 1135564298
GPS second 1135564299
GPS second 1135564300

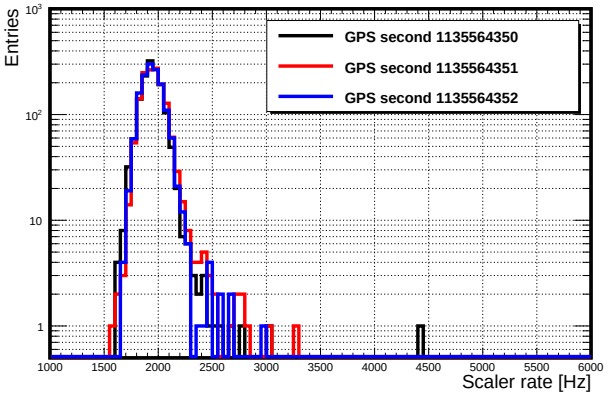
Entries
Scaler rate [Hz]
GPS second 1135564350
GPS second 1135564351
GPS second 1135564352

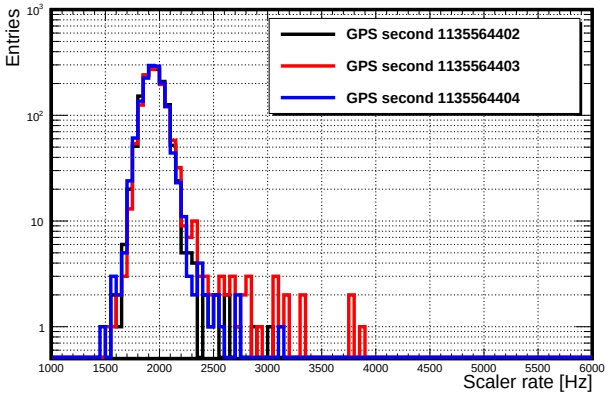
Entries
Scaler rate [Hz]
GPS second 1135564402
GPS second 1135564403
GPS second 1135564404

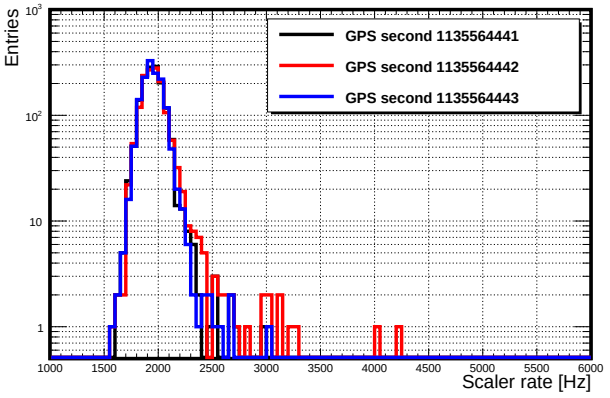
Entries
Scaler rate [Hz]
GPS second 1135564441
GPS second 1135564442
GPS second 1135564443

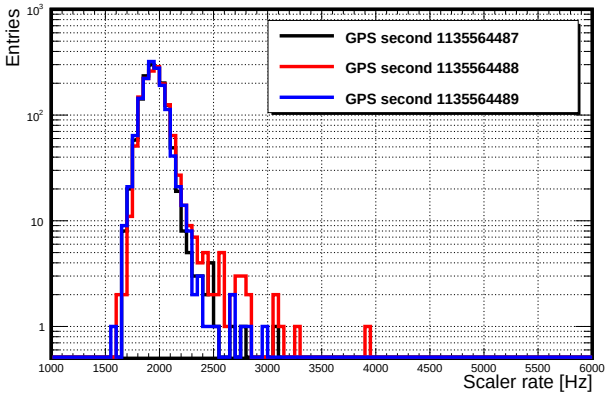
Entries
Scaler rate [Hz]
GPS second 1135564487
GPS second 1135564488
GPS second 1135564489

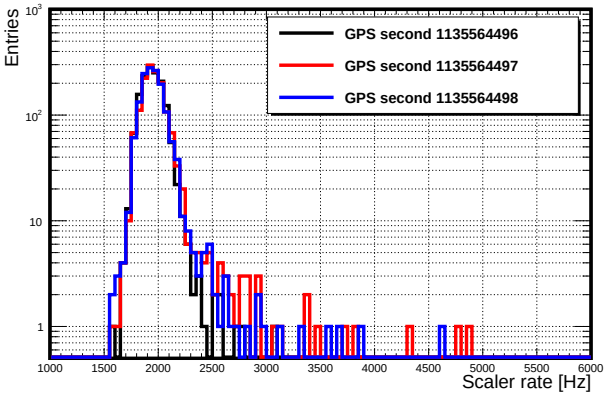
Entries
Scaler rate [Hz]
GPS second 1135564496
GPS second 1135564497
GPS second 1135564498

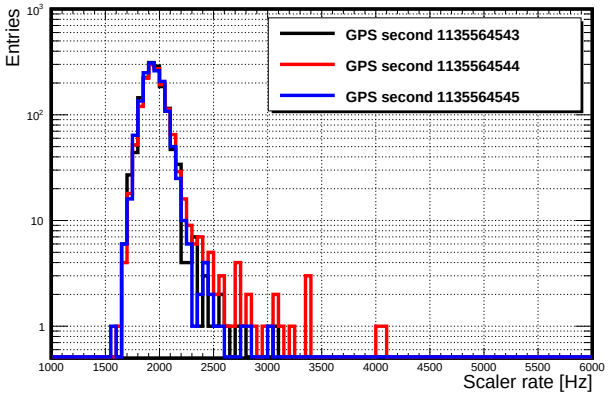
Entries
Scaler rate [Hz]
GPS second 1135564543
GPS second 1135564544
GPS second 1135564545

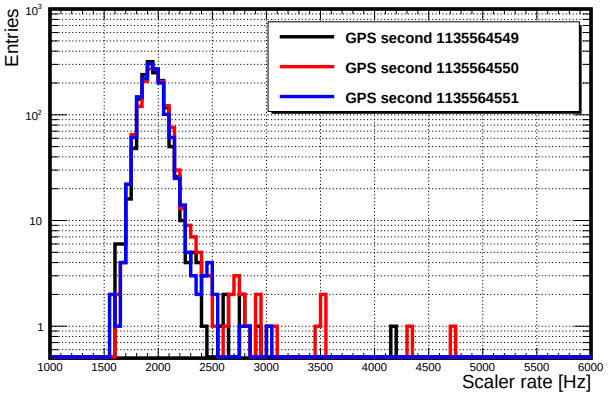
Entries
Scaler rate [Hz]
GPS second 1135564549
GPS second 1135564550
GPS second 1135564551

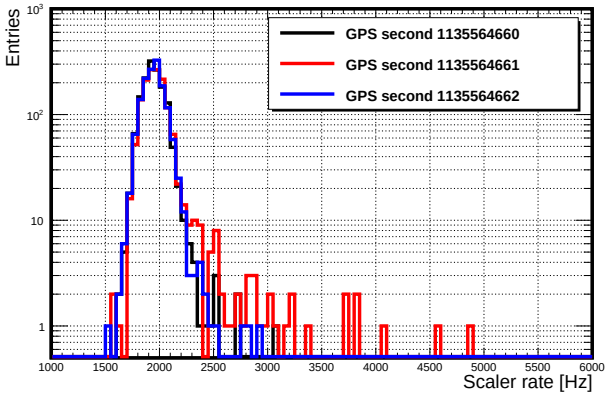
Entries
Scaler rate [Hz]
GPS second 1135564660
GPS second 1135564661
GPS second 1135564662

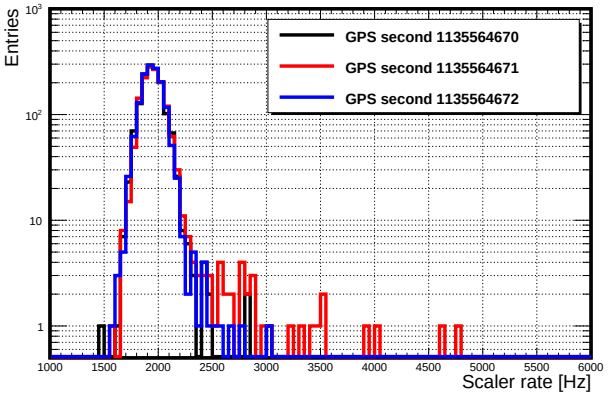
Entries
Scaler rate [Hz]
GPS second 1135564670
GPS second 1135564671
GPS second 1135564672

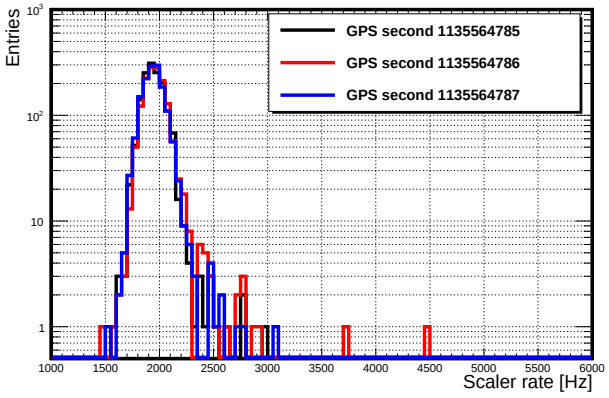
Entries
Scaler rate [Hz]
GPS second 1135564785
GPS second 1135564786
GPS second 1135564787

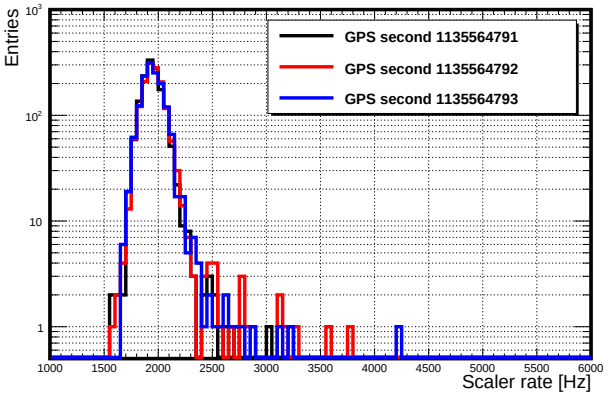
Entries
Scaler rate [Hz]
GPS second 1135564791
GPS second 1135564792
GPS second 1135564793

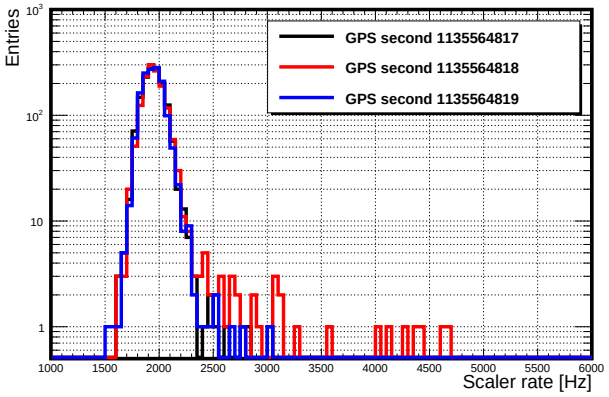
Entries
Scaler rate [Hz]
GPS second 1135564817
GPS second 1135564818
GPS second 1135564819

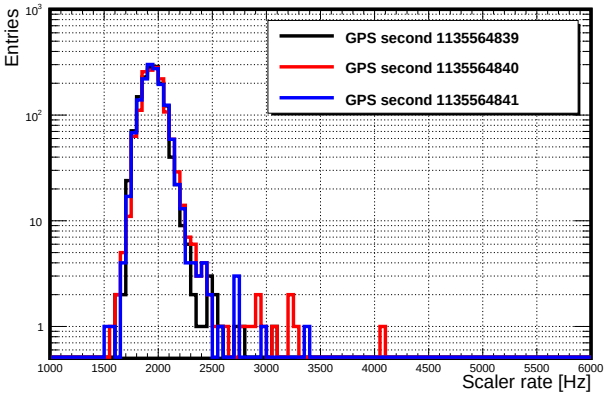
Entries
Scaler rate [Hz]
GPS second 1135564839
GPS second 1135564840
GPS second 1135564841

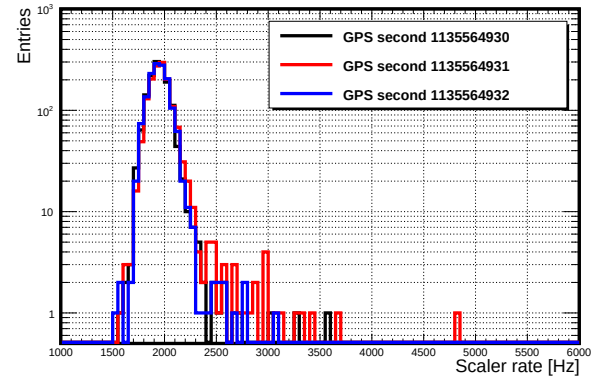
Entries
GPS second 1135564930
GPS second 1135564931
GPS second 1135564932
Scaler rate [Hz]

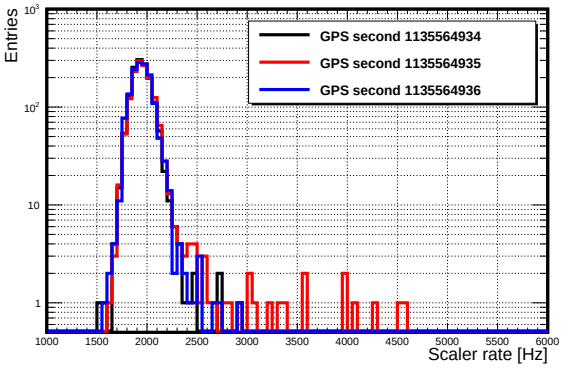
Entries
GPS second 1135564934
GPS second 1135564935
GPS second 1135564936
Scaler rate [Hz]

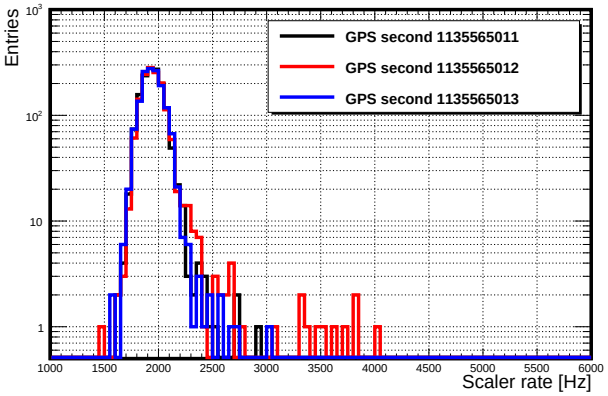
Entries
GPS second 1135565011
GPS second 1135565012
GPS second 1135565013
Scaler rate [Hz]

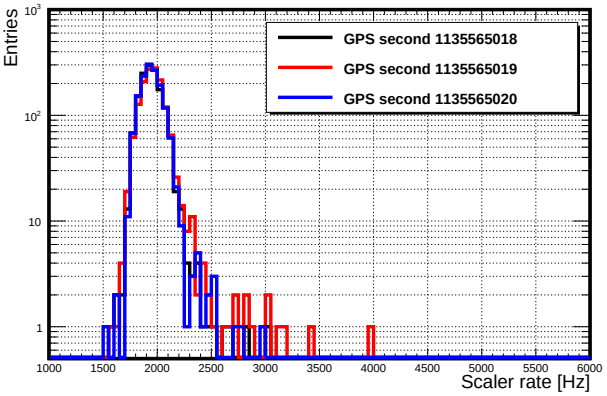
Entries
GPS second 1135565018
GPS second 1135565019
GPS second 1135565020
Scaler rate [Hz]

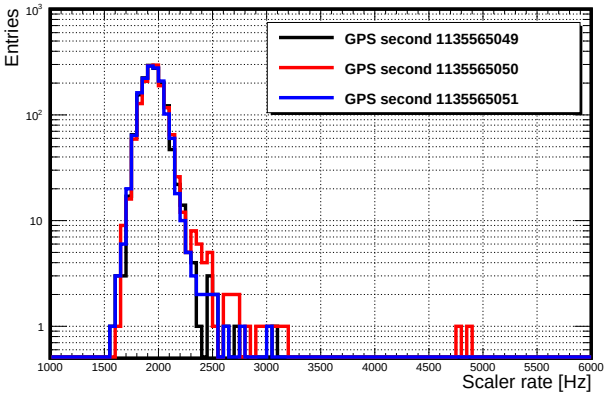
Entries
GPS second 1135565049
GPS second 1135565050
GPS second 1135565051
Scaler rate [Hz]

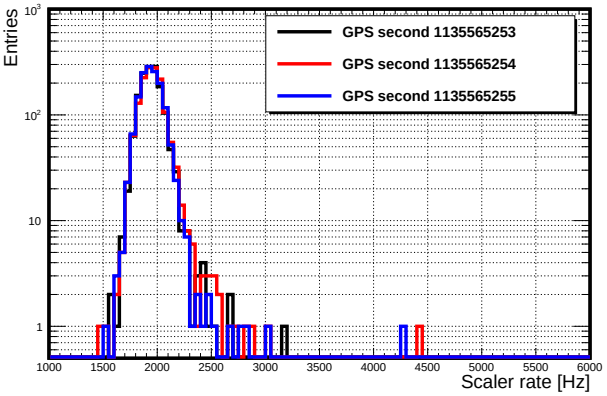
Entries
GPS second 1135565253
GPS second 1135565254
GPS second 1135565255
Scaler rate [Hz]

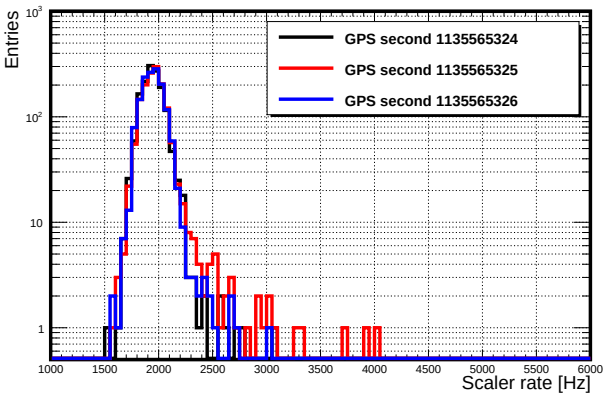
Entries
GPS second 1135565324
GPS second 1135565325
GPS second 1135565326
Scaler rate [Hz]

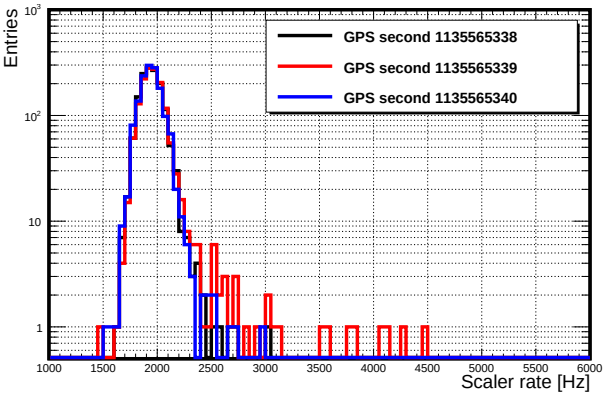
Entries
GPS second 1135565338
GPS second 1135565339
GPS second 1135565340
Scaler rate [Hz]

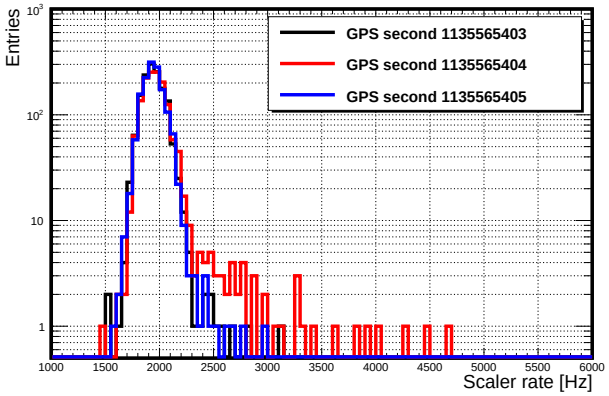
Entries
Scaler rate [Hz]
GPS second 1135565403
GPS second 1135565404
GPS second 1135565405

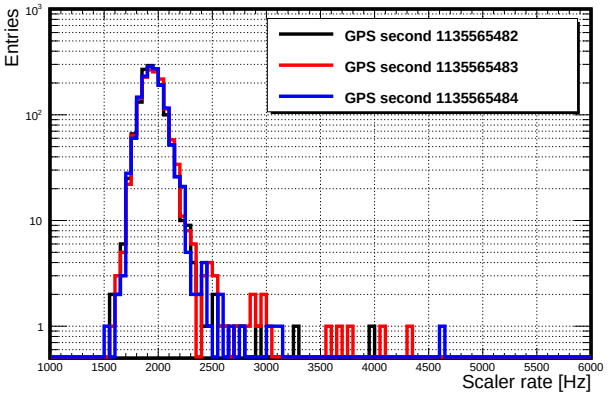
Entries
Scaler rate [Hz]
GPS second 1135565482
GPS second 1135565483
GPS second 1135565484

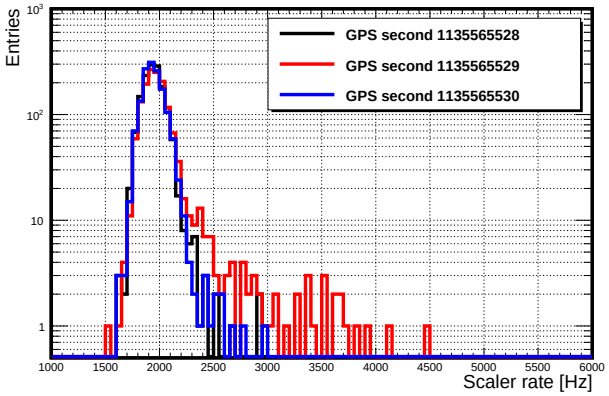
Entries
Scaler rate [Hz]
GPS second 1135565528
GPS second 1135565529
GPS second 1135565530

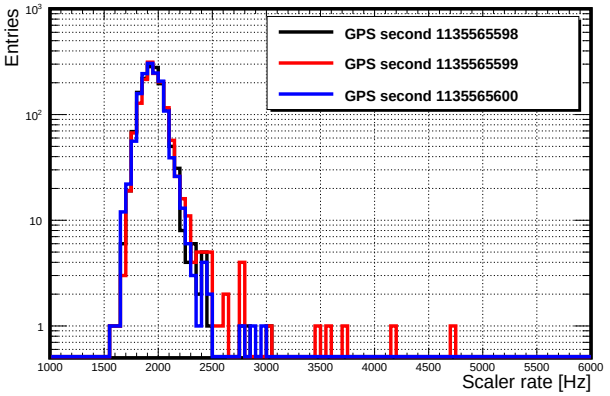
Entries
Scaler rate [Hz]
GPS second 1135565598
GPS second 1135565599
GPS second 1135565600

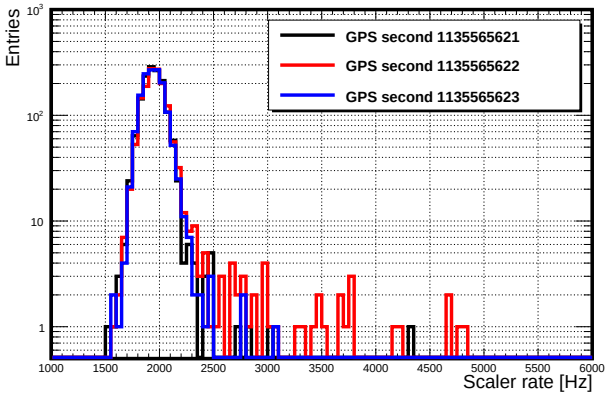
Entries
Scaler rate [Hz]
GPS second 1135565621
GPS second 1135565622
GPS second 1135565623

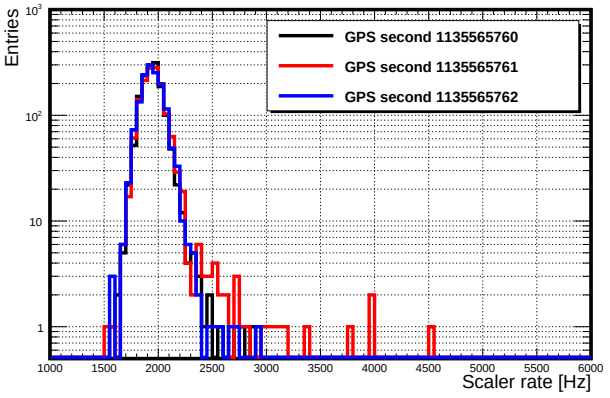
Entries
Scaler rate [Hz]
GPS second 1135565760
GPS second 1135565761
GPS second 1135565762

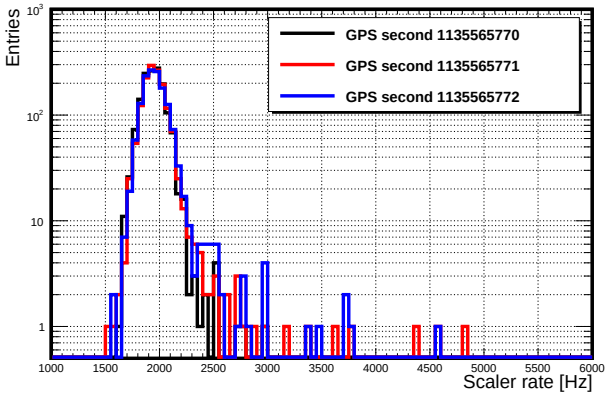
Entries
Scaler rate [Hz]
GPS second 1135565770
GPS second 1135565771
GPS second 1135565772

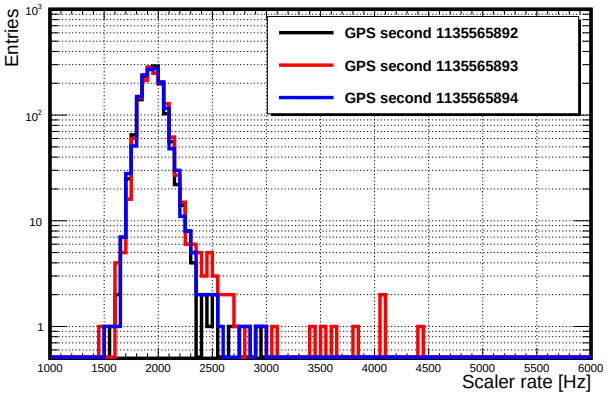
Entries
Scaler rate [Hz]
GPS second 1135565892
GPS second 1135565893
GPS second 1135565894

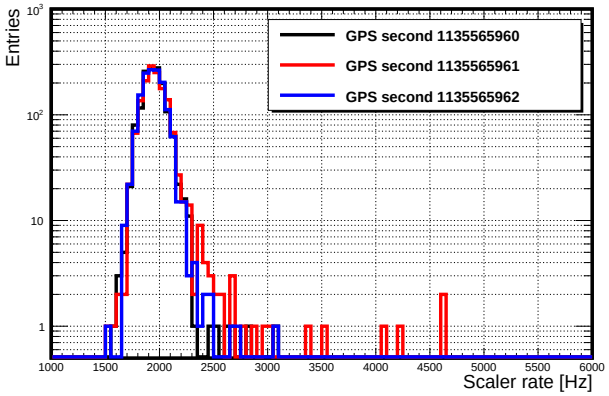
Entries
Scaler rate [Hz]
GPS second 1135565960
GPS second 1135565961
GPS second 1135565962

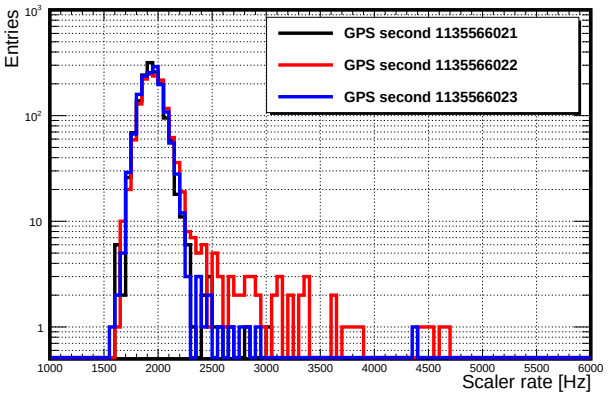
Entries
Scaler rate [Hz]
GPS second 1135566021
GPS second 1135566022
GPS second 1135566023

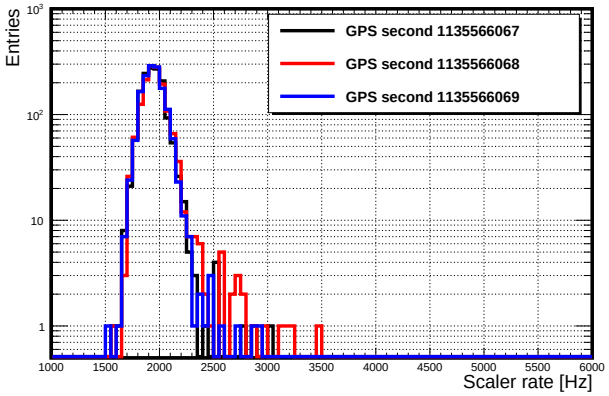
Entries
Scaler rate [Hz]
GPS second 1135566067
GPS second 1135566068
GPS second 1135566069

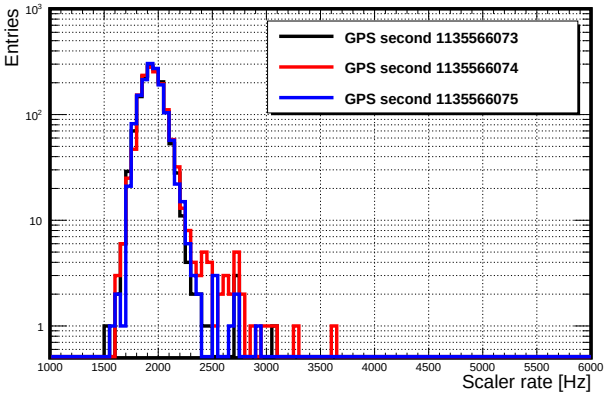
Entries
Scaler rate [Hz]
GPS second 1135566073
GPS second 1135566074
GPS second 1135566075

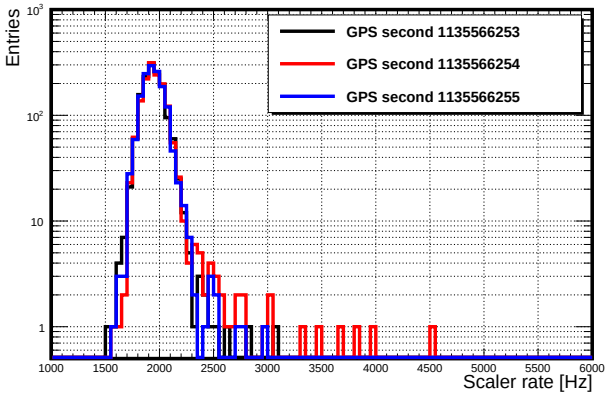
Entries
Scaler rate [Hz]
GPS second 1135566253
GPS second 1135566254
GPS second 1135566255

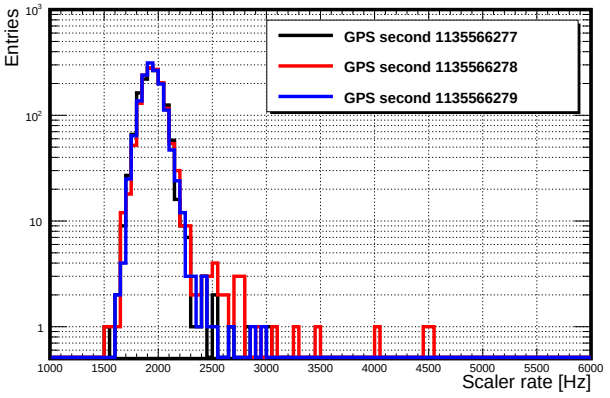
Entries
Scaler rate [Hz]
GPS second 1135566277
GPS second 1135566278
GPS second 1135566279

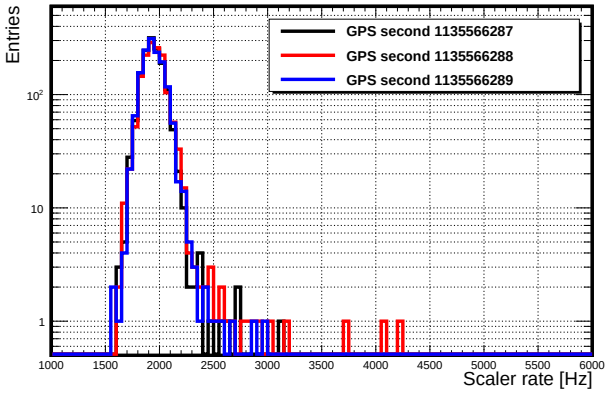
Entries
Scaler rate [Hz]
GPS second 1135566287
GPS second 1135566288
GPS second 1135566289

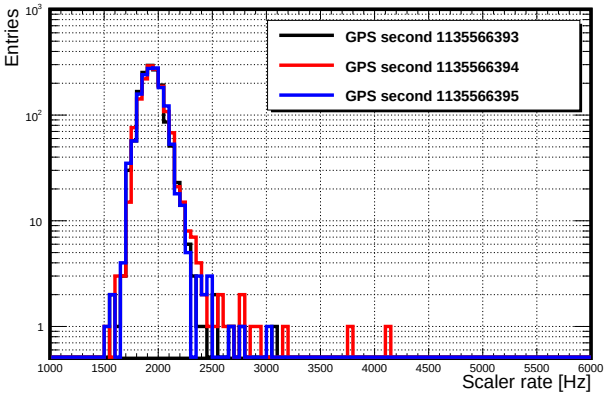
Entries
Scaler rate [Hz]
GPS second 1135566393
GPS second 1135566394
GPS second 1135566395

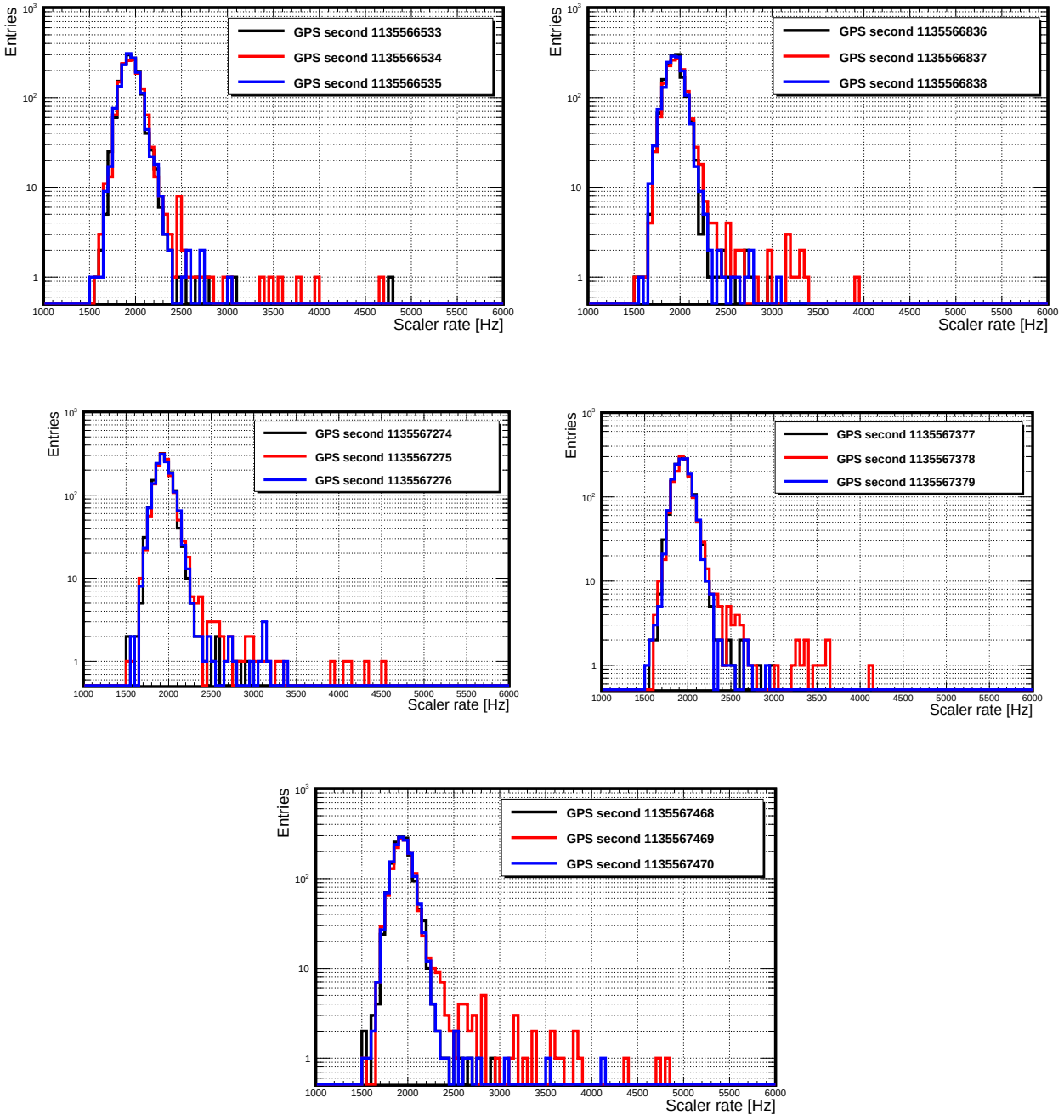

FIGURE A.1: Scaler rate distributions of 75 seconds of excesses (corrected for the AoP and atmospheric pressure) observed in December 2015. In the plots, the second of excess in counting rate is shown in red color. The rate distribution of the previous and next second to the one of excess is marked in black and blue colors, respectively.

A.3 Catalog of the excesses detected in the years 2006-2015 on a minute time scale

This catalog includes all 5-minute intervals of $\sigma^2 \geq \mu + 5\varsigma$ as well as the neighbor (previous and next 5-minute interval) of excess variance $\sigma^2 \geq \mu + 3\varsigma$.

Date [yyyy-mm-dd]	Date [MJD]	Baseline σ^2, $[10^{-6}]$	UTC [hh:mm:ss]	Amplitude excess σ^2, $[10^{-6}]$	Sidereal time [hh:mm:ss]	θ_{CRAB} [°]	ϕ_{CRAB} [°]
2006-05-28	53883	0.97 ± 0.09	01:32:30	1.61 ± 0.07	13:16:20	122.7	275.2
2006-05-28	53883	0.97 ± 0.09	01:37:30	1.55 ± 0.07	13:21:20	123.8	274.5
2006-05-28	53883	0.97 ± 0.09	19:57:30	1.56 ± 0.07	07:44:21	65.0	326.7
2006-06-17	53903	1.00 ± 0.12	19:38:33	1.72 ± 0.09	08:44:12	72.8	314.3
2006-06-29	53915	0.97 ± 0.10	09:37:30	1.57 ± 0.09	23:28:49	103.6	72.5
2006-06-29	53915	0.97 ± 0.10	23:04:19	1.47 ± 0.09	12:57:51	119.0	277.6
2006-07-27	53943	1.00 ± 0.11	05:42:39	1.72 ± 0.08	21:23:43	128.7	88.7
2006-07-30	53946	1.00 ± 0.12	20:47:31	1.65 ± 0.08	12:42:53	116.0	279.6
2006-07-31	53947	1.00 ± 0.11	07:42:30	1.75 ± 0.05	23:39:40	101.5	71.0
2006-08-01	53948	0.99 ± 0.11	09:57:30	1.58 ± 0.04	01:58:59	76.7	50.3
2007-02-22	54153	0.89 ± 0.10	13:57:31	1.55 ± 0.07	19:27:53	151.9	110.4
2007-02-22	54153	0.89 ± 0.10	23:32:35	1.42 ± 0.07	05:04:31	57.7	8.2
2010-09-21	55460	0.64 ± 0.07	10:47:58	1.00 ± 0.05	06:10:46	57.8	350.1
2010-09-21	55460	0.64 ± 0.07	11:01:11	1.11 ± 0.05	06:24:02	58.4	346.5
2010-09-24	55463	0.67 ± 0.06	10:43:08	1.09 ± 0.05	06:17:45	58.1	348.2
2010-09-24	55463	0.67 ± 0.06	11:01:01	0.98 ± 0.05	06:35:41	59.0	343.4
2010-09-24	55463	0.67 ± 0.06	11:06:47	0.99 ± 0.05	06:41:28	59.3	341.9
2010-09-24	55463	0.67 ± 0.06	11:56:05	1.23 ± 0.05	07:30:54	63.5	329.7
2010-09-24	55463	0.67 ± 0.06	12:02:46	1.07 ± 0.05	07:37:36	64.2	328.2
2011-03-27	55647	0.66 ± 0.07	11:02:38	1.13 ± 0.06	18:42:45	160.1	126.9
2011-03-27	55647	0.66 ± 0.07	11:12:39	1.14 ± 0.06	18:52:47	158.4	122.4
2011-04-03	55654	0.68 ± 0.07	11:06:38	1.99 ± 0.05	19:14:21	154.5	114.5
2011-04-03	55654	0.68 ± 0.07	11:11:53	1.03 ± 0.06	19:19:37	153.5	112.8
2011-04-03	55654	0.68 ± 0.07	11:16:53	1.00 ± 0.06	19:24:38	152.6	111.3
2011-04-03	55654	0.68 ± 0.07	11:21:53	0.87 ± 0.06	19:29:39	151.6	109.9
2011-04-04	55655	0.68 ± 0.07	01:07:30	1.33 ± 0.05	09:17:31	77.9	308.4
2011-04-04	55655	0.68 ± 0.07	11:19:48	1.02 ± 0.05	19:31:30	151.3	109.5
2011-04-04	55655	0.68 ± 0.07	18:33:05	1.03 ± 0.05	02:45:58	69.8	41.5
2011-04-08	55659	0.66 ± 0.07	00:29:06	1.28 ± 0.02	08:54:47	74.3	312.4
2011-04-09	55660	0.68 ± 0.06	00:12:30	1.04 ± 0.08	08:42:05	72.4	314.8
2011-04-09	55660	0.68 ± 0.06	00:17:30	1.09 ± 0.08	08:47:06	73.2	313.8
2011-04-09	55660	0.68 ± 0.06	10:52:57	0.92 ± 0.08	19:24:17	152.7	111.5
2011-04-09	55660	0.68 ± 0.06	10:57:57	1.39 ± 0.08	19:29:18	151.7	110.1
2011-04-09	55660	0.68 ± 0.06	11:02:57	1.45 ± 0.08	19:34:19	150.7	108.7
2011-04-12	55663	0.65 ± 0.06	01:17:40	1.18 ± 0.08	09:59:15	84.8	301.6
2011-04-12	55663	0.65 ± 0.06	10:41:27	1.11 ± 0.08	19:24:35	152.6	111.4
2011-04-12	55663	0.65 ± 0.06	11:02:13	1.25 ± 0.08	19:45:25	148.6	106.0
2011-09-24	55828	0.66 ± 0.09	10:40:58	1.15 ± 0.07	06:14:38	57.9	349.0
2011-09-24	55828	0.66 ± 0.09	10:45:58	0.91 ± 0.07	06:19:38	58.2	347.6
2011-10-02	55836	0.70 ± 0.07	10:17:53	1.32 ± 0.04	06:23:01	58.3	346.7
2011-10-02	55836	0.70 ± 0.07	10:22:53	2.93 ± 0.04	06:28:02	58.6	345.4
2011-10-02	55836	0.70 ± 0.07	11:32:53	1.15 ± 0.05	07:38:14	64.3	328.1
2011-10-09	55843	0.65 ± 0.06	00:12:30	1.17 ± 0.06	20:43:35	137.0	94.7

Continued on next page

TABLE A.2: Significant excesses above the baseline variability of the Auger average scaler rate (2006-2015) by using variability method.

Date [yyyy-mm-dd]	Date [MJD]	Baseline σ^2, $[10^{-6}]$	UTC [hh:mm:ss]	Amplitude excess σ^2, $[10^{-6}]$	Sidereal time [hh:mm:ss]	θ_{CRAB} [°]	ϕ_{CRAB} [°]
2011-10-09	55843	0.65 ± 0.06	10:07:46	1.12 ± 0.06	06:40:28	59.3	342.2
2011-10-09	55843	0.65 ± 0.06	10:17:50	1.27 ± 0.06	06:50:34	59.9	339.5
2011-10-09	55843	0.65 ± 0.06	10:31:06	1.04 ± 0.06	07:03:52	61.0	336.2
2011-10-09	55843	0.65 ± 0.06	10:41:13	0.85 ± 0.06	07:14:01	61.8	333.7
2011-10-09	55843	0.65 ± 0.06	11:19:10	0.95 ± 0.06	07:52:04	65.8	324.9
2011-10-09	55843	0.65 ± 0.06	23:09:34	0.97 ± 0.06	19:44:25	148.8	106.2
2011-10-29	55863	0.66 ± 0.06	05:02:30	1.37 ± 0.05	02:53:13	68.8	40.0
2011-10-29	55863	0.66 ± 0.06	09:57:31	1.67 ± 0.05	07:49:03	65.4	325.6
2011-10-29	55863	0.66 ± 0.06	10:07:31	1.70 ± 0.05	07:59:05	66.6	323.5
2011-10-29	55863	0.66 ± 0.06	10:12:31	1.46 ± 0.05	08:04:05	67.3	322.4
2011-10-29	55863	0.66 ± 0.06	10:22:32	1.05 ± 0.05	08:14:08	68.5	320.3
2011-11-22	55887	0.65 ± 0.08	00:52:30	1.28 ± 0.06	00:17:10	94.3	66.0
2012-05-10	56057	0.63 ± 0.07	00:34:26	1.14 ± 0.04	11:09:17	97.6	291.6
2012-05-10	56057	0.63 ± 0.07	01:14:26	1.02 ± 0.05	11:49:24	105.3	286.3
2012-08-05	56144	0.62 ± 0.06	11:52:32	1.03 ± 0.06	04:12:15	60.4	21.9
2012-08-05	56144	0.62 ± 0.06	11:57:32	0.89 ± 0.06	04:17:16	60.0	20.7
2012-08-08	56147	0.64 ± 0.06	11:11:11	1.14 ± 0.06	03:42:37	63.0	29.2
2012-08-08	56147	0.64 ± 0.06	11:21:26	0.91 ± 0.06	03:52:53	62.0	26.7
2012-08-08	56147	0.64 ± 0.06	11:56:26	1.03 ± 0.06	04:27:59	59.3	17.9
2012-09-14	56184	0.62 ± 0.06	03:42:36	0.90 ± 0.05	22:38:41	114.3	79.3
2012-09-14	56184	0.62 ± 0.06	04:17:36	0.97 ± 0.05	23:13:46	107.3	74.9
2012-09-14	56184	0.62 ± 0.06	10:52:39	1.23 ± 0.06	05:49:54	57.3	355.8
2012-09-14	56184	0.62 ± 0.06	10:57:39	0.83 ± 0.06	05:54:55	57.4	354.4
2012-09-14	56184	0.62 ± 0.06	11:02:39	1.12 ± 0.06	05:59:56	57.5	353.0
2012-09-22	56192	0.61 ± 0.07	10:37:53	2.04 ± 0.06	06:06:38	57.7	351.2
2012-09-22	56192	0.61 ± 0.07	10:42:53	2.43 ± 0.06	06:11:39	57.8	349.8
2012-09-22	56192	0.61 ± 0.07	10:47:53	1.00 ± 0.06	06:16:40	58.0	348.5
2012-09-22	56192	0.61 ± 0.07	10:52:53	1.11 ± 0.06	06:21:41	58.2	347.1
2012-09-22	56192	0.61 ± 0.07	10:57:53	0.98 ± 0.06	06:26:41	58.5	345.8
2012-09-22	56192	0.61 ± 0.07	12:58:09	1.16 ± 0.06	08:27:17	69.8	318.4
2012-09-26	56196	0.60 ± 0.06	10:37:33	0.94 ± 0.06	06:22:04	58.3	347.0
2012-09-26	56196	0.60 ± 0.06	10:42:33	0.84 ± 0.06	06:27:05	58.5	345.6
2012-09-26	56196	0.60 ± 0.06	10:47:33	0.91 ± 0.06	06:32:06	58.8	344.4
2012-09-26	56196	0.60 ± 0.06	10:52:33	1.16 ± 0.06	06:37:07	59.1	343.1
2012-09-26	56196	0.60 ± 0.06	22:42:50	0.94 ± 0.06	18:29:21	162.1	134.1
2012-09-26	56196	0.60 ± 0.06	22:47:50	0.86 ± 0.06	18:34:21	161.4	131.2
2012-09-26	56196	0.60 ± 0.06	22:52:50	1.07 ± 0.06	18:39:22	160.6	128.6
2012-09-26	56196	0.60 ± 0.06	22:57:50	1.12 ± 0.06	18:44:23	159.8	126.2
2012-09-26	56196	0.60 ± 0.06	23:02:50	1.26 ± 0.06	18:49:24	158.9	123.8
2012-09-26	56196	0.60 ± 0.06	23:12:50	0.92 ± 0.06	18:59:25	157.2	119.7
2012-09-26	56196	0.60 ± 0.06	23:17:50	0.84 ± 0.06	19:04:26	156.3	117.8
2012-09-29	56199	0.62 ± 0.06	00:02:30	0.97 ± 0.06	19:57:07	147.1	104.2
2012-09-29	56199	0.62 ± 0.06	23:17:48	1.10 ± 0.06	19:16:14	154.1	113.8
2012-09-29	56199	0.62 ± 0.06	23:22:48	1.50 ± 0.06	19:21:15	153.2	112.3
2012-09-29	56199	0.62 ± 0.06	23:57:39	1.00 ± 0.06	19:56:12	146.4	103.5
2012-12-19	56280	0.60 ± 0.06	15:13:04	0.91 ± 0.07	16:29:31	160.6	231.4
2012-12-19	56280	0.60 ± 0.06	15:23:04	1.88 ± 0.08	16:39:33	162.1	225.9
2012-12-19	56280	0.60 ± 0.06	15:28:04	1.43 ± 0.07	16:44:34	162.8	222.9
2012-12-19	56280	0.60 ± 0.06	15:33:29	1.79 ± 0.08	16:50:00	163.6	219.3
2013-01-08	56300	0.62 ± 0.07	00:17:30	1.15 ± 0.06	02:50:21	69.1	40.6
2013-01-08	56300	0.62 ± 0.07	01:07:30	1.39 ± 0.06	03:40:30	63.2	29.6
2013-01-08	56300	0.62 ± 0.07	01:17:30	1.24 ± 0.06	03:50:31	62.3	27.3

Continued on next page

TABLE A.2: Significant excesses above the baseline variability of the Auger average scaler rate (2006-2015) by using variability method.

Date [yyyy-mm-dd]	Date [MJD]	Baseline σ^2, $[10^{-6}]$	UTC [hh:mm:ss]	Amplitude excess σ^2, $[10^{-6}]$	Sidereal time [hh:mm:ss]	θ_{CRAB} [°]	ϕ_{CRAB} [°]
2013-03-03	56354	0.61 ± 0.06	22:02:09	0.99 ± 0.06	04:11:29	60.5	22.2
2013-03-03	56354	0.61 ± 0.06	23:57:57	1.25 ± 0.06	06:07:36	57.7	350.9
2013-03-04	56355	0.61 ± 0.06	00:18:02	1.23 ± 0.06	06:27:44	58.5	345.5
2013-03-04	56355	0.61 ± 0.06	00:33:57	2.28 ± 0.05	06:43:41	59.5	341.3
2013-03-04	56355	0.61 ± 0.06	00:38:57	1.34 ± 0.06	06:48:42	59.8	340.1
2013-03-04	56355	0.61 ± 0.06	00:43:57	1.68 ± 0.05	06:53:43	60.2	338.7
2013-03-04	56355	0.61 ± 0.06	00:58:57	1.20 ± 0.06	07:08:46	61.4	335.0
2013-03-04	56355	0.61 ± 0.06	23:02:14	0.94 ± 0.06	05:15:40	57.4	5.2
2013-03-04	56355	0.61 ± 0.06	23:12:14	1.09 ± 0.06	05:25:42	57.3	2.4
2013-03-04	56355	0.61 ± 0.06	23:57:40	0.92 ± 0.06	06:11:15	57.9	350.0
2013-03-05	56356	0.60 ± 0.07	00:57:30	1.18 ± 0.05	07:11:15	61.6	334.4
2013-03-06	56357	0.60 ± 0.06	23:59:08	3.04 ± 0.03	06:20:37	58.2	347.4
2013-03-08	56359	0.60 ± 0.05	23:29:50	1.17 ± 0.05	05:59:07	57.5	353.2
2013-03-08	56359	0.60 ± 0.05	23:59:51	2.01 ± 0.04	06:29:13	58.6	345.1
2013-03-09	56360	0.60 ± 0.07	00:40:07	0.98 ± 0.05	07:09:35	61.4	334.8
2013-03-09	56360	0.60 ± 0.07	06:53:49	0.95 ± 0.05	13:24:19	124.4	274.1
2013-03-09	56360	0.60 ± 0.07	08:52:05	0.92 ± 0.05	15:22:54	148.4	254.2
2013-03-09	56360	0.60 ± 0.07	23:57:50	1.66 ± 0.05	06:31:08	58.7	344.6
2013-03-10	56361	0.60 ± 0.07	00:52:53	1.16 ± 0.05	07:26:20	63.1	330.8
2013-03-10	56361	0.60 ± 0.07	00:57:53	1.00 ± 0.05	07:31:21	63.5	329.6
2013-03-11	56362	0.60 ± 0.06	00:01:07	2.36 ± 0.03	06:38:22	59.1	342.7
2013-03-11	56362	0.60 ± 0.06	00:16:07	0.81 ± 0.05	06:53:25	60.2	338.8
2013-03-11	56362	0.60 ± 0.06	00:21:08	1.00 ± 0.05	06:58:26	60.5	337.6
2013-03-11	56362	0.60 ± 0.06	00:26:08	1.24 ± 0.05	07:03:27	60.9	336.3
2013-03-11	56362	0.60 ± 0.06	00:31:09	2.94 ± 0.02	07:08:29	61.4	335.1
2013-03-21	56372	0.60 ± 0.06	23:38:41	0.95 ± 0.06	06:59:14	60.6	337.4
2013-03-21	56372	0.60 ± 0.06	23:58:41	2.30 ± 0.05	07:19:18	62.4	332.4
2013-03-22	56373	0.60 ± 0.05	00:03:41	1.20 ± 0.06	07:24:19	62.8	331.3
2013-03-22	56373	0.60 ± 0.05	00:13:43	0.85 ± 0.06	07:34:22	63.8	328.9
2013-03-22	56373	0.60 ± 0.05	00:34:40	0.84 ± 0.06	07:55:23	66.2	324.2
2013-03-22	56373	0.60 ± 0.05	00:44:40	0.91 ± 0.06	08:05:24	67.4	322.1
2013-03-25	56376	0.60 ± 0.06	00:03:31	1.22 ± 0.05	07:35:58	64.1	328.6
2013-03-25	56376	0.60 ± 0.06	23:57:56	0.99 ± 0.05	07:34:19	63.8	328.9
2013-03-26	56377	0.60 ± 0.05	00:02:56	1.18 ± 0.05	07:39:20	64.4	327.8
2013-03-26	56377	0.60 ± 0.05	00:08:12	1.66 ± 0.05	07:44:37	64.9	326.6
2013-03-26	56377	0.60 ± 0.05	05:53:35	0.88 ± 0.05	13:30:56	125.7	273.2
2013-03-26	56377	0.60 ± 0.05	10:59:05	0.90 ± 0.05	18:37:17	160.9	129.7
2013-03-26	56377	0.60 ± 0.05	22:46:03	0.91 ± 0.05	06:26:11	58.5	345.9
2013-04-24	56406	0.58 ± 0.06	11:23:06	0.97 ± 0.07	20:55:42	134.4	92.8
2013-04-24	56406	0.58 ± 0.06	11:28:06	3.24 ± 0.08	21:00:42	133.4	92.0
2013-04-24	56406	0.58 ± 0.06	11:33:06	1.09 ± 0.07	21:05:43	132.4	91.3
2013-04-24	56406	0.58 ± 0.06	11:43:06	0.90 ± 0.07	21:15:45	130.3	89.8
2013-04-24	56406	0.58 ± 0.06	11:53:06	1.02 ± 0.07	21:25:47	128.2	88.4
2013-04-24	56406	0.58 ± 0.06	11:58:06	1.06 ± 0.07	21:30:47	127.2	87.7
2013-04-24	56406	0.58 ± 0.06	23:03:06	1.12 ± 0.07	08:37:37	71.8	315.6
2013-04-27	56409	0.58 ± 0.07	11:27:55	1.01 ± 0.06	21:12:21	131.0	90.3
2013-04-27	56409	0.58 ± 0.07	11:42:55	1.45 ± 0.06	21:27:23	127.9	88.2
2013-04-30	56412	0.58 ± 0.06	02:58:24	0.97 ± 0.06	12:53:16	118.1	278.2
2013-04-30	56412	0.58 ± 0.06	11:10:40	1.74 ± 0.05	21:06:53	132.1	91.1
2013-04-30	56412	0.58 ± 0.06	11:15:40	0.83 ± 0.06	21:11:54	131.1	90.4
2013-04-30	56412	0.58 ± 0.06	11:20:40	1.07 ± 0.06	21:16:54	130.1	89.6
2013-04-30	56412	0.58 ± 0.06	12:00:40	1.03 ± 0.06	21:57:01	121.9	84.2

Continued on next page

TABLE A.2: Significant excesses above the baseline variability of the Auger average scaler rate (2006-2015) by using variability method.

Date [yyyy-mm-dd]	Date [MJD]	Baseline σ^2, $[10^{-6}]$	UTC [hh:mm:ss]	Amplitude excess σ^2, $[10^{-6}]$	Sidereal time [hh:mm:ss]	θ_{CRAB} [°]	ϕ_{CRAB} [°]
2013-07-31	56504	0.58 ± 0.05	11:54:01	1.12 ± 0.05	03:53:04	62.1	26.7
2013-08-05	56509	0.58 ± 0.06	11:39:40	1.04 ± 0.05	03:58:23	61.5	25.4
2013-08-05	56509	0.58 ± 0.06	11:58:49	1.54 ± 0.05	04:17:36	60.1	20.6
2013-08-16	56520	0.59 ± 0.08	11:42:44	1.19 ± 0.05	04:44:50	58.4	13.5
2013-08-16	56520	0.59 ± 0.08	11:47:44	0.81 ± 0.05	04:49:51	58.2	12.2
2013-08-16	56520	0.59 ± 0.08	11:52:44	0.95 ± 0.05	04:54:52	57.9	10.8
2013-08-17	56521	0.59 ± 0.06	11:39:01	1.50 ± 0.06	04:45:03	58.4	13.4
2013-08-17	56521	0.59 ± 0.06	23:34:53	0.95 ± 0.06	16:42:53	162.6	224.0
2013-10-06	56571	0.61 ± 0.06	11:24:25	0.94 ± 0.05	07:47:32	65.3	325.9
2013-10-06	56571	0.61 ± 0.06	11:29:25	1.11 ± 0.05	07:52:33	65.9	324.8
2013-10-06	56571	0.61 ± 0.06	11:34:25	0.93 ± 0.05	07:57:34	66.5	323.7
2013-10-06	56571	0.61 ± 0.06	11:44:25	1.32 ± 0.05	08:07:36	67.7	321.6
2013-10-06	56571	0.61 ± 0.06	23:54:28	0.94 ± 0.05	20:19:39	141.7	98.8
2013-10-29	56594	0.59 ± 0.07	04:49:51	0.83 ± 0.06	02:42:34	70.2	42.2
2013-10-29	56594	0.59 ± 0.07	04:54:51	1.03 ± 0.06	02:47:35	69.5	41.2
2014-02-23	56711	0.61 ± 0.07	01:59:01	1.03 ± 0.06	07:32:33	63.6	329.4
2014-02-23	56711	0.61 ± 0.07	02:04:06	1.51 ± 0.06	07:37:39	64.2	328.2
2014-03-08	56724	0.61 ± 0.06	00:00:40	0.90 ± 0.07	06:25:08	58.4	346.2
2014-03-08	56724	0.61 ± 0.06	02:50:40	0.90 ± 0.07	09:15:36	77.5	308.7
2014-03-08	56724	0.61 ± 0.06	23:54:04	0.93 ± 0.07	06:22:28	58.3	346.9
2014-03-08	56724	0.61 ± 0.06	23:59:23	1.52 ± 0.08	06:27:47	58.5	345.5
2014-03-09	56725	0.63 ± 0.06	00:19:41	0.90 ± 0.07	06:48:09	59.8	340.2
2014-03-15	56731	0.62 ± 0.06	00:33:42	1.76 ± 0.05	07:25:51	63.0	330.9
2014-03-15	56731	0.62 ± 0.06	00:38:43	1.19 ± 0.07	07:30:53	63.5	329.7
2014-03-16	56732	0.62 ± 0.08	00:00:42	1.22 ± 0.02	06:56:42	60.4	338.0
2014-03-16	56732	0.62 ± 0.08	00:20:11	1.72 ± 0.05	07:16:15	62.1	333.2
2014-03-16	56732	0.62 ± 0.08	01:33:37	1.08 ± 0.06	08:29:53	70.7	317.1
2014-03-16	56732	0.62 ± 0.08	21:03:24	1.15 ± 0.06	04:02:52	61.2	24.3
2014-03-16	56732	0.62 ± 0.08	23:55:15	1.22 ± 0.06	06:55:11	60.3	338.4
2014-05-30	56807	0.55 ± 0.06	11:54:07	0.95 ± 0.06	23:47:46	99.9	69.9
2014-05-30	56807	0.55 ± 0.06	11:59:10	0.86 ± 0.06	23:52:50	98.9	69.3
2014-08-06	56875	0.59 ± 0.05	01:09:51	0.97 ± 0.06	17:29:50	166.7	184.7
2014-08-06	56875	0.59 ± 0.05	04:22:05	0.87 ± 0.06	20:42:36	137.1	94.8
2014-08-06	56875	0.59 ± 0.05	04:57:39	0.86 ± 0.06	21:18:16	129.8	89.4
2014-08-06	56875	0.59 ± 0.05	11:48:50	1.13 ± 0.06	04:10:34	60.5	22.4
2014-08-06	56875	0.59 ± 0.05	11:59:03	0.88 ± 0.06	04:20:49	59.8	19.8
2014-08-06	56875	0.59 ± 0.05	12:09:13	0.83 ± 0.06	04:31:01	59.1	17.2
2014-08-06	56875	0.59 ± 0.05	12:55:05	0.97 ± 0.06	05:17:00	57.3	4.8
2014-08-06	56875	0.59 ± 0.05	16:43:28	0.76 ± 0.06	09:06:01	76.0	310.3
2014-08-06	56875	0.59 ± 0.05	16:48:34	0.82 ± 0.06	09:11:07	76.8	309.4
2014-08-06	56875	0.59 ± 0.05	16:53:37	1.02 ± 0.06	09:16:11	77.6	308.6
2014-08-06	56875	0.59 ± 0.05	16:58:44	0.96 ± 0.06	09:21:19	78.4	307.7
2014-08-06	56875	0.59 ± 0.05	17:03:48	0.79 ± 0.06	09:26:24	79.3	306.8
2014-08-06	56875	0.59 ± 0.05	17:08:54	0.86 ± 0.06	09:31:31	80.1	306.0
2014-08-06	56875	0.59 ± 0.05	18:04:26	0.95 ± 0.06	10:27:12	89.8	297.4
2014-08-14	56883	0.59 ± 0.05	09:34:54	0.93 ± 0.08	02:27:49	72.3	45.1
2014-08-14	56883	0.59 ± 0.05	13:08:34	0.81 ± 0.08	06:02:04	57.5	352.4
2014-08-14	56883	0.59 ± 0.05	16:05:52	0.86 ± 0.08	08:59:51	75.1	311.5
2014-08-14	56883	0.59 ± 0.05	22:36:05	0.84 ± 0.08	15:31:08	150.1	252.2
2014-08-19	56888	0.59 ± 0.06	12:55:48	1.15 ± 0.08	06:08:58	57.7	350.5
2014-08-20	56889	0.59 ± 0.06	11:35:14	0.98 ± 0.07	04:52:08	58.1	11.5
2014-08-24	56893	0.59 ± 0.07	11:29:21	1.01 ± 0.07	05:02:00	57.7	8.9

Continued on next page

TABLE A.2: Significant excesses above the baseline variability of the Auger average scaler rate (2006-2015) by using variability method.

Date [yyyy-mm-dd]	Date [MJD]	Baseline σ^2, $[10^{-6}]$	UTC [hh:mm:ss]	Amplitude excess σ^2, $[10^{-6}]$	Sidereal time [hh:mm:ss]	θ_{CRAB} [°]	ϕ_{CRAB} [°]
2014-08-24	56893	0.59 ± 0.07	11:34:26	0.99 ± 0.07	05:07:06	57.5	7.5
2014-08-24	56893	0.59 ± 0.07	11:39:32	1.02 ± 0.07	05:12:13	57.4	6.1
2014-08-27	56896	0.58 ± 0.05	11:13:54	1.06 ± 0.07	04:58:20	57.8	9.9
2014-08-27	56896	0.58 ± 0.05	11:18:55	0.78 ± 0.07	05:03:22	57.6	8.5
2014-08-27	56896	0.58 ± 0.05	11:34:00	0.86 ± 0.07	05:18:29	57.3	4.4
2014-08-27	56896	0.58 ± 0.05	23:06:32	0.86 ± 0.07	16:52:55	163.9	217.3
2014-08-27	56896	0.58 ± 0.05	23:57:44	0.81 ± 0.07	17:44:16	166.6	170.2
2014-08-28	56897	0.59 ± 0.06	09:45:02	1.10 ± 0.07	03:33:10	64.0	31.4
2014-08-30	56899	0.60 ± 0.06	12:25:22	0.98 ± 0.07	06:21:50	58.3	347.1
2014-08-31	56900	0.56 ± 0.05	11:17:47	0.94 ± 0.07	05:18:00	57.3	4.5
2014-08-31	56900	0.56 ± 0.05	11:27:50	1.30 ± 0.06	05:28:05	57.2	1.7
2014-09-02	56902	0.60 ± 0.06	09:43:54	1.08 ± 0.03	03:51:45	62.1	27.0
2014-09-02	56902	0.60 ± 0.06	09:58:54	0.99 ± 0.04	04:06:47	60.8	23.3
2014-11-05	56966	0.67 ± 0.07	00:47:47	1.22 ± 0.09	23:06:29	107.8	75.2
2014-11-05	56966	0.67 ± 0.07	01:02:52	1.11 ± 0.09	23:21:37	104.8	73.3
2014-11-05	56966	0.67 ± 0.07	03:02:55	1.12 ± 0.09	01:21:59	82.6	56.3
2014-11-05	56966	0.67 ± 0.07	19:39:33	1.29 ± 0.09	18:01:21	165.5	153.4
2015-02-02	57055	5.86 ± 0.71	20:19:58	1.52 ± 0.005	00:32:47	91.5	63.8
2015-02-02	57055	5.86 ± 0.71	20:24:58	1.11 ± 0.004	00:37:47	90.6	63.1
2015-04-11	57123	0.60 ± 0.61	12:57:45	1.30 ± 0.004	21:37:26	125.9	86.8
2015-05-10	57152	0.58 ± 0.06	00:22:30	2.51 ± 0.008	10:54:28	94.8	293.6
2015-05-10	57152	0.58 ± 0.06	00:27:38	2.50 ± 0.008	10:59:37	95.8	292.9
2015-05-10	57152	0.58 ± 0.06	00:57:38	1.05 ± 0.004	11:29:41	101.5	288.9
2015-05-10	57152	0.58 ± 0.06	01:02:42	1.74 ± 0.006	11:34:46	102.5	288.3
2015-06-08	57181	0.59 ± 0.06	02:47:30	0.81 ± 0.055	15:14:12	146.7	256.2
2015-06-08	57181	0.59 ± 0.06	02:57:30	0.82 ± 0.055	15:24:13	148.7	254.0
2015-06-08	57181	0.59 ± 0.06	03:12:30	1.23 ± 0.004	15:39:16	151.6	250.1
2015-06-17	57190	0.59 ± 0.07	05:12:30	1.78 ± 0.006	18:15:04	164.1	143.4
2015-06-17	57190	0.59 ± 0.07	05:19:30	0.94 ± 0.003	18:22:06	163.2	138.6
2015-12-18	57374	0.63 ± 0.06	00:02:30	0.80 ± 0.05	01:09:10	84.9	58.4
2015-12-18	57374	0.63 ± 0.06	00:12:30	0.93 ± 0.06	01:19:41	83.1	56.8
2015-12-18	57374	0.63 ± 0.06	00:17:30	0.84 ± 0.05	01:24:42	82.3	56.1
2015-12-18	57374	0.63 ± 0.06	03:27:30	0.80 ± 0.003	04:35:13	58.9	16.1
2015-12-18	57374	0.63 ± 0.06	03:57:30	0.93 ± 0.003	05:05:18	57.6	08.0
2015-12-18	57374	0.63 ± 0.06	04:22:30	0.89 ± 0.003	05:30:22	57.2	01.1
2015-12-25	57381	0.62 ± 0.07	01:42:45	1.04 ± 0.003	03:17:47	65.8	34.8
2015-12-31	57387	0.62 ± 0.08	00:17:30	1.19 ± 0.078	02:15:57	74.1	47.2
2015-12-31	57387	0.62 ± 0.08	00:22:30	1.38 ± 0.078	02:20:58	73.3	46.4
2015-12-31	57387	0.62 ± 0.08	00:32:30	1.46 ± 0.077	02:30:59	71.9	44.5
2015-12-31	57387	0.62 ± 0.08	00:37:30	1.16 ± 0.079	02:36:01	71.2	43.5
2015-12-31	57387	0.62 ± 0.08	00:57:30	1.12 ± 0.079	02:56:03	68.4	39.5
2015-12-31	57387	0.62 ± 0.08	01:02:30	5.92 ± 0.062	03:01:05	67.8	38.4
2015-12-31	57387	0.62 ± 0.08	01:07:30	1.11 ± 0.079	03:06:06	67.2	37.4
2015-12-31	57387	0.62 ± 0.08	01:12:30	1.34 ± 0.078	03:11:06	66.6	36.3
2015-12-31	57387	0.62 ± 0.08	01:17:30	1.71 ± 0.077	03:16:07	66.0	35.2
2015-12-31	57387	0.62 ± 0.08	01:22:30	1.69 ± 0.077	03:21:08	65.4	34.1
2015-12-31	57387	0.62 ± 0.08	01:27:30	1.40 ± 0.078	03:26:09	64.8	33.0
2015-12-31	57387	0.62 ± 0.08	01:37:30	1.24 ± 0.078	03:36:11	63.7	30.7
2015-12-31	57387	0.62 ± 0.08	01:52:30	1.08 ± 0.079	03:51:13	62.2	27.2
2015-12-31	57387	0.62 ± 0.08	01:57:30	2.72 ± 0.073	03:56:14	61.8	25.9
2015-12-31	57387	0.62 ± 0.08	02:02:30	1.41 ± 0.078	04:01:15	61.3	24.7
2015-12-31	57387	0.62 ± 0.08	02:07:30	1.26 ± 0.078	04:06:15	60.9	23.5

Continued on next page

TABLE A.2: Significant excesses above the baseline variability of the Auger average scaler rate (2006-2015) by using variability method.

Date [yyyy-mm-dd]	Date [MJD]	Baseline σ^2, $[10^{-6}]$	UTC [hh:mm:ss]	Amplitude excess σ^2, $[10^{-6}]$	Sidereal time [hh:mm:ss]	θ_{CRAB} [°]	ϕ_{CRAB} [°]
2015-12-31	57387	0.62 ± 0.08	02:12:30	1.48 ± 0.077	04:11:16	60.5	22.2
2015-12-31	57387	0.62 ± 0.08	02:17:30	1.59 ± 0.077	04:16:17	60.1	21.0
2015-12-31	57387	0.62 ± 0.08	02:22:30	1.37 ± 0.078	04:21:18	59.8	19.7
2015-12-31	57387	0.62 ± 0.08	02:27:30	2.32 ± 0.074	04:26:19	59.5	18.4
2015-12-31	57387	0.62 ± 0.08	02:32:30	3.00 ± 0.072	04:31:20	59.1	17.1
2015-12-31	57387	0.62 ± 0.08	02:37:30	2.78 ± 0.073	04:36:20	58.9	15.8
2015-12-31	57387	0.62 ± 0.08	02:42:30	3.20 ± 0.071	04:41:21	58.6	14.5
2015-12-31	57387	0.62 ± 0.08	02:47:30	2.34 ± 0.074	04:46:22	58.3	13.1
2015-12-31	57387	0.62 ± 0.08	02:52:30	5.61 ± 0.063	04:51:23	58.1	11.8
2015-12-31	57387	0.62 ± 0.08	02:57:30	2.59 ± 0.074	04:56:24	57.9	10.4
2015-12-31	57387	0.62 ± 0.08	03:02:30	4.15 ± 0.068	05:01:25	57.8	09.0
2015-12-31	57387	0.62 ± 0.08	03:07:30	1.55 ± 0.077	05:06:25	57.6	07.7
2015-12-31	57387	0.62 ± 0.08	03:12:30	1.77 ± 0.076	05:11:26	57.5	06.4
2015-12-31	57387	0.62 ± 0.08	03:17:30	1.71 ± 0.077	05:16:27	57.4	05.0
2015-12-31	57387	0.62 ± 0.08	03:22:30	2.10 ± 0.075	05:21:28	57.3	03.6

TABLE A.2: Significant excesses above the baseline variability of the Auger average scaler rate (2006-2015) by using variability method.

A.4 Lightning periods discarded from scaler rate acquisition

t_0 [GPS]	t_0 [UTC]	Δt [s]	t_0 [GPS]	t_0 [UTC]	Δt [s]
820354637	2006-01-03 20:17:17	8810	825336904	2006-03-02 12:15:04	7199
821992841	2006-01-22 19:20:41	7651	826476268	2006-03-15 16:44:28	10859
822002153	2006-01-22 21:55:53	9092	827793437	2006-03-30 22:37:17	7199
822079988	2006-01-23 19:33:08	15480	827864317	2006-03-31 18:18:37	7199
822693852	2006-01-30 22:04:12	7260	827878320	2006-03-31 22:12:00	8918
822792045	2006-02-01 01:20:45	8607	841092139	2006-08-31 20:42:19	7199
822857939	2006-02-01 19:38:59	10298	845224993	2006-10-18 16:43:13	10244
822964567	2006-02-03 01:16:07	20223	845494892	2006-10-21 19:41:32	7199
822993931	2006-02-03 09:25:31	8664	846720025	2006-11-05 00:00:25	7199
823385754	2006-02-07 22:15:54	7650	847837795	2006-11-17 22:29:55	7717
823720683	2006-02-11 19:18:03	21240	848607707	2006-11-26 20:21:47	11075
823990720	2006-02-14 22:18:40	7642	849462477	2006-12-06 17:47:57	7352
824061902	2006-02-15 18:05:02	13636	849486394	2006-12-07 00:26:34	17328
824146541	2006-02-16 17:35:41	13771	849558594	2006-12-07 20:29:54	8552
824164986	2006-02-16 22:43:06	7932	849810035	2006-12-10 18:20:35	9772
824240853	2006-02-17 19:47:33	7378	849886371	2006-12-11 15:32:51	11347
824329355	2006-02-18 20:22:35	7199	849981050	2006-12-12 17:50:50	7292
824406758	2006-02-19 17:52:38	27619	850052886	2006-12-13 13:48:06	7199
824501841	2006-02-20 20:17:21	9756	850157501	2006-12-14 18:51:41	8548
824575084	2006-02-21 16:38:04	10173	850238012	2006-12-15 17:13:32	7199
824600483	2006-02-21 23:41:23	10007	850248587	2006-12-15 20:09:47	7199
824654025	2006-02-22 14:33:45	13658	850257192	2006-12-15 22:33:12	7307
825267546	2006-03-01 16:59:06	12494	851472815	2006-12-30 00:13:35	14936
825301143	2006-03-02 02:19:03	7874	851644264	2006-12-31 23:51:04	13043

TABLE A.3: Lightning periods excluded from the analysis in the years 2006.

t_0 [GPS]	t_0 [UTC]	Δt [s]	t_0 [GPS]	t_0 [UTC]	Δt [s]
852147284	2007-01-06 19:34:44	15340	858530056	2007-03-21 16:34:16	12033
852165319	2007-01-07 00:35:19	19478	858559918	2007-03-22 00:51:58	26194
852224504	2007-01-07 17:01:44	15790	858600397	2007-03-22 12:06:37	23773
852322414	2007-01-08 20:13:34	10799	859168658	2007-03-29 01:57:38	11379
852406899	2007-01-09 19:41:39	10799	859184349	2007-03-29 06:19:09	10923
852999976	2007-01-16 16:26:16	40647	859666426	2007-04-03 20:13:46	13566
853179140	2007-01-18 18:12:20	17547	859741267	2007-04-04 17:01:07	17915
853431292	2007-01-21 16:14:52	31028	871227070	2007-08-15 15:31:10	18746
853700766	2007-01-24 19:06:06	10964	873321315	2007-09-08 21:15:15	17496
853783398	2007-01-25 18:03:18	10799	874104603	2007-09-17 22:50:03	15451
853866676	2007-01-26 17:11:16	13467	876073807	2007-10-10 17:50:07	10912
853883574	2007-01-26 21:52:54	10799	876172837	2007-10-11 21:20:37	12280
853894920	2007-01-27 01:02:00	19065	876410895	2007-10-14 15:28:15	10995
854033506	2007-01-28 15:31:46	16885	876423553	2007-10-14 18:59:13	14118
854125254	2007-01-29 17:00:54	29359	878578105	2007-11-08 17:28:25	20842
854312092	2007-01-31 20:54:52	12714	878650178	2007-11-09 13:29:38	39411
854503731	2007-02-03 02:08:51	13446	879698516	2007-11-21 16:41:56	20227
854554013	2007-02-03 16:06:53	17299	879821190	2007-11-23 02:46:30	11296
854737762	2007-02-05 19:09:22	13445	880389715	2007-11-29 16:41:55	12008
855002240	2007-02-08 20:37:20	12887	880470379	2007-11-30 15:06:19	19945
855080199	2007-02-09 18:16:39	24823	880550384	2007-12-01 13:19:44	11809
855252015	2007-02-11 18:00:15	28498	880659278	2007-12-02 19:34:38	10799
856115459	2007-02-21 17:50:59	13026	882123396	2007-12-19 18:16:36	19240
857269876	2007-03-07 02:31:16	13165	882590666	2007-12-25 04:04:26	42075
857289762	2007-03-07 08:02:42	10799	882741393	2007-12-26 21:56:33	17655
857844983	2007-03-13 18:16:23	20509	882811566	2007-12-27 17:26:06	21034
858013650	2007-03-15 17:07:30	24952	882995021	2007-12-29 20:23:41	11561
858044980	2007-03-16 01:49:40	15079			

TABLE A.4: Lightning periods excluded from the analysis in the years 2007.

t_0 [GPS]	t_0 [UTC]	Δt [s]	t_0 [GPS]	t_0 [UTC]	Δt [s]
884292047	2008-01-13 20:40:47	8434	888536585	2008-03-02 23:43:05	19190
884361945	2008-01-14 16:05:45	7199	888777150	2008-03-05 18:32:30	23746
884821189	2008-01-19 23:39:49	7463	888815684	2008-03-06 05:14:44	13471
884981321	2008-01-21 20:08:41	7199	888858637	2008-03-06 17:10:37	18109
885059825	2008-01-22 17:57:05	29924	888952651	2008-03-07 19:17:31	11916
885246756	2008-01-24 21:52:36	15020	891023786	2008-03-31 18:36:26	18600
885274710	2008-01-25 05:38:30	9384	891055171	2008-04-01 03:19:31	7199
885310681	2008-01-25 15:38:01	14214	903881081	2008-08-27 14:04:41	7199
885392148	2008-01-26 14:15:48	9865	906481686	2008-09-26 16:28:06	23546
885403273	2008-01-26 17:21:13	8966	906852999	2008-09-30 23:36:39	7199
885500560	2008-01-27 20:22:40	27334	907869151	2008-10-12 17:52:31	18068
885587625	2008-01-28 20:33:45	9933	908043222	2008-10-14 18:13:42	32103
885598476	2008-01-28 23:34:36	15458	908386239	2008-10-18 17:30:39	7199
885843877	2008-01-31 19:44:37	12819	908899615	2008-10-24 16:06:55	11085
885857254	2008-01-31 23:27:34	7199	908993707	2008-10-25 18:15:07	10851
886198841	2008-02-04 22:20:41	7199	909681477	2008-11-02 17:17:57	13196
886276046	2008-02-05 19:47:26	16934	910291960	2008-11-09 18:52:40	7199
886299401	2008-02-06 02:16:41	7569	910641845	2008-11-13 20:04:05	12125
886323389	2008-02-06 08:56:29	7199	911155022	2008-11-19 18:37:02	12808
886352509	2008-02-06 17:01:49	20362	911238803	2008-11-20 17:53:23	9459
886533441	2008-02-08 19:17:21	9735	911606255	2008-11-24 23:57:35	11069
886620692	2008-02-09 19:31:32	11449	911630737	2008-11-25 06:45:37	9244
886968011	2008-02-13 20:00:11	9826	911660452	2008-11-25 15:00:52	15074
887048678	2008-02-14 18:24:38	11686	911932556	2008-11-28 18:35:56	19879
887062565	2008-02-14 22:16:05	11140	911953394	2008-11-29 00:23:14	12303
887217619	2008-02-16 17:20:19	10621	911968639	2008-11-29 04:37:19	7199
887236334	2008-02-16 22:32:14	8166	912088148	2008-11-30 13:49:08	48670
887305916	2008-02-17 17:51:56	16687	912365424	2008-12-03 18:50:24	9954
887326811	2008-02-17 23:40:11	15763	912461655	2008-12-04 21:34:15	14186
887343233	2008-02-18 04:13:53	7282	912539783	2008-12-05 19:16:23	13337
887350666	2008-02-18 06:17:46	7199	912785078	2008-12-08 15:24:38	15586
887398025	2008-02-18 19:27:05	7199	912801395	2008-12-08 19:56:35	8388
887427256	2008-02-19 03:34:16	7814	912853875	2008-12-09 10:31:15	21747
887436753	2008-02-19 06:12:33	7199	913108301	2008-12-12 09:11:41	13602
887556703	2008-02-20 15:31:43	7322	913127512	2008-12-12 14:31:52	7199
887652874	2008-02-21 18:14:34	14469	913164370	2008-12-13 00:46:10	7249
887669132	2008-02-21 22:45:32	8711	913406801	2008-12-15 20:06:41	30794
887737440	2008-02-22 17:44:00	14095	913508565	2008-12-17 00:22:45	7199
887822797	2008-02-23 17:26:37	10173	913661109	2008-12-18 18:45:09	9778
887922957	2008-02-24 21:15:57	10310	913738639	2008-12-19 16:17:19	8020
888001416	2008-02-25 19:03:36	12122	913748220	2008-12-19 18:57:00	17258
888093215	2008-02-26 20:33:35	19729	913817356	2008-12-20 14:09:16	10756
888183159	2008-02-27 21:32:39	11705	914018874	2008-12-22 22:07:54	20064
888278092	2008-02-28 23:54:52	20139	914207848	2008-12-25 02:37:28	16098
888445347	2008-03-01 22:22:27	16027	914353368	2008-12-26 19:02:48	12217
888516320	2008-03-02 18:05:20	9743	914705664	2008-12-30 20:54:24	7199

TABLE A.5: Lightning periods excluded from the analysis in the years 2008.

t_0 [GPS]	t_0 [UTC]	Δt [s]	t_0 [GPS]	t_0 [UTC]	Δt [s]
915138867	2009-01-04 21:14:27	11262	919294228	2009-02-21 23:30:28	7474
915218687	2009-01-05 19:24:47	7199	919712849	2009-02-26 19:47:29	20639
915293098	2009-01-06 16:04:58	7199	919796236	2009-02-27 18:57:16	17171
915309146	2009-01-06 20:32:26	7199	919881665	2009-02-28 18:41:05	16759
915389399	2009-01-07 18:49:59	12637	920135239	2009-03-03 17:07:19	7541
915647223	2009-01-10 18:27:03	19126	920157001	2009-03-03 23:10:01	17314
915668588	2009-01-11 00:23:08	11683	920401232	2009-03-06 19:00:32	10131
915725415	2009-01-11 16:10:15	16761	920842501	2009-03-11 21:35:01	14963
916026664	2009-01-15 03:51:04	7448	921550571	2009-03-20 02:16:11	22196
916250405	2009-01-17 18:00:05	14049	921714089	2009-03-21 23:41:29	9121
916534544	2009-01-21 00:55:44	7350	922134782	2009-03-26 20:33:02	17930
916595882	2009-01-21 17:58:02	13941	934115840	2009-08-12 12:37:20	7199
916692165	2009-01-22 20:42:45	7199	939830067	2009-10-17 15:54:27	11507
916777010	2009-01-23 20:16:50	13823	943985635	2009-12-04 18:13:55	9691
917067286	2009-01-27 04:54:46	33763	944205158	2009-12-07 07:12:38	12171
917135023	2009-01-27 23:43:43	14701	944221909	2009-12-07 11:51:49	11909
917794791	2009-02-04 14:59:51	12922	944503123	2009-12-10 17:58:43	24702
918279851	2009-02-10 05:44:11	10239	944588961	2009-12-11 17:49:21	16997
918514305	2009-02-12 22:51:45	10813	945102757	2009-12-17 16:32:37	7199
918677298	2009-02-14 20:08:18	7199	945205265	2009-12-18 21:01:05	10246
918684742	2009-02-14 22:12:22	20615	945363214	2009-12-20 16:53:34	10367
918753703	2009-02-15 17:21:43	14280	945530389	2009-12-22 15:19:49	12143
919013983	2009-02-18 17:39:43	15853	945653064	2009-12-24 01:24:24	7199
919101202	2009-02-19 17:53:22	15457	946248493	2009-12-30 22:48:13	12772
919241347	2009-02-21 08:49:07	29191			

TABLE A.6: Lightning periods excluded from the analysis in the years 2009.

t_0 [GPS]	t_0 [UTC]	Δt [s]	t_0 [GPS]	t_0 [UTC]	Δt [s]
946499322	2010-01-02 20:28:42	14155	968172317	2010-09-10 16:45:17	15866
946671045	2010-01-04 20:10:45	8072	968349505	2010-09-12 17:58:25	12291
948138478	2010-01-21 19:47:58	13454	969300161	2010-09-23 18:02:41	7199
948222849	2010-01-22 19:14:09	24120	969550615	2010-09-26 15:36:55	18120
948277593	2010-01-23 10:26:33	11226	969582363	2010-09-27 00:26:03	13031
948365191	2010-01-24 10:46:31	10287	970949585	2010-10-12 20:13:05	8565
948391254	2010-01-24 18:00:54	17544	971802697	2010-10-22 17:11:37	16713
948556253	2010-01-26 15:50:53	7199	971954398	2010-10-24 11:19:58	7199
948564065	2010-01-26 18:01:05	12070	971989854	2010-10-24 21:10:54	11220
948576598	2010-01-26 21:29:58	11619	972192626	2010-10-27 05:30:26	7199
949089088	2010-02-01 19:51:28	11209	973722458	2010-11-13 22:27:38	8725
949503339	2010-02-06 14:55:39	15814	974140916	2010-11-18 18:41:56	8042
949535197	2010-02-06 23:46:37	11817	974218675	2010-11-19 16:17:55	13933
949750507	2010-02-09 11:35:07	7199	974408777	2010-11-21 21:06:17	10755
950228472	2010-02-15 00:21:12	14624	974491180	2010-11-22 19:59:40	9872
950298060	2010-02-15 19:41:00	21840	974651146	2010-11-24 16:25:46	8641
950322581	2010-02-16 02:29:41	7435	974665082	2010-11-24 20:18:02	7199
950462885	2010-02-17 17:28:05	13328	974937719	2010-11-28 00:01:59	19260
950853116	2010-02-22 05:51:56	7484	975000269	2010-11-28 17:24:29	9527
950905597	2010-02-22 20:26:37	7199	975610175	2010-12-05 18:49:35	20379
951179068	2010-02-26 00:24:28	9001	975686385	2010-12-06 15:59:45	7199
951251560	2010-02-26 20:32:40	19267	975709486	2010-12-06 22:24:46	7251
951504517	2010-03-01 18:48:37	13436	976467419	2010-12-15 16:56:59	12315
951584989	2010-03-02 17:09:49	9030	976548923	2010-12-16 15:35:23	10428
951690043	2010-03-03 22:20:43	12116	977003181	2010-12-21 21:46:21	9831
952027286	2010-03-07 20:01:26	7199	977080914	2010-12-22 19:21:54	10866
952038334	2010-03-07 23:05:34	9709	977095223	2010-12-22 23:20:23	9992
952377653	2010-03-11 21:20:53	29901	977427229	2010-12-26 19:33:49	21292
952461950	2010-03-12 20:45:50	16617	977506901	2010-12-27 17:41:41	14266
953713019	2010-03-27 08:16:59	21413	977592941	2010-12-28 17:35:41	11963
958598807	2010-05-22 21:26:47	13368	977675638	2010-12-29 16:33:58	21558
963400912	2010-07-17 11:21:52	7351	977768498	2010-12-30 18:21:38	14598
963574053	2010-07-19 11:27:33	9646			

TABLE A.7: Lightning periods excluded from the analysis in the years 2010.

t_0 [GPS]	t_0 [UTC]	Δt [s]	t_0 [GPS]	t_0 [UTC]	Δt [s]
978112826	2011-01-03 18:00:26	7840	986495691	2011-04-10 18:34:51	18714
978164253	2011-01-04 08:17:33	24161	988039824	2011-04-28 15:30:24	18119
978197374	2011-01-04 17:29:34	26430	1001966177	2011-10-06 19:56:17	7343
978377547	2011-01-06 19:32:27	10275	1002031535	2011-10-07 14:05:35	9087
978390731	2011-01-06 23:12:11	16052	1002041537	2011-10-07 16:52:17	14573
978544680	2011-01-08 17:58:00	8029	1003436999	2011-10-23 20:29:59	13470
978554279	2011-01-08 20:37:59	15182	1003463076	2011-10-24 03:44:36	17252
978730150	2011-01-10 21:29:10	11682	1003526276	2011-10-24 21:17:56	9192
979597917	2011-01-20 22:31:57	14275	1004197024	2011-11-01 15:37:04	12210
979670880	2011-01-21 18:48:00	15785	1004297801	2011-11-02 19:36:41	12584
979692483	2011-01-22 00:48:03	9206	1005151078	2011-11-12 16:37:58	29856
979927569	2011-01-24 18:06:09	9121	1005415303	2011-11-15 18:01:43	30065
980013949	2011-01-25 18:05:49	12196	1005504099	2011-11-16 18:41:39	14214
980099341	2011-01-26 17:49:01	7274	1005586846	2011-11-17 17:40:46	7199
980108079	2011-01-26 20:14:39	8094	1005663998	2011-11-18 15:06:38	12484
980372552	2011-01-29 21:42:32	14443	1005821353	2011-11-20 10:49:13	9300
980534259	2011-01-31 18:37:39	13356	1005830826	2011-11-20 13:27:06	7199
981143026	2011-02-07 19:43:46	23147	1005842021	2011-11-20 16:33:41	7875
981229608	2011-02-08 19:46:48	20861	1006962259	2011-12-03 15:44:19	7199
981324401	2011-02-09 22:06:41	9032	1007004787	2011-12-04 03:33:07	7199
981392496	2011-02-10 17:01:36	16510	1007057621	2011-12-04 18:13:41	8525
981488519	2011-02-11 19:41:59	16862	1007079499	2011-12-05 00:18:19	13638
981677582	2011-02-14 00:13:02	25907	1007141288	2011-12-05 17:28:08	12416
981845165	2011-02-15 22:46:05	9155	1007393247	2011-12-08 15:27:27	7199
981912226	2011-02-16 17:23:46	15012	1007414100	2011-12-08 21:15:00	7199
982349635	2011-02-21 18:53:55	16535	1007486740	2011-12-09 17:25:40	10831
982454117	2011-02-22 23:55:17	7199	1007502565	2011-12-09 21:49:25	15169
982518902	2011-02-23 17:55:02	29008	1008010306	2011-12-15 18:51:46	9377
983154987	2011-03-03 02:36:27	19420	1008024616	2011-12-15 22:50:16	10525
983379906	2011-03-05 17:05:06	21113	1008093670	2011-12-16 18:01:10	12527
983474553	2011-03-06 19:22:33	20924	1009039984	2011-12-27 16:53:04	21141
983735970	2011-03-09 19:59:30	19036	1009066415	2011-12-28 00:13:35	13307
983809494	2011-03-10 16:24:54	22012	1009132407	2011-12-28 18:33:27	13015
985778320	2011-04-02 11:18:40	7199	1009150609	2011-12-28 23:36:49	14478
986476312	2011-04-10 13:11:52	7199	1009227943	2011-12-29 21:05:43	12118

TABLE A.8: Lightning periods excluded from the analysis in the years 2011.

t_0 [GPS]	t_0 [UTC]	Δt [s]	t_0 [GPS]	t_0 [UTC]	Δt [s]
1009676002	2012-01-04 01:33:22	8594	1014155612	2012-02-24 21:53:32	7199
1009741324	2012-01-04 19:42:04	13966	1014560760	2012-02-29 14:26:00	12652
1009816323	2012-01-05 16:32:03	7299	1014928474	2012-03-04 20:34:34	12170
1009832750	2012-01-05 21:05:50	7199	1015280523	2012-03-08 22:22:03	10282
1009896940	2012-01-06 14:55:40	20063	1015355999	2012-03-09 19:19:59	10669
1010612747	2012-01-14 21:45:47	22018	1015387050	2012-03-10 03:57:30	10404
1010682663	2012-01-15 17:11:03	15355	1015443136	2012-03-10 19:32:16	16953
1010763765	2012-01-16 15:42:45	23021	1015466290	2012-03-11 01:58:10	11847
1010877732	2012-01-17 23:22:12	16883	1015480382	2012-03-11 05:53:02	8839
1011029532	2012-01-19 17:32:12	22645	1015543841	2012-03-11 23:30:41	18924
1011119252	2012-01-20 18:27:32	9014	1016062097	2012-03-17 23:28:17	7199
1011200554	2012-01-21 17:02:34	8378	1017343414	2012-04-01 19:23:34	23765
1011211906	2012-01-21 20:11:46	8247	1018035712	2012-04-09 19:41:52	25228
1011254799	2012-01-22 08:06:39	12570	1018116400	2012-04-10 18:06:40	8147
1011278841	2012-01-22 14:47:21	22768	1018366400	2012-04-13 15:33:20	19862
1011343788	2012-01-23 08:49:48	7750	1020635648	2012-05-09 21:54:08	7199
1011364868	2012-01-23 14:41:08	13519	1029196856	2012-08-17 00:00:56	8753
1011728821	2012-01-27 19:47:01	17417	1031111744	2012-09-08 03:55:44	11183
1011812122	2012-01-28 18:55:22	7279	1033059514	2012-09-30 16:58:34	7199
1012150692	2012-02-01 16:58:12	16919	1034103762	2012-10-12 19:02:42	7199
1012168102	2012-02-01 21:48:22	7199	1034188121	2012-10-13 18:28:41	8024
1012237907	2012-02-02 17:11:47	13077	1034197416	2012-10-13 21:03:36	7199
1012338499	2012-02-03 21:08:19	15569	1034229315	2012-10-14 05:55:15	55815
1012431875	2012-02-04 23:04:35	18963	1034865694	2012-10-21 14:41:34	13006
1012520900	2012-02-05 23:48:20	13204	1034880549	2012-10-21 18:49:09	18491
1012537214	2012-02-06 04:20:14	9836	1035522572	2012-10-29 05:09:32	18809
1012551703	2012-02-06 08:21:43	7276	1036461120	2012-11-09 01:52:00	7370
1013099510	2012-02-12 16:31:50	33127	1036877799	2012-11-13 21:36:39	14623
1013206036	2012-02-13 22:07:16	18346	1036948049	2012-11-14 17:07:29	19160
1013282917	2012-02-14 19:28:37	9445	1037036826	2012-11-15 17:47:06	21019
1013332776	2012-02-15 09:19:36	7280	1037097978	2012-11-16 10:46:18	9704
1013358113	2012-02-15 16:21:53	26193	1037202175	2012-11-17 15:42:55	7199
1013387462	2012-02-16 00:31:02	9416	1037467215	2012-11-20 17:20:15	15199
1013416439	2012-02-16 08:33:59	7424	1038177756	2012-11-28 22:42:36	9657
1013443441	2012-02-16 16:04:01	10564	1038192752	2012-11-29 02:52:32	18965
1013454368	2012-02-16 19:06:08	37313	1038229501	2012-11-29 13:05:01	7199
1013536362	2012-02-17 17:52:42	7199	1038249719	2012-11-29 18:41:59	7199
1013559588	2012-02-18 00:19:48	10282	1038678722	2012-12-04 17:52:02	10789
1013645962	2012-02-19 00:19:22	8181	1038786172	2012-12-05 23:42:52	7891
1013806270	2012-02-20 20:51:10	11442	1039987113	2012-12-19 21:18:33	7199

TABLE A.9: Lightning periods excluded from the analysis in the years 2012.

t_0 [GPS]	t_0 [UTC]	Δt [s]	t_0 [GPS]	t_0 [UTC]	Δt [s]
1041266556	2013-01-03 16:42:36	8499	1056894370	2013-07-03 13:46:10	7199
1041433501	2013-01-05 15:05:01	12026	1057703847	2013-07-12 22:37:27	7199
1041446710	2013-01-05 18:45:10	14943	1057761602	2013-07-13 14:40:02	7199
1041888238	2013-01-10 21:23:58	7418	1058021807	2013-07-16 14:56:47	7199
1041980061	2013-01-11 22:54:21	20010	1059839648	2013-08-06 15:54:08	7199
1042054746	2013-01-12 19:39:06	29227	1064339779	2013-09-27 17:56:19	7199
1042145478	2013-01-13 20:51:18	12875	1064763275	2013-10-02 15:34:35	8242
1042313278	2013-01-15 19:27:58	10798	1064789187	2013-10-02 22:46:27	8174
1042404002	2013-01-16 20:40:02	8773	1065810772	2013-10-14 18:32:52	14032
1042479701	2013-01-17 17:41:41	26618	1065977446	2013-10-16 16:50:46	16305
1043270910	2013-01-26 21:28:30	12604	1067240874	2013-10-31 07:47:54	7199
1043341984	2013-01-27 17:13:04	15404	1068033129	2013-11-09 11:52:09	7876
1043434575	2013-01-28 18:56:15	13683	1068057029	2013-11-09 18:30:29	10812
1043599631	2013-01-30 16:47:11	16053	1069105923	2013-11-21 21:52:03	11609
1044057067	2013-02-04 23:51:07	12466	1069268331	2013-11-23 18:58:51	7199
1044129099	2013-02-05 19:51:39	17314	1069517367	2013-11-26 16:09:27	16060
1044205338	2013-02-06 17:02:18	19589	1069544510	2013-11-26 23:41:50	7481
1044311989	2013-02-07 22:39:49	18967	1069656131	2013-11-28 06:42:11	14089
1044378971	2013-02-08 17:16:11	11557	1069786782	2013-11-29 18:59:42	9652
1044464972	2013-02-09 17:09:32	30163	1069865445	2013-11-30 16:50:45	7959
1044906410	2013-02-14 19:46:50	7199	1070522948	2013-12-08 07:29:08	10302
1044987673	2013-02-15 18:21:13	7199	1070550518	2013-12-08 15:08:38	15186
1045433609	2013-02-20 22:13:29	7967	1070580815	2013-12-08 23:33:35	13395
1045699587	2013-02-24 00:06:27	7199	1070824425	2013-12-11 19:13:45	13166
1046197830	2013-03-01 18:30:30	9534	1070839371	2013-12-11 23:22:51	8483
1046297358	2013-03-02 22:09:18	7199	1070994460	2013-12-13 18:27:40	19070
1046720539	2013-03-07 19:42:19	7199	1071022681	2013-12-14 02:18:01	8757
1047072034	2013-03-11 21:20:34	15952	1071078575	2013-12-14 17:49:35	12354
1047144312	2013-03-12 17:25:12	26266	1071162132	2013-12-15 17:02:12	23993
1047176855	2013-03-13 02:27:35	7890	1071254011	2013-12-16 18:33:31	18749
1048098839	2013-03-23 18:33:59	16465	1071283249	2013-12-17 02:40:49	7436
1048545873	2013-03-28 22:44:33	13232	1071357908	2013-12-17 23:25:08	7199
1048638257	2013-03-30 00:24:17	10183	1071397883	2013-12-18 10:31:23	7596
1048699002	2013-03-30 17:16:42	10428	1071418115	2013-12-18 16:08:35	19764
1048719668	2013-03-30 23:01:08	7779	1071505225	2013-12-19 16:20:25	24693
1048753509	2013-03-31 08:25:09	10276	1071603479	2013-12-20 19:37:59	21752
1048976869	2013-04-02 22:27:49	17351	1071685788	2013-12-21 18:29:48	24339
1049617111	2013-04-10 08:18:31	8835	1071775312	2013-12-22 19:21:52	25373
1050978745	2013-04-26 02:32:25	31001	1071852602	2013-12-23 16:50:02	16228
1051014482	2013-04-26 12:28:02	38371	1071870279	2013-12-23 21:44:39	13292
1051500850	2013-05-02 03:34:10	15664	1071949880	2013-12-24 19:51:20	9915
1055771230	2013-06-20 13:47:10	8243	1071962371	2013-12-24 23:19:31	8661
1056105488	2013-06-24 10:38:08	7199	1071980934	2013-12-25 04:28:54	8597
1056243343	2013-06-26 00:55:43	7199	1072052219	2013-12-26 00:16:59	16955
1056840800	2013-07-02 22:53:20	7199			

TABLE A.10: Lightning periods excluded from the analysis in the years 2013.

t_0 [GPS]	t_0 [UTC]	Δt [s]	t_0 [GPS]	t_0 [UTC]	Δt [s]
1073772870	2014-01-14 22:14:30	7384	1092858331	2014-08-23 19:45:31	18178
1073938734	2014-01-16 20:18:54	17909	1093890811	2014-09-04 18:33:31	17636
1074011335	2014-01-17 16:28:55	12347	1093920625	2014-09-05 02:50:25	7797
1074029507	2014-01-17 21:31:47	8023	1095006593	2014-09-17 16:29:53	19515
1074109731	2014-01-18 19:48:51	14009	1095091896	2014-09-18 16:11:36	14649
1074197160	2014-01-19 20:06:00	17916	1097623255	2014-10-17 23:20:55	7199
1074269745	2014-01-20 16:15:45	12029	1098313564	2014-10-25 23:06:04	7199
1074289851	2014-01-20 21:50:51	7199	1098403920	2014-10-27 00:12:00	7262
1074870725	2014-01-27 15:12:05	24333	1098417823	2014-10-27 04:03:43	7540
1074971183	2014-01-28 19:06:23	15506	1099587230	2014-11-09 16:53:50	9600
1076089117	2014-02-10 17:38:37	29474	1099708790	2014-11-11 02:39:50	10707
1076276548	2014-02-12 21:42:28	7592	1099855605	2014-11-12 19:26:45	7661
1076307943	2014-02-13 06:25:43	7199	1099866973	2014-11-12 22:36:13	16552
1076868970	2014-02-19 18:16:10	19285	1100280533	2014-11-17 17:28:53	12969
1076983695	2014-02-21 02:08:15	15543	1100537492	2014-11-20 16:51:32	34926
1077060145	2014-02-21 23:22:25	14552	1100973343	2014-11-25 17:55:43	20163
1077227479	2014-02-23 21:51:19	11763	1102187289	2014-12-09 19:08:09	15116
1077268511	2014-02-24 09:15:11	11047	1102202927	2014-12-09 23:28:47	8811
1077562214	2014-02-27 18:50:14	7199	1102355725	2014-12-11 17:55:25	21848
1077646537	2014-02-28 18:15:37	36795	1102428748	2014-12-12 14:12:28	38036
1077703260	2014-03-01 10:01:00	8736	1102522487	2014-12-13 16:14:47	7424
1077716838	2014-03-01 13:47:18	7754	1102530571	2014-12-13 18:29:31	7649
1077740891	2014-03-01 20:28:11	12670	1102538981	2014-12-13 20:49:41	7336
1078684793	2014-03-12 18:39:53	20445	1102600587	2014-12-14 13:56:27	13829
1078726776	2014-03-13 06:19:36	9626	1102692001	2014-12-15 15:20:01	21972
1078787849	2014-03-13 23:17:29	12424	1102735786	2014-12-16 03:29:46	19797
1080149319	2014-03-29 17:28:39	11134	1102773257	2014-12-16 13:54:17	24054
1080841698	2014-04-06 17:48:18	28610	1102867586	2014-12-17 16:06:26	15272
1083791144	2014-05-10 21:05:44	11534	1103128609	2014-12-20 16:36:49	7797
1086530987	2014-06-11 14:09:47	7199	1103560744	2014-12-25 16:39:04	19931
1086565830	2014-06-11 23:50:30	11274	1103734651	2014-12-27 16:57:31	22122
1087421631	2014-06-21 21:33:51	7199	1103833462	2014-12-28 20:24:22	19295
1092790871	2014-08-23 01:01:11	7199	1103918391	2014-12-29 19:59:51	9828
1092810431	2014-08-23 06:27:11	15811	1104009677	2014-12-30 21:21:17	16933

TABLE A.11: Lightning periods excluded from the analysis in the years 2014.

t_0 [GPS]	t_0 [UTC]	Δt [s]	t_0 [GPS]	t_0 [UTC]	Δt [s]
1104762437	2015-01-08 14:27:17	13924	1127140986	2015-09-24 14:43:06	21548
1104964076	2015-01-10 22:27:56	7820	1127692288	2015-09-30 23:51:28	8305
1105380618	2015-01-15 18:10:18	25095	1127746192	2015-10-01 14:49:52	19330
1105486702	2015-01-16 23:38:22	19000	1128793406	2015-10-13 17:43:26	34634
1105557574	2015-01-17 19:19:34	36072	1128831032	2015-10-14 04:10:32	8684
1105732051	2015-01-19 19:47:31	12213	1128869977	2015-10-14 14:59:37	12400
1106079474	2015-01-23 20:17:54	11984	1129398437	2015-10-20 17:47:17	23763
1106176597	2015-01-24 23:16:37	18375	1129481714	2015-10-21 16:55:14	8712
1106258269	2015-01-25 21:57:49	7199	1130253686	2015-10-30 15:21:26	25199
1106274841	2015-01-26 02:34:01	16106	1130559075	2015-11-03 04:11:15	20876
1106427172	2015-01-27 20:52:52	7199	1130598390	2015-11-03 15:06:30	23821
1106601159	2015-01-29 21:12:39	7334	1130948044	2015-11-07 16:14:04	12150
1106674871	2015-01-30 17:41:11	29059	1131035178	2015-11-08 16:26:18	9204
1106705597	2015-01-31 02:13:17	7199	1131128206	2015-11-09 18:16:46	10156
1106756153	2015-01-31 16:15:53	12149	1131140254	2015-11-09 21:37:34	7440
1106844764	2015-02-01 16:52:44	10751	1131150075	2015-11-10 00:21:15	7199
1106865150	2015-02-01 22:32:30	10229	1131304527	2015-11-11 19:15:27	31561
1106983752	2015-02-03 07:29:12	7213	1131720580	2015-11-16 14:49:40	14661
1107126377	2015-02-04 23:06:17	9659	1131809082	2015-11-17 15:24:42	13199
1107302406	2015-02-07 00:00:06	7199	1132168381	2015-11-21 19:13:01	8291
1107975988	2015-02-14 19:06:28	34289	1132250582	2015-11-22 18:03:02	7199
1108078063	2015-02-15 23:27:43	11761	1132267848	2015-11-22 22:50:48	7199
1108157705	2015-02-16 21:35:05	26819	1132308744	2015-11-23 10:12:24	8547
1108247802	2015-02-17 22:36:42	8946	1132321941	2015-11-23 13:52:21	22103
1108423022	2015-02-19 23:17:02	17256	1132406851	2015-11-24 13:27:31	7199
1108462609	2015-02-20 10:16:49	10541	1132496618	2015-11-25 14:23:38	10610
1108583844	2015-02-21 19:57:24	7199	1132530442	2015-11-25 23:47:22	28729
1108669779	2015-02-22 19:49:39	7979	1132691599	2015-11-27 20:33:19	9027
1108828249	2015-02-24 15:50:49	26270	1132708356	2015-11-28 01:12:36	21597
1108866941	2015-02-25 02:35:41	12449	1132776899	2015-11-28 20:14:59	14924
1109179299	2015-02-28 17:21:39	9092	1132950903	2015-11-30 20:35:03	10254
1109232738	2015-03-01 08:12:18	7199	1133024879	2015-12-01 17:07:59	26522
1109349435	2015-03-02 16:37:15	15078	1133057082	2015-12-02 02:04:42	9291
1109543060	2015-03-04 22:24:20	7740	1133108744	2015-12-02 16:25:44	20550
1109801373	2015-03-07 22:09:33	16895	1133282517	2015-12-04 16:41:57	44108
1109870995	2015-03-08 17:29:55	13412	1133543220	2015-12-07 17:07:00	11832
1110055411	2015-03-10 20:43:31	13500	1133626934	2015-12-08 16:22:14	8632
1110217007	2015-03-12 17:36:47	16732	1133638072	2015-12-08 19:27:52	18265
1110238668	2015-03-12 23:37:48	15491	1133736023	2015-12-09 22:40:23	9293
1110773418	2015-03-19 04:10:18	7199	1133968534	2015-12-12 15:15:34	7199
1111174949	2015-03-23 19:42:29	19706	1134661430	2015-12-20 15:43:50	11480
1111195661	2015-03-24 01:27:41	10256	1134677452	2015-12-20 20:10:52	7284
1111212636	2015-03-24 06:10:36	7451	1135101489	2015-12-25 17:58:09	23285
1111226812	2015-03-24 10:06:52	10988	1135184468	2015-12-26 17:01:08	8565
1111708351	2015-03-29 23:52:31	7960	1135193338	2015-12-26 19:28:58	10659
1111784799	2015-03-30 21:06:39	7199	1135277844	2015-12-27 18:57:24	18774
1112230194	2015-04-05 00:49:54	7199	1135300347	2015-12-28 01:12:27	9302
1125617282	2015-09-06 23:28:02	7199	1135361662	2015-12-28 18:14:22	17964
1126885220	2015-09-21 15:40:20	21184	1135537068	2015-12-30 18:57:48	8133
1127065484	2015-09-23 17:44:44	10378	1135627189	2015-12-31 19:59:49	7199
1127099337	2015-09-24 03:08:57	13636			

TABLE A.12: Lightning periods excluded from the analysis in the years 2015.

t_0 [GPS]	t_0 [UTC]	Δt [s]	t_0 [GPS]	t_0 [UTC]	Δt [s]
1135708306	2016-01-01 18:31:46	9212	1136138766	2016-01-06 18:06:06	22718
1135867314	2016-01-03 14:41:54	7199	1136200091	2016-01-07 11:08:11	11308
1135880154	2016-01-03 18:15:54	24506	1136218058	2016-01-07 16:07:38	18139
1135953590	2016-01-04 14:39:50	11416	1136246899	2016-01-08 00:08:19	20234
1135969921	2016-01-04 19:12:01	27278	1136273648	2016-01-08 07:34:08	12525
1136035664	2016-01-05 13:27:44	7687	1136303130	2016-01-08 15:45:30	12239
1136043923	2016-01-05 15:45:23	21974			

TABLE A.13: Lightning periods excluded from the analysis in the years 2016.

A.5 Bad periods (T3) discarded from scaler rate acquisition

t_0 [GPS]	t_0 [UTC]	Δt [s]	t_0 [GPS]	t_0 [UTC]	Δt [s]
823723200	2006-02-11 20:00:00	10800	830476800	2006-05-01 00:00:00	7200
824065200	2006-02-15 19:00:00	3600	836762400	2006-07-12 18:00:00	3600
824407200	2006-02-19 18:00:00	10800	836938800	2006-07-14 19:00:00	3600
824655600	2006-02-22 15:00:00	3600	849495600	2006-12-07 03:00:00	7200
830296800	2006-04-28 22:00:00	3600	851479200	2006-12-30 02:00:00	7200

TABLE A.14: Bad periods (T3) excluded from the analysis in the years 2006.

t_0 [GPS]	t_0 [UTC]	Δt [s]	t_0 [GPS]	t_0 [UTC]	Δt [s]
852148800	2007-01-06 20:00:00	7200	855270000	2007-02-11 23:00:00	3600
852228000	2007-01-07 18:00:00	3600	858016800	2007-03-15 18:00:00	10800
853005600	2007-01-16 18:00:00	21600	858049200	2007-03-16 03:00:00	3600
853095600	2007-01-17 19:00:00	32400	858574800	2007-03-22 05:00:00	7200
853167600	2007-01-18 15:00:00	3600	858603600	2007-03-22 13:00:00	14400
853437600	2007-01-21 18:00:00	3600	879292800	2007-11-17 00:00:00	54000
853902000	2007-01-27 03:00:00	3600	882594000	2007-12-25 05:00:00	10800

TABLE A.15: Bad periods (T3) excluded from the analysis in the year 2007.

t_0 [GPS]	t_0 [UTC]	Δt [s]	t_0 [GPS]	t_0 [UTC]	Δt [s]
885067200	2008-01-22 20:00:00	7200	888861600	2008-03-06 18:00:00	7200
885315600	2008-01-25 17:00:00	3600	901044000	2008-07-25 18:00:00	10800
885517200	2008-01-28 01:00:00	7200	901306800	2008-07-28 19:00:00	14400
886356000	2008-02-06 18:00:00	7200	901479600	2008-07-30 19:00:00	3600
888004800	2008-02-25 20:00:00	7200	901983600	2008-08-05 15:00:00	3600
888282000	2008-02-29 01:00:00	10800	911664000	2008-11-25 16:00:00	3600
888541200	2008-03-03 01:00:00	7200	912121200	2008-11-30 23:00:00	10800
888822000	2008-03-06 07:00:00	3600			

TABLE A.16: Bad periods (T3) excluded from the analysis in the year 2008.

t_0 [GPS]	t_0 [UTC]	Δt [s]	t_0 [GPS]	t_0 [UTC]	Δt [s]
915732000	2009-01-11 18:00:00	3600	922143600	2009-03-26 23:00:00	7200
918687600	2009-02-14 23:00:00	3600	926164800	2009-05-12 12:00:00	3600
919256400	2009-02-21 13:00:00	3600	926848800	2009-05-20 10:00:00	3600
919886400	2009-02-28 20:00:00	3600	941907600	2009-11-10 17:00:00	7200
920844000	2009-03-11 22:00:00	7200	946256400	2009-12-31 01:00:00	3600
921553200	2009-03-20 03:00:00	3600			

TABLE A.17: Bad periods (T3) excluded from the analysis in the year 2009.

t_0 [GPS]	t_0 [UTC]	Δt [s]	t_0 [GPS]	t_0 [UTC]	Δt [s]
948578400	2010-01-26 22:00:00	7200	975610800	2010-12-05 19:00:00	7200
950238000	2010-02-15 03:00:00	3600	977439600	2010-12-26 23:00:00	3600
951260400	2010-02-26 23:00:00	3600	977511600	2010-12-27 19:00:00	3600
952394400	2010-03-12 02:00:00	7200	977594400	2010-12-28 18:00:00	3600
953715600	2010-03-27 09:00:00	7200	977684400	2010-12-29 19:00:00	10800

TABLE A.18: Bad periods (T3) excluded from the analysis in the year 2010.

t_0 [GPS]	t_0 [UTC]	Δt [s]	t_0 [GPS]	t_0 [UTC]	Δt [s]
978174000	2011-01-04 11:00:00	10800	983480400	2011-03-06 21:00:00	7200
978206400	2011-01-04 20:00:00	14400	983739600	2011-03-09 21:00:00	7200
978393600	2011-01-07 00:00:00	7200	983822400	2011-03-10 20:00:00	3600
979675200	2011-01-21 20:00:00	3600	986590800	2011-04-11 21:00:00	3600
980020800	2011-01-25 20:00:00	3600	987901200	2011-04-27 01:00:00	14400
980380800	2011-01-30 00:00:00	3600	988041600	2011-04-28 16:00:00	14400
981244800	2011-02-09 00:00:00	3600	993675600	2011-07-02 21:00:00	3600
981320400	2011-02-09 21:00:00	7200	996361200	2011-08-02 23:00:00	3600
981680400	2011-02-14 01:00:00	10800	1007085600	2011-12-05 02:00:00	3600
981921600	2011-02-16 20:00:00	3600	1007146800	2011-12-05 19:00:00	3600
982357200	2011-02-21 21:00:00	7200	1007488800	2011-12-09 18:00:00	7200
982522800	2011-02-23 19:00:00	21600	1009044000	2011-12-27 18:00:00	3600
983160000	2011-03-03 04:00:00	10800	1009231200	2011-12-29 22:00:00	7200
983394000	2011-03-05 21:00:00	3600			

TABLE A.19: Bad periods (T3) excluded from the analysis in the year 2011.

t_0 [GPS]	t_0 [UTC]	Δt [s]	t_0 [GPS]	t_0 [UTC]	Δt [s]
1009836000	2012-01-05 22:00:00	3600	1013482800	2012-02-17 03:00:00	3600
1010689200	2012-01-15 19:00:00	3600	1013562000	2012-02-18 01:00:00	3600
1010887200	2012-01-18 02:00:00	7200	1013806800	2012-02-20 21:00:00	7200
1011286800	2012-01-22 17:00:00	3600	1014566400	2012-02-29 16:00:00	3600
1011733200	2012-01-27 21:00:00	10800	1017345600	2012-04-01 20:00:00	172800
1012154400	2012-02-01 18:00:00	3600	1018036800	2012-04-09 20:00:00	21600
1012341600	2012-02-03 22:00:00	7200	1018119600	2012-04-10 19:00:00	75600
1012438800	2012-02-05 01:00:00	3600	1018375200	2012-04-13 18:00:00	3600
1012525200	2012-02-06 01:00:00	18000	1035529200	2012-10-29 07:00:00	3600
1013101200	2012-02-12 17:00:00	158400	1036879200	2012-11-13 22:00:00	7200
1013284800	2012-02-14 20:00:00	3600	1037098800	2012-11-16 11:00:00	7200
1013364000	2012-02-15 18:00:00	18000	1038196800	2012-11-29 04:00:00	10800

TABLE A.20: Bad periods (T3) excluded from the analysis in the year 2012.

t_0 [GPS]	t_0 [UTC]	Δt [s]	t_0 [GPS]	t_0 [UTC]	Δt [s]
1041451200	2013-01-05 20:00:00	3600	1062424800	2013-09-05 14:00:00	18000
1042077600	2013-01-13 02:00:00	3600	1068033600	2013-11-09 12:00:00	3600
1042480800	2013-01-17 18:00:00	10800	1068058800	2013-11-09 19:00:00	3600
1043438400	2013-01-28 20:00:00	3600	1069110000	2013-11-21 23:00:00	3600
1043604000	2013-01-30 18:00:00	3600	1069524000	2013-11-26 18:00:00	3600
1044061200	2013-02-05 01:00:00	7200	1069545600	2013-11-27 00:00:00	3600
1044313200	2013-02-07 23:00:00	14400	1070524800	2013-12-08 08:00:00	7200
1044478800	2013-02-09 21:00:00	10800	1070553600	2013-12-08 16:00:00	7200
1050991200	2013-04-26 06:00:00	3600	1070830800	2013-12-11 21:00:00	3600
1051038000	2013-04-26 19:00:00	3600	1070996400	2013-12-13 19:00:00	3600
1053457200	2013-05-24 19:00:00	3600	1071025200	2013-12-14 03:00:00	3600
1056103200	2013-06-24 10:00:00	3600	1071165600	2013-12-15 18:00:00	18000
1057482000	2013-07-10 09:00:00	3600	1071262800	2013-12-16 21:00:00	3600
1057644000	2013-07-12 06:00:00	3600	1071432000	2013-12-18 20:00:00	3600
1057910400	2013-07-15 08:00:00	3600	1071507600	2013-12-19 17:00:00	18000
1057989600	2013-07-16 06:00:00	3600	1071604800	2013-12-20 20:00:00	14400
1060102800	2013-08-09 17:00:00	7200	1071691200	2013-12-21 20:00:00	7200
1060376400	2013-08-12 21:00:00	7200	1071784800	2013-12-22 22:00:00	10800
1060430400	2013-08-13 12:00:00	10800	1071856800	2013-12-23 18:00:00	21600
1060538400	2013-08-14 18:00:00	7200	1072058400	2013-12-26 02:00:00	7200
1060621200	2013-08-15 17:00:00	7200	1072252800	2013-12-28 08:00:00	32400
1061229600	2013-08-22 18:00:00	7200			

TABLE A.21: Bad periods (T3) excluded from the analysis in the year 2013.

t_0 [GPS]	t_0 [UTC]	Δt [s]	t_0 [GPS]	t_0 [UTC]	Δt [s]
1074200400	2014-01-19 21:00:00	10800	1095012000	2014-09-17 18:00:00	7200
1074542400	2014-01-23 20:00:00	10800	1095098400	2014-09-18 18:00:00	3600
1074585600	2014-01-24 08:00:00	3600	1099591200	2014-11-09 18:00:00	3600
1074880800	2014-01-27 18:00:00	3600	1099868400	2014-11-12 23:00:00	10800
1074981600	2014-01-28 22:00:00	3600	1100538000	2014-11-20 17:00:00	3600
1076094000	2014-02-10 19:00:00	18000	1100559600	2014-11-20 23:00:00	10800
1076871600	2014-02-19 19:00:00	7200	1100980800	2014-11-25 20:00:00	10800
1076986800	2014-02-21 03:00:00	10800	1102031934	2014-12-07 23:58:54	43535
1077066000	2014-02-22 01:00:00	3600	1102204800	2014-12-10 00:00:00	3600
1077274800	2014-02-24 11:00:00	3600	1102246014	2014-12-10 11:26:54	957
1077652800	2014-02-28 20:00:00	28800	1102359600	2014-12-11 19:00:00	7200
1077706800	2014-03-01 11:00:00	3600	1102442400	2014-12-12 18:00:00	18000
1077742800	2014-03-01 21:00:00	3600	1102483510	2014-12-13 05:25:10	685
1080151200	2014-03-29 18:00:00	3600	1102556119	2014-12-14 01:35:19	652
1080849600	2014-04-06 20:00:00	18000	1102600800	2014-12-14 14:00:00	10800
1081609200	2014-04-15 15:00:00	68400	1102698000	2014-12-15 17:00:00	14400
1082242800	2014-04-22 23:00:00	36000	1102741200	2014-12-16 05:00:00	10800
1083794400	2014-05-10 22:00:00	7200	1102777200	2014-12-16 15:00:00	18000
1084262400	2014-05-16 08:00:00	3600	1102870800	2014-12-17 17:00:00	3600
1084676400	2014-05-21 03:00:00	3600	1102893477	2014-12-17 23:17:57	643
1085302800	2014-05-28 09:00:00	3600	1102951145	2014-12-18 15:19:05	4505
1086570000	2014-06-12 01:00:00	3600	1103130000	2014-12-20 17:00:00	3600
1090720800	2014-07-30 02:00:00	3600	1103437268	2014-12-24 06:21:08	913
1092812400	2014-08-23 07:00:00	10800	1103738413	2014-12-27 18:00:13	1782
1092866400	2014-08-23 22:00:00	7200	1103749200	2014-12-27 21:00:00	3600
1093896000	2014-09-04 20:00:00	3600	1103839200	2014-12-28 22:00:00	7200
1093921200	2014-09-05 03:00:00	3600	1104012000	2014-12-30 22:00:00	14400

TABLE A.22: Bad periods (T3) excluded from the analysis in the year 2014.

t_0 [GPS]	t_0 [UTC]	Δt [s]	t_0 [GPS]	t_0 [UTC]	Δt [s]
1105498800	2015-01-17 03:00:00	3600	1127070000	2015-09-23 19:00:00	3600
1106082000	2015-01-23 21:00:00	3600	1127106000	2015-09-24 05:00:00	3600
1106179200	2015-01-25 00:00:00	7200	1127145600	2015-09-24 16:00:00	10800
1106679600	2015-01-30 19:00:00	3600	1127750400	2015-10-01 16:00:00	10800
1107129600	2015-02-05 00:00:00	3600	1128798000	2015-10-13 19:00:00	28800
1107979200	2015-02-14 20:00:00	25200	1128870000	2015-10-14 15:00:00	3600
1108083600	2015-02-16 01:00:00	3600	1129406400	2015-10-20 20:00:00	10800
1108170000	2015-02-17 01:00:00	10800	1130259600	2015-10-30 17:00:00	14400
1108839600	2015-02-24 19:00:00	10800	1130562000	2015-11-03 05:00:00	14400
1109466000	2015-03-04 01:00:00	428400	1130601600	2015-11-03 16:00:00	18000
1110067200	2015-03-11 00:00:00	25200	1131037200	2015-11-08 17:00:00	3600
1110218400	2015-03-12 18:00:00	10800	1131134400	2015-11-09 20:00:00	10800
1110243600	2015-03-13 01:00:00	3600	1131332400	2015-11-12 03:00:00	3600
1110837600	2015-03-19 22:00:00	61200	1131724800	2015-11-16 16:00:00	3600
1111179600	2015-03-23 21:00:00	3600	1131814800	2015-11-17 17:00:00	7200
1111575600	2015-03-28 11:00:00	3600	1132326000	2015-11-23 15:00:00	14400
1118232000	2015-06-13 12:00:00	14400	1132531200	2015-11-26 00:00:00	25200
1120384800	2015-07-08 10:00:00	3600	1132711200	2015-11-28 02:00:00	14400
1120446000	2015-07-09 03:00:00	3600	1132779600	2015-11-28 21:00:00	7200
1121284800	2015-07-18 20:00:00	3600	1133028000	2015-12-01 18:00:00	18000
1123470000	2015-08-13 03:00:00	3600	1133118000	2015-12-02 19:00:00	7200
1123876800	2015-08-17 20:00:00	3600	1133647200	2015-12-08 22:00:00	3600
1124679600	2015-08-27 03:00:00	3600	1134680400	2015-12-20 21:00:00	3600
1126886400	2015-09-21 16:00:00	97200	1135108800	2015-12-25 20:00:00	10800

TABLE A.23: Bad periods (T3) excluded from the analysis in the year 2015.

t_0 [GPS]	t_0 [UTC]	Δt [s]	t_0 [GPS]	t_0 [UTC]	Δt [s]
1135972800	2016-01-04 20:00:00	3600	1136149200	2016-01-06 21:00:00	7200
1136048400	2016-01-05 17:00:00	10800	1136203200	2016-01-07 12:00:00	32400

TABLE A.24: Bad periods (T3) excluded from the analysis in the year 2016.

Appendix B

CORSIKA and $\overline{\text{Off}\underline{\text{line}}}$ simulations of Auger SD scalers

B.1 CORSIKA air shower simulation

The CORSIKA input file is shown, e.g., input file of photon-induced shower at 1 PeV and Crab zenith $\theta = 57.2^\circ$ at Auger site.

```
RUNNR   3665
EVTNR   1
NSHOW   2000
PRMPAR   1
ERANGE   1.E6   1.E6
THETAP   57.2   57.2
PHIP   359.3   359.3
SEED   3665   0   0
SEED   3675   0   0
MAGNET   20.4   -14.3
ARRANG   2.92
OBSLEV   145200
ATMOD   21
FIXCHI   0.
HADFLG   0   0   0   0   0   2
ECUTS   0.05   0.01   0.0008   0.0008
MUADDI   T
```

```
MUMULT   T
ELMFLG   T   T
STEPFC   1.0
RADNKG   200.E2
LONGI    T   10   T   T
ECTMAP   1.E1
MAXPRT   1
DIRECT   '/home/ahmed/sdsimout/'
PAROUT   T   F
USER   'saleh'
DEBUG   F   6   F   1000000
EXIT
```

The corresponding azimuth angles ϕ are following the trajectory of the Crab at Auger sky. The atmospheric and magnetic field parameters are set for Malargüe.

Longitudinal shower profiles Longitudinal shower profiles of secondaries of photon-induced showers at multi-TeV and different Crab zenith angles are shown:

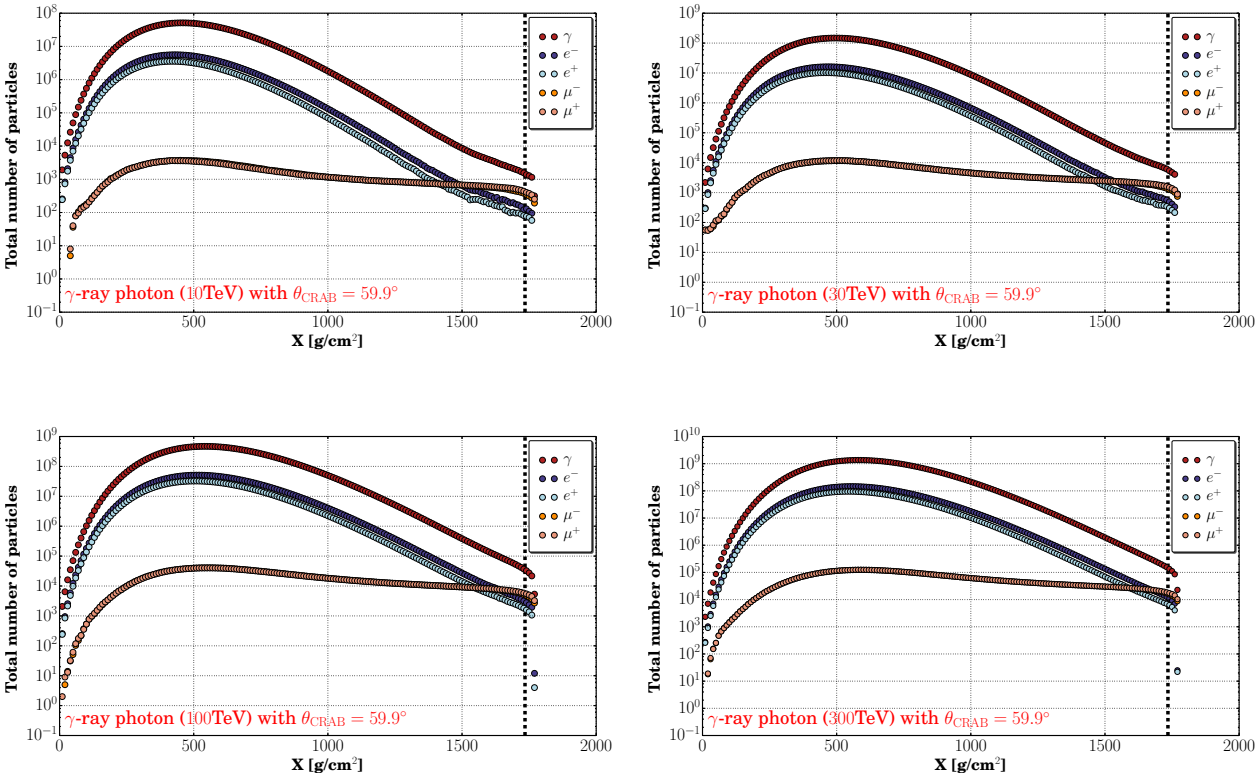

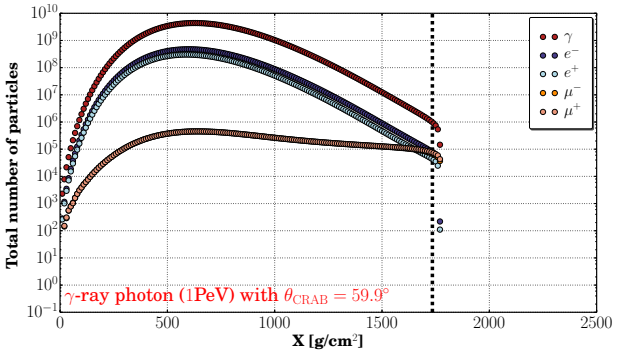

FIGURE B.1: Longitudinal shower profiles of secondaries of photon-induced showers at multi-TeV energies from the direction of the Crab nebula ($\theta_{CRAB} = 59.9°$) with respect to Auger site. The secondaries from inclined photon-induced showers reach the ground level at the Pierre Auger Observatory. The black vertical dashed lines indicate atmospheric depth values at the ground.

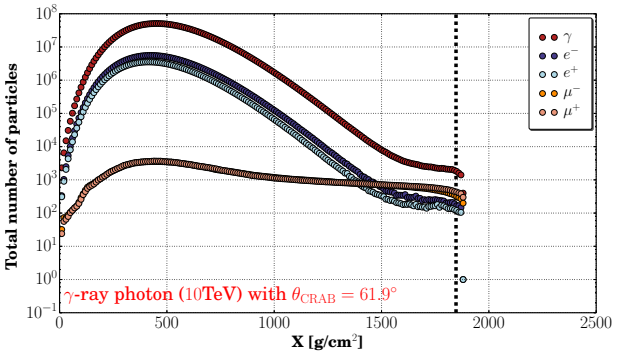

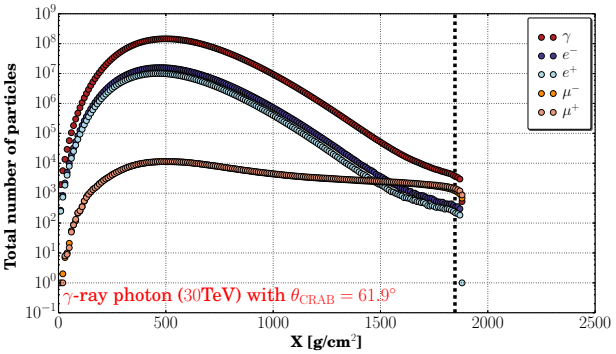

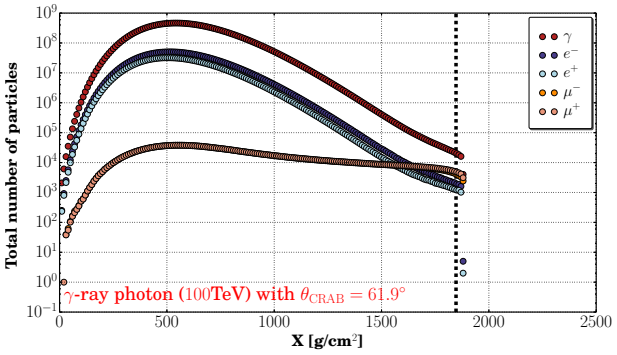

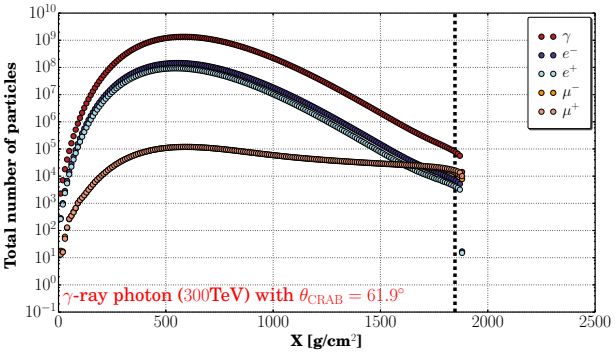

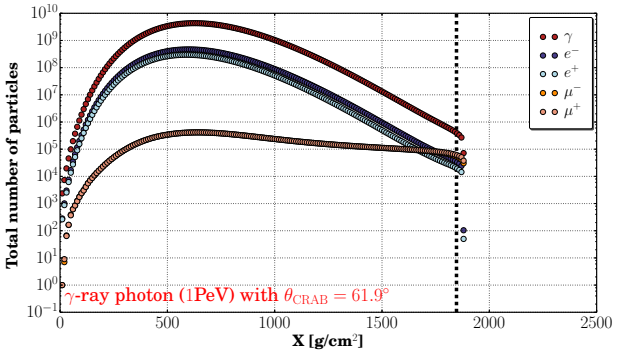

FIGURE B.2: Longitudinal shower profiles of secondaries of photon-induced showers at multi-TeV energies from the direction of the Crab nebula ($\theta_{CRAB} = 61.9°$) with respect to Auger site. The secondaries from inclined photon-induced showers reach the ground level at the Pierre Auger Observatory. The black vertical dashed lines indicate atmospheric depth values at the ground.

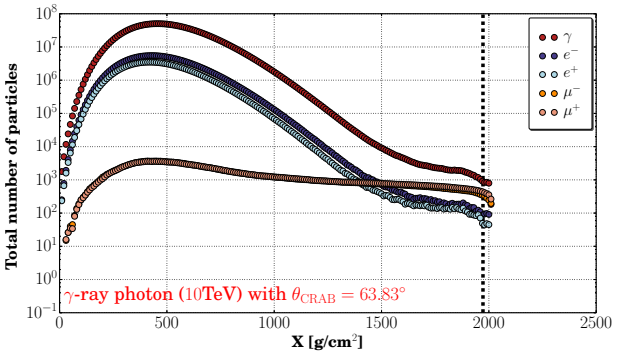

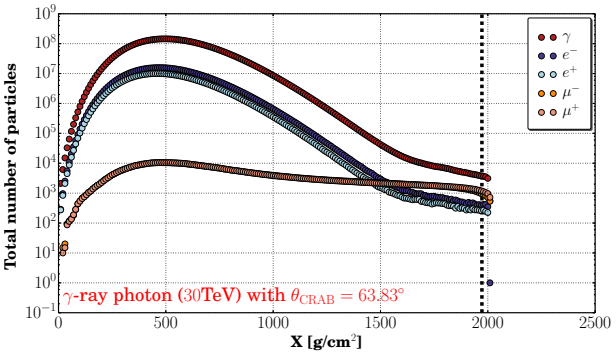

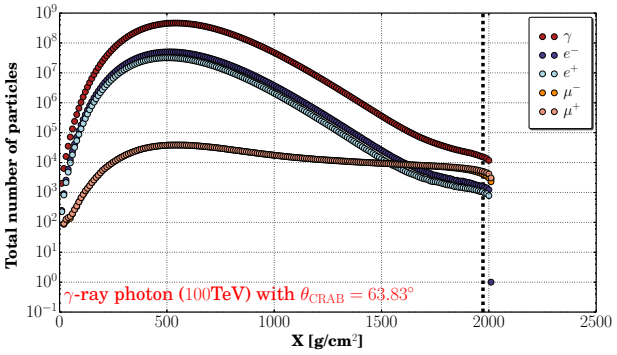

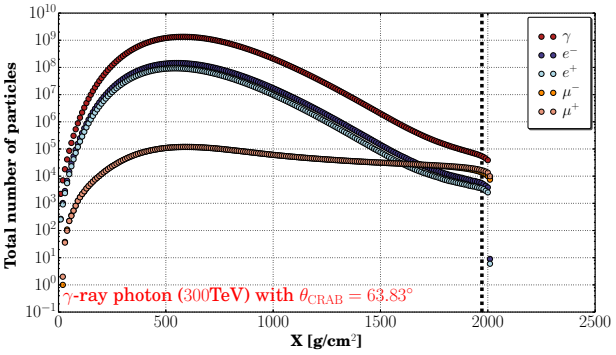

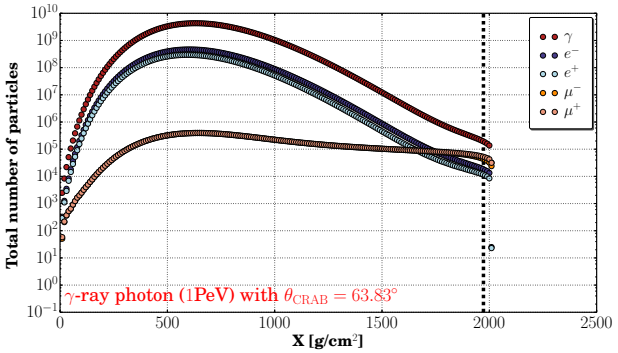

FIGURE B.3: Longitudinal shower profiles of secondaries of photon-induced showers at multi-TeV energies from the direction of the Crab nebula ($\theta_{CRAB} = 63.8°$) with respect to Auger site. The secondaries from inclined photon-induced showers reach the ground level at the Pierre Auger Observatory. The black vertical dashed lines indicate atmospheric depth values at the ground.

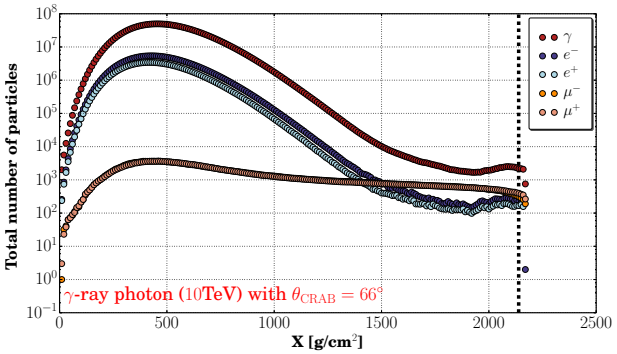

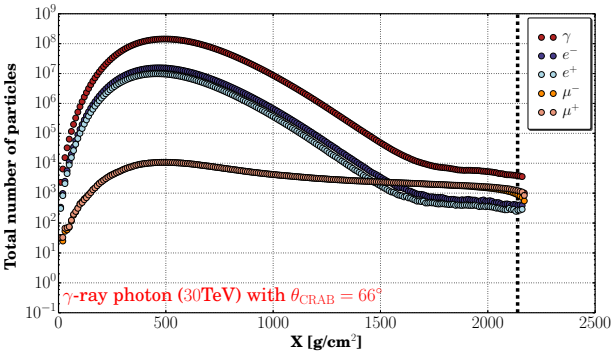

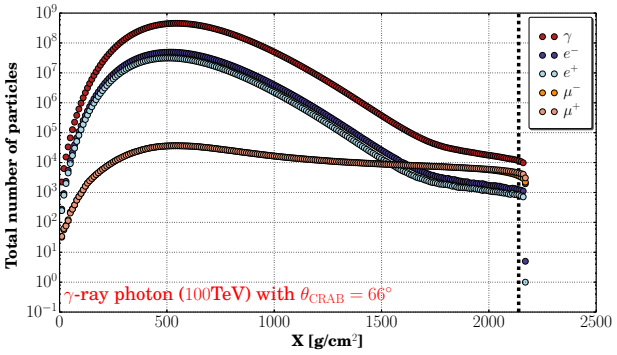

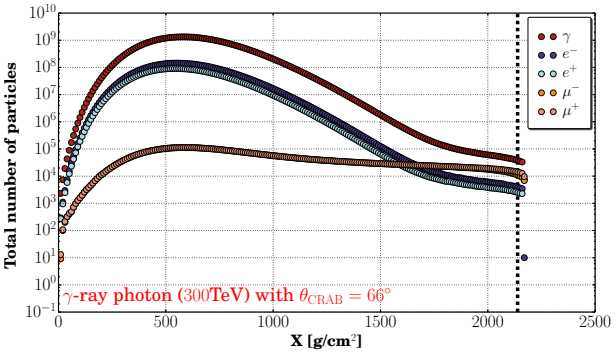

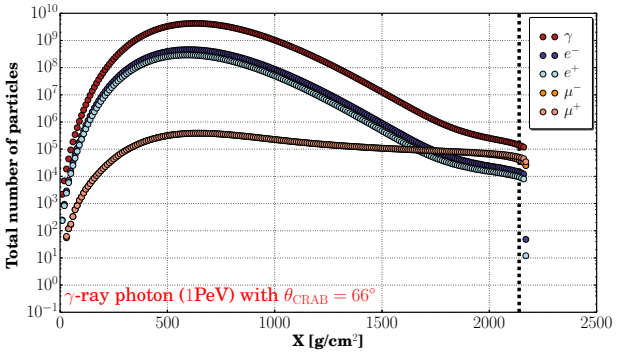

FIGURE B.4: Longitudinal shower profiles of secondaries of photon-induced showers at multi-TeV energies from the direction of the Crab nebula ($\theta_{CRAB} = 66°$) with respect to Auger site. The secondaries from inclined photon-induced showers reach the ground level at the Pierre Auger Observatory. The black vertical dashed lines indicate atmospheric depth values at the ground.

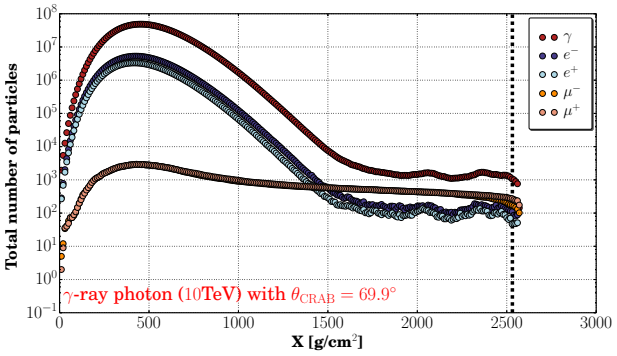

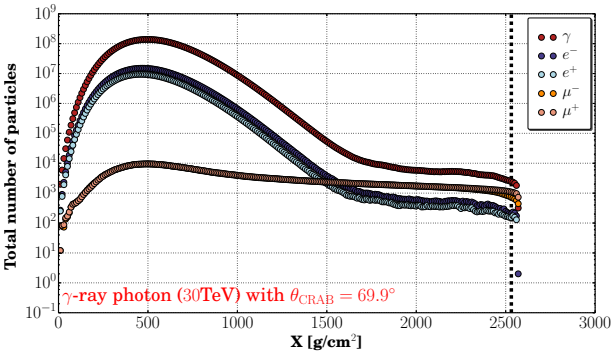

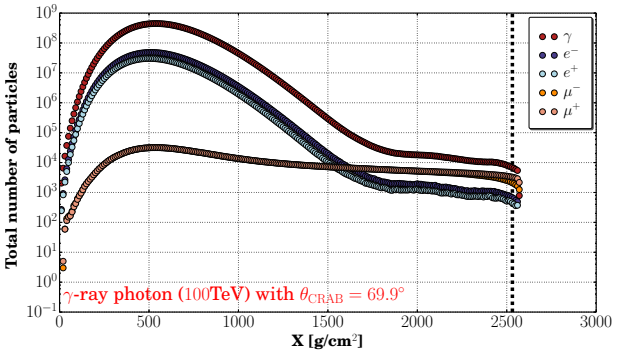

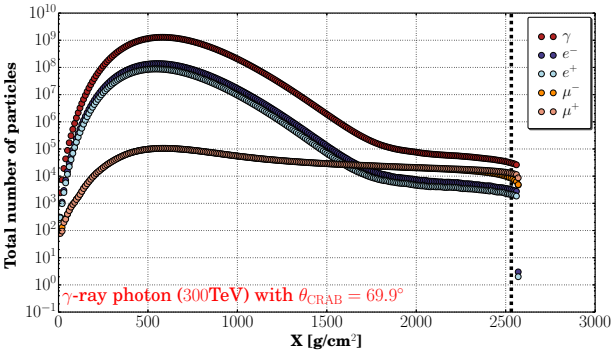

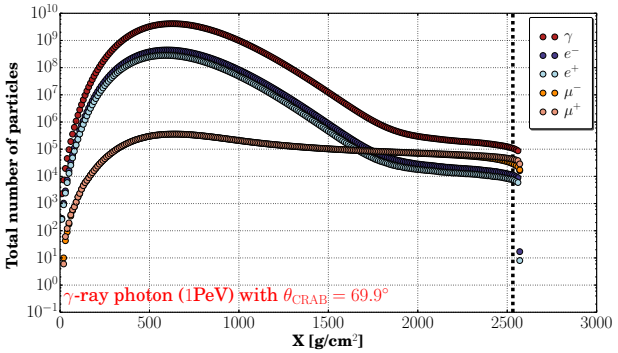

FIGURE B.5: Longitudinal shower profiles of secondaries of photon-induced showers at multi-TeV energies from the direction of the Crab nebula ($\theta_{CRAB} = 69.9°$) with respect to Auger site. The secondaries from inclined photon-induced showers reach the ground level at the Pierre Auger Observatory. The black vertical dashed lines indicate atmospheric depth values at the ground.

Lateral distribution of secondaries Lateral distribution of secondaries of photon-induced showers at multi-TeV and different Crab zenith angles are shown:

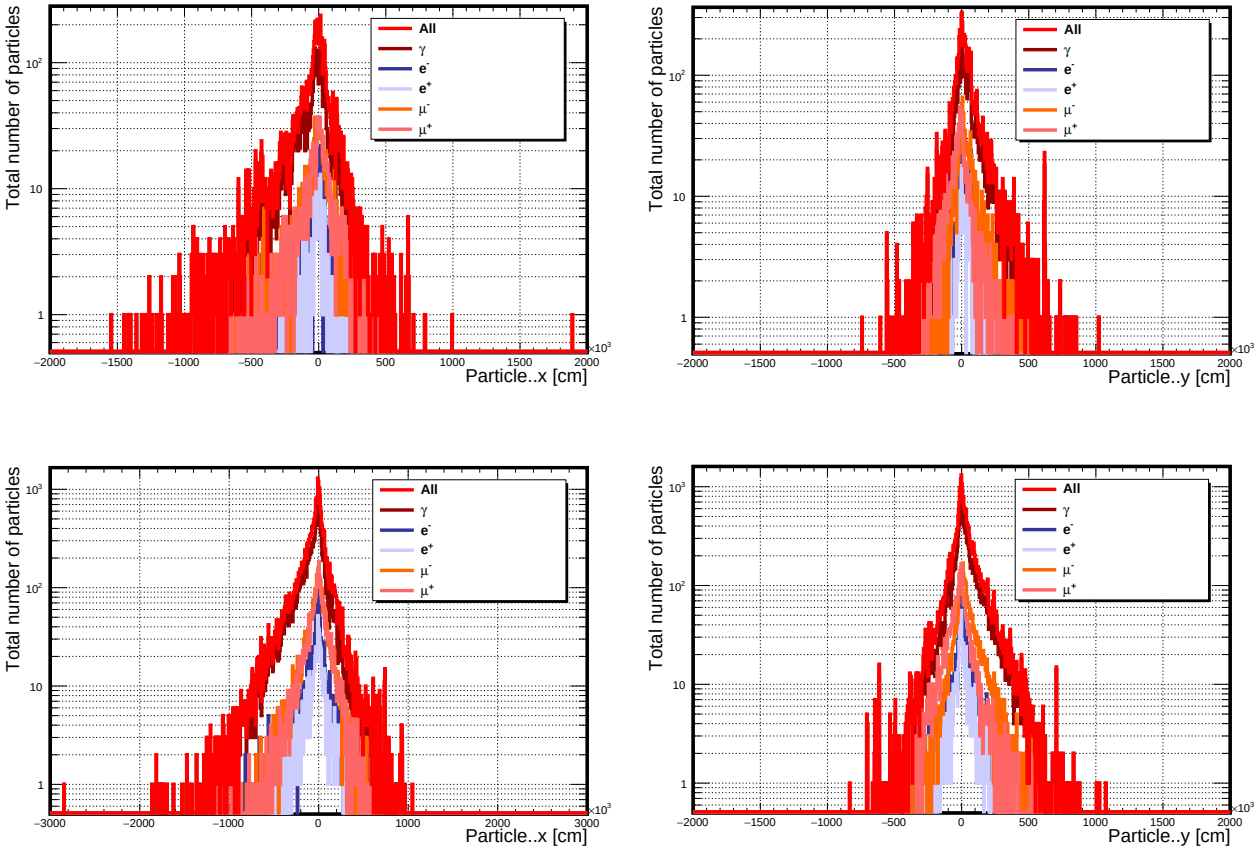

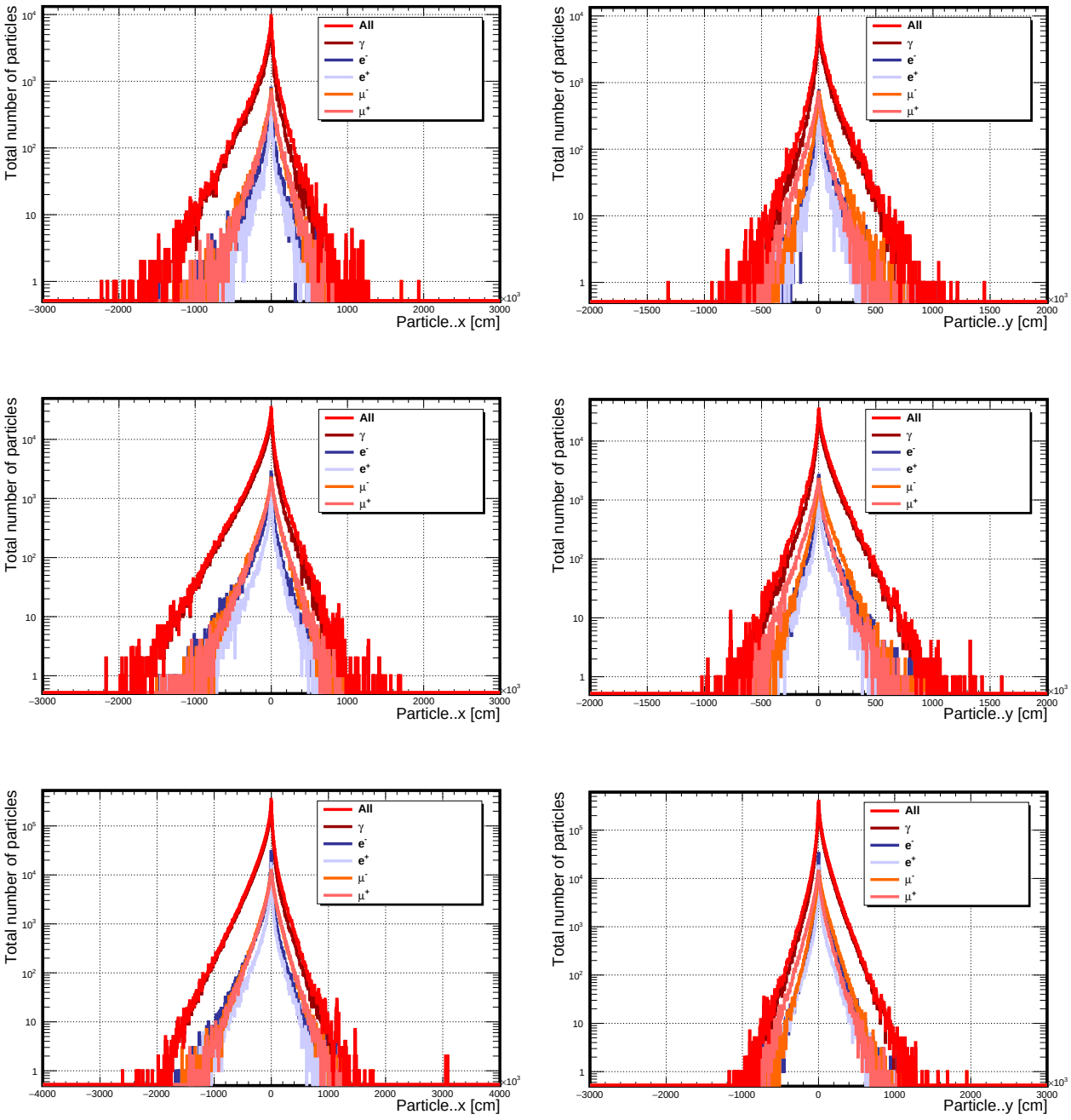

FIGURE B.6: Lateral distribution of secondaries resulted from γ-ray showers at multi-TeV energies, with zenith angle 59.9°.

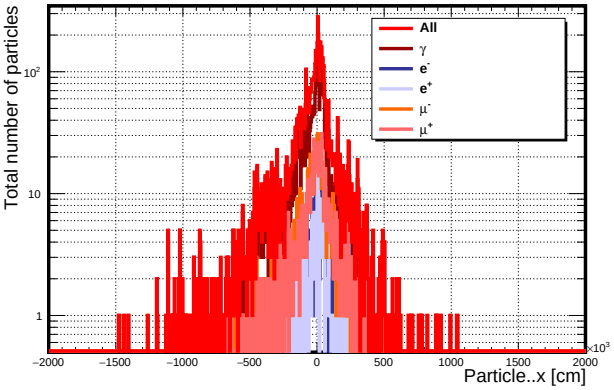
All
γ
e⁻
e⁺
μ⁻
μ⁺
Total number of particles
Particle..x [cm]

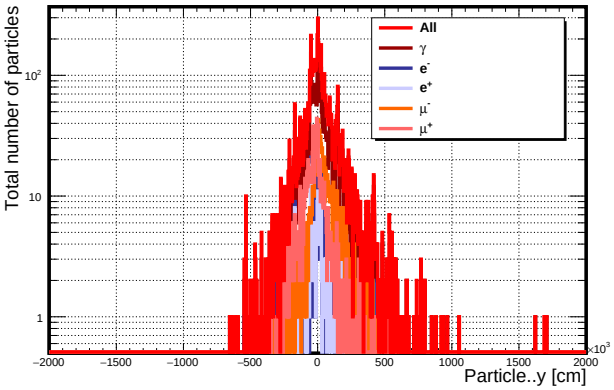
All
γ
e⁻
e⁺
μ⁻
μ⁺
Total number of particles
Particle..y [cm]

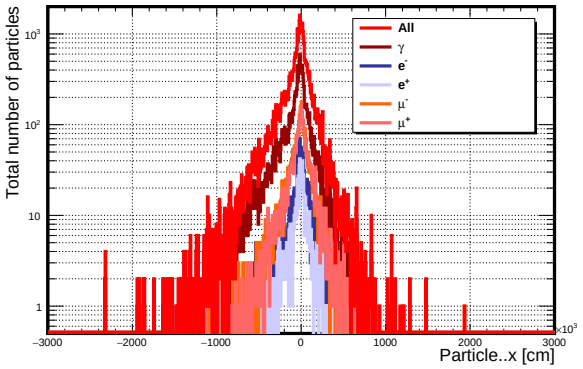
All
γ
e⁻
e⁺
μ⁻
μ⁺
Total number of particles
Particle..x [cm]

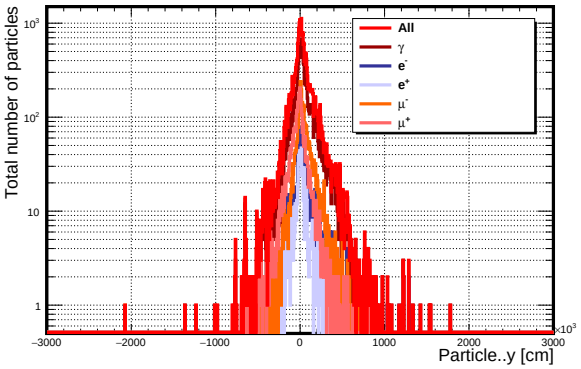
All
γ
e⁻
e⁺
μ⁻
μ⁺
Total number of particles
Particle..y [cm]

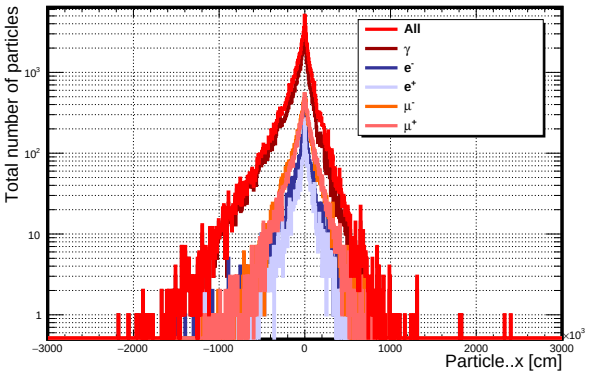
All
γ
e⁻
e⁺
μ⁻
μ⁺
Total number of particles
Particle..x [cm]

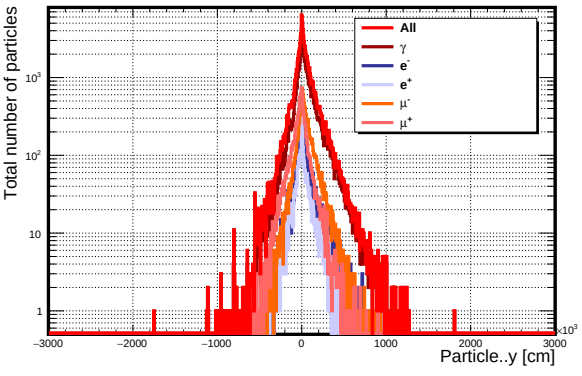
All
γ
e⁻
e⁺
μ⁻
μ⁺
Total number of particles
Particle..y [cm]

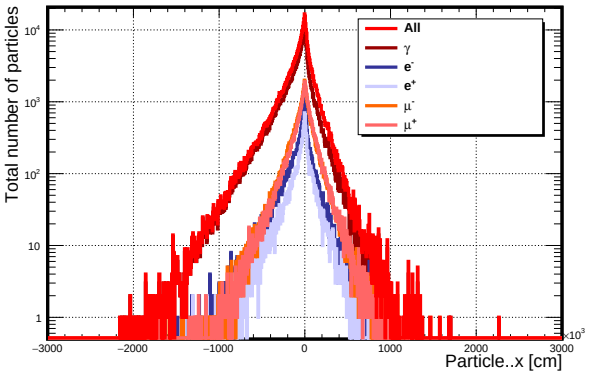
All
γ
e⁻
e⁺
μ⁻
μ⁺
Total number of particles
Particle..x [cm]

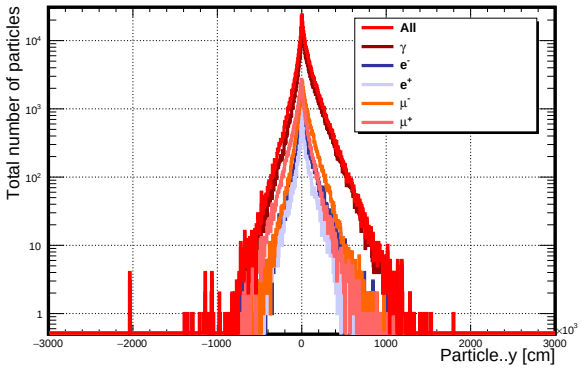
All
γ
e⁻
e⁺
μ⁻
μ⁺
Total number of particles
Particle..y [cm]

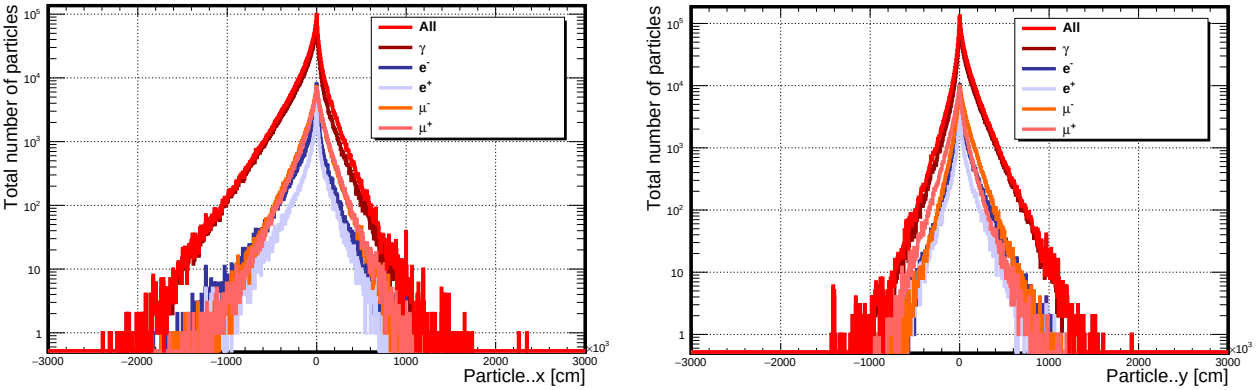

FIGURE B.7: Lateral distribution of secondaries resulted from γ-ray showers at multi-TeV energies, with zenith angle 61.9°.

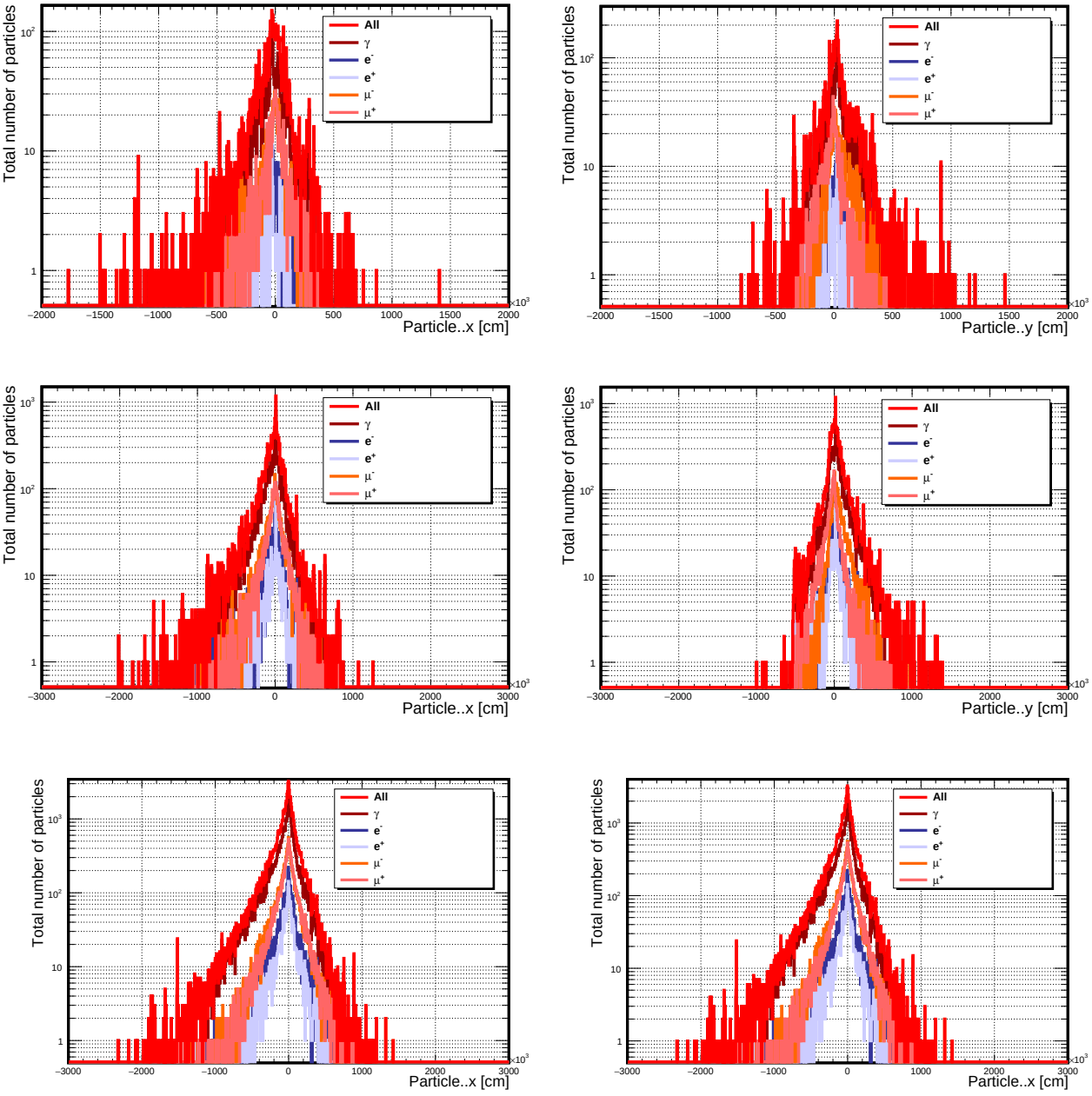

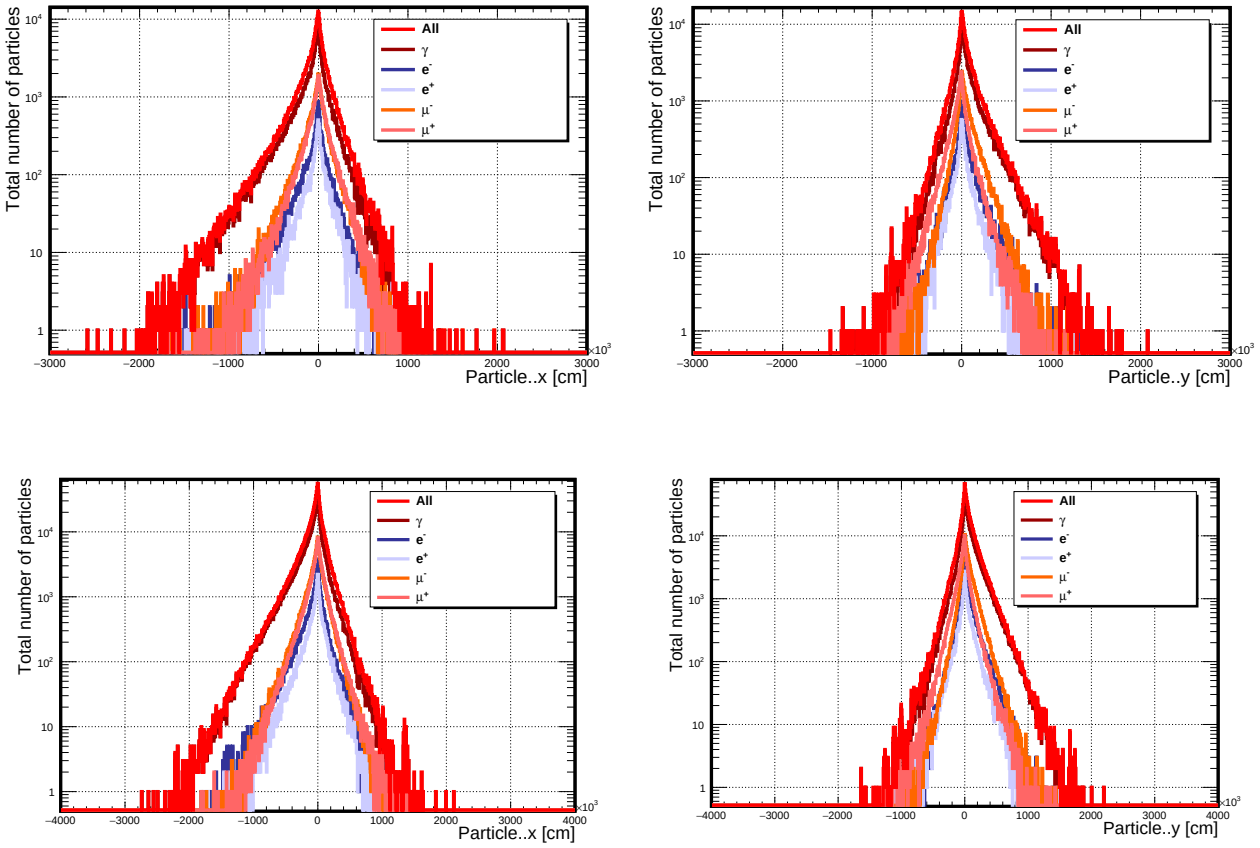

FIGURE B.8: Lateral distribution of secondaries resulted from γ-ray showers at multi-TeV energies, with zenith angle 63.8°.

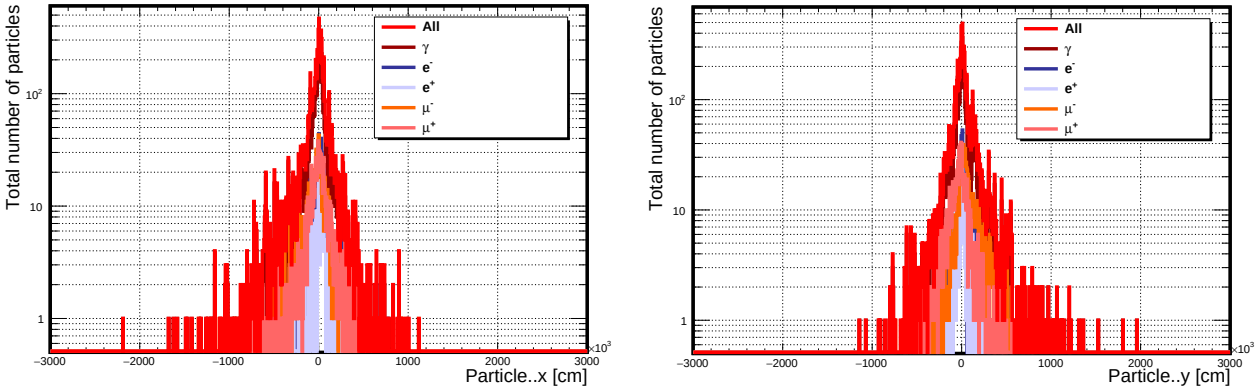

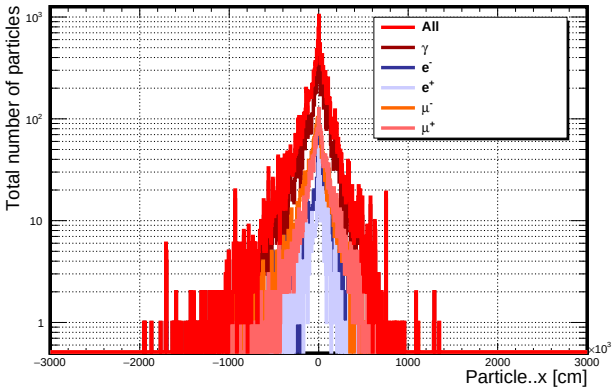
Total number of particles
Particle..x [cm]
All
γ
e⁻
e⁺
μ⁻
μ⁺

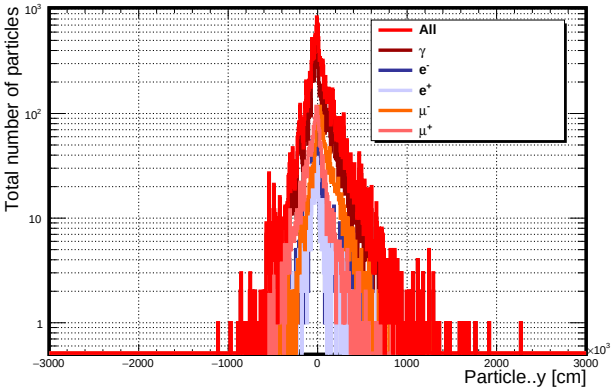
Total number of particles
Particle..y [cm]
All
γ
e⁻
e⁺
μ⁻
μ⁺

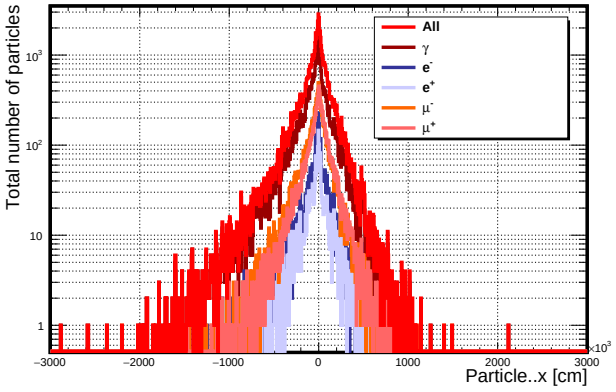
Total number of particles
Particle..x [cm]
All
γ
e⁻
e⁺
μ⁻
μ⁺

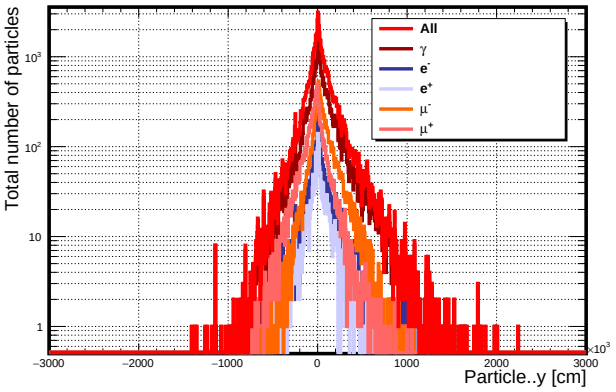
Total number of particles
Particle..y [cm]
All
γ
e⁻
e⁺
μ⁻
μ⁺

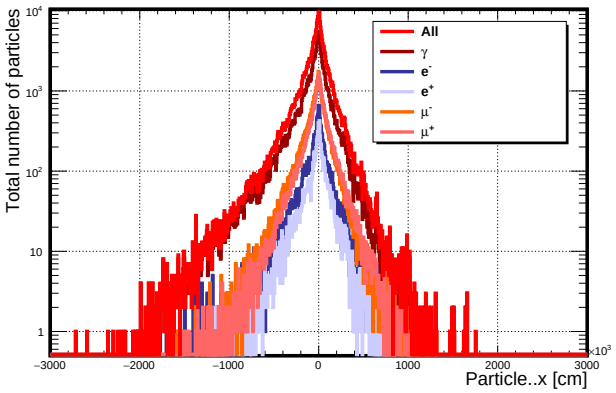
Total number of particles
Particle..x [cm]
All
γ
e⁻
e⁺
μ⁻
μ⁺

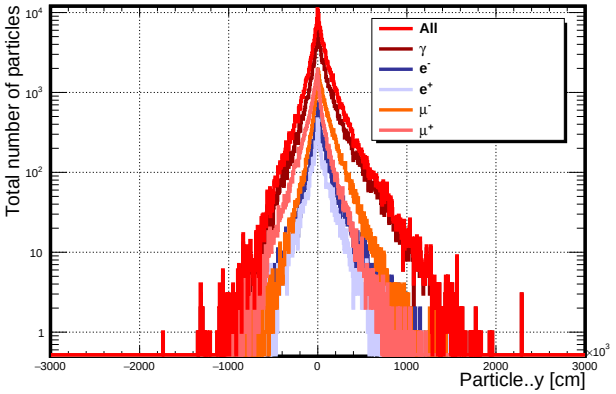
Total number of particles
Particle..y [cm]
All
γ
e⁻
e⁺
μ⁻
μ⁺

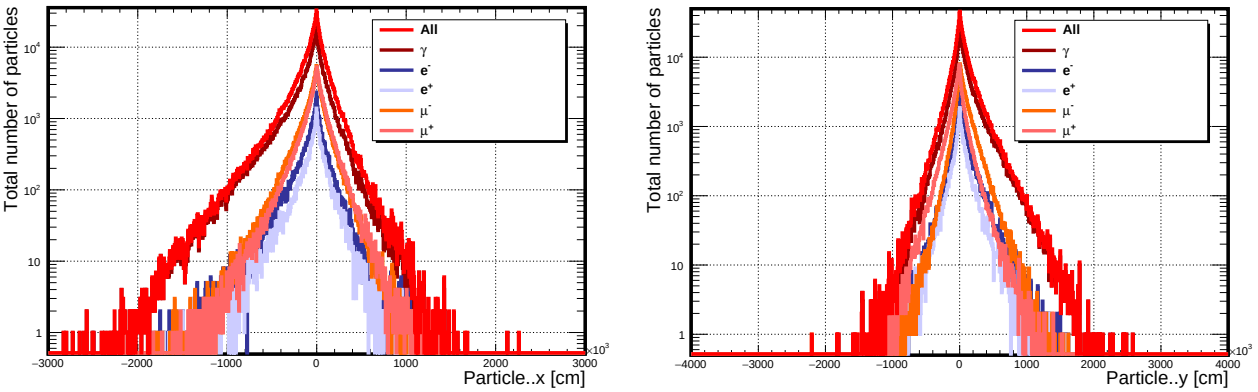

FIGURE B.9: Lateral distribution of secondaries resulted from γ-ray showers at multi-TeV energies, with zenith angle 66°.

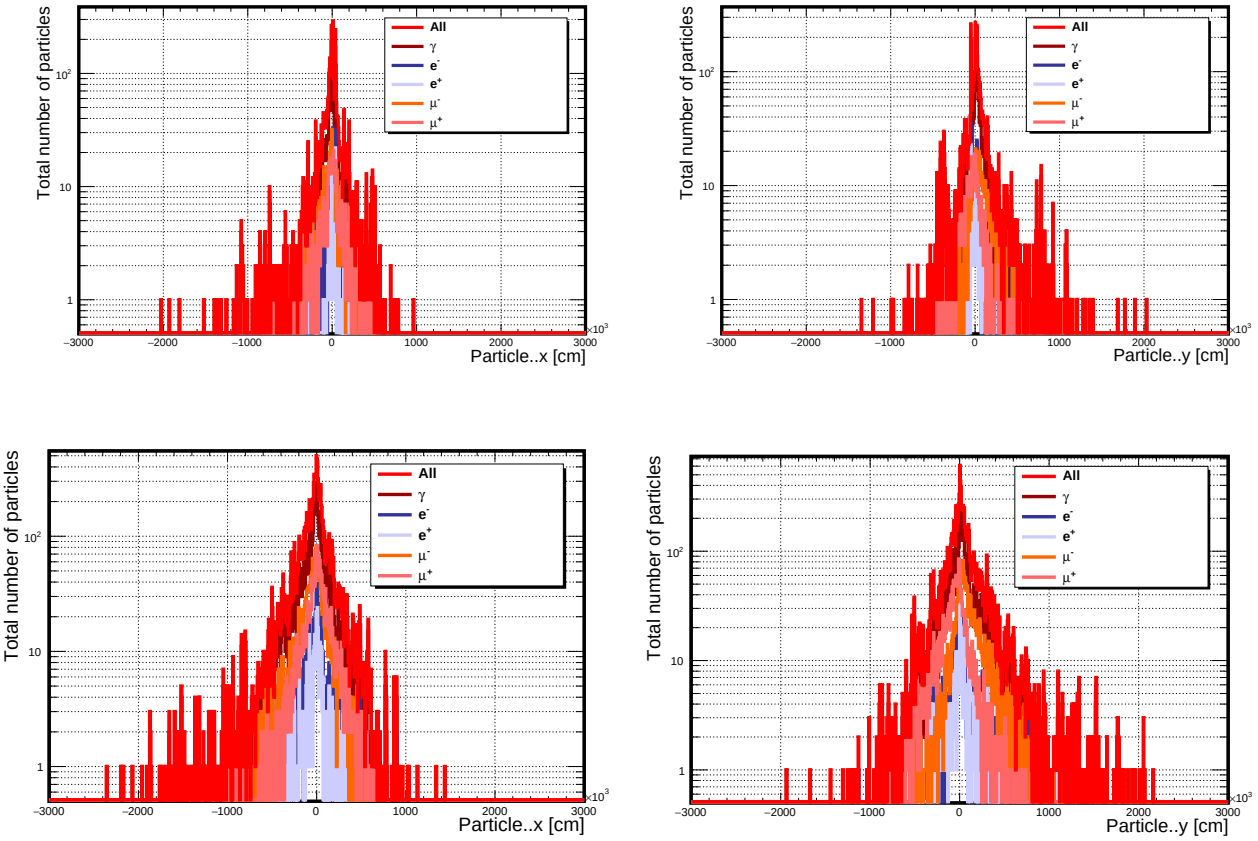

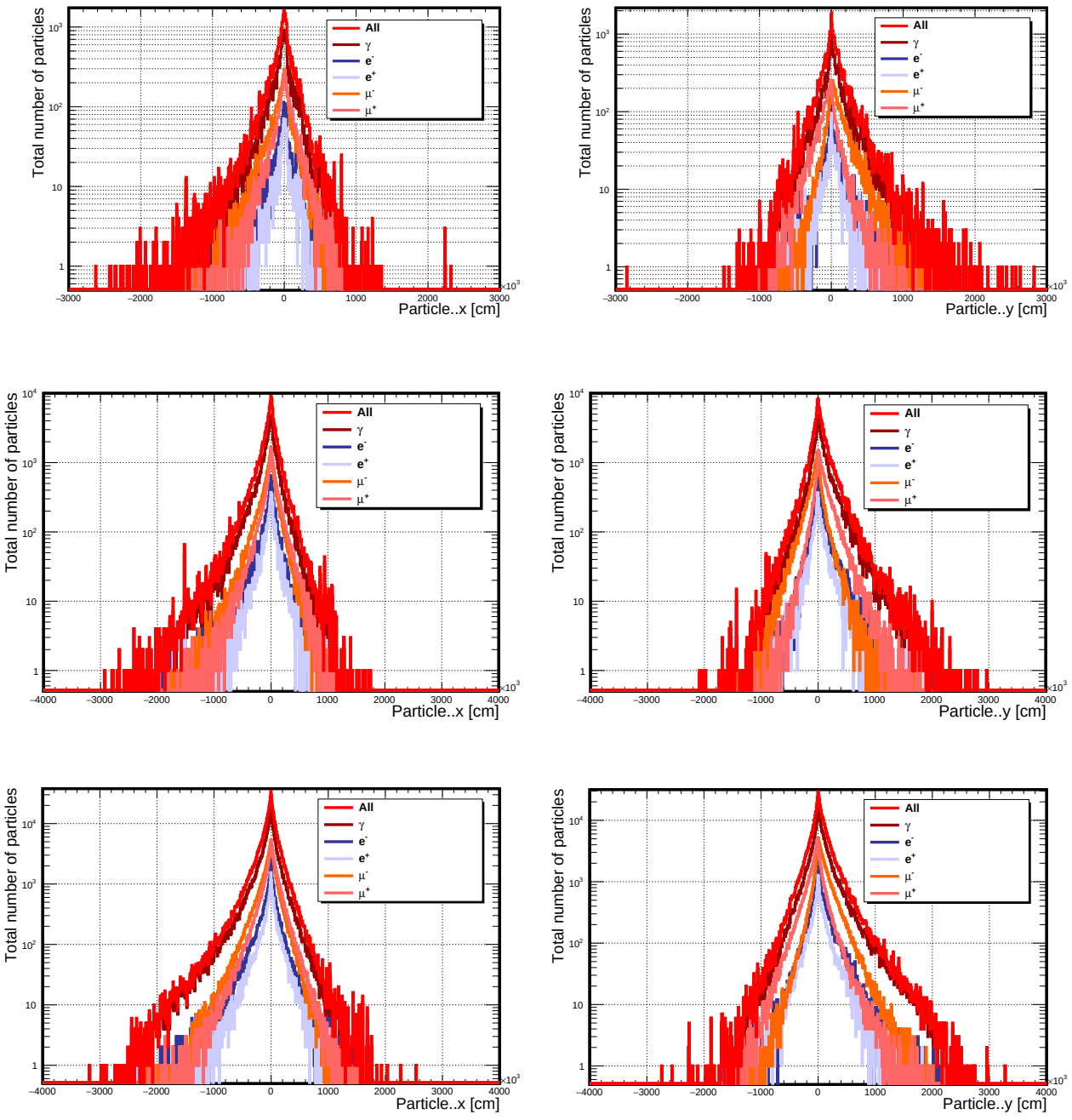

FIGURE B.10: Lateral distribution of secondaries resulted from γ-ray showers at multi-TeV energies, with zenith angle 69.9°.

B.2 Offline detector simulation

Maps of triggered detectors at multi-TeV and different Crab zenith angles are presented:

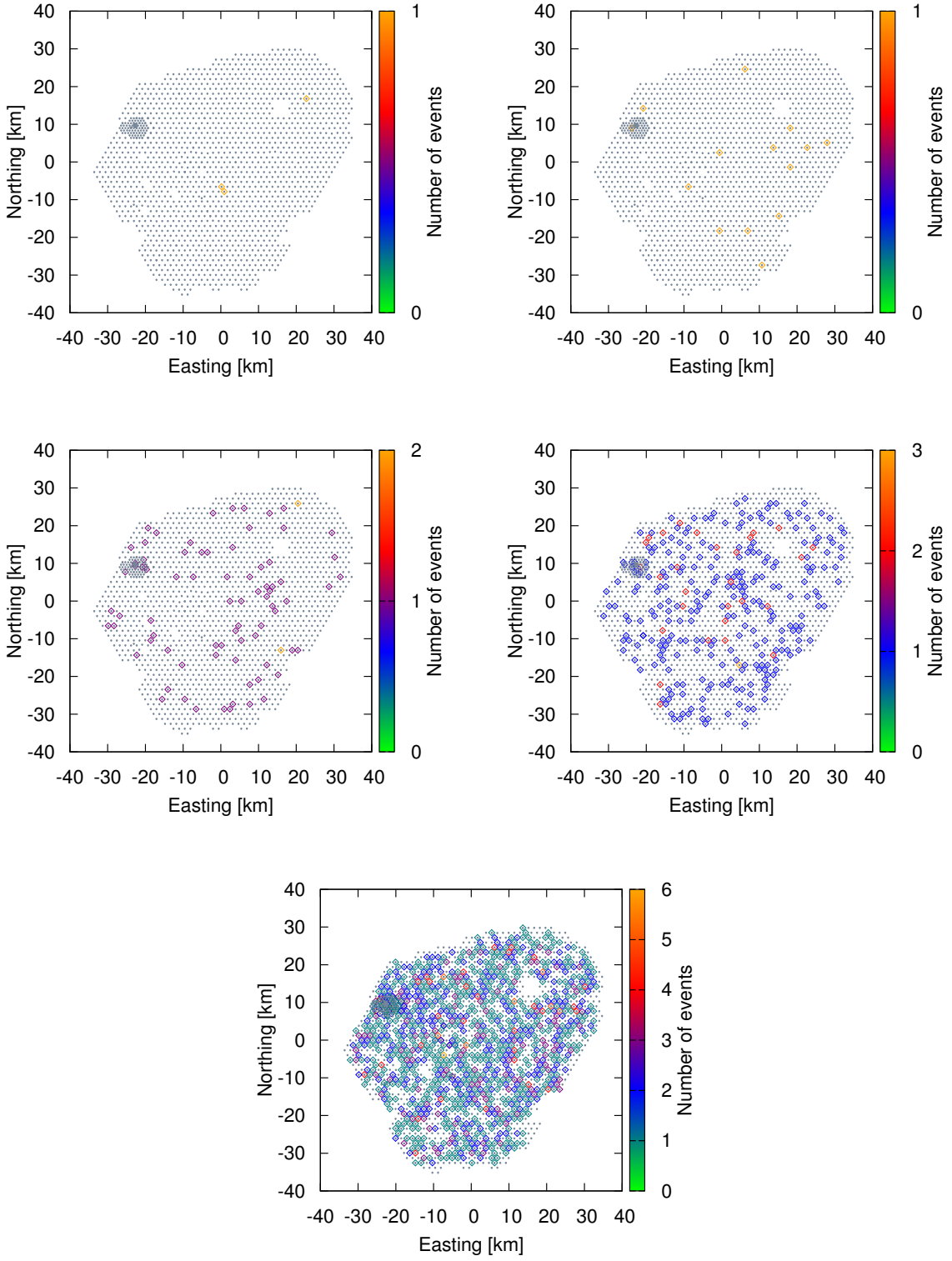

FIGURE B.11: An example of maps of detectors of γ-ray signal at multi-TeV energies and zenith angle 59.9° at Auger sky. Large number of simulated events (4×10^5) at primary photon energies (10, 30, 100, 300, and 1000 TeV), with zenith angle $\theta = 59.9°$, are simulated. Detector multiplicities are clearly visible at high energies >30 TeV.

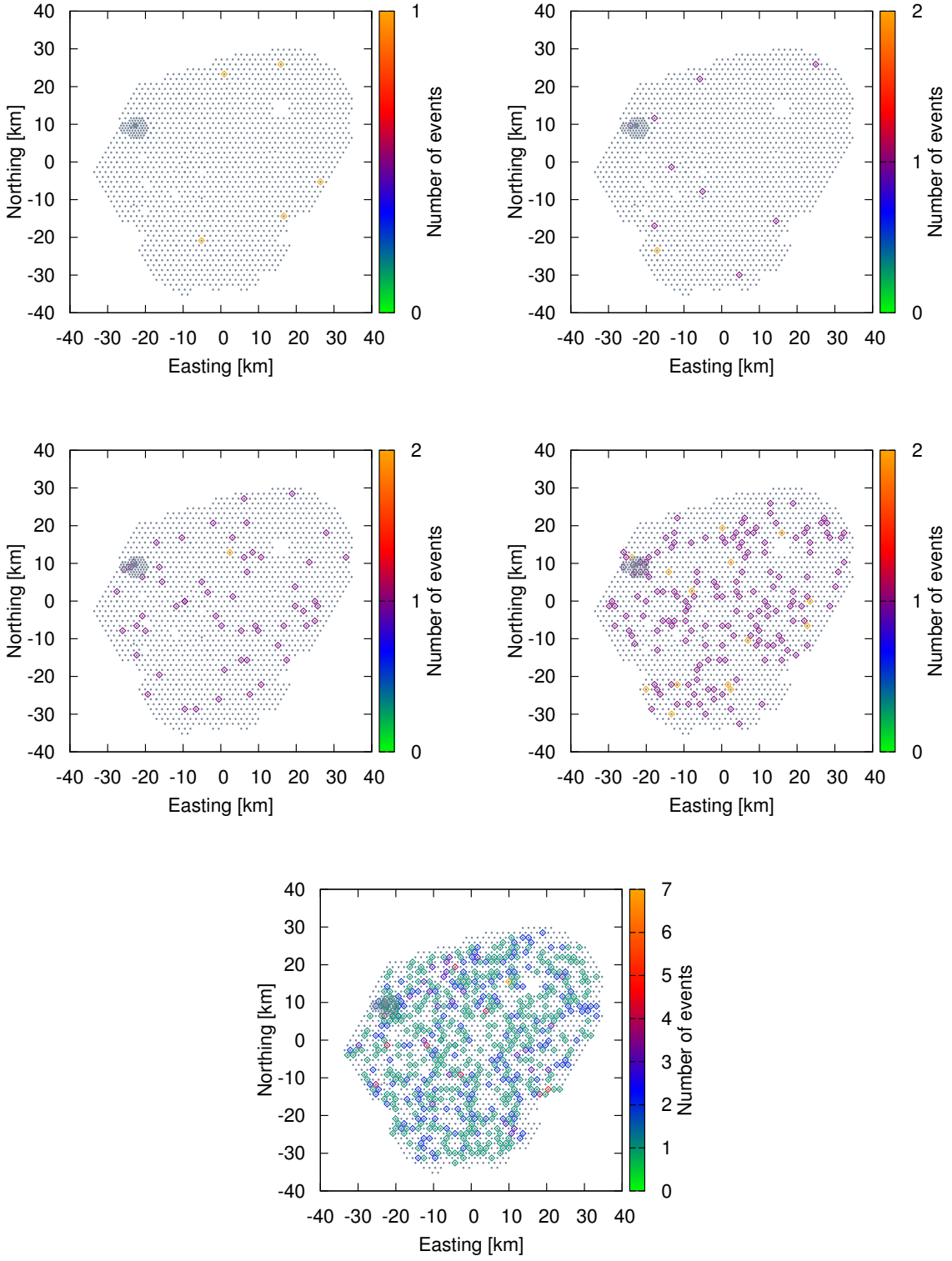

FIGURE B.12: An example of maps of detectors of γ-ray signal at multi-TeV energies and zenith angle 61.9° at Auger sky. Large number of simulated events (4×10^5) at primary photon energies (10, 30, 100, 300, and 1000 TeV), with zenith angle $\theta = 61.9°$, are simulated. Detector multiplicities are clearly visible at high energies >30 TeV.

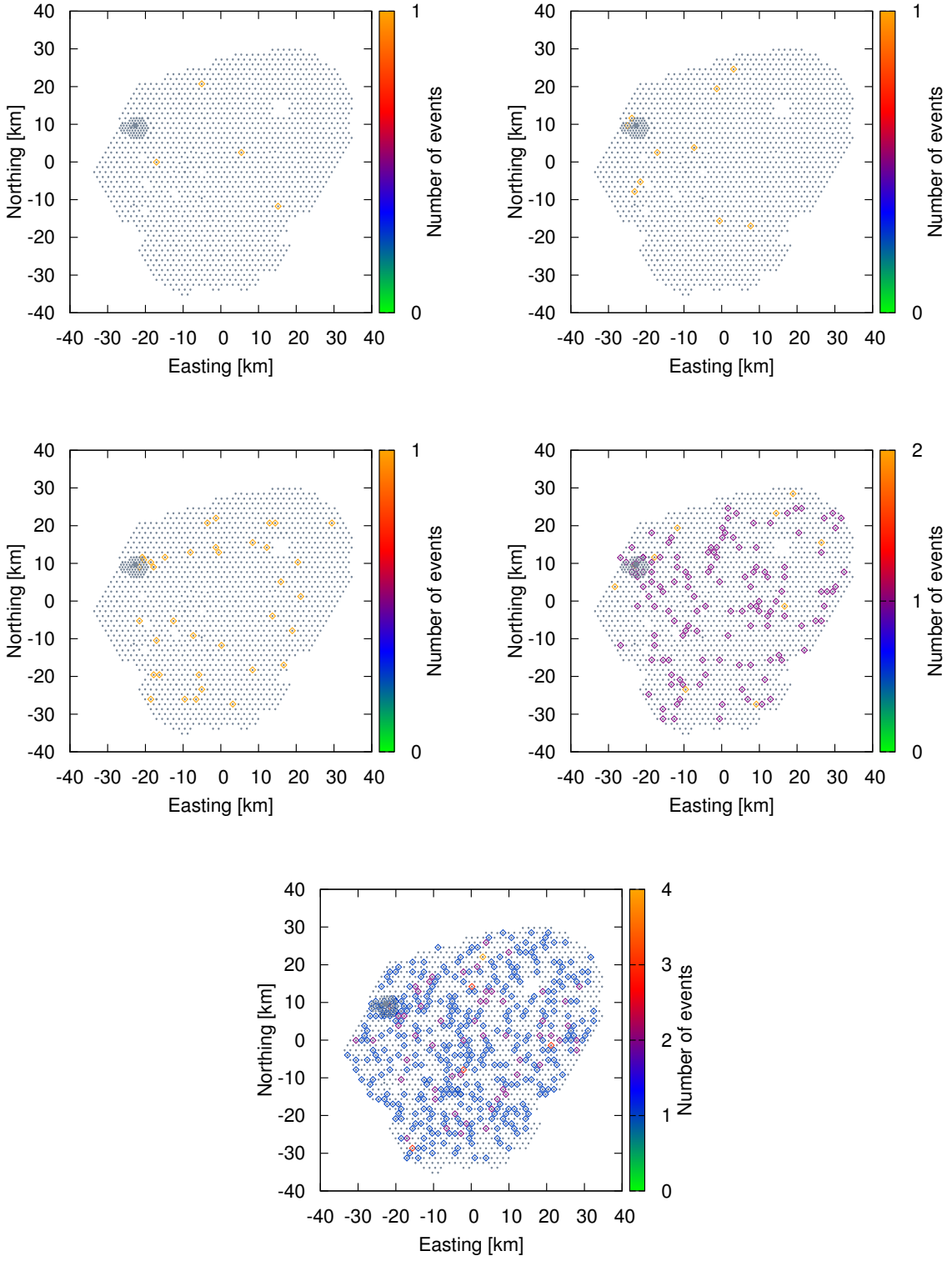

FIGURE B.13: An example of maps of detectors of γ-ray signal at multi-TeV energies and zenith angle 63.8° at Auger sky. Large number of simulated events (4×10^5) at primary photon energies (10, 30, 100, 300, and 1000 TeV), with zenith angle $\theta = 63.8°$, are simulated. Detector multiplicities are clearly visible at high energies >30 TeV.

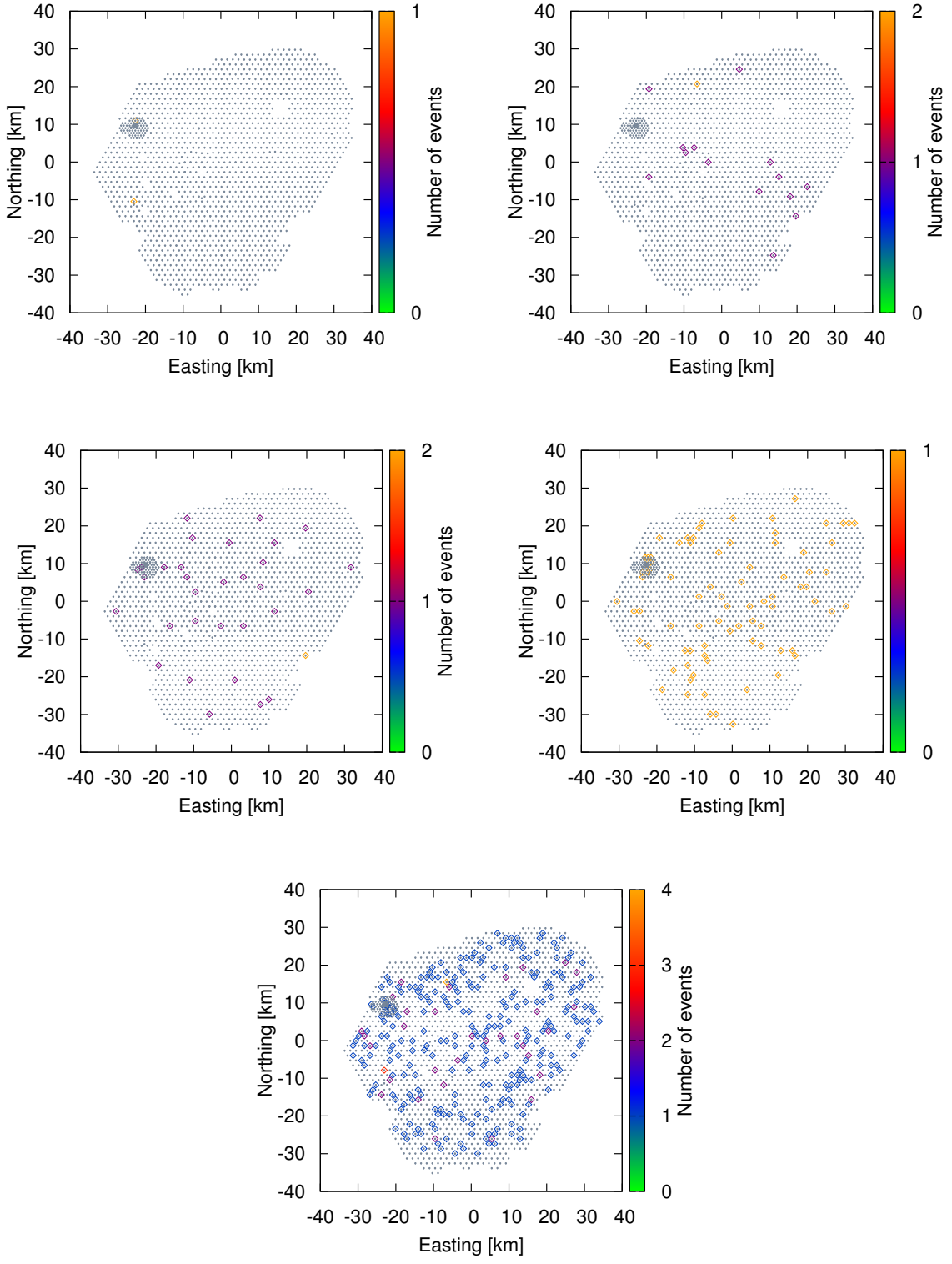

FIGURE B.14: An example of maps of detectors of γ-ray signal at multi-TeV energies and zenith angle 66° at Auger sky. Large number of simulated events (4×10^5) at primary photon energies (10, 30, 100, 300, and 1000 TeV), with zenith angle $\theta = 66°$, are simulated. Detector multiplicities are clearly visible at high energies >30 TeV.

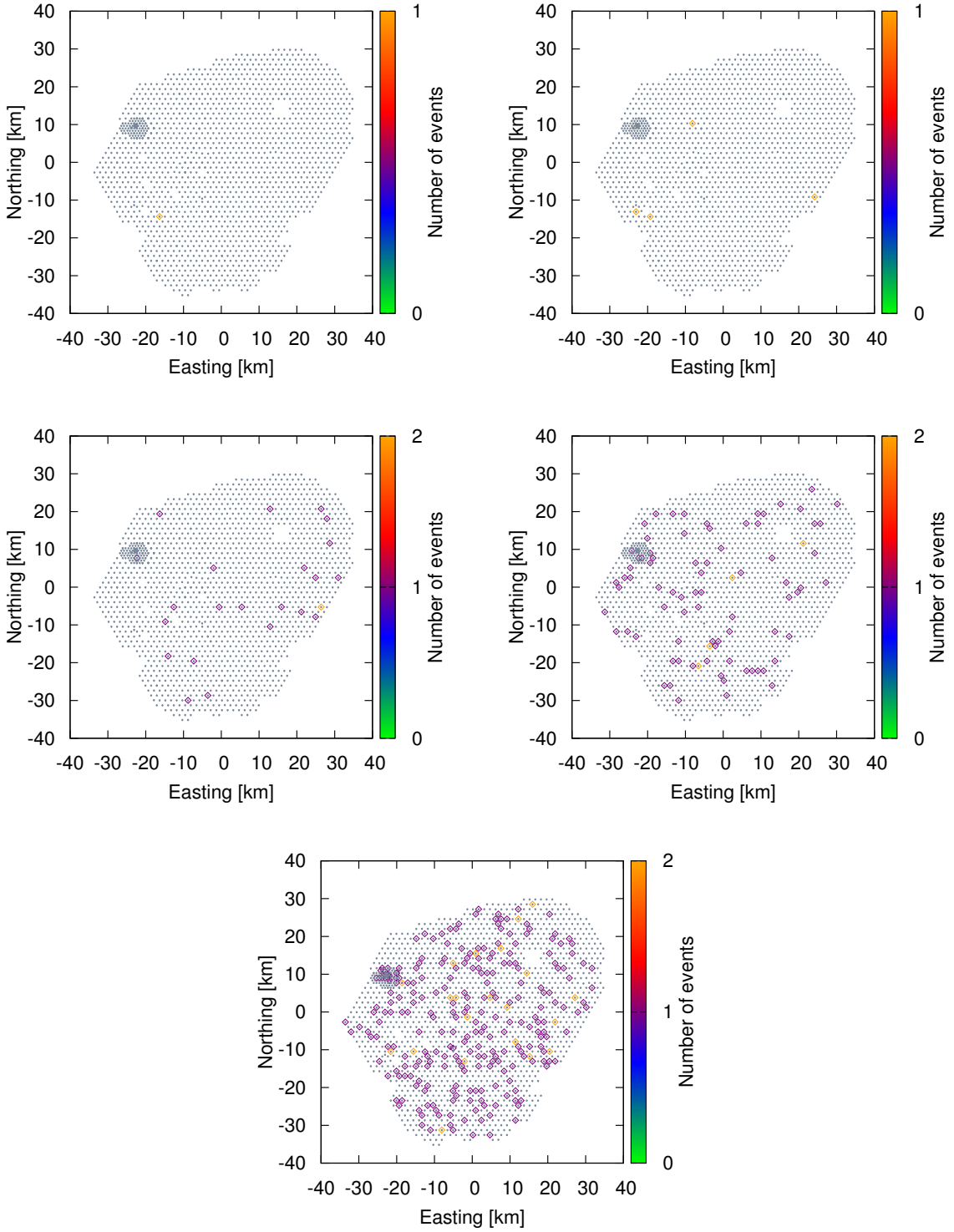

FIGURE B.15: An example of maps of detectors of γ-ray signal at multi-TeV energies and zenith angle 69.9° at Auger sky. Large number of simulated events (4×10^5) at primary photon energies (10, 30, 100, 300, and 1000 TeV), with zenith angle $\theta = 69.9°$, are simulated. Detector multiplicities are clearly visible at high energies >30 TeV.

FADC traces of simulated signals with scaler mode We present examples of FADC traces of simulated γ-ray signal from the Crab direction at multi-TeV and several zenith angles.

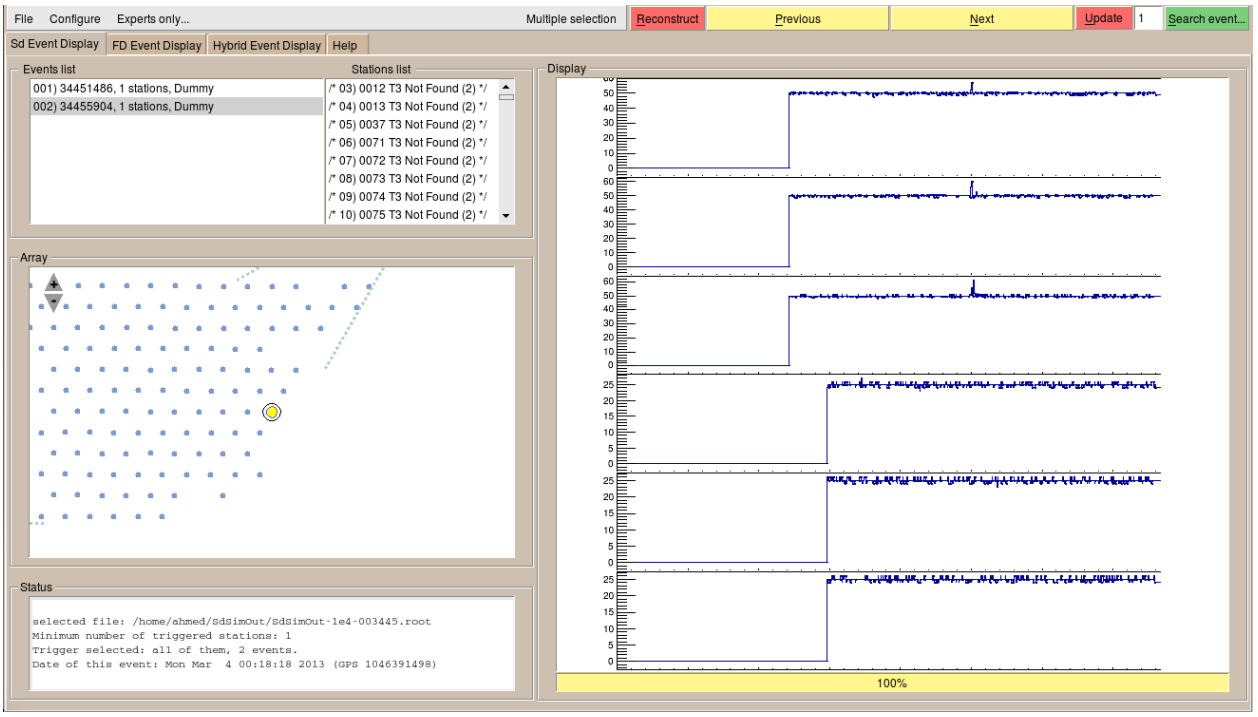
File
Configure
Experts only...
Multiple selection
Reconstruct
Previous
Next
Update
1
Search event...
Sd Event Display
FD Event Display
Hybrid Event Display
Help
Events list
001) 34451486, 1 stations, Dummy
002) 34455904, 1 stations, Dummy
Stations list
/* 03) 0012 T3 Not Found (2) */
/* 04) 0013 T3 Not Found (2) */
/* 05) 0037 T3 Not Found (2) */
/* 06) 0071 T3 Not Found (2) */
/* 07) 0072 T3 Not Found (2) */
/* 08) 0073 T3 Not Found (2) */
/* 09) 0074 T3 Not Found (2) */
/* 10) 0075 T3 Not Found (2) */
Array
Status
selected file: /home/ahmed/SdSimOut/SdSimOut-1e4-003445.root
Minimum number of triggered stations: 1
Trigger selected: all of them, 2 events.
Date of this event: Mon Mar 4 00:18:18 2013 (GPS 1046391498)
Display
100%

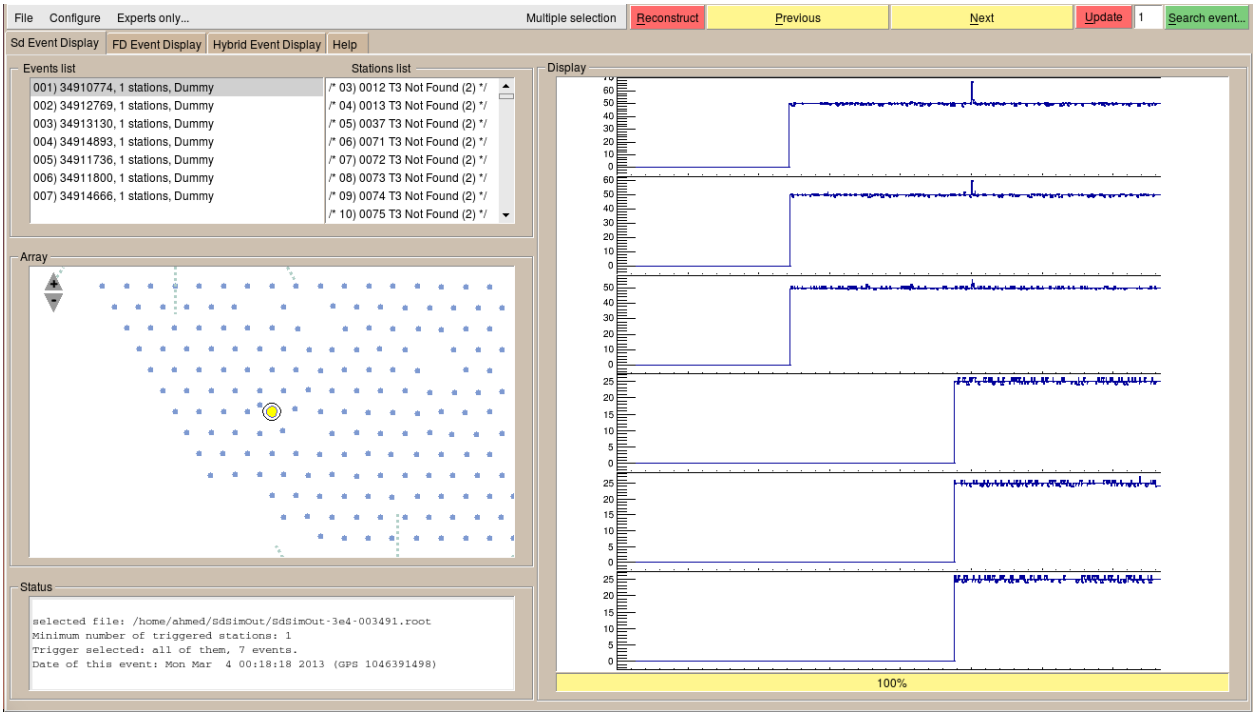
File
Configure
Experts only...
Multiple selection
Reconstruct
Previous
Next
Update
1
Search event...
Sd Event Display
FD Event Display
Hybrid Event Display
Help
Events list
001) 34910774, 1 stations, Dummy
002) 34912769, 1 stations, Dummy
003) 34913130, 1 stations, Dummy
004) 34914893, 1 stations, Dummy
005) 34911736, 1 stations, Dummy
006) 34911800, 1 stations, Dummy
007) 34914666, 1 stations, Dummy
Stations list
/* 03) 0012 T3 Not Found (2) */
/* 04) 0013 T3 Not Found (2) */
/* 05) 0037 T3 Not Found (2) */
/* 06) 0071 T3 Not Found (2) */
/* 07) 0072 T3 Not Found (2) */
/* 08) 0073 T3 Not Found (2) */
/* 09) 0074 T3 Not Found (2) */
/* 10) 0075 T3 Not Found (2) */
Array
Status
selected file: /home/ahmed/SdSimOut/SdSimOut-3e4-003491.root
Minimum number of triggered stations: 1
Trigger selected: all of them, 7 events.
Date of this event: Mon Mar 4 00:18:18 2013 (GPS 1046391498)
Display
100%

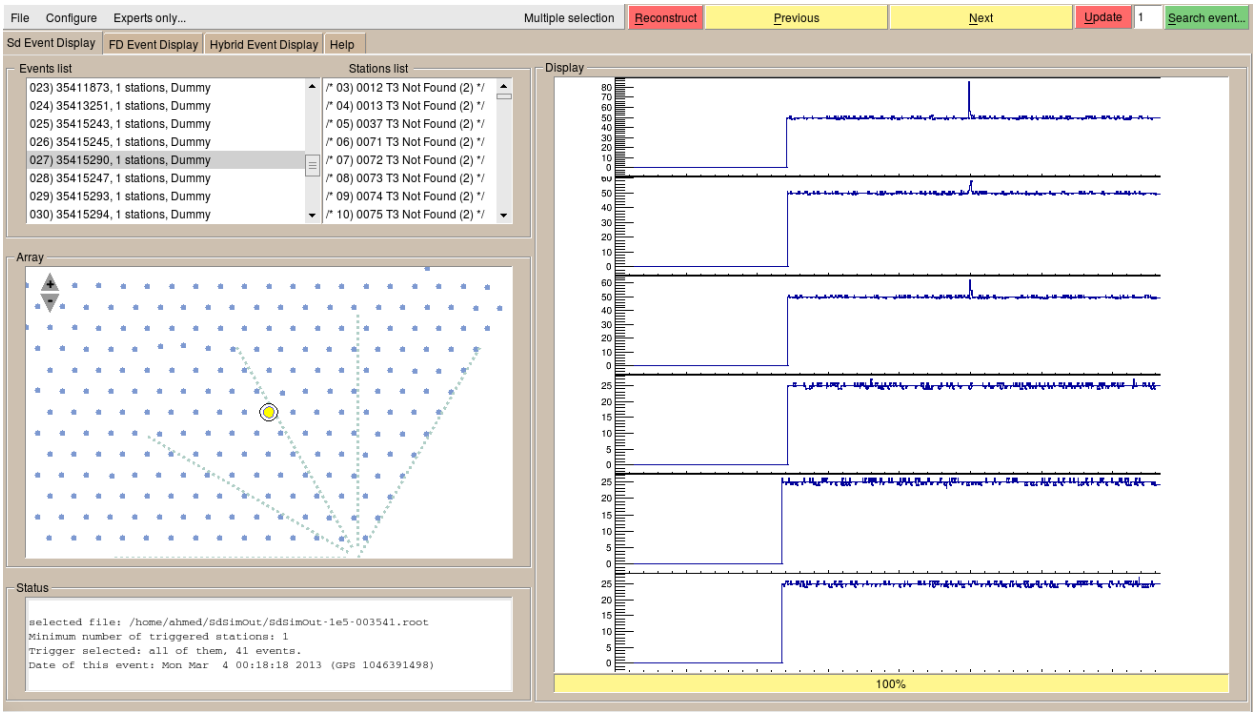
File Configure Experts only... Multiple selection Reconstruct Previous Next Update 1 Search event...
Sd Event Display FD Event Display Hybrid Event Display Help
Events list
Stations list
023) 35411873, 1 stations, Dummy
024) 35413251, 1 stations, Dummy
025) 35415243, 1 stations, Dummy
026) 35415245, 1 stations, Dummy
027) 35415290, 1 stations, Dummy
028) 35415247, 1 stations, Dummy
029) 35415293, 1 stations, Dummy
030) 35415294, 1 stations, Dummy
/* 03) 0012 T3 Not Found (2) */
/* 04) 0013 T3 Not Found (2) */
/* 05) 0037 T3 Not Found (2) */
/* 06) 0071 T3 Not Found (2) */
/* 07) 0072 T3 Not Found (2) */
/* 08) 0073 T3 Not Found (2) */
/* 09) 0074 T3 Not Found (2) */
/* 10) 0075 T3 Not Found (2) */
Array
Status
selected file: /home/ahmed/SdSimOut/SdSimOut-1e5-003541.root
Minimum number of triggered stations: 1
Trigger selected: all of them, 41 events.
Date of this event: Mon Mar 4 00:18:18 2013 (GPS 1046391498)
Display
100%

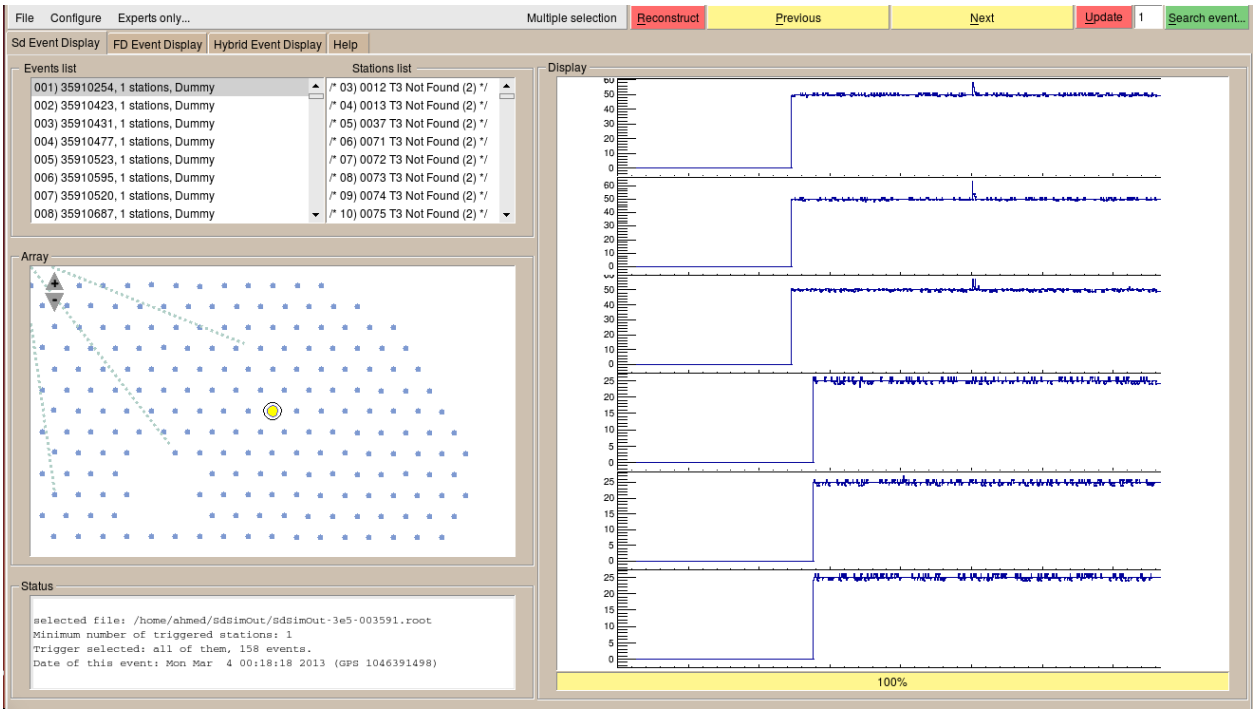
File Configure Experts only... Multiple selection Reconstruct Previous Next Update 1 Search event...
Sd Event Display FD Event Display Hybrid Event Display Help
Events list
Stations list
001) 35910254, 1 stations, Dummy
002) 35910423, 1 stations, Dummy
003) 35910431, 1 stations, Dummy
004) 35910477, 1 stations, Dummy
005) 35910523, 1 stations, Dummy
006) 35910595, 1 stations, Dummy
007) 35910520, 1 stations, Dummy
008) 35910687, 1 stations, Dummy
/* 03) 0012 T3 Not Found (2) */
/* 04) 0013 T3 Not Found (2) */
/* 05) 0037 T3 Not Found (2) */
/* 06) 0071 T3 Not Found (2) */
/* 07) 0072 T3 Not Found (2) */
/* 08) 0073 T3 Not Found (2) */
/* 09) 0074 T3 Not Found (2) */
/* 10) 0075 T3 Not Found (2) */
Array
Status
selected file: /home/ahmed/SdSimOut/SdSimOut-3e5-003591.root
Minimum number of triggered stations: 1
Trigger selected: all of them, 158 events.
Date of this event: Mon Mar 4 00:18:18 2013 (GPS 1046391498)
Display
100%

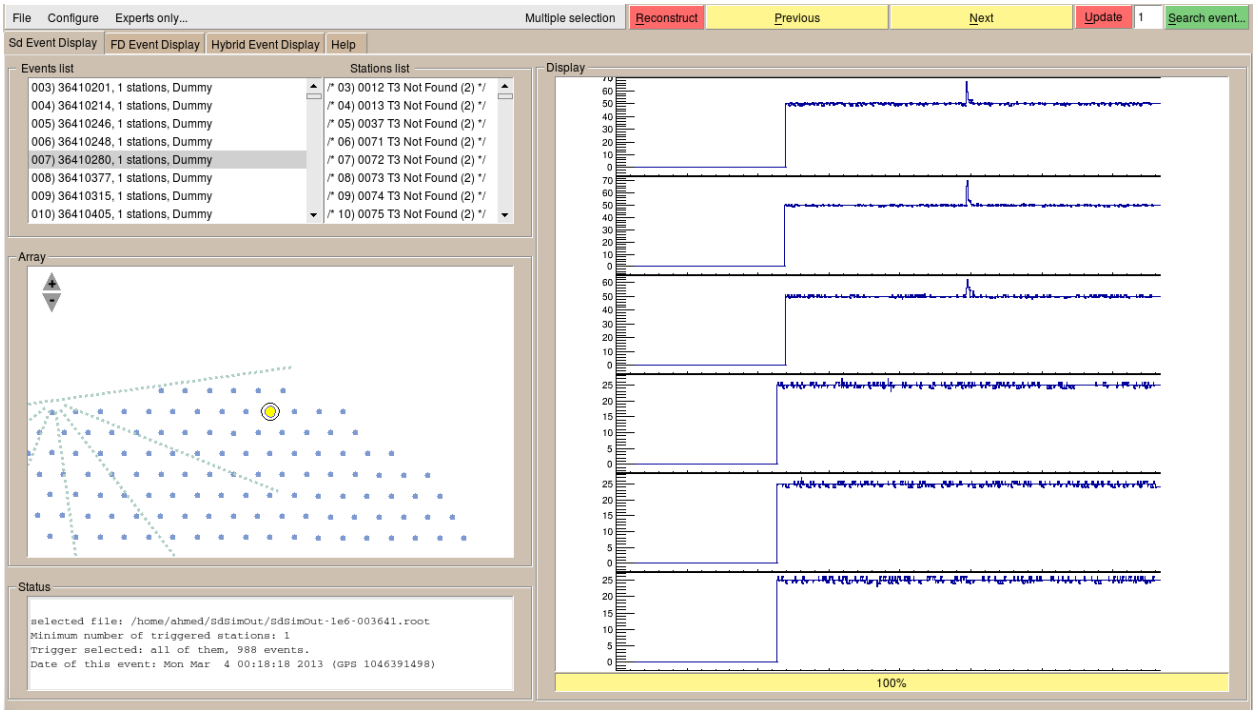

FIGURE B.16: Examples of the Offline FADC traces of simulated VHE γ-ray emission from the Crab nebula.

Appendix C

Scaler rate analysis on individual SD detector

In this appendix we present the results of individual detector analysis. The analysis is carried out to each valid detector of the SD array, via using the following individual scaler rate clean-up and corrections:

- skipping rates outside of [500 Hz-8000 Hz] interval,
- discarding the detectors with abnormal rate distribution and the ones with acquisition efficiency $<$90%,
- skipping periods of lightning, strong wind, and T3 bad periods, which includes famous crisis of 2009,
- performing the AoP and atmospheric pressure corrections for each detector individually,
- calculating the rate variability in consecutive 5-minute intervals (Eq. 3.6).

The implementation of the previous steps enables us to conclude that larger number of high amplitude excesses and high detector multiplicities are observed during the Crab transit at Malargüe (see Fig. C.1 and C.2).

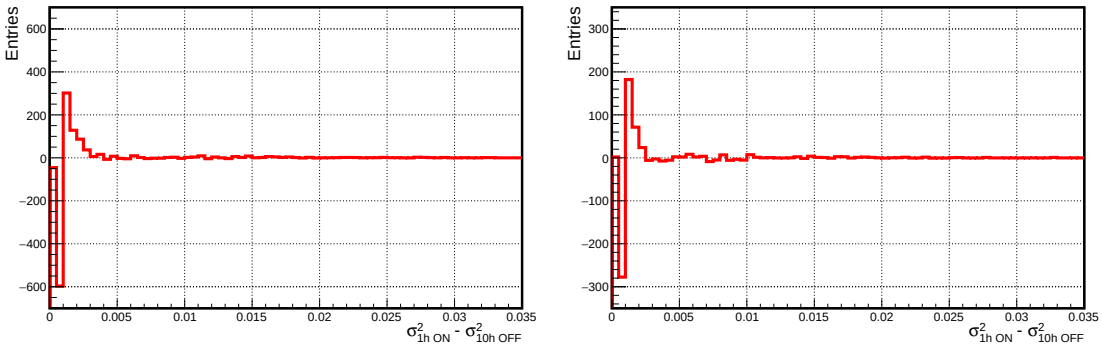

FIGURE C.1: ON-OFF subtraction of histograms of excess variance distributions of March 4, 2013 (left) and March 15, 2014 (right). ON period corresponds to one hour of SD scaler data at the time interval including the observed Crab-compatible extra variability in average scaler rate (Crab at high elevation $>20^\circ$). OFF period corresponds to 10 hr of SD scaler data from the same dates, when the Crab was under horizon. The OFF data shows more detectors with small values of σ^2 amplitude, which is seen as a negative excess in the second bin. Larger σ^2 values is shown as a positive excess, and occurred during the extra variability observed in the average scaler rate. This indicates several hundreds of detectors contributed the observed signal.

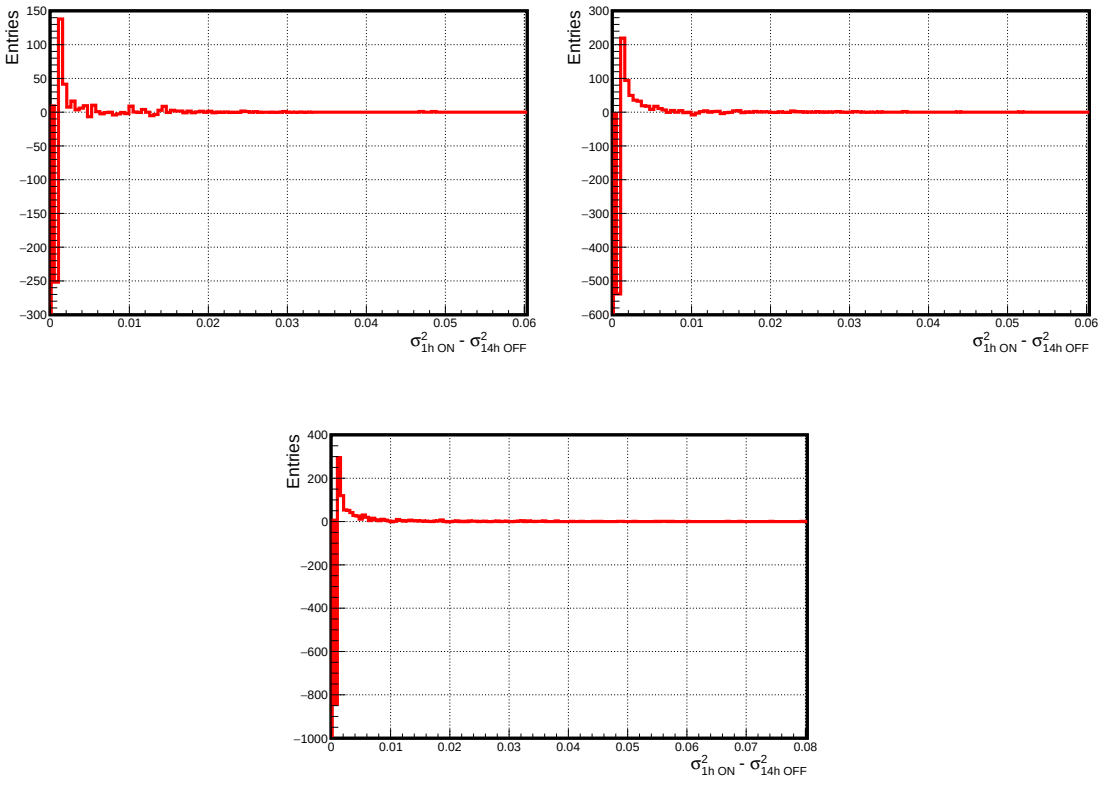

FIGURE C.2: ON-OFF subtraction of histograms of excess variance distributions of three hours intervals on December 31, 2015. ON period corresponds to the time intervals from 00h-01h, 01h-02h, and 02h-03h UTC of SD scaler data, including the observed Crab-compatible extra variability in average scaler rate (Crab at high elevation $>20^\circ$). OFF period corresponds to 14 hr of SD scaler data from the same dates, when the Crab was under horizon. As the same as Fig. C.1, the OFF data shows more detectors with small values of σ^2 amplitude, which is seen as a negative excess. Larger σ^2 values is shown as a positive excess, and occurred during the extra variability observed in the average scaler rate. This indicates several hundreds of detectors contributed the observed signal.

Appendix D

Distributions of average scaler rate variability and *Fermi*-LAT Crab flux

Daily distributions of Auger average scaler rate variability We show daily distributions of the excess variance σ^2 of the dates of strong average scaler rate variability observed during 5 out of the 7 strongest Crab γ-ray flares, as detected by *Fermi*-LAT and AGILE satellites in September 2010, March 2013, March 2014, August 2014, and December 2015.

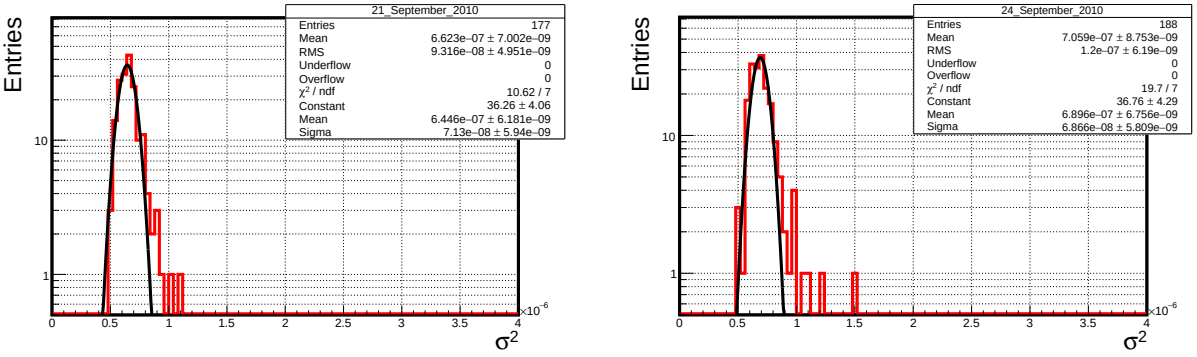

FIGURE D.1: Distribution of σ^2 values for two dates of excesses during September 2010 Crab Nebula flare. The maximal excess amplitude is well above 5 standard deviations.

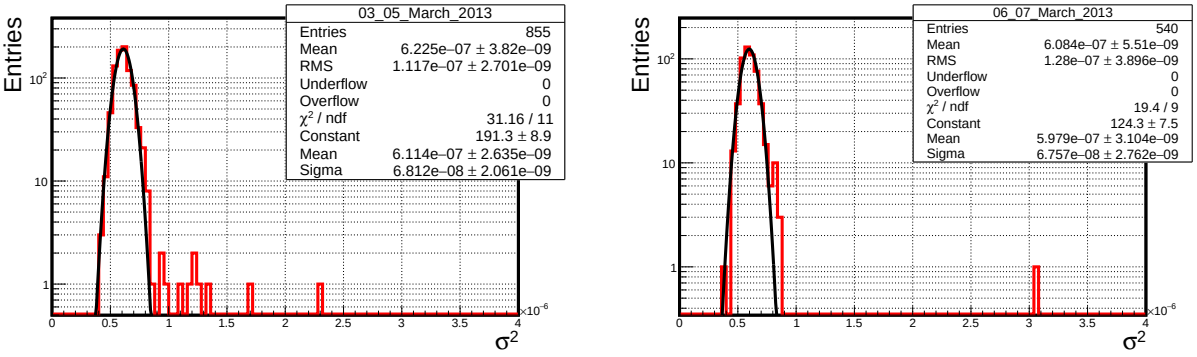

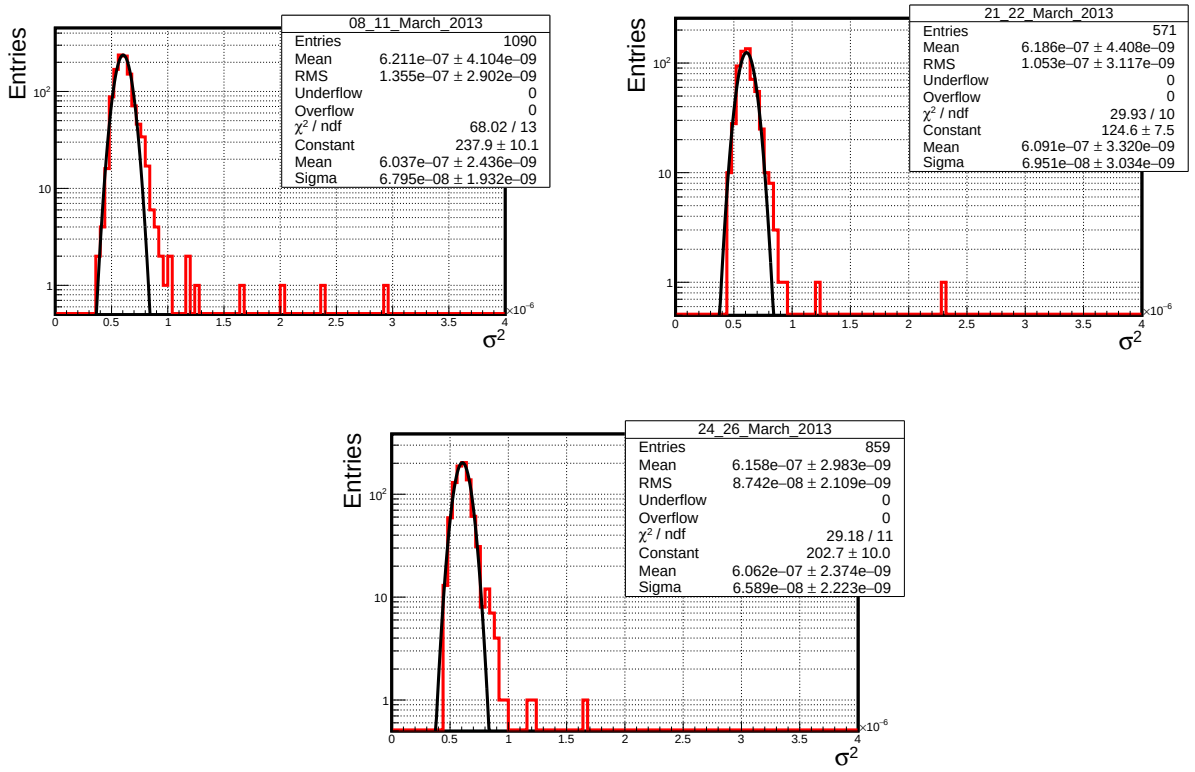

FIGURE D.2: Distribution of σ^2 values for 13 dates of excesses during March 2013 Crab Nebula flare. The maximal excess amplitude is well above 5 standard deviations.

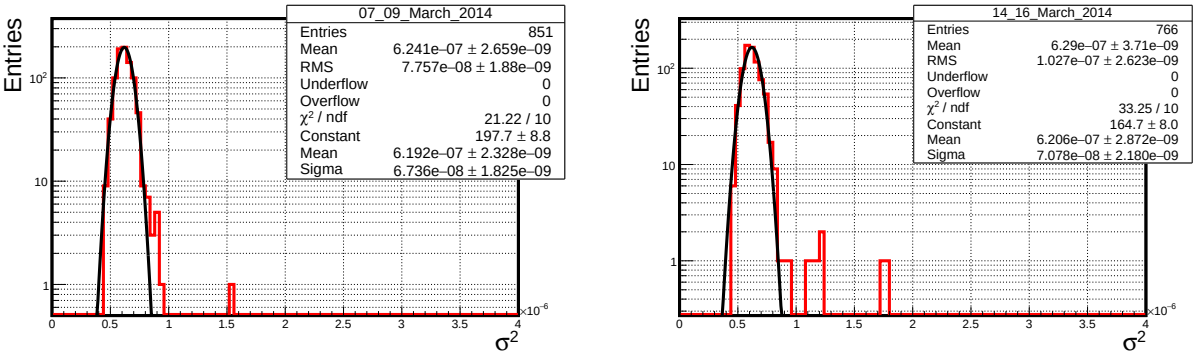

FIGURE D.3: Distribution of σ^2 values for 4 dates of excesses during March 2014 Crab Nebula flare. The maximal excess amplitude is well above 5 standard deviations.

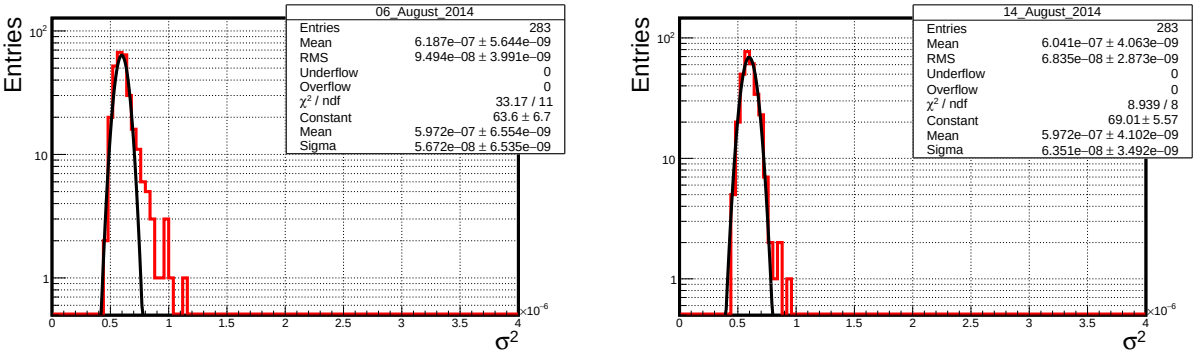

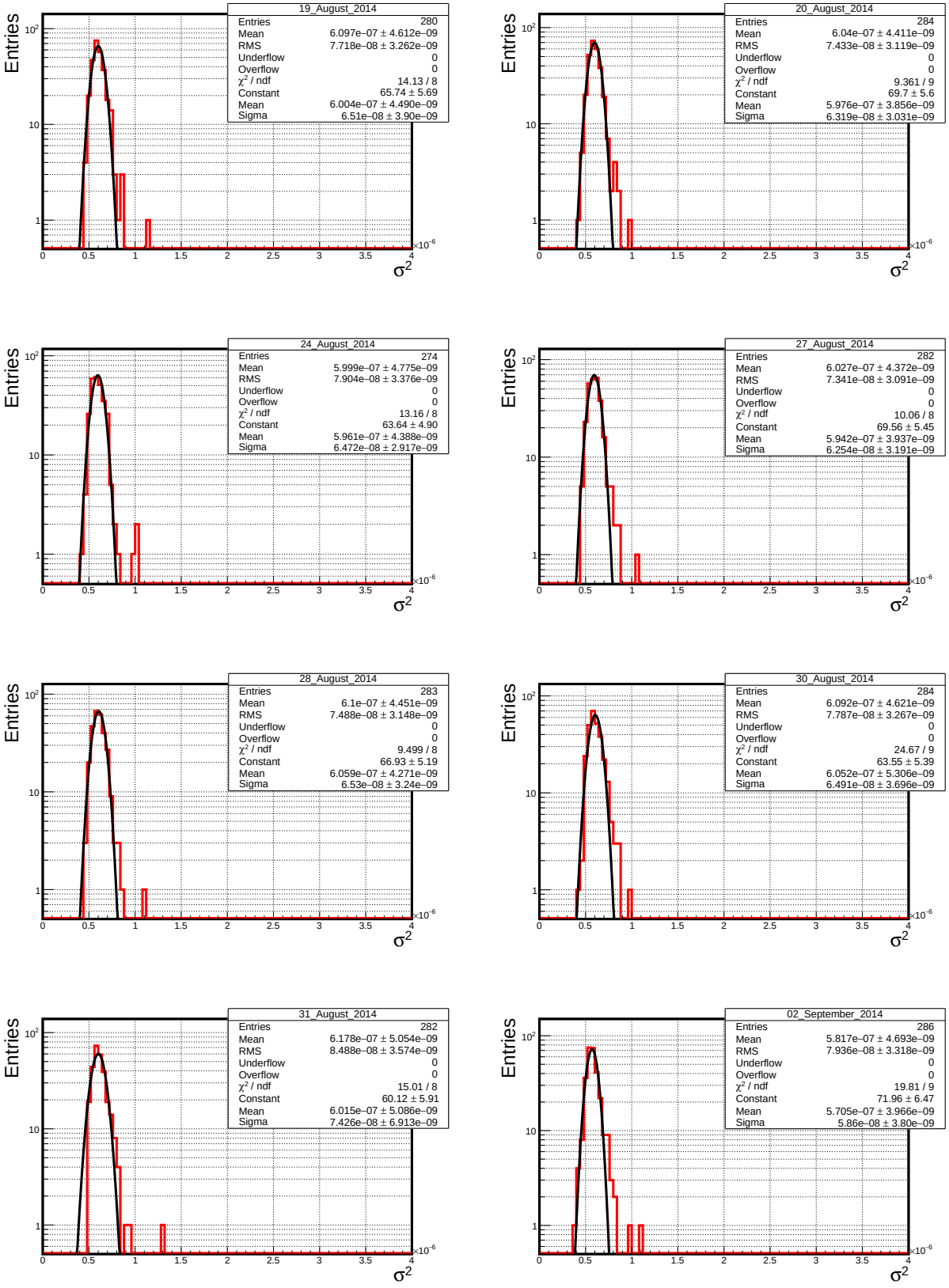

FIGURE D.4: The distribution of σ^2 values for 10 dates of excesses during August 2014 Crab Nebula flare. The maximal excess amplitude is well above 5 standard deviations.

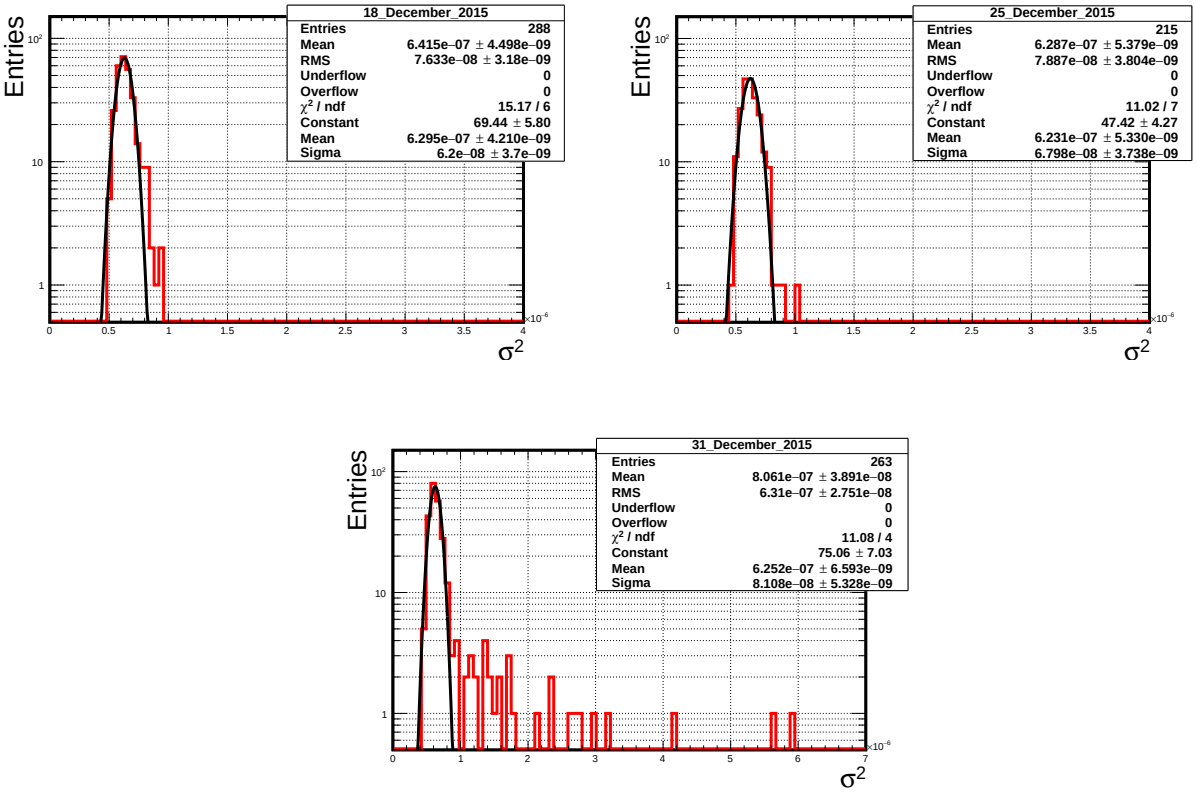

FIGURE D.5: The distribution of σ^2 values for 3 dates of excesses during December 2015 Crab Nebula flare. The maximal excess amplitude is well above 5 standard deviations.

All days show normal distributions with significant excesses on the positive side of σ^2 distribution.

Yearly distributions of the Crab flux measured by *Fermi*-LAT We present yearly distributions of the flux of the Crab nebula and pulsar (Crab in short) measured by *Fermi*-LAT [259].

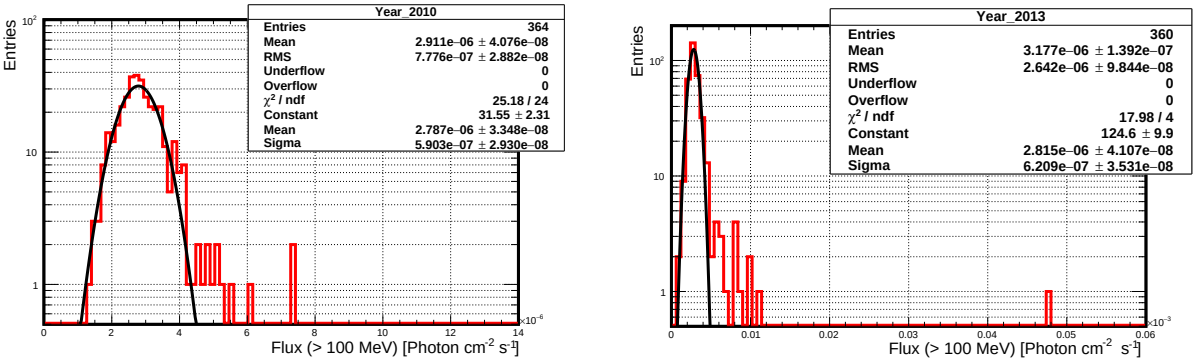

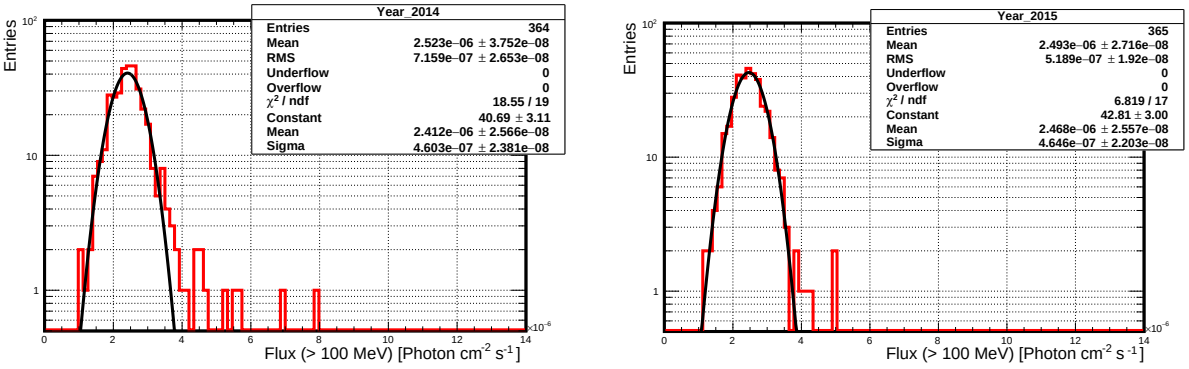

FIGURE D.6: Yearly distributions of the Crab flux measured by *Fermi*-LAT in 2010, 2013, 2014, and 2015.

List of Figures

List of Tables

Bibliography

[1] V. Hess, *Observations of the penetrating radiation on seven balloon flights*, Physik. Zeitschr, **13**, 1084 (1912).

[2] R. Clay and B. Dawson, *Cosmic Bullets - High Energy Particles in Astrophysics*, Helix Books, Addison-Wesley, Australia, (1998).

[3] P. Auger *High Energy Cosmic Rays*, , Proc. of the 17th International Cosmic Ray Conference, **12**, 5 (1981); RevModPhys.11.288.

[4] Phyllis Freier, et al., *Evidence for Heavy Nuclei in the Primary Cosmic Radiation*, Phys. Rev., **74**, 213 (1948).

[5] W. Baade and F. Zwicky, *Remarks on Super-Novae and Cosmic Rays*, Phys. Rev., **46**, 76 (1934).

[6] E. Fermi, *On The Origin of The Cosmic Radiation*, Phys.Rev., **75**, 1169 (1949).

[7] W. I. Axford, E. Leer, and G. Skadron, *The acceleration of cosmic rays by shock waves*, Proc. 15th ICRC, (1977).

[8] Kumiko Kotera, Angela V. Olinto, *The Astrophysics of Ultrahigh Energy Cosmic Rays*, Annual Review of Astronomy and Astrophysics, **49**, 119 (2011).

[9] Roger Blandford, David Eichler, *Particle Acceleration at Particle Astrophysical Shocks: A Theory of Cosmic Ray Origin*, Review Section of Physics Letters, **154**, 75 (1987).

[10] T. W. Jones, *Acceleration of Ultra High Energy Cosmic Rays: Cosmic Zevatrons?*, arXiv:0210477, (2002).

[11] M. Lemoine, G. Sigl, *Physics and Astrophysics of Ultra High Energy Cosmic Rays*, Springer-Verlag Berlin Heidelberg, (2001).

[12] Pijushpani Bhattacharjee, Günter Sigl, *Origin and Propagation of Extremely High Energy Cosmic Rays*, Phys. Rept., **327**, 109 (2000).

[13] Todor Stanev, *Ultra High Energy Cosmic Rays*, Rept. Prog. Phys., **67**, 1663 (2004).

[14] L. Miroshnichenko, *Solar Cosmic Rays*, Kluwer Academic Publishers, (2001).

[15] L. A. Fisk,B. Kozlovsky, R. Ramaty, *An Interpretation of the Observed Oxygen and Nitrogen Enhancements in Low-Energy Cosmic Rays*, ApJ, **190**, L35 (1974).

[16] R. D. Blandford and D. Eichler, *Particle acceleration at astrophysical shocks: A theory of cosmic ray origin*, ApJ., **154**, 1 (1987).

[17] The Pierre Auger Collaboration, *Measurement of the energy spectrum of cosmic rays above* 10^{18} *eV using the Pierre Auger Observatory*, Physics Letters B, **685**, 239 (2010); arXiv:1002.1975.

[18] K. A. Olive and Particle Data Group Collaboration, *Review of Particle Physics*, Chinese Physics C, **38**, 378 (2014).

[19] The HiRes Collaboration, *First Observation of the Greisen-Zatsepin-Kuzmin Suppression*, Phys. Rev. Lett., **100**, 101101 (2008); arXiv:astro-ph/0703099.

[20] The Telescope Array Collaboration, *The Cosmic Ray Energy Spectrum Observed with the Surface Detector of the Telescope Array Experiment*, ApJ, **768**, L1 (2013); arXiv:1205.5067.

[21] Alexander Schulz for the Pierre Auger Collaboration, *The measurement of the energy spectrum of cosmic rays above* 3×10^{17} *eV with the Pierre Auger Observatory*, Proc. 33rd ICRC, (2013); arXiv:1307.5059.

[22] A. A. Penzias and R. W. Wilson, *A Measurement of excess antenna temperature at 4080-Mc/s*, ApJ, **142**, (1965).

[23] Kenneth Greisen, *End to The Cosmic-Ray Spectrum?*, Physical Review Letters, **16**, 748 (1966).

[24] G. Zatsepin and V. Kuzmin, *Upper limit of the spectrum of cosmic rays*, JETP Lett. **4**, 78 (1966).

[25] A. Muecke, et. al., *Monte Carlo simulations of photohadronic processes in astrophysics*, Comput. Phys. Commun., **124**, 290 (2000).

[26] J. L. Puget, F. W. Stecker, and J. H. Bredekamp, *Photonuclear Interactions of Ultrahigh-energy Cosmic Rays and their Astrophysical Consequences*, ApJ, **205**, 638 (1967).

[27] The High Resolution Fly's Eye Collaboration, *Monocular Measurement of the Spectrum of UHE Cosmic Rays by the FADC Detector of the HiRes Experiment*, Astroparticle Physics, **23**, 157 (2005); arXiv:astro-ph/0208301.

[28] Charles C.H. Jui for the High Resolution Fly's Eye Collaboration, *Results from the HiRes Experiment*, Journal of Physics: Conference Series, **47**, 59 (2006).

[29] T. Yamamoto for the Pierre Auger Collaboration, *The UHECR spectrum measured at the Pierre Auger Observatory and its astrophysical implications*, Proc. 30th ICRC, (2007); arXiv:0707.2638.

[30] The Pierre Auger Collaboration, *Observation of the Suppression of the Flux of Cosmic Rays above* $4\times^{19} eV$, Phys. Rev. Lett., **101**, 061101 (2008).

[31] H. Sagawa for the Telescope Array Collaboration, *Telescope Array extension:TA* $\times$ *A*, Proc. 34th ICRC, (2015).

[32] Inés Valiño for the Pierre Auger Collaboration *The flux of ultra-high energy cosmic rays after ten years of operation of the Pierre Auger Observatory*, Proc. 34th ICRC, (2015).

[33] Antoine Letessier-Selvon, Todor Stanev, *Ultra high energy cosmic rays*, Reviews of Modern Physics, **83**, 907 (2011).

[34] J. Matthews, *A Heitler model of extensive air showers*, Astropart. Phys., **22**, 387 (2005).

[35] W. Heitler, *The Quantum Theory of Radiation*, Dover Books on Physics and Chemistry, Dover Publications, (1954).

[36] Stepan G. Mashnik, *On Solar System and Cosmic Rays Nucleosynthesis and Spallation Processes*, arXiv:0008382v1.

[37] Diego Garcia-Pinto for the Pierre Auger Collaboration, *Measurements of the Longitudinal Development of Air Showers with the Pierre Auger Observatory*, Proc. 32nd ICRC, (2011).

[38] Lev Dorman, *Cosmic Rays Interactions,Propagation,and Acceleration In Space Plasmas*, Springer, **339**, 525 (2006).

[39] A. M. Hillas, *The Origin of Ultra-High-Energy Cosmic Rays*, Annual Reviews of Astronomy and Astrophysics, **22**, 425 (1984).

[40] Vassily Beskin, Gills Henri, *Accretion Disks, Jets and High Energy Phenomena in astrophysics*, Springer, 321 (2002).

[41] Malcolm S. Longair, *High Energy Astrophysics, stars, the galaxy and the interstellar medium*, Cambridge University press, (1992).

[42] Graciela B. Gelmini, *High energy cosmic rays*, Journal of Physics: Conference Series, **171**, 012012 (2009); arXiv:0903.4716.

[43] Pranab Ghosh, *Rotation and Accretion Powered Pulsars*, World Scientific Publishing Co. Pte. Ltd., (2007).

[44] Luis Anchordoqui, Thomas Paul, Stephen Reucroft, and John Swain, *Ultra high Energy Cosmic Rays: The state of the art before the Auger Observatory*, Int. J. Mod. Phys., **A18**, 2229 (2003).

[45] C. Megan Urry and Paolo Padovani, *Unified Schemes for Radio-Loud Active Galactic Nuclei*, Publ.Astron.Soc.Pac., **107**, 803 (1995); arXiv:9506063.

[46] http://heasarc.gsfc.nasa.gov/docs/cgro/images/epo/gallery/agns/.

[47] P. Mészáros *Gamma-Ray Bursts*, Rep. Prog. Phys., **69**, 2259 (2006); arXiv:0605208.

[48] G. Vedrenne and J.-L. Atteia, *Gamma-ray Bursts: The brightest explosions in the Universe*, **ISBN 978-3-540-39085-5**, (2009).

[49] The Pierre Auger Collaboration, *Searches for anisotropies in the arrival directions of the highest energy energy cosmic rays detected by the Pierre Auger Observatory*, ApJ, **804**, 15 (2015).

[50] Piera Luisa Ghia for the Pierre Auger Collaboration, *Highlights from the Pierre Auger Observatory*, Proc. 34th ICRC, (2015).

[51] Iván Sidelnik, *Measurement of the first harmonic modulation in the right ascension distribution of cosmic rays detected at the Pierre Auger Observatory: towards the detection of dipolar anisotropies over a wide energy range*, Proc. 33^{rd} ICRC, (2013).

[52] J. Linsley, *Fluctuation effects on directional data*, Phys. Rev. Lett., **34**, 1530 (1975).

[53] R. Bonino et al., *The East-West method: an exposure-independent method to search for large scale anisotropies of cosmic rays*, ApJ, **738**, 67 (2011); arXiv:1106.2651.

[54] Olivier Deligny for the Pierre Auger Collaboration and Telescope Array Collaboration, *Large-Scale Distribution of Arrival Directions of Cosmic Rays Detected at the Pierre Auger Observatory and the Telescope Array above* 10^{19} , Proc. 34th ICRC, (2015).

[55] Geraldina Golup for the Pierre Auger Collaboration, *Search for energy-position correlated multiplets in Pierre Auger Observatory data*, Proc. 32nd ICRC, (2011).

[56] The IceCube, the Pierre Auger, and the Telescope Array Collaborations, *The IceCube Neutrino Observatory, the Pierre Auger Observatory and the Telescope Array: Joint Contribution to the 34th International Cosmic Ray Conference (ICRC 2015)*, Proc. 34th ICRC, (2015).

[57] The IceCube, the Pierre Auger, and the Telescope Array Collaborations, *Search for correlations between the arrival directions of IceCube neutrino events and ultrahigh-energy cosmic rays detected by the Pierre Auger Observatory and the Telescope Array* , Journal of Cosmology and Astroparticle Physics, (2016); arXiv:1511.09408.

[58] The Telescope Array Collaboration, *Indications of Intermediate-Scale Anisotropy of Cosmic Rays with Energy Greater Than 57 EeV in the Northern Sky Measured with the Surface Detector of the Telescope Array Experiment*, ApJ, **790**, L21 (2014); arXiv:1404.5890.

[59] The Pierre Auger Collaboration, *The Pierre Auger Observatory Upgrade "AugerPrime" Preliminary Design Report*; arXiv:1604.03637, (2016).

[60] M. Fukushima for the Telescope Array Collaboration, *Recent Results from Telescope Array*, EPJ Web of Conferences **99**, 04004 (2015); arXiv:1503.06961.

[61] J. Holder, *TeV Gamma-ray Astronomy: A Summary*, Astroparticle Physics, **39-40**, 61 (2012); arXiv:1204.1267.

[62] P. Morrison, *On gamma-ray astronomy*, Annual Review of Astronomy and Astrophysics, **7**, 858 (1958).

[63] G. Cocconi, *An air shower telescope and the detection of* 10^{12} *eV photon sources*, Proc. 6th ICRC, (1960).

[64] W. Galbraith and J. V. Jelley, *Light Pulses from the Night Sky associated with Cosmic Rays*, Nature, **171**, 349 (1953).

[65] T. C., Weekes, et al., *Observation of TeV Gamma Rays from the Crab Nebula Using the Atmospheric Cerenkov Imaging Technique*, ApJ, **342** 379 (1989).

[66] M. Punch, et al., *Detection of TeV photons from the active galaxy Markarian 421*, Nature, **358**, 477 (1992).

[67] J. Quinn, et al., *Detection of Gamma Rays with* $E > 300\,GeV$ *from Markarian 501*, ApJ, **456**, L83 (1996).

[68] A. Daum, et al., *First results on the performance of the HEGRA IACT array*, Astroparticle Physics, **8**, 1 (1997).

[69] Bernard Degrange and Gérard Fontaine, *Introduction to high-energy gamma-ray astronomy*, C. R. Physique, 587, 16 (2015); arXiv:1604.05488.

[70] The *Fermi*-LAT Collaboration, *Fermi Large Area Telescope observations of the Crab Pulsar and Nebula*, ApJ, **708**, 1254 (2010); arXiv:0911.2412.

[71] The H.E.S.S. Collaboration and the *Fermi*-LAT Collaboration, *Simultaneous observations of PKS 2155-304 with H.E.S.S., Fermi, RXTE and ATOM: spectral energy distributions and variability in a low state*, ApJ, **696**, L150 (2009); arXiv:0903.2924.

[72] J.A. Hinton and W. Hofmann, *Teraelectronvolt Astronomy*, Ann.Rev.Astron.Astrophys, **47**, 523 (2010); arXiv:1006.5210.

[73] The Pierre Auger Collaboration, *An upper limit to the photon fraction in cosmic rays above 10^{19} eV from the Pierre Auger Observatory*, Astropart. Phys., **27**, 155 (2006), astro-ph/0606619.

[74] The Pierre Auger Collaboration, *Upper limit on the cosmic-ray photon flux above 10^{19} eV using the surface detector of the Pierre Auger Observatory*, Astropart. Phys., **29**, 243 (2008); arXiv:0712.1147.

[75] The Pierre Auger Collaboration, *Upper limit on the cosmic-ray photon fraction at EeV energies from the Pierre Auger Observatory*, Astropart. Phys., **31**, 399 (2009); arXiv:0903.1127.

[76] The Pierre Auger Collaboration, *A Search for Point Sources of EeV Photons*, ApJ, **789**, 12 (2014); arXiv:1406.2912.

[77] E. Lorenz, R. Wagner *Very-high energy gamma-ray astronomy: A 23-year success story in high-energy astroparticle physics*, The European Physical Journal H, **37**, 459 (2012); 1207.6003.

[78] Gabriele Ghisellini, *Radiative processes in high energy astrophysics*, Lecture Notes in Physics, **873**, (2013); arXiv:1202.5949v1.

[79] Hale Bradt, *Astrophysics Processes: The Physics of Astronomical Phenomena*, Cambridge University Press, ISBN 0521846560 9780521846561, (2008).

[80] V.V. Zheleznyakov, *Radiation in Astrophysical Plasmas*, Kluwer Academic Publishers, ISBN 13:978-94-010-6574-0, (1996).

[81] D. B. Melrose, *Plasma Astrophysics - Nonthermal Processes in Diffuse Magnetized Plasmas*, Gordon and Breach Science Publishers, ISBN 0 677 02340, (1980).

[82] Hiroyasu Tajima for the *Fermi*-LAT, *Fermi*-GBM collaborations, *Fermi Observations of high-energy gamma-ray emissions from GRB 080916C*, Proc. 31st ICRC, (2009); arXiv:0907.0714.

[83] R. W. Klebesadel, I. B. Strong, R. A. Olson, *Observations of Gamma-Ray Bursts of Cosmic Origin*, ApJ, **182**, L85 (1973).

[84] C. A. Meegan, *Spatial distribution of γ-ray bursts observed by BATSE*, Nature, **355**, 143 (1992).

[85] Bohdan Paczyński, *A test of the Galactic origin of gamma-ray bursts*, ApJ, **348**, 485 (1990).

[86] M. Pamini, et. al., *The gamma-ray burst monitor on board the SAX satellite*, Il Nuovo Cimento C, **13**, 337 (1990).

[87] B. Paczyński, *Are Gamma-Ray Bursts in Star-Forming Regions?*, ApJ, **494**, L45 (1998).

[88] http://space.mit.edu/HETE/.

[89] http://sci.esa.int/integral/.

[90] http://swift.gsfc.nasa.gov/.

[91] https://www-glast.stanford.edu/.

[92] The *Fermi*-LAT Collaboration and the *Fermi*-GBM Collaboration, *Fermi-LAT Observations of the Gamma-ray Burst GRB 130427A*, Science **343**, 24 (2014); arXiv:1311.5623.

[93] M. J. Rees and P. Mészáros, *Relativistic fireballs: energy conversion and time-scales*, Mon. Not. R. astr. Soc., **258**, 41 (1992).

[94] M. J. Rees and P. Mészáros, *Unsteady Outflow Models for Cosmological Gamma-Ray Bursts*, ApJ, **430**, L93 (1994); arXiv:9404038

[95] P. Mészáros, et al., *Spectral Properties of Blast Wave Models of Gamma-Ray Burst Sources*, ApJ, **432**, 181 (1994); arXiv:9311071.

[96] Amotz Shemi and Tsvi Piran, *The appearance of cosmic fireballs*, ApJL, **365**, L55 (1990); 1990ApJ...365L..55S.

[97] P. Chris Fragile, et al., *Constraints on models for TeV gamma rays from gamma-ray bursts*, Astroparticle Physics, **20**, 591 (2004); arXiv:0206383.

[98] The LIGO Scientific Collaboration and the Virgo Collaboration, *GW151226: Observation of Gravitational Waves from a 22-Solar-Mass Binary Black Hole Coalescence*, Phys. Rev. Lett., **116**, 241103 (2016).

[99] The *Fermi*-LAT Collaboration, *The Large Area Telescope on the Fermi Gamma-ray Space Telescope Mission*, ApJ, **697**, 1071 (2009); arXiv:0902.1089.

[100] http://agile.rm.iasf.cnr.it/

[101] Frank M. Rieger, et.al., *TeV Astronomy*, Frontiers of Physics, **8**, 714 (2013); arXiv:1302.5603.

[102] C. Pfrommer, *Introduction to extragalactic sources of very high-energy photons*, Proc. 48th Rencontres de Moriond on Very High Energy Phenomena in the Universe, (2013); arXiv:1308.6582.

[103] http://tevcat.uchicago.edu/.

[104] The H.E.S.S. Collaboration, *Acceleration of Petaelectronvolt protons in the Galactic Centre*, Nature, **531**, 476 (2016); arXiv:1603.07730.

[105] F. Acero, et. al., *Study of TeV shell supernova remnants at gamma-ray energies*, A&A, **580**, A74 (2015); arXiv:1506.02307.

[106] The H.E.S.S. Collaboration, *Discovery of extended VHE γ-ray emission from the vicinity of the young massive stellar cluster Westerlund 1*, A&A, **537**, A114 (2012); arXiv:1111.2043.

[107] R. Bühler and R. Blandford, *The surprising Crab pulsar and its nebula: a review*, Rep. Prog. Phys. **77** (2014); arXiv:1309.7046.

[108] The H.E.S.S. Collaboration, *Discovery of gamma-ray emission from the extragalactic pulsar wind nebula N157B with the High Energy Stereoscopic System*, A&A, **545**, L2 (2012); arXiv:1208.1636.

[109] J. Linsley, *Evidence for a Primary Cosmic-Rays Particle with Energy* 10^{20} *eV*, Phys. Rev. Lett., **10**, 146 (1963).

[110] Esteban Roulet, for the Pierre Auger Collaboration, *Latest Results from the Pierre Auger Observatory*, arXiv:1101.1825, (2011).

[111] A.M. Hillas, *Evolution of ground-based gamma-ray astronomy from the early days to the Cherenkov Telescope Arrays*, Astroparticle Physics, **43**, 19 (2013); 2013APh....43...19H

[112] Mathieu de Naurois and Daniel Mazin *Ground-based detectors in very-high-energy gamma-ray astronomy*, Comptes Rendus Physique, **16**, 610 (2015); arXiv:1511.00463.

[113] https://www.mpi-hd.mpg.de/hfm/HESS/.

[114] http://veritas.sao.arizona.edu/.

[115] https://magic.mpp.mpg.de/.

[116] https://portal.cta-observatory.org/Pages/Home.aspx/.

[117] The CTA Collaboration, *Introducing the CTA concept*, Astroparticle Physics, **43**, 3 (2013).

[118] The ARGO-YBJ Collaboration *ARGO-YBJ Observation of the large-scale cosmic ray anisotropy during the solar minimum between cycle 23 and 24*, ApJ, **809**, 90 (2015).

[119] P. Bernardini, on behalf of the ARGO-YBJ Collaboration *ARGO-YBJ experiment in Tibet*, J. Phys.: Conf. Ser., **120**, 062022 (2008); arXiv:0904.1018.

[120] *Milagro observations of multi-TeV emission from galactic sources in the Fermi bright source list*, ApJ, **700**, L127 (2009); arXiv:0904.1018.

[121] http://english.ihep.cas.cn/ic/ip/LHAASO/.

[122] Z. Cao for the LHAASO collaboration, *A Future Project at Tibet: The Large High Altitude Air Shower Observatory (LHAASO)*, Proc. 31st ICRC, (2009).

[123] The HAWC Collaboration, *Search for TeV gamma-ray emission from point-like sources in the inner Galactic plane with a partial configuration of the HAWC observatory*, ApJ, **817**, 3 (2016).

[124] The HAWC Collaboration, *On the sensitivity of the HAWC observatory to gamma-ray bursts*, Astroparticle Physics, **35**, 641 (2012); arXiv:1108.6034.

[125] M. Tluczykont, et al., *The HiSCORE experiment and its potential for gamma-ray astronomy*, Journal of Physics: Conference Series, **409**, 012120 (2013).

[126] M. Tluczykont, et al., *The HiSCORE concept for gamma-ray and cosmic-ray astrophysics beyond 10 TeV*, Astroparticle Physics, **56**, 42 (2014); arXiv:1403.5688.

[127] M. Actis, et al. (CTA Consortium), *Design concepts for the Cherenkov Telescope Array CTA: an advanced facility for ground-based high-energy gamma-ray astronomy*, Experimental Astronomy, **32**, 193 (2011).

[128] C. M. Hoffman, et al., *Gamma-ray astronomy at high energies*, Reviews of Modern Physics, **71**, 897 (1999).

[129] The Pierre Auger Collaboration, *The Pierre Auger Observatory scaler mode for the study of solar activity modulation of galactic cosmic rays*, JINST, **6** P01003 (2011); arXiv:1204.6196.

[130] The Pierre Auger Collaboration, *Properties and performance of the prototype instrument for the Pierre Auger Observatory*, Nucl. Instrum. Meth. A **523**, 50 (2004).

[131] The Pierre Auger Collaboration, *The Pierre Auger Cosmic Ray Observatory*, Nucl. Instrum. Meth. A **798**, 172 (2015); arXiv:1502.01323.

[132] Jakub Vícha, Jiří Chudoba for the Pierre Auger Collaboration, *Data Processing at the Pierre Auger Observatory*, Journal of Physics: Conference Series, **608**, 012077 (2015); arXiv:1509.06319.

[133] The Pierre Auger Collaboration, *The surface detector system of the Pierre Auger Observatory*, Nucl. Instrum. Meth. A **586**, 409 (2008); arXiv:0712.2832.

[134] F. Sanchez for the Pierre Auger Collaboration, *The AMIGA Detector of the Pierre Auger Observatory: An Overview*, Proc. 32nd ICRC, 2011; arXiv:1107.4807.

[135] I. C. Maris for the Pierre Auger Collaboration, *The AMIGA infill detector of the Pierre Auger Observatory: performance and first data*, Proc. 32nd ICRC, (2011); arXiv:1107.4807.

[136] Karl-Heinz Kampert and Alan A. Watson, *Extensive air showers and ultra high-energy cosmic rays: a historical review*, Eur. Phys. J. H, **37**, 359 (2012); arXiv:1207.4827.

[137] X. Bertou, et al., *Calibration of the surface array of the Pierre Auger Observatory*, Nucl. Instrum. Meth. A **568**, 839 (2006).

[138] R. C. Shellard for the Pierre Auger Collaboration, *First results from the Pierre Auger Observatory*, Braz.J.Phys, **36**, 1184 (2006); arXiv:0609060.

[139] The Pierre Auger Collaboration, *Trigger and aperture of the surface detector array of the Pierre Auger Observatory*, Nucl. Instrum. Meth. A **613**, 29 (2010).

[140] Ioana C. Mariş, *Measurement of the Ultra High Energy Cosmic Ray Flux using Data of the Pierre Auger Observatory*, GAP2008_026, 2008.

[141] J. J. Masías-Meza, et al., *Long Term Solar Physics Studies Using the Scalers Rate*, GAP2014_102.

[142] J. J. Masías-Meza for the Pierre Auger Collaboration, *Solar Cycle Modulation of Cosmic Rays Observed with the Low Energy Modes of the Pierre Auger Observatory*; Proc. 34th ICRC (2015); arXiv:1509.03732.

[143] Hernán Asorey for the Pierre Auger Observatory *Measurement of Low Energy Cosmic Radiation with the Water Cherenkov Detector Array of the Pierre Auger Observatory*, Proc. 32nd ICRC, (2011).

[144] The Pierre Auger Collaboration, *The Pierre Auger Observatory Scaler Mode for the Study of Solar Activity Modulation of Galactic Cosmic Rays*, JINST, **6**, P01003 (2011); http://iopscience.iop.org/1748-0221/6/01/P01003; arXiv:1204.6196.

[145] The Pierre Auger Collaboration, *The fluorescence detector of the Pierre Auger Observatory*, Nucl. Instrum. Meth. A **620**, 227 (2010); arXiv:0907.4282.

[146] Federico Suarez for the Pierre Auger Collaboration, *The AMIGA muon detectors of the Pierre Auger Observatory: overview and status*, Proc. 33rd ICRC, (2013).

[147] T. Hermann-Josef Mathes for the Pierre Auger Collaboration, *The HEAT Telescopes of the Pierre Auger Observatory Status and First Data*, Proc. 32nd ICRC, (2011).

[148] John L. Kelley for the Pierre Auger Collaboration, *AERA: the Auger Engineering Radio Array*, Proc. 32nd ICRC, (2011).

[149] Lena Salfenmoser, Ewa Holt, Frank Schröder, Andreas Haungs, *A First Combined Analysis of AMIGA and AERA Measurements*, GAP2015_081, 2015.

[150] Cabrera, et al., Search for GeV GRBs with the INCA experiment, Astron. Astrophys. Suppl. Ser., **138**, 599 (1999).

[151] The EAS-TOP Collaboration, *Search for Gamma-Ray Bursts at Photon Energies* $E \geq 10\,GeV$ *and* $E \geq 80\,TeV$, ApJ, **469** 305 (1996); 1996ApJ...469..305A.

[152] G. Aielli, et al., Search for Gamma Ray Bursts with the ARGO-YBJ Detector in Scaler Mode, ApJ, **699**, 1281 (2009).

[153] B. Bartoli, et al., *Search for GeV Gamma-Ray Bursts with the ARGO-YBJ Detector: Summary of Eight Years of Observations*, ApJ, **794**, 12 (2014);arXiv:1502.05622.

[154] A.N. Gaponenko, Search for very short gamma-ray bursts at the Andyrchy EAS array on millisecond timescale, 33rd International Cosmic Ray Conference, (2013).

[155] V. B. Petkov, et al., *Search for high energy gamma-ray bursts*, Astrophys. Space Sci. Trans., **7** 97 (2011);2011ASTRA...7...97P.

[156] X. Bertou for the Pierre Auger Collaboration, *Search for Gamma-Ray Bursts Using the Single Particle Technique at the Pierre Auger Observatory*, Proc. 30th ICRC, **4** 441 (2008); arXiv:0706.1256.

[157] X. Bertou and D. Allard, *Current Status of the Scalers: Towards the detection of GRBs with Auger?*, GAP2005_053.

[158] H. Asorey, X. Bertou, *First Large Timescale Analysis of Auger SD Scaler Data: Towards cosmic ray solar modulation studies*, GAP2008_072.

[159] The Pierre Auger Collaboration, *Properties and Performance of the Prototype Instrument for the Pierre Auger Observatory*, NIM **A523**, 50 (2004).

[160] The Pierre Auger Collaboration, *The Pierre Auger Cosmic Ray Observatory*, NIM **A798**, 172 (2015); http://dx.doi.org/10.1016/j.nima.2015.06.058.

[161] X. Bertou, *Background Radiation Measurement with the Water Cherenkov Detectors of the Pierre Auger Observatory*, Nuclear Instruments and Methods in Physics Research A, **639**, 73 (2011).

[162] The Pierre Auger Collaboration, *Detecting GRBs with the Pierre Auger Observatory Using the Single Particle Technique*, Nuclear Physics B, **165** , 110 (2007); arXiv:0508441.

[163] A. Manzanera, $\Sigma - \Delta$ *Background Subtraction and the Zipf Law*, L. Rueda, D. Mery, and Kittler (Eds.): CIARP 2007, **LNCS 4756**, 42 (2007).

[164] https://auger.colostate.edu/private/herald/.

[165] http://ipnwww.in2p3.fr/ augers/AugerProtected/ICRC.html/.

[166] http://ipnwww.in2p3.fr/ augers/AugerProtected/ICRC.html/.

[167] X. Bertou, Private Communication.

[168] http://auger.colostate.edu/ED/scaler/.

[169] R. Sato, et al., *Long Term Performance of the Surface Detectors of the Pierre Auger Observatory*, Proc. 32nd ICRC, (2011).

[170] The Pierre Auger Observatory, *Atmospheric effects on extensive air showers observed with the surface detector of the Pierre Auger observatory*, Astroparticle Physics, **32**, 89(2009); arXiv:0906.5497.

[171] D. Allard the Pierre Auger Collaboration, *Detecting GRBs with the Pierre Auger Observatory using the single particle technique*, Nuclear Physics B - Proceedings Supplements, **165**, 110(2007); arXiv:0508441.

[172] The ARGO-YBJ Collaboration, *Search for Gamma Ray Bursts with the ARGO-YBJ Detector in Scaler Mode*, ApJ, **699**, 1281(2009); arXiv:0905.1189.

[173] The H.E.S.S. Collaboration, *GRB 081028 and its late-time afterglow re-brightening*, Mon. Not. R. Astron. Soc., **402**, 46 (2010).; arXiv:0910.3166.

[174] http://www.astronomerstelegram.org/?read=8519/.

[175] K. Nandra, et al., *ASCA Observations Of Seyfert 1 Galaxies. I. Data analysis, Imaging, and Timing*, ApJ, **476**, 70 (1997); arXiv:9608170.

[176] *Handbook of X-ray Astronomy* Edited by Keith A. Arnaud, Randall K. Smith and Aneta Siemiginowska, ISBN 978-0-521-88373-3, Cambridge University Press, 86 (2011).

[177] The H.E.S.S. Collaboration, *An Exceptional Very High Energy Gamma-Ray Flare of PKS 2155-304*, ApJ, **664**, L71 (2007); arXiv:0706.0797.

[178] The VERITAS Collaboration, *Rapid TeV Gamma-Ray Flaring of BL Lacertae*, ApJ, **762**, 92 (2013); arXiv:1211.3073.

[179] https://heasarc.gsfc.nasa.gov/docs/asca/asca2.html/.

[180] E. W. Bonning, et al., *SMARTS optical and infrared monitoring of 12 gamma-ray bright blazars*, ApJ, **756**, 13 (2012); arXiv:1201.4380.

[181] http://ast.noao.edu/facilities/smarts.

[182] http://fermi.gsfc.nasa.gov/.

[183] D. Heck, et al., *CORSIKA: A Monte Carlo Code to Simulate Extensive Air Showers*, Forschungszentrum Karlsruhe **FZKA 6019**, (1998).

[184] S. Ostapchenko, *Monte Carlo treatment of hadronic interactions in enhanced Pomeron scheme: QGSJET-II model*, Phys. Rev. D, **83**, 014018 (2011).

[185] S. Argirò, et al., *The Offline Software Framework of the Pierre Auger Observatory*, NIM, **A 580**, 1485 (2007); arXiv:0707.1652.

[186] V. V. Alexeenko, et al., Burst-Like Event Observed by Baksan EAS Array From The CRAB Nebula 23 Feb 1989, Proc. 22nd ICRC, **1**, 293 (1991); 1991ICRC....1..293A.

[187] M. Aglietta, et al., *Detection of the UHE burst from the Crab Nebula on February 23, 1989, from EAS-TOP array*, Europhys. Lett., **15**, 86 (1991); 1991EL.....15...81A.

[188] J. Jeff Hester, *The Crab Nebula: An Astrophysical Chimera*, Annual Review of Astronomy and Astrophysics, **46**, 127 (2008).

[189] John D. Barrow, Cosmic Imagery: Key Images in the History of Science. Random House, ISBN 978-0-224-07523-7, 45 (2008).

[190] Parsons, William, *Observations on Some of the Nebulae*, Philosophical Transactions of the Royal Society of London, 321 (1844).

[191] Nicholas U. Mayall, *The Crab Nebula, A Probable Supernova*, Astronomical Society of the Pacific Leaflets, **3**, 145 (1939).

[192] S.D. Kawaler, I. Novikov, and G. Srinivasan, *Stellar Remnants: Saas-Fee Advanced Course 25. Lecture Notes 1995. Swiss Society for Astrophysics and Astronomy*, Springer Science & Business Media, 340 (2006).

[193] C. O. Lampland, *Observed Changes in the Structure of the "Crab" Nebula (N. G. C. 1952)*, Astronomical Society of the Pacific, **33**, 79 (1922).

[194] John C. Duncan, *Changes Observed in the Crab Nebula in Taurus*, Proceedings of the National Academy of Sciences of the United States of America, **7**, 179 (1921).

[195] K. Lundmark, *Suspected New Stars Recorded in Old Chronicles and Among Recent Meridian Observations*, Astronomical Society of the Pacific, 33, 225 (1921).

[196] W. Baade, *The Crab Nebula*, ApJ, **96**, 188 (1942); 1942ApJ....96..188B.

[197] Virginia Trimble, *The Distance to the Crab Nebula and NP 0532*, Astronomical Society of the Pacific, **85**, 579 (1973); 1973PASP...85..579T.

[198] http://www.asdc.asi.it/.

[199] http://fermi.gsfc.nasa.gov/ssc/data/access/lat/msl_lc/.

[200] M. F. Bietenholz and R. L. Nugent, *New expansion rate measurements of the Crab Nebula in radio and optical*, MNRAS, **454**, 2416 (2015); arXiv:1509.04687.

[201] Serguei Komissarov and Yuri Lyubarsky, MHD Simulations of Crab's Jet and Torus, Astrophysics and Space Science, **293**, 107 (2004).

[202] I. H. Cairns, *Properties and Interpretations of Giant Micropulses and Giant Pulses from Pulsars*, ApJ, **610**, 948 (2004); astro-ph/0404174.

[203] A. D. Kuzmin, *Giant pulses of pulsar radio emission*, Astrophysics and Space Science, **308**, 563 (2007); astro-ph/0701193.

[204] D. H. Staelin and E. C. Reifenstein, *Pulsating radio sources near the Crab Nebula*, Science, **162**, 1481 (1968); 1968Sci...162.1481S.

[205] J. M. Comella, et al., *Crab Nebula Pulsar NP 0532*, Nature, **221**, 453 (1969); 1969Natur.221..453C.

[206] The MAGIC Collaboration, *Observation of Pulsed γ-Rays Above 25 GeV from the Crab Pulsar with MAGIC*, Science, **322**, 1221 (2008); arXiv:0809.2998.

[207] The MAGIC Collaboration, *Observations of the Crab Pulsar between 25 and 100 GeV with the MAGIC I Telescope*, ApJ, **742**, 14 (2011); arXiv:1108.5391.

[208] The MAGIC Collaboration, *Phase-resolved energy spectra of the Crab pulsar in the range of 50-400 GeV measured with the MAGIC telescopes*, Astronomy & Astrophysics, **540**, A69 (2012); arXiv:1109.6124 .

[209] The VERITAS Collaboration, *Detection of Pulsed Gamma Rays Above 100 GeV from the Crab Pulsar*, Science, **334**, 69 (2011); arXiv:1108.3797.

[210] The *Fermi*-LAT Collaboration, *The Second Fermi Large Area Telescope Catalog of Gamma-Ray Pulsars*, The Astrophysical Journal Supplement, *208*, 59 (2013); arXiv:1305.4385 .

[211] R. J. Gould, *High-Energy Photons from the Compton-Synchrotron Process in the Crab Nebula*, Physical Review Letters, **15**, 577 (1965).

[212] J. E. Grindlay, *Detection of pulsed gamma rays of $\sim 10^{12}$ eV from the pulsar in the Crab nebula*, ApJ, **174**, L9 (1972).

[213] G. G. Fazio, et al., *Detection of high-energy gamma rays from the Crab Nebula*, ApJ, **175**, L117 (1972).

[214] G. Vacanti, et al., *Gamma-ray observations of the Crab Nebula at TeV energies*, ApJ, **377**, 467 (1991).

[215] A. M. Hillas, et al., *The spectrum of TeV Gamma Rays from the Crab Nebula*, ApJ, **503**, 744 (1998).

[216] C. Akerlof, et al., *Detection of very high energy gamma-rays from the Crab nebula*, Proc. of Gamma-Ray Observatory Science Workshop, Greenbelt, MD, 4 (1989).

[217] R. J. Protheroe, *The status of ultra-high-energy gamma-ray observations*, Astrophysical Journal Supplement, **90**, 883 (1994); 1994ApJS...90..883P.

[218] P. Goret, et al., *Observations of TeV gamma rays from the Crab nebula*, **270**, 401 (1993).

[219] THEMISTOCLE Collaboration, *Gamma ray spectrum of the Crab nebula in the multi TeV region*, Astroparticle Physics, **1**, 341 (1993).

[220] R. W. Lessard, et al., *Search for pulsed TeV gamma-ray emission from the Crab pulsar*, ApJ, **531**, 942 (2000).

[221] A. O'Faoláin de Bhróithe for the VERITAS Collaboration, *The search for short-term flares in extended VHE Crab Nebula observations with the Whipple 10 m telescope*, Proc. 34th ICRC, 2015; arXiv:1508.06794.

[222] The HEGRA Collaboration, *The Crab Nebula and Pulsar between 500 GeV and 80 TeV: Observations with the HEGRA stereoscopic air Cherenkov telescopes*, ApJ, **614**, 897 (2004); arXiv:0407118.

[223] The H.E.S.S. Collaboration, *Observations of the Crab Nebula with H.E.S.S.*, Astron. Astrophys., **457**, 899 (2006); astro-ph/0607333.

[224] The MAGIC Collaboration, *Measurement of the Crab Nebula spectrum over three decades in energy with the MAGIC telescopes*, Journal of High Energy Astrophysics, **5-6**, 30 (2015); arXiv:1406.6892.

[225] K. Meagher for the VERITAS Collaboration, *Six years of VERITAS observations of the Crab Nebula*, Proc. 34th ICRC (2015); arXiv:1508.06442.

[226] O. Celik for the VERITAS Collaboration, *Observations of the Crab Nebula and Pulsar with VERITAS*, Proc. 30th ICRC, (2008); arXiv:0709.3868.

[227] C. A. Wilson-Hodge, M. L. Cherry, G. L. Case, et al., *When a standard candle flickers*, ApJL, **727**, L40 (2011); arXiv:1010.2679.

[228] The *Fermi*-LAT Collaboration, *Gamma-Ray Flares from the Crab Nebula*, Science, **331**, 739 (2011); arXiv:1011.3855.

[229] P. V. Ramanamurthy, et al., *A long-term study of high-energy gamma-ray emission from the Vela, Geminga, and Crab Pulsars*, ApJ, **450**, 791 (1995).

[230] M. López, et al., *Search for pulsed VHE gamma ray emission from the Crab Pulsar*, Proc. 29th ICRC, 2005.

[231] M. López, N. Otte, M. Rissi, T. Schweizer, M. Shayduk, S. Klepser for the MAGIC Collaboration, *Detection of the Crab pulsar with MAGIC*, Proc. 31st ICRC, 2009; arXiv:0907.0832.

[232] The MAGIC Collaboration, *Teraelectronvolt pulsed emission from the Crab pulsar detected by MAGIC*, A&A, **585**, A133 (2016); arXiv:1510.07048.

[233] The AGILE Collaboration, *Discovery of Powerful Gamma-Ray Flares from the Crab Nebula*, Science, **331**, 736 (2011); arXiv:1101.2311.

[234] M. Mayer, et al., *Rapid Gamma-Ray Flux Variability During the 2013 March Crab Nebula Flare*, ApJ, **775**, L37 (2013); arXiv:1308.6698.

[235] S. S. Komissarov and M. Lyutikov, *On the origin of variable gamma-ray emission from the Crab nebula*, MNRAS, **414**, 2017 (2011); arXiv:1011.1800.

[236] W. Bednarek and W. Idec, *On the variability of the GeV and multi-TeV gamma-ray emission from the Crab nebula*, Monthly Notices of the Royal Astronomical Society, **414**, 2229 (2011); arXiv:1011.4176.

[237] Q. Yuan, et al., *A Statistical Model for the γ-ray Variability of the Crab Nebula*, ApJL, **730**, 5 (2011); arXiv:1012.1395.

[238] D. A. Uzdensky, B. Cerutti, and M. C. Begelman, *Reconnection-powered Linear Accelerator and Gamma-Ray Flares in the Crab Nebula*, ApJ, **737**, L40 2011; arXiv:1105.0942.

[239] D. A. Uzdensky and A. Spitkovsky, *Physical Conditions in the Reconnection Layer in Pulsar Magnetospheres*, ApJ, **780**, 3 (2014); arXiv:1210.3346.

[240] A. S. Lidvansky, *On the burst activity of the Crab Nebula and pulsar at high and ultra-high energies*, Journal of Physics: Conference Series, **409**, (2013); 2013JPhCS.409a2114L.

[241] http://www.astronomerstelegram.org/?read=2855/.

[242] http://www.astronomerstelegram.org/?read=2856/.

[243] http://www.astronomerstelegram.org/?read=2858/.

[244] http://www.astronomerstelegram.org/?read=2882/.

[245] http://www.astronomerstelegram.org/?read=2921/.

[246] http://www.astronomerstelegram.org/?read=2967/.

[247] http://www.astronomerstelegram.org/?read=2968/.

[248] http://www.astronomerstelegram.org/?read=3276/.

[249] R. Buehler, et al., *Gamma-Ray Activity in the Crab Nebula: the Exceptional Flare of 2011 April*, ApJ, **749**, 26 (2012); arXiv:1112.1979.

[250] http://www.astronomerstelegram.org/?read=3286/.

[251] The AGILE Collaboration, *The Crab Nebula Super-Flare in 2011 April: Extremely Fast Particle Acceleration and Gamma-Ray Emission*, ApJ, **741** (2011); arXiv:1105.5028.

[252] The ARGO-YBJ Collaboration, *Crab Nebula: Five-Year Observation with ARGO-YBJ*, ApJ, **798**, 119 (2015); arXiv:1502.05665.

[253] E. Striani, *Variable gamma-ray emission from the Crab Nebula: Short flares and long "waves"*, ApJ, **765**, 1 (2013); arXiv:1302.4342.

[254] http://www.astronomerstelegram.org/?read=3283/.

[255] http://www.astronomerstelegram.org/?read=3279/.

[256] R. Zanin, et al. for the MAGIC Collaboration, Dieter Horns, M. Meyer *MAGIC measurement of the Crab Nebula spectrum over three decades in energy*, Proc. 32nd ICRC, 2011; arXiv:1110.2987.

[257] http://www.astronomerstelegram.org/?read=4239/.

[258] The *Fermi*-LAT Collaboration, *Fermi Large Area Telescope Second Source Catalog*, The Astrophysical Journal Supplement, **199**, 46 (2012); arXiv:1108.1435.

[259] https://fermi.gsfc.nasa.gov/ssc/data/access/lat/msl_lc/source/Crab_Pulsar/.

[260] http://www.astronomerstelegram.org/?read=4258/.

[261] S. Vernetto for the ARGO-YBJ Collaboration, *Study of the Crab Nebula TeV emission variability during five years with ARGO-YBJ*, Proc. 33rd ICRC, 2011; arXiv:1307.7041.

[262] http://www.astronomerstelegram.org/?read=4855/.

[263] http://www.astronomerstelegram.org/?read=4856/.

[264] http://www.astronomerstelegram.org/?read=4867/.

[265] http://www.astronomerstelegram.org/?read=4869/.

[266] http://www.astronomerstelegram.org/?read=4878/.

[267] The H.E.S.S. Collaboration, *H.E.S.S. observations of the Crab during its March 2013 GeV gamma-ray flare*, A&A, **562**, L4 (2014); arXiv:1311.3187.

[268] The VERITAS Collaboration, *A search for enhanced very high energy gamma-ray emission from the March 2013 Crab Nebula flare*, ApJL, **781**, 7 (2014); arXiv:1309.5949.

[269] http://www.astronomerstelegram.org/?read=5485/.

[270] http://www.astronomerstelegram.org/?read=5506/.

[271] http://www.astronomerstelegram.org/?read=4869/.

[272] http://www.astronomerstelegram.org/?read=4878/.

[273] http://www.astronomerstelegram.org/?read=5971/.

[274] http://www.astronomerstelegram.org/?read=5976/.

[275] http://www.astronomerstelegram.org/?read=6401/.

[276] The *Fermi*-LAT Collaboration, *Fermi Large Area Telescope Third Source Catalog*, The Astrophysical Journal Supplement Series, **218**, 41 (2015); arXiv:1501.02003.

[277] http://www.astronomerstelegram.org/?read=2893/.

[278] J. Rautenberg for the Pierre Auger Collaboration, *Lightning Detection at the Pierre Auger Observatory*, Proc. 34th ICRC (2015); arXiv:1509.03732.

[279] http://wiki.auger.org.ar/monitoring-usage/.

[280] http://paomon.physik.uni-wuppertal.de/pro/AERA/Lightning/.

[281] http://rp5.ru/Weather_archive_in_Malargüe/.

[282] http://rp5.ru/Weather_archive/.